PHYSICAL REVIEW

VOLUME 88

THE PHYSICAL REVIEW

A journal of experimental and theoretical physics established by E. L. Nichols in 1893

Published by the American Institute of Physics for the

AMERICAN PHYSICAL SOCIETY

Officers

President

J. H. Van Vleck
Harvard University
Cambridge, Massachusetts

Vice-President

Enrico Fermi
Institute for Nuclear Studies
University of Chicago
Chicago 37, Illinois

Secretary

K. K. Darrow
Bell Telephone Laboratories
Office:
Columbia University
New York 27, New York

Treasurer

G. B. Pegram
Columbia University
New York 27, New York

Local Secretary for the Pacific Coast

J. Kaplan
University of California at Los Angeles
Los Angeles, California

Managing Editor

S. A. Goudsmit
Brookhaven National Laboratory
Upton, Long Island
New York

BOARD OF EDITORS

Editor

S. A. Goudsmit

Assistant Editor

S. Pasternack

Associate Editors

Harvey Brooks	M. Goldhaber	W. F. Allis
R. F. Christy	R. Hofstadter	F. G. Brickwedde
C. L. Critchfield	A. W. Lawson	W. B. Fretter
M. Deutsch	A. Pais	Converse Herring
T. H. Johnson	R. Serber	H. W. Lewrence
Bruno Rossi	C. H. Townes	Arnold Nordsieck

Manuscripts for publication should be submitted to S. A. Goudsmit, Brookhaven National Laboratory, Upton, Long Island, New York. The authors' institutions are requested to pay a publication charge of $15 per page which, if honored, entitles them to 100 free reprints. Instructions will be sent with galley proofs.

Proof and all correspondence concerning papers in the process of publication should be addressed to the Publication Manager, American Institute of Physics, 57 East 55 Street, New York 22, New York.

Subscription Price

United States and Canada $30.00
Elsewhere $32.00

Back Numbers[1]

Yearly back numbers: only when *complete year is available:*
Prior to 1949: $25.00
Thereafter: $33.00
Single copies: $3.00 each, prior to July, 1929;
$1.50 each, July, 1929–December, 1941;
$3.00 each, January, 1942–December, 1946;
$1.50 each, thereafter.
General Index, 1893–1920: $4.00.

Subscriptions, renewals, and orders for back numbers should be addressed to the American Institute of Physics, 57 East 55 Street, New York 22, New York.

Changes of address in the case of members of the American Physical Society should be addressed to the Treasurer; in the case of other subscribers to the American Institute of Physics.

[1] For Series I (Optical Society of America) Physics Department, Cornell University, Ithaca, New York.

The Physical Review is published semi-monthly at Prince and Lemon Streets, Lancaster, Pennsylvania.

Entered as second-class matter March 6, 1917, at the Post Office at Lancaster, Pennsylvania, under the Act of March 3, 1879.

Acceptance for mailing at special rate of postage provided for in paragraph (d-2), section 34.40, P. L. & R. of 1948, authorized January 27, 1950.

THE
PHYSICAL REVIEW

A journal of experimental and theoretical physics established by E. L. Nichols in 1893

SECOND SERIES, VOL. 88, NO. 2 OCTOBER 15, 1952

The Lifetimes of the π^+ and π^- Mesons*

R. P. DURBIN, H. H. LOAR, AND W. W. HAVENS, JR.
Columbia University, New York, New York

(Received June 25, 1952)

The mean lives of the π^+ and π^- mesons are determined by measurements of the attenuation in flight of a 73-Mev meson beam, using a scintillation counter telescope of variable length. The decay scheme, $\pi^{\pm}\rightarrow\mu^{\pm}+\nu$, is assumed to be isotropic in the rest system of the π-meson. The data, when the Lorentz time dilation is taken into account, give for the mean lives at rest

$$\tau_-=(2.55\pm0.19)\times10^{-8}\text{ sec},$$
$$\tau_+=(2.44\pm0.18)\times10^{-8}\text{ sec}.$$

I. INTRODUCTION

EARLY experiments[1,2] which measured the attenuation of a π-meson beam in flight showed an apparent difference between the mean lives τ_+ and τ_- of the π^+ and π^- mesons. Later, more accurate results, using the decay of the π^+ meson at rest in a scintillator, were obtained.[3,4] With the availability of meson beams of either sign at the Nevis cyclotron, it became possible to measure both lifetimes under the same experimental conditions. Observations have been made on these beams with a cloud chamber,[5] and better agreement has been obtained between τ_+ and τ_-. The following measurements were undertaken to compare the lifetimes with minimum change in experimental conditions.

II. GENERAL METHOD

Mesons produced in a beryllium target by the 385-Mev internal proton beam are brought out through various channels in the concrete shielding. These channels accept π^- mesons produced in a forward direction by a proton beam circulating clockwise and π^+ mesons produced in a backward direction by a counter-clockwise proton beam. The meson beams with energy $\sim$73 Mev were chosen for the experiment, since the percentage of electrons is low and the π^+ intensity is comparable to that of the π^- beam. The lifetimes, τ_+ and τ_-, were obtained in the same series of runs without changes except for the reversal of the magnetic fields of the cyclotron and steering magnet.

The focusing action of the cyclotron fringing field allows mesons to emerge from the shielding in nearly parallel paths. This property of the beam makes it possible to count the mesons with a telescope subtending a very small solid angle. The experimental arrangement is shown in Fig. 1. An effective meson beam is defined by threefold coincidence in the counters C_1, C_2, and C_3. It is seen below that about 3 percent of a π-meson beam decays per foot and that for distances of 2 feet or more between C_3 and $C_4(L\geq2')$ practically all of the decay μ-mesons miss the final counter. The fourfold coincidence rate is then a measure of the fraction of π-mesons surviving for the distance L. This fourfold rate must be corrected for π-mesons decaying to give μ-mesons which traverse C_4. Since the charged π-meson is known to have spin zero,[6,7] the decay is isotropic in the π-rest system. In this system the number decaying within the angle Θ between the π-meson and the decay μ-meson is then proportional to the solid angle included. It can be shown that two angles Θ_1 and Θ_2 in the rest system correspond to the angle θ between the π-meson and the decay μ-meson in the laboratory system. The angles Θ_1 and Θ_2 are given by

$$\sin\Theta=[-B\pm(B^2-4AC)^{\frac{1}{2}}]/2A,$$

* Sponsored by the joint program of the ONR and AEC.
[1] J. Richardson, Phys. Rev. **74**, 1720 (1948).
[2] E. A. Martinelli and W. K. H. Panofsky, Phys. Rev. **77**, 465 (1950).
[3] Jakobson, Schulz, and Steinberger, Phys. Rev. **81**, 894 (1951).
[4] C. Wiegand, Phys. Rev. **83**, 1085 (1951).
[5] Lederman, Byfield, and Kessler, Phys. Rev. **85**, 719 (1952).
[6] Durbin, Loar, and Steinberger, Phys. Rev. **83**, 646 (1951).
[7] Clark, Roberts, and Wilson, Phys. Rev. **83**, 649 (1951).

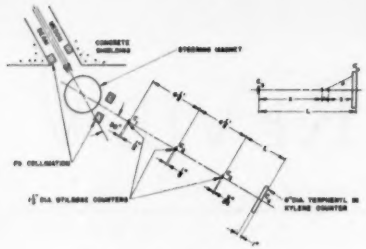

FIG. 1. Experimental layout.

$$A=\frac{M^2}{\tan^2\theta}+E^2, \quad -B=\frac{2MP}{\tan\theta}\left(\frac{1+r^2}{1-r^2}\right),$$

$$C=P^2\left(\frac{1+r^2}{1-r^2}\right)^2-E^2.$$

In the above, P and E are the momentum in Mev/c and total energy in Mev of the π-meson in the laboratory system, and M is its rest mass in Mev/c^2. The quantity $r\equiv M_\mu/M_\pi$ is taken to be 0.759.[8] The probability $P(\theta)$ of decay within the cone of angle θ in the laboratory system is then the sum of probabilities of decay into the solid angles defined by Θ_1, Θ_2, in the rest system. $P(\theta)$ has been calculated for π-meson energies of 70 and 75 Mev, covering the range of energies used in this experiment. The results are shown in Fig. 2. Consider a π-meson traveling along the axis of the counter telescope (the correction for oblique paths is discussed in a later section) which decays at a point s inches from the last counter. The angle C_4 subtends at s is $\tan^{-1}4/s=\theta$. Knowing θ one can find directly from Fig. 2 the probability $P(s)$ that the decay μ will traverse C_4. This efficiency function $P(s)$ is plotted against s in Fig. 3.

The number of fourfold coincidences N', due to the number N_0 of π-mesons traversing the first three counters, is the sum of counts due to those π's which have not decayed and to those which decay to give μ's traversing C_4. Let λ denote the mean free path for

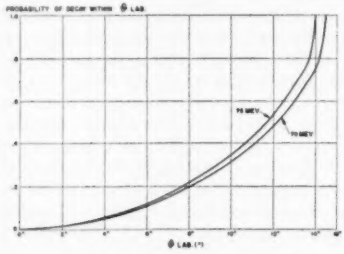

FIG. 2. Probability of a π-meson decaying to give a μ-meson within the angle θ in the laboratory system between the directions of the incoming and outgoing particle.

[8] Barkas, Birnbaum, and Smith, Phys. Rev. **83**, 895 (1951).

decay. The number of π-mesons at the distance x is then $N_\pi=N_0e^{-x/\lambda}$, and the number of decay μ's contributed by Δx to C_{1234} is $\lambda^{-1}N_0e^{-x/\lambda}P(L-x)\Delta x$, where $P(L-x)$ is the geometrical efficiency described above. N' is given by an integration of the above term:

$$N'=N_0e^{-L/\lambda}+\frac{N_0}{\lambda}\int_0^L e^{-s/\lambda}P(L-x)dx \tag{1}$$

$$=N_0e^{-L/\lambda}\left[1+\frac{1}{\lambda}\int_0^L P(s)ds+\frac{1}{\lambda^2}\int_0^L sP(s)ds+\cdots\right], \tag{2}$$

where $s\equiv L-x$ and $e^{s/\lambda}$ is replaced by its series ex-

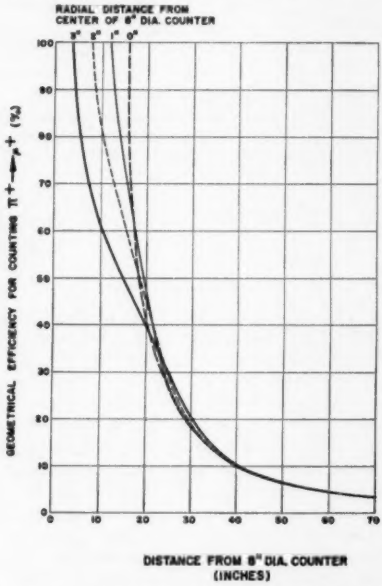

FIG. 3. Geometrical efficiency function $P(s)$ for counting μ-meson given off at s. $P(s)$ is plotted for cases where the projected path of the π-meson strikes C_4 at 0 in., 1 in., 2 in., or 3 in. from the center of C_4.

pansion. The first two terms in the bracket are identical to the first two terms in the series expansion of $\exp 1/\lambda\int_0^L P(s)ds$. Moreover, if the function $P(s)$ of Fig. 3 is approximated by the function $P(s)=1$, $0\leq s\leq s_m$, $P'(s)=0$ for $s>s_m$ (where $s_m\sim 24$ in.), the two expressions (1) and (2) become identical.

Thus, Eq. (2) may be approximated by

$$N'=N_0e^{-L'/\lambda}, \text{ where } L'\equiv L-\int_0^L P(s)ds. \tag{3}$$

This approximation was checked by inserting the correct form of $P(s)$ from Fig. 3 into the exact Eq. (1) and

the approximate expression (3) and performing the integration numerically. The values of N' thus obtained differed by less than 0.1 percent and the more convenient form (3) is hence used throughout the following.

III. EXPERIMENTAL DETAILS AND CALCULATIONS

A. Counters

The dimensions of the counters are shown in Figs. 1 and 4. Two details of importance in the experiment are the thinness of C_3 and the relatively large area of C_4. The third counter is mounted in $\frac{1}{4}$-in. Lucite which tapers down to $\frac{1}{16}$ in. to match the scintillator and to eliminate excessive multiple scattering at its circumference. The response of C_4 to minimum ionizing particles is of the same order of magnitude as that of the small stilbene crystals. The total variation of pulse-height output across the face is about 20 percent, as tested with a beta-source.

The factors which determine the maximum useful distance L are (a) the multiple Coulomb scattering in the third counter (rms value, 0.5°); (b) the angle defined by the monitor telescope (0.6°); (c) the diameter of the final counter (8 in.). If we assume the angular dispersion of the beam entering C_3 is Gaussian, with a mean deviation of

$$\sigma_{\text{geom}}=0.6°,$$

the resultant beam, out of C_3, will have a spread

$$\sigma_{\text{tot}}\leq(\sigma_{ms}^2+\sigma_{\text{geom}}^2)^{\frac{1}{2}}\leq 0.78°.$$

For an 8-in. diameter final counter and maximum separation of 96 in., the angle subtended at C_3 by C_4 is 2.4°; the probability for a particle in the beam which does not decay to exceed this angle is $\leq$0.2 percent.

To locate the center of the beam at large values of L, the 8-in. counter at C_4 is replaced by a scintillation counter with horizontal and vertical dimensions 1 in. and 3 in., respectively. The fourfold count rate C_{1234} is then measured as a function of the horizontal position of the counter. A plot of these data shows a roughly triangular shape; the center of the 8-in. counter is then set at the apex position. At each large value of L several separate runs were taken, and the positions of maximum fourfold counting rate always agreed to $\pm\frac{1}{4}$ in. The final counter is centered vertically by setting all counters at the same height. The distance L is arbitrarily limited to 96 in., since the scanning run shows that some π-mesons begin to appear as far as 3 in. from the center of C_4 at that position.

B. Electronics

A block diagram of the electronics is shown in Fig. 5. The outputs of the RCA type 1P21 photomultipliers were fed directly to bridge coincidence circuits which were located in the cyclotron building near the counters. Since no single counter was fed to all bridges of the monitor, large pulses arising from a single event could not appear in C_{123}. The short resolution time ($\sim 10^{-8}$ sec) of the bridges served to decrease the accidental counting rates. These were evaluated by inserting a long cable into the appropriate bridge so as to eliminate true coincidences. The chief accidental rate was found to be true C_{123} with C_4, varying from 1.9 percent of C_{123} at $L=3\frac{1}{2}$ in. to 1.2 percent at $L=96$ in. There is also an effect due to the decay of the true C_{12} beam to give μ's traversing C_3 and C_4 which cannot be measured with the long cable technique. Calculations show the effect to be 1.0 percent of C_{123}. This, with several of the accidental rates, can be minimized by moving C_2 as far from C_1 as possible. But C_2 cannot be close to C_3 or the effective material for multiple scattering increases; hence, a symmetric position was chosen.

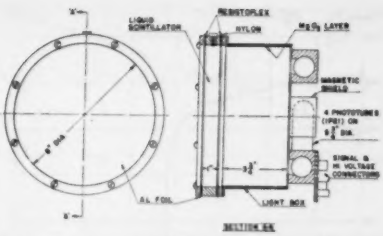

FIG. 4. Construction of 8-in. diameter liquid scintillation counter.

Before each run, plateaus of counter voltage *vs* coincidence counting rate were taken, using cosmic rays. These plateaus checked well with those taken in the meson beam and furnished a convenient starting point for the latter. The plateau on counter C_4 was taken with special care, to insure that its efficiency for counting mesons did not vary across the face. In addition, a timing curve of C_{1234}*vs* cable length was taken at $L=96$ in. to make sure that the cable from C_4 to the bridge 3–4 was not critical (within several feet) at the final voltage and discriminator settings.

C. Range Curves and Beam Impurities

Range curves were taken for both the π^+ and π^- meson beams, using poor geometry. The results for the π^+ beam are shown in Fig. 6. The back of the carbon absorbers was 1 in. in front of C_4, and C_4 was 14 in.

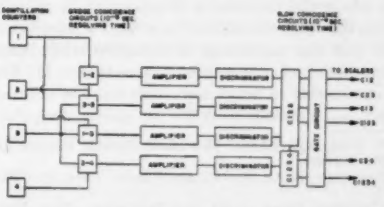

FIG. 5. Block diagram of electronics.

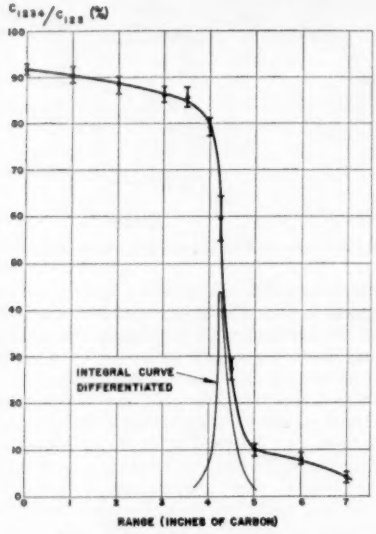

FIG. 6. Range curve in the π^+ beam.

behind C_3. The density of the carbon used was 4.25 g/cm² per inch.

The standard deviations for the Gaussians which gave the best fit to the differentiated range curves were

$$\pi^+,\ \sigma_{\text{exp}}=0.42\ \text{g/cm}^2,$$
$$\pi^-,\ \sigma_{\text{exp}}=0.46\ \text{g/cm}^2.$$

We expect from straggling alone, according to the formula of Bohr,[9]

$$\sigma_{\text{th}}^2=4\pi NZe^4\int_0^{E_0}(dE/dx)^{-3}dE,$$

where dE/dx may be conveniently found from the empirical expression for the range of π-mesons in carbon, $R=0.011E^{1.78}$, where R is in g/cm² and E in Mev. This yields $\sigma_{\text{th}}=0.39$ g/cm² and accounts for σ_{exp} within the accuracy of the experiment. The beam is then assumed to be monoenergetic with an energy corresponding to the mean range. The energy is $W_\pi=73.4\pm2.0$ Mev where the precision is estimated from the difference in the mean energies of the π^+ and π^- range curves.

To find the percentage of π-mesons which survive for the distance L, the accidental counts (Sec. III B) and the counts due to beam impurities must be subtracted from C_{1234}. Previous work[10,11] has shown the principal beam impurities to be electrons and μ-mesons in the negative beam, and μ-mesons in the positive. The particles which originate at or near the target traverse the same momentum channel as the π-mesons and thus have longer ranges due to their lighter mass. On the other hand, μ-mesons which are the result of π-meson decay in the beam after the steering magnet have ranges distributed about the mean π-meson range. However, experiment[11] and an approximate calculation (Sec. III D) show that the number of μ-mesons with shorter range is considerably smaller than the number of those with longer range. Thus the percentage of impurities should be well represented by the tail of the integral curves, i.e., the portion beyond the π-meson range.

The range curve taken in the π^- beam is similar to that shown in Fig. 6. In this case the range curve includes fourfold coincidences due to neutrons[12] and fast protons[13,14] from the stars formed by stopped π^- mesons. These events account for about 2.5 percent of the C_{123} beam.

The estimated impurities are then

$$\pi^+ \text{ beam } (7\pm3) \text{ percent},$$
$$\pi^- \text{ beam } (10\pm4) \text{ percent}.$$

There is a small probability for the electrons in the beam to suffer large radiation losses and stop before the tail of the range curve. The approximate theory of Bethe and Heitler[15] was used to estimate this effect. It was found that the error made in neglecting stopped electrons was small compared with the quoted uncertainties in beam impurities.

TABLE I. Sources of experimental error in τ_+.

Source	Value (units of 10^{-8} sec)
1. Counting statistics	0.09
2. Uncertainty in beam impurities	0.10
3. Uncertainty in energy of beam	0.05
4. Uncertainty in measurement of accidentals	0.07
5. Uncertainty in calculation of L'	0.07

TABLE II. Recent measurements of the mean life of the π-meson.

Martinelli and Panofsky[a]	$\pi^+\left(1.97^{+0.21}_{-0.25}\right)\times10^{-8}$ sec
Jakobson, Schulz, and Steinberger[b]	$\pi^+(2.54\pm0.11)\times10^{-8}$ sec
Wiegand[c]	$\pi^+(2.58\pm0.14)\times10^{-8}$ sec
Lederman, Byfield, and Kessler[d]	$\pi^-(2.79\pm0.25)\times10^{-8}$ sec

[a] See reference 2.
[b] See reference 3.
[c] See reference 4.
[d] Lederman, Byfield, and Kessler (private communication).

[9] N. Bohr, Kgl. Danske Videnskab. Selskab, Mat-fys. Medd. **18**, No. 8 (1948).
[10] Lederman, Booth, Byfield, and Kessler, Phys. Rev. **83**, 685 (1951).
[11] Chedester, Isaacs, Sachs, and Steinberger, Phys. Rev. **82**, 958 (1951).
[12] Menon, Muirhead, and Rochat, Phil. Mag. **41**, 583 (1950).
[13] F. L. Adelman, Phys. Rev. **81**, 650 (1950).
[14] W. Cheston and L. Goldfarb, Phys. Rev. **78**, 683 (1950).
[15] H. Bethe and W. Heitler, Proc. Roy. Soc. (London) **146**, 83 (1934).

D. The Effective Decay Distance

A particle traveling at an angle with the axis of the telescope will have a probability to decay into the final counter somewhat different from that given in Sec. II. Three cases are considered, in which the beam particle (assuming no decay) strikes 1, 2, or 3 inches from the center of C_4. In each case, the counter is divided into zones centered about the point of incidence. The differential probability, at a distance s from C_4, for decay within each zone is found from Fig. 2 (modified to correspond to the actual beam energy). This probability is multiplied by the fraction of the zone subtended by C_4. The sum of the results for all zones then gives the total probability for decay into C_4 at s. This is repeated for a number of positions along the path of the particle, and the resulting curves are plotted (Fig. 3). For each L, we thus get L' (1 in.), L' (2 in.), and L' (3 in.). A mean L' is obtained by weighting these according to the spread in the beam as found by scanning.

A meson approaching C_3 has a small chance to decay and still be counted in C_3 and C_4. This effect may be estimated by scaling down the efficiency curve (e.g., the 3-in. curve of Fig. 3), since the problem is analogous to that discussed in the preceding paragraph. The μ-meson, having passed through C_3, has an average angle of nearly 14° and will miss C_4, unless the latter is closer than 16 in. For L greater than this, the correction amounts to $2\frac{1}{2}$ in. and must be added to the corresponding L'.

IV. RESULTS

Figure 7 is a semilog plot of the number of π-mesons counted per given monitor count as a function of the effective distance L' between the third and fourth counters. The ordinate is

$$y=\log R=\log[(C'-a-b)/C],$$

where C' = measured fourfold coincidences, C = threefold monitor coincidences (the graph is plotted for $C=100$), and a and b are the coincidences due to accidentals and beam impurities, respectively. The errors plotted were obtained from the statistical standard deviation of C' and the estimated precision of the measurements of a and b. A total of about 39,000 π^+ mesons and 54,000 π^- mesons were monitored in obtaining the points of Fig. 7. This corresponds to an observation of about 5000 π^+ meson decays and 6500 π^- meson decays.

The points were then fitted to straight lines using the method of least squares. Each point was weighted according to the inverse square of the corresponding standard deviation. The mean free path thus obtained is divided by the mean velocity of the π-mesons and the result corrected for the Lorentz time dilation to get the mean life in the π-rest system:

$$\tau=(\lambda/\beta c)(1-\beta^2)^{\frac{1}{2}}.$$

The resulting values for the mean life are

$$\tau_-=(2.55\pm0.19)\times10^{-8}\text{ sec},$$
$$\tau_+=(2.44\pm0.18)\times10^{-8}\text{ sec}.$$

The error in τ is calculated by considering the propagation of the statistical errors of the points and the estimated uncertainties, as listed in Tables I and II. The errors shown are for τ_+; the case of τ_- is similar.

The values of τ_+ and τ_- obtained above may be compared with other recent measurements. The last named group also finds a ratio of $\tau_-/\tau_+=1.01\pm0.11$. The results obtained in the present experiment agree quite well with the last three quoted values.

The authors wish to thank Professor J. Steinberger and Professor L. Lederman for their kind advice in the performance of the experiment and Professor L. J. Rainwater and Dr. D. C. Peaslee for help with the analysis of the experimental errors.

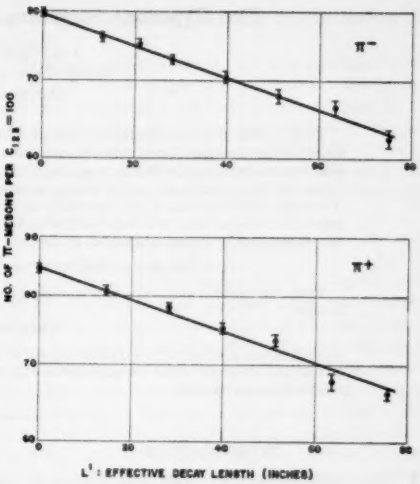

FIG. 7. Lifetime curves.

The Hyperfine Structure of Hydrogen and Deuterium*

A. G. PRODELL AND P. KUSCH
Columbia University, New York, New York

(Received June 18, 1952)

The hyperfine structure separations, ν_H and ν_D, of the ground states of hydrogen and deuterium have been measured by the atomic beam magnetic resonance method. In both cases the determination depends essentially on a measurement with high precision of the frequency of a very nearly field independent line at weak fields and the measurement with reduced precision of the frequencies of one or more field dependent lines. The design of the apparatus and the conditions under which the experiment was performed were such as to permit the accumulation of a large body of significant data and the determination of precise values for the hfs separations by statistical analysis of the data. We find

$$\nu_H=(1420.4051\pm0.0002)\times10^6\ \text{sec}^{-1},\quad \nu_D=(327.38424\pm0.00008)\times10^6\ \text{sec}^{-1}.$$

From these results and the very accurately known ratio of the proton and deuteron magnetic moments, we find

$$\Delta=(1.703\pm0.008)\times10^{-4},$$

where $(\nu_H/\nu_D)_{exp}=(\nu_H/\nu_D)[1-\Delta]$ and (ν_H/ν_D) is calculated from the ratio of the magnetic moments of the proton and deuteron under the assumption that these particles are point dipoles which interact with the electronic magnetic field.

INTRODUCTION

THE measurements by Nafe and Nelson of the hyperfine structure separations of hydrogen and deuterium[1] gave the first definite evidence of the existence of the hyperfine structure anomaly and furnished some of the essential data from which was inferred the existence of the anomalous spin magnetic moment of the electron.[2] In view of the increasing refinement of the theory of the hfs anomaly,[3] a redetermination of the hfs separations of H and D to a precision comparable to that achieved in recent measurements[4] of the ratio of the nuclear magnetic moments of H and D is of interest. The two sets of data, taken together, determine the hfs anomaly and may serve as a critical test of the theory of the interaction of the nucleons within the deuteron and of the electron with the deuteron.

In the following paper an experiment to determine the ratio $g_J(^2S_{\frac{1}{2}}, H)/g_I(H)$ is described. While this quantity is of direct interest in the analysis of the atomic and nuclear interactions which relate the hfs of hydrogen to the magnetic moment of hydrogen, it is also of importance, when combined with the recent measurement by Gardner and Purcell of the ratio $g_l/g_I(H)$,[5] in a determination of the spin gyromagnetic ratio of the electron. The determination of the ratio $g_J(^2S_{\frac{1}{2}}, H)/g_I(H)$ from experimental data requires a prior knowledge of the hfs separation of hydrogen.

It is the purpose of this paper to describe an experiment to determine the hfs of hydrogen and deuterium. A detailed presentation of the methods employed in the experiment, of the data, and of its analysis will be given.

* This research was supported in part by the ONR.
[1] J. E. Nafe and E. B. Nelson, Phys. Rev. **73**, 718 (1948).
[2] G. Breit, Phys. Rev. **72**, 984 (1947).
[3] N. M. Kroll and F. Pollock, Phys. Rev. **84**, 594 (1951); Karplus, Klein, and Schwinger, Phys. Rev. **84**, 597 (1951).
[4] Smaller, Yasaitis, and Anderson, Phys. Rev. **81**, 896 (1951).
[5] J. H. Gardner and E. M. Purcell, Phys. Rev. **76**, 1262 (1949).

METHOD

The general theory of the Zeeman effect of the hyperfine structure is implicit in the Breit-Rabi formula and has been discussed by Nafe and Nelson.[1] The magnetic levels of hydrogen in the $^2S_{\frac{1}{2}}$ state are specified by the quantum numbers (F, m_F) at weak fields. The atom may undergo a transition from one to another of the magnetic levels according to the selection rules, $\Delta F=0$, ±1 and $\Delta m=0, \pm1$, if an oscillating magnetic field of appropriate frequency, amplitude, and polarization is present.

In the experiments performed with hydrogen, measurements were made of the frequency of the σ-line, $(1, 0\leftrightarrow0, 0)$, and with reduced precision, of the frequencies of the π-lines, $(1, 1\leftrightarrow0, 0)$ and $(1, -1\leftrightarrow1, 0)$. The frequency of the σ-line at low fields is almost wholly field independent and gives the hyperfine structure separation ν_H after the application of a small quadratic correction obtained from the frequencies of either of the two π-lines and that of the σ-line. The largest quadratic correction in any of the present measurements was 2.2 kc. Hence, no great accuracy in the measurement of the π-lines $(1, 1\leftrightarrow0, 0)$ and $(1, 0\leftrightarrow1, -1)$ is required to determine the quadratic correction to 0.1 kc, about 1 part in 1.4×10^7 in ν_H. The hyperfine structure separation of hydrogen is also identically equal to the frequency difference, $f(1, 1\leftrightarrow0, 0)-f(1, 0\leftrightarrow1, -1)$. However, since the frequencies of both lines vary at the rate of 1400 kc per gauss, it is evident that extremely small inhomogeneities in the field may severely prejudice the accuracy of ν_H obtained from this frequency difference.

For deuterium, the frequency of the unresolved doublet, $(\frac{3}{2}, \frac{1}{2}\leftrightarrow\frac{1}{2}, -\frac{1}{2})(\frac{3}{2}, -\frac{1}{2}\leftrightarrow\frac{1}{2}, \frac{1}{2})$, and, with a reduced precision, the frequencies of the lines $(\frac{3}{2}, \frac{3}{2}\leftrightarrow\frac{1}{2}, \frac{1}{2})$ and $(\frac{3}{2}, -\frac{1}{2}\leftrightarrow\frac{1}{2}, -\frac{1}{2})$ were measured. As in the case of hydrogen, the last two lines were used to determine the

value of the magnetic field from which the quadratic correction to the almost wholly field independent doublet may be found. The lines of the doublet itself have a frequency separation of $2g_D\mu_0H/h$, or about 1.3 kc per gauss. The field in which all transitions for deuterium were observed was about 0.32 gauss so that the doublet separation was 0.42 kc. Since the probability of transition for each component of the doublet is the same, the center of gravity of the observed line, of 22.5 kc half-width, may be used to fix ν_D without ambiguity after the application of a small quadratic correction.

Because of the rather considerable, inherent width of the resonance lines, it is not possible, from a single observation, to determine the frequency of the line center to the precision which is ultimately ascribed to the quantities ν_H and ν_D. It is, therefore, necessary to resort to a statistical analysis of a large body of data to obtain these quantities to a high degree of precision.

APPARATUS

The source of the atomic hydrogen and deuterium in these atomic beam experiments was a water-cooled Wood's discharge tube of a design which has previously been described.[6] Moist hydrogen or deuterium was admitted to the ends of the discharge tube through two mechanically controlled needle valves from a manifold in which the pressure was approximately atmospheric. The source slit was formed by waxing microscope cover glasses over the opening through the water jacket to the discharge tube.

The beam of atomic hydrogen was detected in a Pirani gauge which was modified from a design proposed by Zacharias.[7] Two glass plates, about 3 mm thick and flat to within 2λ of yellow light, were each grooved with two parallel slots 3.8 cm long, 2 mm wide, and 0.25 mm deep. The two glass plates were separated by pieces of smooth gold foil, 0.0025 cm thick, arranged as shown in Fig. 1. The gold foil served to isolate the cavities, which were formed by opposing pairs of grooves in the plates, from each other and from the external vacuum. Each cavity contained two opposite arms of a Wheatstone bridge, and the connections to the four arms of the bridge were made through the channels A. The connecting ribbons very nearly filled up these channels, but to minimize leakage from the cavities, the external ends of the channels were sealed with Apiezon W40. The channel B served as an entrance slit for the beam, while the channel C connected the cavity N to the vacuum. In principle, the cavities are identical as are the two slits, so that fluctuations in the vacuum surrounding the gauge have, in principle, no effect on the balance of the bridge. The ideal state of affairs is, of course, prejudiced by the difficulty of assembling two identical units. In practice, the gauge was remarkably free of unsteadiness arising from fluctuations in the vacuum.

The atoms of the beam, as they pass through channel B into the Pirani gauge cavity, have a velocity in a preferred direction. Inside the cavity, however, the atoms recombine into molecules and have random velocities. Hence, the resistance offered[8] to a flow of molecules back out through the channel is greater than the resistance offered to the atoms entering the channel by a factor K, where

$$K=lb^{-1}[0.5+\ln(2a/b)]^{-1}, \tag{1}$$

and l is the length, a the height, and b the width of the channel. The equilibrium pressure inside the cavity is increased by the factor K as compared to the pressure when the cavity is closed except for a thin slit of the same cross-sectional dimensions as those of the channel. The higher pressure in the cavity serves to give a more radical cooling of the two arms of the bridge in the cavity. For the Pirani gauge used in these experiments, $K\cong200$. The actual K factor is probably somewhat less than that calculated because of imperfect sealing of the cavities.

The whole assembly was tightly clamped in a massive brass frame. Spring pressure was applied over the surfaces of the glass plates by nine phosphor-bronze Belleville springs bearing on each of the two outside faces of the glass plates. The arms of the Wheatstone bridge were made of platinum ribbon 0.038 cm wide and 1.3×10^{-4} cm thick. A Leeds and Northrup H.S. galvanometer with a nominal sensitivity of 0.0167 microvolts/mm at three meters from the galvanometer was used to detect the off-balance voltage of the Pirani gauge. A total current of 30 ma in the gauge gave a satisfactory sensitivity and stability. With this current and a rate of leakage of gas into the discharge tube of approximately 1 cc per minute at NTP, the off-balance voltage of the gauge due to the beam was about 14 microvolts and resulted in approximately 70 cm of deflection on the galvanometer scale.

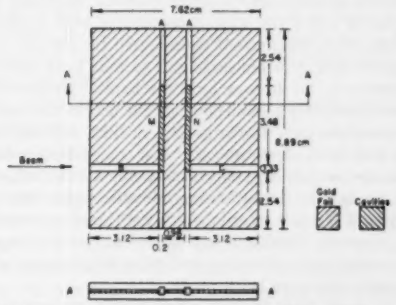

FIG. 1. Schematic diagram of the glass plates of the Pirani gauge showing the arrangement of the gold foil.

[6] Kellogg, Rabi, and Zacharias, Phys. Rev. **50**, 472 (1936).

[7] J. R. Zacharias (private communication); R. Julian, unpublished thesis, Massachusetts Institute of Technology (1947).

[8] I. Estermann, Revs. Modern Phys. **18**, 300 (1946).

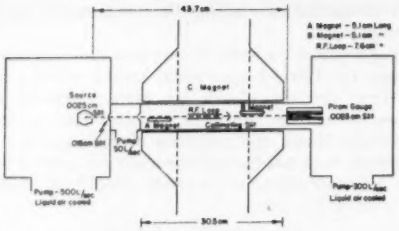

FIG. 2. Schematic diagram of the atomic beam apparatus.

Since the determination of accurate values for ν_H and ν_D depended, in the present work, on the accumulation of a large body of data, it was essential that the gauge have a small time constant. The over-all time constant of the detector system was limited by the period of the galvanometer in the Wheatstone bridge circuit. When the atomic beam was turned on, the galvanometer showed maximum deflection within 7 or 8 seconds. A qualitative opinion is that the Pirani gauge detects a hydrogen beam "like potassium" where the detection of potassium on a hot wire detector is the classic example of efficient, fast, and reproducible detection. Unfortunately, there were intermittent and sometimes long intervals of time during which the gauge was noisy, presumably because of poor alignment of the platinum ribbons in the cavities which caused intermittent contact between the ribbons and the walls of the cavities. In general, the data of June, 1950, were taken with the gauge under remarkably steady conditions, while the data of December, 1950, were taken with a somewhat microphonic gauge.

The apparatus was designed, essentially, for the determination of the ratio $g_J(^2S_{\frac{1}{2}}, \mathrm{H})/g_I(\mathrm{H})$. Although all features of the design are not relevant to the present experiment, a detailed discussion of the design of the apparatus will be given at this point. For the purpose of the subsequent experiment, it was necessary to produce an extremely uniform magnetic field over the region in which the various transitions were to be observed. This requirement necessitated the use of a "*C*" magnet with a rather large gap so that local inhomogeneities in the iron or local mechanical irregularities would have only a small effect on the field in the median plane of the gap. The large gap, in turn, required that the pole faces of the magnet be of comparatively large diameter so that edge effects have only a small influence on the field in the rather considerable region near the center of the pole faces in which the transitions were to be observed. Finally, it was desirable that the magnet be available for shimming and other adjustments while observations were being made.

To meet these various requirements, an apparatus, unique in atomic beam experiments, was designed so that the magnet was external to the vacuum chamber. The minimum gap width, dictated by the construction of the vacuum chamber, was 4.4 cm, and the magnet itself had pole faces 30.5 cm in diameter. In the usual molecular beam apparatus, the "*C*" magnet is internal to the apparatus and has, most frequently, a gap of 0.64 cm. The magnet was supported on a large, heavy frame, and could be rolled on this frame underneath the vacuum chamber, and raised into position by means of four corner jacks.

Because the "*C*" magnet of this apparatus is external to the vacuum chamber, the design of the vacuum chamber is somewhat different from that of the conventional atomic or molecular beam apparatus. The end sections of the vacuum envelope, which are made of 25-cm brass tubing, are connected by a flat vertical section 41 cm long, 4.4 cm wide, and 23 cm high. This central section contains the small separating chamber, the deflecting magnets, usually termed the "*A*" and "*B*" magnets, the rf loop, the collimating slit, and the Pirani gauge detector. A schematic diagram of the apparatus is shown in Fig. 2.

It is always desirable to make a beam as short as possible consistent with the various requirements imposed by the experiment. This is particularly important in the case of a beam of noncondensable matter, such as H, where scattering becomes important and where detection is, at best, inefficient. To keep the beam as short as possible in the present apparatus, the "*A*" and "*B*" deflecting fields were located within the gap of the "*C*" magnet. This arrangement has the additional merit that it increases the deflecting power of the "*A*" and "*B*" fields as used in this apparatus. To avoid the effect of iron block magnets on the homogeneity of the "*C*" field, the deflecting magnets were of the traditional two-wire type fabricated from copper tubing.

It is clear that, consistent with the use of short deflecting magnets, only those transitions can be observed whose high field equivalents are $\Delta m_J=\pm 1$, $\Delta m_I=0$. Those transitions whose high field equivalents are $\Delta m_J=0$, $\Delta m_I=\pm 1$ result in a significant moment change only at very weak fields where the deflecting power of the "*A*" and "*B*" fields is small. The maximum

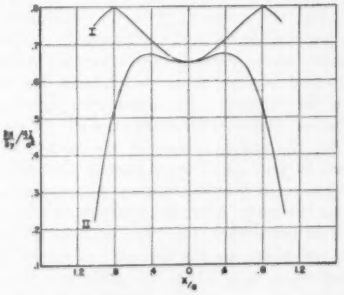

FIG. 3. Plot of the gradient of the magnetic field in terms of the current and the dimensions in the region of the beam. Curve I: $y/a=0.9$, $H_c=0$; Curve II: $y/a=0.9$, $H_c=6(2I/a)$.

field which may be obtained with a two-wire system is rather severely limited. To operate at even a moderate ratio of gradient to field $(\partial H/\partial y)/H$ requires the use of small, closely-spaced conductors, and to develop high fields requires very high current densities. A rather considerable cooling problem thus ensues. In the present case, the maximum field H_{AB}, which can be produced by the deflecting magnets alone, still leaves the hydrogen atom in a relatively weak field region. However, the superposition of a strong dc field, H_C, leaves the atom in a relatively high field region. A transition in the region between the two deflecting fields will therefore correspond to a ΔF transition in H_{AB} and to a Δm_J transition in $H_{AB}+H_C$. The effective deflection of the beam for a fixed gradient is therefore increased by the addition of H_C.

In the case of wires which operate in otherwise field free space, it has been common practice to operate the beam at a distance, $y=1.2a$, from the plane determined by the centers of the wires where $2a$ is the distance between centers. This procedure is followed in order to give a substantial uniformity of both gradient and field along a distance from $x=+0.7a$ to $x=-0.7a$. However, when a fixed field H_C is superimposed on the wires in a direction perpendicular to the plane of the wires, the properties of the field are modified as shown in Figs. 3–5. In Curves I, III, and V, the gradient in terms of the current in the wires and the dimensions is shown for three values of the parameter y/a. When an additional magnetic field is applied to correspond roughly to the conditions anticipated in the experiment on the determination of $g_J(^2S_{\frac{1}{2}}, \mathrm{H})/g_I(\mathrm{H})$, the gradients for the same values of y/a are shown in Curves II, IV, and VI. The case for $y/a=1.2$, with a fixed field H_C superimposed, is evidently poor, since the gradient varies rapidly over a rather small range. For the value $y/a=1$, with the superimposed fixed field, the gradient is substantially uniform from $x/a=+0.4$ to $x/a=-0.4$. When $y/a=0.9$, the gradient of the field is reasonably constant from $x/a=+0.6$ to $x/a=-0.6$. An additional advantage is derived from the small value of y/a in that the magnitude of the gradient is greater than for

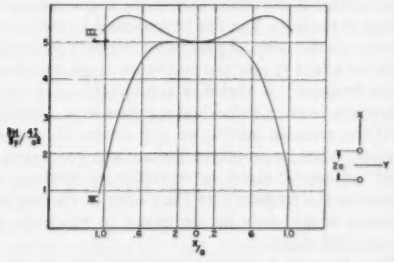

FIG. 4. Plot of the gradient of the magnetic field in terms of the current and the dimensions in the region of the beam. Curve III: $y/a=1$, $H_c=0$; Curve IV: $y/a=1$, $H_c=6(2I/a)$.

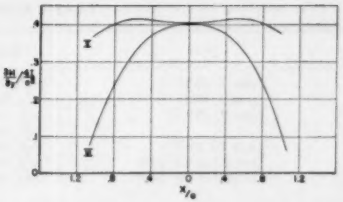

FIG. 5. Plot of the gradient of the magnetic field in terms of the current and the dimensions in the region of the beam. Curve V: $y/a=1.2$, $H_c=0$; Curve VI: $y/a=1.2$, $H_c=6(2I/a)$.

either of the previous cases, and hence there is an increase in the deflecting power. The deflecting fields and other components of the apparatus were, therefore, so adjusted that the beam traversed the apparatus at $y=0.9a$. In the present apparatus, $2a=0.5$ cm. The useful beam height was, therefore, about 3 mm.

The adjustment of beam distance at $y=0.9a$ from the deflecting magnets was made for the purposes of the experiments discussed in the following paper. However, for the present experiments, where the only external field was the residual laboratory field, the chosen value of y is a poor one since the gradient in this case is a marked function of x. Because of the variations in the gradient over the height of the beam, the deflection of the beam, when a transition occurs between the "A" and "B" fields, is not uniform over the beam. Hence, there is a slightly greater sensitivity in the observation of transitions for atoms which traverse the apparatus near $x=\pm 0.6a$ than there is for those atoms that traverse the apparatus near $x=0$. However, since the frequencies of the lines observed in the present experiments are almost wholly field independent and since, in any case, the residual laboratory field will not vary significantly over a distance of 3 mm, the variable gradient will not distort the lines. The fact that the field in the deflecting magnets is low reduces the net deflection at the detector when a transition occurs. The sensitivity of the apparatus is, therefore, less in this experiment than for the one described in the following paper, but is, nevertheless, sufficiently great to permit observation of the appropriate lines.

An oscillating magnetic field in the region of the homogeneous magnetic field is required to induce the atomic transitions. This was produced by rf currents in a loop made of vertical plates of copper, shorted below the line of the beam and tapered from a coaxial line to a length, along the beam, of 7.6 cm. The gap between the plates of the loop was 0.32 cm, and the beam passed between the plates in the median plane. Since the direction of propagation of the electromagnetic wave is perpendicular to the direction of propagation of the beam, the Doppler effect is eliminated and no shift or broadening of the lines occurs because of this effect. The oscillator was connected to the loop through

TABLE I. Results of the measurement of ν_H.

Run	Date	Observed line	No. of observations	$\nu_H \times 10^{-6}$ sec^{-1}	Prob. error
1	June 7, 1950	$\sigma(1, 0 \leftrightarrow 0, 0)$	31	1420.4056	±0.0006
2	June 9, 1950	$\sigma(1, 0 \leftrightarrow 0, 0)$	64	1420.4053	±0.0004
3	June 9, 1950	$\pi(1, 1 \leftrightarrow 0, 0)$	28	1420.4051	±0.0016
		$\pi(1, 0 \leftrightarrow 1, -1)$	25		
4	June 10, 1950	$\sigma(1, 0 \leftrightarrow 0, 0)$	64	1420.4048	±0.0004
5	December 14, 1950	$\sigma(1, 0 \leftrightarrow 0, 0)$	144	1420.4049	±0.0003
6	December 26, 1950	$\sigma(1, 0 \leftrightarrow 0, 0)$	100	1420.4052	±0.0002
			Weighted mean	1420.4051	±0.0002

a transmission line which included attenuation for adjusting the amplitude of the rf current.

The radiofrequency current at 1420 Mc was supplied by a grounded-grid coaxial line oscillator, the transmitter section of Radar Jammer T-85/APT-5, using a 3C22 lighthouse tube. At 327 Mc, current was supplied by a GR Type 757 oscillator. In both cases the frequency could be varied continuously over a small range by moving a plunger, driven by a micrometer screw, in the grid-plate line. A highly stabilized power supply was used with both oscillators and the output was substantially free of modulation. The oscillators were stable over the time interval required to observe the maximum of the line and to measure the frequency at the line center. The low frequency currents were supplied by the GR Signal Generator, 805 C.

FREQUENCY MEASUREMENT AND OBSERVATIONAL PROCEDURE

All frequency measurements were made by beating the frequency of the exciting oscillator with a crystal-controlled frequency adjusted, by comparison with WWV, to an accuracy where residual deviations had no effect on the result. In the case of hydrogen, the standard frequency for most of the runs was 1440 Mc, so that the beat frequency was about 19.6 Mc. The beat frequency was measured in the runs of June, 1950, with a General Radio 620-A heterodyne frequency meter, and in the first run of December, 1950, with a different meter of the same type. Although the least count on this instrument is 1 kc, significant data can be taken to within 0.1 kc with suitable repetition of measurements. The scale on the frequency meters was frequently calibrated against an internal crystal during the course of a run. The correction to be applied to readings on the wave meter varied slowly and smoothly with time. In the course of a single run, the observed variation was as much as 6 kc. The net effect of the variation is to eliminate repetitive readings on the part of the observer and thus to make the readings more truly random. The crystal internal to the frequency meter was calibrated against WWV. Within the precision of the present measurements, the frequency of this crystal was constant.

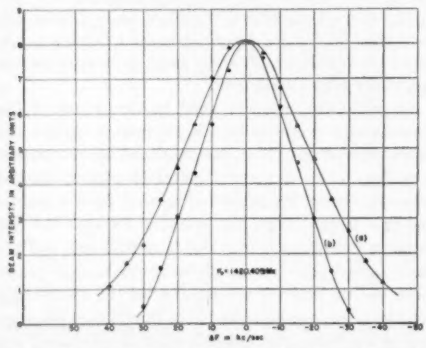

FIG. 6. Plot of the shape of the σ-line of hydrogen. Curve (a): line observed in June, 1950; Curve (b): line observed in December, 1950.

In the second run of December, 1950, the sum frequency of a 1420-Mc signal from the standard and a signal from the GR signal generator, 805-C, was beat against the unknown frequency. The signal generator frequency, about 400 kc, was measured with a BC-221 frequency meter. No special procedures were required to measure this frequency to 0.1 kc.

The frequency measurements to determine ν_D were made by beating the frequency of the exciting oscillator with a standard frequency of 320 Mc. The second harmonic of the beat frequency (7.38 Mc) was measured with a 620A frequency meter as in the case of hydrogen. The excellent agreement among the several independent runs on the determination of ν_H and ν_D indicates the validity of the procedures of frequency measurement.

The principal data of the experiment consisted of a large number of measurements of the frequencies of the centers of the lines. The line centers were located by the observer as the point of maximum intensity in the line. Since the intensity near the maximum varies only slowly as the frequency is varied, a considerable uncertainty is inherent in each individual measurement. However, since the error in setting on the center of a line is random, when appropriate precautions are taken to avoid systematic errors, a repetition of readings will determine the frequency of the center of the line to a precision limited only by the extent to which the line has an ideal shape.

Two observers took turns in adjusting the frequency of the oscillator and in making the frequency measurements. The oscillator, as its frequency was varied, was

tracked with the frequency measuring equipment, and the observer had no prior knowledge of the frequency at which he was setting the oscillator. An effort was made to approach the line center as frequently from high as from low frequencies. In practice, the direction of approach was random, since a disturbance in the beam or an overshoot in the oscillator frequency would prevent the observer from taking a reading at every attempt. In each run, the results obtained by each of the two observers agreed to within the statistical probable errors of the results.

The experiments were carried out in the residual laboratory field. In the runs of June, 1950, the field was about 0.32 gauss, while in those of December, 1950, it was about 0.88 gauss. In all cases the field was so oriented that the rf circuit as used could easily excite both σ- and π-lines.

RESULTS

A tabulation of the results obtained for the hfs of hydrogen in the several runs is given in Table I. In the first two columns are given the number of the run and a date for purposes of identification. In the third column is given the line or lines measured to obtain ν_H. It is to be noted that, with the exception of run 3, the σ-line $(1, 0 \leftrightarrow 0, 0)$ was measured as the primary line. In the fourth column is listed the number of observations made, in each run, on the frequency of the line from which ν_H is primarily determined. The length of all runs was predetermined. In run 3, the frequency of the line $(1, 0 \leftrightarrow 1, -1)$ is subtracted from that of the line $(1, 1 \leftrightarrow 0, 0)$ and has a greater effect on the result than in all other cases. The number of observations for each of the two lines in run 3 is therefore given. In the fifth column is listed the value of ν_H derived from the data of each run, and in the sixth column, the statistical probable error of the result. The value of the hfs of hydrogen obtained from these experiments is, then,

$$\nu_H = (1420.4051 \pm 0.0002) \times 10^6 \text{ sec}^{-1}. \quad (2)$$

It would be extremely difficult to obtain data on the shape of the resonance line of a sufficiently high accuracy to justify belief in the probable error of the result as quoted. In the runs of June, 1950, the σ-line had a half-width of about 46 kc and the line appeared to be symmetrical in shape. A plot of the shape of the observed line is shown in Fig. 6. At the end of the first series of runs, it was discovered that data had been taken with an excessive rf amplitude and that the width of the line would be reduced to a value consistent with the theoretical prediction of 31.5 kc for atomic hydrogen at a source temperature of 300°K and a hairpin 7.6 cm long. In the runs of December, 1950, the half-width of the observed line was, therefore, reduced to 33 kc by a careful adjustment of the rf amplitude. A plot of the shape of the line observed in December is shown in Fig. 6, curve (*b*).

While the accumulation of a large body of data in June, 1950, under less than optimum conditions appears at first sight to be unfortunate, the fact that the value of ν_H is the same for the series of runs in June and in December gives larger credence to the validity of the result than would a repetition of the experiment under identical conditions. Any asymmetry in the line arising from Doppler broadening, Millman effect,[9] and field inhomogeneities would be markedly sensitive to rf amplitude. The complete agreement of the two sets of results gives better evidence of the symmetry of the line than any reasonable amount of data on the line shape itself.

TABLE II. Results of the measurement of ν_D.

Run	Date	No. of observations	$\nu_D \times 10^{-6}$ sec^{-1}	Prob. error
1	June 14, 1950	70	327.3846	±0.0002
2	June 14, 1950	70	327.3840	±0.0002
3	June 16, 1950	70	327.3841	±0.0001
4	June 16, 1950	70	327.3842	±0.0002
5	June 17, 1950	70	327.3843	±0.0001
		Weighted mean	327.38424	±0.00008

The results for the hfs of deuterium obtained in the several runs are given in Table II. The length of each run was predetermined to include 35 observations by each observer. When two runs were made in a single day, only minor experimental modifications were made between runs. The primary datum was the frequency of the unresolved doublet $(\frac{3}{2}, \frac{1}{2} \leftrightarrow \frac{1}{2}, -\frac{1}{2})(\frac{3}{2}, -\frac{1}{2} \leftrightarrow \frac{1}{2}, \frac{1}{2})$. The magnetic field for the runs on deuterium was essentially the same as for the first series of experiments on hydrogen. The hfs of deuterium obtained from the measurements is, then,

$$\nu_D = (327.38424 \pm 0.00008) \times 10^6 \text{ sec}^{-1}. \quad (3)$$

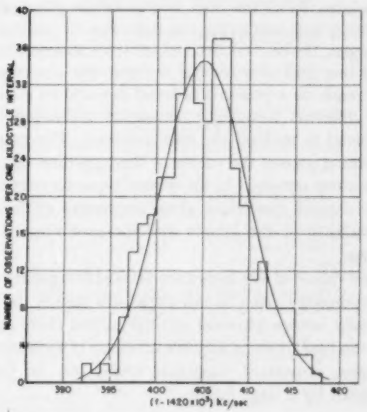

FIG. 7. Histogram showing the distribution of 403 measurements of ν_H obtained from the center of the σ-line of hydrogen with the associated Gaussian error curve.

[9] S. Millman, Phys. Rev. **55**, 628 (1939).

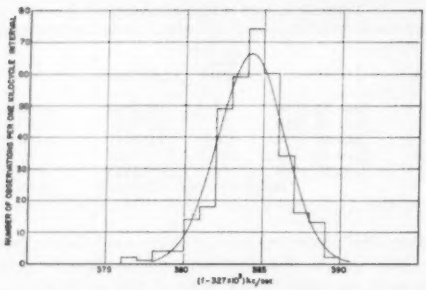

FIG. 8. Histogram showing the distribution of 350 measurements of ν_D obtained from the center of the unresolved doublet of deuterium with the associated Gaussian error curve.

The half-width of the unresolved doublet was found to be 22 kc. The calculated half-width for this line under source conditions similar to those assumed for hydrogen is 23 kc.

Histograms showing the distribution in 1-kc intervals of the 403 measurements of ν_H derived from the center of the σ-line of hydrogen, and 350 measurements of ν_D derived from the center of the unresolved doublet of deuterium are plotted in Figs. 7 and 8. Gaussian error curves,

$$y=h\pi^{-1}\exp(-h^2x^2), \tag{4}$$

are fitted to each histogram. The calculated curves are seen to fit the plotted data very well, and the closeness of the fit is additional evidence of the validity of the statistical reduction of the data.

As has been stated, the several independent runs were made with different experimental conditions and procedures. In all the runs, two observers alternated in adjusting and measuring the unknown frequency. For hydrogen, the hfs was determined from observations on the σ-line and also on the π-lines; the observations were made on a power-broadened line and on a narrow line; different frequency measuring techniques were employed in making the measurements. The excellent agreement among the values of the hyperfine structure separations obtained in the several separate runs under these various conditions gives impressive evidence of the validity of the results and the experimental procedures.

The values of the hyperfine structure separations of the hydrogens given in this paper are among the most precisely known physical constants, and there appear to be no basic reasons why the accuracy of measurement of these important constants could not be further increased by a large factor.

DISCUSSION

The hyperfine structure separation of hydrogen has been used by DuMond and Cohen[10] as a fundamental input datum in their least squares adjustment of the atomic constants. Of the observed quantities used in the adjustment, only the Rydberg constant for infinite mass has been determined with greater accuracy. Of fundamental importance, moreover, is the fact that the corrected Fermi formula[10] for the hyperfine structure separation of hydrogen, allows the calculation of α^2, the square of the fine structure constant, from a knowledge of ν_H and other very accurately known constants. Kroll and Pollock[3] and Karplus, Klein, and Schwinger[3] have recently, by independent methods, calculated higher order radiative corrections to the Fermi formula. Salpeter and Newcomb[11] have calculated still further corrections and give the value $1/\alpha=137.0355$. A more exact analysis of theory and more accurate determinations of the experimental constants in the Fermi formula may possibly permit an evaluation of the corrections proposed by Bethe and Longmire[12] for the finite spatial extension of the nucleus.

From the determination of ν_H and ν_D, the experimental value of the ratio of ν_H to ν_D is

$$(\nu_H/\nu_D)_{exp}=4.3386484\pm0.0000020. \tag{5}$$

If the value of this ratio is computed from the relation

$$(\nu_H/\nu_D)=(4/3)(m_H/m_D)^3(\mu_H/\mu_D), \tag{6}$$

using the very accurate value of (μ_H/μ_D) determined by Smaller, Yasaitis, and Anderson,[4] the discrepancy between these ratios may be written as

$$(\nu_H/\nu_D)_{exp}=(\nu_H/\nu_D)[1-\Delta], \tag{7}$$

where the experimental value of Δ is $[(1.703\pm0.008)\times10^{-4}]$.

Low[13] has discussed in detail, from theoretical considerations, the effect of the structure of the deuteron on the hyperfine structure separation of deuterium. Low and Salpeter[14] introduce certain refinements into the earlier work of Low and indicate that a considerable discrepancy exists between the above observed value of Δ and the calculated value. Salpeter and Newcomb[11] have more recently calculated mass corrections, due to nuclear motion, to the hyperfine structure separations of hydrogen and deuterium. They obtain for the difference between the calculated and experimental values of Δ value of $[(0.6\pm0.4)\times10^{-4}]$.

[10] J. W. M. DuMond and E. R. Cohen, least squares adjustment of the atomic constants as of December, 1950 (report to National Research Council).
[11] E. E. Salpeter and W. A. Newcomb, Phys. Rev. **87**, 150 (1952).
[12] H. A. Bethe and C. Longmire, Phys. Rev. **75**, 306 (1949).
[13] F. Low, Phys. Rev. **77**, 361 (1950).
[14] F. Low and E. E. Salpeter, Phys. Rev. **83**, 478 (1951).

The Anomalous Magnetic Moment of the Electron*

S. H. KOENIG,† A. G. PRODELL, AND P. KUSCH
Columbia University, New York, New York

(Received June 18, 1952)

The ratio of the electron spin g value and the proton g value has been measured with high precision. It is found that $g_s/g_p = 658.2288 \pm 0.0006$, where g_p is the g value of the proton measured in a spherical sample of mineral oil. This result, when combined with the measurement by Gardner and Purcell of the ratio of the electron orbital g value and the proton g value, yields for the experimental value of the magnetic moment of the electron

$$\mu_s = (1.001146 \pm 0.000012)\mu_0.$$

The result is in excellent agreement with the theoretical value recently calculated by Karplus and Kroll:

$$\mu_s = (1.0011454)\mu_0.$$

INTRODUCTION

SEVERAL experiments[1-3] have given direct experimental evidence of the existence of an anomalous electron spin magnetic moment, and have permitted the determination of the magnitude of the anomaly to a moderate precision. New methods developed by Schwinger[4] in quantum electrodynamics have made possible the calculation, to second order, of a radiative correction to the spin magnetic moment of the electron which increased its value from μ_0, given by the Dirac theory, to $\mu_0(1+\alpha/2\pi) = \mu_0(1.00116)$. The experimental results, within the accuracy of measurement and within the validity of the various theoretical approximations which enter into the interpretation of the data, are in excellent agreement with the theoretical prediction.

More recently, Karplus and Kroll[5] have calculated the radiative correction to the electron moment to fourth order and have found for the spin moment μ_s,

$$\mu_s = \mu_0(1+\alpha/2\pi - 2.973\alpha^2/\pi^2) = \mu_0(1.0011454).$$

A critical experimental test of the validity of the result subjects the procedures of quantum electrodynamics to test through one of the two directly measurable experimental quantities discussed by that theory. It is the purpose of the present paper to describe an experiment through which μ_s is measured to high precision.

The ratio $g_J(^2S_{\frac{1}{2}}\mathrm{H})/g_p$ is measured in the present experiment, where g_p is the proton g value. The electron spin g value may readily be obtained from g_J. The present result, combined with the recent measurement of $2g_l/g_p$ by Gardner and Purcell,[6] then determines the quantity $g_s/2g_l = \mu_s/\mu_0$. The present experiment avoids the difficulties in interpretation of data which have occurred in previous experiments and is, in addition, designed to obtain a result of very high accuracy. It is instructive to examine the previous data which have led to a determination of μ_s/μ_0.

PREVIOUS RESULTS

The various experimental results which are used in the calculation of g_s/g_l are given in Table I. A symbol to represent each result in subsequent discussion is also given. The results B, C, D, and H have previously been used[3] to calculate g_s/g_l on the basis of the assumption that the atomic states, $^2S_{\frac{1}{2}}$Na, $^2P_{\frac{1}{2}}$Ga, $^2P_{\frac{1}{2}}$In, $^2P_{\frac{1}{2}}$Ga, $^2P_{\frac{3}{2}}$In, are pure states, and that Russell Saunders coupling adequately describes the states. The result A, however, permits a calculation of g_s/g_l in which it is necessary to assume the purity of the $^2S_{\frac{1}{2}}$ state only.

It is possible from the data of Table I to obtain three values for $g_J(^2S_{\frac{1}{2}}\mathrm{Na})/g_l$.

$$2D/FA = 2(1.00114 \pm 0.00010), \quad \text{(a)}$$

$$2/GEA = 2(1.00109 \pm 0.00003), \quad \text{(b)}$$

$$2IK/A = 2(1.00114 \pm 0.00006), \quad \text{(c)}$$

$$\text{Average: } 2(1.00112 \pm 0.00003). \quad \text{(d)}$$

TABLE I. Data used in the calculation of the spin magnetic moment of the electron.

Symbol	Quantity	Result
A	$2g_l/g_p$	-657.475 ± 0.008[a]
B	$g_J(^2P_{\frac{1}{2}}\mathrm{Ga})/g_J(^2P_{\frac{1}{2}}\mathrm{Ga})$	$2(1.00172 \pm 0.00006)$[b]
C	$g_J(^2S_{\frac{1}{2}}\mathrm{Na})/g_J(^2P_{\frac{1}{2}}\mathrm{Ga})$	$3(1.00242 \pm 0.00006)$[b]
D	$g_J(^2S_{\frac{1}{2}}\mathrm{Na})/g_J(^2P_{\frac{1}{2}}\mathrm{In})$	$3(1.00243 \pm 0.00010)$[b]
E	$g_p/g_J(^2S_{\frac{1}{2}}\mathrm{Cs})$	$-15.1911 \times 10^{-4} \pm 0.0003 \times 10^{-4}$[c]
F	$g_p/g_J(^2P_{\frac{3}{2}}\mathrm{In})$	$-45.6877 \times 10^{-4} \pm 0.0007 \times 10^{-4}$[c]
G	$g_J(^2S_{\frac{1}{2}}\mathrm{Cs})/g_J(^2S_{\frac{1}{2}}\mathrm{Na})$	1.000134 ± 0.000007[d]
H	$g_J(^2P_{\frac{1}{2}}\mathrm{In})/g_J(^2P_{\frac{1}{2}}\mathrm{In})$	$2(1.00200 \pm 0.00006)$[e]
I	$g_J(^2S_{\frac{1}{2}}\mathrm{Na})/g_l(\mathrm{Na})$	-24.8839 ± 0.15[f]
J	$g_J(^2S_{\frac{1}{2}}\mathrm{Ca}^{II})/g_J(^2P_{\frac{1}{2}}\mathrm{Ca}^{II})$	1.5013 ± 0.0003[g]
K	$g_l(\mathrm{Na})/g_p$	0.2645182 ± 0.0000007[h]

[a] See reference 6.
[b] See reference 3.
[c] H. Taub and P. Kusch, Phys. Rev. **75**, 1481 (1949).
[d] See reference 7.
[e] A. K. Mann and P. Kusch, Phys. Rev. **77**, 435 (1950).
[f] R. Logan and P. Kusch, Phys. Rev. **81**, 280 (1951).
[g] Rand McNally, Jr., Phys. Rev. **73**, 1130 (1948).
[h] G. Lindstrom, Arkiv Fysik **4**, No. 1 (1951).

* This research was supported in part by the ONR.
† Predoctoral AEC Fellow; now at Watson Scientific Computing Laboratory, Columbia University, New York, New York.
[1] J. E. Nafe and E. B. Nelson, Phys. Rev. **73**, 718 (1948).
[2] G. Breit, Phys. Rev. **72**, 984 (1947).
[3] P. Kusch and H. M. Foley, Phys. Rev. **74**, 250 (1948).
[4] J. Schwinger, Phys. Rev. **73**, 416 (1947).
[5] R. Karplus and N. Kroll, Phys. Rev. **77**, 536 (1950).
[6] J. H. Gardner and E. M. Purcell, Phys. Rev. **76**, 1262 (1949); J. H. Gardner, Phys. Rev. **83**, 996 (1951).

Inasmuch as an atom in a pure S state has no orbital electronic momentum, $g_J(^2S_{\frac{1}{2}})$ must be associated entirely with the electron spin. It has been shown[7] that the g_J values of the alkalis K, Na, Li^7, and Li^6 are equal within one part in 4×10^4, and it seems reasonable to extrapolate to sequence to include hydrogen. (The following paper by Franken and Koenig justifies the extrapolation.) The ground state of hydrogen can be shown to be a pure S state to about 1 part in 10^6. The g_J value of Na in the $^2S_{\frac{1}{2}}$ state is then, within the present approximation, equal to g_s', the spin g value of the electron bound in the ground state of hydrogen. A relativistic correction of two parts in 10^5, essentially due to the increase of mass with the velocity of the bound electron, gives $g_s=2(1.00114\pm0.00003)g_l$. In view of the limited precision of the experimental data, the excellent agreement with the theoretical prediction must be considered as fortuitous.

The result is limited in precision both by the accuracy of the experimental data and by the limited validity of the assumptions which enter into the calculations. Because of the differential diamagnetic effects of the electrons in various molecules, the magnetic moment of either the proton or the Na nucleus measured in two different molecules will presumably differ by some small, unknown amount. In the results (a) and (b), this effect is neglected. The validity of the result is, of course, also limited by the assumption that $g_J(^2S_{\frac{1}{2}}\mathrm{Na})=g_J(^2S_{\frac{1}{2}}\mathrm{H})$. Finally, it should be noted that in the result (a), use is made of a $^2P_{\frac{1}{2}}$ state as an intermediary in the calculations. The data for D were taken at low magnetic field and those for F at high field. Because of a partial decoupling of the L and S vectors, it is not certain that $g_J(^2P_{\frac{1}{2}})$ is independent of field, to the precision attached to the result (a). The experiment to be discussed in this paper avoids all of these difficulties.

From the data in Table I, it is possible to obtain information on the g values of $^2P_{\frac{1}{2}}$ states. Let

$$N=g_J(^2S_{\frac{1}{2}}\mathrm{Na})/g_l$$

as calculated above. Then

$$N/D=g_J(^2P_{\frac{1}{2}}\mathrm{In})/g_l=\tfrac{2}{3}(1-0.00131\pm0.00010),$$
$$2/AF=g_J(^2P_{\frac{1}{2}}\mathrm{In})/g_l=\tfrac{2}{3}(1-0.00128\pm0.00003),$$
$$N/C=g_J(^2P_{\frac{1}{2}}\mathrm{Ga})/g_l=\tfrac{2}{3}(1-0.00130\pm0.00008).$$

Assuming pure Russell Saunders coupling, $g_J(^2P_{\frac{1}{2}})=4g_l/3-g_s'/3$ and $g_s'/g_l=4-3g_J/g_l$. Then

$$g_s'(^2P_{\frac{1}{2}}\mathrm{In})/g_l=2(1.00129\pm0.00003),$$
$$g_s'(^2P_{\frac{1}{2}}\mathrm{Ga})/g_l=2(1.00130\pm0.00008).$$

These results are significantly higher than for an electron in an S state. The difference may be due in part to a lack of purity of these states at zero field as well as the possibility of a mixing of near lying levels by the magnetic field.

From the remaining data on $^2P_{\frac{1}{2}}$ states, under the assumption of Russell-Saunders coupling where $g_J(^2P_{\frac{1}{2}})=2g_l/3+g_s'/3$, it is found that

$$g_s'(^2P_{\frac{1}{2}}\mathrm{In})/g_l=2(1.00141\pm0.00013),$$
$$g_s'(^2P_{\frac{1}{2}}\mathrm{Ga})/g_l=2(1.00084\pm0.00010),$$
$$g_s'(^2P_{\frac{1}{2}}\mathrm{Ca^{II}})/g_l=2(1.0005\pm0.0002).$$

The significance of these results is not entirely clear, though the values do increase with atomic weight. It is evident that there is an experimental difference in the value of g_s' as measured in S and P states. In view of the greater theoretical simplicity of S states as compared to P states, the result obtained from the S states is probably better.

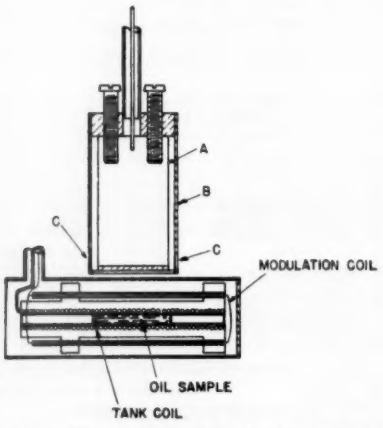

FIG. 1. Cross section of uhf unit and proton resonance probe.

[7] P. Kusch and H. Taub, Phys. Rev. **75**, 1477 (1949).

THEORY OF THE EXPERIMENT

The atomic beams method in combination with nuclear resonance techniques was used to measure the ratio of the electronic g value of hydrogen in the $^2S_{\frac{1}{2}}$ state and the proton g value.

The relevant portion of the term values of the hfs levels of hydrogen in the $^2S_{\frac{1}{2}}$ state is given by

$$W_{F,\,m_F}=m_Fg_p\mu_0H\pm\tfrac{1}{2}h\nu_{\mathrm{H}}(1+2m_Fx+x^2)^{\frac{1}{2}}, \qquad (1)$$

where $x=g_J(1-g_p/g_J)\mu_0H/h\nu_{\mathrm{H}}$, and the $\pm$ sign is to be associated with $F=1$, 0, respectively. The frequency of the line $(1, 0\leftrightarrow1, -1)$ was measured rather than that of the other observable line $(1, 1\leftrightarrow0, 0)$, because its frequency is lower and easier to produce and measure, and because the value of g_J/g_p calculated from the data is less dependent on the frequency of transition for the chosen line than for the other observable line.

From Eq. (1) the transition frequency f of the line $(1, 0\leftrightarrow1, -1)$ is

$$f=\tfrac{1}{2}[(1+x^2)^{\frac{1}{2}}-(1-x)]\nu_{\mathrm{H}}+g_p\mu_0H/h. \qquad (2)$$

The frequency of the proton resonance is

$$P=-g_p\mu_0 H/h. \tag{2a}$$

If f and P are measured in the same magnetic field, Eqs. (2) and (3) give g_J/g_p in closed form

$$g_J/g_p=-[2f(f+P+\nu_H)+P\nu_H]/P[\nu_H+2(f+P)]. \tag{3}$$

g_p in (2) is, of course, the g value of the proton measured in atomic hydrogen. g_p in (2a) is the g value of the proton measured in the environment of the particular sample of proton containing material used in a nuclear resonance experiment. The substitution of (2a) in (2) may, however, be made without any meaningful loss of accuracy since the relative diamagnetic correction does not affect P within the limit to which the frequency f is measured in the present experiment. g_J/g_p is then expressed in terms of three measurable frequencies. P is the Larmor precession frequency of a proton in a magnetic field H and may be measured by use of nuclear resonance absorption techniques. ν_H is known from the preceeding paper, and f is the atomic transition frequency measured in this experiment.

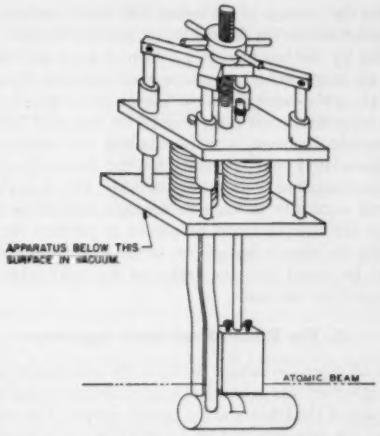

FIG. 2. Probe mount. The mechanism for raising and lowering hairpin and proton sample is indicated.

APPARATUS

A. The Magnet

The major equipment for the present experiment was the atomic beams apparatus described in the previous paper. The large external electromagnet, not used by Prodell and Kusch, was added to produce a uniform magnetic field in the region in which the atomic transitions occurred. The magnet was so designed that an accuracy of one part in 10^6 in the measurement of g_s/g_p appeared to be attainable. The main requirement was an extremely homogeneous field over the transition region, so that neither the atomic line nor the proton resonance line would be excessively broadened by the nonuniformities of the magnetic field.

The magnet, of Armco magnet iron, is a low voltage, water-cooled electromagnet with 30-cm hand lapped pole faces initially parallel within 0.003 cm and with a 5.7-cm gap. The magnetic field was about 1500 gauss. To achieve a high degree of homogeneity, it was necessary to shim the magnet extensively. Geometric factors, such as fringing of the field, and different path lengths of flux for different parts of the pole faces contributed to the variation of the field over the desired region. It was possible to compensate for these effects by large shims near the edges of the magnet faces, and by an adjustment of the assembly bolts so that the gap became slightly wedged shaped. The most important factor contributing to the inhomogeneities of the field were, however, local irregularities in the iron, which to some extent varied from day to day.

The first successful attempts at shimming were by the use of 0.003–0.008 cm steel shims with an area of about 12 cm^2. By trial and error it was possible to improve the character of the field considerably, but not sufficiently to eliminate field broadening of the observed lines. The main difficulty was that effects of the various shims were not independent. Continuous experimentation during the course of this research led to improved shimming procedures, and for the last few runs it was possible to obtain the theoretical line widths. Small nickel shims, about 5 mm square, held in place with Scotch Electrical Tape were used. The small size of the shims greatly reduced their mutual interaction, as did the reduced permeability of the nickel. At best, it was possible to have the field vary less than one part in 10^6 over the transition region. However, the field would retain this character for only about two weeks of use.

B. The uhf Unit

In order to induce the desired transitions in the atomic beam, it is necessary to apply a varying magnetic field perpendicular to the direction of the static field at a frequency of 3655 Mc. The open "hairpin" construction used by Prodell and Kusch was not suitable for the present experiment. Since the transition frequency of the line observed in this experiment is critically dependent on the field, the extent of the rf field must be more closely confined to a known limited region in the present experiment. In addition, the atomic beam apparatus readily propagated energy with a frequency of 3655 Mc, and considerable interference was produced in the Pirani gauge detector by use of an open hairpin.

A resonant, carefully shielded hairpin, shown in Fig. 1, was used. A rectangular box (A), open at both ends and approximately one-half wavelength high, was fed by a loop connected to the rf source through a coaxial line. The cavity had a low Q and could be tuned by means of two screws at the top of the unit. The cavity was enclosed in a copper box (B), with small openings

(*C*) for the passage of the beam. The shield confines the radiation within the desired limits, and the shorted turn formed by the box produces a current sheet and therefore an approximately uniform magnetic field distribution along the beam direction. The hairpin was mounted on a horizontal brass tube, about 9 cm long and 2.86 cm in outside diameter, which contained the sample and the associated coils necessary for the detection of the proton resonance. The entire assembly, Fig. 2, could be moved vertically in vacuum through bellows, so that either the hairpin could be placed in position for observing the atomic transitions, or the water (oil) sample could be raised into the region of the field otherwise occupied by the beam.

C. The Proton Resonance Apparatus

In all cases the sample in which the proton resonance was observed was cylindrical to give the best coincidence in space of the beam and the proton sample. The proton resonance was detected by a circuit[8] which is sensitive only to absorption of energy by the precessing protons. The sample is placed in the tank coil of an rf oscillator which is coupled to an rf amplifier, a detector, and audio amplifiers, so that any change in the level of the oscillator at an audio rate is present at the output of the audio stage. The average dc level at the detector is fed back through a one-second time constant RC circuit to the oscillator to prevent slow wandering of the oscillator level. In actual operation it was found desirable to reduce the filament voltage of all tubes in the circuit to 4 volts. The result was an increased signal to noise ratio as well as increased stability of the feedback circuit.

The magnetic field at the sample was modulated by a pair of rectangular coils. These coils, the oscillator tank coil, and the sample were assembled as a unit to be inserted into the brass tube under the hairpin. In the earlier runs, the tank coil was wound on a glass tube containing the water sample, while the modulating coils were wound on Lucite spacers mounted on the glass tube as well. This unit could be slipped into the brass tube, and electrical contact made by clips. Glass plugs cemented into the glass tube determined the sample length.

For the later runs, a new Lucite holder was designed so that a thin walled glass tube, 4.7-mm i.d., containing the oil sample could be removed without removing the coils. This gave a more flexible working arrangement as well as better electrical stability, since the Lucite holder and coils were permanently mounted in the brass cylinder.

When setting the magnetic field for a run, 60-cycle modulation of about 2 gauss peak to peak was used to display the entire resonance on an oscilloscope. A sinusoidal sweep of 120 cycles derived from the filtered output of a full wave 6H6 rectifier made it possible to adjust the oscillator frequency to the proton resonance frequency corresponding to the unmodulated magnetic field by setting the two resonances occurring on the oscilloscope screen per modulation cycle to coincidence. With large modulation, a 60-cycle signal was induced in the tank circuit from the modulating coils. The interference was conveniently eliminated by injecting a 60-cycle correction voltage of adjustable phase and amplitude through two one-millihenry chokes directly across the parasitic suppressor in the grid lead of the oscillator.

In the actual measurement of the line frequency, a modulation amplitude less than 0.01-gauss rms at a frequency of 99 cycles was used. The frequency was chosen because it is high enough to eliminate flicker effect noise, low enough for the relaxation time of the sample, and not related to 60 cycles in any simple manner so that 60-cycle pick-up could not introduce any errors. The modulation voltage was supplied by a Hewlett Packard 201B audio oscillator feeding the coils through a 6-volt filament transformer.

The output of the audio amplifier, a 99-cycle signal proportional to the slope of the resonance line, in as much as the line in all cases had a width greater than the modulation amplitude, was fed into a narrow band amplifier. The output was displayed on the oscilloscope and the maximum of the resonance curve was determined by setting for null output. By this procedure the resonance could be reset to within 15 cycles out of 6.5 Mc consistently. Repetition of measurements gave a significant improvement in the accuracy of the measurements.

FREQUENCY MEASUREMENT

The main data of the experiment are the frequencies f and P. A 2K42 klystron mounted in a water-cooled oil bath and powered by well-regulated A and B supplies was used to generate f, a frequency of approximately 3655 Mc. The frequency of the klystron was varied by manual adjustment of the repeller voltage. The output was sufficiently free of modulation and constant during the time required to make a setting and measurement of the transition frequency to permit measurement of the frequency to 1 kc. The frequency was measured by beating a part of the klystron output with 3680 Mc from a crystal harmonic generator fed by 240 Mc plus added 80-Mc sidebands from the frequency standard. The 25-Mc beat was heard on a receiver, which was essentially calibrated at each observation by the second harmonic of a General Radio 620A Heterodyne Frequency Meter. The procedure yielded a least count of 2 kc in f.

Measurement of P, a frequency of the order of 6.5 Mc, to the same precision was somewhat more difficult. Initially, 5 Mc from the frequency standard was mixed with 1.5 Mc from a General Radio 805 signal generator. The 6.5-Mc beat was allowed to leak into the oscillator associated with the resonance detection circuit. This

[8] R. V. Pound and W. D. Knight, Rev. Sci. Instr. 21, 219 (1950).

frequency, beating with that produced by the proton resonance oscillator, produced an audiofrequency which appeared on the oscilloscope superimposed on the proton signal. By adjusting the signal generator, zero beat could readily be attained. The tenth harmonic of the signal generator output was measured on a GR Heterodyne Frequency Meter. The least count of this method was 100 cycles at 6.5 Mc. It was necessary, then, to estimate to 0.1 division on the frequency meter to achieve an accuracy of 1 part in 6.5×10^5.

For the later runs, a 10-kc blocking oscillator driven by the 50-kc output of the frequency standard was built. Harmonics of 10-kc in the 6.5-Mc region were received and identified on a National HRO receiver with an internal crystal calibrator. The frequency to be measured was also fed into the receiver. One of the difference frequencies, an audio note less than 5 kc, was measured on a GR Audio Interpolation Oscillator, with a least count of 1 cycle.

In the measurement of both f and P, the procedure was to track the unknown frequency with the frequency measuring device at all times while a setting on a line was made. In this manner effects due to oscillator drift could be minimized. Frequency measurements, then, were not factors which limited the precision of the experiment, especially in view of the statistically significant body of data which was obtained.

EXPERIMENTAL PROCEDURE

The critical point of the experiment was the necessity of placing the sample in the same portion of the field as that occupied by the beam. An exact superposition was impossible, inasmuch as the beam was 2.8 mm high and approximately 0.05 mm wide compared with a proton sample of circular cross section approximately 4.7 mm in diameter. It was attempted to place the sample so that its axis of symmetry coincided with the axis of the beam. This was not always accomplished exactly, and after a run or set of runs, the entire probe mount (Fig. 2) was removed from the apparatus and carefully measured to determine any vertical error in the placement of the sample. At the end of every run the vertical variation of the field was measured. It was at most 1 part in 1.5×10^5 per mm, so that over the height of the sample there could exist field variations as great as 1 part in 3.2×10^4.

To correct for errors due to incorrect positioning of the sample in the face of a gradient of the field, two procedures may be used. The simpler of the two effectively treats the beam and sample as geometric lines defined by their axes of symmetry; if these do not coincide, the measured values of f and P are corrected by an amount determined by the field differential over the distance of separation. The second correction procedure takes account of the fact that the field does not vary linearly but has a second derivative. Therefore, the average value of the field over the beam or sample will not be the same as the field at the axis of the beam or sample. In as much as the beam and sample are of different heights and the varying thickness of the sample weights different parts of the field differently, the second derivative of the field will cause an effective or virtual relative displacement of the beam and sample. A correction can be applied in a straightforward manner, if it is assumed that there is a quadratic variation of the magnetic field in the vertical direction, and no variation of the field in the direction of the field. The validity of this assumption will be discussed in succeeding sections.

TABLE II. g_J/g_p.

Run	I	Ia	II	III	IV
March 17, 1951	658.2123±0.0007		658.2151	658.2176	658.2169
March 20, 1951	.2172±0.0006		.2200	.2169	.2162
March 26, 1951	.2180±0.0005		.2208	.2173	.2172
June 28, 1951	.2131±0.0004		.2141	.2154	.2153
July 12, 1951	.2142±0.0002		.2151	.2181	.2196
July 26, 1951	.2167±0.0002		.2177	.2171	.2163
August 3, 1951*A*	.2170±0.0003		.2180	.2180	.2175
August 3, 1951*B*	.2165±0.0003		.2175	.2175	.2170
Average:			.2173	.2172	.2170
Probable error:			0.0006	0.0002	0.0003

The C field current was monitored by a type K2 L & N potentiometer connected across an L & N 0.001-ohm shunt in series with the magnet windings. In the first two runs no attempt was made to stabilize the current, obtained from two submarine storage batteries. For the remaining runs, however, the current was held constant within 1 part in 2×10^5 by continuous manual adjustment of a mercury rheostat. Drift in the A and B field current as well as geometrical distortions of the C magnet resulting from temperature changes contributed to a variation in time of the magnetic field in the transition region. This variation served the useful purpose of causing each setting on a line to occur at a different position of the dial of the frequency measuring devices, and in this way minimized prejudice of the observer in adjusting and reading the frequency.

The procedure adopted in taking data was to make about 13 sets, alternating between the two lines, of three or four determinations of the frequency of the center of the line. At each observation the time and, in those runs where it was not held constant, the current in the C field were recorded. The data were reduced by interpolating in time or current between the average of the first and third sets of readings to obtain a frequency P to be paired with the average of the second set of readings f. The interpolation process was repeated for all groups of three adjacent sets of readings. Each pair of frequencies was substituted into Eq. (3), and the average of the results of the substitution was taken as the value of g_J/g_p for the run. This value of g_J/g_p depends then on about 21 measurements of P and 18 measurements of f.

EXPERIMENTAL RESULTS

In Table II the values obtained for g_J/g_p in the various runs are tabulated. Column I gives the result of each run without any corrections, that is, the result of Eq. (3) after direct substitution of the measured and interpolated frequencies. The estimated probable error, which gives a measure of the internal consistency of the run, is tabulated in column Ia. Column II lists the results corrected to measurement of the proton frequency in a spherical sample of mineral oil. Several diamagnetic effects to be discussed later are involved. In column III the results of the various runs corrected for variations of the magnetic field over the sample and beam by the first method (see preceeding section on experimental procedure) are tabulated, whereas in column IV the results, after correction for the quadratic variation of the field over the finite samples, are tabulated. It is seen that the spread of the average result in the last three columns is 1 part in 2×10^6. To appreciate this excellent agreement, it is necessary to consider the substantial, accidental or deliberately invoked, variations in the experimental conditions from one run to the next.

In the runs of March 17, 20, and 26, the proton resonance was observed in a 0.13 molar solution of $CuSO_4$ and the proton resonance frequency was measured by the first of the two techniques described in the section on frequency measurements. The sign of the gradient was deliberately changed between the runs of March 17 and March 20 by the simple expedient of altering the angle between the pole faces. To reduce the field inhomogeneity introduced by the change in the shape of the gap, readjustment of shims was required. The vertical gradient of the field in the runs of March 20 and March 26 was approximately the same. However, in the runs of March 17 and 20 the C field was allowed to drift, while in the run of March 26, the current in the C magnet was maintained at a constant value. The total field drift during the course of the two earlier runs was about 1 part in 10^4, while in the later runs, it was only about 1 part in 5×10^4. The atomic line width was about 130 kc on March 17, and about 145 kc on the other two March runs. A theoretical line width of 60 kc is characteristic of a 4-cm hairpin.

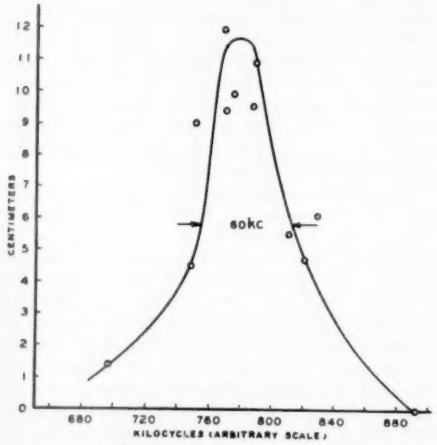

FIG. 3. A plot of the resonance line of hydrogen observed on July 26, 1951. The ordinate is the observed change in beam intensity and the abscissa is the deviation of the applied frequency from a fixed frequency. The scatter of points arises principally from mechanical unsteadiness of the Pirani gauge.

After the series of March runs, a careful measurement of the position of the beam in the transition region as well as a measurement of the position of the water sample under the observational conditions was made. A small relative shift was found; corrections for this shift by each of the two procedures possible in the face of a magnetic field gradient lead to the corrected values in columns III and IV of Table II. In spite of the fact that the corrections are as great as one part in 2×10^5, the maximum discrepancy between the results of the three runs is only about 1 part in 6×10^5. The agreement, in view of the varying field inhomogeneities and different observational procedures, is impressive.

Three runs taken in April, not included in Table II, were made with a new sample holder, tank coil, and modulating coils. The water sample was deliberately made considerably longer than the hairpin. The values of g_J/g_p after reduction to a spherical sample of mineral oil were 658.2208, 658.2141, and 658.2046, with a mean of 658.2132. The large spread of values presumably arises from a differential mean field in the hairpin and the longer water sample. It is significant that the errors of different signs appear in the three runs. Moreover, it should be noted that subsequent examination of the sample holder showed contamination with magnetic particles, and it is not inconceivable that the iron particles gave rise to the total discrepancy. The interpretation of the April runs is, therefore, doubtful, and the data were discarded. No magnetic contamination of relevant portions of the apparatus was detected in any other run.

The runs of June, July, and August were made with the Lucite holder. Squibb's mineral oil was used as the sample material in all these runs. Extraordinary care was taken to prevent magnetic contamination. A new uhf unit was also installed. In this series of runs the current in the C field was held constant, and the proton resonance frequency was measured with an improved procedure, previously described.

The runs of June 28 and July 12 were both taken with a rather poor field and the atomic line widths were 150 and 170 kc, respectively. The shims were adjusted before each run. The vertical gradient was about three times as great in the second of these runs as in the first; the rather poor homogeneity was accompanied by a low intensity of the atomic line and observation was dif-

ficult. In spite of these difficulties, the corrected result is in remarkable agreement with those obtained in the March runs.

The experience during the runs of June 28 and July 12 indicated a progressive deterioration of the magnetic field. A major readjustment and reshimming appeared to be indicated. The magnet yoke was completely disassembled, and all shims removed from the pole faces. The component parts of the yoke were cleaned and lightly greased, and the magnet reassembled. The magnet was then shimmed with small nickel shims, and a portion of the gap was found with a field variation less than 1 part in 10^5 over the transition region.

Mechanisms were provided to insure that the axis of the oil sample coincided with the beam axis in a horizontal plane. Finally, a considerable rearrangement of the uhf unit was made; in particular, the joints were all resoldered, and the tuning screws were adjusted to bring the hairpin closer to resonance at the transition frequency.

The run of July 26, listed in Table II, was taken under the best conditions of any of the runs. The atomic line width was reduced to the theoretical value of 60 kc by careful adjustment of the rf amplitude. The line is shown in Fig. 3. Unfortunately, a mechanical unsteadiness of the beam prevented the observation of a smoother curve. It was apparent from the approximately theoretical magnitude of the "flop" observed that all previous runs had been taken with less than optimum rf amplitude, presumably because of poor tuning of the hairpin.

Though the low rf amplitude in the previous runs made observation difficult because of low intensity of the line, errors arising from an asymmetrical broadening of the line by excessive rf amplitude in the face of field inhomogeneties and other effects are avoided.

An earlier run taken on July 26 with a grossly excessive rf amplitude gave a result of 658.2284 for g_J/g_p. It is possible that the discrepancy with other data arises from effects associated with the large rf amplitude; it is our belief, however, in view of the consistency of all other valid data, that the result is a consequence of a systematic blunder in observation, and the data were rejected.

The two runs of August 3 were taken to determine the effect of rf amplitude on the experimental result. In the first run, the rf amplitude was adjusted so that the flop was only half of its maximum value. The second run was taken at the optimum rf amplitude, and both the line width and intensity had the theoretical value. A third run was taken with an excessive rf amplitude, which broadened the line to about $2\frac{1}{2}$ times its theoretical width and reduced its intensity by about 20 percent. The result for g_J/g_p was 658.2192. This result is in the direction of the previously discarded run, although it is difficult to see how an effect as large as that observed on July 26 could be attributed to any reasonable power broadening. The third result of August 3 is discarded because of the excessive power level in the hairpin and also because of instabilities which appeared in the C field throughout the run.

Data have, therefore, been discarded in arriving at the final result, for well-defined reasons. The agreement of the means of the results in columns II, III, and IV indicates that the effect of the gradient of the magnetic field as well as that of a quadratic variation of field in the vertical direction is random. No direct observation of the gradient and its effect in the two horizontal directions has been made. However, under the widely varying expetimental conditions in the several runs, it appears to be reasonable that effects arising from gradients other than the vertical gradient are also random. In addition, the observed width of the lines could be approximately explained by the vertical gradient alone, so that a total variation of the field over the 4-cm length of the sample larger than that over the height of the sample is precluded.

The result of the experiment is taken to be the mean of the results in columns III and IV since the detailed validity of the assumptions underlying the gradient corrections in both these columns is uncertain. We have, then,

$$g_J/g_p \text{ (spherical sample mineral oil)} = 658.2171 \pm 0.0006,$$

where the stated uncertainty is twice the probable error in column IV and three times that in column III to allow for statistically uncompensated errors arising from gradients not here considered, and to include uncertainties in certain of the diamagnetic corrections.

DIAMAGNETIC CORRECTIONS

The measured proton resonance frequency P' is not identically the frequency corresponding to the externally applied field, but rather that corresponding to the external field modified by several small diamagnetic effects. If P' is substituted into Eq. (3) the result, tabulated in column I of Table II, will be the ratio of g_J to the g value of the proton as measured in a sample of particular shape and material, since the small difference between P and P' will have a negligible effect on the numerator and the bracketed denominator term of the equation. To reduce the result in column I to that of column II, which gives the values of g_J/g_p, before gradient corrections, for g_p measured in a spherical sample of mineral oil, several diamagnetic corrections must be considered. These arise from (1) the bulk diamagnetism of the sample material itself which modifies the field in a cylindrical sample but not in a spherical sample, (2) fields due to paramagnetic ions in the sample, and (3) the differential diamagnetic shielding of the proton by the orbital electrons in the molecules containing the proton. For water, all three corrections must be applied, while for oil the only correction which need be applied is that due to (1). For an infinite cylinder the field at the proton is $H_0(1-\frac{1}{3}\pi k)$, where

H_0 is the applied field and k the diamagnetic susceptibility of the water or oil. The sample used in the present experiment was a cylinder with a ratio of length to diameter of 8.5. The data of Dickenson[9] show that such a cylinder may be considered infinite in calculating the diamagnetic correction. To the present precision the same result is obtained if the cylinder is approximated by an ellipsoid. The ratio of the susceptibility of mineral oil and water is[10] 1.01 and $k_{H_2O}=-0.72\times10^{-6}$. The field at the proton in both materials is, therefore, increased by $H_0 2\pi k/3=1.5\times10^{-6}H_0$. The effect of (1) is to decrease the value of g_J/g_p measured in a cylindrical sample from that measured in a spherical sample. To reduce the observed values to the case of a spherical sample, the value of g_J/g_p is, therefore, to be increased by 0.0010 for both oil and water.

The effect (2) occurs only in the case of the three runs on water. For the 0.13 molar $CuSO_4$ solution used in the water runs, the correction due to the paramagnetism of the Cu^{++} ions is somewhat uncertain. Were the ions derived from $CuCl_2$, the correction would result in a decrease in the measured value of g_J/g_p of 0.7 part in 10^6. Dickenson gives data on the effect of Cu^{++} derived from the chloride, as well as data on the effect of the Ni^{++} ions derived from the sulfate and the chloride. For nickel, the corrections are somewhat different in each case, and it is reasonable to assume that the same may be true for copper. In the absence of further data, however, the correction of -0.7 part in 10^6 will be applied to g_J/g_p. The uncertainty will not affect the final result by more than 1 part in 10^7.

For a fixed magnetic field, the difference in the average magnetic field at the proton in mineral oil and in water due to shielding produced by the different electron configurations in the two molecules is given by Gutowsky and McClure[11] to be 3.4 parts in 10^6. The field at the proton in water is higher than in oil. Then to the uncorrected results for the water runs, a correction of $(1.5+3.4-0.7)\times6.58\times10^{-4}=+0.0028$ must be applied. These corrections, added to the data in the first column of Table II, give the results tabulated in column II. A rough estimate of diamagnetic effects arising from the mechanical structures associated with the apparatus shows a negligible effect.

DISCUSSION

In order to obtain the magnetic moment of the electron, it is necessary to know the relation between g_J of atomic hydrogen and g_s of an unbound electron. A hydrogen atom with a spinless nucleus in zero magnetic field is in a pure S state, and its g value would be entirely due to the electron spin. However, the presence of the nuclear moment as well as the externally applied field mixes a small part of the $^2D_{\frac{1}{2}}$, $m_J=\pm\frac{1}{2}$ levels with the two degenerate ground levels. The amount of mixing may be calculated with the formulas derived by Perl and Hughes.[12] A rough estimate of the mixing may, however, be made. The interaction energy of a Bohr magneton with a magnetic field corresponds to 2.8 Mc per gauss, so that the perturbation energy of the atom in the applied field of 1500 gauss is about 4200 Mc. The $S-D$ separation is approximately 0.9×13.6 ev $=3\times10^9$ Mc. The amount of mixing will then be on the order of $4.2/3\times10^6$ or 1.3 parts in 10^6. The effect on the g value will be proportional to the square of the mixing, or 1.7 parts in 10^{12}, a completely negligible effect.

The effect of the magnetic field due to the nuclear moment is smaller still. The field at the first Bohr orbit due to the proton moment is approximately $\mu/a_0^2=90$ gauss, as compared to the 1500 gauss of the external field. These estimates are in agreement with the more accurately calculated results. Within the limits of the experiment, then, the ground state may be considered pure. $g_J(^2S_{\frac{1}{2}}\mathrm{H})$ is, therefore, equal to g_s', the spin g value of the electron bound in the hydrogen atom.

Relativistic effects, essentially due to the increase in mass of the electron bound in the hydrogen atom, serve to decrease g_s' from g_s, the g value of the free electron.[13]

$$g_s'/g_s=[1+2(1-\alpha^2)^{\frac{1}{2}}]/3\cong1-\alpha^2/3=1-17.8\times10^{-6}.$$

Application of this factor to our experimental result yields

$$g_s/g_p=658.2288\pm0.0006.$$

A combination of this result with that of Gardner and Purcell,

$$2g_l/g_p=657.475\pm0.008,$$

where g_p is also measured in a spherical sample of mineral oil, yields

$$g_s/g_l=2(1.001146\pm0.000012).$$

The greater part of the uncertainty arises from the stated uncertainty in the result of Gardner and Purcell. The agreement with the value calculated by Karplus and Kroll is excellent. Because of the large experimental uncertainties, the result cannot, however, be considered as conclusive evidence of the validity of the theoretical calculation.

The ratio $g_s/g_{p(\mathrm{oil})}$ is not of fundamental significance except when combined with other observations in which a measurement of the proton resonance frequency in a spherical sample of mineral oil is made. There is a rather large diamagnetic shielding of the proton in H_2. Ramsey[14] has calculated the magnetic shielding constant in this case to be $\sigma=26.8\times10^{-6}$. In addition, Gutowsky and McClure[11] have shown that the diamagnetic shielding of the proton in mineral oil is greater by

[9] W. C. Dickenson, Phys. Rev. **81**, 717 (1951).
[10] I. Cooter, Bureau of Standards, private communication.
[11] H. S. Gutowsky and R. E. McClure, Phys. Rev. **81**, 276 (1951).
[12] W. Perl and V. Hughes (to be published).
[13] N. F. Mott and H. S. W. Massey, *Theory of Atomic Collisions* (Clarendon Press, Oxford, 1949), second edition, p. 72.
[14] N. F. Ramsey, Phys. Rev. **78**, 699 (1950).

3.7×10^{-6} than it is in H_2. The net diamagnetic correction is then 30.5×10^{-6}. Accordingly

$$g_s/g_{p(\text{free})}=658.2087\pm0.0006,$$

where the uncertainties in the diamagnetic corrections have not been included in estimating the precision of the result.

The authors wish to express their appreciation to Mr. Jim Woods and his staff in the machine shop for the construction of the apparatus; to Mr. Richard Blume for his work in the design and construction of a suitable frequency standard; and to Dr. Irwin Cooter of the National Bureau of Standards for his measurement of the diamagnetic susceptibility of our mineral oil sample.

PHYSICAL REVIEW VOLUME 88, NUMBER 2 OCTOBER 15, 1952

A Determination of $g_J(^2S_{\frac{1}{2}})$ of Potassium in Terms of the Proton Gyromagnetic Ratio*

PETER FRANKEN† AND SEYMOUR KOENIG
Columbia University, New York, New York

(Received June 18, 1952)

The ratio of the g value of potassium K^{39} in the ground state to the gyromagnetic ratio of the proton in mineral oil has been measured in an experiment combining atomic beam and nuclear resonance techniques. It is found to be $g_J(K)/g_p=658.2274\pm0.0023$. This result, when combined with the measurement of $g_J(H)/g_p$ by Koenig, Prodell, and Kusch, yields

$$g_J(K)/g_J(H)=1.000016\pm0.0004 \text{ percent}.$$

This is to be compared with the recent direct measurement by Pohlman, Bederson, and Eisinger: $g_J(K)/g_J(H)=1.00016\pm0.006$ percent. The present experiment is of superior precision and is in agreement with independent experimental evidence. The present result is found to agree with the theoretically predicted value.

INTRODUCTION

A RECENT direct measurement by Pohlman, Bederson, and Eisinger[1] (PBE) of the ratio of the g_J values of hydrogen and potassium in the ground, $^2S_{\frac{1}{2}}$, states has yielded

$$g_J(K^{39})/g_J(H^1)=1.00016\pm0.006 \text{ percent}.$$

In view of the fact that Kusch and Taub[2] found the g_J values of Li, Na, and K to be identical to within one part in 40,000, this large reported difference between the g_J values of K and H is rather surprising. In addition, it is possible to deduce values of $g_J(K)/g_J(H)$ which are in disagreement with the PBE result both from independent experimental evidence and from theoretical considerations. The experimentally determined quantities to be considered are

$$g_J(H)/g_p=658.2171\pm0.0001 \text{ percent},^3$$
$$g_p/g_J(Na)=15.1927\times10^{-4}\pm0.005 \text{ percent},^4$$
$$g_J(Na)/g_J(K)=1.00000\pm0.002 \text{ percent}.^2$$

Within the stated precision of the results, the different internal diamagnetic corrections to be applied to the g value of the proton as measured in mineral oil and NaOH can be ignored. From these results it is found that

$$g_J(K)/g_J(H)=0.99999\pm0.007 \text{ percent}.$$

While the disagreement between this result and that of PBE cannot be considered as conclusive evidence of the invalidity of either result, the discrepancy is notable.

Calculations by Phillips[5] on the perturbation of the $^2S_{\frac{1}{2}}$ ground state of K by excited states of the inner electronic core yield the estimate $1\leqslant g_J(K)/g_J(H)\leqslant1.00001$. Relativistic and diamagnetic corrections, to be discussed in Sec. C, increase both limits by 6×10^{-6}. While there is some uncertainty in the perturbation calculations, the disagreement of this limit with the result of PBE is marked.

In view of the discrepancy of the PBE result and that obtained from independent experimental evidence and in view of the fact that no effect as large as that found by PBE can be accounted for on the basis of existing theory, it was decided to redetermine the ratio $g_J(K)/g_J(H)$. In the previous paper Koenig, Prodell, and Kusch[3] (KPK) have described a precision measurement of $g_J(H)/g_p$. The present paper discusses a determination of $g_J(K)/g_p$. The combination of the two results yields a value of $g_J(K)/g_J(H)=1.000016\pm0.0004$ percent, which is of a higher precision than the result of PBE and in marked disgreement with it.

A. PROCEDURE

In the experiment of KPK the ratio $g_J(H)/g_p$ was obtained by measuring a field dependent hyperfine

* This research assisted in part by the ONR.

† Submitted by Peter Franken in partial fulfillment of the requirements for the degree of Doctor of Philosophy in the Faculty of Pure Science, Columbia University.

[1] Pohlman, Bederson, and Eisinger, Phys. Rev. 83, 475 (1951).
[2] P. Kusch and H. Taub, Phys. Rev. 75, 1477 (1949).
[3] Koenig, Prodell, and Kusch, Phys. Rev. 88, 191 (1952).
[4] H. Taub and P. Kusch, Phys. Rev. 75, 1481 (1949).
[5] M. Phillips, to be published. We are grateful to Professor Phillips for several discussions relevant to this research.

TABLE I. Tabulation of data. The average of all runs is 658.2264 ±0.0023 average dev. The maximum spread in the data is 0.0098.

Date	Average $g_J(K)/g_p$	Average deviation
Sept. 25, 1951	658.2222	0.0007
Oct. 5	658.2239	0.0009
Oct. 23	658.2282	0.0009
Oct. 24	658.2238	0.0008
Oct. 25	658.2274	0.0006
Oct. 26	658.2223	0.0005
Oct. 30	658.2253	0.0006
Nov. 21	658.2212	0.0006
Nov. 26	658.2251	0.0007
Dec. 11	658.2248	0.0005
Dec. 12	658.2260	0.0010
Dec. 13	658.2294	0.0011
Dec. 17	658.2297	0.0005
Dec. 20	658.2305	0.0003
Jan. 15, 1952	658.2266	0.0009
Jan. 16	658.2268	0.0006
Jan. 19	658.2280	0.0003
Jan. 21	658.2284	0.0009
Jan. 24	658.2249	0.0012
Jan. 28	658.2310	0.0003
Feb. 19	658.2286	0.0013

structure transition in hydrogen in the same magnetic field as that in which the resonance frequency of protons in mineral oil was measured. In the present determination of $g_J(K)/g_p$ a transition was measured in potassium, rather than in hydrogen, with essentially the same apparatus and technique employed in the previous experiment. A correction for the bulk diamagnetism of the cylindrical sample of oil which was used is not critical in the present determination since it is only necessary to compare the ratio of $g_J(K)/g_p$ and $g_J(H)/g_p$ for the same sample of oil to obtain $g_J(K)/g_J(H)$.

The apparatus as described in KPK was modified for this experiment by replacing the hydrogen discharge source with a nickel oven source for potassium and substituting a tungsten hot wire detector for the Pirani gauge. Two stops were attached to the cage surrounding the rf resonant hairpin to provide the same beam height in the transition region as that provided by the aperture of the Pirani gauge in the hydrogen experiment.

The atomic transition

$$(F=2, m_F=-1)\leftrightarrow(F=2, m_F=-2)$$

was observed. The magnetic field was about 10 percent less than in the previous experiment in order that the potassium line would have the same frequency as that observed in the hydrogen experiment. This made it possible to utilize without change the Klystron oscillator, frequency measuring equipment, and resonant hairpin employed in the hydrogen experiment. The data were taken as described by KPK for the later runs on hydrogen.

To reduce the data of the experiment certain auxiliary information is required:

$$\Delta\nu(K^{39})=461.723\pm0.010 \text{ Mc}^2,$$

and $B=g_I(K)/g_p=0.0466\pm0.0002$.[6] The spin of K^{39} is $\frac{3}{2}$. The uncertainty in the value of $\Delta\nu(K^{39})$ introduces an uncertainty in the determination of $g_J(K)/g_p$ of one part in 650,000, while that in B introduces an uncertainty of less than one part in 10^7 in the result. It can readily be shown that the ratio $g_J(K)/g_p$ can be calculated in closed form from the frequency f of the atomic line and the resonance frequency P of the proton:

$$-g_J(K)/g_p=[4f(f+BP+\Delta\nu)+3BP\Delta\nu]/[P(4f+4BP+\Delta\nu)],$$

where g_p is to be interpreted as the nuclear g value of hydrogen measured in a cylindrical sample of mineral oil.

B. ANALYSIS OF DATA

The reduced data of the experiment are listed in Table I. Generally, seven sets of observations of the proton resonance frequency were made, alternating with six sets of observations of the resonance frequency of the atomic transition. The thirteen sets of observations gave twelve values of the ratio $g_J(K)/g_p$, where the magnetic field drift was assumed linear over the time required to make three sets of observations. The mean of each day's determinations together with the average deviation is given in Table I.

An inspection of Table I shows that the spread in the values of $g_J(K)/g_p$ obtained from day to day greatly exceeds the uncertainty in the result for a particular day. A comparison of Table I with the data in Table II of KPK also indicates a greater maximum spread in the results for potassium than for hydrogen. Throughout the present investigation, a continuous search was made for a systematic malfunctioning of the apparatus of the sort which might lead to approximately fixed errors on a particular day but which might vary from day to day. No evidence of such malfunctioning was found, and the apparatus did not appear to be altered in its performance from the hydrogen experiment. The proton resonance and uhf assembly was removed several times during the course of the runs and checked for possible misalignment of the interchange mechanism. Great care was exercised throughout the entire experiment to keep the assembly free of magnetic contaminants. In order to preclude the possibility that the attachment of the beam height stops to the shielding cage gave rise to an asymmetry in the uhf current distribution in the hairpin, a new hairpin was constructed of the same design but with shielding adequate to prevent the stops from perturbing the uhf distribution. The 1952 runs were taken with this new device and indicate no significant change in the dispersion of data. Finally, it is to be noted that on several occasions, runs were taken sequentially on the same day with widely differing amplitudes of the uhf field. The results of the separate runs agreed to within the

[6] H. L. Poss, unpublished Brookhaven National Laboratory report No. 26 (T-10) (1949).

uncertainty of each individual run. The wide range in the results from day to day, therefore, appears to be characteristic of some feature of the apparatus which varies from day to day and was not dependent on easily controlled experimental parameters.

It seems reasonable to attribute the large day to day variation in data to a varying homogeneity of the magnetic field. In view of the fact that detailed information on the actual field distributions could not be obtained, it is not possible to make any exact statements as to the effect of field inhomogeneities on the line shape. Resonance curves were obtained on several occasions and found to exhibit considerable assymmetry, although the field did not appear to be excessively inhomogeneous by the standards of the hydrogen experiment. It is to be noted, however, that the natural width of the potassium line (12 kc) is considerably less than the natural width of the hydrogen line (60 kc), owing to the smaller average velocity of the potassium atoms. The role of the field inhomogeneity in determining the position of the maximum of the line is evidently related to the line width, but no further conclusions can be made at this time.

The average of the seven 1952 runs is 658.2277 and that of the last six runs in 1951 is 658.2276. However, the average of the first eight runs in 1951 is 658.2243. In view of this grouping of individual runs, it is possible that the field distribution may not have varied from day to day in a random manner. In the absence of evidence concerning the actual field distributions leading to an assignment of statistical weights to the individual runs, the best value of $g_J(\mathrm{K})/g_p$ is the mean value of all the runs. In view of the uncertainty in the randomness of the field distributions, it seems doubtful that the statistical probable error (± 0.0005) is a realistic measure of the precision of the result. We have arbitrarily chosen to use as a precision measure the average deviation (± 0.0023). Then,

$$g_J(\mathrm{K})/g_p = 658.2264 \pm 0.0023,$$

where g_p is the gyromagnetic ratio of the proton as measured in a cylindrical sample of mineral oil. After correction to a measurement of the proton resonance frequency in a spherical sample of mineral oil,

$$g_J(\mathrm{K})/g_p = 658.2274 \pm 0.0023.$$

C. INTERPRETATION OF RESULT

The result of this experiment when combined with that of KPK yields

$$g_J(\mathrm{K})/g_J(\mathrm{H}) = 1.000016 \pm 0.0004 \text{ percent}.$$

This is to be compared with the recent result of PBE:

$$g_J(\mathrm{K})/g_J(\mathrm{H}) = 1.00016 \pm 0.006 \text{ percent},$$

which indicates a discrepancy in the g values ten times as great as that found in the present experiment. Two considerations indicate that the present result is more reliable:

(1) The width of the potassium line observed by PBE was one part in 4000 of their resonance frequency; in the present case a typical width was one part in 65,000 of the resonance frequency.

(2) The maximum spread of data in the PBE experiment was 260 parts in a million compared with 15 parts in a million in the present determination.

The present result can be interpreted in terms of three effects: (*a*) the relativistic behavior of the electron, (*b*) the diamagnetism of the electronic core, and (*c*) the perturbation of the potassium ground state arising from exchange interactions with excited states of the electronic core.

The effect of the relativistic behavior of the electron on its observed spin moment has been discussed by Margenau.[7] If g_s' is the spin g value of the bound valence electron and g_s that of a free electron, then $g_s' = 1+\Delta$, where $\Delta \equiv (-2T/3mc^2)$ and T is the average kinetic energy of the valence electron. Δ can be calculated exactly for hydrogen and, as shown by KPK, is equal to -18×10^{-6}. The calculation of the average kinetic energy in many electron atoms requires an approximate treatment. Lamb[8] has derived the approximation $T = 2W - W_0$, where W is the ionization potential of the atom considered and W_0 is the ionization potential of a hydrogen atom in the same electronic state. Foley[9] has compared the Lamb approximation with a numerical calculation utilizing Hartree-Foch functions in the case of sodium and has found an agreement to within four percent. The Lamb approximation yields a Δ for potassium of -10×10^{-6}. The authors place an uncertainty in this calculation of $\pm 2\times 10^{-6}$.

The correction to the observed g value in many electron atoms due to the diamagnetic polarization of the electronic core has been shown by Lamb[8] to be $g_s'/g_s = 1+\delta$, where $\delta \equiv -(T-W)/3mc^2$. The Lamb approximation for $T-W$ yields, for potassium $\delta = -2\times 10^{-6}$.

The difference in the relativistic correction for hydrogen and the relativistic and diamagnetic corrections for potassium produces, then, a shift of $(+6\pm 2)\times 10^{-6}$ in the g value of potassium relative to that of hydrogen. Since the observed shift is $(+16\pm 4)\times 10^{-6}$, there is a discrepancy of $(+10\pm 5)\times 10^{-6}$. Calculations by Phillips[5] on the perturbation of the potassium ground state by excited states of the electronic core indicate a discrepancy equal to or less than $+10^{-5}$. The result obtained in this experiment is in agreement, therefore, with the theoretical estimate.

The authors would like to take this opportunity to express their gratitude to Professor P. Kusch, who proposed the measurement and who gave constant guidance and encouragement throughout the experiment.

[7] H. Margenau, Phys. Rev. **57**, 383 (1940).
[8] W. E. Lamb, Jr., Phys. Rev. **60**, 817 (1941).
[9] H. M. Foley (private communication).

Perturbations of Atomic g Values

M. PHILLIPS
Brooklyn College, Brooklyn, New York
(Received June 25, 1952)

A further investigation of the perturbation by excited core states of gyromagnetic ratios for atoms consisting of a single electron outside closed shells takes account of the spin orbit interaction of the excited core. Although the effect vanishes to lower orders than the fourth, and at least the first term in the expansion of the electrostatic interconfiguration interaction cancels even in that order, there is for alkali atoms a residual correction possibly large enough to account for observed deviations of g values from those expected. Calculations have also been made for ^2P states: The effect in gallium is negligible, but the anomalous observed $g_J(P_{3/2})/g_J(P_{1/2})$ for indium may be at least in part due to perturbations of this kind.

INTRODUCTION

EARLIER discrepancies between experimental and theoretically expected values of atomic gyromagnetic ratios have been mainly resolved by the recognition of the anomalous "intrinsic" magnetic moment of the electron due to radiation reaction.[1-3] More recent[4] calculations of this effect give g for an electron in an s state as $2(1+0.001145)$. Further improvements in experimental technique have made possible a high precision test of the computed value of the anomalous moment,[5] but have also made it necessary to examine all possible factors affecting atomic g values. Variations of these values among the alkalis,[6] and of the ratio of $g(^2P_{3/2})/g(^2P_{1/2})$ for atoms like gallium and indium,[7] while small in comparison to the radiation reaction effect, are not predicted by the quantum electrodynamics. In particular, the observed ground-state g values of cesium and rubidium differ by 13 parts in 10^6 and 5 parts in 10^6, respectively, from that for sodium. The most recently reported g_J value for potassium[8] is greater than the corresponding value for hydrogen by about 1 part in 10^6. The possibility always exists that the atomic gyromagnetic ratio may be affected by interconfiguration interaction with excited core levels for atoms other than hydrogen. The present extension of the perturbation calculation indicates that the perturbations do increase with atomic number, and are of the order of magnitude of the observed discrepancies.

It was previously shown[9] that electrostatic interaction of a one-electron configuration with excited core states, responsible for perturbations of the energies and doublet separations of alkali spectra, does not directly affect the magnetic g values, since it mixes only those states having the same total orbital angular momentum and spin, and therefore the same gyromagnetic ratio. All other interconfiguration interactions are genuinely small. But the excited core states themselves do not exhibit Russell Saunders coupling for the same reason that the rare gases do not: The parameter comparable in magnitude to the electrostatic energy differences is the spin orbit interaction energy of the incomplete core, which gives rise to separations corresponding to that of a high-lying x-ray doublet. Our purpose here is to extend the perturbation calculation to sufficiently high orders that the effect on the g value of the ground state does not vanish.

A consistent fourth-order perturbation calculation is necessary, since the effect vanishes to lower orders. It will be shown later that is is necessary to write the perturbed ground-state wave function only to second order:

$$\psi=\psi_0+\sum_i \frac{V_{0i}}{E_{0i}}\psi_i+\sum_{i,k}\frac{V_{0i}\xi_{ik}}{E_{0i}E_{0k}}\psi_k. \qquad (1)$$

Here ψ_i and ψ_k represent states of the excited core configuration having the same total angular momentum as the ground state, V_{0i} is the nondiagonal electrostatic interaction mixing the ground state and the ith level of the excited core configuration, and ξ_{ik} is the matrix element of the spin orbit interaction between states i and k. We need to consider only the spin orbit interaction for the "hole" in the core, since that for any external electron is negligibly small. The required g value is then found by evaluating the matrix element of $\mathbf{L}+2\mathbf{S}=\mathbf{J}+\mathbf{S}$ with the use of the wave function ψ appropriate to the particular atom under consideration.

ALKALI GROUND STATES

The excited configurations to be considered in the case of alkali atoms are those in which one electron from the last (closed) p shell is excited to a higher p level, i.e., configurations of the kind $(np)^5(n_0s)(n'p)$, where the total quantum number n is n_0-1, and n' is equal to or greater than n_0, the total quantum number of the s valence electron. The energy denominators corresponding to the excitation of electrons lying deeper in the core are very large, and since parity must be preserved the orbital angular momentum of the excited

[1] P. Kusch and H. M. Foley, Phys. Rev. **72**, 1256 (1947); **73**, 412 (1948).
[2] P. Kusch and H. M. Foley, Phys. Rev. **74**, 250 (1948).
[3] J. Schwinger, Phys. Rev. **73**, 416 (1948).
[4] R. Karplus and N. Kroll, Phys. Rev. **77**, 536 (1950).
[5] Koenig, Prodell, and Kusch, Phys. Rev. **83**, 687 (1951).
[6] P. Kusch and H. Taub, Phys. Rev. **75**, 1477 (1949).
[7] A. K. Mann and P. Kusch, Phys. Rev. **77**, 435 (1950).
[8] P. Franken and S. Koenig, Phys. Rev. **88**, 199 (1952).
[9] M. Phillips, Phys. Rev. **60**, 100 (1941).

electron must remain odd. This does not rule out the possibility of virtual transitions to $n'f$, when such orbits are available, but these terms also have larger excitation energies and their wave functions do not appreciably overlap those of the core. The configuration of interest, indicated above, contains six states with $J=1/2$ and thus possibly are capable of affecting the ground state.

In a consistent perturbation calculation the result is independent of the detailed coupling assumed for the perturbing states, but it is instructive to consider two different coupling schemes. Each of the two schemes makes the states diagonal with respect to one set of parameters at the expense of the other. For example, LS coupling makes both V_{0i} and $\mathbf{J}+\mathbf{S}$ diagonal, but ξ_{ik} connects states within the excited configuration that differ in L and S by at most one unit each. We shall consider this scheme first.

The two external electrons, n_0s and $n'p$, may be coupled to form the parent states ^1P and ^3P, which when combined with the incomplete core yield $^2S(^1P)$, $^2S(^3P)$, $^2P(^1P)$, $^2P(^3P)$, $^4P(^3P)$, $^4D(^3P)$, all with $J=1/2$. (The parent terms are indicated in parentheses.) The electrostatic interaction V_{0i} with the configuration $(np)^6(n_0s)$ is then very simple, the sum extending over only the two ^2S states. In fact,

$$\sum_i V_{0i}\psi_i=\tfrac{1}{2}\{(F_0+G_1)\psi_1+\sqrt{3}(F_0-G_1)\psi_2\}, \qquad (2)$$

where ψ_1 is the wave function for $^2S(^1P)$ and ψ_2 that for $^2S(^3P)$. The argument of the direct and exchange radial integrals[10] F_0 and G_1 is $(n_0s, np:n_0s, n'p)$, i.e., the electrostatic interaction refers to the valence electron and the "jumping" p electron. Turning now to the spin orbit interaction: ξ_{ik} has matrix elements connecting $^2S(^1P)$ with $^2P(^1P)$, and $^2S(^3P)$ with $^2P(^3P)$ and $^4P(^3P)$, thus introducing the possibility of foreign g values. The matrix elements of ξ_{ik} may be computed directly from the state wave functions, or by use of the properties of angular momentum matrices according to rules given by C&S, p. 266 ff. They are

$$\begin{aligned}(^2S(^1P):\xi:{}^2P(^1P))&=(1/\sqrt{2})\zeta(np),\\ (^2S(^3P):\xi:{}^2P(^3P))&=(1/3\sqrt{2})\zeta(np),\\ (^2S(^3P):\xi:{}^4P(^3P))&=(2/3)\zeta(np),\end{aligned} \qquad (3)$$

where $\zeta(np)$ is the spin orbit parameter of the "hole" in the incomplete p shell.

In this coupling scheme it is easy to see that the value of $\mathbf{J}+\mathbf{S}$ for the ground state remains unaffected in first, second, and third order, since $\mathbf{J}$ is the same for all states and the matrix for $\mathbf{S}$ is diagonal. It may also be seen that one obtains the whole of the fourth-order correction from the second-order term in the wave function, for the same reason. In the fourth order the contribution to the gyromagnetic ratio of the ground state may be found by evaluating

$$\Delta g=\sum_{i,k}\frac{V_{0i}^2\xi_{ik}^2\Delta g_k}{E_{0i}^2E_{0k}^2}, \qquad (4)$$

where the use of $\Delta g_k=g_k-g_0$ automatically takes care of normalization. Since $g_J(^2P_{1/2})=2/3$ and $g_J(^4P_{1/2})=8/3$, and it is permissible to neglect differences in the energy denominators, the substitution of (2) and (3) gives

$$\Delta g=-\tfrac{4}{9}F_0G_1\zeta^2(np)/E^4. \qquad (5)$$

Whether this correction corresponds to a depression or an elevation of the ground-state g value depends on the relative signs of the direct and exchange electrostatic interaction integrals F_0 and G_1, since both square terms cancel. A knowledge of configuration interaction would be necessary in order to ascertain the values of these integrals directly from spectroscopic data, and even the answer to the question of relative sign cannot be predicted in all cases with absolute certainty. Approximations based on plotting reasonable wave functions for the heavier alkalis, however, indicate that the F_0 and G_1 appearing in (5) are always unlike in sign; and for atoms of lower atomic number, where similar integrals have been evaluated more carefully,[11] the signs have indeed been opposite. It therefore seems safe to conclude that the effect of the perturbation is to raise the ground-state g value by an amount depending on the absolute values of the parameters involved.

With the exception of the electrostatic integrals these parameters may be reliably estimated from spectroscopic data. The energy levels of the rare gas atom having the same electronic configuration as the core of the alkali atom in question yield values of ζ and E, both somewhat too small. The ratio of ζ/E will be appreciably larger for the alkali, however, since ζ varies as the fourth power of the effective nuclear charge and the excitation energy only as Z_{eff}^2. The core doublet separation associated with $\zeta(np)$ increases rapidly with atomic number: $\zeta(np)$ is about 514 cm^{-1} for Ne, 954 for A, 3600 for Kr, and 7100 for Xe. Examination of the data[12] gives a basis for reasonable estimates of ζ/E as follows: 1/200 for Na, 1/70 for K, 1/20 for Rb, and 1/10 for Cs. The excitation potential decreases as one goes to higher atomic number, but so slowly that the ratio ζ/E rises rapidly.

For a rough approximation to the values of F_0 and G_1 one may conclude that the maximum value of F_0 is not likely to be more than one-third to one-half of the average of the diagonal integrals $F_0(np, n_0s)$ and $F_0(n'p, n_0s)$, while the exchange integral G_1 could be nearly equal to the corresponding diagonal value for

[10] E. U. Condon and G. H. Shortley, *The Theory of Atomic Spectra* (Cambridge University Press, Cambridge, 1951), p. 174 ff. This important reference will be referred to hereafter as C&S.

[11] See, e.g., M. Phillips, Phys. Rev. 44, 644 (1933).

[12] C. E. Moore, *Atomic Energy Levels*, Vol. 1, National Bureau of Standards Circular No. 467 (1948), ends with data for $Z=23$. For higher Z no papers consulted show surprising differences from relevant data available systemmatically in R. F. Bacher and S. Goudsmit, *Atomic Energy States* (McGraw-Hill Book Company, Inc., New York, 1932).

electrons within either configuration. The analysis of appropriate spectra for values of these last integrals has been made.[13] Their trend with atomic number, relative to the excitation energy, is opposite to that of ζ/E, decreasing as one goes to heavier atoms, although slowly. For Cs the F_0G_1/E^2 appearing in (5) could hardly be greater than 1/200 for the lowest value of n', and would fall off rather rapidly with increasing n'. Since E increases only very slowly with n', however, and ζ is constant, it is probable that the contributions from all higher excited p orbits amount to at least as much as the first, so that the total Δg for Cs may be as much as 6 or 8 parts in 10^5. It is not possible to rule out surprisingly large F_0 and G_1, and thus the possibility exists that the observed discrepancy may be entirely due to this effect.

For potassium, on the other hand, ζ^2/E^2 is already small, 2 parts in 10,000. If F_0G_1/E^2 is fifty times larger for the first excited p orbit, which seems a reasonable estimate from spectroscopic data and known configuration interactions in this neighborhood, g would be affected by only a few parts in 10^6. This estimate could easily be too small, but more than one part in 10^5 seems out of the question. For sodium the effect of perturbations is still smaller than for potassium. For rubidium we would expect about one-third the perturbation found in cesium.

The whole problem may be set up quite differently, by considering the j of the incomplete shell as a good quantum member and coupling this $j=1/2$, $3/2$ separately to the external $(n_0s)(n'p)$ combination. This scheme is a closer approximation to the actual physical situation, especially for atoms of high atomic number, where the states of any configuration involving an incomplete shell are grouped in two sets corresponding to the two members of the parent doublet. The calculation has been carried out in this way, to check the method. The complications which arise are due to the fact that while $\xi(np)$ is now diagonal all six $J=1/2$ states are mixed with the zero-order ground state by the electrostatic interaction, and cross terms in $\mathbf{J}+\mathbf{S}$ arise. The final answer is just that given by (5).

PERTURBATIONS OF ^2P g VALUES

For atoms like gallium, indium, and thallium, with ground-state configuration $(n_0s)^2(n_0p)$, virtual excitation of the highest filled d shell gives most promise of affecting the g values associated with the two members of the ^2P. The excitation energy of any deep-lying p electron is very large, and s electron excitation does not affect the magnetic moment because it furnishes no parent doublet. The parity limitation permits excitation of a d electron to higher d and unfilled s orbits, but investigation shows so much angular interference in the computation of the electrostatic matrix elements for the latter case that it suffices to consider excited configurations $(nd)^9(n_0p)(n'd)$, $n'\geqslant n_0$.

Again the assumption of LS coupling provides the simplest method of describing the perturbation. Six ^2P states occur in the excited configuration, which may be ascribed to parent terms of the $(n_0p)(n'd)$ combination, ^1P, ^3P, ^1D, ^3D, ^1F, ^3F, coupled with the incomplete core shell $(nd)^9$. The wave function for the ground state of the unexcited atom can be represented as a linear combination of the wave functions for these six states if n' is read as n, a device that simplifies the computation of the electrostatic interaction energy:

$$\psi_0=\frac{1}{2\sqrt{30}}\{-\sqrt{6}\psi(^1P)-3\sqrt{2}\psi(^3P)+\sqrt{10}\psi(^1D)$$
$$+\sqrt{30}\psi(^3D)+\sqrt{14}\psi(^1F)+\sqrt{42}\psi(^3F)\}. \quad (6)$$

Here each ψ is formally the wave function associated with the particular ^3P level of the excited state for which the two-electron parent term is indicated in parentheses. The cancellation of zero-order single electron product functions (antisymmetrized) is such that the sum is compatible with the exclusion principle applied to a closed d shell. The electrostatic interaction between the ground state and any one ^2P of the excited configuration has the same form as that of its $(n_0p)(n'd)$ parent, since just these two electrons are involved, although in the interpretation of each radial integral it must be remembered that the d electron is not diagonal with respect to its total quantum number. There are four terms in the expansion of the electrostatic interaction, but their coefficients may be readily calculated and are, in fact, just those given on p. 200, C&S. These expressions must be multiplied by the appropriate coefficient in ψ_0 as given by (6) to yield a particular V_{0i}.

All that is now needed is the matrix of ξ_{ik} connecting the ^2P states of the excited configuration with neighboring states of different L and S. In this calculation the two terms of the doublet must be considered separately: For $^2P_{3/2}$ there are in all thirteen combining states, whereas only eight states combine with various $^2P_{1/2}$ levels. The values of these matrix elements are given in the appendix, together with the substitution in the expression for Δg.

The final result shows that the largest terms cancel much more completely for the ground state $^2P_{1/2}$ than for the alkali atom ground states. Not only does the coefficient of F_0^2 vanish, but so do those of all cross terms involving F_0. The leading term that remains, in G_1^2, has a negative sign, so that $g_J(^2P_{1/2})$ may be very slightly depressed. In considering G_1, F_2, etc., it must be noted that these symbols already include the denominators resulting from the angular integration, i.e., $G_1=G^1/15$, $F_2=F^2/35$, $G_3=G^3/245$, where G^1, F^2 and G^3 are radial integrals. For the $^2F_{3/2}$ level, however,

[13] E. U. Condon and G. H. Shortley, Phys. Rev. 35, 1342 (1930).

F_0^2 and F_0F_2 have zero coefficients, but F_0G_1 does not:

$$g_J(^2P_{3/2}) = -\tfrac{3}{5}\, F_0G_1\zeta^2(nd)/E^4, \tag{7}$$

in addition to smaller terms. It thus appears that the ratio $g_J(^2P_{3/2})/g_J(^2P_{1/2})$ may be perceptibly perturbed as a result of the perturbation of $g_J(^2P_{3/2})$.

Considerations analogous to those for alkali atoms lead only to very rough quantitative estimates of the effects of these perturbations. The positions of the nodes in the radial wave functions make it highly probable that F_0 and G_1 are opposite in sign, so that the value of $g_J(^2P_{3/2})$ is increased. The spectroscopic data on neighboring metallic ions show that ζ/E again increases markedly with atomic number. (ζ is 2/5 the energy separation of the ^2D associated with $(nd)^9$.) Reasonable estimates $(\zeta/E)^2$ are $16/10^4$ for gallium, 4/100 for indium, 12/100 for thallium. Numerical values of the electrostatic energy parameters, however, are considerably less certain than in the case of the alkalis: The related spectra are much more complicated, with repeated spectral terms of the same character, so that identification of levels with those calculated is almost impossible. In other words, not even the diagonal electrostatic integrals are well known. Nevertheless, it is apparent that the effect would be too small to observe easily in gallium. While the perturbation is greater for indium, the observed discrepancy in the indium ratio seems somewhat too large to be accounted for in this way, if the parameters vary smoothly with atomic number. A check would be furnished by measurements on the thallium ratio, where Δg given by (7) or (10) should be about five times as great as in indium.

APPENDIX

The matrix elements of the incomplete core spin orbit interaction between ^2P states of the excited configuration $(nd)^9(n_0p)(n'd)$ and other states of the same configuration are given below. The $(n_0p)(n'd)$ parent term must be the same for two states in order that ξ_{ik} not vanish, and it is indicated only in the specification of ^2P. The corresponding Δg_k appears on the right.

		Δg_k
$J=3/2$	$(^2P(^1P):\xi:{}^2D) = \frac{3}{4}\zeta(nd)$,	$-8/15$
	$(^2P(^1D):\xi:{}^2D) = \frac{1}{4}\sqrt{21}$	$-8/15$
	$(^2P(^1F):\xi:{}^2D) = \sqrt{(3/2)}$	$-8/15$
	$(^2P(^3P):\xi:{}^2D) = \frac{1}{4}$	$-8/15$
	$(^2P(^3P):\xi:{}^4P) = \frac{1}{2}\sqrt{5}$	$6/15$
	$(^2P(^3P):\xi:{}^4D) = \frac{1}{2}$	$-2/15$
	$(^2P(^3D):\xi:{}^2D) = \frac{1}{4}\sqrt{(7/3)}$	$-8/15$
	$(^2P(^3D):\xi:{}^4S) = \sqrt{(2/3)}$	$2/3$
	$(^2P(^3D):\xi:{}^4P) = \frac{1}{4}\sqrt{5}$	$6/15$
	$(^2P(^3D):\xi:{}^4D) = \frac{1}{2}\sqrt{(7/3)}$	$-2/15$
	$(^2P(^3F):\xi:{}^2D) = 1/\sqrt{6}$	$-8/15$
	$(^2P(^3F):\xi:{}^4P) = -\frac{1}{4}\sqrt{5}$	$6/15$
	$(^2P(^3F):\xi:{}^4D) = \sqrt{(2/3)}$	$-2/15$
$J=1/2$	$(^2P(^1D):\xi:{}^2S) = \sqrt{(3/2)}\zeta(nd)$	$4/3$
	$(^2P(^3P):\xi:{}^4P) = -1/\sqrt{2}$	2
	$(^2P(^3P):\xi:{}^4D) = 1/\sqrt{2}$	$-2/3$
	$(^2P(^3D):\xi:{}^2S) = -1/\sqrt{6}$	$4/3$
	$(^2P(^3D):\xi:{}^4P) = -1/3\sqrt{2}$	2
	$(^2P(^3D):\xi:{}^4D) = \sqrt{(7/6)}$	$-2/3$
	$(^2P(^3F):\xi:{}^4P) = \frac{1}{3}\sqrt{2}$	2
	$(^2P(^3F):\xi:{}^4D) = 2/\sqrt{3}$	$-2/3$

With these values and those for V_{0i} the perturbation of g_J is immediately available.

$$\Delta g_J(^2P_{1/2}) = (-5G_1^2 + 14F_2G_1)\zeta^2/E^4, \tag{8}$$

plus terms in F_2^2 and smaller. To a similar approximation

$$\Delta g_J(^2P_{3/2}) = (-0.6F_0G_1 - 2.5G_1^2)\zeta^2/E^4. \tag{9}$$

The first two terms in the correction of the ratio are

$$\Delta g_J(^2P_{3/2})/g_J(^2P_{1/2}) = (-0.6F_0G_1 + 2.5G_1^2)\zeta^2/E^4. \tag{10}$$

Ionization Chamber Measurements of the Absorption of the *N*-Component of Cosmic Rays in Lead*

H. S. Bridge and R. H. Rediker
Department of Physics and Laboratory for Nuclear Science and Engineering, Massachusetts Institute of Technology, Cambridge, Massachusetts
(Received May 15, 1952)

A detecting system that responds only to ionization bursts produced by nuclear interactions of the so-called *N*-component of cosmic radiation is described. The burst rate observed with this detector has been measured as a function of the thickness of lead absorber above the system at sea level and at 10,600 feet.

The absorption of the *N*-component in lead cannot be represented by an exponential variation of the intensity with absorber thickness; instead the "absorption curve" shows an initial increase in intensity. This behavior may be explained by the assumption that π-mesons with energies of several Bev, which are produced in the nuclear interactions, can give rise to further nuclear interactions.

From the altitude variation of the smallest recorded bursts produced by the *N*-component, one finds a value of 119 ± 5 g cm^{-2} for the absorption thickness of the producing radiation in air. The absorption thickness decreases with increasing energy of the nuclear event detected.

In the same experiment, other kinds of events were also recorded, which could be produced either by *N*-rays or by μ-mesons. The bursts produced by these two components were separated on the basis of the experimental altitude variation of *N*-rays and of the computed altitude variation of the μ-meson induced bursts. For our particular ionization chamber about 50 percent of the bursts at sea level produced by charged particles incident on the 219 g cm^{-2} lead ionization chamber shield were caused by μ-mesons and 50 percent by the *N*-component.

I. INTRODUCTION

THE results reported in this paper were obtained in a continuation of previous experiments[1–5] performed with a lead-shielded ionization chamber and an array of Geiger-Mueller counters above the lead shield. The time coincident pulses of the ionization chamber and of the Geiger counters recorded the arrival of penetrating ionizing particles which could produce ionization bursts below the lead shield. Measurements with this type of detector established the variation of the ionization burst rate with altitude and led to the conclusion that at airplane altitudes most of the observed bursts arise from nuclear interactions of the so-called *N*-component, while at sea level most of the bursts arise from electromagnetic interactions of μ-mesons.[4] From measurements made at 14,300 feet, the absorption of the burst-producing radiation in lead turned out to be much greater than that of the penetrating component of cosmic rays, but smaller than that corresponding to the geometric cross section of the lead nuclei.

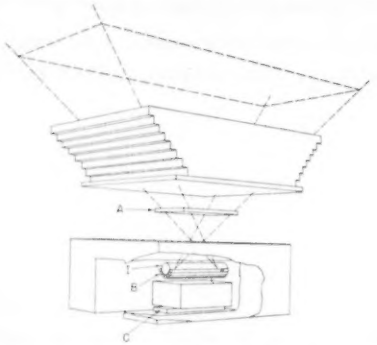

FIG. 1(a). Perspective view of experimental arrangement showing full 455 g cm^{-2} lead absorber as stacked at sea level. For greater clarity the 57 g cm^{-2} of lead in Σ' have been omitted.

As stated above the bursts observed in the ionization chamber are caused either by μ-mesons or nucleons which interact in the shielding material above the chamber. While the first case is well understood, the processes by which nuclear interactions produce ionization bursts are only understood qualitatively. All the charged products contribute to the total ionization but the relative contributions from different products are unknown. However, at energies of several Bev the ionization caused by electron cascades is important. Probably these cascades originate from the decay photons of neutral π-mesons.

Under the assumption that all bursts result from electron cascades initiated by single electrons or photons, a detector such as that described above has some important properties. For a given number of electrons at the chamber there corresponds a minimum initiating energy at a unique position in the shield above the chamber. For our detector the absolute minimum energy transfer required is 3.2 Bev and occurs 48 g cm^{-2} of lead above the chamber.[6] Because

* This work was supported in part by the joint program of the ONR and AEC.

[1] Bridge, Rossi, and Williams, Phys. Rev. **72**, 257 (1947).
[2] Bridge, Hazen, and Rossi, Phys. Rev. **73**, 179 (1948).
[3] Bridge, Hazen, Rossi, and Williams, Phys. Rev. **74**, 1083 (1948).
[4] H. Bridge and B. Rossi, Phys. Rev. **75**, 810 (1949).
[5] McMahon, Rossi, and Burditt, Phys. Rev. **80**, 157 (1950).

[6] These values are obtained from the computations of J. Belenky, J. Phys. (U.S.S.R.) **8**, 305 (1944). The smallest detected burst corresponded to 16 electrons of 10 Mev passing through the chamber perpendicular to its axis. Since many of the electrons in the electronic cascade in the lead are scattered at large angles, sixteen electrons passing through the chamber has been assumed to correspond to a shower of 32 electrons in the lead directly above the chamber. See the appendix for a discussion of the validity of this assumption.

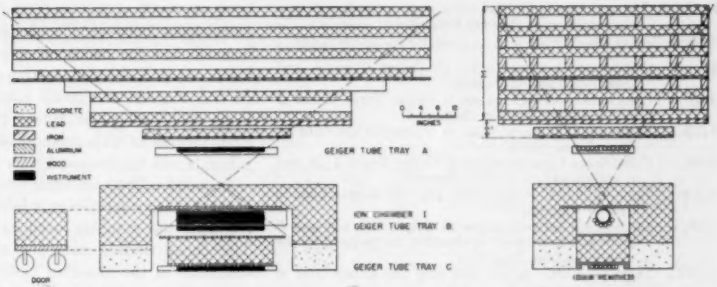

FIG. 1(b). Side and front views of experimental arrangement showing the full 341 g cm^{-2} lead absorber as stacked at 10,600 feet.

the main contribution to the shower rate comes from the lowest energy transfers that can produce the observed effects, the interactions responsible for the ionization bursts are localized mainly in this vicinity.[7] This is important if it is desirable to define a zero thickness of absorber.

In the present experiment, performed at sea level and at 10,600 feet, we have attempted to separate the bursts produced by μ-mesons (to be called μ-bursts) from those produced by the N-component (to be called N-bursts). We have made more accurate measurements of the absorption in air and in lead of the burst-producing radiation and have also tried to determine the collision mean free path for the N-component in lead.

II. EXPERIMENTAL ARRANGEMENT

The experimental arrangement is shown in Fig. 1. The ionization chamber, i, was of the type described previously.[3] It had a diameter of 7.5 cm and an effective length of 52 cm. The chamber used at sea level was filled with purified argon at 7.3 atmospheres (25°C) and contained a fixed source of polonium α-particles placed near the inner surface of the cylindrical wall. The chamber used at 10,600 feet was similar physically but was filled with argon at 7.1 atmospheres (25°C) and contained a removable source of polonium α-particles placed near the inner surface of the cylindrical wall. Tests comparing the counting rates of the two chambers for electron showers showed that for the same number of electrons traversing the chamber the pulses of the chamber used at sea level were 10 percent greater than those of the chamber used at 10,600 feet. The minimum pulse height required from the chambers was 0.3 times that of an α-particle pulse.

A tray of Geiger-Mueller counters, A, was placed above the ionization chamber and was separated from it by 142 g cm^{-2} of lead. This lead served as the producing layer for most of the bursts observed in the ionization chamber. Immediately below the chamber there was a second tray of counters, B. Below tray B and separated from it by 171 g cm^{-2} of lead there was a third tray of counters, C. All counters had diameters of 2.5 cm and effective lengths of 51 cm.

Above tray A one could place an absorber Σ' consisting of 57 g cm^{-2} of lead and 20 g cm^{-2} of iron. Above Σ' one could stack different thicknesses of lead to form the absorber Σ. At sea level the lead in Σ was stacked solid as shown in Fig. 1(a). At 10,600 feet, however, wooden spacers were placed between the layers in lead in Σ as shown in Fig. 1(b). This arrangement facilitated the comparison between absorption measurements in lead and absorption measurements in carbon. The latter will be described in a subsequent paper.

A block diagram of the electronic circuits as used at 10,600 feet is shown in Fig. 2. An electronic discriminator selected pulses of different heights from the

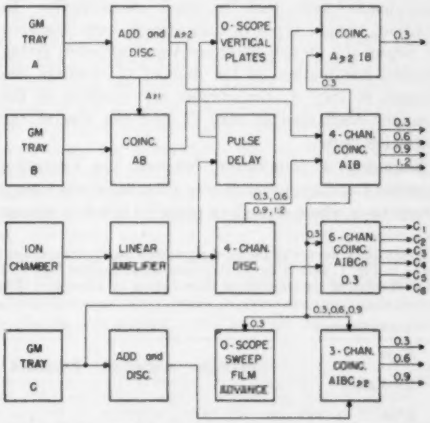

FIG. 2. Simplified block diagram of the equipment. The signal level of the ionization chamber pulse is indicated at appropriate points. Pulse-height discriminators are shown by the abbreviation DISC. Only the more important coincidence outputs which were connected to the Esterline-Angus recorder are given. Pulse shaping circuits are not shown, but all pulses were shaped to be rectangular and 20 μ-seconds wide. At sea level it was not possible to determine whether more than one tube in tray A was discharged but only whether one or both halves of the tray were struck.

[7] See appendix.

TABLE I. The coincidences whose rates were investigated as a function of absorber thickness.

AI	Coincidence between pulse in Geiger Tray A and ionization burst in chamber.
AIB	Coincidence between pulses in Geiger Trays A and B and ionization burst in chamber.
A_1IB	Same as AIB except that only one Geiger tube in Tray A was struck.
$AIBC$	Coincidence between pulses in Geiger Trays A, B, and C and ionization burst in chamber.
A_1IBC	Same as $AIBC$ except that only one Geiger tube in Tray A was struck.
$AIBC_0$	Coincidence between pulses in Geiger Trays A and B and ionization burst in chamber, in anticoincidence with pulse from Tray C.
A_1IBC_0	Same as $AIBC_0$ except that only one Geiger tube in Tray A was struck.
$AIBC_1$	Same as $AIBC$ except that only one Geiger tube in Tray C was struck.
A_1IBC_1	Same as $AIBC$ except that only one Geiger tube in each of the Trays A and C were struck.
$AIBC_2$	Same as $AIBC$ except that at least two Geiger tubes in Tray C were struck (denoted by $AIBC_{\geq 2}$ in the figures).
A_1IBC_2	Same as $AIBC$ except that at least two Geiger tubes in Tray C were struck and only one Geiger tube in Tray A was struck (denoted by $A_1IBC_{\geq 2}$ in the figures).

The size of voltage pulses from the ionization chamber is given in terms of the voltage pulse caused by a polonium α-particle (5.30 Mev) near the wall of the chamber. The relative size is indicated by the subscript following I. I_m means the voltage due to the ionization burst was larger than m times the pulse due to the polonium α-particle.

ionization chamber and addition circuits followed by pulse-height discriminators selected events where more than certain predetermined numbers of counters in individual trays were discharged. Various types of coincidences were then recorded electronically. In addition, certain types of coincidences were analyzed by means of a 20-pen Esterline-Angus recorder, giving detailed information on the number of counters discharged in tray A, the number and position of the counters discharged in tray C, and the size of the ionization burst.

Requiring a coincidence between the ionization chamber I and a counter in tray B excluded low energy interactions whose secondary particles failed to emerge from the wall of the ionization chamber. Requiring a coincidence between I and more than one C counter insured that the event causing the ionization burst in I was one in which penetrating particles were produced. In this manner one could eliminate showers resulting from electromagnetic interactions of μ-mesons. The effectiveness of this method of discrimination against μ-bursts will be discussed later in more detail.

In what follows we shall concern ourselves with the various categories of events listed in Table I, which also contains the symbols used to describe these events. The corresponding counting rates were measured as functions of the absorber thickness above tray A and as functions of the height of the pulses from the ionization chamber. In order to take more extensive data at 10,600 feet, slight changes were made in the equipment between the sea level and the high altitude runs.

III. RESULTS

1. Summary of Experimental Data

The most significant results obtained at sea level with the experimental arrangement shown in Fig. 1(a) are summarized in Table II. Similarly, Table III contains the results obtained at 10,600 feet with the experimental arrangement shown in Fig. 1(b).[8] The counting rates shown in these tables have been corrected for accidental electronic coincidences, and also for the overlap of pen marks on the recording tape of the Esterline-Angus recorder. Both these corrections are of the order of one percent and tend to cancel since they are of opposite sign.

2. Comparison with Previous Results

The altitude variation and the absorption in lead obtained in the present measurements may be compared with previous results from similar experiments. Table IV shows the coincidence rates involving $I_{0.3}$ pulses (i.e., pulses of the ionization chamber greater than 0.3 times an α-particle pulse) observed at sea level and at 10,600 feet with Σ' alone above the chamber. A cor-

TABLE II. Summary of the most significant hourly coincidence rates obtained at sea level by means of the experimental arrangement shown in Fig. 1, with different absorbers above counter tray A. The absorber Σ' consisted of 20 g cm^{-2} of iron plus 57 g cm^{-2} of lead. The reduction of the coincidence rates caused by absorption in 455 g cm^{-2} lead is shown.

	Coincidence event	$AI_{0.1}$	$AI_{0.1}B$	$AI_{0.1}BC_0$	$AI_{0.1}BC_1$	$AI_{0.1}BC_2$	$AI_{0.4}$	$AI_{0.4}B$	$AI_{1.1}$
(a)	Σ' on $\Sigma=0$ g cm^{-2}	2.19±0.06	1.82±0.05	0.99±0.04	0.53±0.03	0.30 ±0.02	0.61±0.03	0.52±0.03	0.21±0.02
(b)	Σ' on $\Sigma=455$ g cm^{-2} Pb	1.38±0.04	1.21±0.03	0.70±0.03	0.38±0.02	0.135±0.01	0.39±0.03	0.36±0.02	0.15±0.01
	Ratio of (b) to (a)	0.64±0.02	0.67±0.02	0.78±0.04	0.72±0.06	0.45 ±0.04	0.65±0.04	0.69±0.06	0.72±0.08

[8] As indicated above, the two experimental arrangements were identical except for the method of stacking the lead in the absorber Σ and the slightly different pressures in the ionization chambers.

TABLE III. Summary of the most significant hourly coincidence rates obtained at 10,600 feet by means of the experimental arrangement shown in Fig. 1, with different absorbers above counter tray A. The absorber Σ' consisted of 20 g cm^{-2} of iron plus 57 g cm^{-2} of lead.

Absorber	Ion chamber pulse size	$A1B$	$A_1 1B$	$A1BC_0$	$A_1 1BC_0$	$A1BC_1$	$A_1 1BC_1$	$A1BC_2$	$A_1 1BC_2$
Σ' off									
Σ 0 g cm^{-2}	$I_{0.3}$	12.25 ±0.45	9.92 ±0.40	6.80 ±0.33	6.00 ±0.30	2.37 ±0.19	1.85 ±0.18	3.08 ±0.21	1.90 ±0.17
	$I_{0.6}$	4.62 ±0.26	3.17 ±0.21	2.40 ±0.19	2.11 ±0.18	0.77 ±0.11	0.68 ±0.10	1.63 ±0.16	0.88 ±0.12
	$I_{0.9}$	2.74 ±0.21	2.10 ±0.18	1.32 ±0.14	1.22 ±0.14	0.32 ±0.07	0.27 ±0.06	1.11 ±0.13	0.61 ±0.10
	$I_{1.2}$	1.72 ±0.16	1.31 ±0.14	0.80 ±0.11	0.74 ±0.11	0.20 ±0.06	0.15 ±0.05	0.72 ±0.10	0.41 ±0.08
Σ' on									
Σ 0 g cm^{-2}	$I_{0.3}$	12.75 ±0.23	7.80 ±0.18	6.27 ±0.16	4.57 ±0.14	2.60 ±0.10	1.64 ±0.08	3.88 ±0.12	1.59 ±0.08
	$I_{0.6}$	4.93 ±0.15	2.85 ±0.12	2.15 ±0.10	1.53 ±0.08	0.809 ±0.059	0.544 ±0.049	1.96 ±0.09	0.774 ±0.058
	$I_{0.9}$	2.93 ±0.11	1.59 ±0.08	1.17 ±0.07	0.832 ±0.058	0.480 ±0.044	0.31 ±0.04	1.26 ±0.07	0.450 ±0.042
	$I_{1.2}$	1.91 ±0.09	0.977 ±0.063	0.702 ±0.053	0.507 ±0.045	0.28 ±0.03	0.16 ±0.03	0.930 ±0.06	0.31 ±0.04
Σ' on									
Σ = 114 g cm^{-2} Pb	$I_{0.3}$	10.05 ±0.23	5.24 ±0.17	4.61 ±0.15	2.92 ±0.12	2.20 ±0.11	1.31 ±0.08	3.24 ±0.13	1.01 ±0.07
	$I_{0.6}$	3.82 ±0.15	1.84 ±0.10	1.48 ±0.09	0.92 ±0.07	0.73 ±0.07	0.46 ±0.05	1.61 ±0.10	0.47 ±0.05
	$I_{0.9}$	2.21 ±0.11	1.02 ±0.08	0.90 ±0.07	0.55 ±0.06	0.33 ±0.04	0.21 ±0.04	0.99 ±0.08	0.28 ±0.04
	$I_{1.2}$	1.39 ±0.09	0.62 ±0.06	0.50 ±0.05	0.30 ±0.04	0.19 ±0.03	0.12 ±0.03	0.69 ±0.06	0.21 ±0.04
Σ' on									
Σ = 341 g cm^{-2} Pb	$I_{0.3}$	5.28 ±0.15	2.51 ±0.11	2.15 ±0.10	1.36 ±0.08	1.21 ±0.07	0.687 ±0.054	1.93 ±0.09	0.467 ±0.044
	$I_{0.6}$	2.16 ±0.10	0.932 ±0.061	0.787 ±0.058	0.452 ±0.044	0.42 ±0.04	0.24 ±0.03	0.963 ±0.064	0.24 ±0.03
	$I_{0.9}$	1.24 ±0.07	0.523 ±0.047	0.41 ±0.04	0.23 ±0.03	0.22 ±0.03	0.13 ±0.02	0.613 ±0.051	0.16 ±0.03
	$I_{1.2}$	0.809 ±0.058	0.37 ±0.04	0.26 ±0.03	0.15 ±0.03	0.15 ±0.03	0.088 ±0.020	0.40 ±0.04	0.12 ±0.02

rection factor taking into account the different response of the chambers used at the two elevations was applied to the sea level rates. Table IV also shows the absorption thickness in air for the different events, computed under the assumption of exponential absorption between 10,600 feet (710 g cm^{-2} atmospheric depth) and sea level. The absorption thickness in air for the event $AI_{0.3}BC_2$ (see Table I) is 119±5 g cm^{-2}, in good agreement with the values found at airplane altitudes for charged particles producing ionization bursts of similar magnitude under thick lead shields.[4,5] Our results are also in good agreement with the results of Tinlot[9] and of Walsh and Piccioni[10] on the altitude variation of penetrating showers. Our instrument selects nearly vertical rays, and thus the values of the absorption thickness refer to approximately vertical incidence.

There is evidence that the absorption thickness in air decreases when events associated with larger ionization bursts are considered. This point will be discussed in Sec. III.6.

Table II shows that at sea level the rate of event $AI_{0.3}BC_2$ is decreased in the ratio of 1 to 0.45±0.04 when Σ is increased from 0 to 445 g cm^{-2} of lead. From Table III one computes a decrease in the ratio of 1 to 0.50±0.03 for the same event in an absorber thickness of 341 g cm^{-2} of lead at 10,600 feet. If for comparison purposes one assumes exponential absorption in Σ, one finds an absorption thickness of 550±70 g cm^{-2} of lead at sea level and an absorption thickness of 490±40 g cm^{-2} of lead at 10,600 feet. These values may be compared with the result of a similar measurement by Bridge and Rossi[4] at 14,300 feet; they obtained 430±90 g cm^{-2} as the absorption thickness in lead. As will be apparent later, the agreement is partly fortuitous.

[9] J. H. Tinlot, Phys. Rev. **74**, 1197 (1948).
[10] T. G. Walsh and O. Piccioni, Phys. Rev. **80**, 619 (1950).

3. Separation of Electromagnetic and Nuclear Interactions

As previously stated, ionization bursts can be caused either by nuclear interactions of N-rays or by electromagnetic interactions of μ-mesons. Table II shows that at sea level the addition of the absorber Σ reduces the rate of the $AI_{0.3}BC_2$ events more strongly than the rate of the $AI_{0.3}BC_0$ or $AI_{0.3}BC_1$ events. Similarly, Table IV shows that 320 g cm^{-2} of atmosphere reduces the rate of the $AI_{0.3}BC_2$ events much more strongly than the rate of the $AI_{0.3}BC_0$ or $AI_{0.3}BC_1$ events. These results together with the well-known difference in penetrating power of N-rays and μ-mesons prove that the requirement of a multiple discharge in tray C discriminates effectively in favor of nuclear interactions as had been anticipated. Indeed, a μ-meson can produce an $AIBC_2$ coincidence only through two successive electromagnetic interactions, one occurring above the ionization chamber and one in the lead between the ionization chamber and tray C. This is necessary because for the energies involved in this experiment, an electronic shower starting above the ionization chamber has virtually zero probability of penetrating the lead block below the chamber. One can easily show that the contribution of such double interactions to the recorded $AIBC_2$ rate is small. It is known that

TABLE IV. Comparison of the coincidence rates obtained at sea level and at 10,600 feet with only absorber Σ' present. (a) The sea level coincidence rates in counts per hour multiplied by 0.86±0.08 to normalize to the chamber used at 10,600 feet. (b) The increase in the coincidence rates from sea level to 10,600 feet (710 g cm^{-2}). (c) The absorption thickness in g cm^{-2} of air computed under the assumption that the absorption is exponential.

	$AI_{0.3}B$	$AI_{0.3}BC_0$	$AI_{0.3}BC_1$	$AI_{0.3}BC_2$
(a) counts/hour	1.56±0.15	0.85±0.09	0.45±0.05	0.26±0.03
(b) factor increase	8.16±0.80	7.39±0.79	5.76±0.67	14.9±1.8
(c) absorption thickness g cm^{-2} of air	153±7	160±9	183±19	119±5

TABLE V. Separation of μ-meson and N-component induced coincidence events for absorber Σ' alone above the detector. Coincidence rates are in counts per hour. The standard errors listed have been calculated under the assumptions that the calculated μ-meson altitude variation has no statistical error and the altitude variation of the N-component is of the same statistical accuracy as the altitude variation of the $AI_{0.3}BC_2$ events.

	$AI_{0.3}B$		$AI_{0.3}BC_0$		$AI_{0.3}BC_1$	
	N-comp.	Mu-meson	N-comp.	Mu-meson	N-comp.	Mu-meson
Sea level	0.79±0.09	0.77±0.11	0.38±0.05	0.47±0.07	0.15±0.03	0.30±0.05
10,600 ft	11.83±0.28	0.92±0.13	5.71±0.19	0.56±0.08	2.24±0.12	0.36±0.06

out of 100 cosmic-ray μ-mesons emerging from a lead block only about 7 are accompanied by an electron.[11,12] If one makes the extreme assumption that all $AIBC_1$ events are caused by μ-mesons, the number of $AIBC_2$ events due to μ-mesons can only be 7 percent of the number of $AIBC_1$ events. This figure may be compared with the experimental results at sea level: with $\Sigma=0$ the ratio of the $AI_{0.3}BC_2$ rate to the $AI_{0.3}BC_1$ rate is 0.57±0.05, and with $\Sigma=455$ g cm^{-2} of lead the ratio is still 0.35±0.03.

Underground experiments substantiate the view that at sea level and above, the N-rays rather than the μ-mesons are responsible for events capable of discharging two heavily shielded Geiger counters in coincidence with an ionization chamber.[13,14] This view is also supported by our finding that the absorption in lead of the radiation responsible for $AIBC_2$ events is approximately the same at 10,600 feet as at sea level. The absorption in lead of the radiation responsible for $AIBC_0$ and $AIBC_1$ events, on the other hand, increases with decreasing atmospheric depth, which shows that at sea level a large part of this radiation consists of μ-mesons.

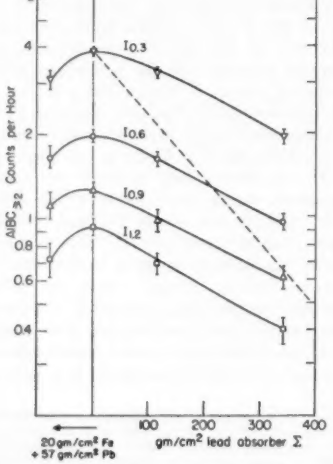

FIG. 3. The coincidence rate $AIBC_2$ at 10,600 feet as a function of the absorber thickness above the detector for four different values of the minimum detected ionization chamber pulse. The 20 g cm^{-2} of iron and 57 g cm^{-2} of lead compose the absorber Σ'. The dashed line shows an exponential absorption $\exp(-x/L)$ with $L=195$ g cm^{-2}.

It is important to evaluate quantitatively the contributions of N-rays and μ-mesons to the $AI_{0.3}BC_0$ and $AI_{0.3}BC_1$ rates recorded at sea level and at 10,600 feet. For this evaluation we computed that the number of $AI_{0.3}BC_0$ and $AI_{0.3}BC_1$ events produced by μ-mesons increases in the ratio 1 to 1.20 between sea level and 10,600 feet.[7] Further, we assumed that the number of $AI_{0.3}BC_0$ or $AI_{0.3}BC_1$ events produced by the N-component increases between these two altitudes in the same ratio as the number of $AI_{0.3}BC_2$ events. From the observed altitude variation in the $AI_{0.3}BC_0$ and $AI_{0.3}BC_1$ rates we then found, with a simple calculation, the results summarized in Table V, which are for absorbers Σ' on and $\Sigma=0$ g cm^{-2}. One sees from the table that at 10,600 feet (91±1) percent of the $AI_{0.3}BC_0$ events and (86±2) percent of the $AI_{0.3}BC_1$ events are due to nuclear interactions, while at sea level (45±5) percent of the $AI_{0.3}BC_0$ events and (33±5) of the $AI_{0.3}BC_1$ events are due to nuclear interactions. For the $AI_{0.3}B$ events at 10,600 feet (92±1) percent of the coincidence rate is due to nuclear interactions, while at sea level (51±5) percent of the coincidence rate is due to nuclear interactions.

4. Absorption of the N-Component in Lead

Figure 3 shows logarithmic plots of the coincidence rates as a function of absorber thickness for the $AIBC_2$ events obtained at 10,600 feet. The various curves correspond to different values of the minimum size of the ionization burst.

From our own results and from those of other experimenters it is known that the absorption curve in air of the N-component of cosmic rays is practically exponential with an absorption thickness close to 120 g cm^{-2}. If one assumes that air and lead absorbers differ only because of the change in nuclear radius, one would also expect an approximately exponential absorption of the N-radiation in lead. From the model of the semi-transparent nucleus[15] and from the experimental value

[11] W. E. Hazen, Phys. Rev. **64**, 7 (1943).
[12] Brown, McKay, and Palmatier, Phys. Rev. **76**, 506 (1949).
[13] E. P. George and A. C. Jason, Nature **160**, 327 (1947).
[14] D. E. Hudson, thesis, Cornell University (1950).
[15] Fernbach, Serber, and Taylor, Phys. Rev. **75**, 1352 (1949).

of the absorption thickness in air, one computes an absorption thickness of 195 g cm^{-2} in lead.[16]

Figure 3 shows the observed absorption in lead for the $AIBC_2$ events compared to the result of the above computation. It is evident that the absorption is much smaller than that predicted. Indeed, the absorption curves are not exponential, but exhibit "transition effects"; the rate of events increases slightly at first with increasing absorber thickness and then decreases again. It thus seems necessary to conclude that the difference in density between the air and lead absorbers has an important effect on the observed absorption curves.

The most likely explanation for this effect is that π-mesons produced in high energy nuclear interactions can give rise to further nuclear interactions capable of producing the observed coincidences. In air, most π-mesons will decay before colliding with nuclei. In lead, instead, most π-mesons will interact before decaying. Thus the total number of interacting particles (nucleons and π-mesons) is greater under an air plus lead absorber than under an equivalent thickness of air alone.

In 1948, when the present experiment was initiated, very little was known about the nuclear interactions of π-mesons. Today, from the work with artificially produced π-mesons, it is known that π-mesons with energies of the order of 100 Mev interact strongly with nuclei,[17] and observations by means of cloud chambers and photographic plates have shown that the same is true for the π-mesons of higher energy which occur in the nuclear interactions of cosmic rays.[18–21] In agreement with these results, the present experiment shows that π-mesons of several Bev such as are necessary to

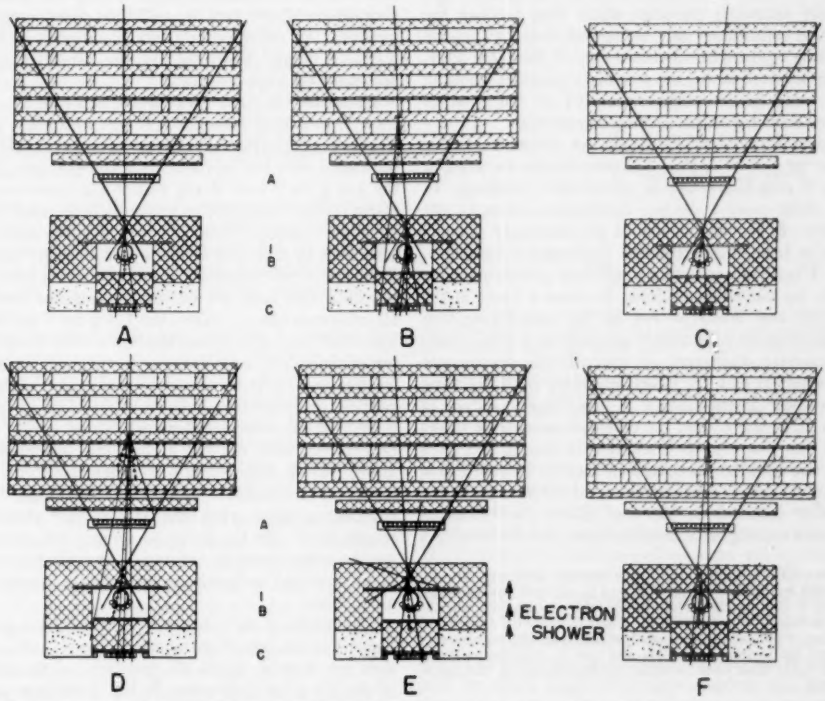

FIG. 4. Schematic representation of six different cosmic-ray processes capable of producing the $AIBC_2$ coincidence events.

[16] This conclusion is not invalidated by the fact that in air there is some reproduction of the N-radiation. For a discussion of this point and for a more detailed description of the method used to determine the collision mean free path in Sec. III.5 see Bruno Rossi, *High Energy Particles* (Prentice-Hall, Inc., New York, 1952), Chap. VIII.
[17] See, for example, Bernardini, Booth, and Lederman, Phys. Rev. **83**, 1075 (1951).
[18] B. P. Gregory and J. H. Tinlot, Phys. Rev. **81**, 675 (1951).
[19] A. J. Hartzler, Phys. Rev. **82**, 359 (1951).
[20] Camerini, Fowler, Lock, and Muirhead, Phil. Mag. **41**, 413 (1950).
[21] M. Annis, thesis, Massachusetts Institute of Technology (1951).

produce the recorded events possess large cross sections for nuclear interactions.

Before accepting this conclusion two other possible explanations of the "transition effect" will be considered. First there is the possibility that the model of the semitransparent nucleus is oversimplified in that the nucleons of a complex nucleus do not act independently of one another in high energy collisions. In this case, a "transition effect" could occur in passing from air to lead. The most convincing evidence that the observed initial increase in the counting rate does not depend on the atomic number but on the density comes from the results obtained with a carbon absorber for Σ.[22] Exactly the same type of absorption curve was obtained in this case as in the experiment here reported.

The second effect considered is the "geometric coherence" of particles produced in Σ. A nuclear interaction that takes place in the absorber may produce two or more secondary particles which then produce the observed coincidence only because of their striking the detecting equipment simultaneously. If the same interaction occurred in air, the secondary particles would in most cases be so widely separated at the detector that no such coincidence would be possible.

Figure 4 shows schematically six different possible causes for events $AIBC_2$. The coincidences recorded in cases D and F are due to geometrical coherence. In both these cases a nuclear interaction occurs in the absorber Σ. In case D, one of the secondary charged particles from this interaction discharges a counter in tray A and then interacts in the lead producing layer above the ionization chamber to cause a burst in the chamber and discharge tray B. The coincidence that results from this secondary particle is A_1IBC_0 (only one counter discharged in tray A and no counter discharged in tray C). Other secondary particles, from the nuclear interaction in Σ, discharge counters in trays A, B, and C, and the detected coincidence shows more than one counter discharged in tray A and more than one counter discharged in tray C. In case F one of the secondary neutrons from the interaction in the absorber interacts in the lead above the ionization chamber causing an ionization burst and discharging a counter in tray B. This event would not be recorded, but associated charged secondaries from the nuclear interaction in Σ discharge counters in trays A and C, and an $AIBC_2$ coincidence is detected.

One may mention another possible coherence effect, which is not illustrated in Fig. 4. In a nucleonic cascade initiated in the lead absorber and propagating through the absorber and the producing layer, the secondary particles remain concentrated in a fairly small region around the trajectory of the initiating particle. Such a cascade may have a sufficient density of ionizing particles at the ionization chamber to produce a detectable burst, while this may not be the case for similar cascades initiated in air.

In order to obtain some information regarding the coherence effects we performed an additional experiment at 10,600 feet; 114 g cm^{-2} of lead were placed, first directly below tray A, then directly above tray A, then 66 cm above tray A, and then were completely removed. All other experimental conditions including the solid angle subtended by the absorber at the detector were kept constant.[23]

When the 114 g cm^{-2} lead shield was directly above tray A, geometric coherence between secondary particles from nuclear interactions in this shield should have been most effective in producing detected events. When the 114 g cm^{-2} lead shield was 66 cm above tray A, many of the events due to geometric coherence should have been missed. (Note, however, that the solid angle presented by tray C to secondary particles produced in interactions 66 cm above tray A is of the order of 0.04 steradian and may not be small enough to eliminate all coherence effects.) When the 114 g cm^{-2} lead shield was below tray A, neutrons incident on this shield could not produce detected events (neglecting back emission). In this case, events caused by associated secondary particles from neutron induced interactions in the 114 g cm^{-2} shield were not detected. These events would be detected with the 114 g cm^{-2} lead shield directly above tray A; they would not be detected in measurements of atmospheric absorption. A change in the coincidence rates when the 114 g cm^{-2} shield was moved from directly above to directly below tray A could also be caused by a change in the relative number of protons and neutrons as the radiation passes from air to lead.

The results of the coherence experiment are given in Table VI. One sees that the rate of the $AI_{0.3}BC$ events does not depend, within the statistics, on the position of the 114 g cm^{-2} absorber. In Fig. 5 we have plotted the absorption data for the $AI_{0.3}BC$ rates given previously in Table III as well as that from the coherence experiment given in Table VI.[24] The dashed line repre-

TABLE VI. The hourly coincidence rates for the events $AI_{0.3}BC$ at 10,600 feet with 114 g cm^{-2} of lead in different positions with respect to the detector. The experimental arrangement was the same as that of Fig. 1 with both Σ and Σ' removed, except that 171 g cm^{-2} instead of 142 g cm^{-2} of lead was kept permanently between the ionization chamber and tray A. The results shown in this table have been corrected for fluctuations in barometric pressure.

114 g cm^{-2} Pb removed	114 g cm^{-2} Pb directly above tray A	114 g cm^{-2} Pb directly below tray A	114 g cm^{-2} Pb 66 cm above tray A
6.28±0.19	6.08±0.23	5.63±0.21	5.94±0.22

[22] R. Rediker, unpublished results. Measurements for carbon and hydrocarbon absorbers will be reported in a subsequent communication.

[23] For all the coherence experiments absorbers Σ and Σ' were removed and an additional 29 g cm^{-2} of lead was added between tray A and the ionization chamber.

[24] The absorption points obtained from the coherence experiment with the 114 g cm^{-2} of lead removed and with the 114 g cm^{-2} of lead directly above tray A fit the absorption curve

sents the expected result computed from the absorption in air as discussed above. The impossibility of explaining solely in terms of a coherence effect, the discrepancy between the observed absorption in lead and that expected from the absorption in air is evident from the figure. The counting rate for the $AI_{0.3}BC$ events with the 114 g cm^{-2} absorber directly above tray A is about 2.2 counts per hour greater than the calculated value, and placing the 114 g cm^{-2} absorber either 66 cm above the tray or directly underneath it, does not change this figure significantly.

Use of the $AI_{0.3}BC$ events rather than $AI_{0.3}BC_2$ events in determining the results of the coherence experiment is justified because the absorption curve for the $AI_{0.3}BC$ events exhibits the same type of "transition effect" as the absorption curves for the $AIBC_2$ events (see Figs. 3 and 5).

We have corrected the results of the coherence experiment for fluctuations in the barometric pressure using an absorption thickness in air for the producing radiation of 119 g cm^{-2}. These are the only results reported in this paper that are corrected for pressure fluctuations. We did not correct the results shown in Table VI and Fig. 5 for μ-bursts because we did not wish to introduce into the comparison of the counting rates the additional statistical errors inherent in making the μ-meson correction. Mu-bursts, which account for only about ten percent of the $AI_{0.3}BC$ coincidence rate, have been included in computing the expected absorption indicated by the dashed line in Fig. 5. The effect of the μ-meson induced events on the barometric correction has been neglected.

There is thus little doubt that π-mesons are mainly, if not totally, responsible for the difference between the absorption curve in lead observed directly and that computed from the experimental absorption curve in air on the basis of the model of the semitransparent nucleus.

Unfortunately, it is not possible to discuss the absorption curves quantitatively. The experimental errors are fairly large, the coherence effects may not be completely negligible, and the "zero thickness" for the lead absorber is somewhat undetermined, for it depends on the position in the lead above the chamber where the detected nuclear interactions occur. It is possible, however, to make some qualitative statements.

(a) If the initial increase in the absorption curves is not entirely due to spurious effects, but represents a real increase in the number of burst producing particles, the average energy of the interacting particles (nucleons and π-mesons) must decrease in passing from air to lead. Obviously the total energy of the particles cannot increase. The decrease in average energy means either that the energy spectrum becomes steeper (i.e., the relative number of lower energy particles is greater in lead than in air) or that the minimum energy necessary to produce a detectable interaction is smaller for π-mesons than for nucleons. It is conceivable that there is a different distribution of available energy between secondary nucleons and π-mesons in the nuclear interactions of the two kinds of particles.

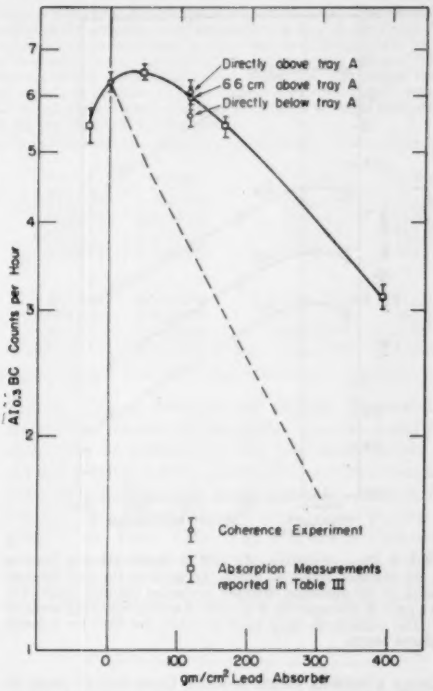

FIG. 5. The results of the "coherence experiment" at 10,600 feet. The rate of $AI_{0.3}BC$ events as a function of absorber thickness as determined from the results given in Table III (assuming the 20 g cm^{-2} of iron equivalent to 20 g cm^{-2} of lead) has been superimposed. The dashed line shows the absorption that would be expected for the $AI_{0.3}BC$ events from the model of the semitransparent nucleus and from the experimental value of the absorption thickness in air.

(b) It is reasonable to assume that after a sufficient thickness of lead, a condition of approximate equilibrium between π-mesons and nucleons will be reached. The absorption curves will then become nearly exponential and the experimental value of the absorption thickness will represent an upper limit for the collision mean free path of all interacting particles. The thickness of lead at which the approximate equilibrium is reached may be much larger than that used in the present experiment. However, the experimental absorption thickness will still give an upper limit (possibly a very high limit) for the collision mean free path of all interacting particles. From Fig. 3, one finds that the absorption at large values of the absorber Σ corresponds to absorption thicknesses of 440±50 g cm^{-2} for the $AI_{0.3}BC_2$ events and 420±100 g cm^{-2} for the $AI_{1.2}BC_2$ events. Thus the collision mean free path for high

(Fig. 5) very well. Since the coherence experiment was performed one year after the experiment reported in this paper, the excellent fit of these points is additional evidence for the reliability of our experimental results.

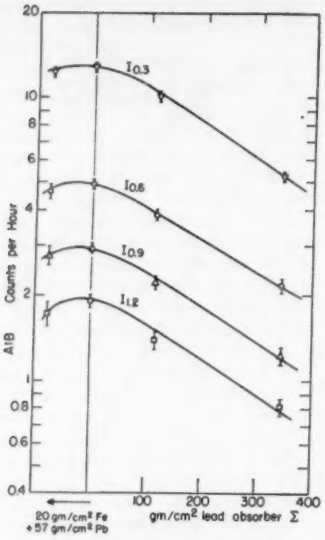

FIG. 6. The coincidence rate AIB at 10,600 feet as a function of the absorber thickness above the detector for four different values of the minimum detected ionization chamber pulse. The 20 g cm^{-2} of iron and the 57 g cm^{-2} of lead compose the absorber Σ'. The coincidence rates have not been corrected for μ-meson induced bursts.

energy π-mesons which produce these events must be smaller than these values.

(c) The "transition effects" in the absorption curves for lead explain the large values of the absorption thickness that have previously been reported from similar ionization chamber experiments.[4,14,25]

The absorption data for events other than those discussed above ($AIBC_2$ and $AIBC$) are given in Fig. 6, Fig. 7, and Table VII. Figure 6 shows the coincidence rate AIB as a function of absorber thickness for the four different values of the minimum pulse required in the ionization chamber. These rates are not corrected for μ-bursts.

Figure 7 and Table VII give the absorption data for the $AI_{0.3}B$, $AI_{0.3}BC_0$, and $AI_{0.3}BC_1$ events corrected for μ-bursts. The μ-meson correction for absorbers Σ' on and $\Sigma=0$ was made using the results of Sec. III.3 above. For other absorbers the additional absorption of the μ-mesons was taken into account only approximately with the assumptions listed in Table VII.[26] The general features of the absorption curves shown in Figs. 6 and 7 are similar to those discussed above (see Figs. 3 and 5).

5. The Interaction Mean Free Path of the *N*-Component in Lead

In Sec. III.4 we have discussed the variation of the various coincidence rates when additional absorbers were placed above tray A. We have interpreted these variations as a direct indication of the effect of the absorber on the number of particles above tray A capable of producing the various types of coincidences.

In this section we will discuss the variation with absorber thickness of the rates of those coincidence events in which one and only one counter in tray A was struck (A_1 events). This requirement rules out many of the events in which the incident particle interacts in the absorber. If the collision in the absorber gives rise to a particle capable of interacting in the lead above the ionization chamber, it is likely that other ionizing particles are produced and that more than one counter in tray A will be discharged (see Fig. 4, cases B, D, and F). If the A_1 requirement could be used to eliminate all collisions in the absorber, the variation with absorber thickness of the rate of occurrence of A_1 events would yield directly the interaction mean free path of the particles responsible for the observed bursts.[16]

The requirement that only one counter be struck in tray A does not, of course, completely eliminate the

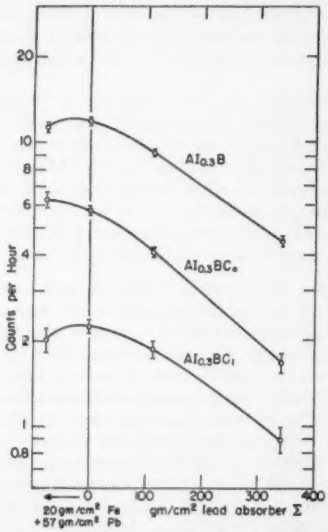

FIG. 7. The coincidence rate as a function of absorber thickness is plotted for the $AI_{0.3}B$, the $AI_{0.3}BC_0$, and for the $AI_{0.3}BC_1$ rates at 10,600 feet. The coincidence rates have been corrected for μ-meson induced bursts. The assumptions listed in Table VII were used to determine the absorption in lead of the burst-producing μ-mesons.

[25] T. G. Stinchcomb, Phys. Rev. **83**, 422 (1951).

[26] A better computation of this absorption similar to that described in the appendix was not performed because the effect of an inaccuracy in the μ-meson absorption on the computation of the N-component rates is small.

TABLE VII. The absorption of the separated N-component that produces different coincidence events at 10,600 feet. The coincidence rates are in counts per hour. We have assumed that in all bursts produced by μ-mesons, only one counter in tray A was struck. We have calculated the absorption in lead of the μ-mesons which produce the bursts by assuming: (a) All μ-mesons of energy above 5×10^9 ev which were incident upon the detector with Σ' on and $\Sigma=0$ g cm^{-2} contributed with equal weight to producing the bursts. (b) The integral range spectrum at sea level for μ-mesons of the energies under consideration was applicable at 10,600 feet. The integral range spectrum given by B. Rossi, Revs. Modern Phys. **20**, 537 (1948), was used in conjunction with the range-energy relation for μ-mesons in lead given by G. C. Wick, Nuovo cimento **9**, 310 (1943). It should be noted when comparing rates at different absorber thicknesses that the standard errors in the rates for the separated N-component are not statistically independent.

Σ'	Σ	$A_1I_{0.3}B$		$A_1I_{0.3}BC_0$		$A_1I_{0.3}BC_1$	
		N-comp.	Mu-meson	N-comp.	Mu-meson	N-comp.	Mu-meson
Off	0 g cm^{-2}	11.31±0.47	0.94±0.13	6.23±0.34	0.57±0.08	2.00±0.20	0.37±0.06
On	0 g cm^{-2}	11.83±0.28	0.92±0.13	5.71±0.19	0.56±0.08	2.24±0.12	0.36±0.06
On	114 g cm^{-2}	9.16±0.27	0.89±0.13	4.07±0.17	0.54±0.08	1.85±0.13	0.35±0.06
On	341 g cm^{-2}	4.45±0.19	0.83±0.12	1.64±0.12	0.51±0.07	0.89±0.09	0.32±0.05
		$A_1I_{0.3}B$		$A_1I_{0.3}BC_0$		$A_1I_{0.3}BC_1$	
Off	0 g cm^{-2}	8.98±0.42	0.94±0.13	5.43±0.31	0.57±0.08	1.68±0.19	0.37±0.06
On	0 g cm^{-2}	6.88±0.22	0.92±0.13	4.01±0.16	0.56±0.08	1.28±0.10	0.36±0.06
On	114 g cm^{-2}	4.35±0.21	0.89±0.13	2.38±0.14	0.54±0.08	0.96±0.10	0.35±0.06
On	341 g cm^{-2}	1.68±0.16	0.83±0.12	0.85±0.10	0.51±0.07	0.37±0.07	0.32±0.05

effects of secondary particles produced in the absorber. The accompanying particles may fail to emerge from the absorber; or they may miss tray A either because they are emitted at wide angles or because they pass through the "holes" between the counters. It is also possible that two or more particles pass through the same counter in tray A. Therefore, the mean free paths deduced from the experimental absorption curves for the A_1 events will be somewhat greater than the actual collision mean free paths.

Figure 8 shows the reduction in coincidence rates with addition of absorber for the $A_1I_{0.3}$ type of coincidences corrected for μ-meson background. Table VIII shows the mean free paths computed from the results shown in Fig. 8. The values have been obtained from a least squares treatment of the data, assuming an exponential decrease of the rates with thickness. Of the events tabulated, it is seen that the $A_1I_{0.3}BC_0$ rate shows the greatest absorption. This is probably related to the fact that when events with multiple counter discharges in tray A are included, secondary particles from nuclear interactions in the absorber contribute to a lesser extent to events of the $AIBC_0$ type than to events of the $AIBC_1$ or $AIBC_2$ type, as shown by the much smaller "transition effect" exhibited by the $AIBC_0$ events compared to the other events (see Figs. 3 and 7).

In Fig. 9, the A_1IBC_0 coincidence rates uncorrected for μ-bursts are plotted as functions of the absorber thickness for different ionization chamber biases. The fact that the points at $\Sigma=341$ g cm^{-2} are high may be explained with the argument that as the absorber gets thicker, tray A becomes less efficient in detecting interactions because of the angular divergence and the absorption of secondaries. The logarithmic slopes of the uncorrected A_1IBC_0 curves increase with increasing pulse height. While the mean free path obtained for the $A_1I_{0.3}BC_0$ events corrected for μ-mesons is 225±14 g cm^{-2} (see Table VIII), Fig. 9 indicates that, with proper μ-meson correction, the absorption of A_1IBC_0 events associated with large bursts is not inconsistent with the geometrical mean free path (167 g cm^{-2} of lead).

TABLE VIII. The mean free path in g cm^{-2} of the various $A_1I_{0.3}B$ type events under the assumption that the rates that are produced by the N-component vary exponentially with absorber thickness.

Event	$A_1I_{0.3}BC_0$	$A_1I_{0.3}BC_1$	$A_1I_{0.3}BC_2$
Mean free path in g cm^{-2}	225±14	292±41	286±23

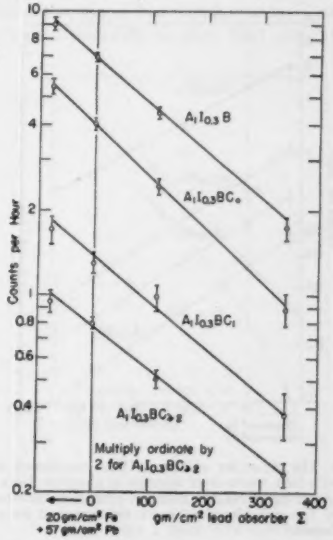

FIG. 8. The reduction of the $A_1I_{0.3}$ type of coincidence rates at 10,600 feet due to addition of absorber. The coincidence rates have been corrected for μ-meson induced bursts under the assumptions listed in Table VII.

6. Pulse-Height Distributions

Figure 10 shows double logarithmic plots of the integral pulse-height distributions observed for various events. The distributions refer to measurements taken at 10,600 feet with the absorber Σ' alone above counter tray A. The experimental results tabulated in Table III show that within the experimental errors the shape of the pulse-height distribution for a given kind of event (with the possible exception of event AIB) is independent of the thickness of absorber above tray A; it is also independent of the requirement that only one counter be discharged in tray A.

From an examination of Fig. 10 it appears that power laws of the type $N(\rho)=\text{constant}\times\rho^{-\gamma}$ represent well the integral pulse-height distributions: for the AIB events, $\gamma=1.35$; for the $AIBC_0$ events, $\gamma=1.52$; and for the $AIBC_2$ events, $\gamma=1.02$. The pulse-height distribution for the $AIBC_1$ events seems to exhibit small deviations from a power law with $\gamma=1.60$. Since the AIB events are merely the sum of the $AIBC_0$, $AIBC_1$, and $AIBC_2$ events, and the sum of three different power laws cannot give a fourth different power law, it appears that the power law assumption is a simplification which is justified only by the crudeness of the experimental data. The subtraction of the ionization bursts due to μ-mesons does not significantly change the above data.[27] Figure 10 shows that the percentage of events associated with multiple counter discharges in tray C increases with the size of the ionization pulse

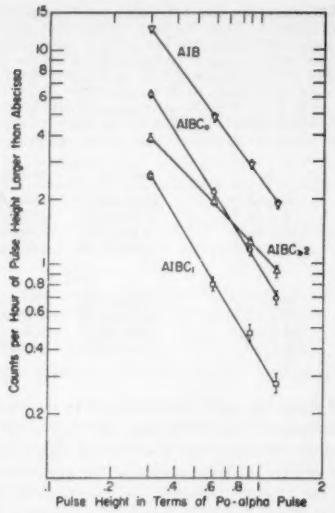

FIG. 10. The integral ionization chamber pulse-height distribution at 10,600 feet for various coincidence events. Only absorber Σ' is present.

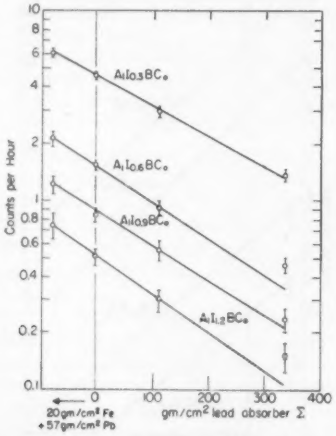

FIG. 9. The reduction of the A_1IBC_0 coincidence rates at 10,600 feet which results from addition of absorber. Data for the four values of the minimum detected ionization chamber pulse are given. The coincidence rates are not corrected for μ-meson induced bursts.

required.[28] (30 ± 1) percent of the $AI_{0.2}B$ events and (49 ± 4) percent of the $AI_{1.2}B$ events are associated with multiple counter discharges in tray C.

The dissimilarity of the integral pulse-height distributions for the $AIBC_0$ and $AIBC_1$ events on the one hand and for the $AIBC_2$ events on the other hand shows that these coincidences are not caused by interactions of the same kind where by chance different numbers of particles strike tray C.

On the basis of the projected zenith angular distribution of penetrating particles from nuclear interactions determined by Brown and McKay,[29] one can estimate that at least 67 percent of the penetrating secondaries from recorded interactions miss tray C. This estimate can only be correct as to the order of magnitude because the angular distribution given by Brown and McKay is an average over many interactions whereas the directions of emission of secondaries from a single interaction are certainly interdependent. It is apparent, however, that most of the $AIBC_2$ events are caused by nuclear interactions in which large numbers of penetrating particles are produced. Most of the $AIBC_0$ and $AIBC_1$ events, instead, are caused by nuclear interactions in which fewer penetrating particles are produced and by interactions of μ-mesons.

Figure 11 shows double logarithmic plots of the pulse-height distributions for the AI, $AIBC_1$, and $AIBC_2$ coincidence events observed at sea level with

[27] To make this subtraction we used the results listed in Table V for the μ-bursts in conjunction with an integral pulse-height distribution with $N(E)=kE^{-1.6}$ (see appendix).

[28] A similar result has been reported by E. P. George and P. T. Trent, Proc. Phys. Soc. (London) **64**, 733 (1951).

[29] W. W. Brown and A. S. McKay, Phys. Rev. **77**, 342 (1950).

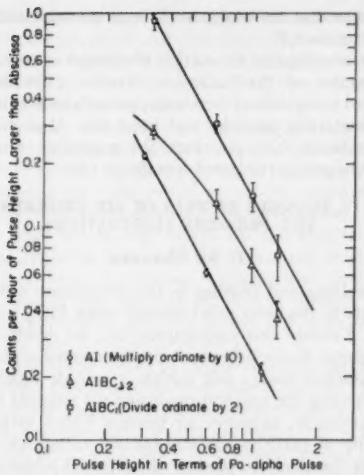
Counts per Hour of Pulse Height Larger than Abscissa
Pulse Height in Terms of Po-alpha Pulse
A (Multiply ordinate by 10)
AIBC₂
AIBC₂(Divide ordinate by 2)

FIG. 11. The integral ionization chamber pulse-height distribution at sea level for various coincidence events. Only absorber Σ' is present.

absorber Σ' alone. It should be noted that the curves obtained with an additional absorber Σ of 455 g cm^{-2} of lead are similar to those shown in Fig. 11. The AI events and the $AIBC_1$ events are distributed according to a power law with $\gamma \approx 1.8$. The pulse-height distribution for the $AIBC_2$ coincidence events, however, shows a definite deviation from a power law, being flatter at small burst size than at large burst size. A similar deviation was also observed in the curve obtained with $\Sigma = 455$ g cm^{-2}. In Fig. 12 the pulse-height distribution for the $AIBC_2$ events at sea level is compared with the pulse-height distribution for the same events at 10,600 feet. The absolute values of the sea level rates are corrected to account for the slightly greater sensitivity of the chamber used at this location. One sees that the atmospheric absorption is stronger for the larger bursts. Under the assumption of an exponential absorption, one finds an absorption thickness in the atmosphere of 119 ± 5 g cm^{-2} for $I_{0.3}$ bursts and of 100 ± 7 g cm^{-2} for $I_{1.3}$ bursts.

An analysis of the AIB pulse-height distributions at sea level and at 10,600 feet also indicates that the atmospheric absorption of the N-component is greater for larger bursts. The observed AIB pulse-height distributions can be represented by power laws with $\gamma = 1.8$ at sea level and $\gamma = 1.4$ at 10,600 feet. In the evaluation of the fractional number of μ-bursts at the two elevations, we have used a computed value of 1.2 for increase factor in the rate of these bursts between sea level and 10,600 feet (see Sec. III.3). The calculation, given in the appendix, from which we obtain the above increase factor also indicates (see Table IX) that the pulse-height distribution of μ-bursts obeys a power law with $\gamma \approx 1.6$ both at 10,600 feet and at sea level. From these results it follows that the observed change in the AIB pulse-height distribution from 10,600 feet to sea level cannot be explained in terms of a change in the proportion of bursts induced by μ-mesons and by N-rays, respectively, unless one also assumes that the pulse-height distribution of the N-bursts becomes steeper at the lower elevation. Such a change in pulse-height distribution is explained by the increased atmospheric absorption of the N-component which produces the larger bursts.

7. Back Emission of Penetrating Particles

The histogram in Fig. 13 shows the number of cases in which either one, or more than one, counter was discharged in tray A for the $AI_{0.3}BC_0$, $AI_{0.3}BC_1$, and $AI_{0.3}BC_2$ events observed at 10,600 feet under different absorber thicknesses. For all absorber thicknesses there is a clear correlation between multiple discharges in tray A and multiple discharges in tray C. The probability for multiple discharges in tray A was least when no counter in tray C was struck. This probability increased slightly when one counter in tray C was struck, and it increased by a large amount when two or more counters in tray C were struck. Even without any lead absorber above tray A, in which case the only solid material above this tray was a canvas tent, in 38 percent of the $AI_{0.3}BC_2$ coincidences more than one counter in tray A was struck, and in 12 percent of the $AI_{0.3}BC_0$ coincidences more than one counter in

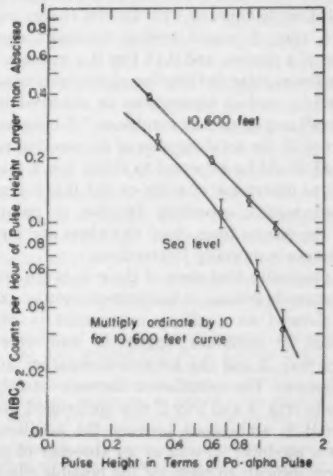
AIBC₂ Counts per Hour of Pulse Height Larger than Abscissa
Pulse Height in Terms of Po-alpha Pulse
10,600 feet
Sea level
Multiply ordinate by 10
for 10,600 feet curve

FIG. 12. The integral ionization chamber pulse-height distribution for the $AIBC_2$ coincidence event at sea level and at 10,600 feet. Only absorber Σ' is present. The sea level rates have been normalized to the ionization chamber used at 10,600 feet.

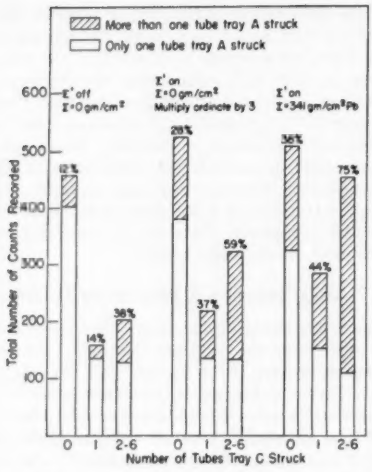

FIG. 13. Histogram showing the number of events in which more than one counter in tray A was discharged as a function of the number of counters in tray C discharged, for the $AI_{0.3}B$ coincidences at 10,600 feet with different absorbers above the detector. The percentages shown are the percentages of coincidence events in which more than one counter in tray A were struck.

tray A was struck. These results show definitely that nuclear interactions giving rise to many penetrating particles often project some of these in the backward direction. If the nuclear interaction occurred 48 g cm^{-2} of lead above the ionization chamber, a charged particle emitted directly upward with kinetic energy sufficient to reach tray A would need a minimum energy of 0.28 Bev if a proton, and 0.15 Bev if a π-meson.

From the angular distribution of penetrating particles produced in nuclear interactions as observed in cloud chambers[29] and in nuclear emulsions,[30,31] between 5 and 10 percent of the total number of penetrating particles produced would be expected to strike the A tray. It is difficult to determine whether or not this is consistent with our results, especially because as pointed out above, the results from cloud chambers and emulsions are averages over many interactions.

The possibility that some of the events are caused by backscattered photons or neutrons cannot be excluded. We performed an auxiliary experiment in which an additional 25 radiation lengths of lead were added between tray A and the ionization chamber to absorb any photons. The correlation between multiple discharges in tray A and tray C was unchanged. However, the result is ambiguous because the additional lead acts as a producer as well as an absorber of photons. It is very difficult to estimate the possible effect of the neutrons that are known to be emitted backwards in large numbers.[32]

An investigation of multiple discharges in tray A as a function of the ionization chamber pulse height showed no significant correlation between back emission of penetrating particles and burst size. It should be remembered, however, that the maximum ratio of pulse heights investigated was one to four.

IV. POSSIBLE EFFECTS OF AIR SHOWERS AND PRESSURE FLUCTUATIONS

1. Air Showers

Electrons and photons in the atmosphere can contribute to the burst rate observed below 142 g cm^{-2} of lead. Crudely this contribution can be divided into two parts: In the first place, single electrons or photons of sufficient energy will initiate a cascade capable of penetrating the lead and producing the required burst; and secondly, extensive air showers with a very high density of particles will still contain enough electrons under the shield to produce the required ionization in the chamber. We have computed the ionization burst rate due to single electrons and photons by extrapolating the energy spectrum of high energy electrons and photons reported by Rossi[33,34] and found a value approximately 3×10^{-3} times the observed AIB rate either at sea level or at 10,600 feet. A calculation using the method developed by Greisen[35] shows that the burst rate caused by dense air showers is approximately 3×10^{-5} times the observed AIB rate either at sea level or at 10,600 feet. If the additional requirement that a counter in tray C be struck is imposed, these values are further reduced. These results are, of course, only correct as to order of magnitude. They indicate, however, that if air showers consisted of electrons and photons exclusively, the number of bursts associated with air showers should be exceedingly small.

In order to test this point experimentally, we performed at 10,600 feet an experiment with essentially the same experimental arrangement as in Fig. 1, except for an additional tray of Geiger counters of 0.15 square meters placed 3 meters from the detector and at the same height as the lower counter in tray B. With no absorber above tray A and with 171 g cm^{-2} of lead between tray A and the ionization chamber (rather than 142 g cm^{-2} as shown in Fig. 1), (5.4±0.5) percent of the $AI_{0.3}B$ events were associated with discharges in the extension shower tray. When the amount of lead between tray A and the ionization chamber was increased to 285 g cm^{-2}, (5.0±0.6) percent of the $AI_{0.3}B$ events were associated with discharges in the

[30] Camerini, Davies, Fowler, Franzinetti, Lock, Perkins, and Yekutieli, Phil. Mag. **42**, 1261 (1951).
[31] L. S. Osborne, Phys. Rev. **81**, 239 (1951).
[32] Cocconi, Cocconi Tongiorgi, and Widgoff, Phys. Rev. **79**, 768 (1950).
[33] B. Rossi, Revs. Modern Phys. **21**, 104 (1949).
[34] Approximation B of the shower theory in B. Rossi and K. Greisen, Revs. Modern Phys. **13**, 240 (1941), has been used in these calculations.
[35] K. Greisen, Phys. Rev. **75**, 1071 (1949).

extension shower tray. In absolute value, the $AI_{0.3}B$ coincidence rate associated with air showers was reduced in the ratio of 1 to 0.70±0.11 when 114 g cm^{-2} of lead were added to the 171 g cm^{-2} of lead between tray A and the ionization chamber.

This small decrease, together with the large discrepancy between the computed and observed numbers of AIB events associated with air showers, shows conclusively that the events cannot be explained by the electronic component of air showers alone. Most likely they are mainly caused by the simultaneous arrival upon the instrument of N-rays and electrons, as part of the same air shower.[36] The electrons discharge the extension tray, whereas the N-rays through their nuclear interactions give rise to the AIB coincidences as in the case of unassociated events.

An experiment similar to the one described above but performed at sea level showed that 5 percent of the $AI_{0.6}$ events were associated with extensive air showers. All of the associated events contained particles of sufficient penetrating power to discharge several counters in tray C under an additional 171 g cm^{-2} of lead.

2. Barometric Effect

The data of the experiments reported here have not been corrected for the fluctuations in the barometric pressure.[37] At 10,600 feet the maximum variation of pressure during the time of the experiment was 12 g cm^{-2}. This pressure change should cause a variation of about 10 percent in the intensity of the N-rays since according to our measurements, the absorption thickness of the N-rays in air is 119 g cm^{-2}. Each measurement, with the exception of the one taken with no absorber above tray A, was run for at least two weeks and none of the severe barometric disturbances lasted more than a few days during the time of the experiment. Thus, the coincidence rates from all measurements (with the possible exception of the measurement with no absorber) should have errors much less than 10 percent from barometric fluctuations.

The authors are greatly indebted to Professor Bruno Rossi for his aid in planning this experiment and for his advice and criticism during the analysis of the results. They wish to thank Mr. Seymour Weiner who helped in performing the experiment at sea level and Mr. Daniel Anderson who did similarly at 10,600 feet. The facilities of the Inter-University High Altitude Laboratory were invaluable, and the aid of Professor Cohn and Professor Iona of the University of Denver was appreciated.

APPENDIX

In order to evaluate the contribution of μ-meson induced bursts to the total burst rates we have attempted to calculate the rate of μ-meson induced bursts at sea level and 10,600 feet. That is, we have tried to determine the number of μ-mesons which could produce, by electromagnetic interactions in the lead above the ionization chamber, electrons or photons capable of initiating the electron showers which cause the bursts.[38] These calculations have been perforce very approximate because of the limitations of present theories regarding the probability for electromagnetic interactions of μ-mesons, because of the difficulty in treating an electron cascade developing partly in lead and partly in air, and because we have neglected fluctuations from average shower behavior.

Neglecting fluctuations, the rate of ionization bursts induced by the μ-mesons is

$$n=\int_0^T dt\int_{E_{\min}(E'')}^{\infty} N_\mu(E)dE\int_{E''(t)}^{E_{\max}'(E)} P(E,E')dE', \quad (1)$$

where t is the number of radiation lengths above the chamber at which the interactions take place, $N_\mu(E)dE$ is the differential number energy spectrum in the vertical direction of μ-mesons,[39] and $P(E,E')dE'$ is the probability per radiation length for a meson of energy E to produce an electron or photon of energy E' in dE'. This yields for n the total number of bursts per second, per cm^2, and per steradian in the vertical direction. The minimum burst size which contributes to n is determined by the limits of the integration of Eq. (1). $E_{\max}'$ is the maximum energy which a μ-meson of kinetic energy E can transfer to an electron or photon, and $E_{\min}(E'')$ is the minimum kinetic energy a μ-meson must have in order to produce an electron or photon of kinetic energy E''. E'' is the minimum energy an electron or photon produced at thickness t of lead above the chamber must possess in order to initiate an electronic shower which will trigger the ionization chamber. The minimum detected ionization burst, $I_{0.3}$, corresponded to 16 minimum ionizing particles traversing the chamber perpendicular to its axis.

Experimental and theoretical results[40,41] show that because of large angle scattering in the lead, not all the electrons in an electronic shower will emerge from the lead and traverse the ionization chamber. In the experiments of this paper an ionization chamber which had a brass wall 0.081 cm thick and was 7.5 cm in diameter and 52 cm long was placed in a cavity in the

[36] Cocconi, Cocconi Tongiorgi, and Greisen, Phys. Rev. **75**, 1063 (1949).

[37] With the exception of the "coherence experiment" as has been noted.

[38] The number of ionization bursts produced by μ-mesons at sea level has been computed by R. F. Christy and S. Kusaka, Phys. Rev. **59**, 414 (1941). The present calculation is for smaller bursts than those considered by Christy and Kusaka. It is for vertically incident mesons on an infinite plane geometry and has been carried out for two elevations, while Christy and Kusaka's calculations are for spherical geometry at sea level. There are salient differences in the two methods of calculation for which the reader is referred to the above article.

[39] $N_\mu(E)$ was assumed independent of the thickness, t, at which the interaction occurred.

[40] S. N. Vernov and O. N. Vavilov, Phys. Rev. **70**, 769 (1946); Blocker, Kenny, and Panofsky, Phys. Rev. **79**, 419 (1950).

[41] R. R. Wilson, Phys. Rev. **86**, 261 (1952).

lead 16 cm×30.5 cm×83 cm. In what follows we have assumed that the lead to air boundaries and the chamber wall reduce the number of shower electrons at the ionization chamber to one-half the number that would be present if the shower developed in lead alone. Thus, a 32-electron shower at the position of lead boundary will be assumed to produce the minimum detected ionization burst and proportionally higher numbers of electrons will be required for the larger size bursts.

In dealing with the development of electronic showers in the lead we have used "Approximation B" of the shower theory in Rossi and Greisen.[42] This approximation is poor for lead because of the breakdown at small energies of the asymptotic formulas for radiation phenomena and pair production which are used in this approximation. Belenky, using the proper cross section for pair production at lower energies, has computed the position of the shower maxima and the number of particles at the maxima for showers initiated by electrons or photons of different energies.[6] He has, however, assumed that the number of particles in a shower is a Gaussian function of the distance from the shower maximum. This assumption is obviously very poor except very close to the shower maximum. It overestimates the number of shower particles at small thicknesses, and it greatly underestimates the number of shower particles at large thicknesses. Therefore, we have used "Approximation B" in preference to the theory given by Belenky.

Figure 14 shows the minimum energy, E'', that an electron must possess to initiate at a thickness t above the ionization chamber a cascade which will produce an $I_{0.3}$ burst. $E''(t)$ can be approximated in the region $2<t<\infty$ by the expressions

$$\begin{aligned} E''&=40e^{-0.77t} && \text{for} \quad 2\leq t<4.5,\\ E''&=0.5e^{+0.22t} && \text{for} \quad 4.5\leq t<\infty,\\ E_{\min}''&=1.25 && \text{for} \quad t=4.5, \end{aligned} \tag{2}$$

as indicated by the dashed lines in Fig. 14. $E''(t)$ is in Bev and t is in radiation lengths. We have assumed in our calculations that $E''(t)$ is identical for photon and electron initiated showers. The errors introduced by this assumption are small because we are interested only in showers that contain at least 32 electrons. A considerable discrepancy exists between the values of $E_{\min}''$ (E'' for t equal to the depth of the shower maximum) obtained using "Approximation B" and the values obtained from the computations of Belenky. As stated in the introduction, the value of $E_{\min}''$ from Belenky is about 3.2 Bev and occurs at about 48 g cm^{-2} of lead above the chamber. The value of $E_{\min}''$ from "Approximation B" is about 1.50 Bev and occurs at about 30 g cm^{-2} of lead above the chamber.[43] This discrepancy again indicates that the results of our calculation will be approximate.

If we substitute E'' for t as the variable of integration, neglect electronic showers initiated in the first two radiation lengths of lead above the ionization chamber, and assume the lead above the chamber to be of infinite thickness, Eq. (1) becomes, for $I_{0.3}$ bursts,

$$\begin{aligned} n=&\int_{1.25}^{\infty}(dt/dE'')dE''\int_{E_{\min}(E'')}^{\infty}N_s(E)dE\\ &\times\int_{E''}^{E_{\max}'(E)}P(E,E')dE'+\int_{1.5}^{1.25}(dt/dE'')dE''\\ &\times\int_{E_{\min}(E'')}^{\infty}N_s(E)dE\int_{E''}^{E_{\max}'}P(E,E')dE'. \end{aligned} \tag{3}$$

The limits for E'' are in Bev. Since t is a doubled-valued function of E'' with a minimum at $t=4.5$ radiation lengths, Eq. (3) is the sum of two terms. The first term includes the electronic showers initiated at thicknesses greater than 4.5 radiation lengths above the chamber in which case $dt/dE''=4.6/E''$. The second term includes the electronic showers initiated at thicknesses between 2 and 4.5 radiation lengths above the chamber in which case $dt/dE''=-1.3/E''$. The error introduced both in neglecting showers initiated in the first two radiation lengths of lead and in assuming the

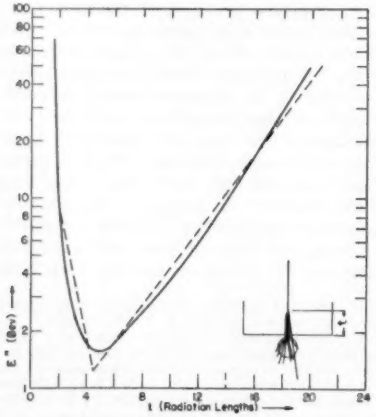

FIG. 14. The electron energy, E'', necessary to initiate at a thickness t of lead above the chamber an electronic cascade which will contain at least 32 electrons in the lead directly above the chamber [after Rossi and Greisen (see reference 42)].

[42] B. Rossi and K. Greisen, Revs. Modern Phys. 13, 240 (1941).

[43] Including the effects of multiple scattering, Wilson has recently applied the Monte Carlo method to the problem of cascade showers in lead. For showers initiated by 500 v Mev photons or electrons, his determination of the depth of the shower maximum agrees more closely with "Approximation B" than with the results of Belenky. Wilson's results indicate that our use of "Approximation B" with the assumption that one-half the shower electrons do not contribute to the ionization in the chamber is a good approximation to the correct shower behavior (see reference 41).

lead above the chamber to extend to infinity is very small.

In order to more easily evaluate the triple integrals of Eq. (3), we wished to integrate last over the differential μ-meson spectrum, $N_\mu(E)$, which could not easily be expressed in analytical form. This required interchanging the order of integration between the variables E and E''. Figure 15 shows the areas of integration in the E, E'' plane for the two terms in Eq. (3). In order to interchange the order of integration the second term in Eq. (3) had to be broken into the sum of two terms. Equation (4) is the equation used in the computation to determine the $I_{0.3}$ ionization bursts due to μ-mesons:

$$n=\int_{E(E''=1.25)}^{\infty} N_\mu(E)dE\int_{1.25}^{E_{\max}''(E)}(4.6/E'')dE''$$
$$\times\int_{E''}^{E_{\max}'(E)}P(E,E')dE'+\int_{E(E''=8.6)}^{E(E''=8.6)}N_\mu(E)dE$$
$$\times\int_{E_{\max}''(E)}^{1.25}-(1.3/E'')dE''\int_{E''}^{E_{\max}'(E)}P(E,E')dE'$$
$$+\int_{E(E''=8.6)}^{\infty}N_\mu(E)dE\int_{8.6}^{1.25}-(1.3/E'')dE''$$
$$\times\int_{E''}^{E_{\max}'(E)}P(E,E')dE'. \quad (4)$$

Similar equations were obtained for the $I_{0.6}$ and $I_{1.2}$ bursts due to μ-mesons. We used the expressions for $E''(l)$ given in Eq. (2) multiplied by a factor of 2 for the $I_{0.6}$ bursts and multiplied by a factor of 4 for the $I_{1.2}$ bursts.

The differential μ-meson spectrum, $N_\mu(E)$, and the probability for μ-mesons to produce electrons and photons by electromagnetic interactions have yet to be discussed. Since our detector selected nearly vertical rays, the differential energy spectrum of vertically incident μ-mesons was used. For energies in the region 1 to 7 Bev the energy spectrum was derived from the differential range spectrum at sea level reported by Rossi.[44] Beyond this point we used the same differential spectrum as that used by Christy and Kusaka.[38] Over the range 1 to 50 Bev the spectrum we used agrees very well with the recent results of Caro, Parry, and Rathgeber,[45] and beyond 50 Bev can be represented by a power law $kE^{-2.9}$. The energy spectrum at 10,600 feet was obtained from the sea level spectrum. We used the survival probabilities computed by Sands[46] to account for those μ-mesons which decay in traversing the

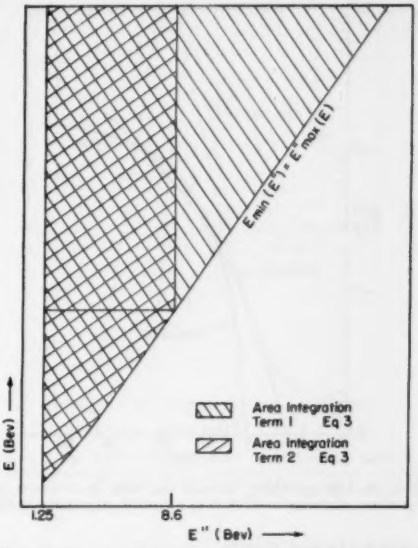

FIG. 15. The area of integration in the E, E'' plane. E'' is the energy of a μ-meson and E' the minimum energy of an electron or photon required to initiate a burst-producing shower.

310 g cm^{-2} of air from 10,600 feet to sea level. We neglected the production of burst-producing μ-mesons (energy over 1.25 Bev) between 10,600 feet and sea level.

There are three known types of electromagnetic interactions in which μ-mesons can produce high energy electrons or photons. These are collisions with atomic electrons, radiation processes in the field of nuclei and atomic electrons, and pair production in the field of nuclei and atomic electrons. The probabilities for μ-mesons to produce high energy electrons by collision and to produce high energy photons by radiation are well known.[47] No general formula is available, however, for the production of high energy electron pairs by charged particles. Hayakawa[48] has shown under simplifying assumptions that the energy lost by μ-mesons of the energy under consideration in pair production is of the same order as that lost in radiation processes. Davisson,[49] however, has shown that in pair production as compared to radiation processes, a considerably greater percentage of the energy loss is in small energy transfers. We have neglected pair production by μ-mesons in the calculation.

We made the following approximations in computing the probabilities for radiation and collision of μ-mesons

[44] B. Rossi, Revs. Modern Phys. **20**, 537 (1948).
[45] Caro, Parry, and Rathgeber, Australian J. Sci. Research **A4**, 16 (1951).
[46] M. Sands, Tech. Report No. 28, LNSE, Massachusetts Institute of Technology (1949).
[47] See probabilities for particles of spin $\frac{1}{2}$ in B. Rossi and K. Greisen, Revs. Modern Phys. **13**, 240 (1941).
[48] S. Hayakawa, Prog. Theoret. Phys. **4**, 287 (1949).
[49] R. J. Davisson, private communication to B. Rossi.

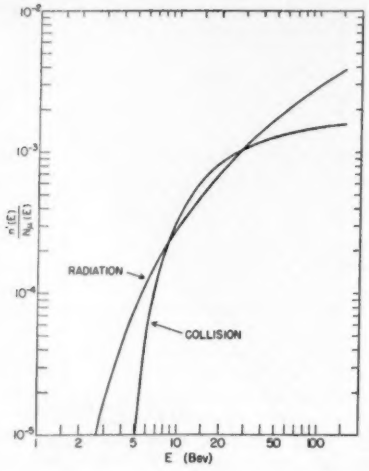

FIG. 16. The probability that an $I_{0.3}$ burst be produced by a μ-meson of energy in dE at E as a function of μ-meson energy.

assumed to have spin $\frac{1}{2}$:

$$mc^2=0.1, \quad p^2c^2 \gg m^2c^4, \tag{5}$$

where m is the mass and p is the momentum of the μ-meson, and all energies are in Bev.

With these approximations we obtained for the probability of collision processes per radiation length

$$P_{\text{col}}(E, E')dE' = 3.9\times 10^{-4}\left(\frac{1}{E'^2}-\frac{10+E}{E'E^2}+\frac{1}{2E^2}\right)dE'. \tag{6}$$

For collision processes, $E_{\max}'$ is given by

$$E_{\max}'(E)=E_{\max}''(E)=E^2/(10+E). \tag{7}$$

Similarly, the probability of radiation processes per radiation length is

$$P_{\text{rad}}(E, E')dE'$$

$$=9.8\times 10^{-6}\left\{\left[\frac{3}{4}\frac{E'}{(E+0.1)^2}+\frac{1}{E'}-\frac{1}{(E+0.1)}\right]\right.$$

$$\left.\times\left[\ln 5.5(E+0.1)(E+0.1-E')/E'-\tfrac{1}{2}\right]\right\}dE'. \tag{8}$$

For radiation processes the maximum transferable energy $E_{\max}'=E_{\max}''$, defined as the value of E' for which P_{rad} goes to zero, is slightly smaller than the μ-meson kinetic energy, E.

Since the limits of integration were different in the two cases, Eq. (4) had to be evaluated separately for collisions and radiation processes of μ-mesons. In evaluating Eq. (4) for the bursts induced by collision processes of μ-mesons, the first two integrations in each of the three terms were performed analytically, while the third integration was performed graphically. For the bursts due to radiation processes of μ-mesons, however, the triple integrals were evaluated numerically.

The probability for a μ-meson of energy E to cause an ionization burst was obtained as an intermediate step in the calculation. In the case of $I_{0.3}$ bursts, this probability for both radiation and collision processes is shown in Fig. 16. The curves of Fig. 16, which are the weighting factors for the differential μ-meson spectrum in calculating the number of $I_{0.3}$ bursts, give an indication of the errors involved in the commonly used assumption that μ-mesons above a certain energy contribute with equal weight to producing bursts, while μ-mesons below this energy do not contribute at all to the bursts.

Figure 17 shows the μ-meson spectrum at sea level weighted by the curves of Fig. 16. This figure gives the burst rate per unit energy interval as a function of the μ-meson energy. Integration of the curves of Fig. 17 gives the $I_{0.3}$ μ-burst rate at sea level.

Table IX shows the final results of calculations for sea level and 10,600 feet for three different values of minimum ionization chamber pulse.[50] From the results in this table we see that for the $I_{0.3}$ bursts induced by μ-mesons incident in the vertical direction, the increase from sea level to 10,600 feet is in the ratio of 1.00 to 1.20.

This increase in the rate of μ-bursts from sea level to 10,600 feet has been used in Sec. III.3 to separate the μ-bursts from N-bursts. While the absolute values of the burst rate due to μ-mesons calculated as described above may be in considerable error, the increase in the burst rate between sea level and 10,600 feet should be much more reliable, because the effects of many of the approximations made in computing the absolute values tend to cancel out when the ratio of these numbers is taken.

Indeed, the results for the μ-meson separation at sea level in Sec. III.3 do not depend critically on the altitude variation of the rate of μ-bursts. Assuming that no error was involved in the computation of the altitude variation of the μ-bursts, we have computed that (51±4) percent of the bursts at sea level are N-bursts. This percentage would be (52±4) if the burst producing μ-mesons did not increase with altitude and would be (48±4) if their intensity doubled between the two elevations. This percentage is, however, strongly dependent on the altitude variation of the N-bursts. In our calculation we assumed that the altitude variation of the $I_{0.3}$ N-bursts was identical to the altitude variation of the $AI_{0.3}BC_2$ events, which corresponded to an absorption thickness in air of 119 g cm^{-2}. We

[50] If we convert these values of n to those which correspond to a $\cos^2\theta$ dependence of the meson intensity about the zenith and to 2π solid angle, they can be compared with the values of Christy and Kusaka for bursts of 100 particles. The agreement is good.

could also have used the absorption thickness for N-bursts of similar size determined from measurements with similar detectors at elevations where the μ-bursts can be neglected.[4] If we take as a lower limit for the absorption thickness 110 g cm^{-2} and as an upper limit 125 g cm^{-2} we find the percentage of bursts due to nuclear interactions at sea level varies between the limits of 41 and 60 percent.

Since for the AIB events the number of μ-bursts is comparable with the number of N-bursts at sea level, and therefore can be neglected in comparison with the number of N-bursts at 10,600 feet, the integral burst size frequency distribution, $(N(E)=kE^{-\gamma})$, at 10,600 feet with $\gamma=1.4$ represents to a first approximation the N-bursts alone. At sea level the size frequency distribution is a power law with $\gamma\approx 1.8$ and represents a mixture of μ-bursts and N-bursts. In order to explain the observed change with altitude in the distribution function without assuming a change in the distribution function of N-bursts, one would have to approximate the distribution of μ-bursts at sea level by a power law with $\gamma\approx 2.5$. However, the results of our calculation

TABLE IX. The ionization burst rate in cm^{-2} sterad^{-1} sec^{-1} at sea level and 10,600 feet resulting from radiation and collision processes of μ-mesons.

Minimum pulse height	$I_{0.3}$	$I_{0.6}$	$I_{1.2}$
Sea level			
Radiation	6.55×10^{-7}	2.59×10^{-7}	0.932×10^{-7}
Collision	5.33×10^{-7}	1.24×10^{-7}	0.273×10^{-7}
Total	11.88×10^{-7}	3.83×10^{-7}	1.205×10^{-7}
10,600 ft			
Radiation	7.78×10^{-7}	3.08×10^{-7}	1.059×10^{-7}
Collision	6.46×10^{-7}	1.45×10^{-7}	0.307×10^{-7}
Total	14.24×10^{-7}	4.53×10^{-7}	1.366×10^{-7}

given in Table IX indicate an integral pulse-height distribution for μ-bursts with $\gamma=1.6$.

This value could only be increased significantly if the production of bursts by collision processes predominated over the production of bursts by radiation processes for μ-meson energies where the μ-meson spectrum is steep. The larger bursts are produced by μ-mesons of energies where the μ-meson spectrum is steep but are produced mainly by radiation processes (see Table IX). Collision processes are important in producing the smaller bursts, but these bursts are mainly produced by μ-mesons of energies where the μ-meson spectrum has begun to flatten off.[51]

In Sec. III.3 we have determined the rate of $AI_{0.3}B$

[51] Because of the nature of Eq. (4) it is difficult to discuss quantitatively the effects of the various parameters. However, assuming that direct pair production by μ-mesons can be neglected, the relative contribution to n by collision and radiation processes depends on the relative radiation and collision probabilities as a function of energy and on the shape of the μ-meson spectrum. We have carried out the calculations with two other spectra, and as long as the meson spectrum does not fall off much faster than we have assumed above, the pulse-height distribution cannot be much steeper than given by our calculation.

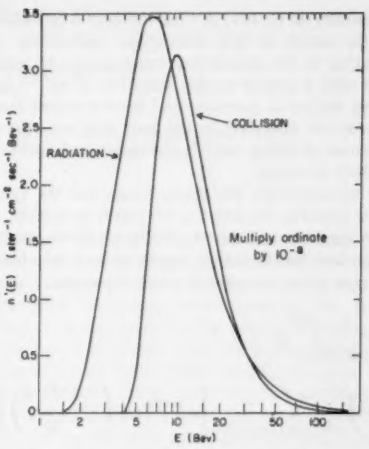

FIG. 17. The number of $I_{0.3}$ bursts contributed by radiation and collision processes per energy interval as a function of μ-meson energy. $n'(E)=dn/dE$ where n has the usual significance and E is the μ-meson energy.

bursts caused by μ-mesons. Table IX gives the calculated burst rate per sterad cm^2 sec for the $I_{0.3}$ bursts caused by μ-mesons. From these data we have determined the effective "area-solid angle product" for our detector to be 183 sterad cm^2.

From this effective "area-solid angle product" of the ionization chamber and from the $AI_{0.3}B$ rate due to the N-component, we can roughly calculate the intensity of the charged burst producing N-rays incident from the atmosphere at sea level and at 10,600 feet. For this calculation we have assumed that the N-bursts are caused by electronic cascades which are initiated by single photons arising from nuclear interactions. Equation (9) gives the number n_P of bursts resulting from interactions of the protons which constitute the charged N-component in the atmosphere. These bursts will be called proton bursts:

$$n_P=\int_0^T dt\int_{E(E'')}^{\infty} N_P(E)dE\int_{E''(1)}^{E_{max}'} P_P(E,E')dE'. \quad (9)$$

In Eq. (9) $N_P(E)$ is the differential number energy spectrum in the vertical direction of protons in the atmosphere, and $P_P(E,E')$ is the probability for a proton of kinetic energy E to cause an interaction from which the kinetic energy E' appears in the electronic component. The terms used in Eq. (9) are defined in identical manner as the similar terms in Eq. (1) except they are for protons and proton bursts, rather than μ-mesons and μ-bursts.

The last integral in Eq. (9) is just the probability for a proton of energy E to produce a burst. For protons above the energy $E(E'')$ we have assumed that this

probability is (1/167) g^{-1} cm^2 or 1/25.6 per radiation length, which is the interaction probability corresponding to the geometrical cross section in lead. We have used a proton energy spectrum of $aE^{-2.5}$ for the energy region in question, and have assumed that the protons are absorbed in the lead with an absorption thickness of 195 g cm^{-2},[52] (30 radiation lengths) independent of energy.

If we substitute the above values and the values of $E''(t)$ from Eq. (2) into Eq. (9) and if we neglect, as we have done for the μ-bursts, electronic showers initiated in the first two radiation lengths of lead, we obtain for the case where absorber Σ' alone is present:

$$n_P=\frac{1}{25.6}\int_2^{4.5}dt \times\int_{E(E''=40\exp[-0.77t])}^{\infty}\left[aE^{-2.5}\exp\left(-\frac{33.6-t}{30}\right)\right]dE +\frac{1}{25.6}\int_{4.5}^{33.6}dt \times\int_{E(E''=0.5\exp[+0.31t])}^{\infty}\left[aE^{-2.5}\exp\left(-\frac{33.6-t}{30}\right)\right]dE, \tag{10}$$

where t is the distance in radiation lengths from the ionization chamber.

In order to evaluate Eq. (10), we have assumed $E(E'')$ (which is the minimum kinetic energy that a proton must possess in order to transfer an energy E'' into the electronic cascade) to be a constant b times E''. Upon integration Eq. (10) becomes

$$n_P=0.030a/b^{1.5}. \tag{11}$$

If we assume that one-third of the proton kinetic energy goes into the electronic cascade, $b=3$, the number of bursts in sterad^{-1} cm^{-2} sec^{-1} becomes

$$n_P=5.7\times10^{-3}a. \tag{12}$$

This calculated value of n_P can be compared with an experimentally measured value to determine a, and we can then calculate the absolute proton intensity in the atmosphere. Unfortunately, the experimental value of n_P must be obtained from the rate of N-bursts which we cannot relate simply to the rate of proton bursts; i.e., the absorption curves cannot be uniquely extrapolated to zero thickness. We assumed that one-half the AIB events observed with Σ' alone above the detector were proton bursts. Using the effective "area-solid angle product" we find

$$\begin{aligned} n_P&=6\times10^{-7}\text{ sterad}^{-1}\text{ cm}^{-2}\text{ sec}^{-1}\quad\text{at sea level,}\\ n_P&=9\times10^{-6}\text{ sterad}^{-1}\text{ cm}^{-2}\text{ sec}^{-1}\quad\text{at 10,600 feet.}\end{aligned} \tag{13}$$

From Eqs. (12) and (13) one obtains the following absolute value for the proton spectrum in the atmosphere:

$$\begin{aligned} N_P dE&=1.05\times10^{-4}E^{-2.5}dE\quad\text{at sea level,}\\ N_P dE&=1.6\times10^{-3}E^{-2.5}dE\quad\text{at 10,600 feet,}\end{aligned} \tag{14}$$

where N_P is in sterad^{-1} cm^{-2} sec^{-1} Bev^{-1} and E is in Bev.

In spite of the many approximations and assumptions we have made in the calculation of the proton intensity, our results agree as to order of magnitude with results previously reported.[53,54] We have assumed that we detect protons of energy above 3.75 Bev. At 10,600 feet Eq. (14) yields at $E=4$ Bev, for N_P, 5×10^{-5} sterad^{-1} cm^{-2} sec^{-1} Bev^{-1}. This compares with the value of 7×10^{-5} sterad^{-1} cm^{-2} sec^{-1} Bev^{-1} for N_P at 4 Bev determined by Whittemore and Shutt at 11,200 feet with a cloud-chamber experiment. Our results also agree with theirs in that at 10,600 feet we find that 5 percent of the charged particles of energy above 4 Bev are protons. At sea level our results are in agreement with those of Mylroi and Wilson, who obtained for the proton spectrum in the range 1–10 Bev/c, $N_P dp=1.0\times10^{-4}p^{-2.5}dp$, where p is the momentum in Bev/c and N_P is in sterad^{-1} cm^{-2} sec^{-1} (Bev/c)$^{-1}$.

[52] Using the model of the semitransparent nucleus, the absorption thickness in lead was calculated from the absorption thickness of 119 g cm^{-2} in air. The "transition effect" in the absorption of the N-component, which obviously contradicts this absorption thickness in lead, was assumed in Sec. III.4 to be due to causes other than the absorption of the protons from the atmosphere.

[53] W. L. Whittemore and R. P. Shutt, Phys. Rev. **86**, 940 (1952).

[54] M. G. Mylroi and J. G. Wilson, Proc. Phys. Soc. (London) **A64**, 404 (1951).

Spallation of Cu with High Energy Neutrons

LUIS MARQUEZ
Institute for Nuclear Studies, University of Chicago, Chicago, Illinois
(Received June 19, 1952)

The yields of spallation products of copper with high energy neutrons have been measured and are given. The results are similar to those obtained with high energy protons. This similarity and some apparent differences are pointed out.

I. INTRODUCTION

So far, there have not been any experimental results of spallation with high energy neutrons, although there are some results of star production with high energy neutrons[1,2] and there are results of spallation in Sb with protons, deuterons, and alpha-particles,[3] in As with deuterons,[4] in Cu with protons, deuterons, and alpha-particles[5] and some others. Of all these spallation works, it seems that the work on Cu by Batzel, Miller, and Seaborg is the most careful and accurate. So it seemed that the study of the spallation of Cu with neutrons and its comparison with the results with protons and deuterons might shed some light on the question of the nuclear forces and more specifically on the question of charge independence.

II. IRRADIATION PROCEDURE

The irradiations were done in the synchrocyclotron at the University of Chicago. The 450-Mev proton beam at a radius of about 76 inches was allowed to strike a Be target of 2-inch thickness. This produced a beam of neutrons mostly in the forward direction, the energy distribution of this beam of neutron has a peak at 370 Mev; it decreases smoothly towards higher energies until it vanishes at about 440 Mev; toward lower energies it is smaller by a factor of five from the peak at 300 Mev and keeps going down smoothly at smaller energies.[6] This neutron distribution is similar to those obtained by other investigators.[7] Throughout this paper, the expression high energy neutrons means this energy distribution just described.

Near the synchrocyclotron tank there is a shield of 12-foot thickness made of concrete and iron in which there is a hole located in such a way as to let the neutron beam go through. Its central axis coincides with the tangent to the orbit at the point where the Be is located inside the tank.

This thick shield was also suitable to study the influence of secondary radiation in our experiments by irradiating samples in the hole near the tank and far from the tank. Secondary protons, mesons, etc., probably do not travel parallel to the neutrons because the magnetic field will deviate them. Only the gamma-rays and slow neutrons would follow exactly the same trajectory as the high energy neutrons. The gamma-rays have a small nuclear cross section and the slow neutrons produce nuclear reactions whose products are, in most cases, different from the spallation products, except Cu^{64} and perhaps Ni^{65} in the irradiation of Cu and Mg^{27} in the irradiation of Al.

The targets consisted of copper foils wrapped in a cylindrical shape and the irradiations were monitored by a foil of Al on one side of the cylinder. In the Al the well-known activity of Na^{24} was produced, and it served to monitor the irradiations. Irradiations lasted from 10 min to 3 hr. The fast neutron flux was of the order 10^5 neutrons/cm^2 sec.

The Cu and Al targets were placed in the hole in the shield in two positions; one close to the tank and the other far from it at the other side of the shield.

It was found that the yields were independent of whether the Cu and Al targets were close to the tank or far from it, except for Cu^{64}. This seems to prove that what was causing the nuclear reactions was coming from the Be target inside the tank in a straight line. The value for Cu^{64} might be somewhat high due to thermal neutron background.

III. CHEMICAL AND COUNTING PROCEDURES

The chemical procedures used were essentially those described by BMS,[5] or some described in the compilation of chemical procedures used in Berkeley,[8] except in the first step of the chemistry in which we usually had a heavy target of 20 to 50 g, from which about 20 mg of carrier had to be separated. This first step was accomplished in a different way for each of the different elements.

Cobalt and Nickel

The target was dissolved with the carriers added in a mixture of concentrated HCl and 30 percent H_2O_2 and boiled. The Cu^{++} was reduced to Cu^{+} with Na_2SO_3

[1] Bernardini, Booth, and Lindenbaum, Phys. Rev. **85**, 826 (1952).
[2] H. Fishman and A. M. Perry, Phys. Rev. **86**, 167 (1952).
[3] M. Lindner and I. Perlman, Phys. Rev. **78**, 499 (1950).
[4] H. H. Hopkins, Jr., Phys. Rev. **77**, 717 (1950).
[5] Batzel, Miller, and Seaborg, Phys. Rev. **84**, 671 (1951), and unpublished University of California Radiation Laboratory Report No. 1077 (1951). Hereafter this paper will be referred to as the BMS paper.
[6] J. Marshall and A. Nedzel (private communication).
[7] Fox, Leith, Wouters, and MacKenzie, Phys. Rev. **80**, 23 (1950). Also J. DeJuren and B. J. Moyer, Phys. Rev. **81**, 919 (1951).
[8] W. W. Meinke, unpublished University of California Radiation Laboratory Report No. 432 (1949).

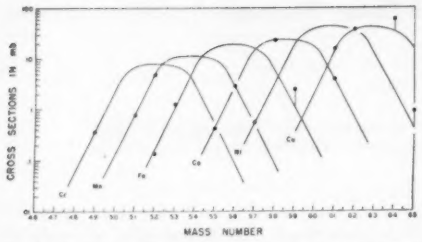

FIG. 1. Yield in millibarns of spallation products of Cu with high energy neutrons, as a function of mass number; each curve represents one element.

and CuSCN precipitated with NH_4SCN. From the filtrate Ni was precipitated with dimethyl glioxime by making the solutions slightly ammoniacal. From the filtrate also the Co was extracted, adding first an excess of NH_4SCN and then extracting with a mixture of amyl alcohol and ether.

Iron

The target with Fe^{+++} carrier was dissolved in a mixture of 12*N* HCl and 30 percent H_2O_2 and boiled. 12*N* HCl was added to make the solution of 8*N* in HCl, and from it the iron was extracted into isopropyl ether.

Chromium and Manganese

The target with Cr and Mn carriers was dissolved in concentrated HNO_3 by heating. From the boiling solution MnO_2 was precipitated by adding $KClO_3$ which also oxidized the Cr. The MnO_2 was separated by filtering through a sintered glass filter. The filtrate was diluted with H_2O and 6*N* NaOH added while heating until the solution was basic and the copper precipitated as CuO. The CuO was filtered and a concentrated solution of $BaCl_2 \cdot 2H_2$ added to the filtrate which gave a precipitate of $BaCrO_4$.

Titanium

The target with titanium carrier added was dissolved in HNO_3. The solution was diluted with water and made basic with ammonia. The copper remained dissolved in the ammonia complex form and the titanium hydroxide was centrifuged.

The samples for counting were spread over a circular area of 1.25-cm radius to have the same area as the aluminum disk used as monitor which also had a circular shape with 1.25-cm radius. All samples and monitors were counted on end-window Geiger counters at a distance of 0.4 cm from the window, and corrections were applied for coincidence, background, absorption, self-absorption, self-scattering, and backscattering. The four last corrections were made using the results of Gleason *et al.*[9] and Nervik and Stevenson.[10]

[9] Gleason, Taylor, and Tabern, Nucleonics **8**, No. 5, 12 (1951).
[10] W. E. Nervik and P. C. Stevenson, Nucleonics **10**, No. 3, 18 (1952).

IV. RESULTS

All cross sections measured in the spallation of copper relative to the cross section for the formation of Na^{24} from Al with high energy neutrons are shown in the third column of Table I. Since there are only one, two, or three points measured for each element, we tried to fit these data with a curve consistent with all of them by interpolating and extrapolating values. After that was done, it was possible to express the results as cross sections by adding the area under all curves, plus an estimate of the area under the lighter elements not measured, and equating this to one-half the total cross section for copper with high energy neutrons,[11] that is, 570 mb. In this way it was found that the cross section for the formation of Na^{24} from Al had to be 24.4 mb and the yield of spallation products of Cu in mb are given in the fourth column of Table I and shown in Fig. 1. We estimate that the error introduced by this method of measuring total cross section is about 50 percent which, however, applies to all results in the same direction. The experimental error of each cross section due to corrections, chemical yield, etc., is between 20 percent and 50 percent.

In the calculation of the cross sections, we used the counting efficiency given by BMS in order to make our results comparable; in the case of 9.2-hr Co^{58} which they did not report, we used 10 percent. The activity of 70-day Co^{58} was probably a mixture of Co^{56} and Co^{58}, since their half-lives are almost the same. In order to get the yield of 70-day Co^{58} we assumed that the yield of Co^{56} was that given by the interpolated yield curve of Co.

In Table II we compare the results of neutron spallation with the results of protons and deuterons. The second column has the yield in mb of the spallation product of copper with 340-Mev protons taken from

TABLE I. Yields of spallation products of copper with high energy neutrons.

Isotope	Observed half-life	Yield relative to yield of Na^{24} from Al	Yield in mb
Ti^{45}	3.5 hr	0.00032	0.0078
Cr^{49}	44 min	0.0142	0.35
Mn^{51}	47 min	0.031	0.76
Mn^{52}	5.9 day	0.192	4.68
Mn^{54}	2.58 hr	0.115	2.81
Fe^{52}	7.4 hr	0.0055	0.134
Fe^{59}	8.9 min	0.051	1.24
Fe^{59}	45 day	0.10	2.44
Co^{55}	18 hr	0.017	0.415
Co^{56}	9.2 hr	~2.0	~49
Co^{58}	70 day	0.95	23.2
Co^{61}	1.62 hr	0.155	3.78
Ni^{57}	36 hr	0.022	0.54
Ni^{66}	2.57 hr	0.036	0.88
Cu^{61}	2.9 hr	0.63	15.4
Cu^{62}	10.4 min	1.52	37.1
Cu^{64}	12.4 hr	2.40	58.6

[11] J. Marshall and A. Nedzel (private communication).

BMS's paper, and whose yield we determined also with high energy neutrons. We used the value of 17 mb for Cu^{64} as given in their University of California Radiation Laboratory report. The third column has the yield with 190-Mev deuterons, but since their value of 60 mb for Cu^{64} was a rough estimate, we used instead 30 mb, which brings the total cross section closer to the value 570 mb that it seems it should be. The fourth column has the ratio of the yield with protons divided by the yield with neutrons, and the fifth column has the ratio of the yields with deuterons divided by the yields with neutrons.

The spallation of Al with high energy neutrons was studied too, and the results are shown in Table III. In the case of neutrons, the high yield of 9.6-min Mg^{27} made it difficult to have an accurate value for the 10.1-min N^{13} and made it impossible to resolve the 20.4-min C^{11} activity. The yield of Mg^{27} was determined radiochemically and the others were measured directly from the irradiated Al foil. The yield of N^{13} is the difference between the total 10-min yield and the yield of Mg^{27}. These results are shown in Table III and compared with the protons results. The results with neutrons have of course the 50 percent error of the value 24.4 mb for Na^{24}, which was found as described previously, and this error also applies to all the neutron yields.

TABLE II. Yields of spallation products of copper with 340-Mev protons and 190-Mev protons according to BMS and ratios of these to the yields with high energy neutrons.

Isotope	Yield in mb with 340-Mev protons	Yield in mb with 190-Mev deuterons	Yield with protons/yield with neutrons	Yield with deuterons/yield with neutrons
Ti^{48}	0.75	0.06	96	7.7
Cr^{49}	0.70	0.30	2.0	0.86
Mn^{51}	1.21	0.87	1.59	1.14
Mn^{52}	5.27	2.61	1.13	0.56
Mn^{54}	1.87	3.00	0.67	1.07
Fe^{52}	0.136	0.090	1.01	0.67
Fe^{55}	1.24	1.41	1.00	1.14
Fe^{59}	0.58	1.35	0.24	0.55
Co^{55}	1.70	0.66	4.1	1.59
Co^{58}	42.5	...	1.83	...
Co^{61}	3.57	2.82	0.94	0.75
Ni^{57}	1.34	1.62	2.48	3.00
Ni^{65}	...	0.81	...	0.92
Cu^{61}	17.0	30	1.10	1.95
Cu^{62}	35.7	45	0.96	1.21
Cu^{64}	16.7	24	0.28	0.41

TABLE III. Yields of spallation products of Al with 420-Mev protons, high energy neutrons and their ratio.

Isotope	Yield in mb with 420-Mev protons	Yield in mb with high energy neutrons	Yield with protons/yield with neutrons
C^{11}	2.8	<3.4	>0.82
N^{13}	0.97	3.2±2.4	0.31±0.26
F^{18}	8.4	6.8±2.4	1.24±0.47
Na^{24}	10.8	24.4	0.44
Mg^{27}	...	5.1±2.0	...

V. CONCLUSION

It can be seen from the cross sections on Table I and II and from the ratios in columns four and five of that Table II that, while the cross sections for different nuclides with a given bombarding particle ranges from about 50 mb to a few tenths of a mb, the ratio of the yields of the same nuclide with different bombarding particles remains very closely the same. In fact, ten out of fifteen of the proton to neutron ratios in column four of the Table II lie between 0.67 and 2.00; and twelve out of fifteen of the deuteron to proton ratios in column five of Table II lie between 0.55 and 1.95.

However, a closer examination of these ratios reveals what seems to us a definite trend, which is very apparent in the proton to neutron ratios and somewhat less apparent in the deuteron case. The ratio is larger than unity for the lightest isotopes of a given element, which are isotopes formed in small yield. It is close to unity for isotopes near stability, which are isotopes formed in large yield. It is less than unity for isotopes on the heavy side, which again are isotopes formed in small yield. This same trend, less pronounced, seems to exist in the deuteron to neutron ratio and perhaps is somewhat blurred, because according to BMS, their results with deuterons are less accurate than their results with protons.

Perhaps we should say why we compared results with particles of quite different bombarding energies. The reason is that the yields in most spallation reactions studied so far in the region of 100 Mev to 450 Mev are slow varying functions of energy. Our results in an indirect way seem to corroborate it.

We are indebted to H. L. Anderson and the crew of the synchrocyclotron for their collaboration in the use of the machine, and to J. Marshall and A. Nedzel for making available to us the results of their experiments before publication.

Rotational Magnetic Moment, Magnetic Susceptibilities, and Electron Distribution in the Hydrogen Molecule*

N. J. HARRICK† AND N. F. RAMSEY
Lyman Laboratory of Physics, Harvard University, Cambridge, Massachusetts

(Received June 19, 1952)

Measurements have been made on the rotational spectrum of H_2 in the state $I=J=1$ and in strong external magnetic fields. These measurements yield a value for the rotational magnetic moment of H_2 in the rotational state $J=1$ of $\mu_{RB}=(0.88291\pm0.00007)$ nuclear magnetons. From this, the high frequency contribution to the diamagnetic susceptibility is calculated to be $\xi_{HF}=(1.64\pm0.16)\times10^{-31}$ erg gauss^{-2} molecule^{-1}. Since the diamagnetic interaction with the external field increases as the square of the field, the high field measurements yield accurate determinations of the dependence of the diamagnetic susceptibility on the molecules' orientations which is found to be $\xi_{a1}-\xi_0=-(3.66\pm0.20)\times10^{-31}$ erg gauss^{-2} molecule^{-1}. ξ_{HF} and $\xi_{a1}-\xi_0$ may be combined to give a measure of the quadrupole moment of the electron distribution relative to the internuclear axis with the result that $Q_e^{expt}=(0.330\pm0.013)\times10^{-16}$ cm^2.

I. INTRODUCTION

MOST of the measurements on the radiofrequency magnetic resonance spectra of H_2 and D_2 up to date[1-3] have been made on the nuclear spectra ($\Delta m_I=\pm1, \Delta m_J=0$). The present experiment is on the rotational spectrum which consists of transitions for which $\Delta m_I=0$, $\Delta m_J=\pm1$. These measurements are somewhat more difficult to make because the signal intensity is lower and also some of the interesting quantities are measurable only with strong external magnetic fields. These measurements are of particular interest because they make possible the evaluation of some of the parameters occurring in the Hamiltonian[4] which are independent of the nuclear orientation and, therefore, cannot be evaluated from measurements on the nuclear spectrum. The measurements on the rotational spectrum at strong external magnetic fields yield values for the rotational magnetic moment, the high frequency contribution to the magnetic susceptibility, and the dependence of the diamagnetic susceptibility on the molecules' orientation. It has been shown[5] that the magnetic susceptibilities determined from measurements on the rotational spectrum may be combined to give a measure of the quadrupole moment of the electron distribution in the molecule. The only previous measurements on the rotational spectrum of H_2 were those of Frisch and Stern[6] which yielded crude values of the rotational magnetic moment, and measurements of Ramsey[7] which improved the numerical value for the rotational magnetic moment but were not accurate enough nor at a high enough external magnetic field to give good measurements of the diamagnetic terms occurring in the Hamiltonian.

TABLE I. Allowed rotational transition frequencies in the strong field limit for H_2 and D_2.

Transition	m_I	m_J	$m_{J'}$	$m_{J'}$	Frequency
AB/KL	∓1	$-1/0$	∓1	$0/+1$	$(1-\sigma_{J1})b\pm(-c+3d/2)$ $\mp f-C_1'+(\sigma_{10}-\sigma_{11})a$
BC/GK	∓1	$0/-1$	∓1	$+1/0$	$(1-\sigma_{J1})b\mp(c+3d/2)$ $\pm f-(C_2-C_1')\pm C_2+(\sigma_{11}-\sigma_{10})a$
DE/EF	0	$-1/0$	0	$0/+1$	$(1-\sigma_{J1})b\mp3d\mp f-C_1'\mp2C_2$

II. APPARATUS AND PROCEDURE

The apparatus used in these experiments is that described previously[2,8] with improvements. The magnet current regulators[8] were improved to enable them to regulate with the required accuracy at strong magnetic fields. Current variations due to noise or battery voltage drift which could not be corrected by the electronic regulators were taken care of by trigger circuits and motor driven rheostats. Special precautions were taken with the motor driven rheostats to avoid contact troubles. Silver buttons with pressure exerted by a bronze spring provided the movable contact on the constantan strips and proved satisfactory. One difficulty with the current regulator was that, due to the slowness of the galvanometer compared to the magnetic circuit, any fast variations were not corrected.

The procedure in recording and treating the data was similar to that discussed elsewhere.[8] Due to the low intensity of the resonances of the rotational spectra, it was often very difficult to distinguish the resonances from the noise.

There are a number of apparatus effects for which special precautions are required. The central magnetic field is not completely homogeneous but varies considerably along its length. This gives rise to a compli-

* This work was assisted by the joint program of the ONR and AEC. The frequency measuring equipment was given to Harvard University by the Shell Oil Company.

† Present address: Philco Corporation, Philadelphia, Pennsylvania.

[1] Kellogg, Rabi, Ramsey, and Zacharias, Phys. Rev. **56**, 728 (1939); **57**, 677 (1940).

[2] Kolsky, Phipps, Ramsey, and Silsbee, Phys. Rev. **79**, 883 (1950); **80**, 483 (1950); **81**, 1061 (1951); Phys. Rev. **87**, 395 (1952).

[3] Harrick, Barnes, Bray, and Ramsey (to be published).

[4] N. F. Ramsey, Phys. Rev. **85**, 60 (1952). It will be noted that Table VIII of this reference disagrees with Table I of the present paper. This is due to a minor error in the earlier table which is corrected in the present Table I.

[5] N. F. Ramsey, Phys. Rev. **78**, 221 (1950). Equation (9) of the present paper corrects some errors of sign in the original paper.

[6] O. Frisch and O. Stern, Z. Physik **85**, 4 (1933).

[7] N. F. Ramsey, Phys. Rev. **58**, 226 (1940).

[8] N. J. Harrick, unpublished Ph.D. thesis, Harvard University, 1952.

cated pattern when Rabi's method[1] of a single oscillating field is used. This pattern is sometimes as much as 25 kc wide and can be altered by shimming the magnetic field. A second apparatus effect is observed even when Ramsey's method of separated oscillating fields[9] is used. Although the resonance observed with this method is not appreciably broadened beyond the theoretical value by the non-uniformities of the field, the intensity of the resonance is markedly reduced. This reduction is particularly serious in strong magnetic fields where it is probably due in part to the slowness of the current regulator for the magnetic field and in part to the non-uniformity of the magnetic field over the height of the beam and over the two oscillatory field regions. The variation of the fixed magnetic field in the region of the oscillatory field is a particularly important cause for concern because it might give rise to a dependence of the resonance frequency upon the oscillatory current. However, observations of the resonance frequency with different currents were made, and no appreciable shift was observed. If such a shift were found it presumably could be eliminated by a shortening of the length of the oscillatory field regions and by an increase in the homogeneity of the fixed fields. The low intensities of the resonances, particularly at high fields and for rotational transitions, made the present observations quite difficult and contributed appreciably to the final error.

TABLE II. Data on the rotational spectrum of H_2 at strong magnetic fields. The values of m_I and m_J, respectively, for the different transitions are as follows: *EF* (0, 0↔±1), *DE* (0, −1↔0), *KL* (+1, 0↔+1), *AB* (−1, −1↔0), *GK* (1, 0↔+1), and *BC* (−1, −1↔0).

No. of observations	Transition	Position of resonance (cps)
1	ν_D	2,268,903±10
	EF	2,508,945±30
	DE	2,163,820±20
2	ν_D	2,267,247±6
	EF	2,507,255±20
	DE	2,162,117±20
5	ν_D	3,287,223±10
	EF	3,557,275±20
	DE	3,212,781±20
2	ν_D	3,287,197±20
	EF	3,557,202±40
	DE	3,212,701±40
2	ν_D	2,431,730±10
	EF	2,676,529±40
	DE	2,331,484±40
2	ν_D	2,420,760±10
	EF	2,665,265±40
	DE	2,320,217±40
2	ν_D	2,407,886±10
	KL	2,506,576±60
	AB	2,452,469±40
3	ν_D	3,184,690±10
	EF	3,451,738±30
	DE	3,107,145±30
2	ν_D	3,184,690±10
	KL	3,306,310±120
	AB	3,252,680±40
3	ν_D	4,403,595±10
	EF	4,706,392±60
	DE	4,362,917±60
3	ν_D	4,373,575±20
	KL	4,530,035±100
	AB	4,477,593±300
2	ν_D	4,353,350±20
	KL	4,509,285±100
	AB	4,457,180±200
2	ν_D	4,318,906±20
	GK	4,646,835±60
	BC	4,243,533±60
1	ν_D	4,318,855±20
	EF	4,619,159±80
	DE	4,275,600±80

TABLE III. Constants required in calculations on rotational spectrum.

$a/H = (4257.84 \pm 0.10)$ cps gauss^{-1}
$6d = 346{,}026 \pm 144$ cps
$2c - 3d = 54{,}800 \pm 80$ cps
$2c + 3d = 400{,}829 \pm 80$ cps
$C_3' = (209{,}430 \pm 300)/H$ cps
$C_3 = (15{,}380{,}000 \pm 5{,}000)/H$ cps
$C_4 = -(455.1 \pm 0.2) \times 10^6/H^2$ cps

III. H_2 ROTATIONAL SPECTRUM AT STRONG MAGNETIC FIELDS

The theory of the hydrogen molecule in a magnetic field has recently been published.[4] In the previous notation,[4] the rotational spectrum consists of the six transitions *AB*, *KL*, *BC*, *GK*, *DE*, and *EF* for which $\Delta m_I = 0$, $\Delta m_J = \pm 1$. The expressions for the rotational transition frequencies are given in Table I.[4]

The measurements on the rotational spectrum are especially interesting in strong fields because one of the quantities of interest is the diamagnetic term, f, which increases as the square of the magnetic field and is just observable at about 3000 gauss. Measurements were made at various fields ranging from 3000 to 7000 gauss. The upper field limit was set by the disappearance of the interference pattern as mentioned earlier.

The experimental data obtained on the H_2 rotational spectrum are given in Table II. Most of the measurements were made on lines *DE* and *EF*. Since $m_I = 0$ for these molecules, there are no deflections due to the nuclear magnetic moment; hence a larger signal is obtained for this pair than for *AB* and *KL* or *BC* and *GK*. Since, at best, the signal on the rotational lines was small, it was easier to make measurements on *DE* and *EF*. The transition frequency, ν_D, of D_2 in the state $I = 2$, $J = 0$ was used to calibrate the magnetic field.[3] Regular and frequent runs were made on this

[9] N. F. Ramsey, Phys. Rev. **78**, 695 (1950); N. F. Ramsey and H. B. Silsbee, Phys. Rev. **84**, 506 (1951).

TABLE IV. Summary of calculations leading to the rotational magnetic moment of H_2.

No. of observations	Transitions	$(1-\sigma_{J1})b/H$ (cps gauss^{-1})
21	DE and EF	673.040±0.036
7	AB and KL	673.053±0.040
2	BC and GK	673.044±0.040

resonance to give an estimate of any magnetic field drift.

The numerical values of quantities required to carry out the calculations on the present experimental results are given in Table III.[8,8]

IV. ANALYSIS OF RESULTS

A. Rotational Magnetic Moment

Since the electronic state of the hydrogen molecule is $^1\Sigma$, the nonrotating molecule has no net electronic magnetic dipole moment. There is, however, a magnetic moment induced by the rotation of the molecule. This rotational magnetic moment arises from the circulating protons and electrons and is of a magnitude comparable to the nuclear magnetic moment. Molecular beams are thus deflected due to the presence of a rotational magnetic moment as well as a nuclear magnetic moment.

The calculation for the rotational magnetic moment is carried out in the following manner. Consider, for example, the pair of resonance frequencies DE and EF of Table I. $(1-\sigma_{J1})b/H$ may be obtained, by iteration, from

$$(1-\sigma_{J1})b/H=(DE+EF)/2H+\left(c-\frac{3d}{2}\right)^2\Big/(a-b)H. \quad (1)$$

In a similar manner, calculations may be carried out on the other pairs of transition frequencies. The results of the measurements on the various pairs of transition frequencies are given in Table IV.

The best value of $(1-\sigma_{J1})b/H$ is

$$(1-\sigma_{J1})b/H=673.043\pm0.036 \text{ cps gauss}^{-1}.$$

Using this value of $(1-\sigma_{J1})b/H$, the rotational magnetic moment, μ_{RH}, of H_2 may be calculated, in the usual notation, from

$$\mu_{RH}/J=\hbar b/H. \quad (2)$$

When the above experimental value is used in the preceding equation along with the DuMond and Cohen[10] values of the fundamental constants, the result is

$$\mu_{RH}=0.88291\pm0.00007 \text{ nuclear magneton}, \quad (3)$$

if the small unknown correction σ_{J1} is neglected.

The contribution of the electrons to the rotational magnetic moment is

$$\mu_{Re}/J=\mu_{RH}/J-1=-0.11709\pm0.00007 \text{ nuclear magneton}.$$

B. High Frequency Terms of the Magnetic Susceptibility

The rotational magnetic moment has been related to the high frequency terms[11] of the H_2 diamagnetic susceptibility by Wick[12,13] under the assumption that the effect of zero-point vibration in the molecule could be neglected. Ramsey[14] has recently discussed the effects of zero-point vibration on this and has shown that if the high frequency terms are assumed to vary with the internuclear spacing, R, as R^l these terms for H_2 in the zeroth vibrational and first rotational state are

$${}_0{}^H\chi_1{}^{HF}=(e^2/12mc^2)R_e^2L\,{}_0{}^H\langle(R/R_e)^l\rangle_1\,{}_0{}^H\langle(R/R_e)^{l-2}\rangle_1{}^{-1}\times\{1-{}_0{}^H\langle\mu_R/J\mu_{NM}\rangle_1\}. \quad (4)$$

TABLE V. Values for the dependence of the diamagnetic susceptibility on the molecules' orientation and of Q_e at various magnetic fields

$EF-DE$ (cps)	H (gauss)	C_1 (cps)	$2f$ (cps)	$(\xi_{a1}-\xi_0)\times10^{31}$ (erg gauss^{-2})	$Q_e\times10^{19}$ (cm^2)
345,125±40	3471.37±0.06	−38	− 749±150	−4.12±0.80	0.362±0.054
345,138±30	3468.84±0.06	−38	− 736±150	−4.05±0.80	0.358±0.054
344,498±30	5029.37±0.10	−17	−1456±150	−3.81±0.39	0.340±0.026
344,500±50	5029.34±0.10	−17	−1458±150	−3.82±0.39	0.341±0.026
345,045±50	3720.49±0.06	−33	− 849±150	−4.06±0.80	0.358±0.054
345,048±50	3703.71±0.06	−33	− 846±150	−4.08±0.80	0.360±0.054
344,594±40	4872.50±0.10	−19	−1356±150	−3.78±0.39	0.348±0.026
344,593±40	4872.50±0.10	−19	−1357±150	−3.78±0.39	0.348±0.026
343,478±80	6737.40±0.10	−10	−2508±150	−3.66±0.21	0.330±0.014
343,559±100	6607.75±0.10	−10	−2427±160	−3.68±0.21	0.327±0.014
$KL-AB$ (cps)					
54,107±60	3684.01±0.06		− 693±100	−3.38±0.49	0.310±0.033
53,630±120	4872.50±0.10		−1170±150	−3.28±0.40	0.303±0.027
52,391±260	6691.47±0.10		−2409±260	−3.56±0.30	0.323±0.020
$GK-BC$ (cps)					
403,301±90	6607.83±0.10	−10	−2452±130	−3.72±0.20	0.339±0.014

[10] J. W. M. DuMond and E. R. Cohen, Phys. Rev. **82**, 556 (1951).
[11] J. H. Van Vleck, *The Theory of Electric and Magnetic Susceptibilities* (Clarendon Press, Oxford, 1932).
[12] G. C. Wick, Z. Physik **85**, 25 (1933).
[13] G. C. Wick, Nuovo cimento **10**, 118 (1933).
[14] N. F. Ramsey, Phys. Rev. **87**, 1077 (1952).

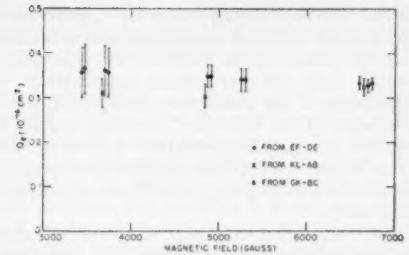

FIG. 1. The quadrupole moment of the electron distribution measured for various transitions and magnetic fields.

The value to be used for l is not determined in the present experiment. However, if one uses a dimensional argument analogous to that used by Newell[15] in a related problem, the value for l in the present case would be 2 ± 2. With this value,[10]

$$ {}_0{}^{H}\chi_1{}^{HF} = (0.0990\pm0.0010) \times 10^{-6} \text{ erg gauss}^{-2} \text{ mole}^{-1}. \quad (5) $$

Per molecule, the high frequency terms of the susceptibility equal

$$ {}_0{}^{H}\xi_1{}^{HF} = (1.64\pm0.16) \times 10^{-31} \text{ erg gauss}^{-2} \text{ molecule}^{-1}. \quad (6) $$

The error in the last two quantities is due almost exclusively to the uncertainty in the value of l to be used for the zero-point vibration correction.

C. Dependence of Magnetic Susceptibility upon Molecular Orientation

The last two terms in the Hamiltonian for H_2 and D_2[4] are included to account for the diamagnetic interaction of the molecule with the external magnetic field. Because these quantities depend only on the rotational quantum number, they can be measured only by observing the rotational transitions and not the nuclear transitions. A value of f may be obtained by taking differences among any pair of rotational transitions in Table I. Consider, for example, the pair of transitions DE and EF:

$$ EF - DE = 6d + 2f + 4c_3. \quad (7) $$

Now, the difference of diamagnetic susceptibility for a molecule with $m_J = \pm1$ and $m_J = 0$ is given[4] by

$$ \xi_{\pm1} - \xi_0 = 2hf/H^2. \quad (8) $$

The quantity f is just observable at about 3000 gauss and increases as the square of the magnetic field. For this reason, the dependence of the susceptibility upon orientation is best determined by experiments in strong magnetic fields. The results of different measurements of the dependence of the diamagnetic susceptibility upon the molecular orientation are given in Table V. The best average value of the 6600-gauss measurements is

$$ \xi_{\pm1} - \xi_0 = (-3.66\pm0.20) \times 10^{-31} \text{ erg gauss}^{-2} \text{ molecule}^{-1}. \quad (9) $$

D. Quadrupole Moment of Electron Distribution

Ramsey[5] has shown that $\xi_{\pm1} - \xi_0$ and ξ^{HF} can be combined to give a measure of the quadrupole moment of the electron distribution of a molecule. Relative to the internuclear axis, the quadrupole moment is given by the following expression:[5]

$$ Q_e = -\sum_j \langle 3\gamma_j^2 - r_j^2 \rangle = -(20mc^2/e^2)[(\xi_{\pm1} - \xi_0) - \tfrac{3}{5}\xi^{HF}]. \quad (10) $$

The results of the different measurements of Q_e are given in Table V. Figure 1 is a plot of Q_e for various magnetic fields as obtained from these measurements. From the resonances DE and EF alone, there appears to be a slight trend for Q_e to decrease with increasing magnetic field, but little significance should probably be attached to this apparent trend because it is less than the estimated experimental error. Since all pairs of transitions give the best agreement in high fields and since the experimental error is least there, the best value of Q_e is the average obtained from high field measurements and is

$$ Q_e = (0.330\pm0.013) \times 10^{-16} \text{ cm}^2. \quad (11) $$

This result agrees, within the experimental error, with the value quoted previously.[16] The previous value was the highest field result available at that time and was taken entirely from measurements on DE and EF. The accuracy of the present value is improved over the previously quoted value.

V. DISCUSSION

This calculated value of Q_e may be compared to a calculated value[5] from the theoretical expression of James and Coolidge.[17] Q_e is related to the quantity $N(R)$ calculated by James and Coolidge by

$$ Q_e = R^2 - [2N(R)/e]a_0^2, \quad (12) $$

where a_0 is the Bohr radius. If James and Coolidge's[17]

TABLE VI. Interaction constants of H_2 obtained from the rotational spectrum of H_2 at strong magnetic fields.

Quantity	Present value
$(1-\sigma_{J1})b/H$	0.673043 ± 0.000036 kcps gauss^{-1}
μ_{RH}/J	0.88291 ± 0.00007 nuclear magnetons
μ_{R_0}/J	-0.11709 ± 0.00007 nuclear magnetons
${}_0{}^{H}\chi_1{}^{HF}$	$(0.0990\pm0.0010)\times10^{-6}$ erg gauss^{-2} mole^{-1}
${}_0{}^{H}\xi_1{}^{HF}$	$(1.64\pm0.16)\times10^{-31}$ erg gauss^{-2} molecule^{-1}
$\xi_{\pm1} - \xi_0$	$-(3.66\pm0.20)\times10^{-31}$ erg gauss^{-2} molecule^{-1}
${}_0{}^{H}(Q_e)_1{}^{\text{exp}}$	$(0.330\pm0.013)\times10^{-16}$ cm^2
${}_0{}^{H}(Q_e)_1{}^{\text{theor}}$	$(0.344\pm0.010)\times10^{-16}$ cm^2

[15] G. F. Newell, Phys. Rev. **80**, 476 (1950).

[16] Harrick, Barnes, and Bray, Phys. Rev. **85**, 716 (1952).

[17] H. M. James and A. S. Coolidge, Astrophys. J. **87**, 447 (1938).

expression for $N(R)$ is used in this equation, one finds

$$ {}_0^{\mathrm{H}}\langle Q_e\rangle_1^{\mathrm{theor}} = a_0^2\left[{}_0^{\mathrm{H}}\langle (R/R_e)^2\rangle_1 (R_e/a_0)^2 - 0.884 - 0.614\ {}_0^{\mathrm{H}}\langle (R-R_e)/R_e\rangle_1 (R_e/a_0) + 0.410\ {}_0^{\mathrm{H}}\langle (R-R_e)^2/R_e^2\rangle_1 (R_e/a_0)^2\right]. \quad (13) $$

The various averages can be obtained from Ramsey's[14] paper on the effects of zero-point vibration and when these are used, the above equation gives

$$ {}_0^{\mathrm{H}}\langle Q_e\rangle_1^{\mathrm{theor}} = (0.344\pm 0.010)\times 10^{-16}\ \mathrm{cm}^2. \quad (14) $$

The agreement between the experimental value of Eq. (11) and the theoretical value of Eq. (14) is within the overlap of the errors.

The results of the present measurements are all summarized in Table VI. These are in good agreement with values previously quoted.[4] There are large improvements in accuracy with the present results. $(1-\sigma_{J1})b/H$ is improved by a factor of 100 over previous measurements.[7] The best existing values for γ_p limits the accuracy of the rotational magnetic moment as calculated from the present results, but, there still is an improvement of about 100 over previous measurements. The dependence of the diamagnetic susceptibility on the orientation of the molecules' rotational angular momentum, $\xi_{\pm 1}-\xi_0$, is improved from a 65 percent uncertainty to only 5 percent; and the quadrupole moment of the electron distribution, Q_e, from 40 percent to 4 percent uncertainty.

The experimental value of Q_e compares favorably to the theoretically calculated value. The usefulness of the experimental value of Q_e lies in a check of the wave functions used in the theoretical calculation of Q_e and the wave function used to calculate the gradient of the electric field at the nucleus resulting from the electrons.

The authors wish to thank Mr. R. G. Barnes and Mr. P. J. Bray for their assistance in making the present measurements.

PHYSICAL REVIEW VOLUME 88, NUMBER 2 OCTOBER 15, 1952

Multiple Scattering of Neutrons. III. Scattering by Spin-Dependent Forces and Polarization Phenomena

OTTO HALPERN
University of Southern California, Los Angeles, California
(Received June 16, 1952)

The treatment presented in two preceding papers is extended to cover the case of spin-dependent forces. A general theorem is derived which reduces the problem of scattering by spin-dependent forces to the problem of scattering by spin-independent forces, which has previously been solved analytically. It is shown that observations on the neutrons returning from the scatterer can be used in many practical cases to determine the ratio of the two scattering amplitudes. Similarly, for very small probability of depolarization per single collision, the depolarization of the neutrons transmitted through the scatterer offers information about the spin dependence of the scattering amplitudes. The necessary material for the evaluation of the observation is presented in table form. A comparison is made with a paper by Borowitz and Hamermesh in which the same subject has been treated by a different method.

I. INTRODUCTION

IN two preceding papers[1] the multiple scattering of slow neutrons in a plane parallel sheet of infinite extension has been discussed. The physical assumptions underlying the treatment were the following: The scattering probability is spherically symmetrical; the scattering is purely elastic; capture processes are admitted. It was also assumed that no correlation exists for the scattering from the various centers. The present paper, as announced at the end of II, extends the treatment to the case of spin-dependent nuclear forces.[2]

The physical interest of the problem here discussed can perhaps best be explained as follows. It has been shown in an earlier paper[3] that the probability Q for the inversion of the spin of the incident neutron during a scattering process is given by

$$ Q = \frac{2i(i+1)}{3(2i+1)}\,\frac{(a_1-a_0)^2}{ia_0^2+(i+1)a_1^2}. \quad (1) $$

Here i denotes the spin of the nucleus in units of $h/2\pi$; a_0 and a_1 stand for the scattering amplitude of the system nucleus plus neutron if its total angular momentum is $i-\frac{1}{2}$ and $i+\frac{1}{2}$, respectively.

One can see by a simple analysis of (1) that Q has a maximum value of $\frac{2}{3}$; this maximum value is taken on for the case of

$$ a_0+3a_1=0. \quad (2) $$

The relation (2) is approximately satisfied, for example, in the case of H. One can see in general that sizeable values of Q will only occur if the two amplitudes have opposite sign.

[1] Halpern, Luneburg, and Clark, Phys. Rev. **53**, 173 (1938) (I); O. Halpern and R. K. Luneburg, Phys. Rev. **76**, 1811 (1949) (II).
[2] O. Halpern, Phys. Rev. **75**, 1633 (1949).
[3] O. Halpern and M. H. Johnson, Phys. Rev. **55**, 898 (1939).

If, on the other hand, a_0 and a_1 differ only by a small percentage, then the value of Q diminishes very rapidly. If, e.g., a_0 and a_1 differ by 20 percent, then Q is of the order of 1/150.

Direct experiments[4] of a single scattering type have successfully demonstrated the spin-dependence of the scattering amplitudes of some elements. The observed values were necessarily somewhat inaccurate; the evaluation of the elaborate experiments led, for example, to values of Q exceeding $\frac{1}{3}$. It can scarcely be hoped that the accuracy of this type of experiment can be very much improved and most obviously an arrangement of this kind will be useful only if Q has sizeable values. If, on the other hand, the two amplitudes differ by a small percentage only, then an arrangement involving multiple scattering becomes necessary so that a sufficiently large depolarization effect be obtained.

The result of a large number of collisions during a diffusion process cannot be foreseen by simple arguments, since the number of collisions undergone by the re-emerging neutrons will show large fluctuations. A theory is therefore required which gives directly the polarization state of the emerging neutrons if that of the incident particles is known. Observation on the amount of depolarization will then allow us, with the aid of the theoretical formulas, to determine the value of Q and thereby the ratio of a_0 and a_1.

The usefulness of the study of multiple scattering for the determination of Q has already been recognized by other authors[5] in an earlier paper, which we shall discuss at the end of the present note.

II. THE INTEGRO-DIFFERENTIAL EQUATION FOR SPIN-DEPENDENT FORCES

We shall now show that the problem of diffusion under the influence of spin-dependent forces can be, without difficulty, reduced to the problem already solved, of diffusion under the influence of spin-independent forces.[1]

Following I and II we write again the specialized Boltzmann transport equation for the diffusion of neutrons in the one-dimensional case,

$$\xi\partial w(x,\xi)/\partial x+Aw(x,\xi)=B\bar{w}(x), \quad \xi=\cos\vartheta. \tag{3}$$

Here, w denotes, as before, the probability of finding neutrons at the distance x from the boundary, the velocity of which makes an angle ϑ with the x direction; $\bar{w}$ is given by

$$\bar{w}(x)=\int_{-1}^{+1} w(x,\xi)d\xi. \tag{4}$$

A and B determine the probability of scattering and capture and of scattering alone, respectively. The ratio B/A is again called σ. In the absence of capture, σ takes on the limiting value $\frac{1}{2}$. As before, the treatment is limited to values of of σ in the neighborhood of $\frac{1}{2}$.

Equation (3) holds true in the presence of polarized neutrons and spin-dependent forces as long as we understand w to represent the distribution of all neutrons independent of their spin. To discuss the polarization, we need a second equation which can be obtained easily. Denoting by Π the function analogous to $w(x,\xi)$ but referring to the polarized part only, we observe that always $\Pi\leqq w$ and that for a completely unpolarized condition Π becomes zero. The ratio Π/w gives the percentage of polarization.

The transport equation for Π reads as follows:

$$\xi\partial\Pi(x,\xi)/\partial x+A\Pi(x,\xi)=B(1-2Q)\bar{\Pi}. \tag{5}$$

In fact, the left side of the transport equation, giving the amount of polarization, leaving a certain x, ξ domain is unchanged as compared with (3). The right side, on the other hand, exhibits two changes: The gain in polarization through the entrance of particles into the specified domain is now given by

$$B\bar{\Pi}(1-Q),$$

since only those particles which retain their polarization can be added. Particles, on the other hand, which change their polarization during collision give a negative contribution, their fraction being

$$B\bar{\Pi}Q.$$

The addition of these contributions gives the right side of (5).

The boundary conditions, as discussed in II, take the same form for w and Π. They read

$$w(0,\xi)=f(\xi), \quad \xi>0, \tag{6a}$$

$$w(l,\xi)=0, \quad \xi<0, \tag{6b}$$

$$\Pi(0,\xi)=g(\xi), \quad \xi>0, \tag{7a}$$

$$\Pi(l,\xi)=0, \quad \xi<0. \tag{7b}$$

Here $f(\xi)$ and $g(\xi)$ are known functions.

Equation (3) has been solved in II. The resultant solution for $w(0,\xi)$ and $w(l,\xi)$ as well as for $w(x,\xi)$ inside of the slab was there given in terms of σ and a new transcendental function $P_\sigma(\xi)$, the values of which in the neighborhood of $\sigma\sim\frac{1}{2}$ and for $\xi>0$ can be found in II in the form of a power series and in tables.

By a simple transformation (5) can now be reduced to (3). Substitute in (5) the following:

$$x'=x(1-2Q), \tag{8a}$$

$$A'=A/(1-2Q). \tag{8b}$$

We then obtain

$$\xi\partial\Pi/\partial x'+A'\Pi=B\bar{\Pi}. \tag{9}$$

(3) and (9) are equivalent if one replaces the old by

[4] W. E. Meyerhof and D. B. Nicodemus, Phys. Rev. **82**, 5 (1951).
[5] S. Borowitz and M. Hamermesh, Phys. Rev. **74**, 1285 (1948).

TABLE I. Values of $P_\sigma^{-1}(z)$.

σ \ z	0.0	0.1	0.2	0.3	0.4	0.5	0.6	0.7	0.8	0.9	1.0
0.500	1.00	1.24	1.45	1.64	1.83	2.01	2.19	2.37	2.55	2.73	2.91
0.499	1.00	1.23	1.42	1.60	1.77	1.94	2.10	2.25	2.40	2.55	2.70
0.498	1.00	1.23	1.41	1.59	1.75	1.90	2.06	2.20	2.35	2.49	2.62
0.496	1.00	1.22	1.40	1.57	1.72	1.86	2.00	2.13	2.27	2.39	2.52
0.494	1.00	1.22	1.39	1.55	1.69	1.84	1.96	2.09	2.21	2.32	2.44
0.492	1.00	1.21	1.38	1.54	1.67	1.81	1.93	2.05	2.17	2.27	2.38
0.490	1.00	1.21	1.37	1.53	1.66	1.79	1.90	2.01	2.13	2.22	2.32
0.485	1.00	1.20	1.36	1.50	1.62	1.74	1.85	1.95	2.05	2.14	2.23
0.480	1.00	1.19	1.35	1.48	1.59	1.70	1.80	1.89	1.98	2.06	2.14
0.470	1.00	1.18	1.32	1.44	1.55	1.64	1.73	1.81	1.88	1.96	2.02
0.460	1.00	1.17	1.30	1.41	1.51	1.60	1.67	1.74	1.81	1.87	1.92
0.450	1.00	1.17	1.29	1.39	1.48	1.55	1.63	1.69	1.74	1.80	1.85
0.440	1.00	1.16	1.27	1.37	1.45	1.52	1.58	1.64	1.70	1.75	1.79
0.430	1.00	1.15	1.26	1.35	1.42	1.49	1.55	1.60	1.65	1.69	1.73
0.420	1.00	1.15	1.25	1.33	1.40	1.46	1.52	1.57	1.61	1.65	1.68
0.410	1.00	1.14	1.24	1.31	1.38	1.44	1.49	1.53	1.58	1.61	1.64
0.400	1.00	1.13	1.23	1.30	1.36	1.41	1.46	1.50	1.54	1.57	1.60

the new variable and also changes the coefficients in the manner indicated. The substitution (8) is legitimate as long as $Q<\frac{1}{2}$. Since we are only interested in the problem of small values of Q, the substitution (8) is always valid in our case.

The presence of spin-dependent forces thus affects the transport equation by changing the unit of length and increasing the "capture cross section." The percentage of polarization can immediately be determined if the ratio of the two solutions of (3) and (9) is formed.

III. DISCUSSION OF THE SOLUTION

The effect of depolarization can be studied observing the returning as well as the transmitted neutrons; the magnitude of Q and perhaps experimental convenience will decide the method to be used. We want to illustrate here the evaluation for some special cases of interest. The discussion will be carried out under the assumption that $A=2B$. This means that there is no direct capture present. A' is, of course, larger than $2B$.

This restriction is only introduced for illustrative purposes, since the formulas in II include the general case, with true capture present.

If observations are made on the returning beam, then it is convenient to assume that the slab is infinitely thick; this restriction again is insignificant, since II, formulas (5.5) and (6.3), are valid also for large but finite thickness of the slab.

The velocity distribution of the returning beam $w(0, \xi)$ then reads

$$w(0,\xi)=\frac{\xi_0}{2(\xi_0-\xi)}\frac{1}{P_0(\xi_0)}\frac{1}{P_0(-\xi)}. \tag{10}$$

In (10) P_0 denotes the new transcendental function $P_\sigma(\xi)$ discussed before for the value of $\sigma=\frac{1}{2}$; ξ is, of course, always negative, while ξ_0 denotes the direction cosine of the velocity of the incident beam. For most practical cases $\xi_0=1$; but, as shown in I and II, the general case of an arbitrary velocity distribution can be obtained by multiplying (10) with the distribution function and integrating over ξ_0.

Similarly, $\Pi(0, \xi)$ is given by

$$\Pi(0,\xi)=\frac{\sigma\xi_0}{(\xi_0-\xi)}\frac{1}{P_\sigma(-\xi)}\frac{1}{P_\sigma(\xi_0)}. \tag{11}$$

The main difference between (10) and (11) is the appearance of σ in place of the factor $\frac{1}{2}$ and the replacement of P_0 by P_σ. We repeat the definition of σ in the present case

$$\sigma=B/A', \tag{12}$$

The percentage of polarization Π/w is now given by

$$\chi(\xi)=\frac{\Pi(0,\xi)}{w(0,\xi)}=2\sigma\frac{P_\sigma(-\xi)P_\sigma(\xi_0)}{P_0(-\xi)P_0(\xi_0)}. \tag{13}$$

It depends, as we see, quite markedly on the direction cosine of the velocity of the returning beam.

Table I gives the values of $P_\sigma(\xi)$ in the range of greatest practical interest. The polarization ratio can be determined with its aid by two simple divisions. We notice that the percentage of polarization of the returning beam increases monotonously with decreasing $-\xi$. Depolarization is by far strongest for neutrons which emerge perpendicular to the boundary.

Numerically, one can see that the method of measuring the depolarization of returning neutrons will require a value of Q which is not too small. Assuming for the sake of discussion that a depolarization effect of about 30 percent is required for sufficiently accurate measurements, then we see from Table I that observation of neutrons returning almost perpendicularly would give such an effect if 2σ is about 0.99. This would mean a depolarization probability Q per collision of approximately 1/200 or a difference in the scattering amplitudes of about 20 percent. Smaller differences between the two scattering amplitudes could then not be measured with the aid of observations on returning beams.

The expressions for transmitted beams are given in II (6.4) and (5.6) with the aid of II (5.13), (6.28), and (4.23). They read as follows:

$$w(l,\xi)=\frac{\xi_0}{2(m+Al)}\frac{1}{P_0(\xi_0)}\frac{1}{P_0(\xi)}. \tag{14}$$

$$\Pi(l,\xi)=\frac{2\sigma\xi_0 e^{-A'l'/\alpha}\alpha\mathcal{S}(\alpha)}{1-\mathcal{S}^2(\alpha)e^{-2A'l'/\alpha}}\times\frac{1}{(\alpha-\xi_0)(\alpha-\xi)}\frac{1}{P_\sigma(\xi_0)}\frac{1}{P_\sigma(\xi)}. \tag{15}$$

The quantities α, $\mathcal{S}(\alpha)$, and m are defined by the relations

$$\sigma=\left(\alpha\log\frac{\alpha+1}{\alpha-1}\right)^{-1}, \tag{16}$$

$$\mathcal{S}(\alpha)=(1/2\alpha)[P_\sigma^2(\alpha)/\rho'(\alpha)], \tag{17}$$

$$\rho(z)=P_\sigma(z)P_\sigma(-z), \tag{18}$$

$$m=1.43. \tag{19}$$

If $\alpha \gg 1$, we have approximately

$$S(\alpha) = 1 - (m/\alpha). \tag{19a}$$

(14) together with the values of Table I shows that the transmitted intensity is approximately given by

$$\mathfrak{s} = \int_0^1 \xi w(l, \xi) d\xi = \frac{\xi_0}{2(m + Al)} \frac{1}{P_0(\xi_0)} \int_0^1 \frac{\xi d\xi}{P_0(\xi)}$$

$$\cong \frac{1.68}{1.43 + \mathrm{Al}} \text{ for } \xi_0 = 1. \tag{20}$$

If the thickness of the slab is about ten mean free paths (Al = 10), then the transmitted current (in the absence of capture) amounts to about 15 percent of the incident or 17 percent of the returning current.

It is rather easy to find the values of $\Pi(l, \xi)$ for various practically occurring values of σ. A simple inspection of the structure of (15) shows that one has it in one's hand by moderately increasing the thickness to obtain sizeable depolarization effects even if σ lies very close to $\frac{1}{2}$; i.e., Q is very small. It is fortunate that the decrease of the transmitted current with thickness is so slow that even for thicknesses which are very large compared to the mean free path, the transmitted intensity forms a substantial fraction of the returning intensity. The experimenter should find no difficulty in choosing the proper arrangement with the aid of the formulas here presented.

The paper by Borowitz and Hamermesh[5] has several points in common with the present investigation; there exist, on the other hand, fundamental differences[2] in the treatment of the problem, the numerical results obtained, and the interpretation of the solution.

The authors named start with the same transport equation and equally use our expression for Q.[3] Since they do not find themselves in the possession of our analytic solution of the diffusion problem, they use an approximate numerical method due to Wick to solve the problem for the special case where the thickness of the slab equals ten mean free paths. The determination of the ratio of polarization is done in the same manner in both papers.

The data given by Borowitz and Hamermesh as a result of their numerical calculations of one single case differ considerably from those obtained by our general analytic solution as specialized for the condition discussed by the authors. Since we have at present no reason to doubt the correctness of our analytic solution, we are forced to conclude that the numerical method used is unsatisfactory. To illustrate the differences occurring, we refer to their value for the transmitted density of 0.3, while our value (in the absence of any capture) is only 0.25. Similarly, they give for the transmitted current, which constitutes probably the best quantity observable, a value of about 8×10^{-3}, while our analytical value leads to 15×10^{-3}. The reflected current is given by those authors, in the absence of capture, as 1, while we have a value of 0.85. Similar differences exist in the values in the presence of capture.[6] We may conclude that these numerical differences are sufficiently big to affect very seriously any attempts to evaluate Q or the ratio of the scattering amplitudes with the aid of these formulas.

The authors did not make calculations for the use of, nor did they discuss, the method of observing the depolarization of returning neutrons; it seems that their calculations would not indicate any sizeable depolarization in this case. The authors give, furthermore, a discussion of the intensity transmitted and the choice of the thickness most advisable for various values of Q, which seems to us to be due to a mistake. They mention in the text on pages 1291 and 1292 as well as in their Table II that the intensity of the emerging beam in case of a thickness of the slab of ten mean free paths is about 10^{-4} of that of the incident beam. Therefore, they advise the experimenter to choose carefully between a very big loss in intensity with increased thickness and a larger depolarization obtained thereby. This statement must be due to a misunderstanding of the formulas. The transmitted current for the case discussed is, as we have shown, not 10^{-4} of the incident or returning current but rather 15 percent or, respectively, 17 percent of it. We have pointed out at the end of the preceding paragraph that the decrease in the transmitted intensity, even for large thicknesses, is so slow that, in the case of very small Q's, thick slabs may be chosen with great advantage.

[6] W. E. Meyerhof and D. B. Nicodemus, Phys. Rev. **82**, 5 (1951), express the opinion (see their footnote 6) that the differences between our results, as announced previously (see reference 2), and those of Borowitz and Hamermesh are due to a wrong labeling of their Fig. 3. We are unable to follow this opinion. In particular, the terminal value for the density of 0.3, as given in Fig. 3 of Borowitz and Hamermesh, is confirmed by their value given in the text, namely 299×10^{-3}. Furthermore, as shown in the text of the present note, there are (even larger) differences which arise from comparison with the other diagrams of Borowitz and Hamermesh.

The Absorption Mean Free Path of Large Hard Showers in Air*

HAROLD K. TICHO
Department of Physics, University of California, Los Angeles, California
(Received April 1, 1952)

In this report an experiment is described in which altitude curves of hard showers of various sizes produced in a lead block were obtained. The sizes were determined by means of a hodoscope; for the largest hard shower group a minimum energy of 260 Bev was estimated by extrapolation to the top of the atmosphere. All altitude curves show an exponential absorption in the atmosphere with a mean free path of ~ 125 g cm^{-2}. It appears that these large attenuation lengths are difficult to reconcile with a geometric collision mean free path for a nucleon-nucleus collision.

I. INTRODUCTION

IN the spring and summer of 1950 an experiment was carried out in which the altitude dependence of the rate of penetrating showers of various sizes produced in a lead block was measured. At the time it was hoped that such altitude curves might yield some information about the dependence, if any, of the collision mean free path of primaries on their energy. Unfortunately the importance of secondaries even in this high energy region was not sufficiently appreciated and as a consequence the experimental results were not unambiguous with respect to a clear differentiation between the collision and the absorption mean free paths.

In the last two years new theories[1] concerning high energy nucleon-nucleon collisions have been published and the existence of some new particles established[2-4] and it will be necessary to perform calculations to see to what extent these new factors involving the primary act succeed in explaining the grosser features of the cosmic radiation. The data obtained in this experiment might be useful as a parameter in such calculations and they are presented in this spirit.

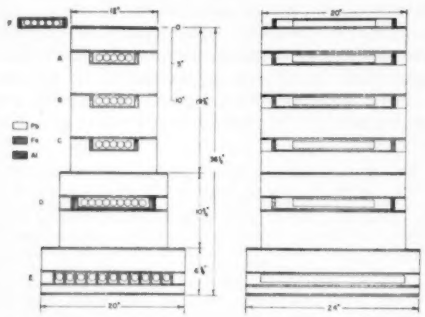

FIG. 1. Cross-sectional view of the counter tube and absorber assembly.

II. APPARATUS

Cross-sectional views of the absorber and counter tube assembly are shown in Fig. 1. Each of the counter trays A, B, C, and F had a sensitive area of 340 cm^2, trays D and E had sensitive areas of 610 cm^2 and 1420 cm^2, respectively. The absorbers, from top to bottom, were 3 in. (86 g cm^{-2}), 4 in. (115 g cm^{-2}), 4 in., 6 in. (172 g cm^{-2}), 8 in. (230 g cm^{-2}), and 1 in. (29 g cm^{-2}) of lead. Steel plates, $\frac{1}{4}$-in. thick, were inserted at various levels indicated in the diagram to give the shield mechanical rigidity. The counters were housed in thin-walled aluminum boxes; those of tray E were separated by $\frac{1}{4}$-in. steel spacers to reduce the chance of multiple firing in that tray due to knock-ons and electron cascades starting in the lead above it. The absorbers were left unchanged throughout the course of the experiment.

The circuit, associated with the counter assembly, consisted of two major parts: (a) a coincidence circuit which generated a master pulse P whenever at least one counter in tray A, at least two counters in tray B, and at least two counters in tray C were discharged simultaneously, and (b) a hodoscope which displayed by means of neon bulbs all those counters in trays D and E which were discharged in coincidence with the master pulse P. The resolving times in the two circuits were shorter than 2 microseconds; as a result all chance coincidences were negligible. P events were caused mainly by hard showers generated in the lead above tray B; the hodoscope permitted classification with respect to their size. Separate neon bulbs also indicated whether a given P event resulted from the firing of one or at least two of the counters in tray A, $P(A_1)$ or $P(A_2)$, and whether or not the P pulse was in coincidence with a pulse from one (or more) of the counters in tray F, $P(F)$ or $P(-F)$; i.e., whether it was an "extensive" or a "local" hard shower. The F tray was used only during the White Mountain part of the experiment. The P pulse also actuated a mechanical register and operated the shutter of a camera which

* The flight time was made available by the ONR and the Air Forces.

[1] E. Fermi, Prog. Theoret. Phys. **5**, 570 (1950); Phys. Rev. **81**, 683 (1951).

[2] G. D. Rochester and C. C. Butler, Nature **160**, 855 (1947); also Seriff, Leighton, Hsiao, Cowan, and Anderson, Phys. Rev. **78**, 290 (1950).

[3] C. O'Ceallaigh, Phil. Mag. **42**, 1032 (1951).

[4] Fowler, Menon, Powell, and Rochat, Phil. Mag. **42**, 1040 (1951).

photographed the panel on which the mechanical register and the hodoscope neon bulbs were displayed.

The equipment was flown in a heated plywood box in the bomb bay of a B-29 at 37,000, 30,000, and 23,000 feet. Subsequently, the equipment was operated at White Mountain Laboratory at an altitude of 10,000 feet. At each altitude, except 23,000 feet, about 10,000 P counts were obtained. The 23,000 foot altitude was abandoned when it became apparent that the counting rate of P pulses was too low to make B-29 flights at that altitude practical. After the flights the B-29 pressure altimeter was recalibrated in the laboratory and the four altitudes were found to correspond to 222, 305, 418, and 720 g cm^{-2} of air. The apparatus was checked hourly during the B-29 flights and daily at White Mountain; subsidiary counting rates obtained during these checks, and the rate of P events in separate time intervals at a given altitude always agreed within statistical error.

Except for one flight at 30,000 feet to a geomagnetic latitude of 52°N, all the data were gathered at 42°N. As no latitude effect was observed, the 30,000 foot data from both latitudes were combined.

TABLE I. Counting rates of P events at four altitudes.

1 Altitude (g cm^{-2})	2 Time (h)	3 Total P count	4 P rate (h^{-1})	5 ($A_1B_1C_1$) (min^{-1})	6 P rate corr.* (h^{-1})
222	12.5	9597	770 ±8	238 ±2	763 ±8
305	28.3	10,648	376 ±4	187 ±1	372 ±4
418	6.0	847	141 ±4.5	131 ±2	138 ±4.5
720	877.3	11,408	13.0±0.1	54.8±0.5	11.7±0.1

* Corrected for P events produced by μ-mesons causing knock-on discharges in both trays B and C.

During the run at White Mountain, the daily record of the apparatus was compared with solar flare data. No correlation was observed.

III. THE ABSORPTION MEAN FREE PATH

The counting rates of P events at the four altitudes are listed in Table I. It has been shown[5] that approximately 0.04 percent of the single μ-mesons passing through a lead absorber produce knock-ons in two successive counter trays imbedded in the lead; such double knock-ons constitute the most serious cause of spurious P events. In the last column of Table I the P events resulting from this cause have been subtracted using the single meson rate given in column 5. The four corrected points fall on a straight line on a semilogarithmic plot and yield an absorption mean free path of 118.5 ±0.4 g cm^{-2} of air, in excellent agreement with the results of Tinlot[6] and other investigators.[5,7]

The hard shower data gathered at each altitude were next classified by means of the hodoscope according to the number of counters discharged in trays D and E, and arranged into a rectangular array $P(m, n)$; $P(m, n)$ is the number of events P with m counters discharged in tray D, and n counters discharged in tray E. Each array was then divided into five categories of increasing hard shower size as shown in Fig. 2. The boundaries in the array $P(m, n)$ were chosen as follows: assuming that the particles which discharged the counters in trays D and E were the only particles produced in the hard shower, the energy corresponding to each element of the array $P(m, n)$ was calculated from range-energy relations and the production spectra of Camerini.[8] The boundaries were then drawn through equienergetic regions and the data of each region were combined.

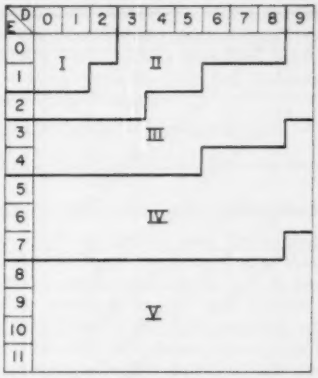

FIG. 2. Boundaries of the hard shower size groups of the array $P(m, n)$.

Figure 3 shows the counting rates of the five hard shower size categories at the four altitudes; it appears that for all hard shower sizes the altitude points may be fitted by straight lines. For each hard shower size the corresponding absorption mean free path resulting from a least squares analysis is also listed. When the array $P(m, n)$ was subdivided into five regions with substantially different boundaries, essentially the same results as above were obtained.

In order to obtain the actual absorption mean free paths from the measured values, a Gross correction due to the finite acceptance solid angle of the instrument must be applied. An approximate calculation based on geometric reasoning indicates that the actual absorption mean free paths are about 10 percent larger than the observed values.

Next, an attempt was made to correlate the hard shower size as exhibited on the hodoscope with the energy of the particle which produced the shower.

[5] E. P. George and A. C. Jason, Proc. Phys. Soc. (London) **A63**, 1081 (1950). See also J. Tinlot, unpublished, Massachusetts Institute of Technology, Technical Report (ONR) No. 18, p. 17.
[6] J. Tinlot, Phys. Rev. **74**, 1197 (1948).
[7] I. J. Lord, Phys. Rev. **81**, 901 (1951).
[8] Camerini, Fowler, Lock, and Muirhead, Phil. Mag. **41**, 413 (1950).

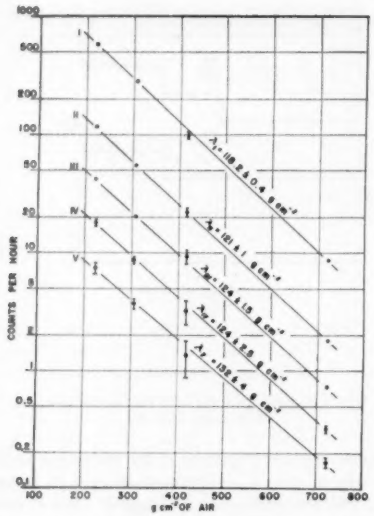

FIG. 3. Absorption curves of hard showers of the five size categories in the atmosphere. The listed values of the mean free path have not been corrected by the Gross transformation.

The energy scale which results from considerations indicated before in connection with the choice of hard shower size boundaries is very likely to be a severe underestimate of the energy of the incident particles for the following reasons: (a) Hard showers are not well collimated and hence some fraction of the particles produced in the original hard shower will miss trays D and E. (b) Particles with insufficient energy to reach tray D, neutral particles, and many electronic cascades resulting from the decay of neutral π-mesons of the original hard shower will not be recorded. (c) In the case of large hard showers several particles may pass through a given E counter. (d) The penetrating particles resulting from the original hard shower are capable of producing hard showers and may disappear by such nuclear encounters. The last point merits closer examination. The collision mean free path of high energy nucleons in lead is geometric, $\lambda_{Pb}=160$ g cm^{-2},[9] and photographic evidence favors a geometric cross section for π-mesons also.[8] The lead between trays A and D, and A and E was equivalent to 2.5 and 4 mean free paths, respectively. As a result it appears very likely that most of the particles which cross trays D and E are the descendants, after several generations,[10,11] of the particles which were produced in the original hard shower which produced the P event. It is therefore reasonable to consider the number of D and E counters discharged as *a measure of the penetration of a hard cascade into the lead block*. Electronic cascades may also be formed in the lead but their effect cannot be disproportionately large, especially in the case of the mutually shielded E counters, since according to Greisen[12] the chance of recording a 1-Bev photon, for example, under 160 g cm^{-2} of lead is less than 2 percent. On the other hand, there is the possibility that occasionally a hard shower may appear more energetic because one of the hard shower particles produces a secondary event in the immediate vicinity of one of the counter trays. An investigation of the hodoscope record, as to the relative number of events when the number of E counters discharged was considerably larger than the number of D counters discharged, revealed that such events comprise about 10 percent of the total in each size category; this will not affect the conclusions of this experiment.

In view of the important role which secondary production plays in an apparatus of this sort, the energy scale computation mentioned before was considered merely as a guide in arranging the hard showers as to their size, under the assumption that in the majority of the hard showers the "apparent" energy obtained from this energy scale is related to the true energy in a monotone fashion.

A better estimate of the energy of the particles which generate the hard showers may be obtained by extrapolating the 37,000 foot data to the top of the atmosphere using the altitude curves. The differential hard shower size distribution of the second column of Table II was first converted to an incident vertical particle flux per cm^2 sec sterad. In this calculation the expression $[1-\exp(-\bar{x}/\lambda_{Pb})]=0.74$ was used for the detection efficiency of shower generating particles, where $\bar{x}$ is the average thickness of lead above tray B; 65.5 cm^2 was used for the area-solid angle product of the apparatus (computed for a $\cos^2\theta$ distribution which presumably exists at 37,000 feet). The energy limits for the five hard shower size groups were then obtained by com-

TABLE II. Extrapolation of the flux at 37,000 ft to the top of the atmosphere and comparison with the spectrum of the primaries.

Shower size	Differential shower size distribution at 37,000 ft	Vertical flux of shower generators[a] at 37,000 ft (cm^2 sec sterad)$^{-1}$	Extrapolated flux at the top of the atmosphere[b] (cm^2 sec sterad)$^{-1}$	Estimated[c] energy band Bev
I	7231	3.3×10^{-3}	1.8×10^{-2}	14–43
II	1449	6.6×10^{-4}	3.5×10^{-3}	43–75
III	520	2.4×10^{-4}	1.2×10^{-3}	75–125
IV	228	1.1×10^{-4}	5.4×10^{-4}	125–260
V	93	4.3×10^{-5}	2.0×10^{-4}	260–∞

[a] $t=12.48\times3600$ sec; solid angle $\times$ area $=65.5$ cm^2 sterad; detection efficiency $=[1-\exp(-\bar{x}/\lambda_{Pb})]=0.74$.
[b] Extrapolation factor $=\exp(222/\lambda_{air})$.
[c] Using the primary spectrum of Winkler (see reference 13).

[9] K. Sitte, Phys. Rev. **78**, 714 (1950); W. D. Walker, Phys. Rev. **77**, 686 (1950).
[10] Cocconi, Cocconi-Tongiorgi, and Widgoff, Phys. Rev. **79**, 768 (1950).
[11] M. B. Gottlieb, Phys. Rev. **82**, 349 (1951).
[12] K. Greisen, Phys. Rev. **75**, 1071 (1949).

TABLE III. Ratio of P events in which more than one counter in tray A is discharged to P events which are due to a single discharge in tray A.

Shower size	Altitude 222 g cm^{-2} ϕ	305 g cm^{-2} ϕ	720 g cm^{-2} ϕ
I	0.95±0.02*	0.96±0.02*	0.86±0.02*
II	1.31±0.07	1.20±0.06	1.25±0.06
III	1.74±0.14	1.49±0.12	1.57±0.13
IV	2.04±0.27	2.21±0.29	2.33±0.31
V	4.5 ±1.1	6.0 ±1.4	6.3 ±1.5

* Corrected for double knock-on phenomena of μ-mesons.

parison of the extrapolated flux with the primary spectrum published by Winkler and collaborators.[13]

According to this computation 14 Bev is the smallest energy a particle must have to be able to produce a recordable hard shower. This is in accord with the absence of a detectable latitude effect during the flight to 52°N geomagnetic latitude and is also substantially in agreement with the measurements of Walsh and Piccioni[14] who concluded from the latitude effect which they observed that for their apparatus the minimum energy was approximately 10 Bev. This reasonable result suggests that the extrapolation procedure is satisfactory *per se* in the low energy region where the primary particle spectrum is known with some precision and questions of ordering the showers into sizes do not arise. At the high energy end the results are rendered much less certain both by the difficulties of reliable size classification and also by the scant knowledge of the primary spectrum. Winkler *et al.* have assumed that in the energy region beyond that accessible to geomagnetic measurements, the primary spectrum goes over into Hillberry's $E^{-1.75}$ power law. Recent experiments[15, 16] suggest that the spectrum of primaries is considerably flatter in the high energy region; in that case the energy values given in Table II are underestimated. On the whole, in view of these uncertainties the energy limits of the large hard shower sizes can be considered no better than estimates correct within a factor of 2.5.

To a first approximation the $P(A_1)$ events are mainly hard showers generated between trays A and B and produced predominantly by charged particles; the $P(A_2)$ events, originating in the lead above tray A, can be caused by both charged and neutral particles. If one neglects the hard showers originating above the apparatus and hard showers generated below tray A which contain particles projected backward which cross tray A, then roughly

$$P(A_2)=(N_e+N_n)\{1-\exp(-x_1/\lambda_{Pb})\}P_1, \quad (1)$$

$$P(A_1)=N_e\exp(-x_1/\lambda_{Pb})\{1-\exp(-x_2/\lambda_{Pb})\}P_2, \quad (2)$$

and

$$\phi=P(A_2)/P(A_1)\sim 1.4(P_1/P_2)(1+N_n/N_e), \quad (3)$$

where x_1 and P_1 are the thickness of lead above tray A and the probability of observing a hard shower originating there, respectively, and x_2 and P_2 are the corresponding quantities for the lead between trays A and B. The effect of the back-projected particles is difficult to assess; if one assumes, for example, that each hard shower has a back-projected particle whose range in lead is 1.25 cm,[11] then

$$\phi\sim 1.9(P_1/P_2)(1+0.7N_n/N_e). \quad (4)$$

The ratio P_1/P_2 must be smaller than one both because trays D and E subtend a larger solid angle when viewed from below tray A than when seen from above A; also generally larger energies are required to produce showers of a given size (as registered on the hodoscope) when they originate above tray A.

The ratios ϕ corresponding to different altitudes and shower sizes are shown in Table III. Since it is hard to see how the ratio N_n/N_e could become appreciably larger than one in this energy region where ionization losses are negligible, it appears that some other phenomenon is contributing to increase ϕ for the largest shower size at all altitudes. Showers originating above the apparatus or a greatly increased number of high energy back-projected particles, or both, could explain this result. To decide between these possibilities tray F was added during the operation of the apparatus at White Mountain. Such an "extension" tray should be very sensitive to electronic showers which are known to accompany hard showers in air.

IV. THE WHITE MOUNTAIN DATA

The detailed results obtained at White Mountain are presented in Table IV. The first four columns list the

TABLE IV. Breakdown of data gathered at 10,000 ft with respect to discharges in the extension tray F and multiple discharges in tray A.

Shower size	(1) $P(A_2,-F)$	(2) $P(A_1,-F)$	(3) $P(A_2,F)$	(4) $P(A_1,F)$	(5) $\phi(-F)$	(6) $P(F)/P$	(7) $\phi(F)$	(8) $\phi(F)_{corr}$[b]
I	3248[a]	3947[a]	207	90	0.82±0.02[a]	0.040±0.002[a]	2.3±0.3	1.54±0.23
II	793	690	102	24	1.15±0.06	0.078±0.007	4.3±1.0	3.1 ±0.8
III	323	234	70	17	1.38±0.12	0.135±0.016	4.1±1.1	2.9 ±0.85
IV	115	71	82	14	1.62±0.25	0.34 ±0.04	5.9±1.7	4.3 ±1.3
V	32	15	94	3	2.13±0.65	0.68 ±0.09	19.0±8.0	14.0 ±6.0

[a] Corrected for double knock-on phenomena of μ-mesons.
[b] Corrected for cascade shower particles penetrating to counter tray A according to $\phi(F)_{corr}=0.77\phi(F)-0.23$.

[13] Winkler, Stix, Dwight, and Sabin, Phys. Rev. **79**, 656 (1950).
[14] T. G. Walsh and O. Piccioni, Phys. Rev. **80**, 619 (1950).
[15] Unpublished report ESN **6**, 1 (1952). Report on work by D. H. Perkins, R. Daniel, J. Davies, and J. Mulvey.
[16] Kaplon, Peters, Reynolds, and Ritson, Phys. Rev. **85**, 295 (1952).

number of P events subdivided according to whether they were due to a discharge of a single counter in tray A or several, and whether or not they were accompanied by discharge(s) in tray F. Column (5) presents the ratios $\phi(-F)$ of $P(A_2)$ and $P(A_1)$ counts not accompanied by discharges in tray F; $\varphi(-F)$ remains compatible with Eqs. (3) and (4) for all shower sizes. It seems reasonable, therefore, to interpret the large values of ϕ obtained previously (Table III) as due to atmospheric events, rather than caused by back-projected particles (for which a very artificial angular distribution would have to be assumed).

Column (6) lists the ratios $P(F)/P$ of P events accompanied by discharges in tray F to all P events in each size group. This ratio for the data of all size groups together is 7 percent in fair agreement with the results of Tinlot,[6] but the contribution of atmospheric events increases with increasing shower size and becomes predominant for size V showers.

In view of this close association between P events and air showers it becomes important to investigate to what extent the electronic component in the atmospheric events could have been instrumental in discharging counters in the lead block. That electronic cascades could not penetrate the lead block to the extent of causing P events may be seen at once: the contribution of atmospheric events to the P rate for the small shower sizes is quite small; furthermore, Cocconi *et al.*[17] have shown that 40 radiation units of lead effectively stop the electronic component of air showers. However, the effect of the electronic component can take another form; an atmospheric shower may arrive at the apparatus inclined, the N-component in this shower produces the P event but some of the counters in trays D and E are discharged by electrons scattered through the rather inadequate shielding on the sides and ends. Spurious results of this sort certainly cannot be ruled out on the basis of the present data, but it can be shown that they cannot constitute an important contribution to the counting rate of large P events. In the first place it is well known that for altitudes larger than 350 g cm^{-2} of air the intensity of air showers decreases with increasing altitude;[18,19] the altitude curves recorded here show no change in slope near 350 g cm^{-2} of air. At 10,000 ft, where the information supplied by tray F was available, the following analysis was carried out. Tray E was actually exposed at its ends much more than tray D. Therefore, in the presence of an air shower ($P(F)$ event) there should be more P events with a large number of E counters but few D counters discharged than in the absence of an air shower. An analysis of the data of size V showers showed that about 10 percent of the $P(F)$ events could be explained as due to electronic cascades. If it is assumed that this contribution due to air showers existed only at 10,000 ft then the measured value of the absorption mean free path should be reduced by about 1.5 percent.

The increase of the ratio $P(F)/P$ with hard shower size has been previously observed.[20] It has been interpreted qualitatively as follows: most of the particles creating penetrating showers at mountain altitudes are secondaries of interactions occurring farther up in the atmosphere. The higher the energy of particle generating the penetrating shower in the lead block the higher is the energy of the interaction in which this particle was created, and the higher, on the average, the energy of the other particles produced in the same event and the greater their collimation. Both of the last-mentioned effects would tend to increase the probability of observing other secondaries in addition to the P event generator. The ratio $P(F)/P$ is a measure of this probability.

The ratios $\phi(F)$ of $P(A_2)$ and $P(A_1)$ events which are accompanied by discharges in tray F are listed in column (7) of Table IV. The ratios obtained in this case are considerably larger than the corresponding ratios $\phi(-F)$. This must be due, at least in part, to the fact that the 3 in. of lead above tray A were inadequate to stop the electronic component. It has been shown[6,20] that the electronic cascades accompanying the N-component are relatively dense, of the order of 200 particles per m^2. Thus it is reasonable to suppose that, had tray A been completely unshielded, it would have been discharged in every $P(F)$ event by the electronic component also. If this premise is accepted then it is possible to calculate how many of the $P(A_1, F)$ events appeared as $P(A_2, F)$ events because of the penetration of the electron cascades to tray A. It has been found that 3 in. of lead over *one* counter tray of a set, detecting extensive air showers, reduces the rate of coincidences to 23 percent,[21,22] hence 23 percent of the $P(A_1, F)$ events will be recorded as $P(A_2, F)$ events. When a correction based on this argument is applied to $\phi(F)$, according to $\phi(F)_{corr}=0.77\phi(F)-0.23$, the last column of Table IV results. The ratios $\phi(F)_{corr}$ are still larger than the ratios $\phi(-F)$ and the discrepancy appears to increase with hard shower size.

V. CONCLUSIONS

The experiment suggests that the absorption mean free path, or perhaps more accurately the attenuation length, of hard showers of all sizes investigated here remains in the vicinity of 125 g cm^{-2} (before Gross correction). By extrapolation to the top of the atmosphere an energy larger than 260 Bev was assigned to the largest hard shower category. The attenuation length observed is approximately twice that which would result from a geometric cross section (67 g cm^{-2} of air). This is in agreement with the results of many

[17] Cocconi, Cocconi-Tongiorgi, and Greisen, Phys Rev. **75**, 1063 (1949).
[18] Biehl, Neher, and Roesch, Phys. Rev. **76**, 914 (1949).
[19] H. L. Kraybill, Phys. Rev. **76**, 1092 (1949).
[20] Greisen, Walker, and Walker, Phys. Rev. **80**, 535 (1950).
[21] Auger, Daudin, Freon, and Maze, Compt. rend. **228**, 178 (1949).
[22] G. T. Reynolds and W. D. Hardin, Phys. Rev. **74**, 1549 (1948).

investigations at lower energies and also with the results of Christy *et al.*[23] in essentially the same energy region and altitude range. For heavy materials the results of investigations by diverse techniques all indicate that the collision cross section is geometric; for light materials the results are not so clear-cut; some experimenters[24,25] have obtained an approximately geometric collision mean free path in carbon, while others[26,27] have observed some transparency.

Since the attenuation length observed in air is longer than the geometric mean free path it would be important to decide to what extent this lengthening is due to the contribution of secondaries originating farther up in the atmosphere and producing hard showers in the apparatus. That secondaries do contribute cannot be doubted in view of the existence of $P(F)$ events. This is also in accord with the finding of several investigators[11,20] that at mountain altitudes neutrons and protons of a few Bev are equally abundant.

If one assumes that the collision mean free path of the nuclear particles in air is geometric, then a question arises as to the nature of the secondary particles which lengthen the absorption mean free path. These may be of three types: nucleons, π-mesons, and heavier mesons of the V, κ, and τ varieties whose existence has recently been established.

The longest mean life that has been quoted for any of these heavy mesons is 10^{-9} sec[4] for the κ-meson whose mass is reported to be about 1200 m_e. A meson with these properties and an energy of 260 Bev should have a mean range before decay of only about 130 m and can therefore not contribute to the hard showers measured in this experiment. Mesons of comparable mass which decay into π-mesons with even shorter mean lives may, for the purposes of this discussion, be considered as π-mesons.

Many investigators have considered the formation of a cascade of nucleons in the atmosphere. In a most recent paper, Caldirola *et al.*[28] have shown that the fact that the attenuation length is about twice the geometric mean free path may be satisfactorily accounted for if one assumes that the nucleon-nucleon collision cross section is near geometric and that the two nucleons which come out of the interaction share on the average 75 percent of the energy of the incident nucleon, while 25 percent is dissipated in π-meson production. It seems unlikely that such a high degree of elasticity should prevail up to the energies involved here; according to this model 260-Bev nucleons should arise from primaries with 700 Bev, or a total energy of 37 Bev in the C-system. According to Fermi,[1] 8 π-mesons should be created in such an interaction; recent work[15] with photographic emulsions suggests that particles with energies larger than 50 Bev lose about 90 percent of their energy to meson production in nuclear collisions. If 10 percent is adopted as the fraction of the energy of the primary nucleons which is retained by the two nucleons issuing from the collision, then, using the relation in reference 28, secondary nucleons will increase the attenuation length beyond the collision mean free path by about 1 percent for a primary power law exponent of -1.8; even if the fraction of energy retained by secondary nucleons is as high as 40 percent, and the power law exponent[16] is -1.35 the lengthening is only 33 percent.

π-mesons with energies above 260 Bev have mean ranges before decay of 14.3 km and therefore can penetrate most of the lower part of the atmosphere. Assuming that π-mesons and nucleons of equal energy create hard showers of comparable size in the lead absorber, the observed altitude curve of hard showers of a given size should be due partly to π-mesons and partly to nucleons in the specified energy interval. The altitude curve of the π-mesons alone then is of the form

$$N_\pi(x)=k\{\exp(-x/\lambda)-\exp(-x/\lambda_n)\}, \qquad (5)$$

with λ the observed attenuation length, λ_n the attenuation length of nucleons alone and k the extrapolated flux for the given size shower at the top of the atmosphere (Table II). From such a π-meson altitude curve, the number of μ-mesons in a corresponding energy range can be estimated from the well-known constants of the π–μ decay, and this number can be compared with the underground μ-meson spectrum given by George.[29] Such a comparison may be used to adjust the parameter λ_n and yields $\lambda_n=0.92\lambda$ for size V events. It is perhaps worth noting that this procedure is relatively insensitive with respect to the energy extrapolation (Table II) since with an increase of the estimated energy both the number of high energy μ-mesons and also the decay probability of the π-mesons decrease.

In conclusion it would therefore appear that in the energy region investigated here the experimental results cannot be explained without assuming an appreciable nuclear transparency effect. Unfortunately its exact value cannot be assessed until the contribution of secondaries is more closely studied. Such experiments are contemplated.

VI. ACKNOWLEDGMENTS

The author is deeply indebted to the ONR and to the Air Force for making available to him the flight time of the B-29. It is a particular pleasure to thank Major W. A. Gustafson and the rest of the B-29 crew for their competent handling of the plane and their cooperative spirit. During the mountain runs, the apparatus was in the charge of Mr. Robert T. Henszey. The author profited greatly from stimulating discussions with Professor David Saxon.

[23] Christy, Biehl, Inonu, and Neher, Phys. Rev. **81**, 647 (1951).
[24] R. R. Brown, Phys. Rev. **85**, 773 (1952).
[25] L. Mezzetti and R. Querzoli, Phys. Rev. **79**, 168 (1950).
[26] Walker, Walker, and Greisen, Phys. Rev. **80**, 546 (1950).
[27] H. W. Boehmer and H. S. Bridge, Phys. Rev. **85**, 863 (1952).
[28] Caldirola, Fieschi, and Gulmanelli, Nuovo cimento **IX**, 5 (1952).
[29] E. P. George, *Progress in Cosmic Ray Physics* (North Holland Publishing Company, Amsterdam, 1951), pp. 403–413.

The de Haas-van Alphen Effect in Enriched Tin Isotopes

TED G. BERLINCOURT*
Sloane Physics Laboratory, Yale University,† New Haven, Connecticut
(Received June 19, 1952)

The de Haas-van Alphen effect has been investigated in tin isotopes in the liquid helium temperature range, and no conclusive evidence has been found indicating a dependence of the effect upon atomic mass. However, some new features of the effect have been investigated which are interpreted as being caused by at least two independent groups of electrons. One group of electrons, having effective masses $m_3=1.1m_0$ (where m_0 is the free electron mass) parallel to the tetragonal axis and $m_1=0.16m_0$ perpendicular to the tetragonal axis, and having a chemical potential of $E_0=0.25$ electron volt, gives rise to short period oscillations in the magnetic susceptibility as the magnetic field is varied. A second group of electrons having a chemical potential $E_0=0.20$ electron volts and for which the effective masses are not so clearly defined gives rise to longer period oscillations such that the observed de Haas-van Alphen oscillations exhibit beats between the long and short period terms.

INTRODUCTION

THE de Haas-van Alphen effect in tin was first observed by Shoenberg[1] who has since completed a more comprehensive investigation[2] of the effect in tin as well as in several other elements. The effect has also been observed in tin by Verkin, Lazarev, and Rudenko[3] and Croft, Love, and Nix.[4] Shoenberg's studies indicated that the periodicity of the oscillations of the anisotropy of the magnetic susceptibility, when plotted against the reciprocal of the magnetic field, was a reasonably reproducible feature in different single crystals of tin, while the amplitude of these oscillations was not in general a very reproducible feature. Furthermore, since the periodicity of the oscillations is determined by rather clearly defined electronic parameters, it was felt that a comparison of the periods would reveal an isotope shift if it existed. Qualitatively, the argument may be stated as follows. The de Haas-van Alphen effect is caused by a relatively few electrons, from 10^{-3} to 10^{-6} per atom, having highly anisotropic effective masses, which therefore occupy some of the positions in phase space for which the curvature of the Fermi surface is very great. Thus, if the electronic structure is altered at all by a variation of the mass of the lattice points, the de Haas-van Alphen electrons might be expected to reflect this change.

TABLE I. Sources, purities, and masses of the tin specimens.

Av. atomic mass	Source	Purity (%)	Mass (grams)
116.17	AEC	99.9	0.1373
118.70 Nat. Sn	JM*530 Lab. No. 4600	99.997	0.1549
121.63	AEC	99.7	0.1240
123.77	AEC	99.7	0.1207

* Johnson, Matthey and Company, Ltd.

In any event, the theory as developed by Peierls,[5] Blackman,[6] and Landau[7] assumes that the de Haas-van Alphen electrons are contained in one or more regions in phase space having ellipsoidal constant energy surfaces which have the symmetry of the particular lattice under consideration. As Shoenberg has shown, one such ellipsoid is inadequate in fully explaining the de Haas-van Alphen effect in tin. The present paper proposes one ellipsoid to account for the short period oscillations and at least one more less simple surface to account for the long period oscillations.

Inasmuch as the theory of the de Haas-van Alphen effect has been covered in detail elsewhere[5-7] only a brief statement of the theoretical results will be given here. Modifications of this theory and methods for determining the pertinent electronic parameters from the experimental data will be discussed in a later section.

For not too high fields nor too low temperatures, Landau's final expression for the difference of magnetic susceptibility ($\Delta\chi$) per unit mass in two directions at right angles to each other is given by

$$\Delta\chi=\sum\frac{A\Delta m}{\rho}\left\{\frac{\pi^2}{6}\left(\frac{k}{E_0}\right)^{\frac{1}{2}}-\frac{1}{T^{\frac{1}{2}}}\left(\frac{2\pi^2kT}{\beta H}\right)^{\frac{1}{2}}\times\exp\left(-\frac{2\pi^2kT}{\beta H}\right)\sin\left(\frac{2\pi E_0}{\beta H}-\frac{\pi}{4}\right)\right\},\quad(1)$$

where A is a constant given by

$$A\equiv\frac{e^2E_0}{\pi^4c^2\hbar(2k)^{\frac{1}{2}}m'^{\frac{1}{2}}},\quad(2)$$

ρ is the density, β is an effective double Bohr magneton

* DuPont Predoctoral Fellow in Physics. This work is part of a thesis submitted in partial fulfillment of the requirements for the Ph.D. degree at Yale University.
† Assisted by the ONR.

[1] D. Shoenberg, Nature **164**, 225 (1949).
[2] D. Shoenberg, Phil. Trans. Roy. Soc. **245** (No. 891) 1 (1952).
[3] Verkin, Lazarev, and Rudenko, Doklady Akad. Nauk. SSSR **69**, 773 (1949). J. Exp. Theor. Phys. USSR **20**, 995 (1950).
[4] Croft, Love, and Nix, Phys. Rev. **86**, 650 (1952).
[5] R. Peierls, Z. Physik **81**, 186 (1933).
[6] M. Blackman, Proc. Roy. Soc. (London) **A166**, 1 (1938).
[7] L. D. Landau, see appendix to D. Shoenberg, Proc. Roy. Soc. (London) **A170**, 341 (1939).

given by

$$\beta = e\hbar/m''c, \tag{3}$$

and m', m'', and Δm are functions of the relevant effective masses which depend upon the geometry of the experiment and the symmetry of the crystal lattice. E_0 is the energy at the ellipsoidal surface of constant energy in phase space which is given in general by

$$E_0 = (1/2m_0)(\alpha_{11}p_x^2 + \alpha_{22}p_y^2 + \alpha_{33}p_z^2 + 2\alpha_{12}p_xp_y + 2\alpha_{23}p_yp_z + 2\alpha_{31}p_zp_x). \tag{4}$$

Here the α_{ij} are the ratios of the true electronic mass, m_0, to the relevant effective masses. As will be illustrated later, these determine the definitions of m', m'', and Δm. Usually, the ellipsoidal constant energy surface is so oriented with respect to the crystal lattice that $\alpha_{12} = \alpha_{23} = \alpha_{31} = 0$.

THE EXPERIMENTAL WORK

I. The Torsion Balance Method

If a magnetically anisotropic single crystal is placed in a homogeneous magnetic field, the magnetization will not in general be in the same direction as the applied field. Hence, the crystal will experience a couple ($\mathbf{C}$) per unit mass given by

$$\mathbf{C} = \mathbf{I} \times \mathbf{H}, \tag{5}$$

where $\mathbf{I}$ is the magnetization per unit mass. For the case of a tin single crystal placed in a horizontal magnetic field with a binary axis and the tetragonal axis horizontal, this becomes

$$C = \Delta\chi \cdot H^2 \sin\phi \cos\phi, \tag{6}$$

where ϕ is the angle between H and the tetragonal axis. $\Delta\chi$ is here the difference between the susceptibilities along the tetragonal axis and a binary axis, i.e., the quantity in which we are interested, as given by Eq. (1).

In this work, a torsion balance similar to that described by Sydoriak[8] was used to determine $\Delta\chi$, the chief difference being that provision was made for transferring liquid helium to the apparatus directly, thus minimizing the probability of disturbing the alignment. Temperatures were determined by observation of the vapor pressure of the helium bath with mercury and oil manometers. The Mond vapor pressure tables[9] were used, and temperatures were held to better than 0.01°K.

The crystal being investigated was mounted on the lower end of a long quartz rod approximately 1 mm in diameter, the upper end of which was rigidly affixed to a small brass frame carrying a front silvered mirror and a damping ring which dipped into Octoil-S. This frame was in turn fastened to the lower end of a flattened nichrome wire torsion member. Light from an illuminated vertical slit placed at the focus of a one meter focal length lens (which also served as a balance case window) was reflected from the mirror and brought to focus so that the diffraction pattern image of the slit could be observed with a traveling microscope. Torsion fibers were calibrated by observation of the periods of oscillation when systems of known moment of inertia were attached.

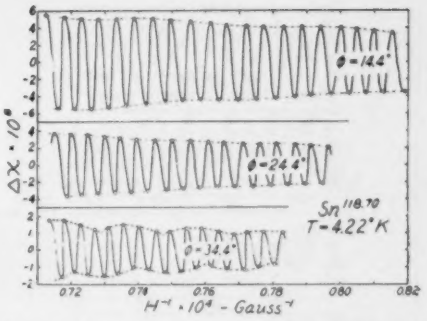

FIG. 1. $\Delta\chi$ in emu *versus* H^{-1} in gauss^{-1} for natural tin, $Sn^{118.7}$, for various angles between the tetragonal axis and the magnetic field. At $\phi = 34.4°$ modulations caused by a short period term become important.

Because of the close spacing of the susceptibility oscillations in tin, it was essential that very small angular displacements be utilized in the measurements. For example, a displacement of a few degrees would be sufficient in some cases to move the crystal from a position of maximum susceptibility to one of minimum susceptibility. Hence, the angular displacements utilized never exceeded 0.2° and were in most cases less than 0.05°. These were reproducible to ±0.0003°, since the slit image observed with the traveling microscope was a well-defined diffraction pattern.

II. The Magnet and Its Calibration

Magnetic fields up to 14 kilogauss were supplied by a water-cooled magnet capable of rotation about a vertical axis and having 6-in. diameter flat pole pieces with a gap of 4 cm. Again because of the close spacing of the susceptibility peaks in tin, it was essential that the field be homogeneous to a high degree over the volume of the sample and also time invariant. Exploration of the gap with a search coil showed the field to be homogeneous (to about two parts in 10^4) within 5 mm in any direction from the center of the gap. This proved to be quite satisfactory since the tin crystals were never larger than 3 mm in any one dimension. A degenerative feedback voltage regulator used in conjunction with the motor-generator set which supplied power to the magnet assured that variations of the field could be limited to one or two gauss during the course of each measurement. The magnetic field was calibrated with a proton resonance fluxmeter to an accuracy of approximately 0.03 percent with proper precautions being taken against hysteresis.

[8] S. G. Sydoriak and J. E. Robinson, Phys. Rev. **75**, 118 (1949).
[9] H. Van Dijk and D. Shoenberg, Nature **164**, 151 (1949).

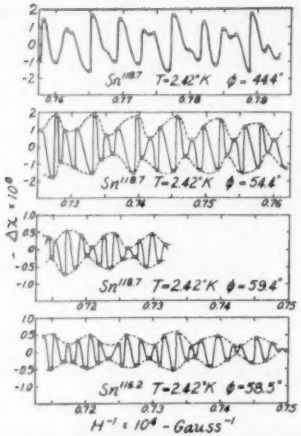

FIG. 2. $\Delta\chi$ in emu *versus* H^{-1} in gauss^{-1} for natural tin, $Sn^{118.7}$, and $Sn^{116.8}$ for various angles between the tetragonal axis and the magnetic field. The long and short period terms are both important at these angles and temperatures. The last two curves illustrate the reproducibility for different isotopes.

III. The Specimens

After several unsuccessful methods for growing small tin single crystals had been tried, the following procedure was finally adopted. A small (approximately 150 mg) bead of tin was placed in a 9-mm Pyrex tube sealed off at one end which was then evacuated. Next the tin was melted with a Bunsen-burner. Upon removal of the Bunsen burner, the portion of the Pyrex tube directly beneath the molten tin was touched to the surface of a beaker of hot water, thus assuring that the crystallization proceeded from the point of contact of the tin with the tube. This procedure produced single crystals with roughly 25 percent efficiency. The resulting crystals were etched with concentrated hydrochloric acid until good reflections were obtained. They were then oriented using an optical method described by Chalmers.[10] While a given crystal, with a binary axis vertical, was still fastened to the goniometer head with Duco cement, the torsion balance was manipulated so that the quartz rod hung plumb above the crystal. The rod was then fastened to the crystal with Duco cement, and in this way the crystal retained the desired orientation during the setting of the cement. The bond between the crystal and the goniometer was then severed by judicious application of acetone with a small brush. Because the anisotropy of tin single crystals is very small at room temperature, the position of the tetragonal axis in the horizontal plane was determined by observation of the position of the magnet for which the amplitude of the de Haas-van Alphen effect just vanished at liquid helium temperatures, a procedure due to Shoenberg.

Pertinent information regarding the tin specimens[11] is recorded in Table I. The $Sn^{116.17}$ and $Sn^{121.63}$ were supplied in the form of SnO_2 and were reduced in a hydrogen furnace. It should also be pointed out that the stated purities are probably not very accurate, for the samples were crystallized and etched several times in general before suitable crystals were obtained.

EXPERIMENTAL RESULTS

The general features of the de Haas-van Alphen effect in tin are illustrated in Figs. 1, 2, and 3, where

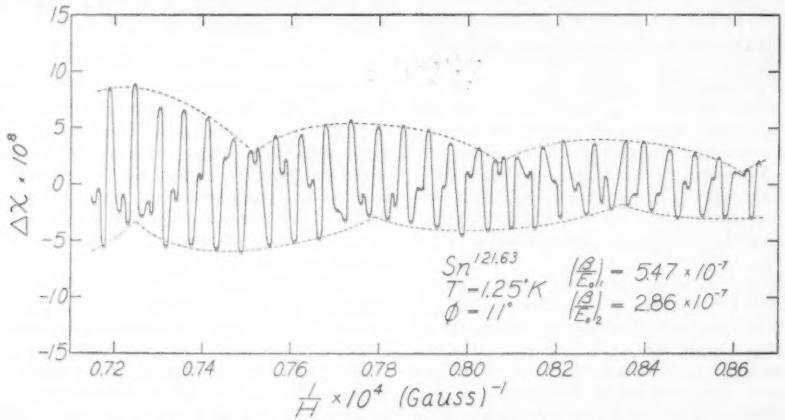

FIG. 3. $\Delta\chi$ in emu *versus* H^{-1} in gauss^{-1} for $Sn^{121.63}$ at 1.25°K and $\phi = 11°$. The presence of two periodic terms accounts for the cusp-shaped envelope.

[10] B. Chalmers, Proc. Phys. Soc. (London) **47**, 733 (1935).

[11] The enriched isotopes were produced by Carbide and Carbon Chemicals Division, Oak Ridge National Laboratory, Y-12 Area, Oak Ridge, Tennessee and obtained on allocation from the Isotopes Division of the AEC.

$\Delta\chi$ in emu has been plotted against H^{-1}. We note that at high temperatures and for small angles between the magnetic field and the tetragonal axis, only one term in Eq. (1) is important, i.e., a long period term. For lower temperatures and larger values of ϕ however, a shorter period term also becomes important, and modulations characteristic of the summation of two sinusoidal variations are observed. For $\phi=34.4°$ and $T=4.22°K$ the cusp-shaped modulation first observed by Shoenberg, and for which he proposed no explanation, begins to appear. The explanation of this unusual type of modulation becomes clear however, in view of Fig. 3, where the temperature was sufficiently low and the magnetic field regulation good enough to permit resolution of both frequencies even for $\phi=11°$. In order to verify that such a curve could be synthesized from two sinusoidal terms, two audiofrequency oscillators were connected in parallel to the vertical plates of a cathode-ray oscilloscope, and with a little manipulation of frequencies and amplitudes such a curve was indeed produced.

At 2.42°K and $\phi=54.4°$ the short period term is most important and the more common types of beats are observed. The final two curves of Fig. 2 for two different isotopes and only slightly different angles illustrate the reproducibility of the measurements from one isotope to another.

If the values of H^{-1} for which maxima in $\Delta\chi$ occur are plotted against successive integers as in Fig. 4, a straight line is obtained verifying the strict periodicity of $\Delta\chi$ in H^{-1} provided, of course, that only one term is important. The slope of such a curve is just β/E_0, the period of the oscillations. For curves of anisotropy *versus* H^{-1} displaying beats, both periods could often be determined unambiguously by standard means. Following Shoenberg, the square of these periods has been plotted against $\cos^2\phi$ in Fig. 5. This permits comparison of the different enriched isotopes investigated, and, as will be discussed later, provides a scheme for determining the electronic structure which gives rise to the two periodic terms. The heavy points refer to cases where both periods were obtained from a single curve of $\Delta\chi$ *versus* H^{-1}. Usually 20, but sometimes as many as 80, periods were observed at each angle ϕ, i.e., each point on Fig. 5 represents a curve of $\Delta\chi$ *versus* H^{-1} such as those in Figs. 1, 2, and 3. It is quite evident that if any isotope shift in the period does exist, it is beyond the accuracy of these measurements.

In Fig. 6 the amplitude, a at 14 kilogauss and 4.22°K for the long period oscillations is plotted as a function

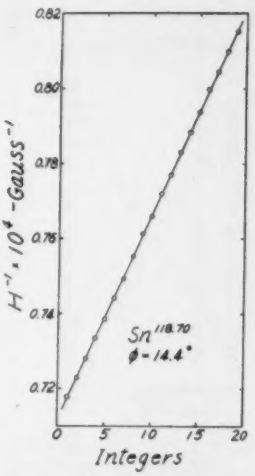

FIG. 4. Typical plot of values of H^{-1} in gauss^{-1} for which maxima in $\Delta\chi$ occur *versus* integers, illustrating the strict periodicity of the susceptibility oscillations in H^{-1}.

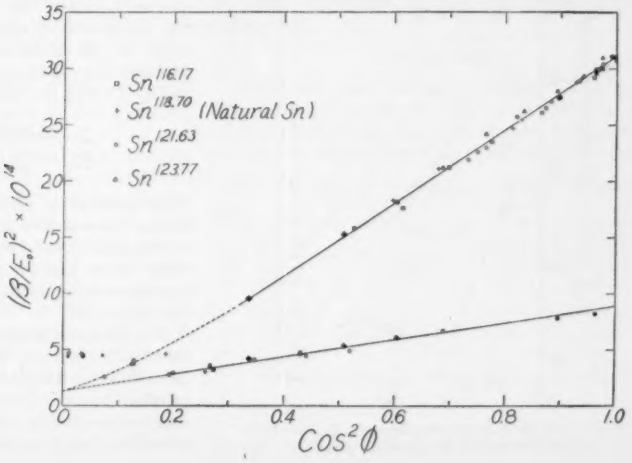

FIG. 5. Comparison of periods for the various isotopes. The linear relation between the period squared, $(\beta/E_0)^2$, and $\cos^2\phi$ provides a scheme for analyzing the electronic structure which causes the de Haas-van Alphen effect.

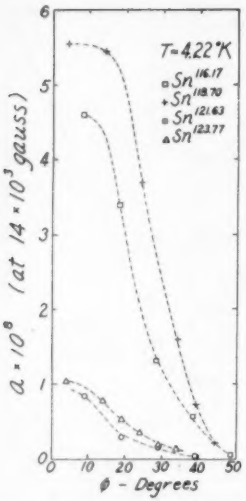

FIG. 6. Comparison at various angles of the long period term amplitudes of the susceptibility oscillations for the various enriched isotopes.

of ϕ for the various isotopes investigated. In order to obtain these amplitudes where strong modulations were present it was necessary to smooth the curves of $\Delta\chi$ *versus* H^{-1}. The large difference in amplitudes is not surprising in view of the purities listed in Table I and in view of Shoenberg's experiments on the effect of impurities. It might be significant that the two heaviest isotopes did exhibit much smaller amplitudes than did the light isotopes, but on the other hand they were also the most impure, so it is doubtful that any definite conclusions can be drawn from Fig. 6.

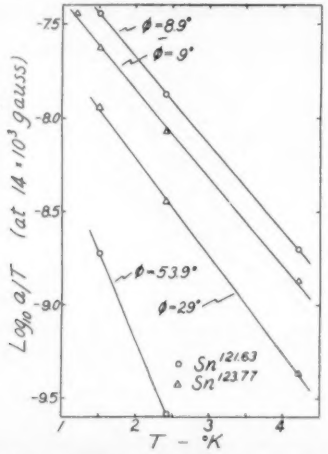

FIG. 7. $\text{Log}_{10}(a/T)$ at 14 kilogauss *versus* T. Values of β are derived from the slopes of such plots.

It should be mentioned in passing that unsuccessful attempts were made to observe the de Haas-van Alphen effect in Te, As, Pb, and Ge. Pertinent data regarding these crystals is listed in Table II. With the exception of the As crystal, all of these specimens were of high quality. Unfortunately, while As appears most likely to exhibit the de Haas-van Alphen effect, it is difficult to obtain as a single crystal.

CALCULATION OF ELECTRONIC PARAMETERS

Inspection of Eq. (1) indicates that β may be calculated from the temperature dependence of the amplitude, i.e., a plot of $\log(a/T)$ *versus* T (for fixed H and ϕ) should yield a straight line from the slope of which β may be calculated. Several such plots appear in Fig. 7 for different values of ϕ. The three upper lines refer to the long period oscillations while the lower one refers to the short period oscillations. Again because of the modulations, it was necessary to smooth the curves of $\Delta\chi$ *versus* H^{-1} in order to obtain a. Once β has been determined, E_0 is readily obtained from the period, β/E_0. Values derived from Fig. 7 are listed in Table III. These values show good agreement with those of Shoenberg, who has verified that E_0 for the long period term is independent of ϕ within experimental error.

TABLE II. Sources, purities, and orientations of crystals not exhibiting the de Haas-van Alphen effect.

Crystal	Source	Purity	Orientation
Te	JM 795 Lab. No. 4938	99.99%	Hex. axis horizontal
As	Lab. Stock	Unknown	Trig. axis horizontal
Pb	JM F688 Lab. No. 1162	99.999%	001 axis vertical
Ge	Dr. R. N. Hall, G. E. Res. Lab.	33 ohm cm	001 axis vertical

Close inspection of Fig. 7 shows that the points could be more accurately fitted to a curve which is slightly concave upward. This is to be expected inasmuch as Eq. (1) is a valid approximation only when $E_0 \gg kT \gg \beta H/2\pi^2$. If the latter half of this inequality is not satisfied, the product of the exponential and the sine in Eq. (1) must be replaced by

$$\sum_{p=1}^{\infty} \frac{\sin(2\pi p E_0/\beta H - \frac{1}{4}\pi)(-1)^{p+1}}{2p^{\frac{1}{2}} \sinh(2\pi^2 pkT/\beta H)}, \qquad (7)$$

which predicts the presence of harmonic terms. For the lowest temperatures and the highest fields in this investigation kT was very nearly equal to $\beta H/2\pi^2$. However, taking account of this fact would change the calculated values of β only slightly, so this discrepancy was neglected.

The presence of apparently independent long and short period terms in the susceptibility variations suggests that it is necessary to postulate at least two independent groups of electrons to account for the de Haas-van Alphen effect in tin. Since a straight line is obtained when the period squared for the short period oscilla-

tions is plotted against $\cos^2\phi$ (see Fig. 5), the assumption is made that for this group of electrons the constant energy surface in phase space is an ellipsoid of revolution. The electrons then have effective masses m_1 at right angles to the tetragonal axis and m_3 along the tetragonal axis. This assumption is made in spite of the fact that, as Shoenberg has shown, an anisotropy does exist in the plane perpendicular to the tetragonal axis. However, since the constant energy surface for the long period term appears more complicated, as may be judged from Fig. 5, it is most convenient to attribute this anisotropy to this group of electrons or to still other groups which cause the irregular dependence of period upon ϕ at large angles.

Then for the short period electrons we have

$$E_0=(p_z^2+p_y^2)/2m_1+p_z^2/2m_3, \tag{8}$$

and

$$\beta=\frac{eh}{c}\left(\frac{m_3\cos^2\phi+m_1\sin^2\phi}{m_1^2m_3}\right)^{\frac{1}{2}}. \tag{9}$$

Using Eq. (9) and values of β derived from Fig. 5 on the basis that $E_0=40.1\times10^{-14}$ erg, the following effective masses are obtained for the electrons causing

TABLE III. Values of the effective double Bohr magneton, the period, and the chemical potential for the de Haas-van Alphen electrons in tin.

Specimen	ϕ	$\beta\times10^{20}$ (erg gauss^{-1})	$\beta/E_0\times10^{7}$ (gauss^{-1})	$E_0\times10^{14}$ (ergs)	
$Sn^{123.77}$	9°	17.9	5.54	32.2	long period
$Sn^{123.77}$	29°	16.1	4.93	32.6	
$Sn^{121.63}$	8.9°	18.2	5.52	32.9	
$Sn^{121.63}$	53.9°	8.02	2.00	40.1	short period

the short period oscillations:

$$m_1=0.16m_0, \quad m_3=1.1m_0, \quad (E_0=0.25 \text{ ev}).$$

The number of electrons per atom involved in the de Haas-van Alphen effect is then given by

$$n=(8\pi/3h^3)(V/N)m_1m_3^{\frac{1}{2}}(2E_0)^{\frac{3}{2}}, \tag{10}$$

where V is the gram molecular volume and N is Avogadro's number. Substituting the values of m_1, m_3, and E_0 listed above yields $n=2.6\times10^{-3}$ electrons per atom for the electrons causing the short period oscillations.

Since the relation between $(\beta/E_0)^2$ and $\cos^2\phi$ for the long period term, if considered linear, would extrapolate to imaginary periods for large values of ϕ, little can be said with finality regarding the electrons causing the long period oscillations. However, using the average value $E_0=32.6\times10^{-14}$ erg$=0.20$ electron volt from Table III and making the assumption that Eq. (9) is suitable for small values of ϕ, a value of $m_1=0.10m_0$ is obtained. No further analysis seems justified here.

According to recent theoretical work by Dingle[2] collision broadening of the energy levels due to impurities will reduce the amplitude of the oscillations by the same amount as if the temperature appearing in the exponential of Eq. (1) were raised by an amount x. It can readily be shown then that $T+x$ is given by the product of $-\beta/2\pi^2k$ and the slope of the straight line obtained when $\log(aH^{\frac{3}{2}})$ is plotted against H^{-1}. Two illustrative plots for the long period term appear in Fig. 8, and values of x for the various isotopes are compared in Table IV with no indications of an isotopic dependence being present. The strong modulations prohibited similar analysis of the short period term. The dependence of x upon T and ϕ might be of interest, but again the data do not justify any analysis. The correlation between x and purity is only fair, since higher values of x are to be expected for the relatively impure $Sn^{123.77}$ crystal. In general, the values of x listed in Table IV are a bit lower than those quoted by Shoenberg which could conceivably be attributed to better equilibrium between the sample and the helium bath.

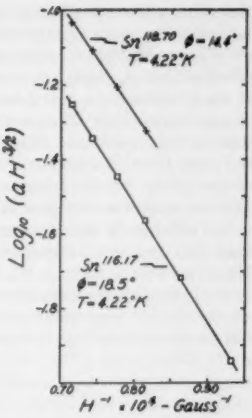

FIG. 8. $\text{Log}_{10}(aH^{\frac{3}{2}})$ *versus* H^{-1}. Values of the amplitude damping parameter, x, resulting from collision broadening of the energy levels are derived from the slopes of such plots.

CONCLUSIONS

Within the experimental error of this work, there is no evidence of an isotope shift in the de Haas-van Alphen effect in tin. However, it now appears that tin is a poor choice for such an investigation because of

TABLE IV. Values of the amplitude damping parameter, x, for the various tin specimens.

Specimen	$\phi(0)$	T(°K)	x(°K)
$Sn^{116.17}$	8.5	4.22	0.9
$Sn^{116.17}$	18.5	4.22	0.4
$Sn^{118.70}$	14.4	4.22	0.2
$Sn^{118.70}$	24.4	4.22	0.6
$Sn^{121.63}$	8.9	4.22	2.1
$Sn^{121.63}$	8.9	1.51	2.8
$Sn^{123.77}$	9.0	4.22	1.1
$Sn^{123.77}$	9.0	2.42	0.9

the relatively large effective masses of the electrons involved. Perhaps a crystal, such as zinc, in which the de Haas-van Alphen electrons have much smaller effective masses, which corresponds to higher curvature of the Fermi surface, would be more likely to show an isotopic dependence. The presence of only one periodic term in this case would also simplify comparison. On the other hand, it is highly probable that the presence of impurities would influence more drastically the effective masses in zinc than in tin.

Nevertheless, it can be concluded that there are at least two groups of electrons responsible for the de Haas-van Alphen effect in tin. While a more thorough investigation of the dependence of the period upon orientation for large values of ϕ might further clarify the electronic structure, it appears doubtful that such an investigation would add much of value to an understanding of the de Haas-van Alphen effect.

It is a pleasure to thank Professor C. T. Lane who suggested and directed this problem. I am also indebted to Professor D. Shoenberg, who sent me, prior to publication, the manuscript of his excellent and comprehensive paper[3] on the de Haas-van Alphen effect. Many thanks are due the staff of the General Electric Research Laboratory where early stages of this work were completed. In particular, I wish to thank Dr. M. D. Fiske of the Low Temperature Group for his interest, Mr. F. C. Kelley for the reduction of the oxides of the tin isotopes, and Dr. R. N. Hall for the germanium single crystal. The magnet used in this research was most generously loaned by the General Electric Company.

PHYSICAL REVIEW VOLUME 88, NUMBER 2 OCTOBER 15, 1952

The Abundances of the Elements

HAROLD C. UREY
Institute for Nuclear Studies, University of Chicago, Chicago, Illinois
(Received June 13, 1952)

The cosmic abundances of the elements were estimated by Goldschmidt (1937) from a study of terrestrial and meteoritic abundances and a comparison of these with Russell's data on the sun. More recently Brown has prepared a table weighting the proportions of the iron and silicate phases according to an estimated proportion of these phases in the earth. The writer has recently proposed that the chondritic meteorites themselves may represent an average sample, and has shown that this assumption is consistent with the density of the moon, which on the basis of his recent discussion in regard to the origin of the solar system should also be approximately a sample of nonvolatile materials. A table of abundances is prepared assuming that these meteorites do represent such a mean sample. This table does not differ markedly from Goldschmidt's, but is distinctly different from Brown's, both because of a different weighting of the phases in meteorites and because of a different choice of data from the literature. Iron is much less abundant than estimated by Brown and somewhat less abundant than Goldschmidt's estimate. There is some indication for markedly low abundances of selenium and tellurium and bromine and iodine, which may indicate some escape of these elements during the formation of the meteorites. Mercury is low, almost certainly because of its loss as a volatile substance during the formation of the meteorites.

THE abundance of the elements in nature is a subject of interest to astronomers, physicists, and geophysicists. These abundances were discussed in great detail by Goldschmidt, and his work has remained a classic in this field up to the present time. He and his co-workers made very many determinations of the abundances of the elements in the rocks of the earth and in the meteorites, and he critically reviewed the work of other people in a classic paper published in 1937–1938.[1] Russell[2] first attempted an estimate of the relative abundances of the elements in the stars and sun, and his conclusion that the composition of the stars and of the earth and meteorites is very nearly the same remains a valid conclusion today; in fact it has not been possible in general to draw a definite conclusion as to whether the stars on the one hand, and the earth and the meteorites on the other have exactly or only approximately the same composition. In the case of certain stars the composition is certainly different from that of other stars, but whether these are or are not unusual stars and therefore the exception to the rule, is difficult to decide.

Goldschmidt weighted the stone, iron, and troilite phases in the proportions of 10:2:1, approximating in this way what he believed to be the composition of the terrestrial planets. He and other workers in the field used these three types of phases, often determining the abundance of the elements in each of the three phases and weighting them in the proportions indicated. In some cases the original determinations were made upon the whole meteorite, and Goldschmidt attempted to separate out the abundances in each one of these

[1] V. M. Goldschmidt, Geochem. Verteilungsgesetze der Elemente IX, Skrifter av det Norske Videnskaps-Akad. i Oslo I. Mat.-Naturv. Klasse No. 4, 1937. Goldschmidt gives references to many other researchers, including his co-workers.
[2] H. N. Russell, Astrophys. J. 70, 11 (1929).

three portions and weight them in the proportions indicated. Brown[3] has published a revised table of the elements using both meteoritic and astronomical data. He gave a table in which he listed the abundances in the silicates, iron, and troilite phases, but included under the silicates, apparently, both the silicate phase of Goldschmidt and the amount of troilite phase that is usually associated with stony meteorites. He then weighted this silicate-troilite phase mixture and the iron phase in the proportions of 60:40, believing that this was the proportion of these materials in the earth. The effect of this weighting procedure was to increase greatly the abundances of iron and the siderophile elements generally. Suess[4] prepared a table which was essentially that of Goldschmidt, but with the addition of certain elements from later data, and he also attempted to estimate what the abundances might be on the basis of regularities relative to the proton and neutron compositions of the nuclei. Rankama and Sahama[5] also revised Goldschmidt's table, adding a few additional estimates. Recently the writer[6] in connection with a general discussion of the possible origin of the solar system concluded that the moon probably was of the approximate composition of the primordial, nonvolatile materials which produced the solar system, arguing that iron had been concentrated in Mercury particularly, in the earth and Venus to a lesser degree, and to a still smaller amount in Mars, and finally to a negligible extent in the case of the moon; and he proposed[7] chemical processes which might reasonably be expected to lead to such a fractionation. He also showed that the mean density of the chondritic meteorites if the iron were oxidized would be approximately the same as that of the moon, and hence suggested that the chondritic meteorites themselves might represent a proper mixture. I. and W. Noddack[8] also made this assumption without giving any reasons for making it. Prior[9] pointed out that the relative proportions of the stone, iron and troilite phases are approximately 85:9:6. Goldschmidt uses 85:9.5:5.5 for these ratios, and the Noddacks used 82.5:12:5.5 for them. The writer prepared a table based on this assumption, but failed to note that Brown's table included under the silicate phase both the silicate phase proper and the approximately 6 parts of troilite phase, and hence doubled the concentrations, approximately, of many chalcophile elements.[10]

In attempting to correct this oversight I have attempted a much more careful study of the whole literature in regard to elemental abundances in meteorites and do not agree with the selection of data used in Brown's table. It appears that the early paper of Noddack and Noddack[11] was in serious disagreement with the work of other people, as repeatedly emphasized by Goldschmidt. In 1934 the Noddacks[11] revised their results and presented a new table differing markedly from the 1930 results for many elements and presenting values much more in accord with those of other researchers. In this second paper they report only their average for the chondritic meteorites and hence it is difficult to compare their analyses with those of others. Goldschmidt rarely accepts the early data of the Noddacks, but does use some of the data of their 1934 paper. The use by Brown of the early results of the Noddacks, often in preference to the later ones, results, I believe, in substantial irregularities in the abundance table for which there is no justification.

In preparing the accompanying table of abundances I have used first of all Goldschmidt's excellent discussion of the subject and have only deviated from his conclusions in the sense of the somewhat different weighting of the stone, iron, and troilite phases in accordance with the idea that chondritic meteorites themselves represent a nearly proper average and the use of some more recent data. In preparing the table it is often possible to use directly the results of investigators for the mean composition of chondrites. When data of this kind seem to be reliable I have used them without attempting to break down the abundances into the three conventional phases. When the data requires, the stone, iron, and troilite phases are weighted in the proportions 85:9.5:5.5.

The objective of such a study is to secure the abundances of the elements in primordial matter, but what is really obtained is only an average of the samples averaged. Whether this does represent the primordial material depends on reasoning of the kind referred to above. The chondritic meteorites are more uniform in composition than are the achondrites, which vary in quite extreme ways as might be expected in silicates differentiated in a fractional crystallization process. However, the ratios of abundances of the more abundant elements in the chondrites, such as the Si:Fe, Si:Mg, Si:Na, and Si:Al ratios, vary by factors up to or even greater than two. It is obvious that the elements have been fractionated in these objects from any possible uniform composition in the original dust cloud from which they were formed, and we do not know whether we have secured representatives of all fractions and whether they are weighted properly. Students of the problems of the origin of the elements and of the uniformity of matter in the universe should bear this

[3] H. Brown, Revs. Modern Phys. **21**, 625 (1949).
[4] H. Suess, Experimentia **5**, 266 (1949).
[5] K. Rankama and T. G. Sahama, *Geochemistry* (University of Chicago Press, Chicago, Illinois, 1950).
[6] H. C. Urey, Geochim. et Cosmochim. Acta **1**, 209 (1951); Amer. Scientist **39**, 590 (1951); *The Planets* (Yale University Press, New Haven, Connecticut, 1952).
[7] See above reference, and a revision to be published in Geochim. et Cosmochim. Acta.
[8] I. and W. Noddack, Svensk kem. Tid. **46**, 173 (1934) [referred to hereafter as Noddack (1934)].
[9] G. T. B. Prior, Mineralog. Mag. **23**, 33 (1933).
[10] In the second printing of *The Planets* the table of abundances given in this paper will be substituted for the one given in the first printing, which is in error for the reasons given.
[11] I. and W. Noddack, Naturwiss. **18**, 757 (1930) [referred to hereafter as Noddack (1930)].

circumstance in mind and not regard the quantitative values given here or elsewhere with too great certainty.

The more abundant elements have been investigated by many analysts and are referred to in Goldschmidt's work. Merrill[12] in 1916 presented a substantial table covering analyses of that time and in 1930 he presented a revised table of averages. The Noddacks (1930) re-analyzed for the abundance of these more abundant elements, and Brown and Patterson[13] in 1947 calculated averages from a table of some 107 stony meteorites covering the work of many people. I have attempted to estimate the abundance of the more abundant elements from these data and have found that it is possible to secure almost exactly the same results in a variety of ways. I have finally selected some 93 chondrites from the table given by Brown and Patterson and have averaged the analyses for the following elements: Si, Mg, Fe, Al, Ca, Na, K, Cr, Ni, Mn, Co, Ti, P, and S. This procedure decreases the abundance of aluminum and calcium and increases that of sodium somewhat as compared to other estimates when all of the stones are included, since the achondrites show a rather marked tendency for high concentrations of the first two elements and low concentrations of sodium. Small changes in the abundances of the other elements occur in this way, but they do not seem to be very important. The analyses are usually given to precisely 0.01 percent, and anything less than this is recorded as a trace, and in many cases the analyses for the rarer elements vary by very large amounts. In taking averages, I have assumed that a trace represents zero abundance as compared with other data in the table. Goldschmidt used a somewhat higher value for sulfur than that indicated by the analyses of the meteorites. I have used the value from the meteorites since the analyses seem to be as consistent in regard to this element as in the case of other elements. Brown estimated sulfur from stellar sources, but a recent discussion by the writer[14] would seem to indicate that there is not much evidence for the loss of this element from the meteorites. Briefly, the argument is that if sulfur was volatilized then other chalcophile elements such as arsenic, zinc, and cadmium should have been lost, which appears not to be true. The abundances of the more abundant elements, Si, Mg, Al, Ca, Na, and Fe may be reliable to about 10 percent. In this connection a recent study by Fairbairn[15] and others on the precision and accuracy of analysis of silicate rocks is most informative.

The P, K,* Ti, Cr, Mn, Co, and Ni values vary considerably and it is doubtful if these values have high precision at all. The value for titanium is lower than Goldschmidt's value since this element is concentrated in the achondrites as compared to the chondrites. The inclusion of five achondrites with the thirty-two chondrites averaged would double the estimated abundance of titanium. For this reason the abundance disagrees with Hevesy's estimates, also.[16]

For Li, Be, and B, I have used the estimates by Goldschmidt. The value for fluorine comes from the 1934 paper of the Noddacks. Rankama and Sahama give a value of 2.1 for the abundance of fluorine based on an analysis by Wasserstein. In a recent paper[14] I have attempted to find some mechanism by which fluorine might have been volatilized from the meteorites and can see no particular reason for believing that this should have occurred unless bromine and iodine have likewise been volatilized. However, the abundance might be perhaps ten times that given in the table. The value for phosphorus may be somewhat low because of its possible volatilization due to reaction of phosphates with hydrogen to give elementary gaseous phosphorus. Goldschmidt used a value for chlorine given by Merrill in his 1916 paper of 0.08 percent. This is the average of four determinations with the analysis of one being 0.27 percent, so that this one analysis contributes substantially to the average. In 1930 Merrill gives in his table 0.03 percent, and the Noddacks (1934) give 0.047 percent by weight. Goldschmidt, however, in compiling his tables uses 0.10 to 0.15 percent. I have used the Noddacks' (1934) value. It is quite obvious that such a common element as chlorine depends upon very few determinations of its abundance in meteorites and the recorded value may be substantially in error. In the study referred to above, I have been unable to find any good reason for believing that chlorine has been lost from the meteorites, unless bromine and iodine have been lost. If the lower values for these elements found by the Noddacks are correct rather than those given by von Fellenburg which are given in the table, some loss of chlorine and fluorine may have occurred also.[14] (the references to bromine and iodine below).

The abundances of the other elements are selected from the literature as follows:

Sc, V, and Cu, Goldschmidt's estimates.
Zn and Ga, Noddacks (1934).
Ge, Goldschmidt and Peters' values, my average.
As, Noddacks (1934).
Se, Goldschmidt's estimate of 1/3000 of sulfur by weight.
Br, Goldschmidt averaged von Fellenburg's results,[17]

[12] G. P. Merrill, U. S. Natl. Museum Bull. 149 (1930); Memoirs Natl. Acad. Sci. 14, 7 (1916).
[13] H. Brown and C. Patterson, J. Geol. 55, 405, 509 (1947).
[14] H. C. Urey, Geochim. et Cosmochim. Acta (to be published).
[15] H. Fairbairn *et al.*, Geol. Survey Bull. 980 (1951).
* *Note added in proof:*—Ahrens, Pinson, and Kearns [Geochim. et Cosmochim. Acta **2**, 229 (1952)] have shown that the abundances of potassium and rubidium in the chondrites are remarkably constant, and their results appear to be the most reliable of any in the literature. Their values have been used in the table, and hence the discussion in the text written previous to their publication does not apply to these elements.
[16] G. Hevesy, *Chemical Analysis by X-Rays and Its Applications* (McGraw-Hill Book Company, Inc., New York, 1932), p. 268.
[17] T. v. Fellenburg, Biochem. Z. **187**, 1 (1927).

securing 0.0025 percent while the Noddacks (1934) give 0.00014 percent. I have used the former value, as did Goldschmidt, but bromine may be too high. It is doubtful if averaging such results has any meaning.

Rb, Ahrens, Pinson, and Kearns.*

Sr, the values of Hevesy and Würstlin.[18]

Y and the lanthanides, Noddack.[19] The weight averages given are calculated from her values for the silicate and troilite phases by assuming an addition of 9.5 percent of iron phase. Her analyses are for two composite samples of chondrites with a small percentage of achondrites.

Zr, Hevesy and Würstlin's value.

Cb, Rankama's estimate.[20]

Mo, the results of Hevesy, Kluver and Noddack (see Goldschmidt's paper); my average.

Ru, Rh, Pd, Ag, Os, Ir, Pt are secured by weighting Goldschmidt's averages for the troilite and metal phases in the proportions of 85:9.5:5.5.

Cd, Noddacks (1934).

In, Goldschmidt's average. Recently Shaw[21] has been unable to detect indium in some stony meteorites.

Sn, Goldschmidt's data, my average.

Sb, Noddacks (1934).

Te, Goldschmidt's estimate of 1/50 of Se by weight.

I, Goldschmidt averages von Fellenburg's data to secure 1.25×10^{-4} percent. Noddacks (1934) give 3.5×10^{-6} percent. I have used the former value, as did Goldschmidt. Averaging two such results would be meaningless.

Cs, Noddacks (1934). Goldschmidt uses their 1930 value. The later value of the Noddacks may be incorrect, but there seems to be no good reason for using a result which the authors themselves have revised.

Ba, Engelhardt's results[22] are used after the elimination of two achondrites. This lowered the mean value from 8×10^{-4} percent to the value of the table.

La to Lu, see Y above. The question mark is used for Tc since it has been observed in certain stars.

Hf, Hevesy and Würstlin's values.[18]

Ta, Rankama's estimate.[20]

W, Noddacks (1934). This value seems much too high.

Re, Brown and Goldberg's values[23] on the iron meteorites assuming no rhenium in the troilite and silicate phases.

Au, Goldschmidt's data on the troilite phase and Brown and Goldberg's data on the iron phase.

Hg, Noddacks (1934).

Tl, Noddacks (1934). Shaw[24] has been unable to detect thallium in meteorites.

Pb, Brown, private communication.

Bi, Noddacks (1934).

Th and U are not estimated because of the great conflicts in data and the lack of good data on the silicate, troilite, and iron phases or on the chondrites as a whole. Davis[25] gives 0.33×10^{-6} percent for U in the iron phase and an average of about 2×10^{-6} percent for two achondrites, and if these are the residue of a crystallization, then this value is too high. Chackett, Golden, Mercer, Paneth, and Reasbeck[26] give about 10^{-5} percent for the recent Beddgelert chondrite. If this latter value is correct, then much more heat has been generated in the moon and earth than seems likely to me, and I have been unable to think of any reasonable process to account for less uranium in the moon and earth than in the meteorites. The blanks in the table represent this uncertainty, though Davis' values seem more probable for the cosmic abundances.

Because of the large variations in analytical results for the rarer elements, the probable errors are very large, at least as large as for the less rare elements represented by P, Cl, K, Ti, etc. Changes in these abundances by a factor of three or even ten in many instances are to be expected. The excellent analyses of Brown and his co-workers using neutron activation methods have not been very useful in this compilation since the method has been applied mostly to the iron meteorites.

The great differences between von Fellenburg's and Noddacks' determinations for bromine and iodine cannot be reconciled. If the first author's values are correct no loss of these elements is indicated, but if the values of the latter authors' are correct some loss is indicated. Selenium and tellurium appear to be rather low. Unfortunately the stabilities of ferrous selenide and ferrous telluride cannot be estimated because of lack of thermodynamic data for these compounds as well as for selenium and tellurium gases. However, it must be kept in mind that all these elements may have been partially lost in high temperature processes to which meteorites have obviously been subjected. Arsenic, zinc, and cadmium sulfides should also have been lost in this case.[14] Because of uncertainties in analyses and inadequate theories relative to what the abundances of the elements should be, it is not possible to be sure in regard to arguments of this kind.

Table I gives the results of these calculations. Columns 1 and 2 give the atomic number and elemental symbol. Columns 3 and 4 give my estimated percent by weight of the element in the average chondrite and the abundance of the element relative to silicon taken as 10,000, respectively. Column 5 gives Goldschmidt's abundances with certain additions and modifications.[27] Column 6 gives Brown's abundances, and column 7

[18] G. v. Hevesy and K. Würstlin, Z. anorg. u. allgem. Chem. **216** 312 (1934).
[19] Ida Noddack, Z. anorg. u. allgem. Chem. **225**, 337 (1935).
[20] K. Rankama, Science **106**, 13 (1947); Bull. Comm. Geol. Finlande No. 133 (1944).
[21] D. M. Shaw, Geochim. et Cosmochim. Acta **2**, 194 (1952).
[22] W. v. Engelhardt, Chemie der Erde **10**, 187 (1936).
[23] H. Brown and E. Goldberg, Phys. Rev. **76**, 1260 (1949); and E. Goldberg and H. Brown, Anal. Chem. **22**, 308 (1950).
[24] D. M. Shaw, Geochim. et Cosmochim. Acta **2**, 131 (1952).
[25] G. L. Davis, Am. J. Sci. **245**, 677 (1947); **248**, 107 (1950).
[26] Chackett, Golden, Mercer, Paneth, and Reasbeck, Geochim. et Cosmochim. Acta **1**, 3 (1950).
[27] H. C. Urey, see reference 6, App. 3.

TABLE I. Abundances of elements (Si = 10,000).

	% by weight	Urey	Goldschmidt	Brown	Kuiper
1 H				3.5×10^{8}	3.7×10^{8}
2 He				3.5×10^{7}	5.1×10^{7}
3 Li	5×10^{-4}	1	1.0		
4 Be	1×10^{-4}	0.16	0.2		
5 B	1.5×10^{-4}	0.2	0.24		
6 C				80,000	4.1×10^{4}
7 N				160,000	8.9×10^{4}
8 O				220,000	1.5×10^{5}
9 F	4×10^{-2}	3	15	90	1.2×10^{3}
10 Ne				9000–240,000	1.7×10^{5}
11 Na	0.75	510	442	462	620
12 Mg	13.55	8700	8700	8870	1.8×10^{4}
13 Al	1.43	820	880	882	830
14 Si	17.96	10,000	10,000	10,000	10,000
15 P	0.15	75	58	130	200
16 S	2.01	980	1140	3500	4600
17 Cl	0.047	21	40–60	170	4000
18 A				130–2,200	2500
19 K	0.09	35	69	69.3	57
20 Ca	1.43	560	571	670	720
21 Sc	5×10^{-4}	0.17	0.15	0.18	
22 Ti	0.058	18	47	26	28
23 V	5×10^{-2}	1.5	1.3	2.5	
24 Cr	0.27	82	113	95	81
25 Mn	0.24	68	66	77	82
26 Fe	24.1	6700	8900	18,300	6200
27 Co	0.11	29	35	99	32
28 Ni	1.45	390	460	1340	380
29 Cu	0.017	4.2	4.6	4.6	
30 Zn	7.6×10^{-2}	1.8	3.6	1.6	29
31 Ga	4.6×10^{-4}	0.10	0.19	0.65	
32 Ge	5.3×10^{-2}	1.1	1.9	2.5	
33 As	1.8×10^{-2}	0.38	0.18	4.8	
34 Se	6.7×10^{-4}	0.13	0.15	0.25	
35 Br	2.5×10^{-2}	0.49	0.43	0.42	
36 Kr					
37 Rb	8×10^{-4}	0.15	0.068	0.071	
38 Sr	2.3×10^{-2}	0.41	0.40	0.41	
39 Y	5.5×10^{-4}	0.097	0.097	0.10	
40 Zr	8×10^{-2}	1.4	1.4	1.5	
41 Cb	4.1×10^{-4}	0.007	0.069	0.009	
42 Mo	3.6×10^{-4}	0.059	0.095	0.19	
43 Tc	?	?			
44 Ru	1.4×10^{-4}	0.021	0.036	0.093	
45 Rh	4.7×10^{-5}	0.0071	0.013	0.035	
46 Pd	9.2×10^{-5}	0.013	0.018	0.032	
47 Ag	1.35×10^{-4}	0.019	0.032	0.027	
48 Cd	1.6×10^{-4}	0.022	0.026	0.026	
49 In	2×10^{-5}	0.0027	0.0023	0.01	
50 Sn	1.4×10^{-3}	0.18	0.29	0.62	
51 Sb	6.4×10^{-5}	0.0079	0.0072	0.017	
52 Te	1.3×10^{-5}	0.0016	0.002		
53 I	1.25×10^{-4}	0.015	0.014	0.018	
54 Xe					
55 Cs	1.1×10^{-4}	0.013	0.001	0.001	
56 Ba	2.9×10^{-4}	0.033	0.083	0.039	
57 La	1.9×10^{-4}	0.021	0.021	0.021	
58 Ce	2.1×10^{-4}	0.023	0.052	0.023	
59 Pr	8.8×10^{-5}	0.0096	0.0096	0.0096	
60 Nd	3.0×10^{-4}	0.033	0.033	0.033	
61 Pm					
62 Sm	1.1×10^{-4}	0.011	0.0115	0.012	
63 Eu	2.7×10^{-5}	0.0028	0.0028	0.0028	
64 Gd	1.7×10^{-4}	0.016	0.0165	0.017	
65 Tb	5.2×10^{-5}	0.0052	0.0052	0.0052	
66 Dy	2.1×10^{-4}	0.020	0.020	0.020	
67 Ho	6.0×10^{-5}	0.0057	0.0057	0.0057	
68 Er	1.7×10^{-4}	0.016	0.016	0.016	
69 Tm	3.1×10^{-5}	0.0029	0.0029	0.0029	
70 Yb	1.7×10^{-4}	0.015	0.015	0.015	
71 Lu	5.4×10^{-5}	0.0048	0.0048	0.0048	
72 Hf	1.6×10^{-4}	0.014	0.015	0.007	
73 Ta	2.8×10^{-5}	0.0026	0.0040	0.0031	
74 W	1.6×10^{-2}	0.13(?)	0.145	0.17	
75 Re	8×10^{-6}	0.0007	0.0012	0.0041	
76 Os	1.2×10^{-4}	0.0097	0.017	0.035	
77 Ir	3.8×10^{-5}	0.0031	0.0058	0.014	
78 Pt	1.9×10^{-4}	0.015	0.029	0.087	
79 Au	2.5×10^{-5}	0.0021	0.0027	0.0082	
80 Hg	$<1\times10^{-6}$	<0.00006	0.0033		
81 Tl	1.5×10^{-5}	0.0011	0.0017		
82 Pb		<0.02	0.091	<0.02	
83 Bi	2×10^{-6}	0.00014	0.0011	0.0021	
90 Th			0.0059		
92 U			0.0023	0.0002	

gives Kuiper's[28] recent estimates of astronomical abundances normalized to silicon equal to 10,000.

The objective of this paper is to show that the use of the chondrites instead of averages of the chondrites, achondrites, and irons does give a reasonable set of values for the abundances of the elements. Tungsten appears to be too high, rhenium too low. Mercury is low because of its volatile characteristics even at low temperatures. It is my belief that this average is the most reasonable of any used thus far, but the table can hardly be regarded as better than that of Goldschmidt to any important degree. However, the table presented here does appear to be definitely better than that of Brown, both because of the choice of weighting given to the iron, troilite, and silicate phases, and the choice of analytical data.

Because of the great interest in the abundances of the elements from the standpoint of the origin of the elements and the most interesting problem of the degree of uniformity in composition of the stars, it is highly desirable that more precise determinations of the abundances be secured.

[28] G. P. Kuiper, *The Atmospheres of the Earth and Planets* (University of Chicago Press, Chicago, 1952), 2nd edition.

Differential Cross-Section Measurements for the Scattering of Protons by Deuterons*

R. J. S. Brown, George D. Freier, H. D. Holmgren, W. R. Stratton, and J. L. Yarnell
Department of Physics, University of Minnesota, Minneapolis, Minnesota

(Received June 16, 1952)

The differential cross section for protons elastically scattered by an incident deuteron beam has been measured in the energy range 0.96 Mev to 3.22 Mev. This corresponds to an extension of previous p-d scattering data down to an energy of 0.48 Mev incident proton energy. The angular range in the c.m. system of coordinates is from 67° to 126° with the cross section showing characteristic minima in the neighborhood of 90° at each energy considered. Values of the cross section vary from 0.147 to 0.280×10^{-24} cm² over this range of parameters.

INTRODUCTION

THE interest in interactions among a small number of nucleons has led us to extend more completely the measurements of p-d scattering[1–6] into lower energy regions. Considerable theoretical work has been done[7–11] on this problem in an attempt to evaluate the equivalence between n-n forces and n-p forces and explain the "anomalous" behavior of the angular distributions. The measurements of Sherr *et al.*[3] covered most extensively the range of working energies of an electrostatic generator when incident protons with laboratory energies in the range of 0.825 Mev to 3.49 Mev were scattered from a deuterium gas target. These data were subsequently analyzed by Critchfield.[9] We have extended the energy range of the measurements for this interaction by reversing the roles of the proton and deuteron while working in the same range of machine energies. An equivalent center-of-mass energy for the interaction is realized in these two experiments when the energy of an incident deuteron beam is twice that of an incident proton beam, so that by working in approximately the same range of machine energies, we have extended the energy range of the earlier data down to 0.48 Mev.

In order to make it easier for the reader to compare results of this experiment with the earlier measurements at Los Alamos and the analysis of the Los Alamos data by Critchfield,[9] we will reduce all of our final data to their equivalent in an experiment where incident protons are scattered by deuterons and present these data as an extension of the earlier work. However, to satisfactorily describe the measurements in the laboratory, we will describe the experiment in terms of measured laboratory coordinates and parameters and then change to the equivalent case in the final tabulation of the data.

SCATTERING CHAMBER

The scattering chamber used in this experiment is shown in Fig. 1. It is the same chamber used for measuring the scattering of protons by tritons[12] with the following modification. The volume of the chamber has been increased from 90 cm³ to 200 cm³ by milling out a large pill-box cavity surrounding the effective scattering volume defined by the incident beam collimating holes and the counter collimating slits. This enlargement moved the walls of the scattering chamber farther from the collimated beam and reduced the amount of gas-to-wall-to-counter scattering which had previously restricted reliable measurements to scattering angles greater than 40°. The enlargement allowed us to go to angles as low as 30° before this trouble again became serious. Data were taken at 26.8°, and the large specified error in these measurements at this angle is due mostly to this phenomenon.

The counter slit system was measured with a comparator and gave a geometry factor $G=2bA/Rh=1.2802\times10^{-4}$ cm, where $A=0.10021$ cm² is the area of the round hole at the counter, which is at a distance $R=13.670$ cm from the center of the effective scattering volume. The defining slit of width $2b=0.1753$ cm is located a distance $h=10.038$ cm away from the counter hole A.

The incident beam was collimated by holes A and C, which have respective diameters of 0.1079 cm and 0.1187 cm. These holes were 5.87 cm apart, thus allowing the beam to diverge into a 1.1° half-angle cone.

The entrance window was of nominally 0.2-mil aluminum foil. The measured energy loss of 1.88-Mev protons in this foil was 130 kev. The exit window to the collector cup was 0.25-mil Mylar[13] coated with a thin layer of evaporated aluminum to help dissipate power from beam losses. This foil would become slightly charred from long use. The centering of the charred

* This work supported by the joint program of the ONR and AEC.

[1] Tuve, Heydenburg, and Hafsted, Phys. Rev. **50**, 806 (1936).
[2] R. F. Taschek, Phys. Rev. **61**, 13 (1942).
[3] Sherr, Blair, Kratz, Bailey, and Taschek, Phys. Rev. **72**, 662 (1947).
[4] Heitler, May, and Powell, Proc. Roy. Soc. (London) **190**, 180 (1947).
[5] Karr, Bondelid, and Mather, Phys. Rev. **81**, 37 (1951).
[6] L. Rosen and J. C. Allred, Phys. Rev. **82**, 777 (1951).
[7] H. Primakoff, Phys. Rev. **52**, 1000 (1937).
[8] K. Ochiai, Phys. Rev. **73**, 1221 (1937).
[9] C. L. Critchfield, Phys. Rev. **73**, 1 (1948).
[10] H. S. Massey and R. A. Buckingham, Phys. Rev. **73**, 260 (1948).
[11] M. M. Gordon, Phys. Rev. **80**, 1111 (1950).
[12] Claassen, Brown, Freier, and Stratton, Phys. Rev. **82**, 589 (1951).
[13] Du Pont's trade name for its polyester film.

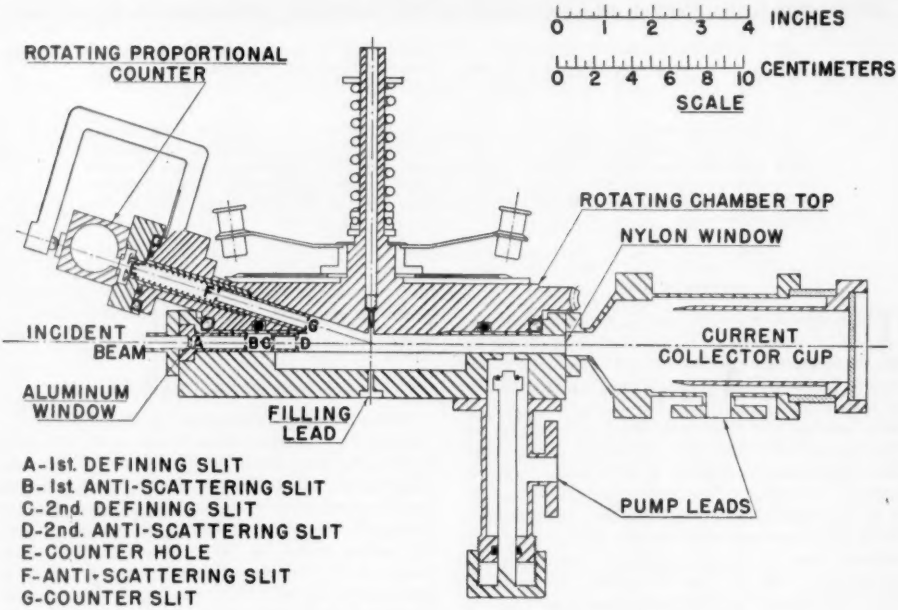

FIG. 1. View of scattering chamber. The figure shows a plane containing the axis of the beam and the axis of cylindrical symmetry of the chamber with the counter set at a maximum scattering angle.

spot indicated that the beam had been passing symmetrically through the chamber and that all of it was properly entering the collector cup. The alignment of the beam was also checked by noting the centering of the fluorescent spot on the quartz window at the far end of the Faraday collector cup.

The integrated incident flux of deuterons which had passed through the chamber into the collector cup was determined by measuring the charge which had accumulated on the cup and a 0.5-μf polystyrene condenser in parallel with the cup. Loss of secondary electrons from the collector cup was prevented by a transverse magnetic field and an electrostatic bias. The accumulated charge was measured with a calibrated ballistic galvanometer at the end of a run. This calibration was checked periodically during the course of the experiment.

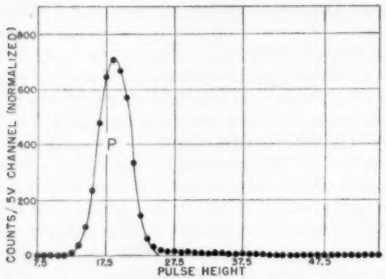

FIG. 2. Typical pulse-height distribution. The tail on the right is due to particles which have suffered gas-to-wall-to-counter scattering and extends into the main peak so as to require a -3 percent correction at this angle.

The scattered particles, which had passed through the counter defining slits, entered the proportional counter through either a thin window made from alternate layers of zapon and evaporated aluminum or a 0.17-mil aluminum window. Our angular range of measurements was limited by the maximum angle at which we could still obtain recoil protons with sufficient energy to give measurable pulses; therefore, the counter window was, in general, made as thin as possible and yet be able to withstand counter gas pressures. The aluminum layers gave the windows added strength and made them impervious to tritium used in a concurrent experiment.

The proportional counter was filled with a mixture of Argon and CO_2 at various pressures between 6 and 15 cm of Hg, adjusted with the window thickness to give maximum pulse height and still allow particles to pass completely through the counter. CO_2 was used as a quenching gas, rather than methane, to cut down the

size of pulses caused by atoms in the counter gas which were recoiling from fast neutrons in the machine background.

The pulses from the counter were amplified by a Model 100 preamplifier and amplifier of Los Alamos design[14] and registered on a 10-channel pulse-height discriminator, also of Los Alamos design. The circuits were modified, and the procedure of taking data was arranged so that a pulse-height distribution was determined from 50 measured points.

The mechanics of this elastic scattering interaction allows no deuteron to be scattered at a laboratory angle greater than 30° so that at all angles between 30° and 90° only a group of recoil protons are involved. At angles less than 30° the scattered deuteron energies are double valued. Measurements were made at only one angle less than 30°—namely, 26.8°, and at this angle sufficient absorbing material was inserted in the counter window to stop the slow group of deuterons, leaving the group of fast deuterons and recoil protons to be resolved. A typical pulse distribution for recoil protons is shown in Fig. 2. The normalized yield was determined by extrapolating the steep edges of the pulse distribution to zero and integrating. This was then corrected for the contribution of a "tail" of large pulses which extended into the main peak. The details of determining the magnitude of this correction are given in a later paragraph.

The number of effective scattering centers was determined from the geometry factors of the counter slit system and the slit system which defined the incident beam. Together these gave an effective scattering volume containing a number of atoms that depended on the measured pressure and temperature of the gas, according to the ideal-gas law.

The pressure was measured with a Wallace and Tiernan differential manometer which was periodically calibrated with a manometer containing Apiezon oil *B* having a measured density of 0.862 ± 0.001 g cm^3 at 20°C and a volume coefficient of expansion of 83×10^{-5} per decree centigrade. The working range of pressure was from 2.0 to 4.0 cm of Hg.

The temperature of the scattering gas was measured with a thermometer in contact with the scattering chamber.

The entire system was checked before and during the experiment by switching to an incident proton beam and scattering protons from protons, protons from helium, and scattering protons from a mixture of hydrogen and helium, at various angles and energies. Further checks were made by scattering deuterons from protons with 3.02-Mev incident deuterons and scattering protons from deuterons with 1.51-Mev incident protons. In all cases we found that at angles of 45° or less, corrections had to be applied similar to those in reference 12. Even though the volume of the scattering chamber had been enlarged, there was evidence of some gas-to-chamber wall-to-counter scattering of the incident particles, which caused the pulse distributions to have a slightly skewed shape arising from counted particles with energies lower than the main group. There were no pulses when the beam passed through an empty chamber. The gas-to-wall-to-counter scattering effect disappeared for deuterons scattered from protons, where the mechanics of the scattering restricts all scattered deuterons to remain within a cone of 30° half-angle and consequently cannot strike the chamber wall area seen by the counter geometry. The corrections applied to the data were −4.5 percent at 26.8°, −4

[14] W. C. Elmore and M. Sands, *Electronics* (McGraw-Hill Book Company, Inc., New York, 1949), p. 166.

TABLE I. Cross sections of protons scattered by deuterons.

Lab angle α			26.8	31.6	34.55	40	44.39[a]	45	49.8	50.3
C.m. angle θ			126.4	116.8	110.9	100	91.22	90	80.4	67.4
E_D	$\sigma(\theta)$ barns		0.275	0.260	0.251	0.250	0.260	0.255		
0.98 Mev	$k^2\sigma(\theta)$		0.295	0.268	0.250	0.255	0.268	0.264		
E_D	$\sigma(\theta)$		0.291	0.282	0.285	0.254	0.226	0.225		
1.20 Mev	$k^2\sigma(\theta)$		0.376	0.333	0.307	0.302	0.262	0.260		
E_D	$\sigma(\theta)$		0.272	0.250	0.216	0.206	0.218	0.208	0.212	0.240
1.46 Mev	$k^2\sigma(\theta)$		0.427	0.381	0.339	0.324	0.342	0.326	0.333	0.377
E_D	$\sigma(\theta)$		0.256		0.208	0.188	0.184	0.180	0.182	0.190
1.97 Mev	$k^2\sigma(\theta)$		0.543		0.441	0.398	0.390	0.382	0.386	0.403
E_D	$\sigma(\theta)$		0.257		0.201	0.184	0.176	0.178	0.174	0.187
2.21 Mev	$k^2\sigma(\theta)$		0.610		0.478	0.437	0.418	0.423	0.413	0.445
E_D	$\sigma(\theta)$		0.244		0.191	0.173	0.163	0.164	0.160	0.178
2.46 Mev	$k^2\sigma(\theta)$		0.645		0.505	0.457	0.428	0.433	0.422	0.470
E_D	$\sigma(\theta)$		0.232		0.182	0.164	0.156	0.153	0.155	
2.71 Mev	$k^2\sigma(\theta)$		0.678		0.530	0.478	0.453	0.445	0.452	
E_D	$\sigma(\theta)$		0.220		0.175	0.160	0.147	0.150	0.152	0.165
2.99 Mev	$k^2\sigma(\theta)$		0.735		0.582	0.515	0.472	0.482	0.489	0.530
E_D	$\sigma(\theta)$				0.166	0.151	0.147	0.148	0.148	0.161
3.22 Mev	$k^2\sigma(\theta)$				0.681	0.623	0.609	0.612	0.612	0.667

[a] Data at 44.39 were obtained by counting deuterons scattered by protons at 26.8 in the laboratory. Data at all other angles were obtained by counting recoil protons.

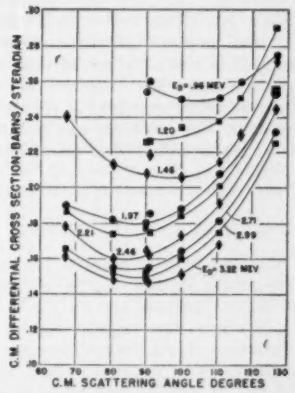

FIG. 3. Center-of-mass cross section in barns/steradian plotted as a function of c.m. scattering angle with incident laboratory deuteron energy as a parameter. The equivalent incident laboratory proton energy would be half of the given deuteron energy. (Note that origin of ordinate is not zero.)

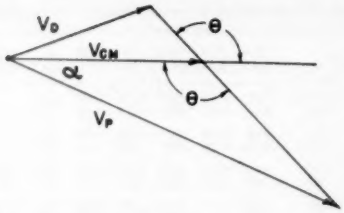

FIG. 4. Vector diagram of laboratory velocities showing angles used in tabulating data. V_P = laboratory velocity of recoil proton at laboratory angle α. θ = center-of-mass angle for a proton scattered from a deuteron at a laboratory angle equal to one-half the given incident deuteron laboratory energy.

percent at 31.6°, −3 percent at 34.5°, −2 percent at 40°, and −1 percent at 45°.

The presence of any contaminant in the scattering gas or the presence of molecular hydrogen in the incident beam could easily be detected by looking for additional small peaks in our pulse distribution curves at angles greater than 30°. Pulse sizes from recoil protons would shift rapidly with changing angle, and deuterons could not be scattered more than 30°, so any scattering from atoms heavier than hydrogen could quickly be detected. The possibility of scattering from large hydrocarbon molecules was ruled out by passing the beam through an empty chamber. No measurable contamination effects were observed.

PROCEDURE

When not in use, the chamber was maintained at approximately 3×10^{-6} mm of Hg with an oil diffusion pump. After the angles and energies were set, the chamber was filled with hydrogen to a pressure of from 2 cm to 4 cm of Hg. The yield was obtained from the integrated pulse distribution curve which required five independent runs to give a smooth curve with well-defined peaks. Data which did not fit onto a smooth pulse distribution curve were rejected. The pressure gauge and galvanometer were read at the end of each of these five runs. This procedure was repeated at an equal angle on the opposite side of the incident beam.

Except for second-order effects, the differential cross section was obtained from the formula

$$\sigma=(Y\sin\alpha)/NnG,$$

where Y is the normalized, integrated, and corrected yield of particles from the pulse distribution curves obtained at the angle α, and N is the number of deuterons incident on the n scattering centers of hydrogen in a volume defined by G. The determination of the yield, Y, as described above involved at least 8000 counts at each angle and energy.

The hydrogen gas was changed before each new angle and energy setting.

RESULTS

The corrected measurements of the differential cross section for protons scattered by deuterons, transformed to the center-of-mass coordinate system, are tabulated in Table I and shown graphically in Fig. 3. The notation for the angles used can be understood best by observing the velocity vector diagram in Fig. 4.

CORRECTIONS

These data have been corrected for the gas-to-wall-to-counter scattering described above. The error in charge measurement was less than ±1 percent. The pressure and geometry measurements were good to $\pm\frac{1}{2}$ percent. We feel that the over-all probable error in the tabulated results is ±2.5 percent for incident deuteron energies greater than 1.20 Mev and ±3.0 percent for incident deuteron energies of 0.96 Mev and 1.20 Mev except at the laboratory angle of 26.8°, where the probable errors are ±4 percent and ±5 percent respectively for these energy ranges. Second-order geometry corrections were found to be negligible.

Incident energies were corrected for loss in the entrance window and loss in the gas target. The quoted values of energy are reliable to ±1 percent.

It is a pleasure to acknowledge the advice and consultations of Professor J. H. Williams and the assistance of Dr. G. R. Keepin and Dr. J. M. Blair and Mr. D. Rankin and Mr. T. F. Stratton during the course of this experiment.

The Elastic Scattering of Deuterons by Tritons*

W. R. STRATTON, G. D. FREIER, G. R. KEEPIN, D. RANKIN, AND T. F. STRATTON
Department of Physics, University of Minnesota, Minneapolis, Minnesota

(Received June 16, 1952)

The differential cross section for the elastic scattering of deuterons by tritons has been measured in the energy range 0.96 Mev to 3.22 Mev. The angular range of data is between 44.3° and 126.4° in the center-of-mass system of coordinates. The values of the cross section have a minimum near 90°, and this minimum decreases steadily and moves to higher angles as the incident deuteron energy is increased. At 1.20 Mev the cross section at the minimum is equal to 0.130 barn, and at 3.22 it is 0.019 barn.

INTRDUCTION

INFORMATION concerning the interactions among the light nuclei has recently been extended at this laboratory to include a measurement of the differential cross sections for elastic scattering of deuterons by tritons as a function of scattering angle and incident deuteron energy. The range of laboratory deuteron energies is between 0.96 Mev and 3.22 Mev, and the angular range for most energies is between 44.3° and 126.4° in the center-of-mass system of coordinates.

The data presented in this paper and those in the preceding paper[1] on p-d scattering were obtained concurrently, using the same equipment. The results of the p-d scattering experiment were essential for completion of the work presented in this paper.

EQUIPMENT AND EXPERIMENTAL PROCEDURE

A beam of collimated, monoergic deuterons from the Minnesota electrostatic generator was passed through a small volume scattering chamber filled with a mixture of hydrogen and tritium gas. Charged particles resulting from passage of the beam through the scattering chamber were detected and identified by a gas-filled proportional counter. This scattering chamber, counter, charge collection and measuring system, and pressure and temperature measuring systems have been previously described.[1,2]

The energy of the incident deuteron beam was controlled and measured by an electrostatic analyzer which operated on the molecular deuterium beam. For purposes of calibrating the energy scale and measuring the thicknesses of aluminum entrance windows to the scattering chamber, a proton beam was used to determine the point at which the 1.882-Mev[3] threshold of the $Li^7(p, n)Be^7$ reaction occurred.

TRITIUM HANDLING SYSTEM

Tritium was obtained and stored, when not in use, in the form of a sintered pellet of uranium tritide. This pellet was in turn contained in a small quartz bottle which was coupled to the scattering chamber and Wallace & Tiernan differential pressure gauge through a Pyrex stopcock.

Prior to use, the scattering chamber, pressure gauge, and quartz bottle were evacuated by an oil diffusion pump and a liquid nitrogen cold trap until a pressure of about 5×10^{-5} mm Hg was obtained. UT_3 is a stable compound at room temperatures and no measurable quantity of gas was lost by this evacuation procedure. The scattering chamber was then isolated from the pump and the UT_3 pellet was heated to about 400°C, evolving the tritium gas[4] directly into the scattering chamber and pressure gauge. When the desired pressure was attained (about 40 mm Hg) the glass stopcock was closed and the current in the heating element around the quartz bottle was reduced in order to maintain the uranium at about 100°C. At the end of 4 to 6 hours the tritium gas which had been used in the scattering chamber was purified by recycling through the uranium. The compound UT_3 was formed very rapidly if the uranium was maintained at about 100°C, and essentially all hydrogen isotopes in the gas sample were taken up within a very few minutes.

The sample of gas was composed of 98 percent tritium and 2 percent hydrogen when first obtained, but the quantity of hydrogen in the gas sample rose constantly during the experiment. The source of this hydrogen was traced to various hydrocarbons that were in or near the scattering volume. Data were taken with the fractional amount of tritium as low as 40 percent.

The method of measuring the percentage of tritium and hydrogen in the gas sample is discussed below.

IDENTIFICATION OF PARTICLES

It should be emphasized that when the deuteron beam passed through the scattering chamber filled with a mixture of tritium and hydrogen, a large number of different charged particles were observed in the proportional counter. Deuterons were scattered by tritons at all angles in the laboratory, recoil protons and recoil tritons could be counted between 0° and 90°, and at angles less than 30° two groups of deuterons which

* This research was assisted by the joint program of the ONR and AEC.

[1] Brown, Freier, Holmgren, Stratton, and Yarnell, Phys. Rev. 88, 253 (1952).

[2] Claassen, Brown, Freier, and Stratton, Phys. Rev. 82, 589 (1951).

[3] Herb, Snowden, and Sala, Phys. Rev. 75, 246 (1949).

[4] Spedding, Newton, Warp, Johnson, Nottorf, Johns, and Daane, Nucleonics 4, 4 (1949).

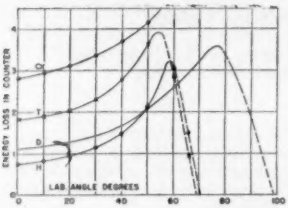

FIG. 1. Curves showing the loss of energy of scattered deuterons, recoil protons, recoil tritons, and alpha-particles in the proportional counter are plotted as a function of angle in the laboratory. The incident deuteron energy is 3.0 Mev.

were scattered by protons could be observed. In addition, alpha-particles from the reaction $T(d, n)\alpha$ were observed[5] at all angles. This last group, however, had a cross section that was small when compared to the other processes. It was absolutely necessary, therefore, that the various voltage pulses coming from the proportional counter be properly identified.

The groups of particles were identified by their relative pulse heights as recorded on a 10-channel pulse-height analyzer. These pulses were in turn proportional to the energy lost by the various charged particles when they passed through the counter. This energy loss for each group of particles was calculated as a function of angle and incident deuteron energy. The result of one such calculation is illustrated in Fig. 1. The incident beam energy in this case is 3.0 Mev. The energies lost (ΔE) by deuterons scattered from tritons, recoil protons, recoil tritons, and $T(d, n)\alpha$ alpha-particles are shown as a function of scattering angle in the laboratory system of coordinates. The ΔE for the two groups of deuterons scattered by protons at angles less than 30° are omitted. These particular curves were calculated assuming an aluminum counter window 130 kev thick for 2-Mev protons and a counter filling of 17 cm Hg of carbon dioxide and argon. Thinner counter windows and lower counter pressures were often used during this experiment, but in all cases the resulting pulse-height distributions could be interpreted by referring to Fig. 1 or similar curves.

Figures 2, 3, and 4 illustrate pulse-height distributions obtained at 34.5°, 49.8°, and 65°. Reference to Fig. 1 readily allows identification of the various groups of particles. It is of interest to note that at 34.5° the pulse resulting from a recoil proton is slightly less than that of a deuteron scattered from a triton, while at 50° the two have almost the same energy loss in the counter. At 65° (and higher angles) all particles except scattered deuterons and disintegration alpha-particles have been stopped in the counter window or produce pulses only slightly larger than normal counter noise. These data (Figs. 2, 3, and 4) were obtained by the methods described in reference 1. They represent the yield observed per mm Hg of gas pressure and per microcoulomb of incident deuteron charge collected.

[5] T. F. Stratton and George D. Freier, Phys. Rev. **88**, 261 (1952).

MEASUREMENT OF THE PERCENTAGE OF TRITIUM

A study of Figs. 1, 2, and 3 shows that the pulse-height distribution resulting from the recoil protons was never completely resolved from both the scattered deuteron and recoil triton pulse-height distributions. Consequently, no direct method of obtaining the concentrations of hydrogen and tritium in the chamber could be carried out and the following somewhat indirect method was used.

At small angles in the laboratory, both recoil tritons and scattered deuterons were observed in the proportional counter. The recoil triton, at these angles, received its momentum from a deuteron scattered, in general, at some larger angle. For example, the yield of recoil tritons observed at 40° in the laboratory gave the laboratory cross section for scattered deuterons at 63.4°. In the laboratory 49.8° is the one angle where the yield of deuterons may be computed from the yield of recoil tritons or vice versa. A recoil triton which entered the detector at 49.8° had deflected a deuteron through an equal angle on the opposite side of the beam. At this angle the deuteron yields from two different peaks can then be obtained simultaneously provided the recoil triton yield is corrected for the larger solid angle presented to the tritons by the detector. The relationship in this case is $Y_D = 0.750 Y_T$, where Y_D and Y_T are the deuteron and triton yields, respectively. By applying this relationship to a pulse distribution such as shown in Fig. 2, the number of pulses in the left-hand peak caused by recoil protons can be determined. Utilizing this proton yield, knowing the cross section for production of recoil protons at 49.8° [1] and knowing the temperature and pressure of the gas in the chamber, the number of hydrogen scattering centers (and consequently the number of tritium nuclei) could be computed.

The tritium concentration was measured about 50 times and during the experiment was observed to decrease steadily from 98 percent tritium to 40 percent

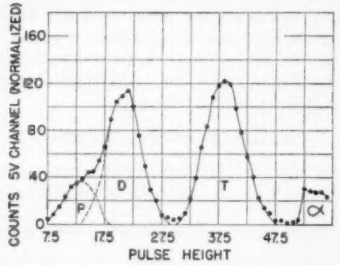

FIG. 2. Pulse-height distribution observed at 34.5°. The yields plotted are normalized per mm Hg pressure and per microcoulomb of charge collected. The abscissa is in volts. Particle groups may be identified by referring to Fig. 1.

tritium. For best resolution of the pulse-height distributions the measurement of tritium concentration was made at energies equal to or greater than 1.96 Mev. The measurement of tritium concentration was independent of the incident deuteron energy used.

METHOD OF OBTAINING DATA

The procedure after filling the scattering chamber was to first measure the percentage of tritium in the gas sample as described above. This value was used for all measurements during this chamber filling. Cross sections were obtained at least twice at each angle and energy—once for each positive and negative value of the scattering angle. If poor agreement existed, or if for some reason (e.g., low percentage tritium) one run appeared to be of doubtful value, additional data were taken. No consistent differences between positive and negative scattering angles were found, and the cross sections observed were independent of the relative amounts of tritium and hydrogen in the gas sample used in obtaining them. Since in the laboratory system of coordinates the cross section for recoil protons averaged between 3 and 7 times the cross section for scattering of deuterons by tritons, data taken with low tritium concentration were relatively less reliable and were generally repeated several times. The method of obtaining a cross section from pulse-height distributions illustrated in Figs. 2, 3, and 4 is discussed in reference 1.

Data were obtained by counting scattered deuterons at all laboratory angles and recoil tritons at small laboratory angles. Recoil tritons observed at small angles corresponded to deuterons observed at large angles (e.g., 34.5° corresponds to 71.65°). Cross sections obtained in these two different ways provided a check on the internal consistency of the data. In general, the agreement was very good, being somewhat less than the estimated errors (discussed below). At angles less than 50° (laboratory) the pulse-height distributions resulting from recoil protons and scattered deuterons were not separated and the expected yield of recoil protons

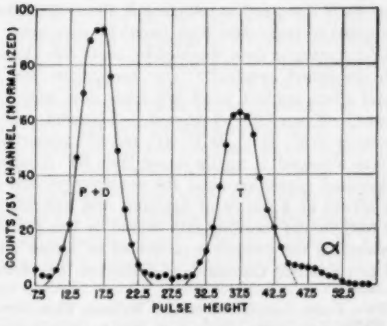

FIG. 3. Pulse-height distribution at 49.8°. At this angle protons and deuterons lose about the same amount of energy in the counter.

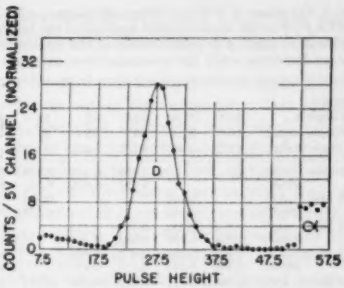

FIG. 4. Pulse-height distribution at 65°. At this angle all particles except scattered deuterons and alpha-particles from the $T(d, n)\alpha$ reaction have been stopped in the counter window.

had to be subtracted from the total peak. Since the percentage of hydrogen in the gas sample was measured for each chamber filling and the cross section for the recoil protons was known (reference 1), this could be done. Above 60°, only scattered deuterons (and alpha-particles) in general could enter the counter.

The largest laboratory angle studied during this experiment was 90° at 3.22 Mev. The maximum angle necessarily decreased as the energy was lowered. The reason for this upper limit is related to the mechanics of this scattering process and to the fact that a rare and radioactive gas, tritium, was used in the scattering chamber. At large scattering angles (above about 90°) a deuteron scattered by a triton retains only a small fraction of its original energy. In addition, it was necessary that the window in the proportional counter be made sufficiently thick in order that it be secure against breaks, leaks, and diffusion processes through it. Consequently, at high angles the deuterons were stopped in the counter window.

During the period that the gas was in the chamber, a very slow pressure rise was noticed. However, the total change in pressure was small, and several checks indicated that impurity scattering was negligible during the period of time mentioned above.

CORRECTIONS TO THE DATA

A correction to the percentage of tritium measured as discussed above was necessary. Reference to Figs. 1 and 3 shows that at 49.8° the voltage pulses resulting from a recoil triton and an alpha-particle differ only slightly. Very often (at this angle) the two pulse-height distributions were, therefore, not resolved. The differential cross section for the production of alpha-particles from the $T(d, n)\alpha$ reaction has been measured as a function of angle and energy,[5,6] and additional values were obtained during this experiment. The expected yield of alpha-particles was calculated and a small correction was made to the number of particles in the

[5] Hanson, Taschek, and Williams, Revs. Modern Phys. 21, 635 (1949).

TABLE I. Summary of *D-T* scattering experiment. $\sigma(\beta')$ is the cross section in the center-of-mass system at the center-of-mass angle β', and $K^2=p^2/\hbar^2$ is the wave number squared of the incident deuteron in the c.m. system. Data were obtained by counting deuterons at the laboratory angle β or recoil tritons at the laboratory angle γ as indicated. At 90° c.m. the starred cross sections were obtained by counting deuterons while the remainder were obtained by counting tritons. The units of $\sigma(\beta')$ are barn/steradian.

Triton angle γ							45	40		34.5		31.6			26.8	
Deuteron angle β	26.8	31.6	34.5	40	45	49.8	56.3		65	75	75		80	83.8		90
Center-of-mass angle β'	44.3	52.1	56.7	65.4	73.2	80.4	90	100	102.2	110.85	115.15	116.75	121.1	125.4	126.4	131.8
Probable error of $\sigma(\beta')$	±9%	±6%	±6%	±6%	±6%	±5%	±5%	±5%	±5%	±5%	±5%	±5%	±5%	±5%	±9%	±5%
$E_D=0.96$ Mev $\sigma(\beta')$			0.195	0.204	0.158	0.181										
$k^2\sigma(\beta')$			0.650	0.680	0.526	0.603										
$E_D=1.20$ Mev $\sigma(\beta')$		0.148			0.133	0.133	0.131*					0.163				
$k^2\sigma(\beta')$		0.616			0.554	0.554	0.546*					0.678				
$E_D=1.46$ Mev $\sigma(\beta')$	0.151	0.138	0.119	0.112		0.101	0.097*	0.103	0.101	0.120		0.133				
$k^2\sigma(\beta')$	0.766	0.700	0.603	0.568		0.512	0.491*	0.522	0.512	0.608		0.674				
$E_D=1.97$ Mev $\sigma(\beta')$	0.103	0.094	0.077	0.072		0.059	0.059*	0.065	0.069	0.087		0.100			0.129	
$k^2\sigma(\beta')$	0.704	0.643	0.526	0.493		0.404	0.404*	0.445	0.472	0.595		0.684			0.882	
$E_D=2.21$ Mev $\sigma(\beta')$	0.086		0.072	0.058	0.052	0.046	0.047	0.052	0.055	0.069	0.077				0.114	
$k^2\sigma(\beta')$	0.660		0.552	0.445	0.399	0.353	0.361	0.399	0.422	0.529	0.594				0.874	
$E_D=2.46$ Mev $\sigma(\beta')$	0.090		0.067	0.056	0.050	0.036	0.034	0.038	0.042	0.055	0.069			0.112	0.113	
$k^2\sigma(\beta')$	0.768		0.572	0.478	0.427	0.308	0.290	0.324	0.359	0.470	0.589			0.959	0.966	
$E_D=2.71$ Mev $\sigma(\beta')$	0.084		0.064	0.052	0.043	0.031	0.027	0.030	0.034	0.045	0.057			0.094	0.109	
$k^2\sigma(\beta')$	0.790		0.602	0.489	0.404	0.291	0.254	0.282	0.320	0.423	0.536			0.884	1.025	
$E_D=2.99$ Mev $\sigma(\beta')$	0.091		0.060	0.044	0.041	0.028	0.023	0.024	0.025	0.036	0.047		0.070		0.099	
$k^2\sigma(\beta')$	0.944		0.622	0.456	0.425	0.290	0.239	0.249	0.259	0.373	0.487		0.726		1.027	
$E_D=3.22$ Mev $\sigma(\beta')$			0.054	0.042	0.032	0.026	0.022	0.019	0.021	0.031	0.041			0.092	0.081	0.139
$k^2\sigma(\beta')$			0.602	0.469	0.357	0.290	0.246	0.212	0.235	0.347	0.458			1.028	0.950	1.554

recoil triton peak and finally to the percentage of tritium. This correction was never greater than 2 percent.

Two corrections to the data were necessary because gas-to-wall-to-counter scattering processes produced extraneous counts. Figure 2 of reference 1 illustrates the appearance of a single group of particles as observed from this scattering chamber. A "tail" of particles whose energy when entering the counter was less than that of the principal group can be seen extending to higher pulse heights. This phenomenon was a function of angle and energy, being most significant at small angles and high energies. This "tail" of particles effected both its parent peak and any neighboring peak of higher pulse height.

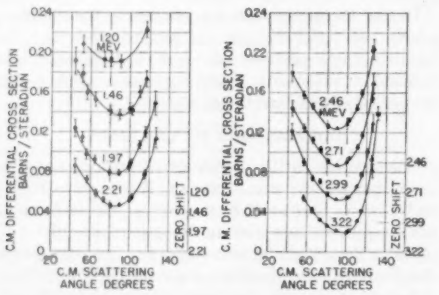

FIG. 5. The differential cross sections per unit solid angle for the elastic scattering of deuterons by tritons is plotted as a function of center-of-mass angle for various incident deuteron energies. Cross sections obtained by counting scattered deuterons which have been resolved from recoil protons are illustrated by squares. Circles represent data obtained from a pulse-height distribution consisting of recoil protons and scattered deuterons; the expected yield of protons was subtracted to obtain the yield of deuterons. Data obtained by counting recoil tritons are plotted as triangles. The zero for each energy is indicated at the right.

The first correction caused by this "tail" of particles was applied to the observed yields of recoil tritons. As is seen by Figs. 2 and 3 the pulse-height distribution resulting from the recoil tritons falls in a region which includes part of the "tail" associated with the yields of scattered deuterons and recoil protons. A correction was therefore made to all recoil triton data. This correction depended on the angle, the beam energy, the percentage tritium in the chamber, and the relative size of the voltage pulses in the two pulse-height distributions. The number of counts subtracted from the triton peak varied a great deal between individual runs. At the smallest angles it averaged about 4 percent. This correction was largest at the smallest angles, was relatively less at 45°, and was zero at all higher angles.

The second correction resulting from multiple scattering processes was applied to all data obtained at low angles. This was necessary since any one peak in the distribution had its own tail which extended into the main peak and would make the measured yield too large. As is discussed in reference 1, the corrections to be applied to these data were found by comparing *p-p* and *d-p* scattering data obtained by use of this chamber with published results.[7–9] The corrections for this second effect applied to all low angle data were −4.5 percent, −4 percent, −3 percent, −2 percent, and −1 percent at 26.8°, 31.6°, 34.5°, 40°, and 45°, respectively.

Data obtained at angles larger than 60° required a background correction since the entrance window and slits served as a source of neutrons and gamma-rays. The background counting rate caused by this radiation increased as the counter was moved to higher angles and hence nearer the source of radiation. In addition,

[7] Blair, Freier, Lampi, Sleator, and Williams, Phys. Rev. **74**, 553 (1948).
[8] Herb, Kerst, Parkinson, and Plain, Phys. Rev. **55**, 998 (1939).
[9] Sherr, Blair, Kratz, Bailey, and Taschek, Phys. Rev. **72**, 662 (1947).

the cross section is quite small in the angular region beyond 60°. Therefore, a background correction was made, when necessary, to data taken above 60° in the laboratory system. This correction fluctuated a great deal from run to run; it averaged about 4 percent. This effect was negligible for data obtained at angles less than 60°.

Errors in the data resulting from the finite size of the entrance slits and counter slits were negligible for this experiment.

RESULTS

The differential cross sections for the elastic scattering of deuterons by tritons in the center-of-mass system of coordinates are listed in Table I. Values of the cross section multiplied by the wave number squared of the incident particle are also included. The probable errors associated with these data (also listed in Table I) vary with angle. The error in $\sigma(\beta')$ was determined by consideration of errors in pressure measurement (±1 percent), charge collection (±1 percent), temperature (±½ percent), geometry (±0.5 percent), uncertainty in measurement of tritium concentration, statistical error of each run, corrections to the data, and a consideration of the internal consistency of the data. The large error reported in data at 44.3° and 126.4° was associated with experimental difficulties which occurred in taking these data.

Figure 5 contains the results of this study in graphical form. Squares and triangles represent data obtained by counting scattered deuterons and recoil tritons, respectively, in resolved pulse-height distributions, while circles represent cross sections obtained after subtracting the expected recoil proton yield from a combined yield of recoil protons and scattered deuterons as is discussed above. The errors illustrated are probable errors. The point of the ordinate representing zero cross section for each energy is indicated on the right side of Fig. 5.

The incident deuteron energies were corrected for loss of energy in the entrance aluminum window and in the target gas. The energies are reliable to ±20 kev at all energies except the lowest two which are considered reliable to ±30 kev.

The authors are pleased to acknowledge the advice of Dr. J. H. Williams and the assistance of Dr. J. M. Blair and Mr. R. J. S. Brown, Mr. H. D. Holmgren, and Mr. J. L. Yarnell during the course of the experiment.

PHYSICAL REVIEW VOLUME 88, NUMBER 2 OCTOBER 15, 1952

The Angular Distribution of Alpha-Particles from the Reaction of Deuterons with Tritons*

T. F. Stratton and George D. Freier
Department of Physics, University of Minnesota, Minneapolis, Minnesota
(Received June 16, 1952)

The distribution, as a function of angle, of the alpha-particles produced in the reaction of deuterons on tritons has been measured using a monoergic beam of deuterons from the Minnesota electrostatic generator. The alpha-particles were detected in the angular range of 40° to 140° in the center-of-mass system of coordinates for an incident deuteron energy of 2.21 Mev in the laboratory. The center-of-mass differential reaction cross section was flat at 8 millibarns from 40° to 90° and rose to about 13 millibarns at 140°.

INTRODUCTION

INFORMATION on the production of neutrons in the reaction of deuterons on tritons is best obtained by measurements on the yield of the associated alpha-particles. The reaction has been studied at Los Alamos[1] with incident deuterons in the energy range of 1 Mev to 2.5 Mev, and over an angular interval of 45° to 90° in the laboratory system. Interest in the reaction for theoretical considerations and as a possible source of fast monoergic neutrons caused an attempt to be made to extend the measurements on the alpha-particle yield to a wider angular range. The availability of an apparatus which allowed measurements in the angular range of 26.8° to 120° in the laboratory system of coordinates made such an investigation possible. Only one energy of incident deuterons was used, this being 2.21 Mev.

EQUIPMENT

A collimated beam of monoergic deuterons produced by the electrostatic generator was allowed to pass through a small volume scattering chamber filled with hydrogen and tritium gas. The alpha-particles produced in the reaction were detected as a function of angle by a movable proportional counter. The chamber and associated current and pressure measuring instruments have been discussed before.[2,3] The tritium handling system was discussed in the previous article.[4]

* This program assisted by the joint program of the ONR and AEC.

[1] Hanson, Taschek, and Williams, Revs. Modern Phys. **21**, 635 (1949).

[2] Claassen, Brown, Freier, and Stratton, Phys. Rev. **82**, 589 (1951).

[3] Brown, Freier, Holmgren, Stratton, and Yarnell, Phys. Rev. **88**, 253 (1952).

[4] Stratton, Freier, Keepin, Rankin, and Stratton, Phys. Rev. **88**, 257 (1952).

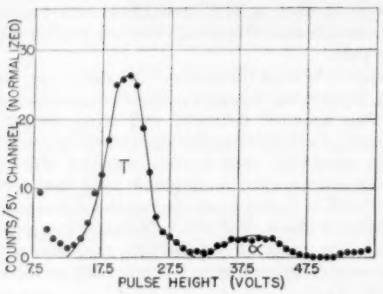

FIG. 1. Pulse-height distribution observed at 49.8°. The yields are plotted normalized per mm Hg and per microcoulomb of charge collected. The abscissa is in volts. Particle groups are recoil tritons and alpha-particles. The counter window was 0.18 mil Al.

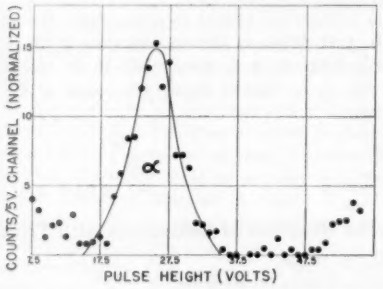

FIG. 2. Pulse-height distribution observed at 100°. All particles except the alpha-particles have been stopped in the counter window (0.5 mil Al).

METHOD

At low angles, the scattered deuterons and recoil protons and tritons had sufficient velocity so that the pulse heights associated with them were much smaller than those coming from the alpha-particles. It was no problem to separate and identify the latter. As the angle of detection was increased, the pulse height from the scattered particles became larger as the particles became slower. The alpha-particles also became slower, and produced larger pulses, but because of the large Q value associated with the reaction, the percentage change was not so great. When the angle of observation was increased to 70° (laboratory), the alpha-particles produced pulse-height distributions in the proportional counter which could not be separated from the pulses of the scattered deuterons. At this point it was possible to adjust the stopping power of the counter window to transmit only the more energetic alphas. Examples of the pulse-height distributions mentioned above are shown in Figs. 1 and 2. Figure 1 is for the counter fitted with a thin window (0.18 mil Al), and Fig. 2 is with a thick window (0.5 mil Al).

The use of a thin window made it possible to obtain a measured value for the concentration of hydrogen contaminant in the tritium sample. The method by which this was done was described in detail in reference 4. Since no concentration measurements could be made while the thick window was in place, the percentage of tritium in the gas sample was measured immediately before the thicker window was substituted for the thin window and immediately after the thin window was replaced. A careful account had been kept throughout the course of the deuteron-tritium scattering experiment[4] of the percentage of hydrogen contaminant as a function of the number of times the tritium sample had been cycled through the uranium. The percentage of tritium in the total gas sample was a monotonically decreasing function of the number of cyclings and averaged very close to 1 percent less tritium per cycling. The data taken with the thicker window required only four cyclings of the gas, so there should have been a 4 percent decrease in the tritium concentration. The measurements before and after inserting the 0.5-mil Al window showed only a 2 percent decrease. Similar fluctuations had been observed before, and it appeared that our concentration estimates could be in error by as much as 2 percent.

At least two measurements were taken at each angle. The statistical error on the large angle data amounted to as much as 5 percent because the chamber geometry was not designed for the measurement of the yields associated with cross sections as small as 10 millibarns.

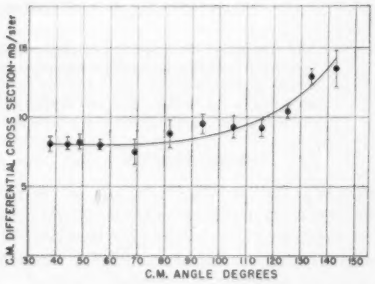

TABLE I.

$\theta_{c.m.}$°	38.0	44.6	48.7	56.1	69.0	81.9	93.9	105.1	115.5	125.1	133.9	143.0
$\sigma_{c.m.}(\theta)$ mb/sterad	8.1	8.1	8.2	8.0	7.5	8.8	9.5	9.2	9.2	10.4	12.9	13.5
$\pm\Delta\sigma_{c.m.}(\theta)$ mb/sterad	0.6	0.4	0.5	0.4	0.9	1.0	0.7	0.8	0.6	0.5	0.6	1.3

FIG. 3 and Table I.

Differential cross section per unit solid angle for the production of alpha-particles from the reaction $T(d, \alpha)n$, as a function of the center-of-mass angle. The deuteron energy was 2.21 Mev. The indicated errors are composite estimates from all causes.

RESULTS

The data have not been subjected to any corrections. The error estimated for the measurement of the beam current was 1 percent. The geometry measurement was good to ½ percent. The concentration of tritium molecules in the gas sample could be estimated to 2 percent. In other experiments using the chamber, 3 percent to 5 percent corrections were necessary to correct the test p-p and p-He^4 scattering data to agree with published results. It was not felt that any correction could be made with confidence on the reaction data. For these reasons an estimated error of ± 8 percent is attached to the results.

Figure 3 and Table I show the cross sections for the production of alpha-particles as a function of alpha-particle angle in the center-of-mass system of coordinates. The indicated errors are, in the main, determined by the average deviation from the mean of the several runs at a given angle. The results are in general agreement with the Los Alamos data but do not seem to indicate so strong a tendency for the alpha-particle to come off in the forward direction.

We wish to thank Professor J. H. Williams for suggesting this problem and for his interest and advice during the experiment. We also wish to thank the members of the electrostatic generator group for their cooperation in obtaining these data.

PHYSICAL REVIEW VOLUME 88, NUMBER 2 OCTOBER 15, 1952

Nuclear Spectroscopy of Ba^{131}

M. W. Elliott, L. S. Cheng, J. R. Haskins, and J. D. Kurbatov
Physics Department, Ohio State University, Columbus, Ohio

(Received June 5, 1952)

The spectra of Ba^{131} have been investigated in permanent magnet spectrographs, a solenoidal beta-spectrometer and a thin lens gamma-spectrometer. Gamma-rays of 122, 214, 241, 370, and 494 kev have been confirmed. In the conversion electron spectrum, there is indication of the existence of three low energy gamma-rays: ~65 kev, ~43 kev, and ~108 kev. The K/L ratios, K-conversion coefficients and relative intensities have been estimated.

I. INTRODUCTION

SEVERAL studies have been made on the energies, relative intensities, conversion coefficients, and multipole orders for the gamma-rays emitted by Ba^{131}.[1-6] Gamma-rays with energies of 122, 196, 206, 213, 241, 371, and 496 have been reported,[5,6] but there is disagreement as to their relative intensities and as to which of those around 200 kev are present. This investigation has therefore been undertaken to check and extend the results which have to date been presented.

II. APPARATUS AND PROCEDURE

Permanent magnet semicircular spectrographs, a solenoidal beta-spectrometer and a thin lens gamma-spectrometer were employed for the studies of the conversion electron spectrum and the photoelectron spectrum of Ba^{131}. The two spectrographs (low and high energy) were calibrated with I^{131}. Resolution of about 1 percent can be expected for gamma-rays of 100 kev or higher. The solenoidal spectrometer, which was used to study the conversion electrons, was equipped with a thin-window counter tube which transmitted electrons down to 17 kev. From 17 kev to 45 kev window correction was carried out on the peak height of conversion electrons. The instrument was calibrated with I^{131} and Cs^{137}. Its resolution setting was 1.5 percent. The thin lens spectrometer was used to study the photoelectron spectrum. It was calibrated with I^{131} diluted with common barium such that the geometries of the two samples, Ba^{131} and I^{131} plus Ba, were made substantially identical. The resolution setting was 2.5 percent.

The activity in the form of barium nitrate, pile activated, was obtained from Oak Ridge National Laboratory. Three samples were made. The one for the spectrographs was prepared by placing Ba^{131} on cellulose tape. Because of the low specific activity, a thick sample was required. The sample for the conversion electron spectrum was approximately 8 mm in diameter and 8 mg/cm² thick. It was covered with 0.2 mg/cm² zapon film. The sample for the photoelectron spectrum was large, having a cylindrical volume of about 1.8 cc and a diameter of 1.7 cm.

The conversion electron spectrum was measured several times so that decay would discriminate the peaks belonging to different radioactive isotopes of barium.

The photoelectron spectrum was measured with a 30 mg/cm² lead radiator and with a 21 mg/cm² ura-

[1] Yu, Gideon, and Kurbatov, Phys. Rev. **71**, 382 (1947).
[2] S. Katcoff, Phys. Rev. **72**, 1160 (1947).
[3] Dale, Rickert, Redfield, and Kurbatov, Phys. Rev. **80**, 763 (1950).
[4] Zimmermann, Dale, Thomas, and Kurbatov, Phys. Rev. **80**, 908 (1950).
[5] E. Kondaiah, Ark. fys. **2**, 295 (1950).
[6] R. Canada and A. B. Mitchell, Phys. Rev. **83**, 76 (1951).

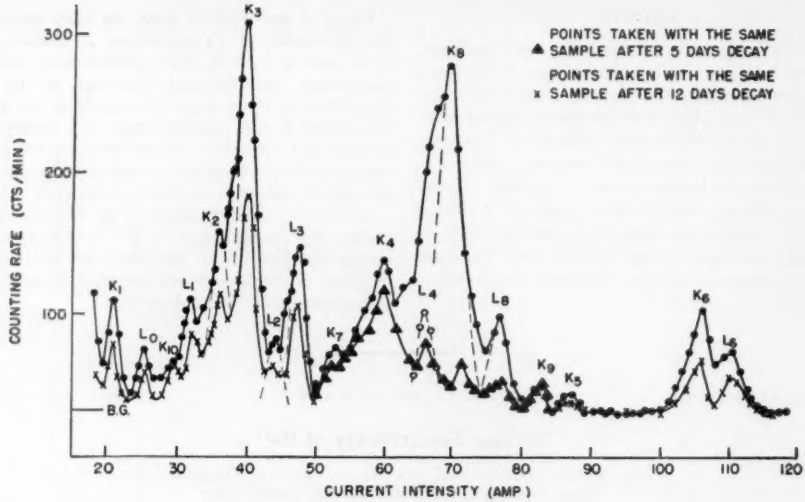
POINTS TAKEN WITH THE SAME
▲ SAMPLE AFTER 5 DAYS DECAY
POINTS TAKEN WITH THE SAME
x SAMPLE AFTER 12 DAYS DECAY
COUNTING RATE (CTS/MIN)
CURRENT INTENSITY (AMP)
B.G.

FIG. 1. Conversion electron spectrum of $Ba^{131, 133, 135}$.

nium radiator. The two radiators were used so that peaks possibly superimposed using one might be separated using the other.

III. CONVERSION ELECTRON SPECTRUM

Figure 1 shows the plot of counting rate against current, for the conversion electrons. The lower curve lying between 50 amp and 85 amp was obtained 5 days after the upper curve. It reveals, in addition to the K- and L-conversion electron peaks of the 214-kev gamma-ray of Ba^{131} (K_4 and L_4 in Fig. 1), the 270-kev gamma-ray emitted by 29 hr Ba^{135m} (K_8 and L_8)[7] and the 340-kev gamma-ray emitted by long-lived Ba^{133} (K_9).[8] The peaks K_4 and L_4 decay with half-life of about 12 days.

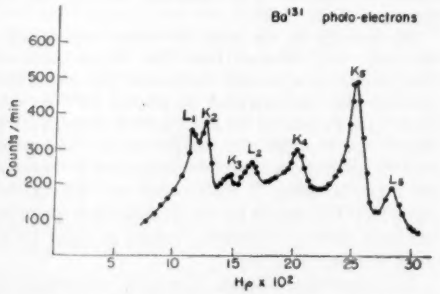

FIG. 2. Photoelectron spectrum Ba^{131} with 30 mg/cm² Pb radiator. Spectrometer set for 3.4 percent resolution.

[7] R. D. Hill and F. R. Metzger, Phys. Rev. **83**, 455 (1951).
[8] F. C. Yu and J. D. Kurbatov, Phys. Rev. **74**, 34 (1948).

A small impurity (K_7) with a half-life of approximately 3 days, and having conversion electrons with kinetic energy of about 142 kev, cannot be identified.

The lower curve between 19 amp and 50 amp was measured 12 days after the upper curve. All peaks, except the peak K_{10}, decay with a half-life of about 12 days, so they are assigned to Ba^{131}. The peaks K_3 and L_3 belong to the highly converted 122-kev gamma-ray of Ba^{131}. In addition there is indicated the existence of three low energy gamma-rays: ~65 kev (K_1 and L_1), ~43 kev (L_0) and ~108 kev (K_2 and L_2). The peak K_{10} was first revealed in the second run and remained practically of the same intensity in the subsequent runs. It may be identified as the 85-kev gamma-ray emitted by long-lived Ba^{133}.[8]

The lower curve between 85 amp and 120 amp was measured 12 days after the upper curve. The three peaks showed about 12 days half-life. The peaks K_6 and L_6 are the K- and L-conversion peaks of the 494-kev gamma-ray. The peak K_5 is the K-conversion peak of the 370-kev gamma-ray.

Conversion electrons for the following energies of gamma-rays were observed in the permanent magnet spectrographs: K- and L-conversion lines for 122 kev, K- and L-lines for 214 kev, K-line for 241 kev, K- and L-lines for 370, and K-line for 494 kev.

The K/L ratios have been estimated by comparing the areas under K- and L-peaks in a plot of counting rate per unit momentum against momentum. Source thickness correction was applied as the result of data obtained from the conversion peaks of thin (carrier-free) and thick (common cerium added to ~10 mg/cm²) Ce^{144} samples.

TABLE I. Gamma-rays emitted by Ba^{131}.

Conversion electrons: Solenoidal spectrometer		Conversion electrons: Permanent magnet spectrograph		Photoelectrons: Thin lens spectrometer, Lead radiator		Photoelectrons: Thin lens spectrometer, Uranium radiator					Multipole order	
Energy of gamma-ray (kev)	Peak obs.	Energy of gamma-ray (kev)	Peak obs.	Energy of gamma-ray (kev)	Peak obs.	Energy of gamma-ray (kev)	Peak obs.	K/L	α_K	Relative intensity	by K/L	by α_K
~43	L											
~65	K, L							~3.5			$E1$	
~108	K, L							~7			$M1$	
124±1	K, L	122±1	K, L	122±1	L	122±1	L	6.0±0.5			$M2$	
214±2.5	K, L	214±2.5	K, L	214±2	K, L	216±2	K, L	2.8±0.4	~0.18	0.10	$E2$	$E2$
		244±2.5	K	244±3	K	239±3	K			0.04		
368±4	K	370±4	K, L	370±4	K	372±4	K		~0.010	0.07		$E1$
491±5	K, L	496±5	K	496±5	K, L	494±5	K, L	2.5±0.8	~0.0045	1.00	$E3$	$E2$

IV. PHOTOELECTRON SPECTRA

Figure 2 shows the photoelectron peaks obtained using a 30 mg/cm² lead radiator. The peaks are: the L photopeak of the 122-kev gamma-ray (L_1 in Fig. 2), the K- and L-peaks of the 214-kev gamma-ray (K_2 and L_2), the K-peak of the 241-kev gamma-ray (K_3), the K-peak of the 370-kev gamma-ray (K_4) and the K- and L-peaks of the 494-kev gamma-ray (K_5 and L_5). No K- or L-peak for the reported 196-kev gamma-ray[6] was observed. Its K-peak, however, would be super-imposed with the L-peak of the 122-kev gamma-ray when a lead radiator is used. When a uranium radiator is used, the K-peak of a 196-kev gamma-ray would be sufficiently separated from other peaks to be resolved.

Figure 3 shows the photoelectron spectrum obtained using a 21 mg/cm² uranium radiator. The photopeaks observed are: the L-peak of the 122-kev gamma-ray (L_1 in Fig. 3) superimposed on the K-peak of the 214-kev gamma-ray (K_2), the L-peak of the 214-kev gamma-ray (L_2), the K-peak of the 241-kev gamma-ray (K_3), the K-peak of the 370-kev gamma-ray (K_4), and the K- and L-peaks of the 494-kev gamma-ray (K_5 and L_5).

K-electron internal conversion coefficients have been estimated by comparison with data obtained from an I^{131} sample diluted with common barium to approximately the same geometry as the Ba^{131} photoelectron sample. The 364-kev gamma-ray with $\alpha_K=0.02$ was used as a standard for this comparison.

Relative intensities were also estimated. Photoelectron efficiency corrections were made using Gray's formula.[9]

V. SUMMARY

The results are summarized in Table I. Gamma-rays of 43, 65, 108, 122, 214, 241, 370, and 494 kev have been assigned to Ba^{131}, although it is noted that the three lowest energy gamma-rays were observed only by conversion electrons in the solenoidal spectrometer and thus evidence for their existence or correct energy is not conclusive.

[9] L. H. Gray, Proc. Cambridge Phil. Soc. 27, 103 (1931).

The K-conversion coefficient for the 122-kev gamma-ray was not estimated, nor was its relative intensity, since the thickness of the counter tube in the thin lens spectrometer precluded observation of the K-photoelectron peak for this gamma-ray. The L-photoelectron peak and the conversion peaks of the 122-kev gamma-ray indicate that it is highly converted.

The multipole assignments were made using the empirical curves for K/L ratio of Goldhaber and Sunyar[10]

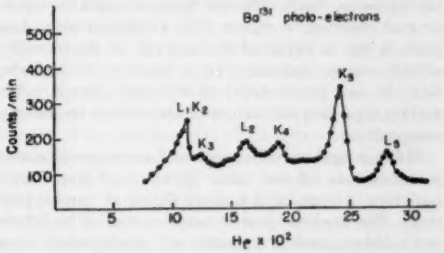

FIG. 3. Photoelectron spectrum Ba^{131}. 0.5-mil uranium radiator. Spectrometer resolution set for 2.4 percent.

and the tables of K-conversion coefficients of Rose *et al.*[11] The multipole orders assigned by these two methods are in conflict for the 494-kev gamma-ray. (An explanation of this discrepancy has not been found by review of experimental work. Further investigation to resolve this conflict is not anticipated unless an enriched isotope becomes available.)

This work was supported in part from funds granted to The Ohio State University by the Research Foundation for aid in fundamental research.

The authors appreciate a grant from The Ohio State University Development Fund for purchase of instruments.

[10] M. Goldhaber and A. W. Sunyar, Phys. Rev. 83, 906 (1951).
[11] Rose, Goertzel, and Perry, Oak Ridge National Laboratory Report No. 1023 (1951) [unpublished].

Intensity of the Soft and Hard Component of the Cosmic Radiation as a Function of Altitude at Geomagnetic Latitudes of 28°N, 41°N, and 55°N*

MARCELLO L. VIDALE†
Department of Physics, University of Chicago, Chicago, Illinois
(Received August 6, 1951)

Counter telescopes have been flown with plastic balloons to a maximum altitude of 94,000 ft. Intensity *vs* pressure curves have been obtained at geomagnetic latitudes of $\lambda=55°$, 41°, and 28° for the total cosmic radiation and for the components capable of traversing several thicknesses of lead. The energy spectrum of primary cosmic-ray particles has been derived from the extrapolation of the intensity of the total radiation to the top of the atmosphere. The integral momentum spectrum of the total primary radiation is given by $N(>pc/Ze)=0.49(pc/Ze)^{-1.0}$. The results show that the radiation originating from primaries in the energy range 1 to 4 Bev (cut-off energies at $\lambda=55°$ and 41°) is predominantly of a nucleonic nature. The absence of an appreciable electronic component can be explained by assuming that, close to the top of the atmosphere, electrons originate predominantly from the decay of neutral mesons and that, within this energy range, the over-all probability of nucleon emission is greater than that of meson production. In sharp contrast, the soft component originating from primaries in the range from 4 to 8 Bev (cut-off at $\lambda=41°$ and 28°) multiplies rapidly in the atmosphere. This large transition effect in air with a maximum at about 10 cm Hg pressure is very characteristic of electron showers. It is concluded that the probability of neutral mesons being produced is comparatively high at primary energies between 4 and 8 Bev. At energies higher than 8 Bev this effect is even more pronounced, due to the contribution of the plural and multiple production of mesons.

I. INTRODUCTION

SEVERAL experiments have been performed in an attempt to gain a better understanding of nuclear events leading to the production of mesons and secondary nucleons. Since different types of particles are in general absorbed in matter with a different mean free path, it can be expected that a study of the intensity of the cosmic radiation as a function of altitude, latitude, and penetrability in lead will provide information regarding the nature of the various cosmic-ray components.

Millikan and his collaborators[1] have made extensive measurements of the total intensity of the cosmic radiation in a series of balloon flights at various latitudes. The hard component has been studied by Schein and collaborators[2] in a number of investigations using counter telescopes with lead absorbers of several thicknesses interposed between the counters. Experiments of a similar nature have been performed by other workers[3–7] during the past few years. In view of many recent improvements in balloon techniques which permit the study of the cosmic radiation up to a pressure equivalent to less than 15 g/cm² of air, it was considered advisable to conduct a further series of flights using counter telescopes of similar geometry so as to obtain results which are directly comparable. In these flights the total, soft, and hard components were measured simultaneously using a technique previously reported by M. Schein at the Pasadena Conference of Cosmic Radiation.[8] This technique permits the comparison of the various components of the cosmic radiation under identical atmospheric conditions. Furthermore, time variations in the intensity of the cosmic radiation due to solar activity and other sources can be recognized by the fact that the variations are not the same for the various components.

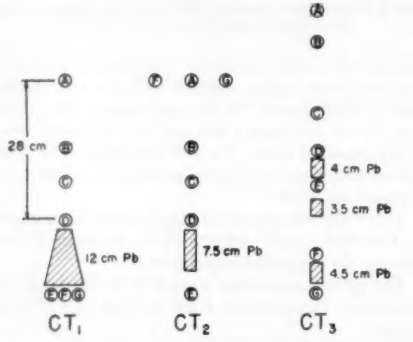

FIG. 1. Counter telescopes used for the measurement of the intensity of the cosmic-ray components.

II. BALLOON FLIGHT TECHNIQUES

The apparatus, consisting of the counters, coincidence circuits, power packs, and recording unit was mounted inside a light Dow-metal frame covered with pyraline, a transparent plastic very opaque to infrared radiation. Bands of aluminum foil around the gondola reflected the proper amount of solar radiation to maintain the equipment close to room temperature. During the flight a record was kept of the temperature inside the gondola, which showed that in most cases the temperature averaged 20°C.

* Assisted by the joint program of the ONR and AEC.
† Now at Princeton University, Princeton, New Jersey.
[1] Millikan, Neher, and Pickering, Phys. Rev. **61**, 396 (1942).
[2] Schein, Jesse, and Wollan, Phys. Rev. **59**, 615 (1941).
[3] M. Pomerantz, Phys. Rev. **75**, 69 (1949).
[4] Winckler, Stix, Dwight, and Sabin, Phys. Rev. **79**, 656 (1950).
[5] M. Vidale and M. Schein, Phys. Rev. **81**, 1065 (1951); Nuovo cimento **VIII**, 10 (1951).
[6] Rao, Balasubrahmanyam, Gokhale, and Pereira, Phys. Rev. **83**, 173 (1951).
[7] J. D. Pullar and E. G. Dymond, Phil. Mag. **42**, 663 (1951).
[8] See J. R. Oppenheimer, Revs. Modern Phys. **21**, 181 (1949).

TABLE I. Summary of flight data.

Flight number	Type of equipment	Date	Geom. lat.	Duration of flight (hours)	Rate of ascent (ft/min)	Maximum cm Hg pressure	Altitude ft
I	Counter telescope CT_1	Nov. 15, 1949	28°	8½	670	1.1	94,000
II	Counter telescope CT_1	June 6, 1950	55°	10½	330 to 60,000 ft 160 above 60,000 ft	1.6	86,000
III	Counter telescope CT_2	Aug. 4, 1950	55°	8½	710	1.2	93,000
IV	Counter telescope CT_3	Jan. 13, 1951	41°	6	120	4.0	66,000
V	Counter telescope CT_3	Feb. 4, 1951	41°	6½	450	1.7	84,000

Each apparatus was tested inside a large tank which was evacuated down to a pressure of 0.5 cm Hg, a pressure lower than the lowest pressure reached in any of the balloon flights. This was done in order to check the performance of the circuits under conditions similar to those found in the stratosphere and, in particular, to guarantee that corona discharges could not occur across the high voltages required for the operation of the Geiger counters.

The counter equipment used in these investigations was flown with plastic, constant level balloons manufactured by the General Mills Company. The cosmic-ray equipment was released from the balloon at a predetermined time and dropped to the ground by parachute. The apparatus was promptly recovered in every case. The essential characteristics of each flight are summarized in Table I.

In every flight, pressure readings were obtained by two or more independent methods. The pressure device consisted of the following:

(1) Barograph with temperature-compensated elements.

(2) Radiosonde or Olland cycle type barometer which transmitted pressure data to the ground station.

(3) In flights IV and V (see Table I) two mercury U-tubes were photographed at 10-minute intervals. The U-tubes gave very accurate (~0.3 mm Hg) altitude data for pressures lower than 12 cm Hg.

III. DESCRIPTION OF THE APPARATUS

The counter telescopes used for the measurement of the vertical intensity of the cosmic radiation are shown in Fig. 1. Each apparatus contained several vertical telescopes of Geiger-Müller counters arranged to detect fourfold coincidences. CT_1 and CT_2 (see Fig. 1) recorded coincidences of the type *ABCD*, *BCDE*, *BCDF*, and *BCDG*, and CT_3 recorded coincidences *ABCD*, *BCDE*, *CDEF*, and *DEFG*.

All Geiger-Müller counters were 2.4 cm in diameter and had an active length of 12.5 cm. The distance between the centers of the two extreme counters in each of the fourfold vertical telescopes was the same and amounted to 28 cm. Assuming that all particles are incident on the equipment isotropically, the correction to be applied to the measured vertical cosmic-ray intensity due to the finite dimensions of the counter telescopes can be shown to amount to less than 2 percent. The effect on solid angle calculations of particles giving rise to secondaries in the lead blocks interposed between the counters will be discussed in Sec. VI. The wall thickness of the brass counters used was 0.08 cm. Hence, in order to produce a fourfold coincidence, an incident particle, depending on its direction, had to penetrate a minimum of 5 to 7 g/cm² of brass.

Each fourfold coincidence caused the flash of a neon bulb which was separately recorded as a narrow line on a photographic film. Corrections arising from the finite resolving time of the recorder are quite negligible except in the measurement of the intensity of the total component at high latitude; however, they are taken into account for all cases.

The length of the coincidence pulses of the circuits used in the equipment was 20 microseconds. Due to the fact that only fourfold coincidences were recorded, the number of accidentals was reduced to a negligible fraction of the counting rate of the telescopes. The dead time of the counters following each discharge was determined in the laboratory under conditions similar to those found in the stratosphere by placing a radium source at a certain distance from the counters. The dead time reduces the fourfold counting rate by 5 percent at a single counter counting rate of 60 counts/sec.

The individual counter telescopes were accurately tested on the ground before each balloon flight. Since the telescopes which were designed to have the same

TABLE II. Counting rate of telescopes at $\lambda = 55°$.

55° geomagnetic latitude					
Pressure (cm Hg)	0 cm Pb absorber (counts/min)	Pressure (cm Hg)	7.5 cm Pb absorber (counts/min)	Pressure (cm Hg)	12 cm Pb absorber (counts/min)
1.2	20.7 ±0.2	1.2	12.0 ±0.2	1.6	10.3 ±0.3
2.5	22.2 ±0.5	2.7	12.8 ±0.7	2.2	10.1 ±0.3
3.8	24.4 ±0.8	7.4	10.7 ±0.6	3.4	10.6 ±0.5
5.0	26.2 ±1.0	17.0	4.8 ±0.6	4.8	10.7 ±0.7
6.5	25.7 ±1.0	28.0	2.4 ±0.8	5.8	9.9 ±0.8
8.5	22.2 ±0.8	76.0	0.57±0.02	7.5	9.1 ±1.0
11.0	21.3 ±0.9			9.5	8.4 ±0.7
14.6	16.7 ±0.9			12.2	6.9 ±0.7
20.8	13.1 ±0.8			16.2	5.2 ±0.7
28.2	6.4 ±0.5			21.8	2.7 ±0.5
36.0	4.3 ±0.4			27.1	2.5 ±0.4
76.0	0.70±0.02			33.6	1.9 ±0.4
				76.0	0.53±0.02

TABLE III. Counting rate of telescopes at $\lambda = 41°$ and 28°.

41° geomagnetic latitude					28° geomagnetic latitude			
Pressure (cm Hg)	0 cm Pb absorber) (counts/min)	4 cm Pb absorber (counts/min)	7.5 cm Pb absorber (counts/min)	12 cm Pb absorber (counts/min)	Pressure (cm Hg)	0 cm Pb absorber (counts/min)	12 cm Pb absorber (counts/min)	
1.9	9.2 ±0.3	7.5 ±0.2	5.6 ±0.2	4.8 ±0.2	1.2	5.0±0.1	3.6±0.1	
5.0	13.4 ±0.5	9.1 ±0.4	6.8 ±0.3	5.4 ±0.3	2.2	5.7±0.4	3.6±0.3	
8.6	15.4 ±0.5	8.3 ±0.3	6.3 ±0.3	5.4 ±0.3	6.1	8.8±0.5	4.3±0.3	
13.9	13.6 ±0.6	7.2 ±0.4	5.1 ±0.4	3.7 ±0.3	12.6	9.4±0.9	4.1±0.6	
20.6	11.1 ±0.4	5.3 ±0.3	3.6 ±0.2	3.3 ±0.2	17.3	6.0±0.5	3.8±0.5	
23.0	8.2 ±0.6	4.6 ±0.5	3.5 ±0.5	2.5 ±0.4	25.0	5.6±0.6	2.1±0.4	
38.0	3.2 ±0.2	2.3 ±0.2	1.8 ±0.2	1.8 ±0.2	35.0	2.3±0.5	1.5±0.3	
65.3	0.88±0.03	0.79±0.03	0.66±0.03	0.62±0.03				

geometry gave the same counting rate within a statistical error of 3 percent, it has to be concluded that the individual counters were lined up correctly within the precision of the experiment. Tests were also made to guarantee that the lead blocks covered completely the active area of the counters.

IV. EXPERIMENTAL RESULTS

In a series of balloon flights (see Table I) at $\lambda = 55°$, 41°, and 28° N, the intensity of the various cosmic-ray components was measured as a function of altitude using counter telescopes with varying amounts of lead interposed between the counters. In most of the flights the rate of rise of the balloon was sufficiently low to give statistically significant data for the dependence of cosmic-ray intensity on altitude. As a consequence, these series of flights had considerable advantages over those of previous investigators in studying cosmic-ray components of low intensity and in considering differences between counting rates of various components at one particular altitude.

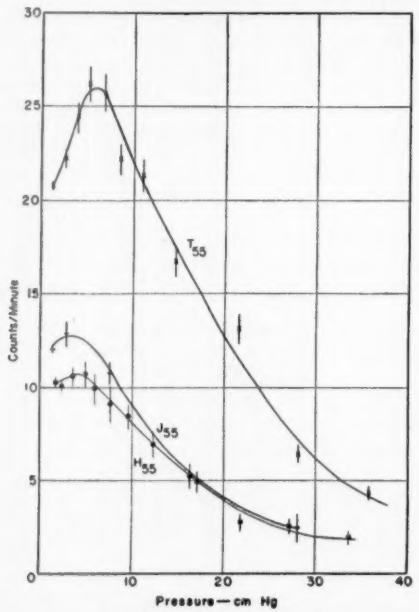

FIG. 2. Altitude dependence of the intensity of the cosmic radiation at $\lambda = 55°$ as measured through 0 cm of lead (T_{55}), 7.5 cm of lead (J_{55}), and 12 cm of lead (H_{55}).

Tables II and III give the counting rate of the fourfold coincidences[9] in telescopes CT_1, CT_2, and CT_3 (see Fig. 1) at $\lambda = 55°$, 41°, and 28°. Each value has been corrected for accidental coincidences, dead time losses, and losses due to the resolving time of the recording unit as discussed in Sec. III. The error given for each experimental point represents the standard statistical error obtained from the square root of the number of counts in the individual telescopes.

Curves T_{55}, T_{41}, and T_{28} in Figs. 2, 3, and 4 are plots of the total vertical intensity of the cosmic radiation at the three latitudes of $\lambda = 55°$, 41°, and 28°, respectively. For comparison these curves are presented together in Fig. 5. All three curves show a pronounced maximum which occurs at an increasing altitude at higher latitudes.

Curves H_{55}, H_{41}, and H_{28} in Figs. 2, 3, and 4 represent the vertical intensity of the penetrating component of the cosmic radiation capable of traversing 12 cm of lead. For comparison these three curves are given in Fig. 6. It can be seen that the intensity of the penetrating component increases up to a pressure of 5, 7, and 9 cm Hg at $\lambda = 55°$, 41°, and 28°, respectively. At these pressures the three curves show relatively flat maxima.

The vertical intensity through 4 and 7.5 cm of lead was measured in order to obtain intermediate points between the total and the hard component. The intensity of the cosmic radiation through 4 cm of lead was obtained at $\lambda = 41°$ (curve I_{41} in Fig. 3) and through 7.5 cm of lead at $\lambda = 55°$ and 41° (curves J_{55} and J_{41} in Figs. 2 and 3).

The intensity *vs* altitude curves obtained at $\lambda = 55°$ (Fig. 2) do not extrapolate to a common point at the top of the atmosphere. At $\lambda = 41°$ and 28° (Figs. 3 and 4) a similar effect seems to exist; however, it is less pro-

[9] Re-evaluation of the pressure data in flight *II* at $\lambda = 55°$ has indicated a small discrepancy in the time *vs* altitude curve between 0 and 45,000 ft. (This change results in a shift toward higher pressures of the intensity measurements reported in reference 5.)

nounced because of the better collimation of penetrating secondaries in the forward direction due to the considerably higher cut-off energy of the primary radiation. At $\lambda=55°$ the difference in the extrapolated intensity of the total and the hard component through 12 cm of lead amounts to approximately 50 percent, as compared to about 30 percent at $\lambda=41°$ and to about 15 percent at $\lambda=28°$. This effect can be understood by noting that primary cosmic-ray particles incident on the equipment at these latitudes interact with nuclei of the lead absorber. These interactions, which are known to occur with a collision cross section approximately equal to the geometrical area of the lead nucleus, lead to the emission of secondary particles which in turn can be absorbed or scattered out of the counter telescope. At low latitudes, where the primary particles have a higher average energy, this effect is considerably smaller, as secondary particles which are produced in 12 cm of lead and which are emitted forward have often sufficient energy to traverse the remaining amount of lead and trigger the lower counter of the telescope. The effect of the presence of the lead absorber on the geometry of the counter telescope will be discussed in Sec. VI.

The latitude effect (intensity at $\lambda=55°$ or 41°/intensity at $\lambda=28°$) of the total and hard components of the cosmic radiation at $\lambda=55°$ and 41° is given in Table IV for a few selected altitudes in the atmosphere. One can see that at all altitudes the total radiation shows a larger latitude effect than the hard component. For both components, the latitude effect reaches its highest value at the top of the atmosphere.

From Figs. 2, 3, and 4 one can obtain the difference curves representing the contribution to the intensity of the cosmic radiation of primaries in the energy range 1 to 4 Bev (cut-off energy from the vertical at $\lambda=55°$ and 41°), 4 to 8 Bev (cut-off at $\lambda=51°$ and 28°) and >8 Bev (cut-off at $\lambda=28°$). Curves H_{55-41} and S_{55-41} in Fig. 7 represent, respectively, the intensity of the penetrating radiation and of the radiation absorbed in 12 cm of lead originating from primaries in the energy range 1 to 4 Bev. From the absorption of these two components in air, it appears that electrons cannot be present in large numbers, as they would produce a strong transition effect close to the top of the atmosphere and would not contribute to the penetrating component. μ-mesons would be absorbed in air less rapidly than indicated by H_{55-41}. Hence, it is concluded that primary and secondary nucleons are mainly responsible for the two components represented by these curves.

Curves H_{41-28} and S_{41-28} in Fig. 7 represent the penetrating component and the component absorbed in 12 cm of lead originating from primaries in the energy range between 4 and 8 Bev. The large increase by a factor of 2 in the intensity of the soft component between the atmospheric pressure of 1.5 and 12 cm Hg is strong evidence that primaries in the energy range 4 to 8 Bev give rise to electronic cascades in the atmosphere. This effect can be explained by assuming

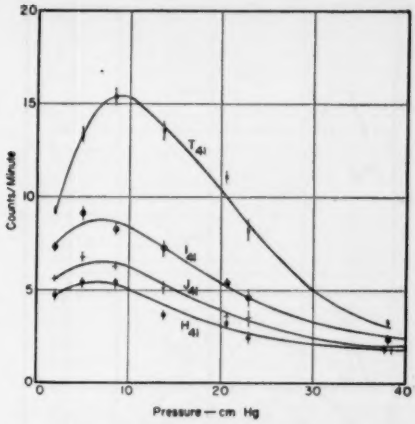

FIG. 3. Altitude dependence of the intensity of the cosmic radiation at $\lambda=41°$ as measured through 0 cm of lead (T_{41}), 4 cm of lead (I_{41}), 7.5 cm of lead (J_{41}), and 12 cm of lead (H_{41}).

that, as the result of the decay of neutral mesons into two γ-rays, electron showers of moderate multiplicity are initiated in air.[10] The very low intensity of the penetrating component is apparently due to the fact that charged π-mesons produced in the primary interaction decay into μ-mesons with a short mean life and hence do not give rise to subsequent nucleonic cascades.

Curves H_{28} and S_{28} in Fig. 7 represent, respectively, the penetrating component and the component stopped in 12 cm of lead originating from primaries of energy greater than 8 Bev. Both components show a marked transition effect with a maximum intensity at approximately 9 cm Hg pressure. From 1.5 to 9 cm Hg pressure the soft component increases by a factor of 3.2 and the hard component by 1.2. This strong multiplication in

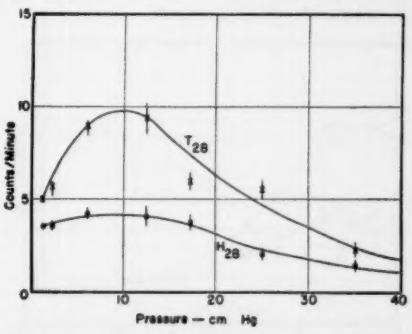

FIG. 4. Altitude dependence of the intensity of the cosmic radiation at $\lambda=28°$ as measured through 0 cm of lead (T_{28}) and 12 cm of lead (H_{28}).

[10] B. Rossi, Revs. Modern Phys. 21, 104 (1949).

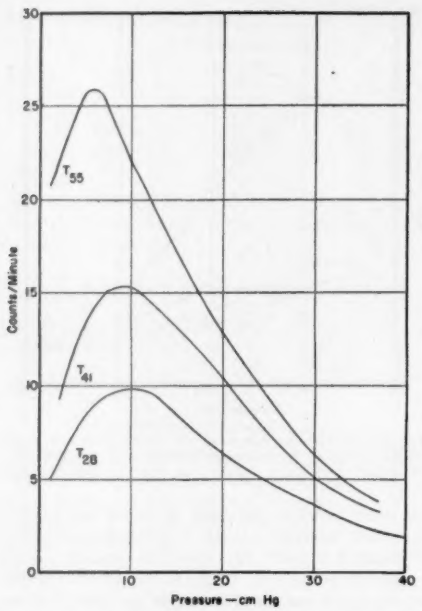

FIG. 5. Altitude dependence of the total vertical cosmic radiation at $\lambda=55°$ (T_{55}), $\lambda=41°$ (T_{41}), and $\lambda=28°$ (T_{28}).

the first few mean free paths in the atmosphere indicates that primaries having an energy greater than 8 Bev can produce, in their interactions with air nuclei, nucleonic cascades of higher multiplicity. The fact that the soft and hard components reach their maximum intensity at approximately the same atmospheric depth is an added indication that both must have a common origin, namely, those nuclear interactions which give rise to neutral and charged mesons.

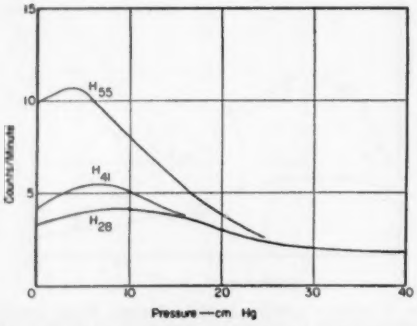

FIG. 6. Altitude dependence of the hard component of the cosmic radiation as measured through 12 cm of lead at $\lambda=55°$ (H_{55}), $\lambda=41°$ (H_{41}), and $\lambda=28°$ (H_{28}).

Figure 8 gives the absorption of the radiation in lead at $\lambda=41°$ for atmospheric pressures of 8, 2, and 0 cm Hg (curves A, B and C, respectively). The primary cosmic radiation (obtained by extrapolating curves T_{41}, I_{41}, J_{41}, and H_{41} to the top of the atmosphere, see Fig. 3) is absorbed in lead with a mean free path of 300 g/cm², approximately. From these results the following conclusions can be drawn:

(*a*) The number of primary and secondary electrons present at the top of the atmosphere is negligible (less than a few percent) since they would show a rapid absorption in lead, which is clearly not the case.

(*b*) The value obtained for the absorption mean free path of the primary radiation is approximately two times the geometrical mean free path of protons and is in good agreement with results of other investigators[11] on the absorption of high energy nucleons in lead at lower altitudes. An admixture of 10–15 percent alpha-particles is consistent with the shape of the absorption curve in Fig. 8.

(*c*) The contribution of particles originating within the apparatus and of low energy albedo nucleons from the lower atmosphere must be small since their presence

TABLE IV. Latitude effect of the total and hard components.

Pressure (cm Hg)	55° geomagnetic latitude		41° geomagnetic latitude	
	Total	Hard	Total	Hard
0.0	4.9	3.0	1.7	1.3
1.2	4.2	3.0	1.7	1.3
6.0	2.9	2.5	1.6	1.3
10.0	2.2	1.9	1.5	1.2

in appreciable numbers would tend to make the absorption curve considerably steeper.

At an atmospheric pressure of 8 cm Hg (corresponding to the maximum intensity of the total radiation at $\lambda=41°$), the large drop in the absorption curve of Fig. 8 between 0 and 4 cm of lead is typical for electrons and hence clearly shows the presence of an abundant electronic component (~30 percent) at these lower altitudes (50,000 ft).

V. INTENSITY OF THE PRIMARY RADIATION

The magnetic field of the earth determines,[12,13] as a function of latitude, the minimum energy that cosmic-ray particles must have in order to enter the atmosphere from outer space. This cut-off energy for particles incident from the vertical direction at $\lambda=55°$, 41°, and 28° is given in Table V.

The vertical flux of the radiation (number of particles/cm² sterad sec) traversing a counter telescope can be obtained by multiplying the observed counting rate (counts/sec) by a factor f which is calculated from the known geometry of the telescope. In the present

[11] T. A. Stinchcomb, Phys. Rev. **83**, 422 (1951).
[12] M. S. Vallarta, Phys. Rev. **74**, 1837 (1948).
[13] R. A. Alpher, J. Geophys. Rev. **55**, 437 (1950).

case, a standard telescope subtends a solid angle × area $f=1.06$ cm²-sterad for isotropic distribution of the incident radiation. Table VI gives the flux of the primary radiation incident on the atmosphere at $\lambda=55°$, 41°, and 28° as extrapolated from curves T_{55}, T_{41}, and T_{28} (Fig. 5) of the total radiation to the top of the atmosphere after subtraction of those events due to showers originating within the equipment (see Sec. VI).

The total primary flux can be approximated by an integral power spectrum of the following type:

$$N(>pc/Ze)=(0.49\pm0.04)(pc/Ze)^{-1.0\pm0.1}.$$

Recent measurements of the total cosmic radiation made above the atmosphere in experiments carried out in rockets[14] give a spectrum in substantial agreement with the one obtained here, though the absolute intensity is 20 percent less than here. This difference may be due to the different geometry of the telescopes and to the different disposition of the heavy material in the apparatus. It may be noted that in rocket experiments events which were due to showers originating in the equipment and were subtracted from the total counting rate in the estimate of the total primary flux represent a contribution several times larger than in the present work.

TABLE V. Geomagnetic cut-off of primary cosmic-ray particles incident from the vertical direction.

Geom. lat.	Protons Energy (Bev)	Heavy nuclei ($Z\geq2$) Energy per nucleon
55°	1.0	0.35
41°	4.0	1.5
28°	8.1	3.5

The primary spectrum can also be compared with the results obtained by Winckler *et al.*[4] using telescopes with 3 cm of lead interposed between the counter trays. However, due to the absorption in lead of a fraction of the radiation of lower energy, the results indicate that the flux given by Winckler at 55° is 15 percent lower than the flux found with counter telescopes without lead absorber.

VI. EFFECT OF SHOWERS, SCATTERING, AND GEOMETRY OF TELESCOPES

In the determination of the intensity of the cosmic radiation by means of counters, the effect of local and air showers has to be considered. In order to reduce the number of showers originating in the equipment that might discharge the coincidence arrangements, no heavy material was placed alongside or above the counters. The importance of this effect can be estimated from the number of coincidences *FBCD* and *GBCD* detected in equipment CT_2 (see Fig. 1) at $\lambda=55°$, where the highest out-of-line counting rate was found to be

[14] J. A. Van Allen and S. F. Singer, Phys. Rev. 78, 819 (1950).

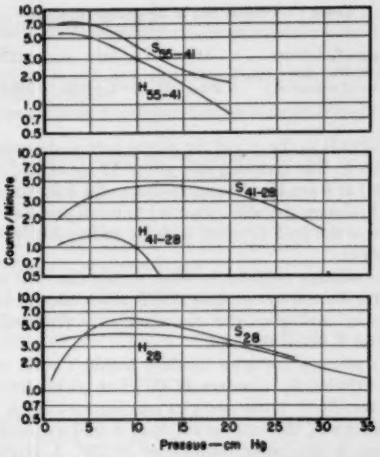

FIG. 7. Altitude dependence of the intensity of the penetrating radiation (H) and of the radiation absorbed in 12 cm of lead (S) originating from primaries in the energy range: 1 to 4 Bev (cut-off energy at $\lambda=55°$ and 41°), 4 to 8 Bev ($\lambda=41°$ and 28°) and >8 Bev ($\lambda=28°$).

7 percent of the corresponding rate for counters *ABCD*. Other investigators with similar counter arrangements have obtained values of the same magnitude.[15,16]

The location of the lead in the counter train affects the geometry of the counter telescope due to the interactions of incident particles within the absorber. These types of interactions were studied with apparatus CT_1 at $\lambda=55°$ and 28°. Let I be the extrapolated flux (number of particles per cm² per sterad per sec) of the cosmic radiation incident on telescope *BCDF* ($f=1.06$

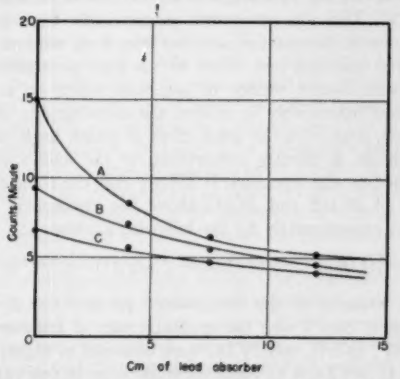

FIG. 8. Absorption of the cosmic radiation in lead at $\lambda=41°$ measured at an atmospheric pressure of: *A*, 8 cm Hg; *B*, 2 cm Hg; *C*, 0 cm Hg.

[15] T. H. Johnson and J. G. Barry, Phys. Rev. 57, 245 (1940).
[16] Schein, Wollan, and Groetzinger, Phys. Rev. 58, 1027 (1940).

TABLE VI. Primary flux of the cosmic radiation.

Geomagnetic latitude	55°	41°	28°
Total primary flux (per cm² sterad sec)	0.296±0.02	0.102±0.01	0.059±0.01

cm²-sterad) at the top of the atmosphere as determined in Sec. V. The counting rate under 12 cm of lead (132 g/cm²) at 0 cm Hg pressure is due to the following:

(a) primary particles, assumed to be all protons, that traverse the lead absorber without undergoing nuclear collisions,

(b) primary particles incident within the solid angle × area defined by counters *BCDF* which interact in the absorber and give rise to secondaries detected by counter *F* below the lead,

(c) primary particles incident within a solid angle not included by counters *BCDF*, but which traverse counters *BCD*. These particles may interact in the lead absorber and, through the action of secondary particles, register a quadruple coincidence *BCDF*. A graphical integration of their path length in lead gives, for events of this type, an effective solid angle × area $f'=2.33$ cm²-sterad.

At the top of the atmosphere the counting rate of telescope *BCDF* will be given therefore by the following expression:

$$F=1.06Ie^{-12/\lambda_{Pb}}+(1.06a+2.33a')I(1-e^{-12/\lambda_{Pb}}),$$

where λ_{Pb}(g/cm²) is the collision mean free path of protons in lead and a and a' are constants giving the probability that after collision one or more of the secondary particles traverse the bottom counter of the telescope.

The solid angle subtended by counters *BCDE* and *NCDG* (see Fig. 1) was half as wide as that of telescope *BCDF*. This was determined geometrically from the location of the counters and also from their respective ground counting rate. Since at sea level penetrating particles consist mainly of μ-mesons which do not interact appreciably in matter, the counting rate observed, neglecting the small effect of zenith angle dependence, is directly proportional to the solid angle defined by the telescope. It follows that the counting rate of *BCDE* and *BCDG* above the atmosphere is given approximately by the following expression:

$$G=\tfrac{1}{2}(1.06)Ie^{-12/\lambda_{Pb}}+(1.06a+2.33a')I(1-e^{-12/\lambda_{Pb}}).$$

The intensity of the extrapolated primary flux I is given in Sec. V and the counting rates of telescopes *BCDF*, *BCDE*, and *BCDG* were obtained in flights I and II (see Table I). Since the collision mean free path λ_{Pb} is 160 g/cm², one finds:

$$F_{55}=0.137+0.192a_{55}+0.420a_{55}'=0.163 \text{ counts/sec};$$
$$G_{55}=0.068+0.192a_{55}+0.420a_{55}'=0.102 \text{ counts/sec};$$
$$F_{28}=0.027+0.038a_{28}+0.083a_{28}'=0.055 \text{ counts/sec};$$
$$G_{28}=0.014+0.038a_{28}+0.083a_{28}'=0.035 \text{ counts/sec}.$$

Since secondary particles of high energy are known[17] to be collimated in the direction opposite to the incoming particle, it will be assumed that $a'=a/2$. From the above equations one can solve for two independent values of a at each latitude. Their average value is very approximately $a_{55}=0.075$ and $a_{28}=0.31$.

These results indicate that particles incident on the equipment from outside the solid angle defined by counters *BCDF* (and that would be affected seriously by the geometrical disposition of the absorber) contribute roughly a maximum of 10 and 25 percent at 55° and 28° geomagnetic latitude, respectively, to the observed counting rate of the hard component. Consideration of the effect of Coulomb scattering, of knock-on electrons, and of the presence of heavy nuclei in the primary radiation would decrease the value of a in the above equations and therefore also the contribution to the hard component of particles incident within the solid angle not defined by counters *BCDF*.

Apparatus CT_1 registered the counting rate of the coincidence sets *BCDE*, *BCDF*, and *BCDG* discharged simultaneously. Such events require the tripping of all the counters below the lead block so that a minimum of three penetrating particles must be involved in the process. Since the contribution of penetrating air showers and electronic side showers is found to be negligible in such high order coincidences, events of this type must be due to penetrating events of moderate energy originating in the lead. (Coincidences between counters *ABCDGH* in equipment CT_2 at $\lambda=55°$ occurred at the rate of 0.11 counts/min at a pressure of 1.2 cm Hg.) In flights I and II at 28° and 55°, the counting rate of counters *BCDFGE* was found to be 0.52 and 0.72 counts/min, respectively. The largest latitude effect for this kind of high energy events occurs at the highest altitude reached (1.6 cm Hg) and amounts to 1.5±0.3 as compared to 2.9 for the hard component and 4.1 for the total radiation.

I wish to express my sincere gratitude to Professor Marcel Schein for his guidance and encouragement during the course of this work. The cooperation of the ONR and of the staff of the General Mills Company in arranging the balloon flights and in making every effort to make these experiments successful is deeply appreciated. Thanks are due to Mr. Raymond Foster and Mr. John Bjorkland for their valuable help in the construction and operation of the equipment, and Professor G. Puppi for a very interesting discussion.

[17] Brown, Camerini, Fowler, Heitler, King, and Powell, Phil. Mag. **40**, 862 (1950).

The Range of Alpha-Particles in Water

HERVASIO G. DE CARVALHO* AND HERMAN YAGODA
National Institute of Arthritis and Metabolic Diseases of the National Institute of Health, Public Health Service, Federal Security Agency, Bethesda, Maryland
(Received May 16, 1952)

A photographic method is described for measuring the ranges of alpha-particles in liquids whose properties are compatible with emulsion sensitivity utilizing a surface deposit of radiocolloid aggregates as point sources of alpha-radiation. The method has been applied to both water of normal isotopic composition and to heavy water containing 97 percent deuterium oxide. Using polonium radiocolloids as a source of 5.3-Mev alpha-particles ranges of 38.1±0.5 and 38.0±0.5 microns were measured in the respective liquids. By conducting the exposure at temperatures below the freezing point the method is also applicable to certain solid media. The ranges of RaF alpha-particles in normal and heavy ice were found to be 41.6±0.5 and 41.5±0.5 microns. The integral molecular stopping power of water is computed to be 1.56±0.02 for an alpha-particle energy of 5.3 Mev. Similar measurements with radium sulfate radiocolloids indicates a molecular stopping power of 1.56±0.02 for the alpha-particles from RaC′, as compared with a computed value of 1.54±0.02. Larger estimates for this constant may originate from water-air interface effects inherent in experiments with an external detector.

I. INTRODUCTION

THE stopping power of water for alpha-particles is an important constant in the evaluation of their radiochemical action in aqueous solutions. Since living biological tissues are composed to a large extent of water the range of alpha-particles in this medium is of fundamental importance in the quantitative interpretation of the biological action of densely ionizing radiations, particularly with reference to the number of primary ionizations produced per micron of path, and in the determination of the rate of energy dissipation. The experimental measurements of the range of 5.30-Mev and 7.68-Mev alpha-particles in water employing essentially monoenergetic sources of RaF and RaC′, respectively, are few in number, and the experimental values are in poor agreement with both the empirical stopping power law of Bragg-Kleeman[1] and that derived from modern stopping power theory as elaborated by Livingston and Bethe,[2] Cüer,[3] and Webb.[4] The early measurements were made chiefly with the aid of scintillation screens as detectors for the residual range of the alpha-particles after traversing paths of known length in water, and are therefore of low accuracy, because the microscopic detection of scintillations produced by low energy alpha-particles is subject to a large subjective error. The tendency has been, therefore, to rely on a computed value of 71 microns for the range of RaC′ alpha-particles in tissue of unit density in radiobiological studies as those described by Lea.[5]

The first investigation of the range of alpha-radiations in water was reported by Michl[6] using thin wires coated with polonium placed in contact with photographic plates covered with water. From the geometry he derived a total range of 32 microns from the maximum width of the shadow of photographic blackening. In the course of these investigations Michl observed that "poloniumteilchen" became detached from the source and recorded individual black circular areas varying in radius between 28 to 38 microns. This phenomenon, now understood as radiocolloid aggregation, provided an alternate estimate of the range in water. Michl, however, selected 32 microns on the basis of the more reproducible shadow blackenings. Michl's methods were fundamentally sound, but the emulsions available at that early period were not of adequate sensitivity, particularly when swollen with water, for the microscopic recognition of the short tracks defining the entire path of the rays through the liquid. The few long-range tracks noted were possibly recorded shortly before development and hence escaped fading of the latent image. As seen in Sec. V his upper limit of 38 microns is identical with results of the present study.

An independent set of measurements for the range of RaC′ alpha-particles in water has been reported by Philipp.[7] Using scintillation screens as detectors of the residual range of the particles he measured a range of 59.5 microns in water, and one of 67 microns in water vapor. The measurement in liquid water is low compared with estimates of 77 microns deduced from the Bragg-Kleeman stopping power relationship, or the more reliable value of 68 microns computed with the aid of electronic stopping theory. The investigations of Rutherford[8] on the sensitivity of the scintillation method show that the flash of light is discernible microscopically when the alpha-particle has a residual range in air of 3.5 mm and that the limit of visibility is reached at a residual air range of 0.2 mm. These limits would tend

* Public Health Service Research Fellow of the National Institute of Arthritis and Metabolic Diseases. Present address: Laboratorio de Producao Mineral, Rio de Janeiro, Brazil.

[1] W. H. Bragg and R. Kleeman, Phil. Mag. (6), **10**, 318 (1905).
[2] M. S. Livingston and H. A. Bethe, Revs. Modern Phys. **9**, 263 (1937).
[3] P. Cüer, Compt. rend. **223**, 1121 (1946).
[4] J. H. Webb, Phys. Rev. **74**, 511 (1948).
[5] D. E. Lea, *Actions of Radiations on Living Cells* (Cambridge University Press, Cambridge, 1947) pp. 17 and 351.
[6] W. Michl, Sitz. Akad. Wiss. Wien **123**, 1965 (1914).
[7] K. Philipp, Z. Physik **17**, 23 (1923).
[8] Rutherford, Chadwick, and Ellis, *Radiations from Radioactive Substances* (Cambridge University Press, Cambridge, 1930), p. 547.

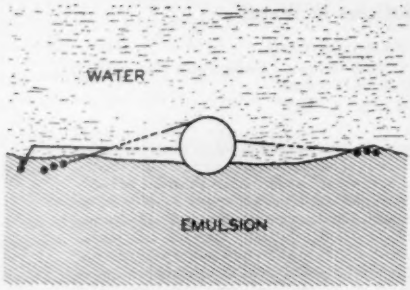

FIG. 1. Schematic representation of liquid range measurements with radiocolloid sources.

to reduce the measured range in water by about 2.3 to 0.13 microns, depending on the acuity of the observer.

The stopping power of liquid water has more recently been investigated by Appleyard[9] by measuring with a Geiger counter the effective thickness of a deep source of polonium dispersed in water acidified with hydrochloric acid. After application of geometric and counter-window corrections his measurements yield a range of 33.2 microns, and he concludes that the stopping power of liquid water is anomalous as compared with the water vapor measurements of Philipp.

The stopping power of water is also an important factor in correlating range measurements of ionizing particles in nuclear emulsions which differ in moisture content. This subject has been investigated in detail by Wilkins,[10] who concludes that the value measured by Appleyard leads to marked inconsistencies in the evaluation of the net stopping power of water-loaded emulsions. Wilkins' work indicates that ranges of 38 and 69 microns for RaF and RaC′ alpha-particles, respectively, would be in best conformity with the more recent evaluation of atomic stopping numbers for hydrogen and oxygen.

A photographic method for measuring the range of alpha-particles in water utilizing radiocolloid aggregates, described briefly by one of us,[11] gave preliminary estimates of 39 and 67 microns for the ranges of RaF and RaC′ alpha-particles in water. In view of the marked disparity between different experimental methods of liquid range measurement it is worth while to describe details of the technique and to attempt an evaluation of the factors which contribute to the spread in the values for the stopping power of water.

II. METHOD OF RANGE MEASUREMENT

The microscopic examination of nuclear type emulsions shows that the tracks of slow alpha-particles can be discriminated from the background fog when the recorded range exceeds one micron. This suggested that under proper experimental conditions it should be possible to measure the range of alpha-particles in liquids with an accuracy of about 2 percent provided adequate sensitivity could be maintained during contact of the emulsion with the liquid. In our exploratory work efforts were made to make the emulsion surface water-repellant by application of thin films of hydrophobic materials such as zinc stearate and petroleum jelly. This approach was not successful, as films impervious to water caused absorption of the greater part of the alpha-particle energy. During these experiments it was observed that occasionally a radiocolloid aggregate would separate from the polonium source and float onto the emulsion surface, and the tracks originating from it could be discerned in the wet emulsion even after traversing the greater part of their range through water. Further exploration of the method using specially prepared dispersions of polonium and radium sulfate as point sources showed that the method gave consistent results, provided the liquid wetted the emulsion, and the radiocolloids remained fixed in position during the duration of the exposure.

The principle of the method is shown diagramatically in Fig. 1 in which a radiocolloid aggregate (size greatly exaggerated, true dimension being less than 0.1 micron) is adsorbed on an emulsion surface covered with a thick layer of liquid. Alpha-particles directed normal to the plane of the emulsion and those ejected at small angles to its produce a black core of developed silver whose diffuse diameter varies with the activity of the radiocolloid, the energy of associated alpha-particles and the duration of the exposure. The center of this core defines the position of the point source. Particles ejected at near glancing incidence expend their energy almost entirely in the liquid and a small number of suitably oriented particles will define the range by

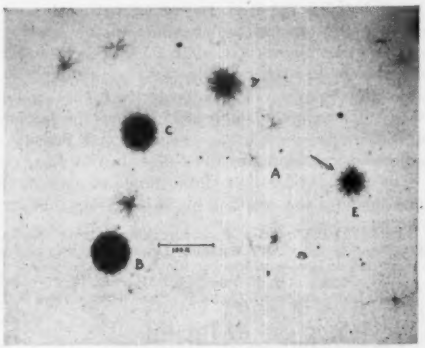

FIG. 2. Low power field of polonium radiocolloid images recorded on emulsion exposed below water.

[9] R. K. Appleyard, Nature **163**, 527 (1949); Proc. Cambridge Phil. Soc. **47**, part 2, 443 (1951).
[10] J. J. Wilkins, Atomic Energy Research Establishment Report AERE 664 (1951) (unpublished).
[11] H. G. de Carvalho, Phys. Rev. **78**, 330 (1950).

rendering several grains developable before coming to rest in the emulsion. In so far as the radiocolloids are almost dimensionless, the method is abetted by the following considerations:

1. The emulsion surface is not a true mathematical plane, but contains an appreciable number of microscopic hills and valleys. Radiocolloids deposited on high points, such as embedded dust particles, are in a favored geometrical position for the recording of the range defining tracks.

2. Alpha-particles close to the end of their range frequently exhibit large angle scattering, so that rays ejected at near glancing incidence have an appreciable chance of being projected into the recording medium before coming to rest.

3. Because of the minute size of the radiocolloids corrections for internal absorption and geometry are negligibly small. In particular, the end point tracks are recorded at very small angles with the plane of the recording medium, and hence their horizontal projections as measured in the dry gelatin is a close approximation to their original lengths in the water-swollen emulsion.

In plates where the fog background is kept at a low level by suitable development, as little as 2 or 3 grains suffice to indicate the termination point provided they reside in an axial direction with the center of the radiocolloid. A very small part of the alpha-particle energy is expended in the activation of the end point silver halide grains. This does not introduce appreciable error in the measurement, because the emulsion is heavily loaded with water and the recorded range is rarely more than 2 percent of the entire trajectory. The distance between the last grain recorded and the center of the radiocolloid can therefore be taken as a measure of the range in the liquid. When the point sources emit several types of alpha-particles originating from radioactive series decay, such as radium, the end point tracks define the range of the most energetic member, RaC'.

A low power view of the processed plate Fig. 2, shows a random distribution of radiocolloid images varying in blackening in proportion to the particle size of the colloids. Images produced by particles of low activity, Fig. 2, *A*, are not suitable for measurement, owing to an inadequate number of end point tracks. Images of very high activity, *B*, are not suitable for precise measurements because it is difficult to establish the exact center of the core by microscopic inspection. Range measurements were restricted to radiocolloids of intermediate size, such as, for example, *C*, *D*, and *E*. To avoid confusion of the end point tracks the concentration of the radiocolloids should be kept low, and in general measurements were taken from plates with a population about one-third that exhibited by Fig. 2. Occasionally, the radiocolloid image is produced by two closely adsorbed particles. These are readily noted by the ellipticity of the core and are not selected for measurement.

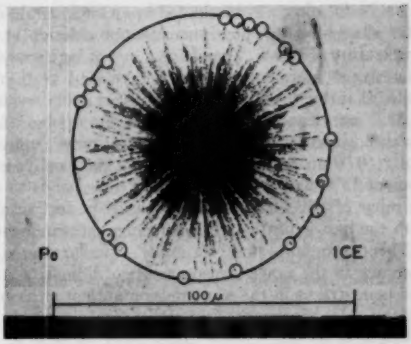

FIG. 3. Photomicrograph of a polonium radiocolloid recorded in an emulsion exposed in water frozen at −5°C. Typical end point tracks are encircled.

The average distance between the center of the radiocolloid and the periphery grains defining the range was measured with a fluorite oil immersion objective of 1.30 N.A. and a filar micrometer ocular standardized by a stage micrometer. Radiocolloid images were selected for measurement which contained at least 10 recognizable end point tracks and the average of the readings taken as a measure of the mean range for that particular point source. The center of the radiocolloid can be judged visually when the blackening of the core is not excessive. Units recording a large number of end point-tracks are also of high total activity and visual judgment of the center is subject to greater error. This can be minimized by making a photomicrograph of the unit and determining the exact center on an enlargement print by drawing radial lines through the grains of the tracks, and taking the average point of intersection as the center. This method, while somewhat laborious, increases the precision because it permits a measurement of the average diameter for the zone of endpoint-tracks. A typical photomicrograph of one of the diametric measurements is exhibited in Fig. 3. In general, the photomicrographic and the visual measurements were in good agreement as noted in the tabulation:

Radiocolloid	Polonium	Radium
Photomicrographic range	38.1±0.1μ	67.0±0.1μ
Visual range	38.1±0.5μ	67.2±0.5μ

The distribution in range values for water of normal isotopic composition and a sample containing 97 percent D_2O is shown in Fig. 4.

In order to ascertain the reliability of this method of range determination a macroexposure simulating the radiocolloid method was made which would yield the range of polonium alpha-particles in air. The tip of a fine-pointed steel needle was coated with polonium electrolytically and supported about 0.3 mm above the surface of a dry Ilford C2 emulsion. The exposure of

24 hours duration was conducted in an enclosed desiccator charged with anhydrous calcium chloride at a temperature of 23±0.1°C and 768.5 mm of Hg pressure. Microscopic examination of the developed plate revealed that the tracks of minimum discernibility resided at 37.8 mm distance from the tip of the needle. This distance, corrected for residual end point range (equivalent to 0.09 air-cm) and converted to standard conditions of 15°C and 760-mm pressure, corresponds to an air range of 3.82±0.02 cm in practically perfect accord with the best ionization chamber range measurements.

This concordance does not imply a similar degree of accuracy in the range measurements of liquids, as the end point-tracks in the wet emulsion are not as clearly defined. Also the errors of microscopic measurement in a length of 38 microns are about twice as large as in the macroscopic measurement of the 38-mm air range.

III. PREPARATION OF RADIOCOLLOIDS AND DEVELOPMENT

For the preparation of radium radiocolloids a solution composed of 10 micrograms of radium and 2 mg of barium chloride per liter was saturated with sodium sulfate crystals. After aging for several days, the solution was diluted about 100-fold. No visible precipitate or turbidity forms at this concentration, but as indicated by photographic exposure, the bulk of the radium activity is concentrated in colloidally dispersed particles, presumably a mixture of barium and radium sulfates. It is important that the preparation contain a minimum of ionically dispersed radium, as the decay of isolated atoms gives rise to the well-known alpha-stars, and a large population of these structures interferes with the recognition of the short end point-tracks. Aging of the stock dispersion increases the ratio of radiocolloids to stars.

The polonium chloride employed in these experiments

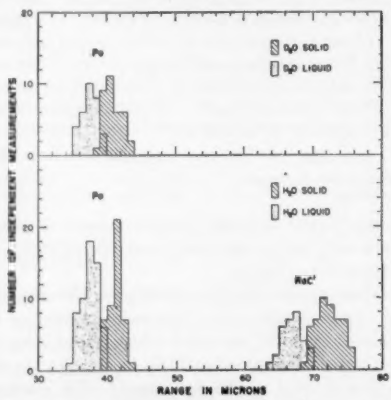

FIG. 4. Histogram of radiocolloid range measurements in water at 5°C and ice at −5°C.

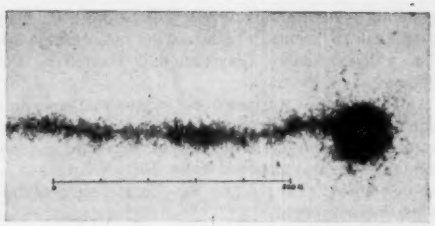

FIG. 5. Path of a radium sulfate radiocolloid recorded on surface of emulsion. The colloidal particle moved a distance of 3 mm before becoming permanently fixed to the gelatin. The test plate contained several similar tracks, and it is possible that the linear movement originated from vibrations initiated by the starting and stopping of the refrigeration mechanism. The lateral small angle scatter may represent the Brownian movement of the colloidal particle.

was a slightly acid solution having an activity of roughly 0.1 microcurie per ml at the time of the investigations. It was prepared about 3 years prior to the tests and the bulk of the activity was found to be concentrated in radiocolloids. We, therefore, have no recipe to offer, but it would appear that in starting with a fresh solution the desired degree of aggregation could be accelerated by rendering the solution faintly ammoniacal.

The slides were prepared by spreading several drops of the dispersions over the center area of 1×3, in. Eastman NTA plates (devoid of a gelatin T-coat). After several minutes the plates were rinsed with distilled water to remove excess electrolytes (Na_2SO_4, HCl) and placed in a paraffined paper box containing a layer of water about 5 mm deep. Most of the colloidal particles are strongly adsorbed to the gelatin surface, and even persist in the gelatin after photographic processing. This can be demonstrated by making an autoradiograph of the processed slide. We have, however, observed occasional instances where some of the particles migrate slowly over the surface of the emulsion for several millimeters before coming to rest. A striking example of this unusual behavior is shown in Fig. 5. The path of dislocation is clearly delineated by recorded alpha-particle tracks and the sinuous, monopole-like trajectory is suggestive of the Brownian movement of a colloidal particle.

In order to avoid dislocation of the particles during exposure and to minimize fading of the latent image the preparations were kept in a refrigerator at a temperature of 5±1°C. For measurements in the solid state, the slide was prepared in a similar fashion, leaving about 1 mm of the liquid on the surface, and the tray was left inside the freezing compartment (about −5°C) for the duration of the exposure.

Slides were developed after peiods of 1 to 10 days, by a brief immersion in 1:20 Eastman D-19 solution. The success of the method is dependent on the ability to develop the end point grains with the production of a minimum of random fog grains. The tracks of interest

TABLE I. Range measurements.

Molecule	State	Density g cm^{-3}	α-particle energy, Mev	Range in microns Meas.	Calc.	Diff.
H_2O	liquid	1.000	5.30	38.1±0.5	37.4	+0.7
	solid	0.917	5.30	41.6±0.5	40.7	+0.9
	liquid	1.000	7.68	67.2±0.5	68.0	−0.8
	solid	0.917	7.68	72.8±0.5	74.3	−1.5
D_2O	liquid	1.104	5.30	38.0±0.5	37.6	+0.4
	solid	1.017	5.30	41.5±0.5	40.9	+0.6

reside at depths of less than 2 microns; hence no effort was made to secure uniform depth development. The process was usually terminated soon after the appearance of surface abrasion marks by immersing the plate in a 1 percent acetic acid stop bath.

IV. PURIFICATION OF TEST LIQUIDS

The range measurements were made on freshly distilled air-free water. The sample of heavy water was observed to contain peroxides. This was removed by acidifying 25 ml of the preparation with 0.1 ml of sulfuric acid and adding crystals of potassium permanganate until in excess as evidenced by the formation of a stable pink coloration. The mixture was distilled, giving a distillate of specific gravity 1.104 at 25°C indicating a D_2O content of 97 percent. Most commercial samples of heavy water contain peroxides, which probably originate during the electrolytic decomposition of the water employed in the concentration process. The peroxides have a destructive action on the latent image of nuclear particle tracks[12] and purification of the heavy water is essential when making exposures of long duration.

While purified liquids were brought in contact with the emulsion, some contamination doubtlessly occurred during the course of the exposure as a result of the extraction of water soluble components from the emulsion layer. In manufacture, small amounts of glycerine and potassium bromide are incorporated in the sensitive material.[13] Measurements of the water extractable components in the plates showed the presence of 2.3 mg of solubles per cm^2 of a 100-micron thick emulsion. The diffusion of these constituents into the test liquid does not affect the range measurements materially, as a large part of the surface water solubles are removed in the operations of applying the radiocolloids to the emulsion. In the early stages of the exposure the alpha-particles traverse pure test fluid. At later stages a maximum concentration of about 2 percent solute may possibly be built up at the emulsion-liquid interface. Calculations based on glycerine as the principal contaminant indicate that the incorporation of this solute would tend to diminish the range in water by about 0.6 percent. Since the range is established by the most remote end point tracks, contamination tends to diminish their number without influence on the path length. In range measurements in the solid state, a layer of pure liquid is frozen and subsequent contamination is inhibited. In so far as the molecular stopping power of water deduced from the measurements appears to be independent of the state, the contamination of the test liquids was probably inappreciable.

[12] H. Yagoda and N. Kaplan, Phys. Rev. 73, 634 (1948).
[13] H. Yagoda, *Radioactive Measurements with Nuclear Emulsions* (John Wiley and Sons, Inc., New York, 1949), p. 128.

V. DISCUSSION OF RESULTS

The several range measurements in water and ice are compared with the theoretical ranges in Table I. The latter were evaluated from the general relationship for the stopping power of polyatomic media derived by Webb:[4]

$$\frac{\Delta R_0}{\Delta R}=\frac{dA_0}{d_0}\left[\frac{p_1 s_1}{A_1}+\frac{p_2 s_2}{A_2}+\cdots+\frac{p_i s_i}{A_i}\right], \tag{1}$$

in which R and d refer to the range and density of the test substance, A_0 represents the atomic weight of the average air atom 14.56, and $d_0=0.001226$ g/cc is the density of dry air at 15°C and 76 cm of Hg pressure. It is assumed in the derivation of Eq. (1) that the stopping power of the molecule or mixture of atoms is an additive property of the atomic stopping powers s_i of component atoms of atomic weight A_i and fractional abundance p_i. As applied to water, using the chemical symbols as subscripts to designate the individual atomic components:

$$\frac{\Delta R_0}{\Delta R}=\frac{dA_0}{d_0}\left[\frac{2s_H+s_O}{2A_H+A_O}\right]. \tag{2}$$

Since $2A_H+A_O=M$, the molecular weight of water, and

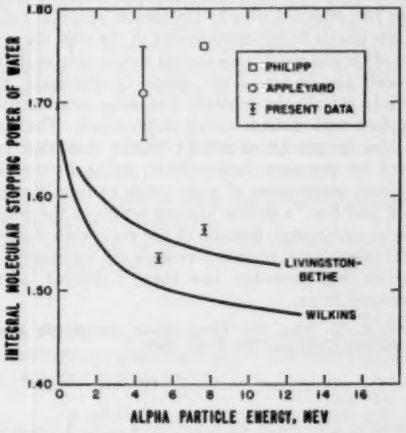

FIG. 6. Comparison of experimental and theoretical values of the stopping power of water.

designating $2s_H+s_O$ by $s(H_2O)$, this simplies to

$$\Delta R_0/\Delta R=(dA_0/d_0M)s(H_2O). \quad (3)$$

Integral values of $s(H_2O)$ were evaluated by a graphical integration of the Livingston-Bethe[2] values for the differential atomic stopping powers of hydrogen and that estimated by Webb[4] for oxygen as a function of alpha-particle energy, and the range in water was computed from

$$R=R_0d_0M/dA_0s(H_2O). \quad (4)$$

On this basis the integral molecular stopping power of water for Po and RaC′ alpha-particles is estimated at 1.56 ± 0.02 and 1.54 ± 0.02, respectively, and the corresponding ranges in liquid water are 37.4 ± 0.5 and 68.0 ± 0.9 microns, respectively. The indicated limits originate from uncertainties in the extrapolation of $s(H_2O)$ at small alpha-particle velocities. Uncertainties in the absolute values of s_i are of a larger magnitude and introduce an additional variation of about 6 percent in the evaluation of $s(H_2O)$, as indicated by the curves in Fig. 6.

The range measurements with polonium alpha-particles are about 1 to 2 percent larger than theory, and the RaC′ values are about 2 percent low. In the evaluation of different factors which might introduce errors in the measurements as a result of photographic processing only the Ross effect appears to be significant. In the development of a large circular area equidistant between two small circles, the images of the latter tend to contract towards the area of major blackening. The degree of the contraction depends on the nature of the developer and the tanning of the gelatin during processing. Mees[14] states that for most developers close doubles separated by 100 microns or less sufier a contraction of about 1.6 microns when the gelatin dries. The radiocolloid image is a close approximation to the Ross test object. Owing to the greater chemical action on the gelatin in the development of the core, the position of the end point tracks might conceivably be drawn towards the center of the image. Qualitatively, this helps to explain the generally low range measurements obtained with radium sulfate radiocolloids. The cores of these images are of greater density than that produced by polonium radiocolloids; owing to the concomitant registration of alpha-particles from Ra, Rn, RaA, and RaC′ a greater tanning action on the gelatin can be anticipated. Because of the very weak development employed in these experiments the maximum contraction was probably less than 1 percent of the measured range.

[14] C. E. K. Mees, *The Theory of the Photographic Process* (MacMillan Company, New York, 1946).

To facilitate comparison of our measurements with that of other investigators, the data have been placed on a common basis by computing the molecular stopping power of the water molecule. The present work indicates an essentially constant stopping power which is independant of the state of the molecule[15] or its isotopic composition, in accord with modern concepts on the stopping of ionizing particles by interaction with the electrons in the medium.[16] As shown in Fig. 6 the present measurements are in fair agreement with the stopping power evaluated by Wilkins from range measurements in thorium-loaded emulsions containing high concentrations of water, and agree closely with the Bethe stopping power theory.

The several independent estimates of the stopping power of water appear to fall into two groups of high (1.76–1.71) and low (1.53–1.51) values. The experiments yielding the smaller value were made under conditions such that the entire range is measured in a thick layer of water in the absence of a liquid-air interface. In the experiments yielding high stopping powers the alpha-particles dissipate the greater part of their energy in a thin film of water immediately below the air interface. The discrepancy between the methods of measurement may originate in the following factors:

1. Inadequate corrections for the stopping power of the air gap and counting windows between the surface of the water and the detector.

2. The existence of an anomalous electronic density at the air-water interface.

These factors do not affect the measurements with submerged photographic detectors as employed by Wilkins and in the present investigation, but may be significant with external detectors. If the interface factor per se is of appreciable magnitude, it should be possible to demonstrate anomalous surface densities in liquids of high cohesive pressure by precise differential range measurements using submerged and external detectors in conjection with monoenergetic alpha-particle sources of low energy.

[15] In the course of these experiments a measurement of the range of polonium alpha-particles in water vapor at 25.3°C was made by exposing an emulsion at glancing incidence to a point source of polonium enclosed in an evacuated tube containing water vapor at equilibrium with the liquid. From the position of the tracks of minimum discernibility (1 micron) a range in water vapor of 3.76 mg per cm² was estimated, which is equivalent to a molecular stopping power of 1.55 ± 0.04. This estimate, based on a single determination, is in good agreement with the value of 1.57 reported by Philipp using a scintillation screen to measure the range of RaC′ alpha-particles in water vapor.

[16] It is noteworthy that the Bragg-Kleeman stopping power rule (see reference 1) valid over a wide range of media composition, fails in the case of heavy water, owing to its assumed dependence of range on the square root of the mass of the atoms rather than their charge.

Some Consequences of Invariance under Charge Conjugation

L. WOLFENSTEIN AND D. G. RAVENHALL
Carnegie Institute of Technology, Pittsburgh, Pennsylvania
(Received July 7, 1952)

The charge conjugation operator, which transforms charged fields to their charge-conjugate fields and reverses the sign of the electromagnetic field, is explicitly constructed. States of zero net charge are eigenstates of this operator; the eigenvalues are $(-1)^n$ for states of n photons and $(+1)$ and (-1) for the singlet and triplet S states of positronium, respectively. The effect of charge conjugation on neutral boson fields is also discussed. Physical consequences of the invariance of field theory under this transformation include:
1. For usual interactions a spin-zero particle (including the singlet S state of positronium) cannot decay into three photons, although this decay is shown to be allowed by angular momentum and parity considerations.
2. The $m=1$ and $m=-1$ levels of triplet positronium cannot be split by a magnetic field.

I. INTRODUCTION

IN considering the decay of a neutral spin-zero particle into three photons, we were struck by the fact that, although this was not forbidden by standard selection rules, the decay probability calculated for the usual interactions was zero. For the case of a neutral scalar meson decaying via intermediate pairs of fermions, the process had been shown to be forbidden[1] as a consequence of Furry's theorem, and this was found to be still true if the fermions were replaced by charged bosons. It was also pointed out to us[2] that the probability for the decay of the singlet S states of positronium into three photons was zero to the lowest order in $e^2/\hbar c$, a result which cannot be derived from Furry's theorem. If these results represent absolute selection rules, we should expect them to be related to a general invariance principle. It is the purpose of this paper to show that these results do follow from the invariance of field theories under charge conjugation and to consider some of the consequences of this invariance principle.[3]

II. CHARGE CONJUGATION IN SPINOR ELECTRODYNAMICS

Charge conjugation for a charged matter field is the operation of reversing the signs of the charges of all the particles, while not altering their other properties—momentum and spin, for example. It is well known that if U is this (unitary) charge conjugation operator the effect of charge conjugation on the field operators $\psi(x)$, $\bar{\psi}(x)$ of a charged spinor field is given by[4]

$$U\psi(x)U^{-1}=C\bar{\psi}(x), \tag{1a}$$

$$U\bar{\psi}(x)U^{-1}=C^{-1}\psi(x), \tag{1b}$$

where C is a four-by-four matrix having the properties that

$$C^{-1}\gamma_\mu C=-\tilde{\gamma}_\mu, \quad \tilde{C}C^{-1}=-1, \tag{2}$$

and is undefined to the extent of a constant of modulus unity. After this operation the Dirac equation for charged particles, and consequently the equations of motion for the field operators $\psi(x)$ and $\bar{\psi}(x)$, become those for particles with charges of the opposite sign.

If it is required that the Hamiltonian of the interacting matter field and electromagnetic field $A_\mu(x)$,

$$H=H_{\text{matter}}+H_{\text{photons}}-\frac{1}{c}\int d^3x j_\mu(x)A_\mu(x), \tag{3}$$

is invariant under charge conjugation, the transformation property of $A_\mu(x)$ must be

$$UA_\mu(x)U^{-1}=-A_\mu(x). \tag{1c}$$

U leaves invariant the commutation relations of the fields and commutes with the Hamiltonian (3); it is therefore a constant of the motion. Since two successive charge conjugations reproduce the initial state, U has two eigenvalues, $+1$ and -1, just like the parity operator. Furthermore, U commutes with the total angular momentum and the parity, but it anticommutes with the total charge Q,

$$Q=\frac{1}{c}\int d^3x j_0(x).$$

Hence U and Q can be made simultaneously diagonal only for states of zero charge.

It is of interest to construct the operator explicitly; to do this we factor U:

$$U=U_D U_{ph}, \tag{4}$$

where U_D and U_{ph} operate on the matter field and the electromagnetic field, respectively. The potentials $A_\mu(x)$ are expanded in plane waves,

$$A_\mu(x)=\sum_{\mathbf{k},\lambda}\left(\frac{2\pi\hbar c}{V|\mathbf{k}|}\right)^{\frac{1}{2}}(a_{\mathbf{k},\lambda}(\varepsilon_{\mathbf{k},\lambda})_\mu e^{ik\cdot x}+a_{-\mathbf{k},\lambda}{}^*(\varepsilon_{\mathbf{k},\lambda})_\mu e^{-ik\cdot x}),$$

[1] H. Fukuda and Y. Miyamoto, Prog. Theoret. Phys. 4, 392 (1949).
[2] R. Drisko, private communication.
[3] While writing this paper we learned of a paper by A. Pais and R. Jost [Phys. Rev. 87, 871 (1952)] on the same general subject. We have attempted to minimize the overlapping of the two papers, and in particular have omitted consequences of simultaneous use of charge conjugation and charge symmetry.
[4] J. Schwinger, Phys. Rev. 74, 1439 (1948). We use the same notation as is used in that paper; in particular, $\bar{\psi}(x)=\psi^*(x)\gamma_4$.

where $a_{\mathbf{k},\lambda}$ and $a_{\mathbf{k},\lambda}^*$ are absorption and emission operators for photons with wave-vector $\mathbf{k}$ and polarization vector $\boldsymbol{\varepsilon}_{\mathbf{k},\lambda}$. Then an operator which anticommutes with $A_\mu(x)$, and which is therefore a suitable representation for U_{ph}, is

$$U_{ph}=(-1)^N;\ N=\sum_{\mathbf{k},\lambda}a_{\mathbf{k},\lambda}^*a_{\mathbf{k},\lambda}. \tag{5}$$

The Dirac matter field operators may be expanded in plane waves using positron theory:[5]

$$\psi(x)=V^{-\frac{1}{2}}\sum_r[a_r u_r(x)+b_r^* v_r(x)],$$

where we choose $u_r(x)$ and $v_r(x)$ to be related by

$$v_r(x)=C\bar{u}_r(x),\quad u_r(x)=C\bar{v}_r(x).$$

Here $u_r(x)$ and $v_r(x)$ are electron spinors of positive and negative energies, respectively, r standing for a particular value of the momentum $\mathbf{p}$ and one of two values for the spin s.[6] The relations (1) can now be expressed in terms of the creation and annihilation operators a_r^*, b_r^*, a_r, b_r; from (1a),

$$\begin{aligned}V^{-\frac{1}{2}}\sum_r[U_D a_r U_D^{-1}u_r(x)+U_D b_r^* U_D^{-1}v_r(x)]\\ =CV^{-\frac{1}{2}}\sum_r[a_r^*\bar{u}_r(x)+b\bar{v}_r(x)]\\ =V^{-\frac{1}{2}}\sum_r[b_r u_r(x)+a_r^* v_r(x)],\end{aligned}$$

so that

$$U_D a_r U_D^{-1}=b_r,\quad U_D b_r^* U_D^{-1}=a_r^*. \tag{6a}$$

Similarly from (1b)

$$U_D a_r^* U_D^{-1}=b_r^*,\quad U_D b_r U_D^{-1}=a_r. \tag{6b}$$

In order to construct U_D[7] we define operators α_r^*, β_r^*, α_r, β_r, by

$$\alpha_r=(a_r+b_r)/\sqrt{2},$$
$$\beta_r=(a_r-b_r)/\sqrt{2},$$

and the Hermitian conjugate equations. These operators satisfy the relations

$$\begin{aligned}U_D\alpha_r U_D^{-1}=\alpha_r,\\ U_D\beta_r U_D^{-1}=-\beta_r,\end{aligned} \tag{7}$$

and the usual anticommutation rules among themselves; by applying these rules it may be shown that (7) is satisfied if U_D is replaced by

$$1-2\beta_r^*\beta_r.$$

Thus U_D may be written

$$\begin{aligned}U_D&=\prod_r(1-2\beta_r^*\beta_r)\\ &=\prod_r(1-a_r^*a_r-b_r^*b_r+a_r^*b_r+b_r^*a_r).\end{aligned} \tag{8}$$

The effect of U_D on a state vector may be found either by using the explicit construction (8) or by expressing the state vector in terms of creation operators acting on the vacuum state and employing (6). By either method it can be seen by inspection that U_D multiplies each empty state r by unity, and for each occupied state r changes an electron to a positron and vice versa; for the exceptional case when both an electron and a positron are present in the state r, U_D multiplies the state by -1, as is to be expected from the antisymmetry properties of Dirac particles.

III. STATES OF TWO AND THREE PHOTONS

It will first be shown that the decay of a scalar or pseudoscalar particle into three photons is not forbidden by angular momentum and parity considerations. This has previously been stated,[8] but no explicit construction of a scalar or pseudoscalar state of three photons was demonstrated.

In order to illustrate the method to be used, the states of two photons previously discussed by Landau[9] and Yang[10] will be considered. The state of two photons must be described in terms of three vectors: the polarization vectors of the two photons, $\boldsymbol{\varepsilon}_1$ and $\boldsymbol{\varepsilon}_2$, and the relative momentum vector $\mathbf{p}$. The polarization vectors are directly associated with the photon creation operators which act on the vacuum state. Since each creation operator acts only once our expression must be bilinear in $\boldsymbol{\varepsilon}_1$ and $\boldsymbol{\varepsilon}_2$. Because of the transversality condition ($\boldsymbol{\varepsilon}_1\cdot\mathbf{p}=0=\boldsymbol{\varepsilon}_2\cdot\mathbf{p}$) the only spherically symmetrical states are

$$\boldsymbol{\varepsilon}_1\cdot\boldsymbol{\varepsilon}_2 f(|\mathbf{p}|),\quad \text{(scalar)} \tag{9a}$$
$$(\boldsymbol{\varepsilon}_1\times\boldsymbol{\varepsilon}_2)\cdot\mathbf{p}f(|\mathbf{p}|),\quad \text{(pseudoscalar)} \tag{9b}$$

where $f(|\mathbf{p}|)$ stands for an arbitrary function of the magnitude of $\mathbf{p}$. It is seen from these representations of the states that the planes of polarization of the photons are parallel and perpendicular in the scalar and pseudoscalar states, respectively. Since the only vector state satisfying the above conditions,

$$\boldsymbol{\varepsilon}_1\cdot\boldsymbol{\varepsilon}_2\mathbf{p},$$

is antisymmetrical on interchange of the two photons (which changes $\mathbf{p}$ to $-\mathbf{p}$), it is evident that there exists no such state of two photons.[10] Similarly there is no pseudovector state.

The states (9) can be expressed in a manifestly Lorentz-invariant and gauge-invariant manner by using the field strengths $F_{\mu\nu}(x)$ instead of the potentials $A_\mu(x)$.

For three photons there are the three polarization vectors $\boldsymbol{\varepsilon}_1$, $\boldsymbol{\varepsilon}_2$, $\boldsymbol{\varepsilon}_3$, and two independent vectors to be chosen from $\mathbf{p}_1$, $\mathbf{p}_2$, and $\mathbf{p}_3$, the three momentum vectors. From these it is possible to construct spherically symmetrical states satisfying all the above conditions; two of the simpler ones are

$$\boldsymbol{\varepsilon}_1\cdot(\mathbf{p}_2-\mathbf{p}_3)\boldsymbol{\varepsilon}_2\cdot(\mathbf{p}_3-\mathbf{p}_1)\boldsymbol{\varepsilon}_3\cdot(\mathbf{p}_1-\mathbf{p}_2)g(p_1,p_2,p_3),\quad \text{(scalar)} \tag{10a}$$
$$\boldsymbol{\varepsilon}_1\cdot(\boldsymbol{\varepsilon}_2\times\boldsymbol{\varepsilon}_3)g(p_1,p_2,p_3),\quad \text{(pseudoscalar)} \tag{10b}$$

[5] See, for example W. Pauli, Revs. Modern Phys. 13, 203 (1941). Our notation is not the same as his.

[6] For a given value of r, $v_r(x)$ is the spinor of the negative-energy electron whose absence corresponds to a positron with spin and momentum the same as those of the electron whose spinor is $u_r(x)$.

[7] We are indebted to Professor G. C. Wick for this construction of U_D.

[8] D. Peaslee, Helv. Phys. Acta 23, 845 (1950).

[9] L. D. Landau, Doklady Akad. Nauk, S.S.S.R. 60, 207 (1948).

[10] C. Yang, Phys. Rev. 77, 242 (1950).

where g is a function antisymmetric on interchange of any two of the three (independent) scalars p_1, p_2, and p_3 [for example, $(p_1-p_2)(p_2-p_3)(p_3-p_1)$]. Thus it is possible for three photons to exist in scalar and pseudoscalar states.

By applying the charge conjugation operator (5) to state vectors for a given number of photons we obtain the result that for an even number of photons U_{ph} has the eigenvalue $+1$, and for an odd number of photons the eigenvalue -1.

IV. THE EFFECT OF CHARGE CONJUGATION ON STATES OF POSITRONIUM

It has been pointed out in Sec. II that U can be diagonalized for states of zero charge, and can be diagonalized simultaneously with angular momentum **J** and parity P. Therefore, states of positronium with specified values of **J** and P may be chosen so that U is diagonal. In fact, U also commutes with the orbital angular momentum **l** and the spin s. Hence the ^1S and ^3S states, which are specified uniquely by their **J** and **l** values, must be eigenstates of U. The state function of any state of positronium can be expanded in terms of free-particle state functions,

$$\Psi_{\text{positronium}}=\Big(\sum_{\mathbf{p},s_1,s_2} c(\mathbf{p},s_1,s_2)a_{s_1}^*(\mathbf{p})b_{s_2}^*(-\mathbf{p}) +\sum_{r}\cdots a_{r_1}^* a_{r_2}^* b_{r_3}^* b_{r_4}^*+\cdots\Big)\Psi_{\text{vac}}, \quad (11)$$

where the second term represents the effect of virtual pair production. Since U commutes with the number of free particles, it will be sufficient to determine the behavior under U of the first term in (11). Performing the operation, we have

$$\begin{aligned} U_D\Psi_{\text{positronium}} &= \sum_{\mathbf{p},s_1,s_2} c(\mathbf{p},s_1,s_2)U_D a_{s_1}^*(\mathbf{p})U_D^{-1} \times U_D b_{s_2}^*(-\mathbf{p})U_D^{-1}U_D\Psi_{\text{vac}} \\ &= \sum_{\mathbf{p},s_1,s_2} c(\mathbf{p},s_1,s_2)b_{s_1}^*(\mathbf{p})a_{s_2}^*(-\mathbf{p})\Psi_{\text{vac}} \\ &= -\sum_{\mathbf{p},s_1,s_2} c(\mathbf{p},s_1,s_2)a_{s_2}^*(-\mathbf{p})b_{s_1}^*(\mathbf{p})\Psi_{\text{vac}} \\ &= -\sum_{\mathbf{p},s_1,s_2} c(-\mathbf{p},s_2,s_1)a_{s_1}^*(\mathbf{p})b_{s_2}^*(-\mathbf{p})\Psi_{\text{vac}}. \end{aligned}$$

For S states $c(-\mathbf{p},s_1,s_2)=+c(\mathbf{p},s_1,s_2)$; thus

$$U_D\Psi_s=-\sum_{\mathbf{p},s_1,s_2} c(\mathbf{p},s_2,s_1)a_{s_1}^*(\mathbf{p})b_{s_2}^*(-\mathbf{p})\Psi_{\text{vac}}. \quad (12)$$

The three triplet S states must behave in the same way on operation by U_D, and for the particular states with $s_1=s_2$, $c(\mathbf{p},s_2,s_1)=+c(\mathbf{p},s_1,s_2)$. Consequently from Eq. (12) the triplet states must belong to the -1 eigenvalue of U_D. In the same way it follows that the singlet state belongs to the $+1$ eigenvalue. Comparing these results with those of the last part of Sec. III, we see that

(1) the ^1S states cannot decay into three photons;
(2) the ^3S states cannot decay into two photons, a result already known from space-symmetry considerations.

TABLE I. Values of J, P, and U for states of positronium.

State	J	P	U
^1S	0	odd	$+1$
^3S	1	odd	-1
^1P	1	even	-1
^3P	0, 1, 2	even	$+1$

Clearly these results can be generalized to states of higher **l**, with the result that the eigenvalues of U_D involve an extra factor $(-1)^l$. A classification of the S and P states of positronium is given in Table I, according to the eigenvalues of **J**, P, and U_D. It may be noted that the states which are odd under charge conjugation are just those which would not exist if the two particles were identical.

By using the property of invariance under charge conjugation it is possible to deduce another result for positronium—that the $m=+1$ and $m=-1$ levels of the ^3S states are not separated by a magnetic field. Since the interaction of external electromagnetic fields with the charged particles is formally the same as for the radiation field, we require such fields also to change sign on charge conjugation. We then consider the behavior of states of positronium under the two successive transformations of charge conjugation and of rotation through 180° about an axis perpendicular to the axis of quantization, which is parallel to the magnetic field. Under the first transformation the magnetic field is reversed, while the states are unaltered (apart from a change of sign, which does not affect the energy eigenvalues of the states). Under the rotation the magnetic field is re-reversed, while the $m=+1$ and $m=-1$ states are interchanged. Since the only effect of the two transformations, which each leave the Hamiltonian invariant, is the interchange of the two states, the energies of the two must be exactly equal.

A third result that can be deduced, of less practical value, is that in electron-positron scattering there is no mixing of singlet and triplet states, since for the same values of **J** and P they belong to different eigenvalues of U_D.

These results are absolute selection rules, independent of any perturbation expansion.

V. CHARGED BOSON FIELDS

For the sake of completeness we give the explicit form of U for a charged scalar field ϕ. The transformation laws for such a field under charge conjugation are

$$U\phi(x)U^{-1}=\eta\phi^*(x),$$
$$U\phi^*(x)U^{-1}=\eta^{-1}\phi(x),$$

where η is an arbitrary factor of modulus unity, which can be set equal to unity without loss of generality. In a way similar to that used in Sec. II we find the following transformation laws for a_s^*, b_s^*, a_s, b_s, the free particle creation and annihilation operators:

$$Ua_sU^{-1}=b_s,$$
$$Ua_s^*U^{-1}=b_s^*.$$

As in Sec. II we define new operators α_s^*, β_s^*, α_s, β_s by

$$\alpha_s=(a_s+b_s)/\sqrt{2}, \quad \beta_s=(a_s-b_s)/\sqrt{2},$$

and the Hermitian conjugate equations. These new operators satisfy

$$\begin{aligned} U\alpha_s U^{-1}&=\alpha_s, \\ U\beta_s U^{-1}&=-\beta_s, \end{aligned} \tag{13}$$

and the usual commutation relations among themselves. The operator satisfying Eq. (13) is $(-1)^{\beta_s^*\beta_s}$, so U may be represented as

$$U=(-1)^{\Sigma_s\beta_s^*\beta_s}.$$

VI. EXTENSION TO NEUTRAL FIELDS

Although a neutral field is not generally assumed to interact directly with the electromagnetic field, one can attempt to determine the behavior of a neutral field under charge conjugation from its interaction with charged fields. For any single interaction term an appropriate assumption about the transformation law of the neutral field will make this term invariant under charge conjugation; for a neutral boson field $\varphi(x)$ this assumption will be either

$$U\varphi(x)U^{-1}=\varphi(x), \tag{14a}$$

or

$$U\varphi(x)U^{-1}=-\varphi(x). \tag{14b}$$

Once one of these has been chosen there exist a whole set of interaction terms which are forbidden by the condition that the Hamiltonian be invariant under charge conjugation; consequently, selection rules concerning neutral particles may be derived from this invariance principle. It should be noted that it is possible formally to retain invariance under charge conjugation without drawing any conclusions about neutral particles; this can be done by assuming that the charge-conjugate of a neutral field is a different neutral field (the field of the antiparticle). For example, if a neutral particle consisted of a bound state of a proton and a negative μ-meson, the charge-conjugate state would involve a negative proton and a positive μ-meson. Thus the requirement that a neutral boson field follow either Eqs. (14a) or (14b) is really an additional assumption.

The interactions of a neutral scalar field φ with a single charged field are of the form

$$\begin{aligned} &\varphi(x)\phi^*(x)\phi(x), \\ &\varphi(x)\bar{\psi}(x)\psi(x), \\ &\varphi(x)\Phi_\mu^*(x)\Phi_\mu(x), \end{aligned} \tag{15}$$

(ϕ, ψ, and Φ_μ are scalar, spinor, and vector fields, respectively) where only terms linear in φ have been included. As long as only a single charged field is involved, vector interactions of the form $\partial_\mu\varphi j_\mu(x)$, where j_μ is the current of the charged field, can be reduced to contact interactions of the charged field and terms quadratic in φ, neither of which contribute to the decay of a single neutral meson. Each of the forms (15) corresponds to a decay of the neutral meson via a charged pair and each requires the transformation law (14a) for invariance under charge conjugation. Thus for all of these interactions the decay of the neutral scalar meson into three photons is forbidden, as previously noted. If interactions involving two charged fields are considered it is possible to get interaction terms which require (14b). One such interaction is a modified form of the vector interaction,

$$\partial_\mu\varphi(x)j_\mu(x)\bar{\chi}(x)\chi(x).$$

Here j_μ can be $\bar{\psi}\gamma_\mu\psi$ or the gauge-invariant currents of either of the fields ϕ or Φ_μ, and χ is another spinor field. This interaction should allow the decay into three photons. Similar considerations hold for a pseudoscalar neutral field; in this case both the pseudovector and the pseudoscalar interactions with a single charged field require Eq. (14a).

For the neutral vector field the simple vector and tensor interactions both require Eq. (14b) (for each component of the vector field). Interaction terms requiring Eq. (14a) can also be constructed; for example,

$$\partial_\mu\varphi_\nu\bar{\psi}\gamma_\mu\psi\bar{\chi}\gamma_\nu\chi.$$

A vector meson field obeying Eq. (14a) could not permit decay into two or three photons, but only into four. For the neutral pseudovector field the pseudovector interaction requires Eq. (14a) while the tensor interaction requires Eq. (14b) so that only one of these is allowed by our assumptions, as has been pointed out by Pais and Jost.[3]

In addition to the decays into a number of photons, some other selection rules for the decay of neutral bosons may be established. If the neutral boson field is even under charge conjugation (14a) the following decay scheme is forbidden:

$$B^0\rightarrow\pi^0+\pi^0+\gamma, \tag{16}$$

where π^0 is the usual neutral meson. This has been pointed out[11] as a consequence of Furry's theorem for a pseudoscalar B^0, but is independent of the spatial transformation properties of B^0. More generally, the decay into any number of neutral mesons (assumed to be even under charge conjugation) and an odd number of photons is impossible. If the neutral boson field is odd under charge conjugation (14b) many decay schemes are forbidden, including

$$\begin{aligned} &B^0\rightarrow\pi^0+\pi^0, \\ &B^0\rightarrow\pi^+\pi^- \text{ for scalar } B_0, \\ &B^0\rightarrow e^+e^- \text{ for scalar or pseudoscalar } B^0. \end{aligned}$$

On the other hand, (16) now becomes possible.

We should like to thank Professor R. E. Peierls for several very useful comments. We are deeply indebted to Professor G. C. Wick for many helpful discussions and suggestions.

[11] A. Pais, Phys. Rev. 86, 663 (1952).

The Scattering of 31.5-Mev Protons from Several Elements*,†

ROY BRITTEN‡,§
Palmer Laboratory, Princeton University, Princeton, New Jersey
(Received January 30, 1952)

The elastic and inelastic scattering of 31.5-Mev protons from the Berkeley linear accelerator from Be, C, Al, Pb, and Pt have been observed, using a sodium iodide (Tl) crystal and photomultiplier for particle detection and energy measurement. Inelastic scattering led to the excitation of states or closely spaced groups of states at 2.5, 6.8 and 11.6 Mev in beryllium; 4.3, (7.5), and 9.5 in carbon; and a group of states between 11 and 17 in carbon. Deuterons have been observed from the reaction $C^{13}(p, d)C^{12}$, leading to the ground state of C^{12}. Differential cross sections have been measured for all these reactions at two or three angles. The differential cross sections for the elastic scattering of 31.5-Mev protons have been measured at several angles for Be^9, C^{13}, Al^{27}, and Pb. A comparison with the results of calculations based on several different nuclear models is made. The extreme sensitivity of the calculated cross sections (in the backward hemisphere) to the individual phase shifts and amplitudes indicates that moderately rough measurements of the backward scattering cross sections of nuclei for neutrons in this energy range would give accurate determinations of the individual phase shifts.

I. INTRODUCTION

ALTHOUGH a thorough understanding of the scattering of nucleons by nucleons may not be achieved for some time, information of importance to the development of concepts of nuclear structure may be obtained at present from the scattering of nucleons by complex nuclei. Such experiments supply two quite distinct kinds of information. From the inelastic scattering process information may be obtained about some of the excited states of the bombarded nucleus. From the angular distribution of the elastically scattered particles information may be derived about some aspects of the structure of the nucleus, or better, about the "external" characteristics of the nucleus that influence the colliding particle.

The present work is an exploration of the scattering of 31.5-Mev protons by means of the thallium-activated sodium iodide crystal photomultiplier[1] technique. With this technique it is possible to record on film the entire energy spectrum of outgoing particles at one time.

II. APPARATUS AND METHOD

A. The Linear Accelerator

The linear accelerator[2] produces a beam of approximately 32-Mev protons with an energy spread of about 0.6 Mev (full width at half-maximum). The proton current occurs in pulses of 150 to 200 microsecond duration at a 15 cps repetition frequency. The energy produced and the energy spread depend critically on adjustments of the end drift tubes which affect the distribution of radio frequency power along the cavity. As a result, it is necessary to check the beam energy regularly. This was done for these experiments by measuring the range of the protons in aluminum, using a remote control foil changing device.

At the exit end of the accelerator a magnet deflects the beam. This magnet is principally used for switching the beam from one experimental set-up to another. In this work it was not practical to use the magnet to reduce the energy spread of the main group of protons. The magnet did, however, remove a small number of protons of intermediate energies and a group of 8-Mev protons. This group of 8-Mev protons results from the acceleration on alternate cycles of H_2^+ ions. These ions remain approximately in resonance and achieve an energy of about 16 Mev. A 16-Mev H_2^+ ion has the same momentum as a 32-Mev H^+ ion, and therefore a thin nylon foil is placed in the beam ahead of the magnet to convert the H_2^+ (16-Mev) ions to H^+ (8-Mev) ions.

The angular divergence of the proton beam is quite small ($\pm 0.1°$). The pre-magnet collimator A (Fig. 1) was set to a $\frac{1}{4}$-in. square aperture and most of the proton current passed through a $\frac{3}{16}$-in. diameter circular aperture at C. Under these conditions, the principal spot of proton beam at the scattering foil F was about $\frac{1}{4}$ in. in diameter. A 1-in. diameter collimator was placed at G to prevent slit-scattered protons from striking the foil holder.

This arrangement gave only a small gamma-ray background for several reasons. The main part of the excess proton current was stopped at A which was a long distance (10 ft) from the scattering chamber, with the magnet acting as shielding. A relatively small amount of current was stopped at C. The current density at the edges of aperture C was much smaller than that at the center. Seven hundred pounds of lead

* This article is based on a thesis submitted in partial fulfillment of the requirements for the degree of Doctor of Philosophy at Princeton University.

† This work supported in part by the ONR and AEC.

‡ Now at the Department of Terrestrial Magnetism, Carnegie Institution of Washington.

§ U. S. Public Health Service-National Cancer Institute Predoctorate Fellow during the period in which this work was carried out.

[1] Franzen, Peelle, and Sherr, Phys. Rev. **79**, 742 (1950).

[2] L. W. Alvarez, Phys. Rev. **70**, 799 (1946); Science **106**, 506 (1946); unpublished Manhattan District Declassified Contribution No. 85 (1946); unpublished Atomic Energy Commision Unclassified Report No. 120 (1948); unpublished University of California Radiation Laboratory Report No. 236 (1948).

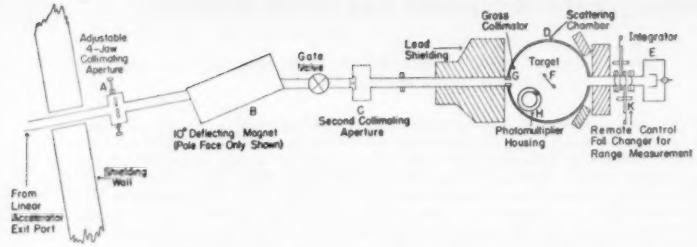

FIG. 1. Arrangement of scattering chamber in linear accelerator bombardment area.

shielding was placed around the scattering chamber as shown in Fig. 1.

In Fig. 3 is shown the resulting background taken with the scattering foil removed from the proton beam. Before the careful collimation and shielding was completed, the background was so great as to mask the deuteron peak, at channel 16, in the 90° carbon curve.

B. The Scattering Chamber

A cross section of the scattering chamber at 90° to the beam direction is shown in Fig. 2. The main body of the chamber is a brass cylinder 19 in. in diameter with $\frac{1}{2}$-in. thick walls. This chamber carries the connections to the beam tube and integrator and is rigidly mounted to the table top.

The base plate which carries the photomultiplier housing and foil holder is a 19-in. diameter $1\frac{1}{4}$-in. thick iron plate. This plate is supported by three adjustable ball bearing wheels and is accurately centered by three guides attached to the supports for the brass cylinder. When the chamber is let down to atmospheric pressure, the weight of the base plate is carried by the ball bearing wheels, and it may easily be rotated for angle changes. When it is set at the desired angle, the foil angle is adjusted by laying a scale across the foil holder and setting it to one of several angle marks on the inside of the brass cylinder.

The controlling aperture for particles striking the crystal was a $\frac{1}{4}$-in. diameter hole located $4\frac{5}{8}$ in. from the center of the scattering chamber. This corresponds to a solid angle subtended of 2.29×10^{-3} steradian. The proton beam struck the target principally within a circular region $\frac{1}{4}$-in. in diameter, which was centered over the center of the scattering chamber to an accuracy of about $\pm\frac{1}{8}$-in. As a result, the scattering angle for the center of the counter aperture could be set to an accuracy of $\pm1.5°$ and the angular resolution was about 6°.

The gross collimator (G) on Fig. 1 was intended to prevent slit-scattered protons from striking the foil holder. Tests were made at both 90° and 160° with the foil holder but no scattering foil in place. No counts were observed in excess of the usual γ-ray and neutron background.

C. The Photomultiplier Assembly

A type 5819 photomultiplier was used with a thallium-activated sodium iodide crystal (0.5 in.$\times$0.5 in.$\times$0.2 in.) mounted on edge in silicone grease under a polished aluminum dome on the photosensitive window. This assembly is shown in Fig. 2. The dome was sealed to the window with silicone grease and had a $\frac{1}{2}$-in. diameter hole in one side, through which the particles entered. This aperture was covered with 0.0003-in. Al foil cemented on with silicone grease. The surfaces of the crystal were thus preserved from the damaging effects of atmospheric water vapor by a silicone grease seal for the immediate crystal housing. In addition, the photomultiplier housing was filled with dry argon and sealed with Q-wax. Under these conditions, the resolving power of the crystal remained stable for a week or longer, indicating that the crystal surfaces did not appreciably deteriorate in that time.

The resolving power in energy is to a great extent determined by the fraction of the light pulse from the crystal which arrives at the photosensitive surface. This fraction is determined by the area of contact between the crystal and the window, the condition of the crystal surfaces, and the effectiveness of the reflecting surface. Because of limitations in space available in the scattering chamber, the photomultiplier had to be mounted vertically. To reduce background, the crystal thickness in the direction of passage of the particles was just greater than the maximum proton range (about 0.2 in.).. Its face was $\frac{1}{2}$ in. square to simplify alignment with the $\frac{1}{4}$-in. aperture and the target. It was necessary to set the crystal on edge and this probably seriously affected the resolving power, which was not as good as that reported for protons by Franzen, Peelle, and Sherr.[1]

The sodium iodide was cleaved under Nujol and mounted on the photomultiplier without removing the oil film. There were 17.6 mg/cm^2 (Al equivalent) of material interposed between the scattering foil and the crystal consisting of the Al foil vacuum window, the Al foil crystal housing window, and the argon in the path from the vacuum window to the crystal.

D. Pulse-Height Discrimination

The photomultiplier was operated with about 600 volts, total, across it or 60 volts per stage. Under these conditions, a 30-Mev proton produced a pulse of about one volt out of the cathode follower. These pulses were fed through a delay line clipping circuit into a Los Alamos model 501 amplifier. The pulse produced had a rise time of about 0.5 microsecond and a base width of about 1.5 microseconds followed by a small (1–2 percent) undershoot lasting about 50 microseconds.

It was found convenient to adjust the counting rate for the major part of a spectrum to about 15 counts per second or 1 count per beam pulse. With the 150 microsecond duration beam pulse, the pile-up of large pulses was negligible, and the γ-ray and neutron background pulses may have contributed through pile-up a small amount to the spread of peaks in the spectrum.

The output of the amplifier was fed both to a 10-channel pulse-height discriminator and to one vertical plate of a Tektronix model 411 AD synchroscope, with a blue screen for photography.

The 10-channel discriminator was very useful for exploration and monitoring but when used with a 2-volt channel width introduced uncertainties which reduced its value for taking a full spectrum. There were unreproducible variations in channel width as well as shifts in the location on the voltage scale of the whole set of channels, introducing errors somewhat greater than the statistical error. With a resolving power such that the full width at half-maximum of the elastic peak was about 5 percent, it was necessary to use channel widths of about 2 percent of the elastic pulse height (2 v in ~100 v). As a result, a minimum of 5 runs was required for one spectrum at one angle.

As an alternative method for taking pulse-height distributions, the vertical pulses on the synchroscope screen were photographed on a continuously-moving horizontal 35-mm film strip. In order to make economical use of the film without increasing greatly the chance of one pulse masking another, a slow horizontal sweep was used, triggered from the linear accelerator circuits. A trigger pulse was available which occurred about 500 microseconds before the beam pulse. At this time a horizontal sweep was started from the left at a rate of about 150 microseconds/cm. The pulses then occurred over a 1-cm region at the center of the screen. The screen was masked except for this central region to avoid over-exposure of the base line. In addition, a small piece of yellow plastic filter was cemented over the base line in the central region. The film was moved continuously at 1-in. per second and under these conditions, each interval corresponding to a beam pulse was recorded on the film as a region about $\frac{1}{16}$ in. long without overlap. A particle pulse appears as a faint vertical line with a dark spot corresponding to the 0.5 microsecond duration flat top. This is convenient for analysis of the film since the center of this dark spot can be used to estimate the pulse height.

With a counting rate for the major part of the spectrum of 15 counts per second, a spectrum consisting of 20,000 counts can be recorded in 20 minutes on a 100-foot film strip.

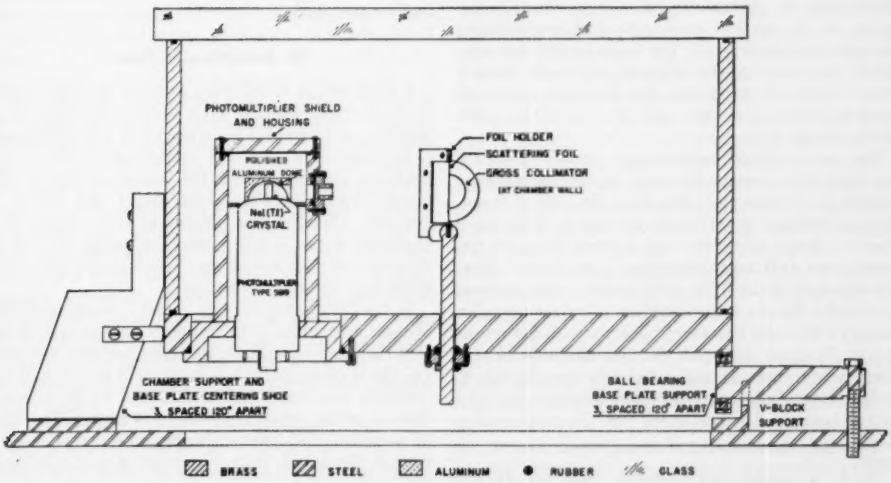

FIG. 2. Cross section of scattering chamber at 90° to beam direction. The chamber is set for observation at 90° to the beam direction.

E. Method of Film Analysis

After consideration of various methods for automatic analysis of the films using multichannel phototube circuits, etc., it was decided that the investment of development time would be prohibitive if good precision were to be obtained and counts from dirt and scratches eliminated. On the other hand, a strictly manual method of analysis was inconveniently slow.

As a practical compromise, a bank of 80 electrical registers was assembled connected to a row of 80 small microswitches. The microswitches were mounted directly on the face of a large ground glass screen in a horizontal row. An image of the film was projected onto the screen with the base line vertical, so that the pulses extended along the row of switches. As the film moved, the ends of the pulses passed individual switches which were then depressed manually. With this arrangement an increase in speed of analysis of a factor of five or ten was obtained over any strictly manual method of recording pulse heights from the film strip.

F. The Integrator

All bombardment current integrations were made with the integrator constructed by Lee Aamodt several years ago. This integrator has been used in a number of investigations with the linear accelerator[3,4] and has given good, consistent results. It is unlikely that any significant error in the absolute cross sections has been introduced from this source.

G. The Energy Scale

In all of this work it has been assumed that the pulse height from the photomultiplier is proportional to the energy of the particle (proton or deuteron) striking the sodium iodide crystal. The beam energy was estimated by measuring the range in aluminum. With a proper correction for recoil, the elastically scattered group of protons was then used as a calibration point for the energy scale.

The semi-empirical range-energy relation of Smith[5] was used. An approximate check on the range-energy relation is available at 32 Mev from the data of Panofsky and Phillips.[4] In this work, the energy of the beam from the linear accelerator was inferred from the frequency and drift tube dimensions to be 32 ± 0.1 Mev. The threshold of the $B^{11}(p, n)C^{11}$ reaction was measured as 3.0 ± 0.6 Mev by using absorbers to reduce the beam energy. This value checks within error with the results of Van de Graaf work. At the time of this work, the linear accelerator was not sufficiently reproducible in its behavior to allow such a precise inference as to the energy output. Another check on the range-energy relation at 18 Mev is available from the work of Hubbard and MacKenzie,[6] using a 180° deflection method inside the cyclotron at the University of California, Los Angeles.

The most precise check on the linearity of the crystal is the comparison of the Q values for various excited states from this work with previously obtained values. Another good check is the energy estimated for the deuteron group from the $C^{12}(p, d)C^{11}$ reaction (see Fig. 4), where an error of 0.3 Mev is indicated.

An attempt to check the linearity of the crystal was made using aluminum absorbers to reduce the beam energy. The results of this method are not entirely satisfactory since the original beam energy spread of greater than 0.6 Mev (full width half-maximum) is increased greatly as the energy is reduced. The results are good to about ±3 percent from 12 Mev to 32 Mev and are consistent with proportionality between pulse height and proton energy.

The shape of peaks in the pulse-height distribution in general appears to be symmetrical except for a slight distortion toward low energies at the foot of large peaks. The following criterion for the location of a peak on the pulse height or energy scale has been chosen: A smooth curve is drawn through the points on the peak, and a point halfway between the sides of the peak, about $\frac{3}{4}$ of the way up, has been taken as the location of the peak. Since there is an energy spread of about 0.6 Mev (full width at half-maximum) in the proton beam from the linear accelerator, the measurement of the beam energy by measuring the extrapolated range will introduce an error as far as the mean energy of the beam is concerned. As a result, 0.3 Mev has been subtracted from the value of beam energy obtained by extrapolated range measurement.

H. Reduction of Data

A pulse-height distribution recorded on film or with 10-channel discriminator gives directly the number of particles per interval of pulse height for a known charge of bombarding protons. The bombarded nucleus, target thickness, and solid angle of the counter are known, and proportionality between pulse height and energy is assumed. Therefore, the differential cross section at a particular angle for any interval of energy referred to the center of mass system may be calculated, if the outgoing particle can be identified.

In the calculations for Figs. 4 and 7, where the center of mass differential cross section is plotted against the Q of the reaction, inelastic scattering has been assumed, i.e., the outgoing particle is taken to be a proton. If the outgoing particle actually turns out to be different from a proton, small errors in cross section (less than 10 percent for laboratory energies greater than 8 Mev) appear, along with shifts of several Mev in calculated

[3] Levinthal, Martinelli, and Silverman, Phys. Rev. **78**, 199 (1950).
[4] W. K. H. Panofsky and R. Phillips, Phys. Rev. **74**, 1732 (1948).
[5] J. H. Smith, Phys. Rev. **71**, 32 (1947).
[6] E. L. Hubbard and K. R. MacKenzie, Phys. Rev. **85**, 107 (1952).

Q value. Some examples of the shifts appear on Figs. 4 and 7 and will be discussed later.

The first step in the reduction is to obtain the relationship between pulse height and laboratory energy for the particular run. The peak in the pulse-height distribution due to elastic scattering from the target nucleus is identified. The energy of the elastically scattered protons is calculated from the usual recoil formula, and a correction is made for the loss in the (17 mg/cm² Al equivalent) material interposed between the target and crystal to obtain the energy actually lost in the crystal. This energy value is used to calibrate the crystal for the particular run and by again applying the appropriate correction for the energy lost in the "window," the laboratory energy corresponding to any pulse height may be calculated.

If the outgoing particle is assumed to be a proton, then, by using the usual recoil formula, the reaction energy change Q can be calculated for any given pulse height. Actually the Q value was calculated for several points over the range of interest and the remainder of the values were obtained graphically. It was found that from a laboratory energy of 8 Mev up to the maximum, a linear relationship holds between Q and the pulse height to better than 0.1 Mev, for beryllium and carbon.

The next step in the reduction is to calculate the center-of-mass differential cross section corresponding to each point in the pulse-height distribution. The number of particles counted in a particular interval of Q is

$$n = n_0 N \frac{d^2\sigma}{d\omega dQ} \Delta Q \Delta\omega \frac{\sigma(\theta)}{\sigma(\eta)},$$

where n_0 is the number of bombarding protons, N the scattering nuclei per cm² of target, $d^2\sigma/d\omega dQ$ the center-of-mass differential cross section in cm² steradian^{-1} Mev^{-1}, $\Delta\omega$ the solid angle of the counter in the laboratory system, η the center-of-mass scattering angle, and θ the laboratory scattering angle. This expression is accurate in general if the resolution width for energy is small compared with ΔQ, or if $d^2\sigma/d\omega dQ$ does not change significantly within the resolution width. Since neither of these conditions is met in general in this work, the value of $d^2\sigma/d\omega dQ$ calculated will be strongly modified by the resolution width. Sharp peaks will be reduced in height and smeared out. Nevertheless, the calculated $d^2\sigma/d\omega dQ$ is useful since the resolution width is independent of θ to our accuracy and a comparison of the variation of cross section with Q can be made between different angles. In addition, if correction is made for overlapping of peaks, the area under any given peak is the corresponding differential cross section in millibarns per steradian.

If P is the pulse height, $\Delta Q = \Delta P dQ/dP$. dQ/dP can be easily evaluated from the slope of the graph of Q against P for each run. $\sigma(\theta)/\sigma(\eta)$ is evaluated from the usual recoil formulas and is a minor correction amounting to a maximum of 16 percent in this work.

III. RESULTS

A. Carbon

A 2-mg/cm² polystyrene foil was used as a target for the work on carbon. Since the spectra were taken at angles of 90° or greater, there was no interference from the hydrogen content of the foil.

Several spectra were taken using the 10-channel discriminator and spectra at 90° and 160° were recorded on film. Since there are no inconsistencies between the 10-channel data and the film data and the accuracy and background of the film data are better, only the film data are included.

In Fig. 3 are given the actual pulse-height distributions as read from the films, less background. In Fig. 4 the calculated center-of-mass differential cross section in 10^{-27} cm²/steradian Mev is plotted against the calculated Q value, assuming inelastic scattering. The probable errors shown are just those due to statistics. In addition, there is about ± 15 percent error in absolute cross section, and a smaller relative error between the data at the two angles.

Referring to Fig. 3, the peaks occurring at greatest pulse height have been taken as due to elastic scattering. Note the peak at 52 on the 90° curve (marked K) which is probably due to elastic scattering from a heavy impurity in the target. The peaks due to elastic scattering from carbon have been plotted at $Q=0$ on Fig. 4 (marked A). The peaks marked (B) and (D) can be identified as due to inelastic scattering leading to the excitation of known levels in C^{13}. Table I gives the Q values and cross sections measured in this work.

The excitation of the 7.4-Mev level (peak C) has not been previously observed in the inelastic scattering process. An analysis of the various experiments in which this level has been observed indicates that its existence is uncertain. The groups identified with the 7.4-Mev level in this work occur with such small cross section as to make the identification doubtful.

The broad peak (E) can, with reasonable certainty, also be identified as due to inelastic scattering from C^{13}. Because of the large negative Q values for all competing reactions, the broad peak (E) cannot be due to any particles but protons resulting from $C^{12}+p$, although a contribution may be present from various particles resulting from reactions in C^{13} and impurities. The Q values for reactions competing with inelastic scattering, calculated from mass tables, are as follows: $(p-d)$, -16.3; $(p-p,n)$, -18.7; $(p-\alpha)$, -7.5; $(p-He^3)$, -19.6; $(p-p,2n)$, -32.7; $(p-H^3)$, -24.1; $(p-n)$, -18.5; $(p-3He^4,p)$, -7.3. The calculated location of the peak on the 90° curve due to alpha-particles from the reaction $C^{12}(p,\alpha)B^9$ to the ground state is shown on Fig. 4 (H′). Although this Q is only -7.5 Mev, the combination of recoil and energy loss in the window reduces the energy of this group of alpha-particles to about 7 Mev, at the time they strike the crystal.

C^{13} is present in the target (1.1 percent) and other

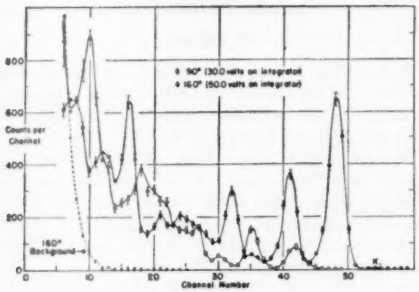

FIG. 3. Pulse-height distributions, recorded on film, for the scattering of 31.5-Mev protons from a polystyrene target. Background has been subtracted. The background for the run at 160° is included as an example.

impurities may be present in smaller quantities. However, no reaction has been suggested which, with reasonable cross section, could give the peak (*E*). This broad peak may be due either to the excitation of broad levels or to the excitation of closely spaced sharp levels. A better resolving power is apparently necessary to show which is the case. Some evidence for levels in this region has been obtained in other reactions.[7]

The peaks (*B*) and (*D*) show a strong anisotropy. The ratio of the 90° cross section to the 160° cross section is about five to one. However, for the peaks (*C*) and (*E*) no anisotropy is indicated. This may indicate that so many levels contribute to the peak (*E*), that the individual angular distributions are washed out, or that the levels concerned give roughly isotropic angular distributions.

The spectrum at 90° may be compared with the results of Levinthal, Martinelli, and Silverman[8] obtained as range distributions using nuclear emulsions

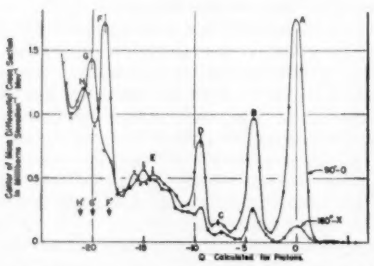

FIG. 4. C^{12} center-of-mass differential cross section, calculated from the pulse-height distributions in Fig. 3, plotted against calculated Q in Mev, assuming inelastic scattering.

[7] E. Stuhlinger, Z. Physik **114**, 185 (1939); V. R. Johnson, Phys. Rev. **81**, 316 (1951); Fowler, Gaerttner, and Lauritsen, Phys. Rev. **53**, 628 (1938); A. H. Morrish, Phys. Rev. **76**, 1651 (1949); R. Tangen, Kgl. Norske Videnskab. Selskabs Skrifter, No. 1 (1946); McLean, Ellett, and Jacobs, Phys. Rev. **57**, 1083 (1940).

in bombarding carbon with protons of about the same energy. Levinthal *et al.* do not give absolute cross section figures, but the relative height and locations of the peaks (*B*) and (*D*) check well, and in addition, there is evidence in their data for the group (*E*).

The peaks (*F*) and (*G*) are due to deuterons from the reaction $C^{12}(p, d)C^{11}$. The range distribution of Levinthal *et al.* shows a peak with the proper range, if it is assumed to be deuterons from a reaction ending in the ground state of C^{11}. The energy distributions in Fig. 3 show a peak at both 90° and 160° which has the proper energy under the same assumption.

Since the peaks (*F*) and (*G*) are due to deuterons, they will not fall at the proper Q values on Fig. 4, where the Q was calculated assuming the the outgoing particle was a proton. The arrows marked (*F'*) and (*G'*) on Fig. 4 are located at the expected positions on the 90° and 160° curves, respectively, of the deuteron peaks, assuming $Q=-16.5$ Mev, calculated from the masses given in Bethe.[8]

TABLE I. C^{12} Q values and differential cross sections.

Group	Differential cross section (millibarns/steradian)	
	90°	160°
Elastic	3.0 ±0.4	0.29±0.05
Resolved inelastic, centered at:		
$Q=-4.3\pm0.2$ Mev	1.5 ±0.2	0.34±0.05
$Q=-7.5\pm0.4$ Mev	0.16±0.1	0.12±0.06
$Q=-9.5\pm0.2$ Mev	0.90±0.2	0.19±0.1
Unresolved inelastic between $Q=-11$ and $Q=-17$ Mev	2.8 ±0.4	2.7 ±0.4
Deuteron	1.3 ±0.6	1.1 ±0.6

The differential cross sections for the $C^{12}(p, d)C^{11}$ reaction at 90° and 160° are 1.3 and 1.1×10^{-27} cm²/steradian. These are lower limit figures, obtained from the areas of the peaks on Fig. 3, above smooth curves drawn to represent background from other reactions. The error is probably not greater than 50 percent. If isotropy is assumed, the total cross section becomes 15 millibarns. This figure can be compared with the total cross section for the production of C^{11} of 75 millibarns measured by Panofsky and Phillips,[4] using 32-Mev protons. Thus, as a lower limit, 10–20 percent of the production of C^{11} is by the (p, d) reaction. It is possible that the figure should be very much higher than this, since a forward peak in the angular distribution may occur. Such a peak would be expected to occur if the reaction were considered as a pick-up process. Harvey[9] has measured the angular distribution of the ground-state deuterons in the $Be^9(p, d)Be^8$ reaction with bombarding energies from 5 to 8 Mev and observed a very strong forward peak. The intensity at 20° was 15

[8] H. A. Bethe, *Elementary Nuclear Theory* (John Wiley and Sons, Inc., New York, 1947).

[9] J. A. Harvey, Phys. Rev. **82**, 298 (1951).

times that at 70° and the distribution was roughly isotropic at larger angles.

It is conceivable that the production of C^{11} with 32-Mev protons on C^{12} may be predominantly by the (p, d) reaction.

B. Beryllium

A 4.8 mg/cm² rolled metallic foil of beryllium was used as a target, and charged particle spectra were obtained at 90°, 125°, and 160°. The 90° and 125° spectra shown in Fig. 5 were recorded on film and the 160° spectrum shown in Fig. 6 was recorded with the 10-channel analyzer.

Small peaks which have been identified as due to elastic scattering from impurities in the target occur at large pulse height on Fig. 6. The peak with a pulse height of 94.5 on Fig. 6 is due to elastic scattering from

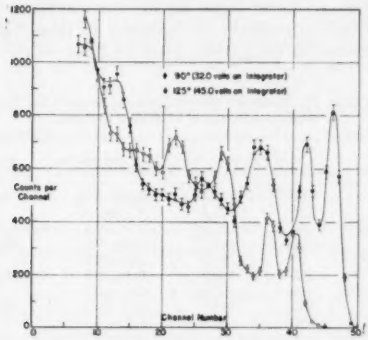

FIG. 5. Pulse-height distributions, recorded on film, for the scattering of 31.5-Mev protons at 90° and 125° from a beryllium foil target. Background has been subtracted.

Be^9 and is used to calibrate the energy scale for the 160° data. The peaks with pulse heights of 46.0 and 40.5 on Fig. 5 are due to elastic scattering from Be^9 at 90° and 125°, respectively, and are used to calibrate the energy scales for the data at these angles.

On Fig. 7 the calculated center-of-mass differential cross section is plotted against the calculated Q, assuming inelastic scattering from Be^9, for the spectra at the three angles.

Some of the groups appearing in these spectra can be identified as due to inelastic scattering leading to the excitation of previously unobserved levels in Be^9. As a result, it is important to rule out the possibility of impurities in the target having a strong influence on the spectra. An analysis of a sample of beryllium foil from the same lot as the target indicated the following impurities: Al, 0.1–1 percent; Ca, Mg, 0.01–0.1 percent; Cr, Fe, <0.01–0.1 percent. In addition, there was a barely visible layer of oxide on the surface of the foil.

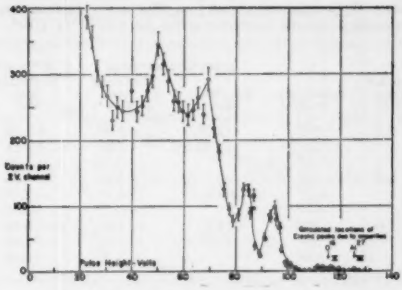

FIG. 6. Pulse-height distribution, recorded with the 10-channel discriminator for the scattering of 31.5-Mev protons at 160° from a beryllium foil target. Background has been subtracted.

On Fig. 6 the calculated locations of elastic peaks due to O^{16} and Al^{27} are plotted, assuming the peak at 94.5 is due to elastic scattering from Be^9. The peaks occurring in this region of pulse height are apparently due to impurities of about the mass of oxygen and aluminum. Since these are the principal expected impurities, for the purpose of estimating the effect on the remainder of the spectrum, we can assume that these are the only significant impurities.

Taking the peak marked *VI* to be due to aluminum, and using the values of the cross sections for elastic scattering listed in Table IV, the amount of aluminum impurity is estimated to be 2±1 percent by weight. It can be seen by referring to the 160° aluminum spectrum, Fig. 9, that this amount of aluminum will have an entirely negligible effect on the spectrum. The peak presumably due to oxygen is somewhat greater, amounting to about 5 percent of the beryllium elastic peak.

The spectrum caused by oxygen is unknown. However, any peaks in the beryllium spectrum that were due to oxygen would exhibit a shift with angle on Fig. 7, where the differential cross section is plotted against Q calculated for inelastic scattering of protons from Be^9. As an example of this shift, the calculated positions

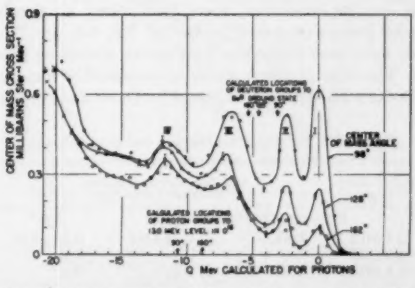

FIG. 7. Be^9 center-of-mass differential cross section calculated from the pulse-height distributions in Figs. 5 and 6, plotted against calculated Q in Mev, assuming inelastic scattering.

TABLE II. Q values calculated from film and 10-channel data, assuming inelastic scattering or the reaction $Be^9(p, d)Be^8$.

Excited state, Mev	Laboratory angle	Q, Inelastic scattering Film data Mev	Q, Inelastic scattering 10-channel data Mev	Q, $Be^9(p, d)Be^8$ 10-channel data Mev
2.5	90°	−2.45	−2.49	+1.34
	125°	−2.50	−2.41	+3.11
	160°		−2.70	+3.49
6.8	90°	−6.7	−6.61	−3.26
	125°	−7.1	−6.85	−2.15
	160°		−6.72	−1.06
11.6	90°	−11.5	−11.43	−8.68
	125°	−11.8	−11.48	−7.45
	160°		−11.55	−6.82

of peaks due to inelastic scattering from O^{16} leading to excitation of a 13.0-Mev level are plotted. The shift from 90° to 160° for this case is 1.8 Mev, and the amount of this shift does not change strongly with energy, being 2.0 Mev at $Q=0$ and about 1.6 Mev at $Q=-18$.

It cannot be said with certainty to what extent the spectra are made up of protons, deuterons, or other particles. However, with considerable certainty the peaks marked II, III, and IV on Fig. 7 can be identified as due to protons. Table II lists the Q values corresponding to the center of these peaks, assuming that they are due either to protons or deuterons. These values were calculated from the pulse-height distributions shown in Figs. 5 and 6 and from two additional 10-channel distributions which are not reproduced.

The values in column 5 vary between 90° and 160° by 2 Mev or more, which is clearly outside error. The values in column 3, however, vary by less than 0.3 Mev which is the order of precision to be expected in locating fairly broad and occasionally unsymmetrical peaks. If these peaks can be identified with each other as they have been in Table II, they are due to protons. No alternative identification has been successful.

If a reaction were to lead to a discrete group of particles heavier than deuterons, say He^3 or He^4, the apparent shift in Q with angle on Fig. 7 would be considerably larger than that shown for the deuterons to the ground state of Be^8.

It can be concluded, then, that states, or closely-spaced groups of states, in Be^9 at 2.5, 6.8, and 11.6 Mev have been excited in the inelastic scattering process. The first of these states is presumably identical with the 2.41-Mev level observed by Davis and Hafner[10]

TABLE III. Be^9 excitation energies and cross sections.

Excited state Mev	Differential cross section (millibarns/steradian) 90°	125°	160°
2.5±0.2	0.64±0.3	0.34±0.1	0.18±0.05
6.8±0.3	0.6	0.2	0.1_4
11.6±0.4	0.1_7	0.1_8	0.2_1

[10] K. E. Davis and E. M. Hafner, Phys. Rev. **73**, 1473 (1948).

from the inelastic scattering of protons up to 7.1 Mev, and by Rhoderick,[11] also from the inelastic scattering of protons. The 6.8- and 11.6-Mev states have not been observed previously in any reaction. However, there do not appear to be any reports in the literature of experiments in which the observation of these states could be expected.

In Table III are listed the average values for the energies of the excited states and the approximate differential cross sections at three angles.

The principal source of error in the evaluation of these cross sections is the continuous background in the pulse-height distribution due to particles from other reactions. In order to estimate the cross sections for the 6.8- and 11.6-Mev levels, a smooth curve representing the background has been drawn through the valleys between the peaks. The figures listed in Table III are based on the area under the peaks above this curve and therefore are lower limits for the cross sections. It is is difficult to estimate the accuracy of these figures. The figures for the 2.4-Mev level are based on the area above the baseline of symmetrical peaks, allowing for some overlapping.

TABLE IV. Measured differential cross sections for the elastic scattering of 31.5-Mev protons.

Element	Lab angle	c.m. angle	c.m. cross section (millibarns steradian^{-1})	Ratio 90°/160°
Be^9	160	162.4	0.19±0.04	7±1
	125	127.5	0.32±0.05	
	90	97.9	1.3 ±0.3	
C^{12}	160	161.7	0.29±0.05	10±1
	90	95.6	3.0 ±0.4	
Al^{27}	160	160.7	0.59±0.1	6±2
	90	92.3	3.5 ±0.5	
Pb	155	155	0.79±0.2	9±3
	90	90.1	6.8 ±2	

C. Aluminum

The target for the aluminum bombardments was a 3.36 mg/cm² sample of commercial pure aluminum foil.

On Fig. 8 are shown the pulse-height distributions taken with the 10-channel discriminator. On Fig. 9 is shown the differential cross section in millibarns steradian^{-1} Mev^{-1} as a function of the laboratory energy of the outgoing particles. Figure 9 is given as a semilog plot in order to show the approximately exponential shape of the spectra, which is similar to the results of Gugelot[12] and others on neutron spectra.

Included for comparison purposes on Fig. 9 is a dotted curve representing the results of Levinthal, Martinelli, and Silverman.[9] This curve is a transformation to proper scales of a smooth curve drawn through their experimental points. Their results were obtained

[11] E. H. Rhoderick, Proc. Roy. Soc. (London) **A201**, 348 (1950).
[12] P. C. Gugelot, Phys. Rev. **81**, 51 (1951); P. H. Stelson and C. Goodman, Phys. Rev. **82**, 69 (1951).

as range distributions using nuclear emulsions, at an angle of 96° with 30.4 Mev bombarding protons. The vertical dotted bars represent their quoted probable errors, which are just those due to statistics. The errors shown on the 90° and 160° curves are also just those due to statistics.

Levinthal *et al.* quote 4.1 millibarns steradian^{-1} as the differential cross section for elastic scattering at 96°. The result from this work, appearing in Table IV, is 3.5±0.5 millibarns steradian^{-1}.

D. Platinum and Lead

Spectra taken with the 10-channel discriminator at 90° for platinum and lead are shown in Fig. 10. A number of other runs were taken with broad channels and all check the shape of the spectra within statistical error. These data were taken in the earlier stages of the work before the background and resolution had been improved to the degree later obtained. Also included on Fig. 10 is the peak for elastic scattering taken at 25° from the same target immediately after the 90° lead spectrum was taken. The 90° lead elastic peak has been spread, possibly due to the excitation of low-lying levels.

IV. ELASTIC SCATTERING

A. Experimental Results

Measurements of the differential cross section for elastic scattering were obtained from each of the spectra reproduced in Sec. III. In addition, values were obtained from a number of exploratory runs using the 10-channel discriminator. Table IV gives average values of the measured differential cross sections in millibarns per steradian.

The probable errors quoted in Table IV, column 5 include ±15 percent due to various errors in measurement of target thickness, solid angle, integrated current, target angle, as well as the effect of variations in beam position on the effective solid angle. In addition, allowance has been made for counting statistics and in some cases for possible contribution of unresolved, low-lying levels to the apparent elastic peak. The ratio of the cross section at 90° to that at 160° is generally known with greater precision since some of the errors drop out.

The ratio of the differential elastic scattering cross section at 90° to that at 160° does not vary among the four elements by an amount which is significantly greater than the probable errors quoted. In addition, there is a fairly smooth increase in differential cross section with atomic weight. From the smooth behavior of the elastic scattering cross section as a function of A, it appears very unlikely that the experimental results are fortuitously located in sharp valleys in the angular distributions. If the spectra showed sharp peaks and valleys, the location and spacing of the peaks would be expected to change radically as kR changes from 5 (Be) to 14 (Pb).

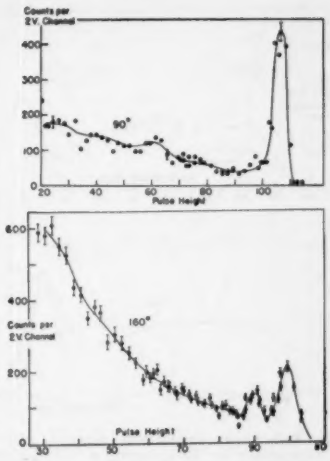

FIG. 8. Pulse-height distributions, recorded with the 10-channel discriminator for the scattering of 31.5-Mev protons from an aluminum foil target. Background has been subtracted.

B. Discussion of Elastic Scattering

These results suggest that the constitution of the individual nuclei has a relatively minor effect on elastic scattering at this energy. As a result, it is conceivable that some simple nuclear model might be chosen which would give predictions in agreement with experimental results.

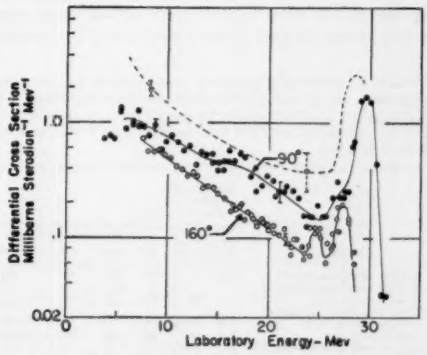

FIG. 9. Semilog plot of Al^{27} center-of-mass differential cross section calculated from the pulse-height distributions in Fig. 8, assuming inelastic scattering. The broken curve represents the results of Levinthal, Martinelli, and Silverman (see reference 3) obtained as a range distribution using nuclear emulsions with a laboratory angle of 96° and 30.5 Mev bombarding energy.

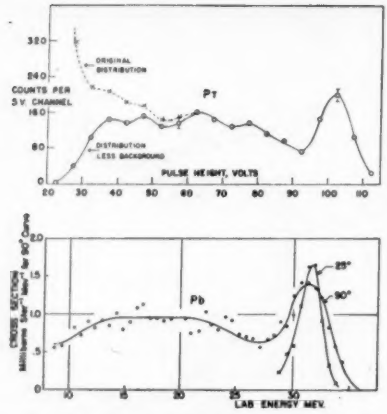

FIG. 10. Pulse-height distributions recorded with the 10-channel discriminator for the scattering of 31.5-Mev protons at 90° from lead and platinum. Background has been subtracted.

A number of models have been investigated, and agreement in order of magnitude has not been obtained. Table V summarizes the results. In addition, Fig. 11 shows the angular distributions calculated for the various models.

The total cross sections for neutron scattering and absorption are listed as well as the differential cross sections since they are fairly well known experimentally[13] and give a good control on the choice of models.

In all but one case, the differential cross sections have been calculated for neutrons, to avoid the use of Coulomb wave functions. It is reasonable to expect that the 2- or 3-Mev Coulomb barrier (beryllium) compared with a 30-Mev nuclear potential and a 32-Mev bombarding energy will have a small effect on scattering cross section at large angles. This is corroborated by the comparison of the results of calculations for neutron scattering and proton scattering from a totally reflecting sphere, with a Z of 4, shown in Table V. It is apparent from this case that if a close comparison were required between calculated and experimental results for proton scattering at 32 Mev for light elements, the Coulomb field could not be neglected. However, since in these calculations the order of magnitude only is of interest, the Coulomb field has been neglected.

TABLE V. Calculated scattering cross sections. In row 7, for comparison, are given the experimental results for beryllium. The differential cross section figures are from this work and the total cross section figures are from neutron scattering work (see references 13 and 16).

Model	Total cross sections (barns) Scattering	Absorption	Differential cross sections (millibarns steradian^{-1}) 90°	125°	160°	180°
1 Totally reflecting sphere	1.4	0	33	40	48	32
2 Totally reflecting sphere +Coulomb field	—	0	68	7	74	97
3 Total absorption of partial waves up to $l=4$	0.55	0.55	6.1	3	6.5	44
4 Square well	2.3	0	24	14	33	193
5 Square well with absorption	1.4	0.55	16	5	1.5	24
6 Adjusted phase shifts	0.47	0.51	1.0	0.12	0.17	0.01
7 Experimental, beryllium	0.5	0.5	1.3	0.32	0.19	—

Discussion of the calculations[14] will be limited to a brief description of the various models. The partial wave analysis of Rayleigh[15] has been used throughout. The bombarding energy has been taken as 31.5 Mev and the nuclear radius has been chosen such that $kR=5$. This value for the nuclear radius is based on various fast neutron scattering cross section measurements for beryllium.[13,16]

1. The Totally Reflecting Sphere

The boundary condition for this case is just that the wave function is zero at the surface of the "nucleus." There is no field external to the "nucleus."

2. The Totally Reflecting Sphere+Coulomb Field

In this case, the boundary condition is again that the wave function is zero at the surface of the "nucleus." The external field is that due to a nuclear charge of 4 (beryllium). We were very fortunate in obtaining a pre-publication copy of the tables of Coulomb wave functions[17] from Dr. Gregory Breit. This table lists the necessary functions from $l=0$ to $l=4$, and values for $l=5$ to $l=7$ were obtained by extrapolation. These higher angular momenta had little effect on the scattering at large angles so that the accuracy of the extrapolation was unimportant.

3. Total Absorption of Partial Waves up to $l=4$

The outgoing part of each partial wave from $l=0$ to $l=4$ is set equal to zero. In turn, the absorption and phase shift for all waves with $l>4$ are set equal to zero. This case corresponds to a semiclassical picture of the nucleus in which the waves corresponding to particles with collision parameters such that they will strike the nucleus are completely absorbed and all others are unaffected. It also corresponds roughly to the optical analogy of a black disk if diffraction at the edges is

[13] Amaldi, Bocciarelli, and Caccipuoti, Nuovo cimento **3**, 15, 203 (1946); translated in Report of Cambridge Conference on Fundamental Particles, pp. 97–113 (Phys. Soc., London, 1947).

[14] A more detailed description, including tables of the phase shifts and amplitudes for the important angular momenta appears in the author's thesis (Princeton University, 1951) and in a project report, "The Scattering of 32 Mev Protons from Several Elements," June, 1951, Palmer Physical Laboratory, Princeton, New Jersey (unpublished).

[15] J. W. Rayleigh, *Theory of Sound* (Dover Publications, New York, 1945), second edition, p. 323; N. F. Mott and H. S. W. Massey, *The Theory of Atomic Collisions* (Oxford University Press, London, 1949), p. 19 ff; D. Bohm, *Quantum Mechanics* (Prentice-Hall, Inc., New York, 1951), Chap. 21, p. 557 ff.

[16] R. Sherr, Phys. Rev. **68**, 240 (1945).

[17] Bloch, Hull, Broyles, Bouricius, Freeman, and Breit, Phys. Rev. **80**, 553 (1950).

ignored.[18] This model is closely related to the picture used in the usual definition of the nuclear radius from scattering experiments, since it gives for both the total scattering and total absorption cross sections

$$\frac{\pi}{k^2}\sum_{l=0}^{kR-1}(2l+1)=\pi R^2.$$

On Fig. 11 the angular distribution for the case of total absorption from $l=0$ to $l=3$ is also given in order to judge the sensitivity to the point at which the cutoff is made.

4. *Square Well*

In this case, a square well with radius $=4.17\times10^{-13}$ cm and depth $=30$ Mev was taken to represent the nucleus. The boundary condition is that the wave function outside the well is continuous with the wave function inside. Owing to the complexity of the numerical calculation, it has not been possible to vary the parameters of the well.

5. *Square Well with Absorption*

For this model, a square well with a complex potential was used. The imaginary part of the potential was chosen to be 6 Mev, which gives a total absorption cross section about equal to the experimental value. The radius and depth of the well were the same as in case 4, above. This case is similar to the partially transparent nuclear model used by Fernbach, Serber, and Taylor[18,19] to explain the results of high energy scattering experiments. The absorption coefficient, for the wave function inside the nucleus, chosen here (corresponding to the 6 Mev imaginary part of the potential) is, however, about twice the value resulting from the adjustment to the high energy scattering results made by Fernbach *et al.*

The boundary condition is again that the wave function be continuous passing from inside to outside the well. The solution inside involves Bessel functions of complex argument, and since tabulations of these functions are not available, a Taylor expansion of the solution was used.

6. *Adjusted Phase Shifts*

The models described give differential cross sections at large angles a factor of 10 or so larger than the experimental values. Although not leading to any specific model, it has been possible, as a result of experience with the above calculations, to specify a set of amplitudes and phase shifts which give an order of magnitude agreement between the calculated and experimental differential cross sections. These amplitudes and phase shifts give, at the same time, about the experimental values for the total cross sections.

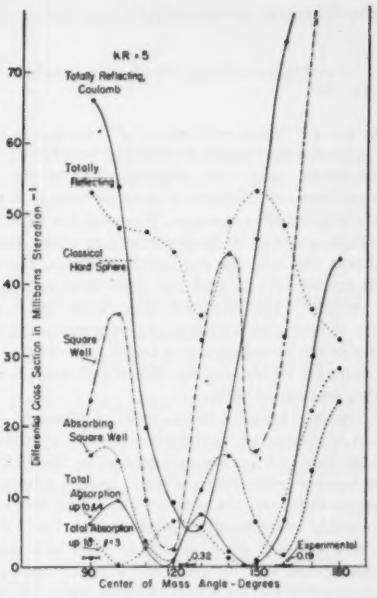

FIG. 11. Calculated angular distributions for elastic scattering into the backward hemisphere for the various models described in the text. The three horizontal bars are the experimental points for beryllium, the length of the bar representing the 6° angular aperture of the counter.

In terms of the phase shift $\delta_l=a_l+ib_l$ the total scattering and absorption cross sections are

$$\sigma_s=\frac{\pi}{k^2}\sum_{l=0}^{\infty}(2l+1)(1+e^{-4b_l}-2e^{-2b_l}\cos 2a_l),$$

$$\sigma_a=\frac{\pi}{k^2}\sum_{l=0}^{\infty}(2l+1)(1-e^{-4b_l}),$$

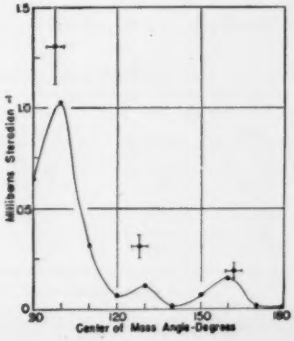

FIG. 12. Differential cross section calculated from the adjusted phase shifts, compared with the experimental values for beryllium.

[18] Fernbach, Serber, and Taylor, Phys. Rev. **75**, 1352 (1949).
[19] S. Pasternack and H. S. Snyder, Phys. Rev. **80**, 921 (1950); R. Serber, Phys. Rev. **72**, 1114 (1947).

and the differential cross section is

$$\frac{d\sigma}{d\omega}=\frac{1}{4k^2}\{|\sum_l(2l+1)\chi_l P_l|^2+|\sum_l(2l+1)y_l P_l|^2\},$$

where $\chi_l=e^{-2b_l}\cos 2a_l-1$ and $y_l=e^{-2b_l}\sin 2a_l$. In principle, within broad limits, it would be possible to solve for the phase shifts and amplitudes, given the total cross sections and differential cross sections at a sufficiently large number of angles. However, for $kR=5$ the set a_l+ib_l consists of twelve numbers which have a significant effect on the angular distribution. (In none of the models investigated has there been any significant contribution to the cross sections for $l>kR$. As a matter of fact, the contributions approach zero quite rapidly in the neighborhood of $l=kR$.) In addition, the equations for $d\sigma/d\omega$ are not linear and contain both the sine and cosine of $2a_l$.

The method followed was to make an educated guess at a set of phases and amplitudes controlled by the total cross sections and, for a starting point, by the idea that if the nuclear potential were softer than a square well the phase shifts and absorption for $l=2$ and $l=6$ would be smoothly converging. Total absorption for $l=0$ and $l=1$ was assumed for convenience since this seemed reasonable and had no great influence on the result. It was possible by inspection of the resulting $d\sigma/d\omega$ to judge which $P_l(\cos\theta)$ was predominant and to make small corrections in the phase shifts. Actually, two corrections were sufficient to bring the $d\sigma/d\omega$ to the result shown in Fig. 12. Further slight corrections, of the order of 10 percent in x_l and y_l could be made which would reduce the average value of $d\sigma/d\omega$ in the region shown by a factor of five and have almost any desired effect on the shape of the angular distribution, without importantly influencing the total cross sections. It did not seem valuable to make further adjustments in view of the possible effect of the Coulomb field, the small number of angles for which data are available, and the limited accuracy with which the total cross sections are known.

An extreme sensitivity to the individual phase shifts of the differential cross section for backscattering results from the small value of the cross section. Almost complete cancellation has occurred in both parts of the expression for $d\sigma/d\omega$.

It appears, from this result, that fairly rough experimental results on the backscattering of neutrons could lead to accurate determination of the phases and amplitudes for the different angular momentum waves. This will be particularly true if the cross sections for backscattering are as low as would be indicated by the proton scattering results reported here. Given the phases and amplitudes, for several bombarding energies, considerable insight into the structure of a complex nucleus might be obtained.

The author is grateful to the Chairman and members of the Department of Physics at Princeton University for generous advice and assistance at all points and for making possible the trip to Berkeley to carry out the experimental work, and to the Radiation Laboratory of the University of California, in particular to Dr. Luis Alvarez for the opportunity to use the linear accelerator.

Professors Rubby Sherr and H. W. Fulbright have given many hours of advice and assistance without which this work would not have been completed. Dr. David Bohm has given a great deal of assistance on the calculations.

The Coulomb Scattering of Relativistic Electrons and Positrons by Nuclei*

HERMAN FESHBACH
Department of Physics and Laboratory for Nuclear Science and Engineering, Massachusetts Institute of Technology, Cambridge, Massachusetts
(Received June 25, 1952)

The Mott series for the Coulomb scattering of electrons and positrons of high energy is summed numerically for angles varying from 30° to 150° and for nuclear charge varying from 13 to 80.

INTRODUCTION

MEASUREMENT of the deviations from the Coulomb scattering of electrons by point nuclei is of great physical interest. In the low energy range, where the electron wavelength is much greater than the nuclear radius, such deviations measure the radiative correction to scattering and thus form the basis of another test of quantum electrodynamics. Recent measurements by both Paul and Reich[1] and Kinzinger and Bothe[2] indicate that for scattering angles greater than 60° a discrepancy exists between theory and experiment. In the higher energy range, where the electron wavelength is of the same order or smaller than the nuclear radius, scattering experiments should furnish information on nuclear charge and current distributions. Such experiments have been recently performed by Lyman, Hanson, and Scott[3] at 15.7 Mev. At the much higher energies available with synchrotrons, the large angle scattering will be sensitive to the charge and current distribution of the nucleons forming the nucleus.[4]

The theoretical cross sections for Coulomb scattering, which are clearly essential for the above studies, have been given by Mott[5] in the form of a conditionally convergent series. Bartlett and Watson[6] have summed the series numerically for Hg($Z=80$) for a range of energies up to $(v/c)\cong 1$; Massey[7] has employed their results to evaluate the corresponding cross section for the scattering of positrons. McKinley and Feshbach[8] have expanded the Mott series in a power series in α and α/β where

$$\alpha=(Ze^2/\hbar c), \quad \beta=v/c, \tag{1}$$

the coefficients depending only on ϑ, the angle of scattering. The series is accurate up to middle Z elements. For light Z they obtained the following formula, since verified by Dalitz,[9] by the second Born approximation:

$$\sigma=\sigma_R[1-\beta^2\sin^2\tfrac{1}{2}\vartheta+\pi\alpha\beta\sin\tfrac{1}{2}\vartheta(1-\sin\tfrac{1}{2}\vartheta)], \tag{2}$$

where σ_R is the Rutherford cross section,

$$\sigma_R=(Ze^2/2m_0c^2)^2(1-\beta^2)/\beta^4\csc^4\tfrac{1}{2}\vartheta. \tag{3}$$

In the present paper, the Mott series is evaluated for $\beta\simeq 1$, for $Z=13$, 29, 47, 62, 80 for $\vartheta=30°$, 45°, 60°, 80°, 90°, 100°, 135°, 150° for both electron and positron scattering. These results should be adequate for electron energies greater than 4 Mev.

THEORY

Mott's result for the differential scattering cross section is

$$\sigma=\lambda^2\{q^2(1-\beta^2)|F|^2\csc^2\tfrac{1}{2}\vartheta+|G|^2\sec^2\tfrac{1}{2}\vartheta\}, \tag{4}$$

where $q=(\alpha/\beta)$. The functions F and G are defined as follows:

$$\begin{aligned}
&F=F_0+F_1, \quad G=G_0+G_1,\\
&F_0=(i/2)\exp[iq\ln\sin^2\tfrac{1}{2}\vartheta]\Gamma(1-iq)/\Gamma(1+iq),\\
&G_0=-iqF_0\cot^2\tfrac{1}{2}\vartheta,\\
&F_1=i/2\sum_{k=0}^{\infty}[kD_k+(k+1)D_{k+1}](-)^kP_k(\cos\vartheta),\\
&G_1=i/2\sum_{k=0}^{\infty}[k^2D_k-(k+1)^2D_{k+1}](-)^kP_k(\cos\vartheta),
\end{aligned} \tag{5}$$

where Γ is the gamma-function and P_k the Legendre

TABLE I. Comparison of values for G_1.

ϑ	Re G_1 B and W[a]	Re G_1 Euler transformation	Im G_1 B and W	Im G_1 Euler transformation
30°	1.349	1.349	−0.026	−0.027
45°	0.851	0.851	0.292	0.290
60°	0.538	0.538	0.331	0.330
90°	0.213	0.213	0.227	0.228
130°	0.0734	0.0735	0.107	0.107
150°	0.0159	0.0158	0.0272	0.0272

[a] J. H. Bartlett and R. E. Watson (see reference 6).

* This work has been supported in part by the joint program of the ONR and AEC.

[1] W. Paul and H. Reich, Z. Physik **131**, 326 (1952).
[2] E. Kinzinger and W. Bothe (to be published).
[3] Lyman, Hanson, and Scott, Phys. Rev. **84**, 626 (1951).
[4] Amaldi, Dedecaro, and Mariani, Nuovo cimento **I**, 757 (1950).
[5] N. F. Mott, Proc. Roy. Soc. (London) **A124**, 426 (1929); N. F. Mott, Proc. Roy. Soc. (London) **A135**, 429 (1932).
[6] J. H. Bartlett and R. E. Watson, Proc. Am. Acad. Arts Sci. **74**, 53 (1940).
[7] H. S. W. Massey, Proc. Roy. Soc. (London) **A181**, 14 (1942).
[8] W. A. McKinley, Jr., and H. Feshbach, Phys. Rev. **74**, 1759 (1948).
[9] R. H. Dalitz, Proc. Roy. Soc. (London) **A206**, 509 (1951).

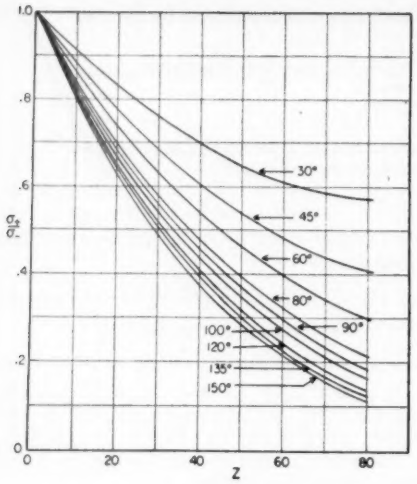

FIG. 1. The ratio of positron to electron scattering (note that β is taken to be one).

polynomial of order k. The coefficients D_k are

$$D_k=\frac{e^{-\pi ik}}{k+iq}\frac{\Gamma(k-iq)}{\Gamma(k+iq)}-\frac{e^{-\pi i\rho_k}}{\rho_k+iq}\frac{\Gamma(\rho_k-iq)}{\Gamma(\rho_k+iq)}, \tag{6}$$

where

$$\rho_k=(k^2-\alpha^2)^{\frac{1}{2}}.$$

The D_k coefficient may be expressed in terms of phases and amplitudes of the complex numbers in (6) as follows:

$$(-)^kD_k=(k^2+q^2)^{-\frac{1}{2}}\exp\{-i[\tan^{-1}(q/k)+2\eta_k]\}$$
$$-(\rho_k^2+q^2)^{-\frac{1}{2}}\exp\{-i[\pi(\rho_k-k)$$
$$+\tan^{-1}(q/\rho_k)+2\sigma_k]\}, \tag{7}$$

where

$$\eta_k=\text{phase}\Gamma(k+iq),\quad \sigma_k=\text{phase}\Gamma(\rho_k+iq).$$

In evaluating D_k we have placed $\beta=1$, that is, $q=\alpha$, from which it follows that

$$\rho_k^2+q^2=k^2,\quad \tan^{-1}(q/\rho_k)=\sin^{-1}(\alpha/k),\quad \text{for}\quad \beta=1.$$

The phases η_k were evaluated for nearly all k by Stirling's approximation which gives the following

TABLE II. Values of the function G defined in Eq. (5).

Z	Real G	Imag G	$\lvert G\rvert^2\sec^2\frac{1}{2}\vartheta$	Real G	Imag G	$\lvert G\rvert^2\sec^2\frac{1}{2}\vartheta$	Real G	Imag G	$\lvert G\rvert^2\sec^2\frac{1}{2}\vartheta$
		$\vartheta=30°$			$\vartheta=45°$			$\vartheta=60°$	
−80	−1.222	−3.512	14.82	−0.980	−1.146	2.664	−0.614	−0.444	0.765
−62	−1.785	−2.281	8.99	−0.965	−0.678	1.628	−0.541	−0.244	0.470
−47	−1.759	−1.352	5.27(5)	−0.824	−0.376	0.961	−0.439	−0.127	0.278
−29	−1.296	−0.521	2.091	−0.558	−0.136	0.386	−0.288	−0.042	0.113
−13	−0.634	−0.104	0.442	−0.265	−0.026	0.0831	−0.136	−0.007	0.0247
13	0.675	−0.102	0.499	0.288	−0.023	0.0978	0.150	−0.005	0.0303
29	1.514	−0.504	2.729	0.680	−0.110	0.556	0.364	−0.019	0.177
47	2.395	−1.303	7.97	1.183	−0.270	1.725	0.657	−0.028	0.576
62	2.996	−2.223	14.92	1.656	−0.439	3.439	0.957	−0.008	1.221
80	3.405	−3.537	25.83	2.270	−0.649	6.530	1.382	0.095	2.559
		$\vartheta=80°$			$\vartheta=90°$			$\vartheta=100°$	
−80	−0.320	−0.142	0.209	−0.230	−0.082(5)	0.119	−0.164	−0.048	0.0707
−62	−0.266	−0.070	0.129	−0.188	−0.038	0.0736	−0.133	−0.020	0.0438
−47	−0.210	−0.032	0.0769	−0.148	−0.016	0.0443	−0.104	−0.007	0.0263
−29	−0.136	−0.007	0.0316	−0.095	−0.002	0.0181	−0.067	0.001	0.0109
−13	−0.064	−0.001	0.0070	−0.045	0.000	0.0040	−0.031	0.000(4)	0.0023
13	0.072	0.000(5)	−0.0088	0.051	0.001	0.0052	0.036	0.001	0.0031
29	0.177	0.008	0.0535	0.126	0.010	0.0320	0.089	0.010	0.0194
47	0.327	0.040	0.185	0.233	0.043	0.112	0.166	0.039	0.0704
62	0.484	0.107	0.419	0.346	0.107	0.262	0.246	0.095	0.168
80	0.706	0.279(5)	0.982	0.502	0.266	0.646	0.354	0.230	0.431
		$\vartheta=120°$			$\vartheta=135°$			$\vartheta=150°$	
−80	−0.078	−0.015	0.025	−0.040	−0.006	0.011	−0.017	−0.0023	0.0044
−62	−0.063	−0.005	0.016	−0.032	−0.001	0.0070	−0.013(5)	−0.000	0.0026
−47	−0.049	−0.001	0.0096	−0.025	0.000	0.0043	−0.010(3)	0.000	0.0015
−29	−0.031	0.001	0.0038	−0.016	0.000	0.0017	−0.007	−0.001	0.0007
−13	−0.015	0.000(4)	0.0009	−0.008	0.000	0.0004	−0.003	0.0001	0.0001
13	0.017	0.001	0.0012	0.009	0.001	0.0006	0.004	0.0003	0.0002
29	0.043	0.007	0.0076	0.022	0.004	0.0034	0.009	0.002	0.0013
47	0.080	0.025	0.0281	0.041	0.015	0.0130	0.017	0.007	0.0050
62	0.117	0.060	0.0692	0.060	0.035−	0.0329	0.025	0.016	0.0132
80	0.164	0.142	0.188	0.083	0.082(5)	0.0935	0.034	0.037	0.0377

TABLE III. Values of the function F defined in Eq. (5).

Z	Real F	$\vartheta=30°$ Imag F	$\lvert F\rvert^2\csc^4\frac{1}{2}\vartheta$	Real F	$\vartheta=45°$ Imag F	$\lvert F\rvert^2\csc^4\frac{1}{2}\vartheta$	Real F	$\vartheta=60°$ Imag F	$\lvert F\rvert^2\csc^4\frac{1}{2}\vartheta$
−80	−0.4841	0.1889	4.031	−0.3825	0.3661	1.914	−0.2821	0.4585	1.1592
−62	−0.3939	0.3290	3.932	−0.2778	0.4392	1.844	−0.1849	0.4920	1.1050
−47	−0.2989	0.4108	3.853	−0.1936	0.4741	1.791	−0.1164	0.5027	1.0650
−29	−0.1789	0.4703	3.780	−0.1050	0.4939	1.741	−0.0536	0.5038	1.0267
−13	−0.0767	0.4947	3.741	−0.0411	0.4994	1.715	−0.0167	0.5012	1.0059
13	0.0703	0.4956	3.740	0.0320	0.5000	1.714	0.0053	0.5015	1.0061
29	0.1484	0.4792	3.757	0.0602	0.5008	1.737	−0.0036	0.5076	1.0307
47	0.2266	0.4468	3.747	0.0795	0.5020	1.764	−0.0336	0.5171	1.0741
62	0.2844	0.4051	3.657	0.0878	0.4988	1.752	−0.0740	0.5202	1.1043
80	0.3436	0.3298	3.386	0.0932	0.4780	1.619	−0.1353	0.5007	1.0760
		$\vartheta=80°$			$\vartheta=90°$			$\vartheta=100°$	
−80	−0.1737	0.5208	0.7295	−0.1303	0.5382	0.6133	−0.0932	0.5503	0.5309
−62	−0.0924	0.5248	0.6873	−0.0565	0.5331	0.5748	−0.0264	0.5384	0.4952
−47	−0.0424	0.5190	0.6563	−0.0142	0.5227	0.5468	0.0094	0.5247	0.4693
−29	−0.0055	0.5088	0.6266	0.0127	0.5097	0.5199	0.0280	0.5100	0.4446
−13	0.0059	0.5019	0.6098	0.0145	0.5020	0.5044	0.0216	0.5020	0.4303
13	−0.0200	0.5018	0.6104	−0.0296	0.5017	0.5052	−0.0378	0.5015	0.4310
29	−0.0653	0.5078	0.6344	−0.0892	0.5064	0.5288	−0.1094	0.5045	0.4541
47	−0.1466	0.5124	0.6875	−0.1908	0.5056	0.5841	−0.2283	0.4978	0.5111
62	−0.2403	0.5022	0.7502	−0.3059	0.4848	0.6572	−0.3615	0.4654	0.5918
80	−0.3773	0.4446	0.8230	−0.4726	0.4005	0.7675	−0.5531	0.3530	0.7337
		$\vartheta=120°$			$\vartheta=135°$			$\vartheta=150°$	
−80	−0.0358	0.5643	0.4263	−0.0052	0.5696	0.3801	0.0160	0.5724	0.3514
−62	0.0198	0.5437	0.3947	0.0441	0.5452	0.3505	0.0608	0.5457	0.3231
−47	0.0454	0.5261	0.3718	0.0643	0.5261	0.3291	0.0773	0.5257	0.3026
−29	0.0512	0.5097	0.3499	0.0633	0.5092	0.3085	0.0716	0.5087	0.2828
−13	0.0326	0.5017	0.3370	0.0384	0.5015	0.2964	0.0424	0.5014	0.2714
13	−0.0503	0.5009	0.3379	−0.0570	0.5005	0.2973	−0.0616	0.5003	0.2723
29	−0.1407	0.5004	0.3603	−0.1572	0.4976	0.3190	−0.1687	0.4955	0.2936
47	−0.2865	0.4816	0.4187	−0.3174	0.4712	0.3781	−0.3387	0.4631	0.3528
62	−0.4474	0.4269	0.5099	−0.4928	0.4023	0.4741	−0.5240	0.3835	0.4519
80	−0.675(3)	0.2608	0.6987	−0.7385	0.2022	0.6869	−0.7812	0.1578	0.6808

asymptotic series:

$$\eta_k \cong (q/2)\ln(k^2+q^2)+(k-\tfrac{1}{2})\tan^{-1}(q/\rho_k) - q[1+(1/12)(k^2+q^2)^{-1} - (1/360)(3k^2-q^2)(k^2-q^2)^{-3}]. \quad (8)$$

To obtain σ_k replace k by ρ_k in Eq. (8). Equation (8) could almost always be employed down to $k=2$ with little error. For $k=1$, the standard formula given by Jahnke-Ende[10] or the gamma-function recurrence relation was employed.

The values of D_k so obtained were inserted into the series for F_1 and G_1 which were then summed numerically. Since the series are only conditionally convergent, a summation method appropriate to a series being evaluated on its circle of convergence was employed. This is the Euler transformation,[11] which was found to be accurate in reference 8. Another check is provided by comparison with Bartlett and Watson's results for $Z=80$, as given in Table I.

The B and W values will differ somewhat from the values they quote because we have included several more terms in the infinite series they needed to sum. It was also necessary to extrapolate in β to $\beta=1$.

The results of these calculations are given in Tables II and III. The negative Z refers to positron scattering, the positive Z to electron scattering. In Fig. 1 we plot the ratio of the cross section for positron scattering to that for electron scattering. We note that this ratio is less than one, decreasing as either ϑ or Z increases. Effects of this kind have been observed by Lipkin and White.[12]

[10] E. Jahnke and F. Ende, *Funktionlafeln* (B. G. Teubner, Leipzig, 1933).

[11] See, for example, T. J. I. 'A, Bowmwich, *Introduction to the Theory of Infinite Series* (The MacMillan Company, New York, 1947).

[12] H. J. Lipkin and M. G. White, Phys. Rev. **79**, 892 (1950).

Deuteron Bombardment of Be^9 and Classification of Levels of B^{10}†

FAY AJZENBERG*
University of Wisconsin, Madison, Wisconsin
(Received June 17, 1952)

Previous measurements on the $Be^9(d,n)B^{10}$ neutron spectrum at 0° and 80° have been extended to 10°, 30°, and 45° to check the energy level assignments and to deduce the parity of the levels from a Butler analysis of the angular distributions. The observed neutron groups correspond to levels of B^{10} at 0.72, 1.75, 2.15, 3.53, 4.78, 5.14 (doublet), 5.37 (?), 5.58, 5.72 (?), 5.93, 6.12 (possibly doublet), 6.38, 6.58, and 6.77 Mev. The estimated uncertainty is 0.06 Mev for the first five states of B^{10} and 0.04 Mev for the higher energy levels. The Butler analysis of the angular distribution data indicates that the ground state and the first four excited states of B^{10} are of even parity and that both components of the 5.14-Mev doublet are probably odd parity states. Parity assignments for some of the other energy levels have been attempted. The spins of these states cannot be uniquely determined on the basis of the Butler analysis, but the possible spin limits are listed. A $Be^9(d,p)Be^{10}$ exposure was also made. There do not appear to be any states in Be^{10} between the ground state and the known 3.37-Mev level.

INTRODUCTION

IN the past couple of years, a great deal of progress has been made in the determination of the values of the excitation energies of light nuclei. While large energy regions in various nuclei[1] are still unexplored, it is desirable to attempt a more complete description of particular states in the hope that it may contribute to an understanding of nuclear structure and nuclear forces.

There are a number of methods available for the determination of spins and parities. The one with which this investigation is concerned is the deuteron stripping theory of Butler.[2] The theory has been applied in this work to the angular distributions of neutrons resulting from the deuteron bombardment of Be^9.

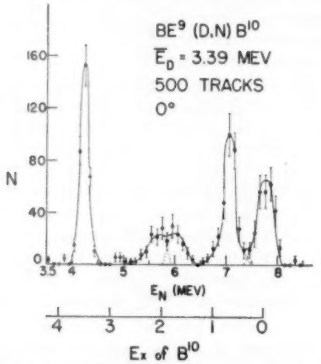

FIG. 1. 0° data. N is the relative number of neutrons/100-kev interval.

EXPERIMENTAL PROCEDURES—(d,n) EXPOSURE

Deuterons from the Wisconsin electrostatic generator, after passing through the 1-meter cylindrical analyzer and a $\frac{1}{8}$-inch defining aperture in 0.01-inch tantalum, struck a thin Be^9 metallic target[3] mounted on a tantalum backing. The average deuteron energy was 3.39 Mev. The resulting neutrons were observed by means of NTA (Eastman-Kodak) emulsions, 200 microns thick, mounted 10 centimeters from the target, and at angles of 0°, 10°, 30°, 45°, and 80° to the incident beam.

The following processing technique, suggested by Mrs. M. J. Wilson Laubenstein, was employed: The plates, supported in a Lucite holder, were immersed in a solution of 1 part D-19 and 1 part distilled water. This solution was at 5°C. After 30 minutes, 4 parts of distilled water at room temperature (approximately 22°C) were added. The plates remained in this mixture of 1 part D-19 to 5 parts distilled water for 30 minutes, and were then placed in a solution of 1.5 percent acetic acid at 5°C for another thirty minutes. After this stopping treatment, the plates were transferred to a hypo solution (30 percent sodium hyposulfite by weight, 70 percent distilled water) for a length of time 1.5 times the period necessary for clearing the emulsion. The plates were then washed in running water for about 6 hours, dipped in a solution of 50 percent ethyl alcohol and 50 percent water for a couple of minutes, and then allowed to dry in a reasonably dust-free room.

The acceptance criteria that were applied to the proton recoil tracks are similar to the ones discussed in a paper by Johnson, Laubenstein, and Richards.[4] The range-energy relation used to compute the energy of

† Work supported by the Wisconsin Alumni Research Foundation and by the AEC.
* Now at the Department of Physics, Smith College, Northampton, Massachusetts, and the High Voltage Laboratory, Building 46, Massachusetts Institute of Technology, Cambridge, Massachusetts.
[1] Hornyak, Lauritsen, Morrison, and Fowler, Revs. Modern Phys. 22, 291 (1950).
[2] S. T. Butler, Proc. Roy. Soc. (London) A208, 559 (1951).
[3] The foil was kindly furnished by Dr. Hugh Bradner. Its thickness corresponds to a stopping power of approximately 50 kev for deuterons of 3.5 Mev.
[4] Johnson, Laubenstein, and Richards, Phys. Rev. 77, 413 (1950).

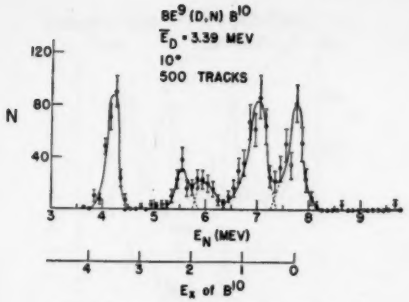

FIG. 2. 10° data. N is the relative number of neutrons/100-kev interval.

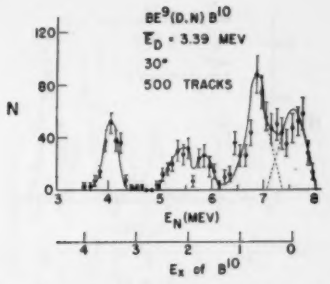

FIG. 4. 30° data, E_n<4 Mev. N is the relative number of neutrons/100-kev interval.

the recoil protons has been discussed previously.[5] The data, after being corrected for geometry[6] and for variation of the neutron-proton scattering cross section,[7] is plotted as relative number of neutrons/energy interval (N) *versus* the neutron energy. For the angular distribution data, the total number of neutrons in a given group is usually obtained by adding the corrected experimental ordinates. In some cases, neutron groups have not been completely resolved, and thus decisions have had to be made as to whether neutrons were part of one group or of another. Whenever the choice has not been obvious, dotted lines on the data plots show the lines of demarcation. The uncertainties indicated for the angular distribution points are statistical uncertainties only. They do not include possible errors in the assignment of the neutrons to the group.

The total number of neutrons in a given group, at a given laboratory angle, were then converted to the center-of-mass system values by means of Moskow's tables.[8] The relative number of neutrons is then corrected for the different areas scanned at the various angles. A $1/r^3$ correction is not necessary since strips of approximately equal lengths are scanned at all angles, the only varying parameter being the number of strips. Thus angular distribution points may be plotted. These are directly proportional to the differential cross section for the reaction to a given state of B^{10}, and therefore comparison may be made with Butler's theoretical curves.

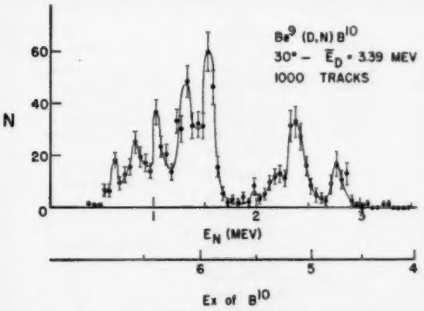

FIG. 3. 30° data, E_n>4 Mev. N is the relative number of neutrons/50-kev interval.

EXPERIMENTAL RESULTS—(d,n) EXPOSURE

The results of a first exposure on the $Be^9(d,n)B^{10}$ reaction, carried out under conditions similar to the ones in this exposure, but with plates exposed only at 0° and 80°, have been reported previously.[9] This first exposure will be designated throughout the remainder

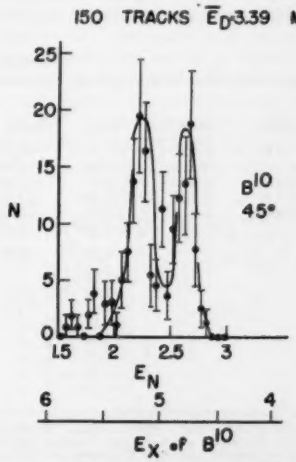

FIG. 5. 45° data, 4.5 Mev<E_n<5.8 Mev. N is the relative number of neutrons/50-kev interval.

[5] Richards, Johnson, Ajzenberg, and Laubenstein, Phys. Rev. **83**, 994 (1951).
[6] H. T. Richards, Phys. Rev. **59**, 796 (1941).
[7] R. K. Adair, Revs. Modern Phys. **22**, 249 (1950).
[8] Morris Moskow, unpublished Master's essay, The Johns Hopkins University (1948).
[9] Fay Ajzenberg, Phys. Rev. **82**, 43 (1951).

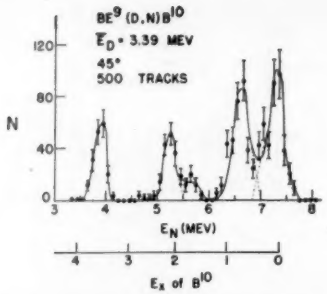

FIG. 6. 45° data, $E_x < 4$ Mev. N is the relative number of neutrons/100-kev interval.

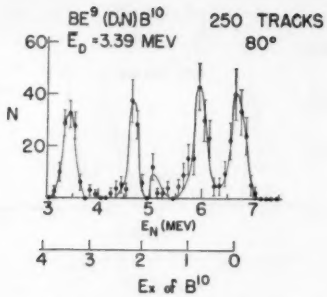

FIG. 7. 80° data. N is the relative number of neutrons/100-kev interval.

of the paper by I, and the present exposure by II. Exposure II was made primarily to obtain the angular distributions of the neutrons from the first five states of B^{10}, because from I it was known that the first five states could be resolved fairly satisfactorily. Therefore, only "long" tracks were measured at 0°, 10°, and 80°. At 30° and 45° shorter tracks were also measured to aid in checking on some "doubtful" high energy levels tentatively identified during the scanning of I. Five hundred "long" tracks have been measured on each of the following plates: II–0°, II–10°, II–30°, and II–45°. Two-hundred and fifty long tracks have been measured on II–80°. In addition, 1000 short tracks have been measured on II–30°, and 150 tracks corresponding to 4.5 Mev $\leq E_x \leq$ 5.8 Mev have been measured at 45°. The data are shown as Figs. 1–7.

A secondary scale, showing the excitation energy (E_x) of the B^{10} nucleus, has been drawn on all the data figures so that the value of the energy level corresponding to a given neutron group can be seen directly.

The same groups, some of which were quite doubtful from the original 0° and 80° data (exposure I), have been observed again at the various angles. Better values of the energies of these levels are available from a combination of the new and the old data (Table I). There is indication from the 30° data (Fig. 3) of a previously unreported group corresponding to a level at approximately 5.37 Mev. At other angles, this group, if it is real, is submerged in the low energy tail of the 5.14-Mev doublet.[10] The level at 5.58 Mev, listed as uncertain in I, apparently reappears at 30° and 45°, but its neutron groups remain low in intensity. A very "weak" level at 5.72 Mev, suggested by I, cannot be either supported or excluded on the basis of the 30° and the 45° data. The doubtful 6.38-Mev level, sug-

TABLE I. Q-values of states of B^{10}.

I-0°	II-0°	II-10°	II-30°	II-45°	I-80°	II-80°	Av. Q from present data	Other Q-values	B^{10} energy levels
+4.33	+4.40	+4.36	+4.35	+4.31	+4.29	+4.44	+4.35±0.06	+4.363±0.016[a]	0
+3.59	+3.68	+3.69	+3.66	+3.59	+3.60	+3.67	+3.64±0.06	+3.644±0.016[b]	0.72
+2.57	+2.65	+2.63	+2.61	+2.61	+2.54	+2.69	+2.61±0.06	+2.627±0.016[c]	1.74
+2.16	+2.29	+2.20	+2.20	+2.26	+2.11	+2.24	+2.21±0.06	+2.223±0.015[c]	2.15
+0.78	+0.92	+0.88	+0.75	+0.86	+0.75	+0.90	+0.83±0.06	+0.779±0.030[c]	3.58
−0.44	—	—	−0.40	−0.40	−0.43	—	−0.42±0.04		4.78
−0.76	—	—	−0.79	−0.80	−0.78	—	−0.78±0.04	−0.752±0.016[d]	5.12
								−0.805±0.016	5.17
—	—	—	−1.01	—	—	—	−1.01±0.04		5.37
−1.24	—	—	−1.17	−1.23	−1.22	—	−1.22±0.04		5.58
−1.35	—	—	—	−1.41	−1.33	—	−1.36±0.04		5.72
−1.55	—	—	−1.57	—	−1.58	—	−1.57±0.04	−1.566±0.017[d]	5.93
−1.73	—	—	−1.79	—	−1.77	—	−1.76±0.04		6.12
−2.03	—	—	−2.02	—	−2.00	—	−2.02±0.04		6.38
−2.22	—	—	−2.21	—	−2.22	—	−2.22±0.04		6.58
−2.45	—	—	−2.38	—	—	—	−2.41±0.04		6.77

[a] Computed from $Q = (2D - He^6) - (Q_d + Q_{dp} + Q_{da})$. The details of this computation are given in reference 5.
[b] Computed from reference a and from Craig, Donahue, and Jones, Phys. Rev. **87**, 206 (1952).
[c] Computed from reference b and from Rasmussen, Hornyak, and Lauritsen, Phys. Rev. **76**, 581 (1949); and Chao, Lauritsen, and Rasmussen, Phys. Rev. **76**, 582 (1949).
[d] Computed from references 10 and a.

[10] T. W. Bonner and J. W. Butler's work [Phys. Rev. **83**, 1091 (1951)] has indicated the existence of two levels at 5.115 and 5.168 Mev. The energy of these levels has been recalculated on the basis of the best known Q-value for the $Be^9(d,n)B^{10}$ reaction (see Table I).

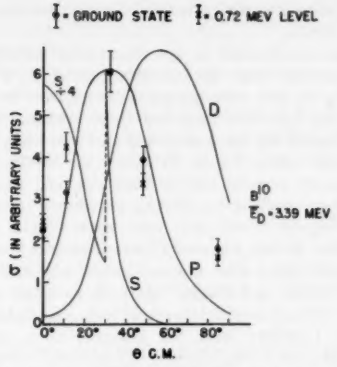

FIG. 8. Angular distributions of neutrons from the ground state and the 0.72-Mev state of B^{10} and the theoretical Butler curves.

gested by I, is well resolved, and its neutron group is fairly intense at 30° in the present exposure.

The standard deviation is 60 kev or less for the first five states of B^{10}, and 30 kev or less for the higher energy levels. The estimated uncertainty shown in Table I is based on the standard deviation and is larger than the standard deviation in the case of the high energy levels which were observed at relatively few angles.

ANALYSIS OF THE ANGULAR DISTRIBUTION DATA

One of the main reasons for exposure II was the possibility of observing the angular distributions of the neutrons from the first five states of B^{10}. It was hoped that by plotting the Butler curves for the various states, and by comparing the angular distributions with these curves, the parity of the five states could be determined.

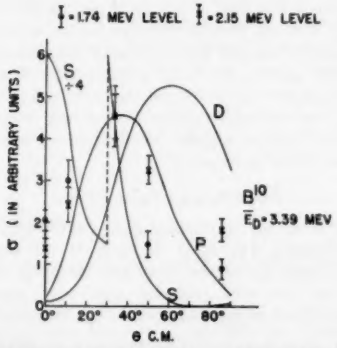

FIG. 9. Angular distributions of neutrons from the 1.74-Mev and the 2.15-Mev states and the theoretical Butler curves.

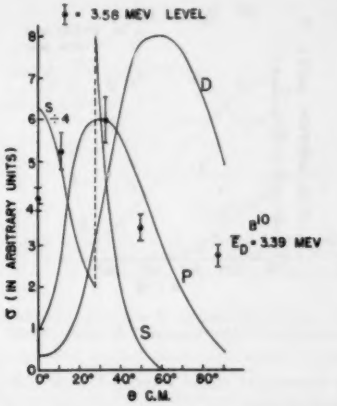

FIG. 10. Angular distributions of neutrons from the 3.58-Mev state and the Butler curves.

Equation 34 of Butler's paper[2] has been used in the calculation of the theoretical curves. "r_0" has been taken to be 4.53×10^{-13} cm by appropriate substitution in the formula

$$r_0=1.47\times10^{-13}(A^{\frac{1}{3}}+1)\text{ cm}.$$

To test the sensitivity of shape to choice of r_0, some curves were also calculated for a 20 percent larger r_0. The shape was qualitatively unaffected, and the peaks were shifted to smaller angles by only a few degrees. Such a small shift is not sufficient to lead to confusion as to which curve best fits given experimental data.

No attempt has been made to evaluate any of the constant multiplicative factors in Butler's equation. The ordinates in Figs. 8–12 are therefore arbitrary, but the units used are the same for all the figures.

The "shape" of the experimental points determines the choice of the Butler curve which best fits it. The ordinate scale was then adjusted so that the maximum

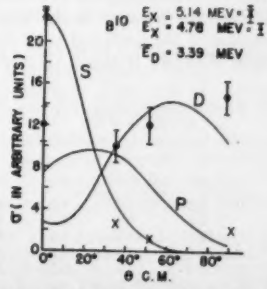

FIG. 11. Angular distributions of neutrons from the 4.78-Mev state and the 5.14-Mev doublet and the Butler curves.

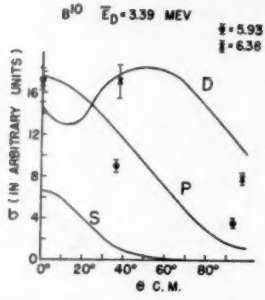

FIG. 12. Angular distributions of neutrons from the 5.93-Mev and the 6.38-Mev states and the Butler curves.

of the theoretical curve coincided with the highest experimental point.

Since the ground state of Be^9 is believed to have odd parity, then, because of conservation of parity, the angular distributions of the neutrons fix the parity of the final states in B^{10} as odd or even, depending upon whether the angular momentum transfer is even or odd.

Figures 8, 9, and 10 show the Butler curves as well as the experimental points for the ground state, and for the 0.72, 1.74, 2.15, and 3.58 Mev levels (data from both exposure I and exposure II are incorporated in the points). All these points fit the corresponding $P(l_p=1)$ curve which means that these B^{10} levels are of even parity. Table II shows the relative number of neutrons per unit solid angle as a function of angle. It also indicates the relative total cross section for each level.

An attempt was also made to ascertain the parity of some of the higher energy levels. Measurements of the neutrons from the 4.78-Mev level have been carried out at I-0°, II-30°, II-45°, and I-80°. Figure 11 shows the corresponding Butler curves and the experimental points. These points do not seem to fit any one of the curves. Some possible explanations are: (1) Compound nucleus formation may be more likely than stripping. (2) There may be two closely spaced levels which were not resolved in the neutron work. (3) A combination of the $l_p=0$ and $l_p=2$ distributions may have been observed. If this is the correct explanation, then the parity is fixed as odd and the J is either 1 or 2.

It was also decided to plot the angular distribution of the neutrons from the 5.14-Mev doublet. At 0°, 45°, and 80°, the data may include some neutrons from an unresolved 5.37-Mev level, but these neutrons should be comparatively few and should thus not bring in an appreciable error. Figure 11 shows the results. It is immediately obvious that at least one, and probably both, of the levels in the doublet are formed by s-wave proton capture ($l_p=0$) and hence have $J=1$ or 2 and odd parity. In fact, the strong forward neutron bunching associated with s-wave proton capture is probably the reason Bonner and Butler[10] see both members of the doublet by their neutron threshold technique but do not see the 4.78-Mev level, for instance, as a neutron threshold.

It was not possible to resolve completely any of the other high energy levels except, possibly, the 5.93- and the 6.38-Mev levels which were observed at I-0°, II-30°, and I-80°. Figure 12 shows the Butler curves and the experimental points for both levels. The 5.93-Mev level points could fit either the S or the P curve, and therefore nothing can be said about the parity of this state. The 6.38-Mev level seems, perhaps, to fit the D curve, and thus it may be of odd parity.

While it is not possible to make unique spin assignments on the basis of Butler's theory since the spin of the target nucleus Be^9 is $\frac{3}{2}$,[11] conservation of angular momentum places limits on the maximum and minimum angular momentum available to the final state. For protons of orbital angular momentum l_p which are captured, these limits are

$$|J+j+s_p|_{\min} \leq l_p \leq J+j+s_p,$$

where J is the spin of the final state, j is the spin of the target nucleus, and s_p is the spin of the captured proton. Table III shows these spin limits as well as guesses of the most probable spin value whenever possible. These suggestions (made by Richards[12]) are

TABLE II. Relative number of neutrons from the first five states of B^{10}.

Angle	E_x of B^{10} (Mev) 0	0.72	1.74	2.15	3.58
0°	5.2	5.7	1.6	1.6	4.6
10°	7.4	9.7	2.7	2.4	6.0
30°	14.1	13.8	3.4	5.2	6.9
45°	9.1	7.7	1.5	3.3	3.9
80°	4.2	3.7	0.7	2.1	3.2
Relative total cross section	4.4	4.1	0.9	1.7	2.3

TABLE III. Spins and parities of states of B^{10}.

E_x of B^{10} (Mev)	Butler spin limits	Parity	Probable spins[a]
0	0, 1, 2, 3	even	3[b]
0.72	0, 1, 2, 3	even	1
1.74	0, 1, 2, 3	even	0
2.15	0, 1, 2, 3	even	1
3.58	0, 1, 2, 3	even	2
4.78	? (see text)	?	0, 1, 2
5.14(*d*)	1, 2	odd	
5.93	0, 1, 2, 3	?	
6.38	0, 3, 4	odd	

[a] See reference 12.
[b] Spin measured by Gordy, Ring, and Burg, Phys. Rev. **74**, 1191 (1948).

[11] N. A. Schuster and G. E. Pake, Phys. Rev. **81**, 886 (1951).
[12] H. T. Richards, unpublished University of Pittsburgh conference on Medium-Energy Nuclear Physics, June, 1952.

based on the known gamma-ray intensities and on the known allowed gamma-ray transitions[13] as well as on beta-decay evidence.

El-Bedewi[14] has interpreted his data on the angular distributions of the protons from the $Be^9(d,p)Be^{10}$ reaction as showing that the first excited state of Be^{10} at 3.37 Mev is of even parity. It is not clear that his results exclude the possibility of this state being of odd parity. If the 3.37-Mev level in Be^{10} is of even parity, then an analogous state in B^{10} (which should appear at about 5.1 Mev) has not been observed unless the corresponding state in B^{10} has been greatly shifted in energy. It would be extremely useful if the question of the parity of the 3.37-Mev state in Be^{10} were reinvestigated.

EXPERIMENTAL PROCEDURE AND RESULTS—(d,p) EXPOSURE

Dr. R. Sherr of Princeton University suggested to the author that perhaps the 413.5-kev gamma-ray observed[13] when Be^9 is bombarded with deuterons might be due not to a cascade transition in B^{10} but

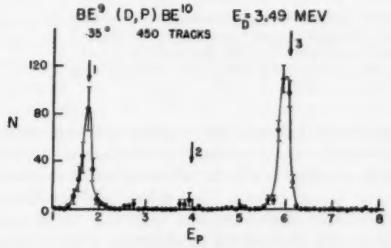

FIG. 13. $Be^9(d,p)Be^{10}$ data at 35°. N is the number of protons/100-kev interval.

instead to a level at approximately 0.4 Mev in Be^{10}, a level which would therefore be analogous to the 2.15-Mev level in B^{10}. Other investigators have previously covered this region in Be^{10}, but the work was performed either with fairly poor resolution[14,15] or with good resolution but with a fairly intense alpha-group appearing in the region where the possible 0.4-Mev level group might have been observed,[16] and the alpha-group might possibly have concealed it. Therefore, it was deemed advisable to test Dr. Sherr's hypothesis by observing the $Be^9(d,p)Be^{10}$ reaction again under favorable conditions.

The protons emitted at 35°±2° in the laboratory system were observed by means of a 100-micron NTA plate.[17] The number N of protons per 100-kev interval was then plotted against the proton energy. Figure 13 shows the data.

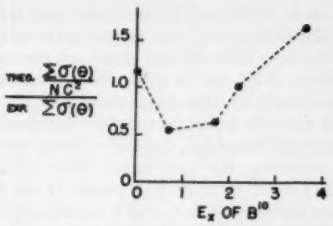

FIG. 14. Plot of the ratio of the integrated Butler equations for the $l_p=1$ cases, with the nuclear factors considered constant, to the relative total experimental cross sections for the first five states of B^{10}.

If the ground state of Be^{10} is analogous to the 1.74-Mev level of B^{10}, we know that it must have the same parity, and therefore its maximum yield should occur at the same angle (about 35° in the laboratory system). Similarly, if there is a state of Be^{10} at 0.4 Mev, its maximum yield should likewise be at that same angle. This is why the exposure was made at 35°.

The ground state and the known excited state at 3.37 Mev have been observed. The corresponding proton groups are indicated as "3" and "1," respectively, on Fig. 13. The group indicated as "2" is of the correct energy to be due to protons from the $C^{12}(d,p)C^{13}$ reaction. There is no indication of a group corresponding to a 0.4-Mev state in Be^{10} of intensity greater than 5 percent of the intensity of the ground-state group. From charge independence considerations and from the corresponding angular distributions in B^{10}, one would expect the 0.4-Mev level in Be^{10}, if it exists, to have an intensity comparable in magnitude to the intensity of the proton group from the ground state. The fact that there is no such intense group seems to be extremely strong evidence that there is no level in Be^{10} at 0.4 Mev and that the 413.5-kev gamma must be fitted into the Be^{10} level scheme.

DISCUSSION AND ACKNOWLEDGMENTS

Buechner's group at M.I.T.[18] have studied the inelastic scattering of 7-Mev protons from B^{10}. Their results confirm the existence of the first five excited states of B^{10} observed in this investigation.

Schecter[19] has bombarded Be^9 with 20-Mev deuterons and has observed the angular distributions of the neutrons by the method of foil activity. He assumed that all the neutrons he observed derived from the

[13] See reference c in Table I.
[14] F. A. El-Bedewi, Proc. Phys. Soc. (London) **A65**, 64 (1952).
[15] Lattes, Fowler, and Cuer, Proc. Phys. Soc. (London) **59**, 883 (1947), and others.
[16] Strait, Van Patter, Buechner, and Sperduto, Phys. Rev. **81**, 747 (1951).
[17] The details of the experimental arrangement and procedure are discussed in the author's doctoral dissertation: Fay Ajzenberg, unpublished PhD thesis, University of Wisconsin (1952).
[18] Buechner, Browne, Elkind, Sperduto, and Bockelman, Phys. Rev. **87**, 237A (1952).
[19] L. Schecter, Phys. Rev. **83**, 695 (1951).

ground state of B^{10}, and he concluded from the shape of the distribution that the ground state is of even parity. Actually Schecter was observing the first four or five states of B^{10}, but his conclusion was not incorrect since apparently all these states are of even parity and therefore have the same characteristic distribution.

Throughout this paper, the Butler curves have been drawn neglecting the spin factor $(2J+1)/[(2s_p+1)\times(2j+1)]$ in Eq. 34 of Butler's paper.[2] It was decided to assume spins of 3, 1, 0, 1, and 2, respectively, for the first five states of B^{10} and to plot the ratio of the integrated Butler equations for the $l_p=1$ cases, with the nuclear factors considered constant, to the relative total experimental cross sections. Figure 14 indicates that if the assumed spin assignments were correct, then the nuclear factors affecting the stripping process are constant within a factor of about 3 for these states.

The author deems it a pleasure to be able to acknowledge her profound indebtedness and gratitude to Professor H. T. Richards for suggesting this investigation and for his invaluable criticisms and suggestions. She also wishes to thank Eugene Goldberg for his very valuable help in the exposure of the plates and for several interesting discussions, and R. E. Benenson, F. J. Eppling, and R. W. Hill for their generous assistance in the operation of the generator.

PHYSICAL REVIEW VOLUME 88, NUMBER 2 OCTOBER 15, 1952

The Energy Spectrum of Positrons from the Decay of the μ-Meson*

H. J. Bramson, A. M. Seifert, and W. W. Havens, Jr.
Columbia University, New York, New York

(Received June 23, 1952)

The energy of the positrons from $301\ \pi\rightarrow\mu\rightarrow\beta$ decays have been determined in electron sensitive emulsions by measuring the multiple scattering of the positron tracks. The annihilation properties of the charged particle emitted in the decay of the μ^+ meson confirm its identity as a positron. This spectrum has a maximum about 36 Mev and a nonzero cutoff at the high energy end. A statistical analysis of the data, using the Michel theory, yields a value of $\rho=0.41\pm0.13$.

I. INTRODUCTION

EARLIER experiments[1] have demonstrated that the β-decay of the μ-meson is consistent with the scheme

$$\mu\rightarrow\beta+\nu+\nu. \qquad (1)$$

However, the possibility that β-decay of the μ-meson might be merely one phase of a universal interaction between fermions has raised interest in the exact shape of the spectrum of the β-particle. It is here that previous experiments have given contradictory results, due either to poor energy resolution of individual β-particles, to the low number of such events obtained, or both. A brief report on the preliminary results of our measurements has been given previously.[2]

II. METHOD

A. Detector

Minimum ionization emulsions were used to detect the $\pi\rightarrow\mu\rightarrow\beta$ decay. Emulsions have several important advantages in a study of the β-decay of the μ-meson. The grain density for all β's of relativistic energies is substantially the same;[3] hence, all decay β's are recorded with virtually equal sensitivity. Whereas it is characteristic of other methods of detection that massive material is used to stop the μ-meson and the decay β observed only after emergence from this "dead mass," the β-track is unobscured at any stage when emulsions are employed. Emulsions are also able to be used inside the 381-Mev Nevis cyclotron, where the meson flux is such that even in restricting entrance to the emulsion to pions of an 11- to 14-Mev band and less than a $\pm10°$ spread, some 10^4 pions/sec/cm^3 of emulsion are obtained.

Problems peculiar to the photographic technique for this purpose include the substantial labor required for high energy resolution per track through multiple scattering measurements, the discrimination against low energy β's because of outscattering from an emulsion of finite depth, and the necessity to obtain an accurate calibration of energy with multiple scattering measurements. As with other techniques, the uncertainty in energy degradation must be evaluated. These points will be discussed in greater detail below.

B. Multiple Scattering Measurements

The technique of determining the energy of a fast particle through the average magnitude of Coulomb scatterings in emulsion has been analyzed by Gold-

* This work was supported by a joint program of the ONR and AEC.

[1] Leighton, Anderson, and Seriff, Phys. Rev. **75**, 1432 (1949); Davies, Locke, and Muirhead, Phil. Mag. **40**, 1256 (1949); J. Steinberger, Phys. Rev. **75**, 1136 (1949); Sagane, Gardner, and Hubbard, Phys. Rev. **82**, 557 (1951).

[2] H. J. Bramson and W. W. Havens, Jr., Phys. Rev. **83**, 861 (1951).

[3] E. Pickup and L. Voyvodic, Phys. Rev. **80**, 89 (1950).

schmidt-Clermont.[4] A variation developed by Fowler[5] has been used, consisting of measuring the ordinates of a track at fixed intervals, and obtaining from the second differences a measure of the average scattering angle. The mathematically equivalent Molière[6] and Snyder-Scott[7] theories then permit a unique equivalence of average scattering angle with energy.

In principle, the only serious limitations in energy resolution of a particular trajectory are those given by the number of scattering angles n that can be obtained and by the abrupt radiation losses that may be masked by the normal fluctuations in Coulomb scattering. The first factor decreases with track length as $\sigma_{stat}=0.80/\sqrt{n}$, the latter increases with track length as $\sigma_{rad}=(\text{const})L$, where L is the track length. Thus ideally, maximum energy resolution would be obtained with an L sufficiently long so that $\sigma_{stat}=\sigma_{rad}$. In practice, track lengths employed are considerably shorter than this optimum length. First, the thickness of emulsions that can be used with the high resolution microscope lenses, which are necessary to minimize errors in ordinate readings, discriminate seriously against slow particles remaining in the emulsion for this optimum distance. Second, improved energy resolution must be balanced against obtaining a greater number of events.

For these reasons, a minimum track length of 1500 microns was adopted as the criterion of acceptance for analysis on the 600 micron thick emulsions, and 2500 microns long on the 1000 micron thick emulsions. The magnitude of this outscattering effect is shown in Fig. 1. For the minimum track lengths used the effect of outscattering on the determination of the Michel parameter ρ is negligible (see below).

Where a β-trajectory of a prescribed length is to be analyzed, the shortest interval between ordinate readings (cell length) is employed which for that trajectory will result in a nonobjectionable error in the final estimate of average scattering angle. Both by using a "straight line" obtained from the Bausch and Lomb ruling engine and a test devised by Corson,[8] the minimum average error in second differences of ordinates obtainable was found to be 0.03 micron. With this low value of reading noise, the effect on the square of the true scattering angle is less than 1 percent even for the fastest particles. The ability to use cell lengths of 25 to 60 microns (depending on track energy and length available) resulted in an average energy resolution due to the statistical factor n of 10 percent.

To reduce the tedium of realigning the β-trajectory relative to the base line during scattering measurements, and to provide a reliable, accurate movement of the trajectory along the base line, a special stage motion was devised for this experiment. The rotating turntable of a Spencer research microscope was removed from its stand and attached to a heavy carriage that rode on a lathe bed. Thus any arbitrary direction in the emulsion could be rotated about a mechanical axis that coincided closely with the optic axis, and aligned with the direction of motion of the carriage. This carriage rested on a vee and flat of the bed over a length of 18 inches to reduce rotational play, and was pushed by a precision screw.

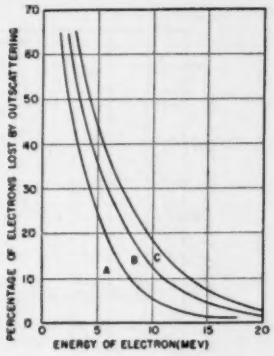

FIG. 1. Outscattering losses for various emulsion thicknesses for minimum track lengths adopted. Curve A gives the loss for the bulk of the data: 600μ thick emulsion and 1500μ minimum track length; curve B for the remainder of the data: 1000μ emulsion and 2500μ track length; curve C for a 200μ emulsion and 1000μ track length.

It is perhaps worth noting that the distance pushed by the screw is the cell length only if the dip of the track in the emulsion is ignored; otherwise, the cell length is greater by a factor of the secant of the angle of dip. This factor if ignored can cause an error in cell length of 1 percent for a track even as long as 4000 microns in a 600-micron emulsion, and as much as 8 percent in the extreme case of a 1500-micron track, which represents an error of 1.4 percent and 11 percent respectively in energy.

Finally, account was taken of the correction due to the averaging of grains about a given abscissa. This averaging, adopted to obtain a weighted mean ordinate and thus mitigate the grain fluctuations, causes the underemphasis of the peaks and valleys in a track, resulting in a falsely high energy. By restricting this region about the abscissa over which the grains were averaged to ± 10 percent, the error in the average scattering angle is less than 2 percent, and so has a negligible effect on the mean squared scattering angle.

C. Energy Degradation

In photographic emulsion where the energy of a particle is determined by a dispersion measure of a statistical distribution of the scattering along its track, a sudden loss of energy of considerable magnitude may be masked by the fluctuations normal to that distribution. Only when the number of scattering angles after the point of sudden loss is sufficient to establish a trend distinguishable from that of the earlier portion, can the loss be noted. Since the estimate of energy of the particle is based upon measurements made during energy degra-

[4] Y. Goldschmidt-Clermont, Nuovo cimento **7**, 1 (1950).
[5] P. H. Fowler, Phil. Mag. **41**, 169 (1950).
[6] G. Moliere, Z. Naturforsch. **2a**, 133 (1947); **3a**, 78 (1948).
[7] W. T. Scott, Phys. Rev. **85**, 245 (1952).
[8] D. R. Corson, Phys. Rev. **80**, 303 (1950).

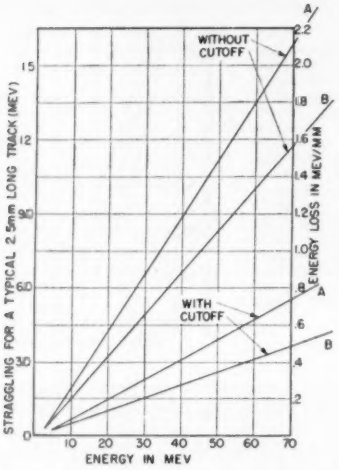

FIG. 2. *A*: Radiation loss and *B*: straggling of positrons in Ilford G-5 emulsion, with and without radiation cutoff.

dation, it becomes important to take into account the continual, but not continuous, loss of energy along the track.

The degradation of energy due to inelastic collisions resulting from excitation of atoms along the trajectory causes little difficulty, since the number of such collisions is sufficiently large ($>10^4$), for the shortest tracks observed, to reduce the straggling to a low value (about 0.3 Mev for the length tracks used). This is not the case for inelastic collisions resulting from radiation. While, as above, there is a high number of collisions in all tracks analyzed, the probability of losing a given amount of energy through many collisions of small loss each is approximately the same as of losing a large fraction in a single collision. This results in a large straggling about the mean radiation loss; e.g., for track lengths used in this experiment, about 8 percent of the time one radiative collision can be expected to occur with an energy loss of at least 30 percent.[9] Actually, in 301 positron tracks analyzed, some 21 were observed to suffer such large losses. If no allowances were made for these large losses, an average radiation loss of 2.7 Mev for a typical 2.5 mm long 40-Mev track would be accompanied by a straggling ($\sigma^2=\langle E^2\rangle_{Av}-\langle E\rangle_{Av}^2$) of 6.3 Mev about this average! Hence in a sense the small average radiation loss is deceptive; the large straggling about the average is more indicative of the accuracy to which energy losses are known.

This sizable straggling can be reduced by eliminating from consideration all positrons whose radiation losses exceed a given amount. The lower this cut-off radiation loss, the lower will be the average radiation loss and straggling. However, too low a cutoff will sacrifice many tracks already analyzed, again prejudicing against the total number of events in favor of better energy resolution per event. Since a cutoff at 30 percent loss maintains the radiation straggling small as compared to the statistical straggling, yet eliminates only 8 percent of the total number of analyzed events, this loss has been selected as cutoff. The effect of this cutoff upon the average radiation loss and straggling is shown in Fig. 2 for one mm of track and for a typical 2.5 mm long track, respectively. Since track lengths scanned are generally less than a tenth the radiation length, the total loss is very nearly proportional to the track length. The relative straggling, on the other hand, varies slowly with L, increasing by only 1 percent when L is doubled. For the example cited above, our cutoff reduces the average radiation loss to 1.0 Mev and the straggling to 2.0 Mev.

III. RESULTS

A. Annihilation of the Positrons

As has been shown previously,[2] the observed annihilation of the minimum ionization particle from μ-meson decay offers further substantiation of its positron nature. The study of these emitted charged particles has covered about 230 cm in emulsion in the course of which we have found five annihilations. According to Heitler,[10] the cross section for annihilation of a positron is given by

$$\phi=\frac{\pi r_e^2 m_e}{E}\left(\ln\frac{2E}{m_e}-1\right), \qquad (2)$$

where m_e is the mass of the positron, and r_e the classical electron radius. Averaging over the constituents of G-5 emulsion and the energy spectrum of these particles, a value of 57 cm is obtained for the annihilation length. Thus the observed annihilation length is consistent with that of a positron.

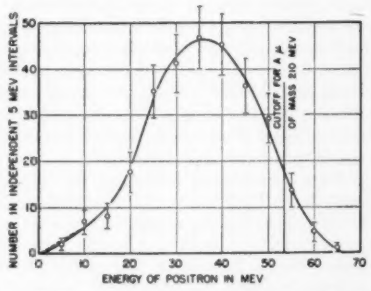

FIG. 3. Differential energy spectrum of 286 positrons from $\pi\to\mu\to\beta$ decay. Dashed portion at low energies gives correction for outscattering.

[9] H. Bethe and W. Heitler, Proc. Roy. Soc. (London) **146**, 83 (1934).

[10] W. Heitler, *The Quantum Theory of Radiation* (Oxford University Press, London, 1947), second edition, p. 208.

B. Energy Spectrum of Positrons

Of the 301 tracks energy-analyzed by the technique of multiple-scattering measurements, 21 were observed to have lost more than the maximum energy (30 percent) acceptable under our criterion; of these, however, there were 6 for which the track length prior to the large energy loss was adequate to warrant using that section alone to salvage the event for the purpose of the energy spectrum. In Fig. 3, the unsmoothed spectrum for these 286 events is shown. The dashed portion of the curve at the low energy end indicates the extent of the calculated correction because of the outscattering referred to in Sec. IIB. This correction amounts to 0.4 percent of the mean of the untabulated, uncorrected energies, (35.7 Mev), and only 0.01 percent of $\langle E^4\rangle_{Av}$ (see below).

In Michel's theory,[11] it is shown that for any linear combination of the five well-known β-decay interactions that may be responsible for the interaction energy of (1), the shape of the positron spectrum is given by

$$P(E)=(4E^2/W^4)[3(W-E)+\tfrac{2}{3}\rho(4E-3W)], \quad (3)$$

where W represents the maximum energy available to the positron. The effect of a particular specification of the linear combination is contained in the single parameter ρ to a high degree of accuracy, which improves with increasing E. For the particular prescriptions similar to nucleon decay, e.g., $\mu\rightarrow\nu$, $e\rightarrow\nu$, ρ would be given by

$$\frac{3[(g_s-g_t)^2+(g_t+g_{ps})^2+2(g_v+g_{pv})^2]}{4[g_s^2+4g_v^2+6g_t^2+4g_{pv}^2+g_{ps}^2]}, \quad (4)$$

and

$$\frac{3[g_s+g_{ps}-2(g_v+g_{pv})]^2}{2[(g_s+6g_t-g_{ps})^2+16(g_v-g_{pv})^2+2(g_s+g_{ps}-2g_v+g_{pv})^2]}, \quad (5)$$

according to whether the neutrinos are distinguishable or indistinguishable[12] and where the g's are the usual coupling constants. For all combinations, $\rho<\frac{3}{4}$ for identical neutrinos, and <1 otherwise. For the particular case of the Critchfield-Wigner interaction,[13] unique in that it is independent of the order of the particles in the Hamiltonian, ρ always equals $\frac{1}{2}$.

The most that can be concluded from any positron spectrum is the value of ρ. For this purpose, two experimental limitations must inevitably be considered: the effect of the limited number of events comprising the spectrum, and the uncertainty involved in the energy measurement of each event. To compensate for the latter effect, the distribution of uncertainties in the measuring process is folded into the theoretical Michel curves to yield, for various values of ρ, the curves shown in Fig. 4. The few events observed at low energies, the large number at very high energies, and the position of the mode are all indicative of a ρ near $\frac{1}{2}$.

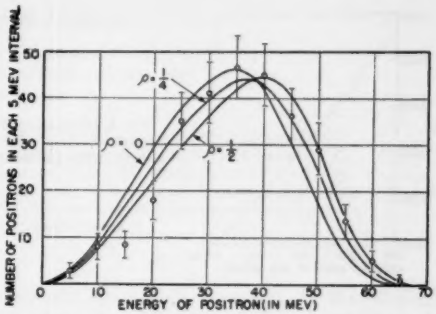

FIG. 4. Comparison of data with Michel curves for $\rho=0$, $\frac{1}{4}$, $\frac{1}{2}$, with the experimental error folded in.

C. A Statistical Estimation of ρ

The photographic and cloud chamber techniques are similar in that both yield a low number of satisfactory events (<1000). It therefore is desirable to exercise care in the choice of an optimum statistical criterion to estimate ρ. Two procedures have been offered which are based on the fact that $P(3W/4)$ is independent of ρ: (a) One[14] then compares the theoretical ratio of events before and after this E, (which is a linear function of ρ), with the experimental ratio, thus determining ρ. While this has the advantage of simplicity, it does not extract the maximum available information from the spectrum, effectively ignoring the spectral shape away from the $E=3W/4$ point. (b) The second[15] takes advantage of the fact that $P(E)/E^2$ is linear in E, and finds ρ as the slope of a least squares line. Unfortunately, the fewest number of events occur at the extreme energies, and although these have the least statistical accuracy, they exercise a high "lever-arm" on a least squares curve. A different approach is to use various moments of E of the experimental distribution. On taking these as estimates of the true moments, ρ follows from the relation

$$\text{expectation}(E^i)=\frac{4W^i}{(i+3)(i+4)}\left\{3+\frac{2i\rho}{3}\right\}, \quad (6)$$

which follows from (3). If we denote the value of ρ estimated in this fashion by ρ', then the straggling is a function of ρ itself:

$$\sigma_{\rho'}{}^2=\sigma_{\rho'}{}^2(\rho)=\frac{(i+3)^2(i+4)^2}{16i^2n}\left[\frac{(9+4i\rho)3}{(2i+3)(2i+4)}-\frac{4(9+2i\rho)^2}{(i+3)^3(i+4)^2}\right], \quad (7)$$

[11] L. Michel, Proc. Phys. Soc. (London) **63**, 514 (1950).
[12] See, however, E. R. Caianiello, Phys. Rev. **86**, 564 (1952).
[13] L. Critchfield and E. Wigner, Phys. Rev. **60**, 412 (1941); L. Critchfield, Phys. Rev. **63**, 417 (1943).
[14] A. Lagarrique and C. Peyrou, J. phys. et radium **12**, 848 (1951).
[15] H. W. Hubbard, thesis, unpublished University of California report UCRL 1623 (1952).

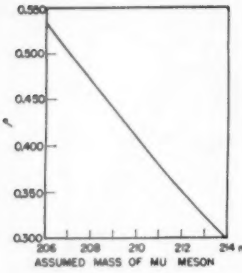

FIG. 5. Dependence of estimate of ρ with μ-meson mass assumed.

where n is the number of events ($=286$). For $\rho=\frac{1}{2}$, this has a minimum of 2.09 for the fourth moment ($i=4$), for an $n=1$.

One might wonder whether perhaps another means of estimating ρ might lead to a still smaller value of $\sigma_\rho{}^2$. It is possible to compute the lower bound of this variance. Following Cramer,[16] for $\rho=\frac{1}{2}$ and $i=4$, this is found to be 2.08 for $n=1$. Hence, there is no other means of estimation which is theoretically capable of much further refinement. This in turn may be compared with the variance resulting from test (a), e.g., which for $\rho=\frac{1}{2}$, $i=4$, $n=1$ is 3.04.

A preliminary check of our data shows that $\rho\approx 0.5$. Hence from the above, it is most advisable to choose the fourth moment to estimate ρ. Further, this moment will tend to eliminate the slight effect of outscattering and the effect of small discrepancies in (2) at lowest energies. Our fourth moment of energy is 2.59×10^6 (Mev)^4, leading to an estimate of $\rho=0.41$ from the folded curves with a standard deviation of about 0.13. As shown in Fig. 5, this estimate depends on the mass assumed for the μ meson. Since the latter is known with considerable accuracy,[17] the resultant variation in ρ is small.

[16] H. Cramer, *Mathematical Methods of Statistics* (Princeton University Press, Princeton, 1946), pp. 477–485.

IV. DISCUSSION

Our earlier result of a distinct finite cutoff has persisted with little change, being quite compatible with a ρ of $\frac{1}{2}$, or a Critchfield-Wigner interaction. Since this value is higher than generally reported elsewhere, it is of interest to see where in this experiment bias could have been introduced to lead to higher energies. The usual pitfalls of the multiple-scattering technique—"noise" distortion and dip effects—would tend to lower the energy. The radiation correction does tend to increase energy slightly, but as indicated in II C, if any error were present one would tend to suspect that the loss was underestimated. Therefore, it is difficult to see an intrinsic error which will increase the energies. On the other hand, in techniques where the positron is observed only after emerging from a "dead mass," there is the possibility discussed above that occasional tracks are accepted which have lost more than average energy, before emerging from the absorber. This effect would be in the direction of lower ρ, and it is perhaps worthy of note that more recent Wilson cloud-chamber experiments with less dead mass present have resulted in higher values of ρ.

The authors are indebted to Dr. Helen Friedman and Dr. L. James Rainwater for the use of their exposure chamber and some of their plates, to Dr. H. Yukawa and Dr. R. Serber for helpful discussions, to Mr. R. Beckhofer and colleagues for a study on the statistical analysis of ρ, to Mrs. Carol Major and Marjorie Boehlert for painstaking scanning of our plates, and to members of the cyclotron crew, the nuclear emulsion group, and others too numerous for individual mention but whose assistance is deeply appreciated.

[17] Lederman, Booth, Byfield, and Kessler, Phys. Rev. **83**, 685 (1951).

Superconductivity of Rhenium*

J. G. DAUNT AND T. S. SMITH
Department of Physics, Ohio State University, Columbus, Ohio
(Received July 7, 1952)

Measurements have been made in the liquid helium temperature region of the magnetic threshold curve of rhenium by observations of the magnetic moment of a powdered sample. The transition temperature T_c in zero magnetic field was found to be 2.42°K, and the observed slope of the threshold curve at $T=T_c$ was 235 gauss per degree. Assuming a reversible transition, the value of the normal electronic specific heat coefficient γ obtained from the magnetic data is 4.6×10^{-4} calories per mole per degree^2, a value which would be expected from the correlation between γ/V and T_c previously proposed.

I. INTRODUCTION

THE investigation of superconductivity in metals may be carried out by two methods; first, by the observation of the electrical resistance of the specimen, and second, by the observation of its diamagnetism. In the second method superconductivity is noted by perfect or partial diamagnetism (the Meissner effect[1]). For metals which are difficult to obtain in a chemically or physically pure form the two methods may give divergent results.[2] In particular, the measurement of zero electrical resistance in a specimen will not disclose what percentage of the total volume of the specimen may be in the superconducting state. Because of this, and since it also yields information of the reversibility of the transition, the measurement of the susceptibility is accepted as the more trustworthy method[3] of investigation of superconductivity.

We here report on magnetic measurements on rhenium which we have found to be a superconductor in the liquid helium temperature region.

II. THE EXPERIMENTAL ARRANGEMENTS

Rhenium, kindly loaned to us by Dr. C. A. Beuhler of the University of Tennessee, was prepared from ammonium perrhenate by hydrogen reduction and was in powder form of purity 99.8 percent, as observed by spectrographical analysis; 0.68 grams were used in the experiments.

This metal was mounted in a Teflon holder, immersed in liquid helium as shown diagrammatically in Fig. 1. A uniform magnetic field was produced at the specimen by means of a large air-core solenoid. The magnetic moment of the specimen was observed by moving a 5000 turn search coil, by means of a magnetic lifting mechanism, parallel to the applied field from a position around the specimen to a remote position at which the magnetic field was sensibly uniform. This method has been used satisfactorily previously by Mendelssohn[4] and by Daunt and Mendelssohn.[5]

The temperature of the helium cryostat was measured in the usual way by observation of the liquid helium vapor pressure and by using the 1949 temperature scale.[6]

Before the rhenium sample was investigated, a spherical tin sample of the same total volume as the rhenium was measured in order to calibrate the sensitivity of the apparatus and in order to distinguish by the direction of the galvanometer deflections between diamagnetic and paramagnetic effects.

The rhenium was annealed in vacuum at 800°C for 2½ hours before the investigations.

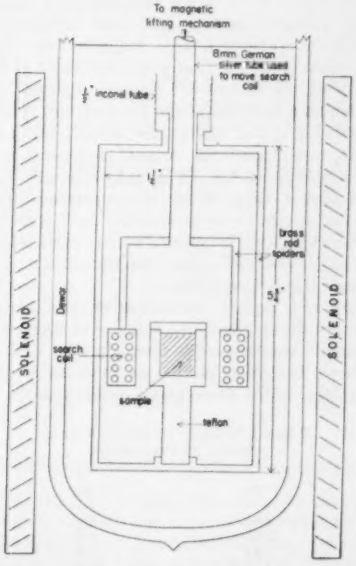

FIG. 1. Diagram of apparatus.

* Assisted by a contract between the AEC and The Ohio State University Research Foundation.

[1] W. Meissner and R. Ochsenfeld, Naturwiss. **21**, 787 (1933).

[2] J. G. Daunt, Phil. Mag. **28**, 24 (1939); J. G. Daunt and C. V. Heer, Phys. Rev. **76**, 715 (1949).

[3] J. G. Daunt and K. Mendelssohn, Proc. Roy. Soc. (London) **A160**, 127 (1937); D. Shoenberg, *Superconductivity* (Cambridge University Press, London, 1938).

[4] K. Mendelssohn, Proc. Roy. Soc. (London) **A155**, 558 (1936).

[5] H. Van Dijk and D. Shoenberg, Nature **164**, 151 (1949).

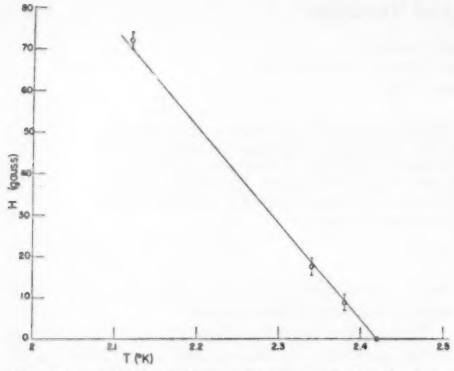

FIG. 2. Magnetic threshold curve for superconducting rhenium.

III. THE RESULTS

The results of three separate helium runs are shown in Fig. 2 and in Table I, which give the magnetic threshold curve as a function of temperature. The transition temperature T_c in zero magnetic field was found to be 2.42°K, and the slope of the transition curve at $T=T_c$ was 235 gauss per degree.

In observing the transition in zero magnetic field the specimen was allowed to warm up from a low temperature (~1.5°K) at which temperature a superconducting magnetic moment had been "frozen-in" by momentarily applying a large magnetic field. Typical observations in such a "warm-up" are shown in Fig. 3, which plots the "frozen-in" magnetic moment of the specimen as a function of the temperature. It will be seen from Fig. 3 that, whereas the temperature at which the last trace of magnetic moment disappears is quite sharply defined (point "A"), the transition itself is spread over a broad range of temperature. This is attributed largely to the geometrical form of the specimen, which, having irregularly shaped particles of different sizes, would also make the transition in a magnetic field highly irreversible.[6]

A plot of a typical observation of the diamagnetic moment of the specimen as a function of magnetic field at constant temperature is shown in Fig. 4. The galvanometer deflection plotted as ordinate is directly proportional to the diamagnetic moment of the specimen. The isothermal observations of Fig. 4 were made at 2.12°K. For the observation the specimen was first cooled from above T_c in zero magnetic field. The virgin isothermal magnetization is the curve "A" of Fig. 4. After a field of 61.6 gauss (point "a", Fig. 4) had been reached, the field was reduced again and the magnetic moment followed the curve "a"–"b," showing at zero field a large frozen-in magnetic moment. Then the direction of the applied field was reversed and a complete hysteresis cycle taken as shown in Fig. 4. After the cycle had been once completed, it was found that subsequent repetitions produced exactly the same curve. The hysteresis is probably due, as indicated above, to shape and size effects in the powder specimen.

From the data obtained from the virgin curve "A" and from the known calibration of the system on the tin specimen of volume equal to that of the rhenium, it was deduced that 100 percent of the total volume of the rhenium showed zero induction at the virgin curve. In fact, the slope of the virgin magnetization curve (curve "A" of Fig. 4) at the origin indicated that the average demagnetization factor of the rhenium particles was about 0.8. This could be expected for flat shaped particles.[7] It was concluded, therefore, that the diamagnetism observed could be associated with the superconductive properties of the rhenium as a whole and was not due to unknown impurities present in small quantities in the specimen.

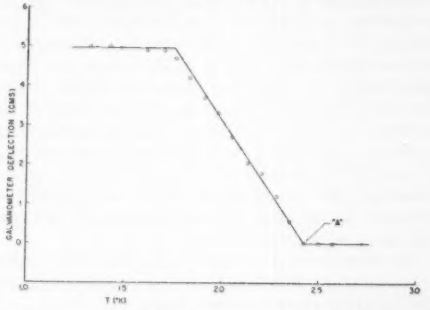

FIG. 3. Warm-up curve in zero magnetic field. Galvanometer deflection is proportional to diamagnetic moment of specimen.

The complete threshold curve was obtained both by observation of the hysteresis cycles and by warm-up curves taken in constant magnetic fields.

TABLE I. Magnetic threshold values of superconducting rhenium.

T(°K)	H(gauss)
2.42	0
2.38	8.8
2.34	17.6
2.12	72.0

IV. DISCUSSION

Owing to the position of rhenium in the periodic table, in the same subgroup (VII*a*) as manganese (which is not a superconductor) and technetium, its superconductivity may at first seem surprising. In view, however, of the recent discovery by Goodman[8] of the super-

[6] Mendelssohn, Daunt, and Pontius, Proc. of VII International Congress of Refrigeration **I**, 445 (1936).

[7] E. R. Andrew and J. M. Lock, Proc. Phys. Soc. (London) **A63**, 13 (1950).

[8] B. B. Goodman, Nature **167**, 111 (1951).

conductivity of osmium and ruthenium in Group VIII*a*, it is not clear that the periodic grouping has considerable significance.

Our observed superconducting transition temperature for rhenium of 2.42°K differs considerably from that initially reported by Aschermann and Justi[9] of 0.85°K. It must be remembered, however, that the latter authors used resistance measurements on a sintered powder whose properties may well have been different from the annealed powder used by us.

If it is supposed that the magnetic threshold curve given in Fig. 2 would reflect a reversible transition if the shape and size effects of our specimen were not present, then a calculation may be made of the specific heat γT of the electrons in the normal state.[2] By assuming that $\gamma=(V/8\pi)(\partial H/\partial T)^2_{T=T_c}$ and using the observed value of $(\partial H/\partial T)_{T=T_c}$ of 235 gauss per degree, the value of γ is 4.6×10^{-4} calories per mole per degree.[2]

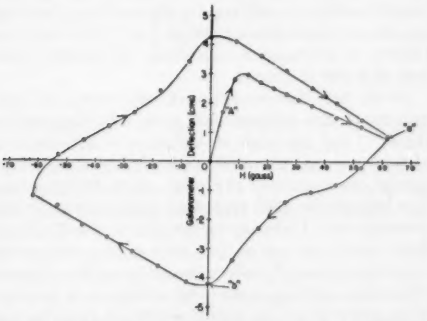

FIG. 4. Isothermal magnetization curve for $T=2.12$°K. Galvanometer deflection is proportional to diamagnetic moment of specimen.

It is of interest to compare this value of γ for rhenium with values for other superconducting elements using the correlation previously proposed by one of us.[10] In Fig. 5 is shown a plot of γ/V, where V is the atomic volume, against the transition temperatures for all the superconducting elements for which reliable data are now known. The data used in this plot for Pb, Hg, Sn, In, Tl, Al, Zn, Th, Ta are the same as those previously reported,[10] whereas new data for other elements are included as follows: Al, Cd, Zn, Ga from Goodman and Mendoza,[11] V from Wexler and Corak,[12] Zr from Smith and Daunt,[13] and Nb from Brown, Zemansky, and Boorse.[14] A tabulation of this new data is given in Table II. It is clear from this plot (Fig. 5) that not only does rhenium fall exactly where such a transition

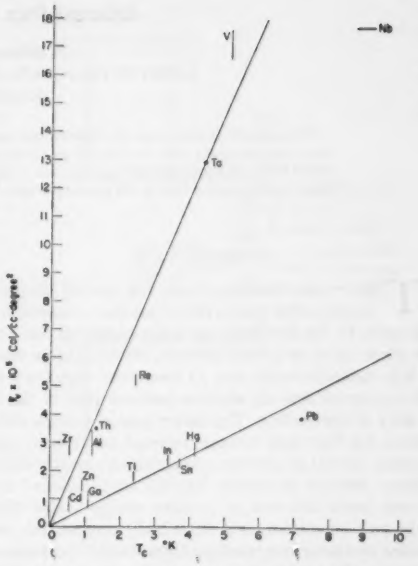

FIG. 5. Plot of γ/V against T_c from latest data on superconductors.

element would be expected, according to Daunt's correlation curve, but also that the distinct grouping of the superconducting elements into two subgroups, for each of which γ/V seems an approximately linear function of T_c, is very outstanding. It is considered that, whereas the terminology previously employed of "hard" and "soft" superconductors is not clearly defined, nevertheless the known superconductors seem to form two definite groups characterized by distinct ratios of γ/VT_c or, expressed in terms of the magnetic threshold field H_0 at zero degrees K, by two distinct ratios of H_0^2/T_c^2. A more detailed discussion of this correlation will be given in a subsequent paper.

TABLE II. Values of transition temperature T_c; the atomic volume, V; normal electronic specific heat coefficient, γ; the Debye temperature, θ; and γ/V from recent measurements on superconductors.

Element	T_c(°K)	V(cc)	$\gamma\times10^{-4}$ cal/mole/deg²	$\gamma/V\times10^4$ cal/cc/deg²	θ°K	Ref.
Al	1.197	9.99	2.95	2.95	390	11
Cd	0.560	13.0	1.28	0.98	172	11
Zn	0.905	9.17	1.16	1.27	290	11
Ga	1.103	11.8	0.91	0.77	125	11
V	5.12	8.39	15	17.6		12
Zr	0.54	14.0	3.92	2.76	288	13
Nb	8.65–9.22	10.8	21	17.65	254	14
Re	2.42	8.8	4.6	5.2		this paper

[9] V. G. Aschermann and E. Justi, Physik. Z. **43**, 207 (1942).
[10] J. G. Daunt, Phys. Rev. **80**, 911 (1950).
[11] B. B. Goodman and E. Mendoza, Phil. Mag. **42**, 194 (1951).
[12] A. Wexler and W. Corak, Phys. Rev. **85**, 85 (1952).
[13] T. S. Smith and J. G. Daunt, Phys. Rev. **86**, 818 (1952).
[14] Brown, Zemansky, and Boorse, Phys. Rev. **86**, 134 (1952).

Internal Pair Conversion in Mg^{24}

STEWART D. BLOOM*
Institute for Nuclear Studies, University of Chicago, Chicago, Illinois
(Received June 2, 1952)

The positron spectra from the internal pair conversion of the two γ-rays following the β^- decay of Na^{24} have been observed, and the internal pair conversion coefficients found to be 7.1×10^{-4} in the case of the 2.758-Mev γ-ray and 0.6×10^{-4} in the case of the 1.380-Mev γ-ray. The value of the coefficients and the shape of the spectra lead to the conclusion that both γ-rays are electric quadrupole transitions.

INTRODUCTION

THE γ-rays resulting from the excited states of nuclei suffer two types of internal conversion in general. In the first type the entire energy of the γ-ray is given up to an orbital electron, resulting in an essentially monochromatic line. In the second type the γ-ray is converted into an electron-positron pair in the vicinity of the nucleus. This latter type of process differs from the first type (atomic internal conversion) principally in that an electron comes from a negative energy state, whereas in atomic internal conversion all electrons begin and end in positive energy states. Since the pair conversion is a three-body process, the electrons and positrons resulting from it exhibit continuous spectra. Moreover, the γ-ray undergoing such conversion must have an energy of at least $2m_0c^2$ (1.022 Mev), and the process, therefore, does not compete with internal conversion below this energy. However, above this energy, pair conversion not only competes with, but rapidly becomes more frequent than internal conversion. The former increases, while the latter decreases with energy. For instance, for electric dipole radiation ($Z=0$) the total pair conversion coefficient is $\sim3\times10^{-4}$ at 1.5 Mev and $\sim1\times10^{-3}$ at 2.5 Mev. For the same two energies, respectively, the coefficient of internal conversion ($Z=10$, K-shell) decreases from 2.5×10^{-6} to 1.2×10^{-6} for electric dipole radiation, and from 2.3×10^{-5} to 5.4×10^{-6} for electric 5-pole radiation. Furthermore, pair conversion possesses a marked advantage over internal conversion as far as detectability goes, when using β-ray spectrometers: namely, that while the monochromatic lines due to internal conversion may be concealed in the negatron spectrum, the positron spectrum, due to pair conversion, may be observed free from these effects by simply reversing the field of the spectrometer.

Aside from the intrinsic interest of the process of pair conversion itself, additional interest stems from the fact that conclusions may be drawn concerning the spin and parity assignments of the excited levels of the relevant nuclei from the value of the internal pair conversion coefficients and also the shape of the continuous spectra of the electron-positron pair. This may lead further, to information concerning the internal structure of nuclei in general.

At the time this present work was begun, the major aspects of the process had been well described in theory[1–4] and the work of Alichanov *et al.*[5] as well as of Rae[6] had demonstrated the feasibility of the experimental observation of the event. Both Alichanov and Rae utilized the 180° type β-ray spectrometer in their investigation, Alichanov in the case of the ThC″ and RaC, Rae in the case of Na^{24}, thus making effective use of the advantage of positron detection mentioned above. This same advantage may be utilized in a lens-type β-ray spectrometer by installing twisted vanes between the source and the detector conforming to the helical trajectories of the electrons (or positrons). In the lens-type spectrometer there is the further advantage that the transmission may be from ten to a hundred times larger than it is in simple semicircular type spectrometers.

With the above considerations in mind it seemed that the high luminosity and low instrumental scattering of the lens-type spectrometer[7] in this laboratory was well adapted, with a few minor modifications, to a detailed study of the phenomenon. Na^{24} was chosen for the subject of the study because of the apparent discrepancy between Rae's[6] deduction of an electric dipole character for the 2.758-Mev γ-ray (hereinafter to be referred to as γ_1), and the work of Brady and Deutsch,[8]

TABLE I. Tabulation of observed and theoretical values of I_1 and I_2.

	Observed value	Theoretical values					
	$\times10^4$	$E1\times10^4$	$E2\times10^4$	$E3$ $\times10^4$	$M1$ $\times10^4$	$M2$ $\times10^4$	$M3$ $\times10^4$
$I_1(\gamma_1=2.76$ Mev)	7.1 ± 0.2	11.20[a]	6.95[a]	4.62[a]	5.30[a]	3.45[a]	2.58[a]
$I_2(\gamma_2=1.38$ Mev)	0.6 ± 0.1	1.87[b]	0.57 ($Z=0$) / 0.38 ($Z=84$) [b]	0.19[a]	0.25[a]	0.07[a]	0.02[a]

[a] See reference 4.
[b] See reference 1.
[c] M. E. Rose (private communication).

* AEC Predoctoral Fellow.

[1] J. C. Jaeger and H. R. Hulme, Proc. Roy. Soc. (London) **148**, 708 (1935).
[2] M. E. Rose and G. E. Uhlenbeck, Phys. Rev. **48**, 211 (1935).
[3] G. K. Horton, Proc. Phys. Soc. (London) **60**, 457 (1948).
[4] M. E. Rose, Phys. Rev. **76**, 678 (1949).
[5] G. D. Latyshev, Revs. Modern Phys. **19**, 132 (1947).
[6] E. R. Rae, Phil. Mag. **40**, 1155 (1949).
[7] H. M. Agnew and H. L. Anderson, Rev. Sci. Instr. **20**, 869 (1949).
[8] E. L. Brady and M. Deutsch, Phys. Rev. **74**, 1541 (1948).

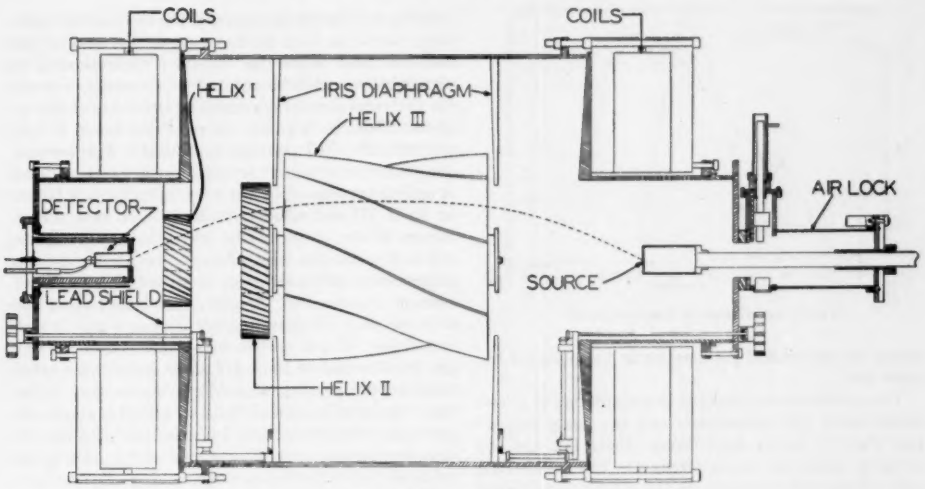

FIG. 1. Diagram of spectrometer.

who had studied the angular correlation of γ_1 and γ_2 (the 1.380-Mev γ-ray) by $\gamma-\gamma$ coincidences, and had found a scheme consistent with two electric quadrupole transitions. Furthermore, as yet the value of the internal pair conversion coefficient of γ_2 (hereinafter to be referred to as I_2) was unknown.

During the course of this work two experiments[9,10] were done which measured I_1 (the internal pair conversion coefficient of γ_1) using essentially the same technique as Brady and Deutsch.[8] In the paper of Cleland *et al.*[10] the results of these two experiments are combined in the value $I_1=(7.5\pm0.8)\times10^{-4}$, strongly suggesting the $E2$ (electric quadrupole) nature of γ_1. This may be compared with the results of this experiment and theoretical prediction by referring to Table I.

While the present work was in progress a similar investigation was carried out by Slatis and Siegbahn[11] for the case of Na^{24} as well as for ThC'', Mn^{56}, and Co^{60}, using a lens-type spectrometer. The method they used was the same, in the essentials, as the one used here, and is described below. They found the values $I_1=8.0\pm0.4\times10^{-4}$ and $I_2=3.0\times10^{-5}$. Although these values differ from the ones obtained here, they yet indicate clearly the $E2$ nature of γ_2 as well as γ_1 (see Table I).

It should be especially noted that in spite of the differences among the various values obtained for I_1 and I_2 in different experiments, with the one exception of Rae's work, they all agree as to the multipolar nature of γ_1 and γ_2. This can be understood from a glance at the graphs of I *versus* γ-ray energy for the various multipole orders as given by Rose.[4] The lower the energy the larger the difference, in percent of any particular coefficient, between coefficients for different multipolarities (see Table I). For γ_1, for instance, it is easy to discriminate between pure $E3$, $E2$, or $E1$ radiation, since I for these changes, respectively, in the ratio 1.0:1.5:2.4 (as predicted by Rose).[4] For γ_2, I (as predicted by Jaeger and Hulme)[12] varies by a factor of more than three from $E3$ to $E1$ radiation. However, I_2 is very low and must be expected to be measured with far less precision than I_1. Nevertheless, in this experiment, as in the experiment of Slatis and Siegbahn, the precision turned out to be adequate to indicate the $E2$ character of the γ_2 radiation. The same considerations apply to magnetic transitions and to comparisons between magnetic and electric transitions.

The possibility of mixed radiation (not considered in any of the above remarks) was examined in this work by comparing the positron spectrum with theoretically predicted spectra for various multipole orders, as well as by considering the absolute value of I.

SPECTROMETER

The beta-ray spectrometer used in this work was the instrument of Agnew and Anderson[7] with modifications to adapt it to the special purposes involved here. The basic outline of the spectrometer is given in Fig. 1. It is double-lensed, the source being located at the

[9] Mims, Halban, and Wilson, Nature **166**, 1027 (1950).
[10] Cleland, Townsend, and Hughes, Phys. Rev. **84**, 298 (1951).
[11] H. Slatis and K. Siegbahn, "*Determination of Multipole Orders from Internal Pair Formation*," *Manne Siegbahn; 1886–3/12–1951* (Almqvist and Wicksell, 1951), p. 153.

[12] See reference 1. The graphs for I *vs* γ-ray energy as given by Rose (reference 4) were calculated only as far down on the energy scale as $3m_0c^2$ (private communication from M. E. Rose).

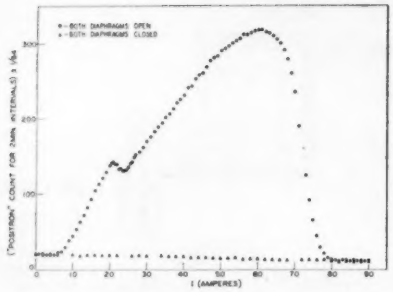

FIG. 2. Actual positron count *vs* current.

center of one coil and the detector at the center of the other coil.

The modifications consisted in the addition of a lead shield inside the spectrometer and two brass helices[12] (see Fig. 1), one of sixty leaves (Helix II), and the other of thirty-six leaves (Helix I). The nine-leaved helix (Helix III) originally in the machine was found to be inadequate for discriminating sufficiently between electrons and positrons. In a test run with P^{32} (before any additions were made to the spectrometer) it was found that with the current in the coils adjusted for positrons, a false "positron" spectrum was observed which roughly followed the shape of the negatron spectrum. The total number of these "positrons" was about 10^{-3} of the negatrons observed and actually consisted of electrons fortuitously scattered through the helix. The addition of the two brass helices and the lead shield in the positions shown (see Fig. 1) brought this figure down to less than 10^{-6}. This electron-positron discrimination ratio was more than sufficient, even for detecting γ_2 internal pair conversion.

A danger of drastically reduced transmission was involved in the use of these helices. Therefore, considerable care was taken to insure that the leaves of the helices were twisted to fit the shape of the trajectories for all values of the radial displacement (r) of the electrons from the axis of the spectrometer. The angle of rotation of the orbit (the angle through which the radial displacement vector moves as the electron moves along its trajectory) is approximately independent of r and is given[7] by

$$\theta_2-\theta_1=K\int_{z_1}^{z_2}H(z)dz,$$

where $\theta_2-\theta_1$ is the angle of rotation between z_1 and z_2, K is a constant, and $H(z)$ is the magnetic field along the axis. The $\frac{1}{32}$ in. thick brass leaves were made to conform to this turbine-like shape by being stamped between appropriately machined forms.

The original helix used had nine leaves and a $36\frac{1}{2}°$ rotation over its 39-cm length. If the fields in the region were altered so as to produce one degree more or less rotation than might be expected theoretically, its transmission would be reduced 2.74 percent, whereas for the same percentage errors in the fields at the regions of Helices II and I, the reduction would be 7.02 percent and 17.62 percent, respectively. Furthermore, the region over which the negatron or positron beam is spread (as defined by the iris diaphragms) is largest at Helix III and smallest at Helix I, so that the accuracy of the shape of the leaves at any particular value of r has the least effect in the former and the largest effect in the latter, as far as reducing the transmission is concerned. Actually, the transmission was reduced about 35 percent after Helices I and II were introduced. This is not too bad if it is considered that the introduction of Helix III alone reduced the transmission by 5 percent, according to Agnew and Anderson.[7] The combination of Helices I and II is about nine times as sensitive to field irregularities as Helix III and, furthermore, cuts off 16 percent of the beam by the cross section of the leaves alone.

The only other change was the addition of the lead shield in which Helix I was supported (see Fig. 1). This was introduced to shield against the background effects due to γ-radiation from the source hitting various parts of the spectrometer and scattering electrons into the counter or being scattered into the counter itself. A series of experiments using a 200-μC Co^{60} source was performed and the characteristics of this type of background were investigated. Co^{60} has two γ-rays (1.16 Mev, 1.32 Mev) and is therefore closely analogous to Na^{24} in that it would produce very much the same type of background as far as γ-radiation alone is concerned.

With the Co^{60} source it was found that when the current in the spectrometer coils was adjusted for positrons and a current survey made, a current-dependent background was found which was unchanged in character whether both or either one of the iris diaphragms (see Fig. 1) were completely closed or open. This meant that all current-dependent background effects due to the γ-radiation were produced by electrons scattered beyond the diaphragm closest to the counter. An experiment with the counter enclosed in a brass shield

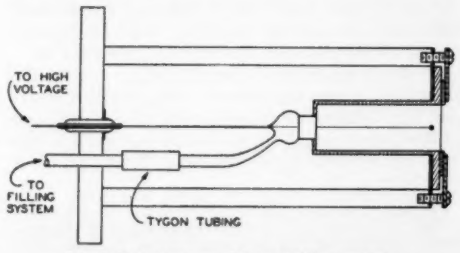

FIG. 3. Detail picture of Geiger-Müller counter.

[12] The original model for these helices was one made by Dr. M. Friedman of the Argonne National Laboratory.

showed that about $\frac{1}{3}$ of the background was due to these scattered electrons.

Because this type of background is independent of the opening or closing of the iris diaphragms, a genuine positron spectrum is corrected for background of this nature by closing the iris diaphragms, repeating the survey, and taking the difference of the two resulting spectra, which is the desired true positron spectrum. An important consideration when measuring the γ-background in this fashion is whether electrons or positrons can leak through small openings between the closed down iris diaphragm and the lead core (see Fig. 1). This contingency was provided against by arranging for the iris diaphragm closest to the counter to close down behind a $\frac{1}{4}$-in. high aluminum lip. Penetration through the iris diaphragm to the detector is quite unlikely, since at the openings used each iris diaphragm had a mean thickness of 0.635 cm ($\frac{1}{4}$-in. Al) except at the edges, where the thickness was that of the individual leaves ($\frac{1}{32}$ in.). The mean thickness corresponds to a range of 3.41 Mev for electrons (using a modified Feather's Rule),[14] more than twice greater than the maximum negatron energy involved here. The individual leaf thicknesses were enough to scatter the electrons so that they would not be detected. All this is also true for the positrons, since the same considerations apply to both.[15]

The introduction of the lead shield alone lead to a reduction in the γ-background by a factor of two. The addition, then, of Helix I accounted for an additional factor of two. This can easily be understood since all scattered electrons entering the window of the Geiger-Müller counter must first pass through the spiral leaves of Helix I, and few of them could be expected to have either the proper momentum or the proper orbit orientation. The effect of Helix II was negligible in this connection, which is consistent with the experimental evidence described above.

The high efficiency of this type of shielding against high energy γ-radiation background can be clearly seen from Fig. 2, which shows a plot of the actual number of counts counted on the Geiger-Müller counter *versus* the positron current, in the case of Na^{24}. The true positron count is, on the average, about ten times as large as the γ-background count obtained with both iris diaphragms closed. Since the magnitude of the positron effect in this case is 7×10^{-4}, it could be expected that under similar conditions spectra spreading over roughly the same momentum interval could be measured reasonably accurately down as low as 7×10^{-6}; and if the momentum interval should be shorter, the lower limit of the coefficient would be smaller but still determinable to a comparable accuracy.

In its final running condition the spectrometer had a transmission of 2.2 percent and a resolution of 10.23 percent. The poor resolution was largely the result of two factors: (1) The relatively wide openings used in the iris diaphragms (see Fig. 1); (2) The large size of the source (diameter=1.2 cm). The wide opening of the iris diaphragms was necessary in order to have a high transmission, and the large size of the source was dictated by the need of having a low source thickness so as to distort the positron and negatron spectra as little as possible (see below).

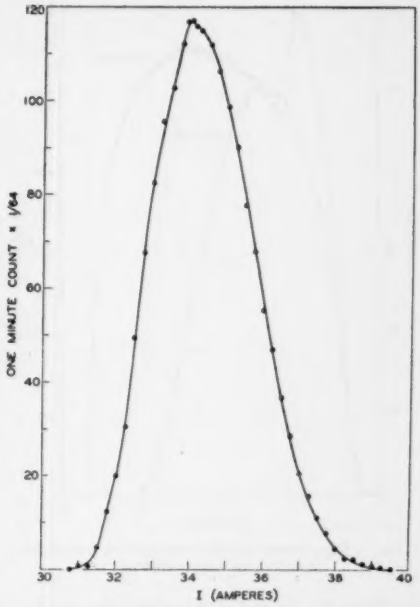

FIG. 4. Ba^{137} K-conversion line.

DETECTOR

The detector used was a Geiger-Müller counter (see Fig. 3) with a 1.19 mg/cm² window sealed in place with Araldite. The center wire was made of 5-mil platinum wire with a 2-millimeter bead on the unsupported end. The counter was pumped and filled *in situ*, since the window was too thin and too large to sustain atmospheric pressure.

Thin window counters (<0.1 mg/cm²) were tried in the initial phases of the experiment but abandoned because they necessitated the use of grids reducing the transmission by $\frac{2}{3}$ or more.

The counter had a plateau of 20-volts width using a filling mixture of ethyl acetate vapor (7 percent) and neon at a total pressure of 8.9 cm. Since batteries were used for the high voltage supply, the short plateau was no serious problem, although the region of the plateau did shift upwards for a period of a day immediately

[14] L. E. Glendenin, Nucleonics **2**, No. 1, 12 (1948).
[15] W. Heitler, *The Quantum Theory of Radiation* (Oxford University Press, London, 1947).

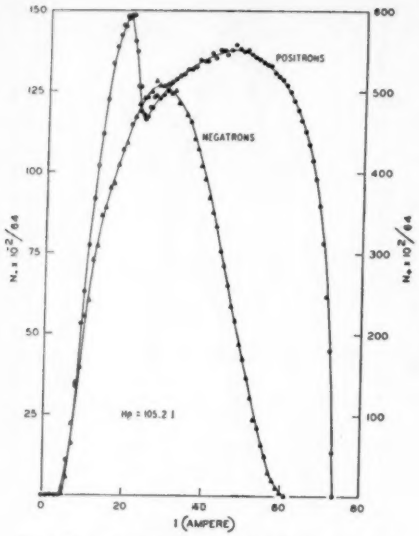

FIG. 5. Experimental negatron and positron momentum spectra (resolution corrected).

after filling. At the end of this period the counter remained stable for the rest of the experiment.

SOURCES

There were three sources used in the experiment. The first was the Na^{24} source, the second Cs^{137}, and the third Co^{60}. The cesium source was used for calibrating the spectrometer and for measuring its resolution, using the 0.6253-Mev K-conversion line[16] of Ba^{137}. The Co^{60} source was used in source and window thickness corrections (see below).

The Na^{24} source was deposited on an aluminum-coated Nylon film <0.08 mg/cm² in thickness, in the form of sodium fluoride solution. This solution was spread out over a circular area 1.2 cm in diameter, and, when dried, left a deposit of 4.5 mg of sodium fluoride. The effective thickness of the source, as derived from the Fermi plot of the beta-spectrum (see below), was indicated to be from 6–10 mg/cm². This was due to clumping of the NaF crystals. Because of this effect sources of larger area produced no significant decrease in effective thickness while sources of smaller area tended to pile the crystals on top of each other and increase the effective thickness.

The Nylon film backing was stretched on a light Bakelite frame[7] two inches in diameter and was made conducting by evaporating an aluminum layer on to it <0.02 mg/cm² in thickness. The edge of the foil was then grounded to the machine through a layer of Aquadag painted on one of the thin Bakelite columns supporting the frame.

Both the Cs^{137} and Co^{60} sources were made so as to be exact duplicates of the Na^{24} source in size and location, and were deposited on a similar backing. The shape of the Ba^{137} K-conversion peak is shown in Fig. 4. The resolution is 10.23 percent and $H\rho = 105.2I$, where

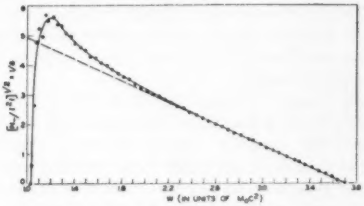

FIG. 7. Fermi plot of Na^{24} β^- spectrum.

I is the current in amperes. The formula for $H\rho$ is based on the assignment of the K-conversion kinetic energy[16] to the position of the peak at 34 amperes.

The activity of the Na^{24} at the beginning of the experiment was 2.5 millicuries and the activity of the Cs^{137} source was about 1.5 microcuries.

EXPERIMENTAL PROCEDURE

The experimental procedure used here consisted of a series of spectrometer current surveys of the radioactive emanations from Na^{24} and Mg^{24}. The first survey was that of the positron spectrum emitted by the excited states of Mg^{24}, the positron decay of Na^{24} being energetically impossible.[10] The second survey was that of the current dependent γ-produced background, conducted with both iris diaphragms closed down (see Fig. 1). The iris diaphragms were then reopened to their original aperature and the third survey was made on the negatron spectrum of Na^{24}. This last survey was conducted after a few days lapse, to allow the source to decay to an activity practicably observable. The observed spectra were then converted to momentum spectra (see Figs. 2 and 5), and procedures were intro-

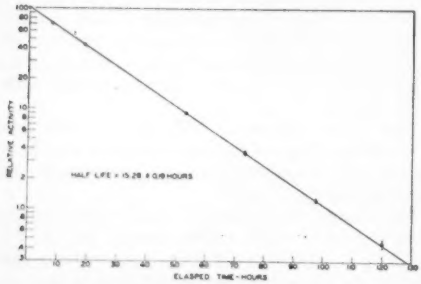

FIG. 6. Semilog plot of decay curve.

[16] L. M. Langer and R. D. Moffat, Phys. Rev. 78, 75 (1950).

duced (see below) to remove distortions due to source and window thickness and finite resolution. After a separation of the two overlaid positron spectra due to γ_1 and γ_2 (see below), a comparison of the areas of each of these spectra with the total area of the negatron spectrum gave numerical values for I_1 and I_2 (see Table I).

RESULTS

The experimental results are contained in Figs. 2 and 5. Figure 2 is a plot of the actual counts obtained as a function of current from the positron run, for the two conditions of the iris diaphragms open and closed. Figure 5 is a plot of the observed positron and negatron momenta spectra, the positron spectrum having first been corrected for γ-background in the manner described above. The data of both Figs. 2 and 5 are corrected for the counter background, which amounted to 10.3 counts per minute, and for radioactive decay back to a time about an hour before the actual beginning of the experiment. The half-life used in the decay correction was the latest published value, 15.06 hours.[17] The half-life of the source (checked after the spectrometer runs) was found to be 15.28±0.19 hours (see Fig. 6). The error is within range of Sreb's measurement.

The positron and negatron spectra in Fig. 5 are also corrected for the effect of resolution. This was done by assuming a perfect-resolution shape for each spectrum and then folding it into the resolution curve (see Fig. 4). The resulting curve (i.e., the fold of the resolution curve and the assumed spectrum) should reproduce the observed spectrum in each case. This process was iterated until the actual spectrum and the derived one agreed to within about 1 percent, except in the vicinity of the end point where the agreement is necessarily more uncertain.

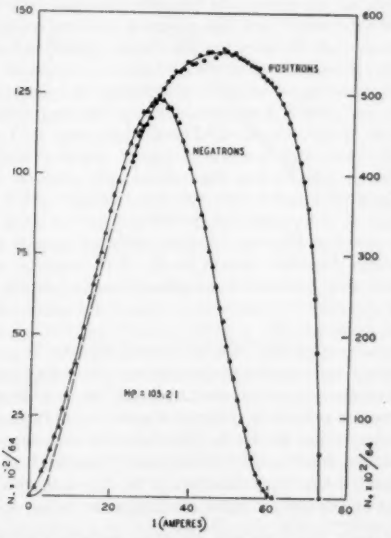

FIG. 8. Negatron and γ_1 positron momentum spectra of Na^{24}. Both spectra are corrected for source and window thickness distortion and resolution distortion. The extrapolation of the γ_1 positron spectrum below 24 amperes (0.36 Mev) is based on the method described under "Positron Spectra."

[17] J. H. Sreb, Phys. Rev. **81**, 469 (1951); he finds the half-life to be 15.060±0.039 hours.

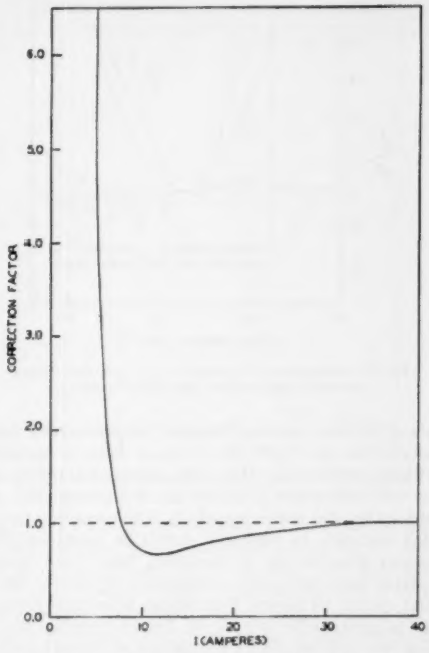

FIG. 9. Correction curve as derived from Na^{24} Fermi plot.

THE POSITRON SPECTRA

The observed positron spectrum is distorted by the effects of source and window thickness. This distortion has been corrected to some extent by studying suitable negatron spectra whose effective source thickness was made identical with that of the positron source and whose true shape is that given by the allowed Fermi distribution. The γ_1 positron spectrum was corrected with a correction function derived from the β^- spectrum of Na^{24}, which is emanated along with the γ_1 positrons from the same NaF source. The γ_2 positron spectrum was corrected with a function similarly derived from the β^- spectrum of Co^{60}.

The Fermi plot of the observed negatron spectrum (see Figs. 5 and 7) starts to depart from linearity at

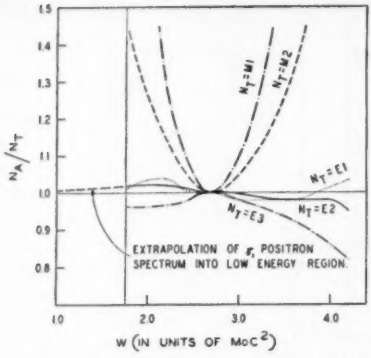

FIG. 10. Comparison of observed γ_1 spectrum and various theoretical spectra (see "Discussion" section).

about 0.7 Mev, whereas Siegbahn[18] showed with a thin source that the Fermi plot is linear down to energies at least as low as 0.2 Mev. This distortion is produced by the finite source thickness and is a combination of absorption and scattering effects. The correction function necessary to remove it should be approximately correct also for the γ_1 spectrum, since both these spectra have end points considerably beyond 0.7 Mev and, as will be shown, their shapes below this energy are roughly similar (see Fig. 8). Thus a correction function was derived from a comparison of the extrapolation of the straight line portion of the negatron Fermi plot and the observed Fermi plot (see Figs. 8 and 9), and applied to both the negatron spectrum and the γ_1-positron spectrum. In the case of the γ_1 positron spectrum this correction could not be applied below 0.36 Mev because of the presence of the γ_2 spectrum in this range, which made it necessary to separate the

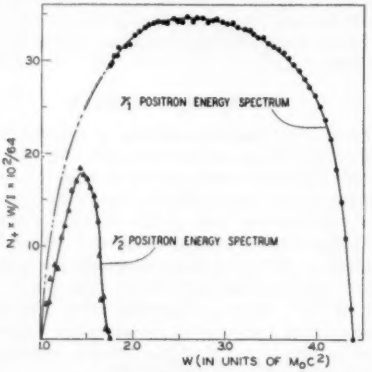

FIG. 11. Energy spectra of γ_1 and γ_2 positrons.

[18] Kai Siegbahn, Phys. Rev. **70**, 127 (1946).

spectra in order to calculate I_1 and I_2. To this end, the corrected γ_1-positron spectrum was referred to an appropriate theoretical spectrum and an extrapolation of the curve of this comparison was made from 0.36 Mev down to zero energy (see Fig. 10). The theoretical spectrum chosen was based on the $E2$ spectrum for a γ-ray energy of 2.76 Mev as predicted by Rose.[4,19] The appropriateness of this choice was well borne out by the results and is further discussed later in this report. The results of all these corrections are given in Figs. 8 and 11.

After the source and window thickness distortion correction and the extrapolation into the low energy region had been applied to the observed γ_1 spectrum, the inverse of the source and window correction function was applied to the corrected spectrum in order to gain an idea as to how much of an effect was involved. The uncorrected spectrum gave 5 percent more positrons than the corrected spectrum. Since the shape of the corrected negatron spectrum corresponds closely to the shape of the γ_1 positron spectrum, as extrapolated in its corrected form, in the region where the correction is necessary (see Fig. 8), it is felt that a 50 percent uncertainty in the correction of the γ_1 positron spectrum area is a liberal estimate, which means a probable error of 2.5 percent in the deduced value of I_1.

In order to obtain the positron spectrum due to γ_2, the extrapolated part of the γ_1 positron spectrum, uncorrected for source and window thickness distortion, was subtracted from the observed positron spectrum, uncorrected. In order to obtain some correction for the effect of source and window thickness, a source of Co^{60} was made up, of identical distribution and location as the Na^{24} source. A survey of the negatron spectrum was made at the original thickness, which was <0.1 mg/cm^2. Four and five-tenths mg of inactive NaF in aqueous solution was then added and, after the artificially thickened source was dry, a second survey was made. A comparison of the Fermi plots of these two surveys (see Fig. 12), identical with the type of comparison described above for the Na^{24} negatron spectrum, then produced a correction function (see Fig. 13) for the effect of source and window thickness, which was applied to the γ_2 positron spectrum. The corrected γ_2 momentum spectrum is shown in Fig. 14. It gave 7 percent more positrons than the uncorrected spectrum. Since the γ_2 positron spectrum and the Co^{60} β^- spectrum not only have different shapes but different end points, it can hardly be expected that the correction function is an entirely reliable one; however, it can be expected that the correction is in the right direction and of the proper order of magnitude, as far as the

[19] Rose's calculation uses the Born approximation ($Z=0$), whereas in the present case the emitted nucleus (Mg) has a positive coulombic charge of $12e$. The Z-dependence was inserted by multiplying his formula by the factor

$$f(\xi_+,\xi_-)=\frac{(2\pi\xi_+)(2\pi\xi_-)}{(e^{2\pi\xi_+}-1)(1-e^{2\pi\xi_-})},$$

where $\xi_+=Ze^2/\hbar v_+$ (see reference 15).

calculation of I_2 is concerned. The energy spectrum with the correction included is given in Fig. 11.

The shape of the derived γ_2 spectrum and its total integrated value is also affected by the degree of accuracy of the extrapolation of the γ_1 positron spectrum. This statement applies to the γ_1 spectrum as well, but to a different degree, the γ_2 positron spectrum being about ten times as sensitive to extrapolation inaccuracy as the γ_1 spectrum. Also, the two are oppositely affected, a too high answer in I_1 giving a too low answer in I_2, and vice versa. In order to ascertain how much of a change a different extrapolation would cause in the values of I_1 and I_2, it was assumed that below 0.8 Mev the shape of the observed γ_1 spectrum should correspond exactly to the theoretical $E2$ spectrum (see Fig. 10). On the basis of this extrapolation the deduced value of I_1 was decreased 1 percent and that of I_2 was increased 12 percent, which magnitudes give a reasonable estimate as to the uncertainties in I_1 and I_2 due to this correction.

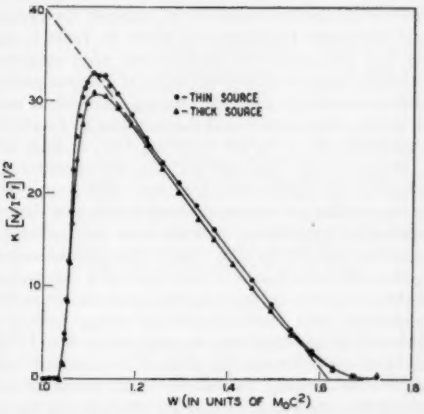

FIG. 12. Fermi plot of thin and thick Co^{60} sources.

EXTERNAL PAIR-PRODUCTION

The errors due to external pair-production (within the source itself) amounts to less than 0.1 percent for both I_1 and I_2. This estimate is based on the values of the cross section for pair-production as calculated from the Bethe-Heitler formula[15] and an assumed effective thickness of 8 mg/cm² for the NaF source. The effective source thickness was estimated by comparing the Fermi plot obtained here (see Fig. 7) with Fermi plots obtained with similar sources of known uniform thickness. The energy at which deviation from the straight line Fermi plot began was assumed to be proportional to the effective source thickness, and a value was calculated for the effective source thickness of the NaF source used in this experiment. This is a very rough

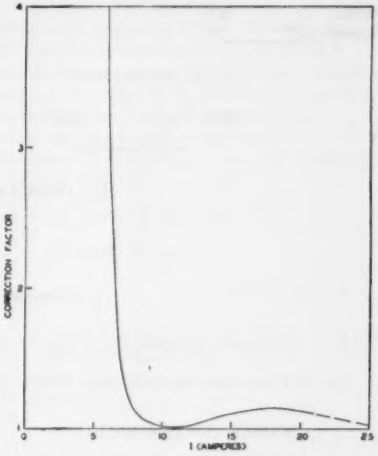

FIG. 13. Correction curve as derived from Co^{60} Fermi plot.

approach, but for the purposes involved here it was quite adequate. It generally gave values far in excess of the average thickness (3.9 mg/cm²), although these values were quite scattered. Two criteria used in selection were (1) that the sources should be of the same order of magnitude thickness as the average thickness of the NaF source used in this experiment; (2) that the energy end point of the spectrum should be greater than 1 Mev. With reference to criterion (2) it should be pointed out that it was felt that electrons or positrons whose energies were greater than 1 Mev contributed little to distortions in the Fermi plot beginning at energies equal to or less than 0.7 Mev, as was the case here (see Fig. 7). For this reason it could be expected that the results of this method should be fairly insensitive to the energy end point of the Fermi plot used for comparison, and this was found to be the case. The figure obtained by this method was 8 ± 2 mg/cm².

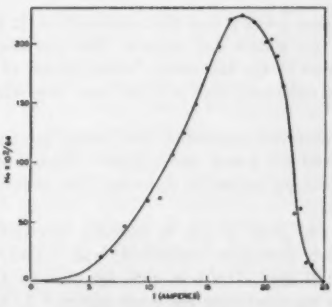

FIG. 14. γ_2 positron momentum spectrum.

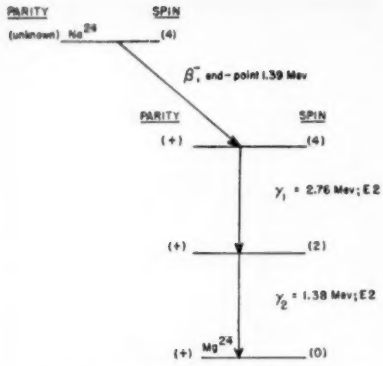

FIG. 15. Energy level diagram for decay of Na^{24}.

SOURCE CONTAMINATION

Since the half-life determination was carried out over a period of thirteen days after the beginning of the spectrometer runs and since, in that time, the source did not exhibit a half-life significantly different from the expected one (see Fig. 4), the contamination level of long-lived positron emitters (such as Na^{22}) must have been of the order 10^{-6}, during the time of the positron run. Such contamination could cause at most an error of the order of 0.1 percent in the value of I_1 or 1 percent in the value of I_2. Since these errors are insignificant compared to the actual uncertainties, they have been ignored.

2.758-Mev γ-Ray (γ_1)

The internal pair conversion coefficient of γ_1 was computed by taking the ratio of the area of the γ_1-positron spectrum to the area of the negatron spectrum, both spectra being corrected for source and window thickness distortion and resolution distortion (see Fig. 8). The result was

$$I_1=(7.1\pm0.2)\times10^{-4}.$$

The error given is that due to uncertainty in the correction for source and window thickness distortion, and errors in the low energy extrapolation of the γ_1 positron spectrum, both of which have been estimated above.

The observed momentum and energy spectra, after corrections for source and window thickness spectral distortion and resolution distortion, are given in Figs. 8 and 11.

The end point of the γ_1 positron spectrum, after resolution distortion correction, was found to be 1.73 ± 0.02 Mev. This is in good agreement with what is to be expected from the γ-ray energy,[18] 2.758 Mev, after subtracting $2m_0c^2$.

1.380-Mev γ-RAY (γ_2)

By taking the ratio of the corrected γ_2 spectrum area (Fig. 14) to the corrected negatron spectrum area (Fig. 8), the internal pair conversion coefficient for γ_2 was found to be

$$I_2=(0.6\pm0.1)\times10^{-4}.$$

The error given is much larger than that for I_1 because of the much greater uncertainties in the correction for source and window thickness and in the extrapolation of the high energy spectrum. For the same reasons the localization of the end point of the γ_2 spectrum is less certain than for the γ_1 spectrum. The measured end point was (0.35 ± 0.02) Mev. The error includes the end-point energy to be expected from the γ-ray energy,[18] 1.380 Mev, after subtracting $2m_0c^2$.

DISCUSSION

A comparison of the measured values of I_1 and I_2 with the theoretical values to be expected for various pure multipolar transitions, as shown in Table I, and the fact that only odd electric and even magnetic transitions may occur between states of different parity, while even electric and odd magnetic transitions may occur only between states of the same parity, limits the possibilities for γ_1 to the following two: 1. Pure $E2$. 2. Mixture of $E1$, $E3$, and $M2$. The experimental observations of Brady and Deutsch,[6] who found the $\gamma_1-\gamma_2$ angular correlation consistent with two electric quadrupole transitions, indicate that the radiations should be pure $E2$ for both γ-rays. The conclusion that γ_1 is an $E2$ transition is a result also of a comparison of the γ_1 positron energy spectrum, as measured in this experiment, with various theoretical energy spectra of pure multipolar transitions as predicted by Rose,[4] with an added correction for the effect of the Coulomb field of the Mg^{24} nucleus (see above). The results of this comparison are shown in Fig. 10, which is the plot of the ratio of the observed energy spectrum (N_A) to various theoretically predicted energy spectra (N_T) as a function of energy, for all energies from 0.36 Mev to close to 1.73 Mev. This plot shows that only two theoretical spectra, those for $E1$ and $E2$, have a close resemblance to the observed shape. However, any mixture of $E1$, $E3$, and $M2$ arranged to yield the observed value of I_1 will produce a theoretical spectrum differing far more from the observed spectrum than the pure $E2$ spectrum, aside from deviations near the end-point, which are relatively large in all cases. Thus we see that the pure $E2$ spectrum provides the best fit to the data of all possible combinations.

In the case of γ_2 the value of I_2 seems to limit the possibilities to pure $E2$ radiation alone. However, we cannot substantiate this by a comparison with theoretical spectra because of distortions affecting the entire observed spectrum. Nevertheless, the evidence for pure $E2$ radiation as against other alternatives is very persuasive, since the $\gamma_1-\gamma_2$ angular correlation is also

characteristic of an $E2$ transition. Thus we make the assignment of pure $E2$ radiation in the case of γ_2 as well as γ_1. This conclusion is very much in line with the recently published work of Goldhaber and Sunyar,[20] who find that the first excited state of about 30 even-even nuclei has spin 2 and + parity (all spin 0 and + parity in the ground state).

Figure 15[21] summarizes the conclusions of this section.

[20] M. Goldhaber and A. W. Sunyar, Phys. Rev. **83**, 906 (1951).
[21] D. E. Alburger and E. M. Hafner, Revs. Modern Phys. **22**, 373 (1950).

No conclusions from the data in this experiment can be derived as to the parity of Na^{24}. The spin assignment of Na^{24} comes from the recent work of Smith.[22]

I should like to express my profound gratitude to my sponsor, Professor H. L. Anderson, whose interest and encouragement made possible this work.

I would also like to express my thanks to C. Y. Fan, David Saxon, M. Goldberger, and M. Friedman for their generous help.

[22] K. F. Smith, Nature **167**, 942 (1951).

PHYSICAL REVIEW VOLUME 88, NUMBER 2 OCTOBER 15, 1952

Rocket Determination of the Ionization Spectrum of Charged Cosmic Rays at $\lambda = 41°N$

G. J. Perlow,* L. R. Davis, C. W. Kissinger, and J. D. Shipman, Jr.
U. S. Naval Research Laboratory, Washington, D. C.
(Received June 30, 1952)

In a V-2 rocket measurement at $\lambda = 41°N$ an analysis has been made of the various components of the charged particle radiation on the basis of ionization and absorption in lead. The ionization was determined by two proportional counters, the particle paths through which were defined by Geiger counters. With increasing zenith angle toward the north, the intensity is found to be substantially constant until the earth ceases to cover the under side of the telescope. The intensity of all particles with range ≥ 7 g/cm² is 0.079 ± 0.005 (cm² sec steradian)$^{-1}$. Of this an intensity 0.012 ± 0.002 is absorbed in the next 14 g/cm². The ionization measurement is consistent with $\frac{1}{4}$ of these soft particles being electrons of $<\sim 60$ Mev, the remainder being slow protons and alpha-particles. For the particles with greater range an ionization histogram is plotted, the smaller of the two ionization measurements for a single event being used to improve the resolution. The particles divide into protons, alpha-particles, and one carbon nucleus, with $N_p/N_\alpha = 5.3 \pm 1.0$. Their absorption is exponential with mean free path 440 ± 70 g/cm² Pb. Extrapolating to zero thickness, the total primary intensity is 0.070 ± 0.005 (cm² sec steradian)$^{-1}$ with 0.058 ± 0.005 as protons, 0.011 ± 0.002 as alpha-particles, and 0.001 ± 0.001 as $Z > 2$.

INTRODUCTION

THIS paper reports on some measurements made on February 17, 1950, by apparatus flown in a V-2 rocket. The launching occured at White Sands, New Mexico (geomagnetic latitude 41°N). The purpose was to distinguish among and count the various components of the charged particle cosmic radiation above the atmosphere. For each particle which entered the solid angle of a Geiger tube telescope, the ionization was measured twice, using proportional counters for the purpose. The subsequent history of each particle in traversing lead absorbers was then recorded. In this way the poor statistics of a rocket flight were somewhat compensated by detailed knowledge of each recorded event.

THE EXPERIMENTAL METHOD

Figure 1 shows the telescope schematically. The rocket nose in which it was mounted was a conical shell of $\frac{1}{16}$-inch Al joining at the wide end and about halfway down the telescope to an Al cylinder $\frac{1}{4}$-inch thick. The coincidence ABC (which we shall abbreviate as T) defined a beam of particles which traversed the proportional counters P_1 and P_2. No event of any sort was registered unless the threefold T occured coincidently. The discharge of either group S_1 or S_2 indicated a "side" shower, as did the discharge of both counters A_1, A_2 comprising tray A or C_1, C_2 of tray C. The side showers were presumably undesired events but were registered for information. Counter trays D, E, and F beneath their respective lead absorbers covered the solid angle of T with some overlap. Thus, each selected particle was interrogated as to its range in lead within certain limits. Trays D and E were further subdivided into threefold sets and tray F into a fourfold set. In this way showers produced in the absorbers could be detected, provided of course that T was tripped.

The proportional counters contained argon with 2 percent of CO_2 and were filled to atmospheric pressure. Figure 2 is a plot of multiplication vs voltage obtained by irradiating the active region with γ-radiation and measuring the current with a vibrating reed electrometer. The counters behaved identically, although this was actually not essential to the reduction of flight data. The counters were operated finally at a multiplication ~ 2000. The stability of voltage was not a problem at any time.

The electronic coincidence circuits were of the diode

* Now at the University of Minnesota, Minneapolis, Minnesota.

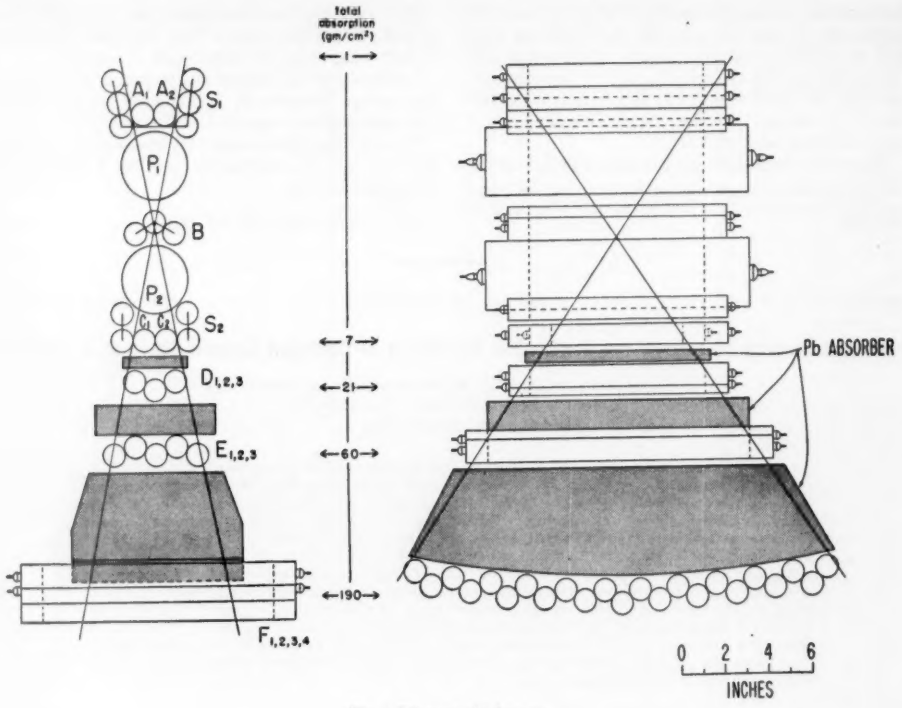

FIG. 1. Diagram of telescope.

type,[1] with resolving times ~5 μsec. The proportional counter pulses were separately amplified, gated by a pulse derived from the event T, stretched to 20 milliseconds for radio telemetering,[2] and then annihilated. By using high and low sensitivity scales the range $0 \leq I \leq 35I_0$ was covered with good accuracy. Here I_0 is the most probable ionization of a fast singly charged particle in one proportional counter. The ionization system was calibrated with the sea-level hard component.

Figure 3 shows two sections of the flight telemetering record with various events identified on the basis of ionization and penetration.

The zenith angle of the rocket, hence of the telescope, was determined to $\pm 2°$ by motion picture photography of the horizon using a simple sort of wide-angle lens (~110° angular aperture). The rocket's azimuth was determined by land marks and by the position of the sun's image during parts of the flight. Gyroscopes confirmed the camera data.

[1] Howland, Schroeder, and Shipman, Rev. Sci. Instr. **18**, 551 (1947).
[2] N. R. Best, Electronics **23**, No. 8, 82 (1950).

INTENSITY OF THE TOTAL RADIATION

The rocket rose to a maximum height of 150 km, 220 seconds after launching. At the maximum, the zenith angle was 68° and continuing a nearly linear increase with time. The azimuth angle was 10° west of geographic north (19.5° west of geomagnetic north) and slowly turning toward geographic north. The azimuth of the rocket may be generally summarized in the statement that whenever the telescope was not nearly vertical, it pointed nearly north.

Table I is a summary of data without regard to ionization. They are divided into five 50-second intervals starting at 68 seconds from take-off. At that time the atmospheric depth was 2.5 g/cm² and decreasing about 20 percent per second. The range of zenith angle variation is listed for each time interval. The rows of the table refer to events of different penetration, *TDEF*, for example, denoting penetration of the total absorber. The supports and counter walls are an appreciable part of the absorber for events of small penetration, but are lumped together with the lead as g/cm². In each time interval for each type of event we list the number of events R to be retained because they are not associated

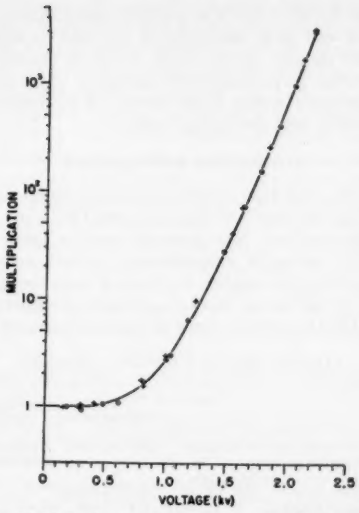

FIG. 2. Multiplication *vs* voltage for the proportional counters.

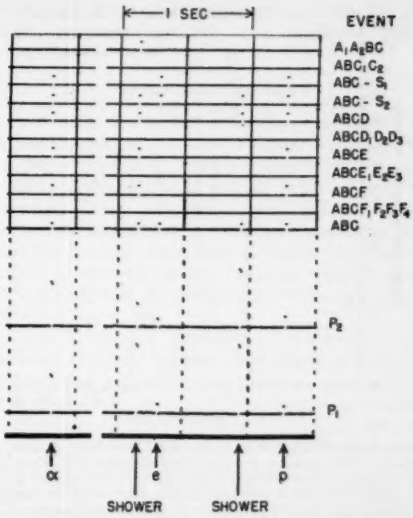

FIG. 3. Two samples of the telemetering record. The low sensitivity scales of ionization do not appear on this record. The particle marked α penetrates at least 190 g/cm² Pb without a detectable shower and ionizes at about $4I_0$. The particle marked p has the same history except that the ionization is $\sim I_0$. The particle marked e stops in the first absorber with ionization $\sim I_0$ and is considered an albedo electron. Two events showing showers above the lead fall in the Δ class (deleted events).

with showers above the absorber (i.e., no A_1A_2, C_1C_2, S_1, or S_2). The columns marked Δ, list events deleted for the opposite reason. The following observations may be made:

(1) The total number of retained events R does not change within statistics in the first three intervals comprising the zenith angle spread $6° \leq \theta \leq 63°$ and leads to a value 0.079 ± 0.005 (cm² sec sterad)$^{-1}$ for the intensity from the neighborhood of the vertical for 7 g/cm² telescope thickness and rocket skin. This is in agreement with the measurements of others.[3]

(2) The total intensity apparently increases abruptly by a factor of 1.5 for the last two intervals $63° \leq \theta \leq 101°$. The increase is nearly all in the penetrating component *TDEF*, and examination of the ionization shows it attributable mainly to partizles of $Z=1$.

(3) The rate of *deleted* events increases monotonically with θ to a value in the fourth and fifth time intervals 2.4 times that in the first. This increase is not specific to any particular type of event but changes in about the same ratio for all except the softest particles T. Excluding these, the increase in Δ is found to be strongly associated with showers below the lead. Thus, comparing 6°–42° with 63°–101°, the increase in Δ, *TDEF* is 33 per 100 seconds while the increase in the subclass of these events which show showers somewhere below the lead is found to be 25 per 100 seconds. This suggests that the increase in Δ events is caused by nuclear interactions in the lead due to primaries coming from outside of the solid angle of T. Figure 4 illustrates the

TABLE I. Summary of events without regard to ionization.[a]

Time (sec)		68–117		118–167		168–217		218–267		268–317	
Zenith angle		6°–19°		19°–42°		42°–63°		63°–82°		82°–101°	
Event	Range (g/cm²)	*R*	Δ	*R*	Δ	*R*	Δ	*R*	Δ	*R*	Δ
T	$7 \leq X < 21$	6	4	4	4	8	14	9	7	7	9
TD	$21 \leq X < 60$	1	11	1	11	5	10	7	18	3	23
TDE	$60 \leq X < 190$	11	8	8	15	5	19	4	31	10	25
TDEF	$190 \leq X$	21	15	20	19	25	18	40	33	36	34
Total		39	38	33	49	43	61	60	89	56	91

[a] The columns marked Δ represent events accompanied by a shower above the absorber and are to be discarded finally. The columns marked *R* represent the opposite case and are to be retained.

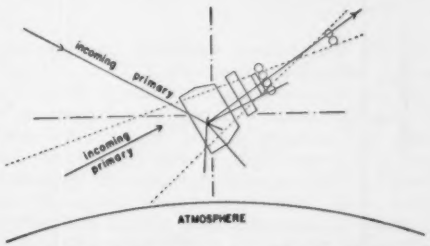

FIG. 4. The particle coming in from the upper left produces a shower in the lower absorber and an event classified as Δ, *TDEF*. The figure also serves to illustrate the cause of the apparent increase in intensity with zenith angle as the effective atmospheric layer ceases to shade the telescope from radiation as at the lower left.

[3] Winckler, Stix, Dwight, and Sabin, Phys. Rev. **79**, 656 (1950); J. A. Van Allen and S. F. Singer, Phys. Rev. **78**, 819 (1950).

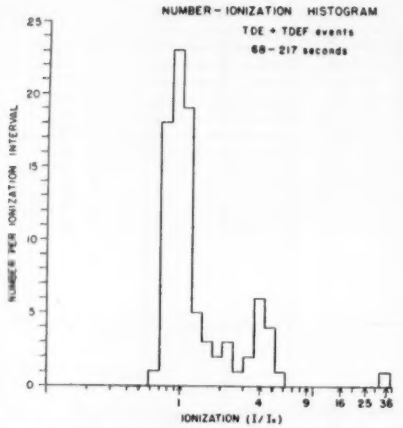

FIG. 5. Distribution in ionization for 150 seconds of flight, of particles which produce a count below 60 g/cm² Pb. There are two ionization measurements of each particle. The smaller of the two is plotted in this histogram. I_0 is the most probable ionization of a fast singly charged particle in one proportional counter.

process which becomes more probable with increasing θ. With the aid of this figure one may also visualize the main cause of the increase in retained events R for $\theta > 60°$. During the time of interest the tangent to the earth lies 12° below the plane $\theta = 90°$. The effect of the atmosphere is to decrease this dip angle to 10° for the process to be considered. The angular aperture of the telescope is $\pm 35°$ in one plane and $\pm 6°$ in the other. The rocket rolled about its axis with a period of about 20 seconds. After the zenith angle reached 45° it was possible, depending on the roll angle, to receive radiation through both ends of the telescope, the effect becoming

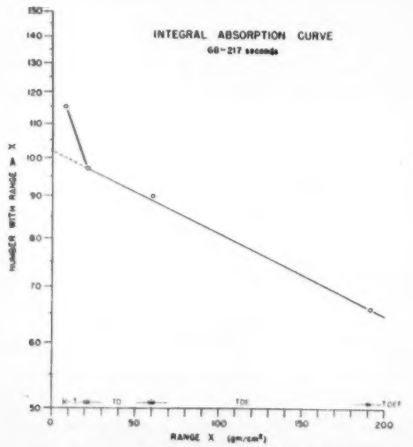

FIG. 6. Absorption in lead of the total radiation.

serious for $\theta > \sim 65°$. The particles going through the bottom end must penetrate all the lead to register, thereby showing up as *TDEF* events as observed. A calculation gives qualitative agreement but does not rule out some increase in the intensity of the penetrating component near the (north) horizon.[4]

IONIZATION DISTRIBUTION

In Fig. 5 we have plotted a number-ionization histogram for the combined class of events *TDEF* and *TDE* for the first three time intervals listed in Table I. Of the two ionization measurements for each event we have chosen the smaller. It is known[5] that the general shape of the energy loss and ionization distribution in cases like the present, where the particle loses very little

TABLE II. Intensities of the various components.

	Present measurements	Measurements of others
Total ionizing particle intensity (range ≥ 7.0 g/cm²)	0.079 ± 0.005	0.082 ± 0.002[a] 0.073 ± 0.006[b]
Total primary intensity (extrapolation to zero g/cm², Fig. 6)	0.070 ± 0.005	
Proton/alpha ratio	5.3 ± 1.0	
Primary proton intensity	0.058 ± 0.005	
Primary alpha-particle intensity	0.011 ± 0.002	
Primary $Z > 2$ intensity	0.001 ± 0.001	$(8.3 \pm 0.7) \times 10^{-4}$[c]
Albedo particle intensity ($7 \leq$ range ≤ 21 g/cm²)	0.012 ± 0.002	
Electrons ($< \sim 60$ Mev)	0.008 ± 0.002	
Slow protons	0.003 ± 0.001	
Slow protons or alpha-particles	0.001 ± 0.001	

Intensities in (cm² sec steradian)⁻¹

[a] Range ≥ 34 g/cm² Pb at 15 g/cm² depth [Winckler, Stix, Dwight, and Sabin, Phys. Rev. **79**, 656 (1950)].
[b] Range $> \sim 4$ g/cm² Cu in rocket [J. A. Van Allen and S. F. Singer, Phys. Rev. **78**, 819 (1950)].
[c] Primary $Z \geq 6$ intensity at $\lambda = 41.7°$N [Kaplon, Peters, Reynolds, and Ritson, Phys. Rev. **85**, 295 (1952)].

of its energy in the measuring instrument, is a Gaussian curve with a tail toward high energies. Taking the smaller of two measurements greatly diminishes the tail. The ionization scale is logarithmic, the interval size increasing proportionally with the ionization. Monoenergetic groups of different Z have distributions of nearly equal width on such a plot.

The proton peak at $I/I_0 \sim 1$ and the alpha-particle peak centered about $I/I_0 \sim 4$ may be seen clearly. One particle was observed with $Z = 6$ and none between this and the alpha-particle group. The statistics do not, however, permit conclusions to be drawn regarding the presence of Li, Be, or B primaries. The division into alpha-particle and proton peaks is uncertain by a few particles, but using $I/I_0 = 2.5$ as a dividing line we get a ratio of 5.3 protons for each alpha-particle.

The event *TD* corresponding to a range $21 \leq X < 60$

[4] A similar increase with θ in a rocket flight has been reported by S. F. Singer, Phys. Rev. **77**, 729 (1950). The explanation given here seems to apply to his observations.
[5] E. J. Williams, Proc. Roy. Soc. (London) **A135**, 108 (1932); L. Landau, J. Phys. (U.S.S.R.) **8**, 201 (1944); N. Bohr, Det Kgl. Danske Videnskab. Selskab, Mat.-fys. Medd. **18**, No. 8 (1948).

g/cm² occurs only once in each of the first 50-second intervals of Table I and 5 times in the third for a total of 7 to be considered. On the other hand, 31 cases are deleted because of showers above the absorbers. Thus there is some doubt as to whether all the events are real. A histogram of them shows 6 in the $Z=1$ category and 1 in the $Z=2$. They will not therefore affect the proton/alpha-particle ratio obtained above. With some reservation we shall consider them as primaries which stop without producing penetrating secondaries. According to Camerini *et al.*[6] such events (O_p in their notation) have still some probability of occurrence for the primary energies at this latitude (>4 Bev for vertical incidence).

The T events appear to be a real phenomenon but not attributable to primaries. Of the 18 listed in the first three columns of Table I, 11 have ionization consistent with their being low energy electrons, 5 with protons, and 2 with protons or alpha-particles. It has not been found possible to explain away any but a quite small fraction as due to events in the rocket skin, counter walls, or absorber below. On the other hand, they are considerably too numerous to be regarded as stopped primaries having no penetrating secondaries. We conclude that they are returning particles of the earth's albedo. They form 15 percent of the incoming charged particle radiation. This compares to 13 percent found to be absorbed in 2 cm Pb by Golian and Krause[7] and 22 percent by Perlow and Shipman[8] in 2 cm Pb. The latter experiment probably had insufficient shower protection.

[6] Camerini, Davies, Fowler, Franzinetti, Muirhead, Lock, Perkins, and Yekutieli, Phil. Mag. **42**, 1241 (1951).
[7] S. E. Golian and E. H. Krause, Phys. Rev. **71**, 918 (1947).

ABSORPTION IN LEAD

It is instructive to plot as in Fig. 6 an integral absorption curve of the total charged radiation. The number of counts at a given thickness is not independent of the number at another thickness, only the difference being independent. The line drawn has therefore somewhat better statistical basis for its slope than the numbers might seem to imply. The T events appear as an extra group. The main portion of the curve corresponds to an absorption mean free path of 440 ± 70 g/cm² in lead.

Table II lists the intensities of the various components. The total primary intensity is obtained by extrapolating to zero thickness the main portion of the absorption curve of Fig. 6. The proton and alpha-particle intensities are obtained by applying the ratio 5.3 mentioned before to this number. The events of type T are considered as albedo particles.

The authors wish to acknowledge the aid given by their colleagues in the Rocket Sonde Research Branch, Naval Research Laboratory, and by personnel of the White Sands Proving Grounds. We are especially indebted to T. A. Bergstralh, C. A. Schroeder, C. Y. Johnson, H. M. Caulk, and P. R. McCray.

[8] G. J. Perlow and J. D. Shipman, Jr., Phys. Rev. **71**, 325 (1947).

PHYSICAL REVIEW VOLUME 88, NUMBER 2 OCTOBER 15, 1952

The Superconductive Transition in Tantalum

H. PRESTON-THOMAS*
Division of Physics, National Research Council, Ottawa, Canada
(Received June 9, 1952)

The construction of small coreless coils allows the simultaneous measurement of resistive and magnetic transitions in tantalum. As is the case with the other "hard" superconductors, these measurements give evidence of the presence of "filaments" in the metal. The results are explained on the basis of a modification of a two-phase model used previously, and critical field-temperature curves are derived for the bulk metal and for the filament material.

MAGNETIC and resistance measurements have been made on tantalum wire supplied by Fansteel Metallurgical Corporation that had been cold drawn to a diameter of 0.25 mm and heated in high vacuum at 2800°K for 100 hours. To prevent distortion and work hardening of the very soft wire resulting from this treatment, close fitting search coils were preformed and then slipped onto the specimen.[1] Nickel terminals were spot welded to the ends of the specimen, the potential and current leads being soft soldered to the nickel. This arrangement allowed magnetic and resistive measurements to be made simultaneously on the same specimen. Resistance measurements over the range 5°K to 300°K were made in a modified Collins A. D. Little cryostat[2] with a galvanometer amplifier[3] as the measuring instrument. θ-values based on the Bloch-Grüneisen formula were obtained from these measurements, the value of 210°K over a large part of the range comparing with the value of 245°K derived from the specific heat measurements. These results together with the low value of the residual resistance ($R/R_0=0.008$ and 0.0074 in the two specimens) suggest that the metal had a rather high degree of physical and chemical purity.

* National Research Laboratories, Postdoctorate Fellow.
[1] H. Preston-Thomas, (to be published).
[2] D. K. C. MacDonald, Phil. Mag. **43**, 479 (1952).
[3] D. K. C. MacDonald, J. Sci. Instr. **24**, 323 (1947).

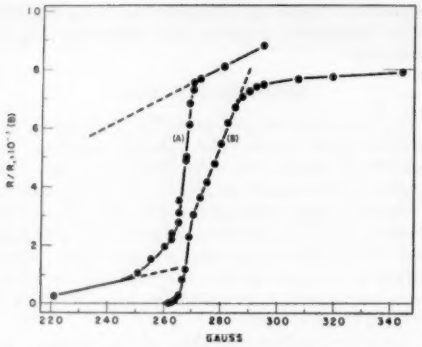

FIG. 1. Superconductive transition of tantalum at 3.61°K. The ballistic curve (A) has an arbitrary ordinate scale.

The ballistic method of Keeley and Mendelssohn[4] was used to determine field penetration changes in the specimen. In this method the external longitudinal magnetic field is abruptly removed, the resulting throw of the ballistic galvanometer being a function of the field strength and the shielding effect of the superconductor. Both resistance and magnetic measurements were made isothermally for a series of temperatures.

The observed results differed substantially from those obtained by Jackson and Preston-Thomas[5] from similar measurements on niobium which were accounted for on the basis of a model postulating a superconducting sponge (compare with Mendelssohn[6]) consisting of material which differed from the bulk metal in its critical field-temperature slope and normal transition temperature. The three main points of difference in the case of tantalum are that the penetration of magnetic field always takes place over a small range of field, indicating there is a low or zero coefficient of demagnetization; that there is no measurable frozen-in flux, indicating that no bulk metal is enclosed by filaments of higher critical field; and that the transition from zero to normal resistance is not sharp (except at temperatures very close to the normal transition temperature) but increases rapidly in width as the temperature is lowered (commencing at the same field at which substantial penetration of flux into the specimen begins to occur) and is a function of the flux penetration. Figures 1 and 2 show the form of the transition at 3.61°K and 2.635°K.

The form of these curves is explicable on the basis of a two-phase model similar in some respects to that postulated for niobium but with the difference that the sponge filaments are now so dispersed that they can no longer shield any part of the bulk metal. In Fig. 1

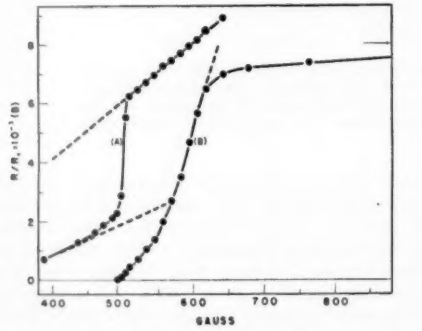

FIG. 2. Superconductive transition of tantalum at 2.635°K. The ballistic curve (A) has an arbitrary ordinate scale.

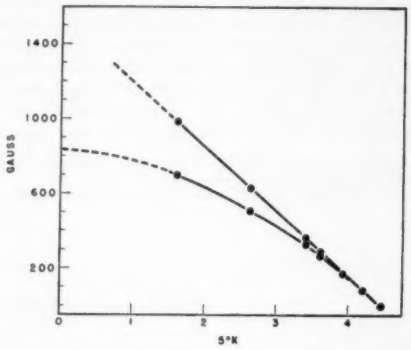

FIG. 3. Critical field curves of tantalum for the bulk material (lower curve) and for the filament structure.

it may be seen that during the penetration of the magnetic flux into the bulk metal the resistance rises rapidly. The discontinuity of slope in the resistance curve then corresponds to the resistance of that part of the bulk metal that is connecting the still superconducting filaments. An assumed random orientation of the filaments with respect to the field (with corresponding variation in demagnetizing coefficient) accounts for the gradual rise of resistance from this point, the continuation of the straight portion of the curve to the normal value of the resistance of the tantalum giving the critical field for the filaments. In Fig. 2 the increased difference between the bulk and the filament critical fields allows the effect of those filaments so oriented as to have a higher demagnetizing coefficient to be observed. The final decrease in the rate of rise of resistance with field and the very slow approach to the normal value of resistance may

[4] T. C. Keeley and K. Mendelssohn, Proc. Roy. Soc. (London) **A154**, 378 (1936).
[5] L. C. Jackson and H. Preston-Thomas, Phil. Mag. **41**, 1284 (1950).
[6] K. Mendelssohn, Proc. Roy. Soc. (London) **152**, 34 (1935).

tentatively be ascribed to the existence of a number of filaments so thin that their critical field has risen in a manner comparable with that observed in superconductors of small dimensions.[7]

Figure 3 shows the critical field-temperature curves for the bulk material and for the filaments as deduced from these measurements. It appears that the normal transition temperature of the filaments is the same as or slightly lower than that of the bulk material.

This work forms part of the program of the Low Temperature and Solid State Physics group, and the writer is grateful to Dr. D. K. C. MacDonald for very helpful discussions.

[7] R. B. Pontius, Phil. Mag. 24, 787 (1937).

PHYSICAL REVIEW VOLUME 88, NUMBER 2 OCTOBER 15, 1952

Neutron Capture Cross Sections*†

B. MARGOLIS
Physics Department and Laboratory for Nuclear Science and Engineering, Massachusetts Institute of Technology, Cambridge, Massachusetts

(Received June 26, 1952)

Cross section formulas for neutron capture are developed by means of statistical theory, for intermediate and heavy weight nuclei for energies of the order of 1 kev to a few Mev. The formulas do not exhibit resonances, but are rather averages over resonances in the energy region where these exist. The case is treated where the residual nucleus levels are well separated, although the method is applicable in principle where these levels form a virtual continuum. The processes competing with capture in the energy range considered are elastic and inelastic scattering. The energy dependence of radiation widths is estimated. The ratio of energy level spacing to radiation width at the dissociation energy of a neutron enters as a parameter in the cross-section formulas. This ratio is chosen to make experiment and theory agree as well as possible. Taking the spacing of levels of a given spin and parity at the dissociation energy of a neutron to be 25 ev, the values of the radiation widths are found to be 0.08 ev for Ag^{108} and In^{116}, 0.10 ev for Ag^{110}, and 0.20 ev for Au^{198}.

INTRODUCTION

THE cross sections of atomic nuclei for bombarding particles of low enough energy are characterized by resonances and are explained by the well-known Breit-Wigner type formulas. For increasing kinetic energy of the bombarding particles, the resonances become more and more closely spaced until finally they overlap, i.e., the cross sections become smoothly varying functions of energy. Formulas will be developed here for neutron capture cross sections representing an average over resonances in the resonance region and the actual cross sections where they become smooth functions of energy. The validity of the compound nucleus concept underlies the development so that one cannot use this treatment for excessively high energies. (For energies of the order of 50 Mev the compound nucleus ceases to have any meaning, since the mean free path of the bombarding particles becomes of the order of size of a nuclear diameter.[1]) The paper may be considered a sequel to those of Feshbach, Peaslee, and Weisskopf[2]; and Feshbach and Weisskopf,[3] which consider nuclear reaction theory in which the target and bombarding particles are taken to have spins of zero. The approach here follows a similar one for inelastic scattering of neutrons by Hauser and Feshbach.[4]

The treatment is subject to the validity of the usual assumptions of statistical theory. In particular, the expression (17) for the partial neutron widths is used, an expression which can be true only on the average. Fairly large fluctuations from the widths given by (17) must be expected for any individual level. Since the (n, γ) cross sections are the result of competitions among several emissions by the compound nucleus, it is expected that these fluctuations are cancelled out to a large extent.

DERIVATION OF CROSS SECTION FORMULAS

Let i be the spin quantum number of the target nucleus. This spin can combine with the incident neutron spin $s=\frac{1}{2}$ to give a "channel spin" quantum number $j=j^{(\pm)}=i\pm\frac{1}{2}$ if $i\neq 0$, with azimuthal quantum number $m=-j,\ -j+1,\ \cdots,\ j$.[5] Let the z axis be chosen in the direction of the incident neutron beam. The cross section for the formation of a compound nucleus of spin J, by incident neutrons of orbital angular momentum l and energy E in the channel of spin j with z component m then, following H.F., is written

$$\sigma(l, j, J, m, E)=(2l+1)\pi\lambda^2 T_l(E)\,|(lj0m\,|\,Jm)|^2, \quad (1)$$

where $2\pi\lambda$ is the wavelength of the incoming neutrons, $(lj0m\,|\,Jm)$ is the Clebsch-Gordan coefficient relating to

* This work was supported by the ONR and AEC.
† Part of a doctoral thesis submitted to the Physics Department at the Massachusetts Institute of Technology.
[1] V. F. Weisskopf, Helv. Phys. Acta XXIII, 187 (1950).
[2] Feshbach, Peaslee, and Weisskopf, Phys. Rev. 71, 145 (1947).
[3] H. Feshbach and V. F. Weisskopf, Phys. Rev. 76, 1550 (1949).
[4] W. Hauser and H. Feshbach, Phys. Rev. 87, 366 (1952). This paper will be called H.F.
[5] If $i=0$ the channel spin is $\frac{1}{2}$.

TABLE I. Energies, spins, and parities of low-lying states of Ag^{107}, Ag^{109}, In^{115}, and Au^{197}.

Target	Ag^{107}			Ag^{109}			In^{115}		Au^{197}				
n	0	1	2	0	1	0	1	2	0	1	2	3	4
E_n, Mev	0	0.094	0.94	0	0.088	0	0.338	1.04	0	0.077	0.268	0.541	1.22
i_n	1/2	7/2	···	1/2	7/2	9/2	1/2	···	3/2	(3/2)	(5/2)	(11/2)	···
Parity	odd	even	···	odd	even	even	odd	···	even	(even)	(even)	(odd)	···

the probability that l and j with z components 0 and m combine vectorially to give a spin J with z component m. The $T_l(E)$ are wave mechanical penetration factors due to the sharp change in potential at the nuclear surface and to the centrifugal barrier. For electrically charged particles, there is in addition the effect of the Coulomb barrier. The $T_l(E)$ depend on the nuclear radius R. For neutrons Feshbach and Weisskopf[5] show that

$$T_l(E)=4xXv_l/[X^2+(2xX+x^2v_l')v_l], \quad (2)$$

where $x=R/\lambda$, $X^2=X_0^2+x^2$ with $X_0\simeq 10^{13}\times(R \text{ in cm})$,

$$v_l=|x[j_l(x)+in_l(x)]|^{-2},$$
$$v_l'=|(d/dx)\{x[j_l(x)+in_l(x)]\}|^2,$$

$j_l(x)$ and $n_l(x)$ being spherical Bessel and Neumann functions. The notation in (2) is that of Blatt and Weisskopf,[6] not that of the original authors.

The part of (1) due to neutron capture is then

$$\sigma(l, j, J, m, E)\Gamma_r^{(J)}/\Gamma^{(J)}, \quad (3)$$

where $\Gamma_r^{(J)}$ and $\Gamma^{(J)}$ are the radiation and total widths of the compound nucleus of spin J at the appropriate excitation energies. Summing over the possible J and l values and averaging over j and m, one gets the neutron capture cross section for unpolarized neutrons, if $i\neq 0$,

$$\sigma_{cap}=\frac{\pi\lambda^2}{2(2i+1)}\sum_{l=0}^{\infty}\left[T_l(E)\sum_{J=0}^{\infty}\frac{\epsilon_{jl}{}^J(2J+1)\Gamma_r^{(J)}}{\Gamma^{(J)}}\right], \quad (4)$$

$\epsilon_{jl}{}^J=2$, $|J-l|\leqslant j\leqslant J+l$ for $j=j^{(\pm)}$,
$=1$, $|J-l|\leqslant j\leqslant J+l$ for $j=$ only one of $j^{(\pm)}$,
$=0$, otherwise;

if $i=0$, one obtains

$$\sigma_{cap}=\frac{\pi\lambda^2}{2}\sum_{l=0}^{\infty}\left[T_l(E)\sum_{J=|l-\frac{1}{2}|}^{l+\frac{1}{2}}\frac{(2J+1)\Gamma_r^{(J)}}{\Gamma^{(J)}}\right]. \quad (5)$$

In the energy range considered below, the Coulomb barrier renders the emission probability of charged particles negligible so that the total width $\Gamma^{(J)}$ can be taken to be the sum of the partial neutron widths and the radiation width $\Gamma_r^{(J)}$. The radiation width is to be determined semi-empirically. In order to compare (4) or (5) with experiment, the form of the radiation width, in particular, its increase with energy is needed. Formula (16) in the appendix gives an estimate of this energy dependence. Among other things, it depends on the form used for the density of levels of the compound nucleus. Whatever the energy dependence of radiation widths, however, the general features of the work presented here are preserved. The width for emission of a neutron of orbital angular momentum l' and energy E' from a nucleus of spin J is denoted by $\Gamma_N^{(J,l')}(E')$. The following estimate for the ratio of neutron width to radiation width is derived in the appendix:

$$\frac{\Gamma_N^{(J,l')}(E')}{\Gamma_r^{(J)}(B+E)}\simeq\frac{D^{(J)}(B)}{\Gamma_r^{(J)}(B)}T_{l'}(E')\times\frac{\int_0^B\epsilon^{2\lambda+1}\rho(B-\epsilon)d\epsilon}{\int_0^{B+E}\epsilon^{2\lambda+1}\rho(B+E-\epsilon)d\epsilon}\equiv\frac{D^{(J)}(B)}{2\pi\Gamma_r^{(J)}(B)}T_{l'}(E')f_\lambda(E). \quad (6)$$

In the above, B is the binding energy of the neutron emitted, $B+E$ is the excitation of the compound nucleus, $D^{(J)}(\epsilon)$ is the spacing of levels of the compound nucleus of spin J and given parity at excitation, ϵ, $\rho(\epsilon)$ is the density of levels of all kinds of the compound nucleus at excitation ϵ, and 2^λ is the multipole type of the radiation in the gamma-ray decay of the

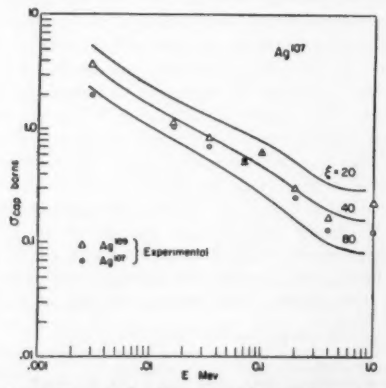

FIG. 1. Theoretical and experimental values for neutron capture cross sections for Ag^{107}, Ag^{109}.

[6] J. M. Blatt and V. F. Weisskopf, *Theoretical Nuclear Physics* (John Wiley and Sons, Inc., New York, 1952).

compound nucleus. It is assumed that a single multipole predominates.

Using (6) the form of (4) becomes

$$\sigma_{cap}\simeq\frac{\pi\lambda^2}{2(2i+1)}\sum_{l=0}^{\infty}\left[T_l(E)\sum_{J=0}^{\infty}\times\frac{\epsilon_{jl}{}^J(2J+1)}{1+\xi_J f_\lambda(E)\sum_{l'}\sum_n\epsilon_{jn}l'^J T_{l'}(E-E_n)}\right]\equiv\sum_{l=0}^{\infty}\sigma^{(l)}, \quad (7)$$

where

$$\xi_J=D^{(J)}(B)/[2\pi\Gamma_\gamma{}^{(J)}(B)]. \quad (8)$$

E_n is the energy of the nth excited state of the residual nucleus for $n>0$, $E_0=0$ being the ground-state energy; the corresponding spins are denoted by $i_n(i=i_0)$ and $j_n=i_n\pm\frac{1}{2}$. The sum over l', the angular momenta of the scattered neutrons must include only those terms that conserve the parity of the system, i.e., for each E_n there must be only odd or even l' values depending on whether the parity of the ground state and the nth excited state are opposite or the same. The sum over n is to include only excited states such that $E_n<E$, of course.

EXAMPLES

Silver

The capture of neutrons by Ag^{107} will be considered in the energy region from $E=3$ kev up to the point where inelastic scattering due to the second excited state becomes important, near $E=1$ Mev. Table I lists the spins, energies, and parities of pertinent states of the residual nucleus. The spin and parity of the E_1 level has been determined by Goldhaber and Sunyar[7] from its lifetime (44 sec) and from its internal conversion coefficients. The other information on Ag has been obtained from *Nuclear Data*.[8] The following

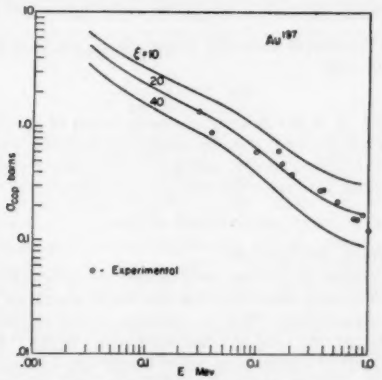

FIG. 2. Theoretical and experimental values for neutron capture cross sections for Au^{197}.

[7] M. Goldhaber and A. W. Sunyar, Phys. Rev. **83**, 906 (1951).
[8] *Nuclear Data*, Circular No. 499 (1950).

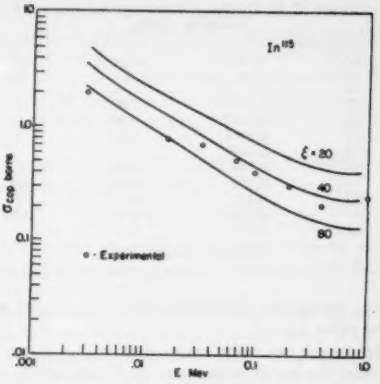

FIG. 3. Theoretical and experimental values for neutron capture cross sections for In^{115}.

are sample $\sigma^{(l)}$ for this case:

$$\sigma^{(0)}=\frac{\pi\lambda^2}{4}T_0(E)\left[\frac{1}{1+\xi_0 a_0}+\frac{3}{1+\xi_1 a_1}\right],$$

$$\sigma^{(1)}=\frac{\pi\lambda^2}{4}T_1(E)\left[\frac{1}{1+\xi_0 b_0}+\frac{6}{1+\xi_1 b_1}+\frac{5}{1+\xi_2 b_2}\right], \quad (9)$$

$$\sigma^{(2)}=\frac{\pi\lambda^2}{4}T_2(E)\left[\frac{3}{1+\xi_1 a_1}+\frac{10}{1+\xi_2 a_2}+\frac{7}{1+\xi_3 a_3}\right],$$

where

$$\begin{aligned}
a_0&=f_\lambda(E)[T_0(E)+T_3(E-E_1)],\\
a_1&=f_\lambda(E)[T_0(E)+T_2(E)+2T_3(E-E_1)+T_5(E-E_1)],\\
a_2&=f_\lambda(E)[2T_2(E)+T_1(E-E_1)+2T_3(E-E_1)\\
&\qquad+2T_5(E-E_1)],\\
a_3&=f_\lambda(E)[T_2(E)+T_4(E)+2T_1(E-E_1)\\
&\quad+2T_3(E-E_1)+2T_5(E-E_1)+T_7(E-E_1)],\\
b_0&=f_\lambda(E)[T_1(E)+T_4(E-E_1)],\\
b_1&=f_\lambda(E)[2T_1(E)+T_2(E-E_1)+2T_4(E-E_1)],\\
b_2&=f_\lambda(E)[T_1(E)+T_3(E)+2T_2(E-E_1)\\
&\qquad+2T_4(E-E_1)+T_6(E-E_1)]. \quad (10)
\end{aligned}$$

Indium and Gold

The information on the lowest three levels of In^{115} that appears in Table I has been taken from references 6 and 7. For Au^{197} Huber *et al.*[9] have found the first three excited levels given in Table I. In accordance with the lifetime of the 0.541-Mev level (7.3 sec) and the gamma-ray decay scheme, and using predictions of shell theory, spins and parities have been written down. These values are perhaps not as certain as those for In and Ag and are in parentheses. The $\sigma^{(l)}$ for In^{115} and Au^{197} will not be written down, but curves of σ_{cap} against

[9] O. Huber *et al.*, Helv. Phys. Acta **XXIV**, 127 (1950).

TABLE II. $f_\lambda(E)$, part of the energy dependence of radiation widths.

$x=R/\lambda$ 0	E, Mev 0	$f_1(E)$ 1	$f_2(E)$ 1
0.1	0.00293	1.00	···
0.2	0.0117	0.99	···
0.3	0.0264	0.97	···
0.4	0.0469	0.95	···
0.7	0.144	0.84	···
···	0.384	0.64	0.60
1.2	0.422	0.61	···
···	0.769	0.41	0.36
1.7	0.847	0.38	···
	$\alpha B=210$,	$\alpha=26$ Mev^{-1}	

energy are given. The energy range considered is the same as for Ag.

Before one can make calculations with (7), one must consider the set of parameters ξ_J. These will be taken to be independent of J, $\xi_J=\xi$. The validity of this will be discussed in the appendix.

COMPARISON WITH EXPERIMENT

Figures 1, 2, and 3 show the theoretical values of σ_{cap} plotted against the energy of the bombarding neutrons for Ag^{107}, Au^{197}, and In^{115} targets for several values of ξ. At the maximum energy considered, $E=0.847$ Mev, l values from 0 to 4 contribute appreciable $\sigma^{(l)}$. The value of the nuclear radius in all cases was taken to be $R=8\times10^{-13}$ cm. To calculate $f_\lambda(E)$ the form for the density of energy levels of the compound nucleus was taken to be

$$\rho(E)=C\exp[(\alpha E)^{\frac{1}{2}}], \tag{11}$$

with $\alpha=26$. B was taken to be 8 Mev. Values of $f_\lambda(E)$ are tabulated in Table II. The cross section plotted in Figs. 1, 2, and 3 are for $\lambda=1$.

Figure 4 has σ_{cap} curves for Ag^{107} with $\xi=40$ showing the effect of (a) neglecting inelastic scattering, (b) changing the parity of the E_1 level. There is also a curve (c) for Au^{197} with $\xi=40$ to show the sensitivity of σ_{cap} to the level scheme of the excited states of the target nucleus. From curve (a) it is seen that inelastic scattering is not a negligible effect in calculating σ_{cap}.

For Ag^{107} and In^{115} the best agreement of theory with the experiments of Segrè *et al.*[10,11] and Hughes and Sherman[12] is obtained with $\xi\simeq50$. For Ag^{109}, $\xi\simeq40$. (Experimental points for Ag^{109} as well as Ag^{107} are plotted in Fig. 1, since the lowest two levels of these isotopes have very similar properties.) For Au^{197} a good fit of theory to experiment is obtained with $\xi\simeq20$. The experimental results have been compiled by Adair.[11]

Using (8) and taking a level spacing $D^{(J)}(B)=25$ ev, the radiation widths are for In^{116} and Ag^{108}, $\Gamma_\gamma(B)=0.08$ ev; for Ag^{110}, $\Gamma_\gamma(B)=0.10$ ev; for Au^{198}, $\Gamma_\gamma(B)=0.20$ ev. For dipole radiation using (16) the widths are 1.3 times as large at an excitation 0.85 Mev higher.

[10] Segrè, Greisen, Linenberger, and Miskel (unpublished).
[11] R. K. Adair, Revs. Modern Phys. **22**, 249 (1950).
[12] D. J. Hughes and D. Sherman, Phys. Rev. **75**, 632 (1950).

Professor H. Feshbach suggested this problem. I wish to thank him and Professor V. F. Weisskopf for valuable suggestions and criticisms. I thank too Miss Hannah Paul who made many of the calculations.

APPENDIX

Weisskopf[13] shows that the probability per unit time of a radiative transition of multipole 2^λ (electric or magnetic) from a nuclear quantum state a to a state b of energy ϵ lower is given by

$$T_\lambda(a,b)\propto\epsilon^{2\lambda+1}|M_\lambda|^2, \tag{12}$$

the proportionality constant depending only on λ, the nuclear radius R, and fundamental physical constants. M_λ is the matrix element for the transition, and Blatt

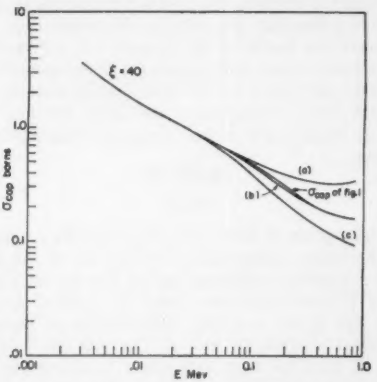

FIG. 4. Theoretical curves showing the effect on the neutron capture cross section for Ag^{107} of (a) neglecting inelastic scattering and (b) changing the parity of the first excited state. The curve (c) is the cross section for Au^{197}, to show the sensitivity of σ_{cap} to the level scheme of the target nucleus. All curves are for $\xi=40$.

and Weisskopf[6] show that its magnitude can be written in the form

$$|M_\lambda|^2=n_\lambda(a,b)D_a, \tag{13}$$

where D_a is the spacing of energy levels of the same spin and parity as a at the energy of a, a strongly varying function of energy, and $n_\lambda(a,b)$ is a slowly varying function. One can write then an approximation

$$T_\lambda(a,b)\simeq K_\lambda\epsilon^{2\lambda+1}D_a, \tag{14}$$

where K_λ is a constant.

Consider a nucleus with initial excitation B and having many levels between this initial excitation and the ground state. Then on a statistical basis the probability per unit time of a transition of multipole 2^λ from the state of energy B to one of energy ϵ to $\epsilon+d\epsilon$ lower is given by

$$P(\epsilon)d\epsilon\simeq K_\lambda\epsilon^{2\lambda+1}D(B)\rho_\lambda(B-\epsilon)d\epsilon, \tag{15}$$

[13] V. F. Weisskopf, Phys. Rev. **83**, 1073 (1951).

where $D(B)$ is the spacing of levels of the same spin and parity as the initial state at energy B, and $\rho_\lambda(B-\epsilon)$ is the density of levels at energy $B-\epsilon$ that can be reached through the radiative transitions of multipole 2^λ. The radiation widths are obtained by integrating $hP(\epsilon)$ from $\epsilon=0$ to B.

The ratio of radiation widths of states of spin J and given parity with excitations B and $B+E$ then takes the following form:

$$\frac{\Gamma_\gamma^{(J)}(B+E)}{\Gamma_\gamma^{(J)}(B)} \simeq \frac{D^{(J)}(B+E)}{D^{(J)}(B)} \cdot \frac{\int_0^{B+E} \epsilon^{2\lambda+1}\rho(B+E-\epsilon)d\epsilon}{\int_0^{B} \epsilon^{2\lambda+1}\rho(B-\epsilon)d\epsilon} = \frac{1}{f_\lambda(E)} \cdot \frac{D^{(J)}(B+E)}{D^{(J)}(B)}, \quad (16)$$

where $D^{(J)}(B)$ is the spacing of levels of spin J and given parity at excitation B. It is assumed that for all spins J the energy dependence of the level densities is as in (11), the constant preceding the exponential alone having J dependence. This allows the use of ρ, the density of levels of all types, instead of ρ_λ on the right side of (16).

Many authors, for example, Feshbach, Peaslee, and Weisskopf,[2] have shown that

$$\Gamma_N^{(J,l')}(E') \simeq T_{l'}(E')D^{(J)}/2\pi, \quad (17)$$

where the value of $D^{(J)}$ is to be taken at the excitation energy of the compound nucleus. Equation (6) follows directly from (16) and (17).

ρ_λ has no obvious J dependence. Hence, from (15) it can be seen that the main dependence of $\Gamma_\gamma^{(J)}(B)$ is in its proportionality to $D^{(J)}(B)$. This is the basis for taking ξ_J to be independent of J.

PHYSICAL REVIEW VOLUME 88, NUMBER 2 OCTOBER 15, 1952

The Spread of the Soft Component of the Cosmic Radiation

H. S. GREEN AND H. MESSEL
University of Adelaide, Adelaide, South Australia
(Received June 3, 1952)

The fundamental diffusion equations describing the three-dimensional development of the electron-photon component of the cosmic radiation, are formulated. These equations take into account exactly ionization loss and variation of density in the medium, and enable one to determine all angular and radial moments of the distribution functions, as explicit functions of depth and energy for arbitrary initial conditions.

The exact general solution of these equations obtained in this paper are readily adapted to any physical situation of interest. The method is similar to that devised by the authors in considering the three-dimensional development of the nucleon component. The only approximations involved are those inherent in the Bethe-Heitler cross sections in the full screening approximation, and the neglect of angular deflections in processes other than elastic Coulomb scattering.

It is shown that all previous work is subject to very large errors on the following counts: (1) the neglect of fourth and higher angular moments for the Coulomb scattering in Landau's equation and equivalent integral equations; (2) the neglect of variation of density in the atmosphere—which alone can lead to errors as high as 5000 percent; (3) elimination of the depth dependence either by integration over all depths, or evaluation in the neighborhood of the cascade maximum; (4) miscellaneous errors introduced in the evaluation of already approximate integrals; (5) use of results due to Moliere, hitherto unpublished in detail, which involve errors of several orders of magnitude in the higher moments; and also in the distribution functions concerned.

No calculation of the actual distribution functions in the atmosphere or elsewhere has yet been made on the basis of a realistic physical model. The results obtained in this paper will allow the authors to do this in the future.

1. INTRODUCTION

IT is difficult to find any topic in theoretical physics which has received so much attention, with results so lacking in precision, as the spread of the soft component of the cosmic radiation in the atmosphere. Both the physical assumptions and the mathematical techniques employed have been of such a crude nature that no confidence whatever can be placed in either the qualitative or quantitative aspects of the theories advanced.

All theories hitherto put forward which have not consisted of purely qualitative considerations, have been based either on equations due to Landau[1] or on completely equivalent integral equations due to Roberg and Nordheim.[2] These equations are actually inapplicable to the atmosphere, since they relate only to media of constant density. Janossy[3] has argued that "no great error arises from the fact that the variation of the cascade unit with air density has been neglected," but our exact calculations will show that the error actually attains a maximum of 5000 percent. Another defect of the equations of Landau, and Roberg and Nordheim, is the neglect of the higher angular moments of the Coulomb scattering of the electrons. In consequence of this neglect, the mean square angular deviation of particles from the shower axis can be calculated accurately for a medium of constant density, but the mean fourth power obtained is in error by 18 percent, the mean sixth power by 45 percent, and higher moments are completely inaccurate. Similar corrections apply to

[1] L. Landau, J. Phys. (U.S.S.R.) **2**, 234 (1940).
[2] J. Roberg and L. W. Nordheim, Phys. Rev. **75**, 444 (1949).
[3] L. Janossy, *Cosmic Rays* (Oxford University Press, London, 1948).

the moments of the radial distribution function. The so-called "exact" values of the higher moments computed by Eyges and Fernbach[4] and Nordheim *et al.*[5] are thus subject to large corrections. Furthermore, the angular and radial distribution functions constructed from such moments are necessarily incorrect.

Moliere[6–8] attempted to obtain the distribution functions by a method not requiring the previous determination of the moments. The details of the method have never been published, but since it involves the use of Landau's equation, it is necessarily inexact. Further, if Landau's equations are accepted, Moliere's results are still incorrect, both quantitatively and qualitatively. His calculation has so little relation to the physical problem that it is a strange coincidence that experimental evidence[9] should appear to support his results. This coincidence has unfortunately led to an almost universal acceptance[10] of an incorrect theory, which has obstructed further advance.

Errors of principle have been introduced in the treatment of the depth dependence of the angular and radial spread. Some authors[2–5,11] have averaged over all depths; however, it will be shown presently that the spread is by no means constant, whether one assumes constant or variable density. Others[6,7] have obtained results only for the cascade maximum, or attempted by very approximate methods to extrapolate from the cascade maximum.[12] In view of these and other approximations which have been introduced, it seems futile, as some authors have attempted[2–4,6] to take ionization loss into account; this may be done after a theory valid for high energies has been established.

The conclusion is inevitable that all work hitherto on the angular and lateral spread of the soft component is incorrect or so inexact as to be severely in need of amendment.

From the physical point of view, two distinct problems need to be considered: the determination of the spread of the electron and photon components of the cosmic radiation in the atmosphere, and in a medium of constant density such as lead. It is now almost certain that in the atmosphere the soft component is secondary to the nucleon-mesonic component, so that the spread of the nucleon component, previously determined by the present authors,[13] provides the initial condition required for the determination of the spread of the soft component. The problem thus raised will be considered by us in a subsequent publication in which we shall obtain the correct radial and angular distribution functions. In media of constant density, the angular and radial distributions of interest result from two initial conditions, corresponding to either incident electrons or incident photons at the top of the layer considered. This is the problem which we presently considered, since it is that which has been treated by all previous authors. It has applications to the spread of showers in slabs of material with uniform density, and also to the spread of atmospheric showers through *shallow layers well down in the atmosphere*, where the density is almost constant. For purposes of comparison, we have, however, determined the mean square lateral spread of showers initiated by electrons (though few, if any, of these exist) at the top of the atmosphere.

Our theoretical results are applicable to an arbitrary distribution of particles incident on the absorbing layer concerned, within which the density may vary in an arbitrary manner, and are thus completely general. However, for purposes of numerical discussion, we have always considered an incident power law spectrum for the particles concerned. Numerical results for all other types of spectra can be obtained by a single complex integration, which in most cases is readily performed by the method of steepest descents. We have confined our attention in this paper to the determination of nth moments of the angular and radial distribution functions; it is possible, however, to reconstruct the functions from the moments by a method given by us in a previous publication[13] and this we shall do presently. The present theory is valid only in the region of high energies where ionization loss is negligible, but the consideration of an additional term in our fundamental equations will enable us to extend the theory to low energies in the near future.

2. FUNDAMENTAL EQUATIONS FOR THE SPREAD OF THE SOFT COMPONENT

We denote by $f^{(i)}(\mathbf{p}, \mathbf{r}, t)d\mathbf{p}d\mathbf{r}/(2\pi p^2)$ the probability that a particle of the ith kind ($i=1$ refers to electrons; $i=2$ to photons) be found with momentum in the range $\mathbf{p}d\mathbf{p}$ at height t cm, and with horizontal displacement $\mathbf{r}$, $d\mathbf{r}$ from the shower axis, assumed to be vertical.[14] Further, we denote by $w^{(i)}(\mathbf{p}', \mathbf{p})d\mathbf{p}/(2\pi p^2)$ the well-known Bethe-Heitler cross sections[15] in the full screening approximation, and by $w(\mathbf{p}', \mathbf{p})d\mathbf{p}/(2\pi p^2)$ the corresponding differential cross section for the elastic scattering of an electron[16] by an atom of the absorber considered. The total cross sections corresponding to $w^{(i)}$ and w are represented by $\alpha^{(i)}$ and α, respectively;

[4] L. Eyges and S. Fernbach, Phys. Rev. **82**, 23 (1951).
[5] Nordheim, Osborne, and Blatt, unpublished Echo Lake Proceedings (1949).
[6] G. Moliere and W. Heisenberg, *Cosmic Radiation* (Dover Publications, New York, 1946).
[7] G. Moliere, Naturwiss. **30**, 87 (1942); Z. Physik **125**, 250 (1948).
[8] G. Moliere, Phys. Rev. **77**, 715 (1949).
[9] Cocconi, Cocconi-Tongiorgi, and Greisen, Phys. Rev. **76**, 1020 (1949).
[10] J. M. Blatt, Phys. Rev. **75**, 1584 (1949) is one of the few authors who appear to have appreciated that Landau and Moliere's theory was incorrect, though he was not able to amend it.
[11] S. Z. Belenky, J. Phys. (U.S.S.R.) **8**, 9 (1944).
[12] S. Fernbach, Phys. Rev. **82**, 288 (1951).
[13] H. Messel and H. S. Green, Phys. Rev. **87**, 378 (1952).
[14] The method of generalization to the case where the shower axis is not vertical was described in our previous paper (reference 13).
[15] Multiplied by 2 for $i=2$.
[16] B. Rossi and K. Greisen, Revs. Modern Phys. **13**, 240 (1941).

the fact that $\alpha^{(1)}$ is mathematically divergent leads to no difficulty in this instance. The ionization loss for the electrons per cascade unit is represented by β; the depth in the absorber, measured in cascade units is denoted by $l(t)$. In a medium of constant density δ g/cm^3, $l=-\delta t/k$, where k is the radiation length in g/cm^2 ($k=43$ for air). In an isothermal atmosphere, on the other hand, $l=(p_0/43g)\exp(-g\delta_0 t/p_0)$, where p_0 and δ_0 are the surface pressure and density, and g the acceleration due to gravity.

The rate of change of $f^{(i)}$ per unit path length is $\mathbf{p}/p\cdot\partial f^{(i)}/\partial\mathbf{r}$, where $r_3=-t$; this results from a loss $(\alpha^{(i)}+\alpha\delta_{i,1})(dl/dt)f^{(i)}$ from the momentum range $\mathbf{p}$, $d\mathbf{p}$ to the other momenta, a gain

$$\frac{dl}{dt}\int[w^{(3-i)}(\mathbf{p}',\mathbf{p})f^{(3-i)}(\mathbf{p}')+\{w^{(i)}(\mathbf{p}',\mathbf{p}'-\mathbf{p})+w(\mathbf{p}',\mathbf{p})\}f^{(i)}(p')\delta_{i,1}]d\mathbf{p}'/(2\pi p'^2),$$

from other momenta, and a loss $\beta(dl/dt)\times(\partial f^{(i)}/\partial p)\delta_{i,1}$ due to ionization. Hence,

$$\frac{dt}{dl}\frac{\mathbf{p}}{p}\cdot\frac{\partial f^{(i)}}{\partial\mathbf{r}}=-(\alpha^{(i)}+\alpha\delta_{i,1})f^{(i)}+\beta\frac{\partial f^{(i)}}{\partial p}\delta_{i,1}+\int[w^{(3-i)}(\mathbf{p}',\mathbf{p})f^{(3-i)}(\mathbf{p}')+\{w^{(i)}(\mathbf{p}',\mathbf{p}'-\mathbf{p})+w(\mathbf{p}',\mathbf{p})\}f^{(i)}(\mathbf{p}')\delta_{i,1}]d\mathbf{p}'/(2\pi p'^2). \quad (1)$$

Transforming to polar coordinates by writing

$$r=(r_1^2+r_2^2)^{\frac{1}{2}},\quad E=p=(p_1^2+p_2^2+p_3^2)^{\frac{1}{2}},\quad p_1r_1+p_2r_2=ErS\cos\Psi,\quad C=p_3/p,\quad S=(1-C^2)^{\frac{1}{2}}, \quad (2)$$

one obtains

$$\frac{dt}{dl}\left(C\frac{\partial f^{(i)}}{\partial t}-S\cos\Psi\frac{\partial f^{(i)}}{\partial r}+\frac{S\sin\Psi}{r}\frac{\partial f^{(i)}}{\partial\Psi}\right)+(\alpha^{(i)}+\alpha\delta_{i,1})f^{(i)}=\beta\frac{\partial f^{(i)}}{\partial E}\delta_{i,1}+\int_E^\infty[w^{(3-i)}(E/E')f^{(3-i)}(E')+w^{(i)}(1-E/E')f^{(i)}(E')\delta_{i,1}]dE'/E'+\int_0^{2\pi}\frac{d\Psi'}{2\pi}\int_{-1}^1 dC'\int_E^\infty dE'w\{E',E,CC'+SS'\cos(\Psi-\Psi')\}f^{(i)}(E',C',\Psi')\delta_{i,1}. \quad (3)$$

Expanding $f^{(i)}(E',C',\Psi')$ about the value $C'=C$, $\Psi'=\Psi$, by means of associated Legendre operators, and substituting[16]

$$w(E',E,c)=\delta(E'-E)V/E^3(1-c)^2,\qquad V=\tfrac{1}{2}\pi[137m_e^2/\ln(181z^{-\frac{1}{3}})], \quad (4)$$

the last term in (3) reduces to

$$\sum_{l=0}^\infty 4^{-l}(l!)^{-2}E^{-2l}w_lP(P+1.2)\cdots\times\{P+l(l-1)\}f^{(i)}(E)\delta_{i,1}, \quad (5)$$

where P is the operator

$$P=\left(\frac{\partial}{\partial C}S^2\frac{\partial}{\partial C}+\frac{1}{S^2}\frac{\partial^2}{\partial\Psi^2}\right), \quad (6)$$

and

$$w_l=2^lV\int_{c_0}^{c_1}(1-c)^{l-2}E^{2l-2}dc,$$

$$c_0=1-\tfrac{1}{2}(137m_ez^{-\frac{1}{3}})^2/(0.57E)^2,$$

$$c_1=1-\tfrac{1}{2}(m_ez^{\frac{1}{3}})^2/(137E)^2. \quad (7)$$

The term with $l=0$ in (5) yields the total cross section for elastic scattering, and cancels the equivalent term $(\alpha\delta_{i,1}f^{(i)})$ on the left-hand side of (3). The latter is then

$$\frac{dl}{dl}\left(C\frac{\partial f^{(i)}}{\partial t}-S\cos\Psi\frac{\partial f^{(i)}}{\partial r}+\frac{S\sin\Psi}{r}\frac{\partial f^{(i)}}{\partial\Psi}\right)+\alpha^{(i)}f^{(i)}=\beta\frac{\partial f^{(i)}}{\partial E}\delta_{i,1}+\int_E^\infty[w^{(3-i)}(E/E')f^{(3-i)}(E')+w^{(i)}(1-E/E')f^{(i)}(E')\delta_{i,1}]dE'/E'+\sum_{l=1}^\infty 4^{-l}(l!)^{-2}E^{-2l}w_lP(P+2)\cdots\times\{P+l(l-1)\}f^{(i)}(E)\delta_{i,1}. \quad (8)$$

This equation is exact, within the limitations of the assumed Bethe-Heitler cross sections. One may legitimately approximate C by 1, and P by $\partial^2/\partial\theta_1^2+\partial^2/\partial\theta_2^2$, where

$$\theta_1=S\cos\Psi\quad\text{and}\quad\theta_2=S\sin\Psi, \quad (9)$$

since this merely amounts to dropping terms of order $(m_ec^2/E)^2$ compared with unity. At sufficiently high energies (above the critical energy) one may also set $\beta=0$, neglecting ionization loss. If in addition, all terms with $l>1$ are dropped from the summation in (8), and dt/dl is replaced by the constant $-k/\delta$ (appropriate only to a medium of constant density), then (8) reduces to Landau's equations.[1] The last two procedures mentioned account for the substantial errors involved in the use of Landau's equations, or the equivalent integral equations of Nordheim and Roberg. It might be supposed that the error in neglecting the term with $l=2$ in (8) in comparison with the first is of the same order of magnitude as that resulting from the substitution $C=1$, for example; this is not so, however, as it makes a direct contribution to the fourth angular and radial moments. This is evident on physical grounds, and will appear so in subsequent mathematical developments.

3. SOLUTION OF THE FUNDAMENTAL EQUATIONS

If the Mellin transform $f^{(i)}(v)$ of $f^{(i)}(E)$ is defined by

$$f^{(i)}(v)=\int_0^\infty E^{v-1}f^{(i)}(E)dE, \tag{10}$$

then (8) reduces to

$$\frac{dt}{dl}\left\{C\frac{\partial}{\partial t}-S\cos\Psi\frac{\partial}{\partial r}+\frac{S\sin\Psi}{r}\frac{\partial}{\partial\Psi}\right\}f^{(i)}(v)$$
$$=-(v-1)\beta f^{(i)}(v-1)\delta_{i,1}+B^{(i)}(v)f^{(3-i)}(v)$$
$$-D^{(i)}(v)f^{(i)}(v)+\sum_{l=1}^{\infty}4^{-l}(l!)^{-2}w_l P(P+2)\cdots$$
$$\times\{P+l(l-1)\}f^{(i)}(v-2l)\delta_{i,1}, \tag{11}$$

where

$$B^{(1)}(v)=2\left\{\frac{1}{v}-\frac{(4/3+\alpha_0)}{(v+1)(v+2)}\right\},$$
$$B^{(2)}(v)=\frac{1}{v+1}+\frac{(4/3+\alpha_0)}{v(v-1)},$$
$$D^{(1)}(v)=(4/3+\alpha_0)\{\Psi(v)-\Psi(1)\}+\tfrac{3}{2}-\frac{1}{v(v+1)}, \tag{12}$$
$$D^{(2)}(v)=7/9-\alpha_0/6,$$

and

$$\Psi(v)=\frac{d}{dv}\ln(v!), \quad \text{while} \quad 9\alpha_0=\{\ln(181z^{-4})\}^{-1}.$$

Introducing the polar Fourier transform

$$g^{(i)}(v,k,\beta')=\int_0^{2\pi}d\Psi\int_0^\infty rdr$$
$$\times\exp\{ikr\cos(\Psi-\beta')\}f^{(i)}(v,r,\Psi), \tag{13}$$

whose inverse is

$$f^{(i)}(v,r,\Psi)=(2\pi)^{-2}\int_0^{2\pi}d\beta'\int_0^\infty kdk$$
$$\times\exp\{-ikr\cos(\Psi-\beta')\}g^{(i)}(v,k,\beta'), \tag{14}$$

one has

$$\frac{dt}{dl}\left\{C\frac{\partial}{\partial t}+ikS\cos\beta'\right\}g^{(i)}(v)$$
$$=-(v-1)\beta g^{(i)}(v-1)\delta_{i,1}+B^{(i)}(v)g^{(2-i)}(v)$$
$$-D^{(i)}(v)g^{(i)}(v)+\sum_{l=1}^{\infty}4^{-l}(l!)^{-2}w_l Q(Q+2)\cdots$$
$$\times\{Q+l(l-1)\}g^{(i)}(v-2l)\delta_{i,1}, \tag{15}$$

where

$$Q=\left(\frac{\partial}{\partial C}S^2\frac{\partial}{\partial C}+\frac{1}{S^2}\frac{\partial^2}{\partial\beta'^2}\right). \tag{16}$$

In order to solve the simultaneous Eqs. (15) with $\beta=0$ (the general case $\beta\neq0$ is postponed for future consideration), we formulate the equation satisfied by

$$h(v)=g^{(1)}(v)+\mu(v)g^{(2)}(v), \tag{17}$$

where $\mu(v)$ is independent of depth. If $\mu(v)$ satisfies the quadratic equation

$$B^{(2)}(v)\mu^2(v)+\{D^{(2)}-D^{(1)}(v)\}\mu(v)-B^{(1)}(v)=0, \tag{18}$$

one obtains

$$\left\{C\frac{\partial}{\partial l}+\frac{iKS\cos\beta'}{l'(l)}\right\}h(v)+a(v)h(v)=R(v,l), \tag{19}$$

where

$$R(v,l)=\sum_{l=1}^{\infty}4^{-l}(l!)^{-2}w_l Q(Q+2)\cdots$$
$$\times\{Q+l(l-1)\}g^{(1)}(v-2l), \tag{20}$$

and

$$a(v)=D^{(1)}(v)-\mu(v)B^{(2)}(v). \tag{21}$$

Inserting the two admissible values

$$\mu_1(v)=[(D^{(1)}-D^{(2)})+\{(D^{(1)}-D^{(2)})^2$$
$$+4B^{(1)}B^{(2)}\}^{\frac{1}{2}}]/2B^{(2)}, \tag{22}$$

$$\mu_2(v)=[(D^{(1)}-D^{(2)})-\{(D^{(1)}-D^{(2)})^2$$
$$+4B^{(1)}B^{(2)}\}^{\frac{1}{2}}]/2B^{(2)}, \tag{23}$$

of $\mu(v)$ into (19), and writing

$$G_1^{(1,1)}(v)=\frac{D^{(2)}-a_1(v)}{a_2(v)-a_1(v)}, \quad G_2^{(1,1)}(v)=\frac{a_2(v)-D^{(2)}}{a_2(v)-a_1(v)},$$
$$G_1^{(1,2)}(v)=\frac{B^{(2)}(v)}{a_2(v)-a_1(v)}, \quad G_2^{(1,2)}(v)=-G_1^{(1,2)}(v),$$
$$G_1^{(2,1)}(v)=\frac{B^{(1)}(v)}{a_2(v)-a_1(v)}, \quad G_2^{(2,1)}(v)=-G_1^{(2,1)}(v), \tag{24}$$
$$G_1^{(2,2)}(v)=G_2^{(1,1)}(v), \quad G_2^{(2,2)}(v)=G_1^{(1,1)}(v),$$

one obtains

$$g^{(i)}(v)=g^{(j)}(v,l=\lambda)G_m^{(j,i)}(v)\exp(-C^{-1}[a_m(v)(l-\lambda)$$
$$+iSk\cos\beta'\{t(l)-t(\lambda)\}])$$
$$+C^{-1}G_m^{(1,i)}(v)\int_\lambda^1\exp(-C^{-1}[a_m(v)(l-l')$$
$$+iSk\cos\beta'\{t(l)-t(l')\}])R(v,l')dl', \tag{25}$$

where $t(l)$ is the height, expressed as a function of l, and the repeated affixes j and m are summed over the values 1 and 2, as in relativity theory. In practice an iteration procedure using (20) and (25) is employed in solving these equations. The integrals which arise may

be simplified by expanding the exponential factor

$$\exp[-iSk\cos\beta'\{t(l)-t(l')\}/C]$$

in a power series, and integrating by parts a sufficient number of times to replace $t(l)$ everywhere by its derivative. The result may be expressed in terms of the operator

$$Y_i=C^{-1}G_m^{(1,i)}(v)\exp\{-C^{-1}a_m(v)l\}$$
$$\times\sum_{u=0}^{\infty}(SC^{-1}\cos\beta')^u\sum_{s=1}^{\infty}w_sA^{-s}(s!)^{-u}Q(Q+2)\cdots$$
$$\times\{Q+s(s-1)\}\left\{-ik\int_{t(\lambda)}^{t(l)}dt(l)\right\}^u$$
$$\times\int_{\lambda}^{l}dl\exp\{C^{-1}a_m(v)l\}E_v^{-2u}, \quad (26)$$

where E_v is the incremental operator which raises the value v by unity. One has, in fact, the solutions

$$g^{(1)}(v)=\left(\sum_{u=0}^{\infty}Y_1^u\right)g^{(i)}(v,l=\lambda)$$
$$\times G_m^{(i,1)}(v)\exp(-C^{-1}[a_m(v)(l-\lambda)$$
$$+iSk\cos\beta'\{t(l)-t(\lambda)\}]), \quad (27)$$

and

$$g^{(2)}(v)=g^{(i)}(v,l=\lambda)G_m^{(i,2)}(v)\exp(-C^{-1}[a_m(v)(l-\lambda)$$
$$+iSk\cos\beta'\{t(l)-t(\lambda)\}])+Y_2g^{(1)}(v). \quad (28)$$

This gives the exact values of the $g^{(i)}(v)$ throughout the atmosphere or other medium, for an arbitrary given distribution of electrons and photons at depth λ, for all depths and for an arbitrary distribution of density.

4. SIMPLE APPLICATIONS

The nature of the solutions (27) and (28) depends on the initial conditions supplied by the physical situation considered. In the atmosphere, a correct initial condition for the soft component is the distribution function for the neutral π-mesons, which is governed by the distribution function of the nucleonic component. Since we have already determined the distribution function for the nucleonic component of the cosmic radiation in the atmosphere, this problem is ready for solution. In the present paper, however, we are concerned with assessing the merits of previous work on the soft component, in which it was customary to take initial conditions corresponding to a particle or spectrum of particles incident on the top of the atmosphere, and therefore adopt the same initial conditions ourselves, namely,

$$g^{(i)}(v,l=0)=g_0{}^{(i)}(v)\delta(1-C), \quad (29)$$

where $g_0{}^{(i)}(v)$ is independent of C. When this is substituted into (27) and (28), one obtains a result of the form (see reference 13)

$$g^{(i)}(v)=\sum_{l,m,n}\frac{(-2)^{-n}}{l!m!n!}(ik\cos\beta')^l(ik\sin\beta')^m$$
$$\times\delta^{(n)}(1-C)f_{(l,m,n)}{}^{(i)}(v). \quad (30)$$

This gives, on applying the transform defined by (13) and (14),

$$f^{(i)}(v)=\sum_{l,m,n}\frac{(-1)^{l+m+n}2^{-n}}{l!m!n!}f_{(l,m,n)}{}^{(i)}(v)$$
$$\times\delta^{(l)}(r\cos\Psi)\delta^{(m)}(r\sin\Psi)\delta^{(n)}(1-C), \quad (31)$$

from which it may be deduced by integration that

$$f_{(l,m,n)}{}^{(i)}=2^n\int\int\int f^{(i)}(r_1,r_2,C)r_1{}^lr_2{}^m(1-C)^n dr_1dr_2dC, \quad (32)$$
$$r_1=r\cos\Psi, \quad r_2=r\sin\Psi,$$

is a typical moment of $f^{(i)}(v)$ with respect to r_1, r_2, and $2(1-C)$.

By comparison of (27), (28), and (29) with (30) we obtain for the $2n$th pure angular moment of the electron distribution

$$f_{(0,0,n)}{}^{(1)}(v)=(n!)^2g_0{}^{(i)}(v-2n)\exp\{-a_m(v-2n)\}$$
$$\times\sum{}'\prod_k\left\{\frac{w_{n(k)}}{\{n(k)!\}^2}G_{m(k)}{}^{(1,1)}\left\{v-2\sum_{q=1}^{k}n(q-1)\right\}\right.$$
$$\times\exp\left[-a_{m(k)}\left\{v-2\sum_{q=1}^{k}n(q-1)\right\}l\right]$$
$$\left.\times\int_0^l\exp\left[a_{m(k)}\left\{v-2\sum_{q=1}^{k}n(q-1)\right\}l\right]\right\}, \quad (33)$$

where $\sum'$ indicates summation over all products for which $\sum_k n(k)=n$, with $n(0)=0$. The corresponding formula for the photons is obtained by changing $G_{m(1)}{}^{(1,1)}(v)$ to $G_{m(1)}{}^{(1,2)}(v)$ in (33). These formulas are independent of the variation of density in the absorber, except insofar as it affects the cascade unit. The formulas for the radial moments, however, depend very sensitively on the law of variation of density adopted. One has

$$f_{(2,0,0)}{}^{(1)}(v)=2w_1g_0{}^{(i)}(v-2)G_m{}^{(i,1)}(v-2)G_n{}^{(1,i)}(v)$$
$$\times\exp\{-a_n(v)l\}\chi_{m,n}(v,l), \quad (34)$$

where

$$\chi_{m,n}(v,l)=\int_0^l dl'(l)\int_0^l dl'(l)\int_0^l dl$$
$$\times\exp[\{a_n(v)-a_m(v-2)\}l]. \quad (35)$$

Substituting, for an isothermal atmosphere, $t'(l) = -p_0/(g\delta_0 l)$ one has

$$\chi_{m,n}(v,l) = \left(\frac{p_0}{g\delta_0}\right)^2 \frac{J_1[\{a_n(v)-a_m(v-2)\}l]}{a_n(v)-a_m(v-2)} \times \exp[\{a_n(v)-a_m(v-2)\}l], \quad (36)$$

$$J_1(x) = e^{-x}\sum_{n=1}^{\infty} x^n/n^2 n!$$

and for an absorber of constant density, with $t'(l) = -k/\delta$, one has

$$\chi_{m,n}(v,l) = \left(\frac{k}{\delta}\right)^2 \frac{J_2[\{a_n(v)-a_m(v-2)\}l]}{\{a_n(v)-a_m(v-2)\}^2} \times \exp[\{a_n(v)-a_m(v-2)\}l], \quad (37)$$

$$J_2(\tau) = e^{-\tau}(e^{\tau}-1-\tau-\tau^2/2).$$

The moments $f_{(0,2,0)}{}^{(i)}(v)$ which describe the horizontal spread in a direction normal to the instantaneous motion, are of order E^{-2} compared with $f_{(2,0,0)}{}^{(i)}(v)$. and make no effective contribution to the total radial moments,

$$f_{(0,2,0)}{}^{(i)}(v) + f_{(2,0,0)}{}^{(i)}(v).$$

We have written down corresponding expressions for the higher radial moments, but as these expressions are somewhat complicated we shall not reproduce them here.

For a single incident particle of energy E_0, $g_0{}^{(j)}(v-2n) = E_0{}^{v-2n-1}\delta_{j,i}$, where $i=1$ for an incident electron and $i=2$ for an incident photon. For an incident power law spectrum of electrons or photons,

$$g_0{}^{(j)}(v-2n) = \{\gamma E_c{}^{v-2n-1}/(\gamma+2n+1-v)\}\delta_{j,i},$$

where E_c is the geomagnetic cut-off energy and $\gamma = 1.5$ is the primary power law exponent; it should, however, be remembered that this substitution has little relation to the physical reality. With this latter substitution, the inverse Mellin transform which has to be applied to the formulas of this section is readily evaluated for energies $E > E_c$; the pole at $v = \gamma+2n+1$ is the only one within the contour completed by a semicircle in the right-hand half of the complex plane, and one has therefore only to take the residue at this pole.

TABLE I. Values of the mean square distance of particles of energy E from the shower axis, in units of $(kE_s/\delta E)^2$, where k is the radiation length, $E_s = 21$ Mev, and δ is the constant density of the medium considered. In all cases, figures are for a primary power law spectrum of exponent $\gamma = 1.5$.

Primary	Secondary	$l=1$	$l=2$	$l=3$	$l=4$	$l=5$	$l=6$	$l=\infty$
Electron	Electron	0.1625	0.5252	0.7913	1.023	1.261	1.505	2.623
	Photon	0.07139	0.3962	0.9294	1.556	2.189	2.808	5.543
Photon	Electron	0.04386	0.1900	0.3721	0.5637	0.7674	0.9758	2.623
	Photon	0.00454	0.07028	0.2704	0.6092	0.053	1.542	5.543

Hence, one has

$$f_{(0,0,n)}{}^{(i)}(E,l) = \lim_{v=\gamma+2n+1} (\gamma+2n+1-v)E^{-v} f_{(0,0,n)}{}^{(i)}(v), \quad (38)$$

$$f_{(2,0,0)}{}^{(i)}(E,l) = \lim_{v=\gamma+3} (\gamma+3-v)E^{-v} f_{(2,0,0)}{}^{(i)}(v). \quad (39)$$

The expressions (38) and (39) relate to particles with energy E; to obtain results for particles with energies $> E$ one simply integrates the expressions from E to E_0. The values of the G's required for the numerical evaluation of (38) and (39) are:[17]

$$\begin{aligned} G_1{}^{(1,1)}(2.5) &= 0.30628, \quad G_1{}^{(1,1)}(4.5) = 0.049882, \\ G_1{}^{(1,2)}(2.5) &= 0.46833, \quad G_1{}^{(1,2)}(4.5) = 0.18567, \\ G_1{}^{(2,1)}(2.5) &= 0.45368, \quad G_1{}^{(2,1)}(4.5) = 0.25525, \\ G_1{}^{(1,1)}(6.5) &= 0.013816 \\ G_1{}^{(1,1)}(6.5) &= 0.093836 \\ G_1{}^{(2,1)}(6.5) &= 0.14520, \end{aligned} \quad (40)$$

and those of the a's

$$\begin{aligned} a_1(2.5) &= 0.35001, \quad a_1(4.5) = 0.70167, \\ a_2(2.5) &= 1.73328, \quad a_2(4.5) = 2.14525, \\ a_1(6.5) &= 0.74846 \\ a_2(6.5) &= 2.57416. \end{aligned} \quad (41)$$

The numerical results will be presented with the discussion in the next section.

5. RESULTS AND DISCUSSION

To assess the error introduced by the neglect of the higher angular moments for the Coulomb scattering in Landau's equation, we have evaluated the exact asymptotic values of the second, fourth, and sixth angular moments for large depths, valid for inhomogeneous as well as homogeneous media.

For an incident electron power law spectrum one has

$$\frac{f_{(0,0,1)}{}^{(1)}(E, l=\infty)}{f_{(0,0,0)}{}^{(1)}(E, l=\infty)} = \frac{G_m{}^{(1,1)}(4.5)w_1 E^{-2}}{a_m(4.5)-a_1(2.5)} = 0.6711(E_s/E)^2, \quad (42)$$

where $E_s{}^2 = (4\pi)137 m_e{}^2$; and

$$\frac{f_{(0,0,2)}{}^{(1)}(E, l=\infty)}{f_{(0,0,0)}{}^{(1)}(E, l=\infty)} = \frac{G_m{}^{(1,1)}(6.5)(w_2+2.684w_1{}^2)E^{-4}}{a_m(6.5)-a_1(2.5)} = 1.519(E_s/E)^4. \quad (43)$$

The ratio of w_2 to $2.684w_1{}^2$ is 0.184, so the error involved in the use of Landau's equation (or other equivalent equations) is 18.4 percent for the mean fourth power of

[17] L. Janossy and H. Messel, Proc. Roy. Irish Acad. **A54**, 217 (1951).

the angular deviation from the shower axis. For the corresponding mean sixth power,

$$\frac{f_{(0,0,3)}{}^{(1)}(E, l=\infty)}{f_{(0,0,0)}{}^{(1)}(E, l=\infty)} = \frac{G_m{}^{(1,1)}(8.5)(w_3+10.34w_1w_2+11.55w_1{}^3)E^{-\gamma}}{a_m(8.5)-a_1(2.5)}. \quad (44)$$

The ratio of $10.34w_1w_2$ to $11.55w_1{}^3$ is 0.443, so, even if one neglects w_3, the error in using Landau's equation exceeds 44 percent. This error varies somewhat with the initial condition applied; however, the order of magnitude remains unchanged. Thus, not only are the "exact" moments previously determined[4,5] subject to increasingly large corrections, but the determinations of the distribution function which employ these moments are seriously affected. Moliere[6,7] apparently used a different method to determine his angular distribution function from Landau's equation; however, according to Eyges and Fernbach,[4] the sixth angular moment (for example) derived from his distribution function is in error by an order of magnitude, and the distribution function itself is thus in even greater error than that determined by Eyges and Fernbach.

The depth dependence of the angular moments can be computed readily from our formula (33). However, the radial moments are of more interest in this connection, and we have selected the mean square distance from the shower axis for special consideration. Values for a medium of constant density derived from (34) are given in Table I.

It will be noticed that the spread approaches its asymptotic value only very slowly; there is thus no support for the assertion by Janossy[3] that "most of the scattering takes place in a layer of about one cascade unit above the observer."

Another interesting feature of the results is that the spread of the electrons at depths greater than 4 cascade units is less than that of the photons—in spite of the fact that only the elastic scattering of the electrons contributes appreciably to the spread of the shower. What happens is that the electrons are absorbed more quickly than the photons, with the result that the photons are ultimately left further from the shower axis. Only at depths less than 4 cascade units does the spread of the electrons exceed that of the photons. Moreover, this conclusion is independent of whether the primary particles are photons or electrons.

It is clear on physical grounds that the spread at great depth must be independent of the type of primary particle. A photon primary generates a pair at some lower depth, so that the spread is delayed throughout the medium. These conclusions are confirmed by our calculations, and are indeed elementary consequences of our Eqs. (27) and (28).

As can be seen from (34), in media of constant or variable density the mean square distance from the shower axis is a linear combination of four terms, namely, the $\chi_{m,n}(4.5, 1)$ given by (35), divided by the average numbers. It can be seen from (36) and (37) that the behavior of the $\chi_{m,n}$ is determined by the *spread function* $J_1(x)$ in the atmosphere, or $J_2(x)$ in a medium of constant density. Since the function $J_1(x)$ describes the spread of all components of the cosmic radiation (see reference 13) in the atmosphere, it has been tabulated for us by Dr. E. A. Cornish of the Commonwealth Scientific and Industrial Research Organization, with results given in the Appendix. After several cascade units, only the term derived from $\chi_{1,1}$ makes an essential contribution to the spread; and we have therefore singled out this term for special consideration.

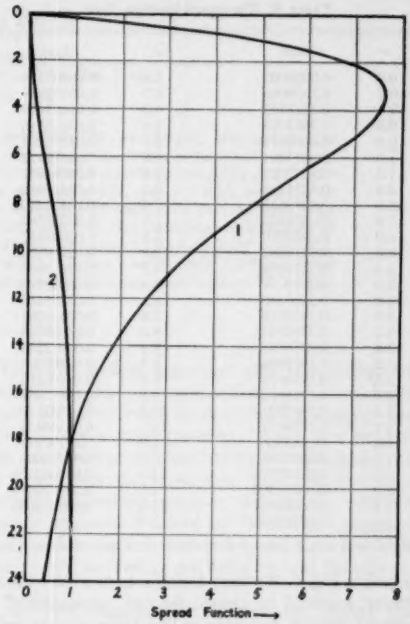

FIG. 1. The spread function normalized in such a way that, multiplied by $(E_s/E)^s$, it gives the mean square distance of electrons of energy E from the shower axis. The curves are calculated for an electron primary power law spectrum with exponent $\gamma=1.5$. The vertical scale gives the atmospheric depth l measured in cascade units. Curve 1 is for an isothermal atmosphere; curve 2 for an atmosphere assuming a constant mean density.

In order to compare the behavior of the mean square spread of showers initiated by a spectrum of electrons in the atmosphere, assumed to be (a) of constant density and (b) isothermal, we have plotted the J_1 and J_2 as functions of depth, multiplied by the appropriate

TABLE II. The spread function $J_1(x)$.

x	$J_1(x)$	x	$J_1(x)$
0.0	0.0000000	5.8	0.06681354
0.2	0.1679646	6.0	0.06119279
0.4	0.2823759	6.2	0.05613459
0.6	0.3563793	6.4	0.05158116
0.8	0.4002031	6.6	0.04748001
1.0	0.4217734	6.8	0.04378372
1.2	0.4272021	7.0	0.04044957
1.4	0.4211756	7.2	0.03743916
1.6	0.4072634	7.4	0.03471810
1.8	0.3881625	7.6	0.03225562
2.0	0.3658910	7.8	0.03002427
2.2	0.3419402	8.0	0.02799953
2.4	0.3173958	8.2	0.02615959
2.6	0.2930317	8.4	0.02435576
2.8	0.2693846	8.6	0.02295855
3.0	0.2468114	8.8	0.02156481
3.2	0.2255345	9.0	0.02029013
3.4	0.2056768	9.2	0.01912236
3.6	0.1872884	9.4	0.01805071
3.8	0.1703675	9.6	0.01706557
4.0	0.1548762	9.8	0.01615839
4.2	0.1407521	10.0	0.01532155
4.4	0.1279177	10.5	0.01349454
4.6	0.1162866	11.0	0.01197937
4.8	0.1057688	11.5	0.01071006
5.0	0.09627376	12.0	0.009636510
5.2	0.08771300	12.5	0.008720378
5.4	0.08000181	13.0	0.007932085
5.6	0.07306021		

factors, in Fig. 1. We were doubtful as to what constant density δ should be chosen for the "atmosphere" of constant density, but have in fact taken a mean value equal to the actual density at 12 cascade units. In the case of the isothermal atmosphere, δ_0 is the surface density; thus, no such difficulty is encountered.

It is obvious from Fig. 1 that the variation of the shower spread with height depends very sensitively on the law of variation of density which is adopted. The values calculated for constant density would be much more applicable to the actual atmosphere if they were multiplied by the ratio of the assumed density to the actual density at each level. This procedure would, of course, be quite inconsistent, and even if applied would result in a percentage error.

Results have hitherto been calculated, either in the neighborhood of the cascade maximum,[6,7] which varies widely with the energy and initial condition considered, or averaged over all depths.[2-5,10] It is clear from Fig. 1 that neither of these procedures could result in values bearing even an approximate relation to those at sea level, or other given depths. This conclusion holds whether one assumes media of constant or variable density.

It should, of course, be borne in mind that the concept of incident electrons at the top of the atmosphere is probably unphysical. However, since all previous work has adopted this concept, it is interesting to note that the maximum spread of particles with a given energy is attained in the upper half of the atmosphere. No such maximum is attained in a medium of constant density, where the spread tends to a constant value.

To the errors already noted in work by previous authors, should be added those arising from miscellaneous approximations introduced in evaluating the already approximate integrals obtained. In view of the above it is obvious that treatments which have endeavored to account for the low energy showers, by the introduction of ionization losses, are practically meaningless.

APPENDIX

Table II gives the spread function $J_1(x)$, defined in (36). It can be expressed in terms of an indefinite integral:

$$J_1(x)=e^{-x}\int_0^x\{\mathrm{Ei}(x)-\ln x-\gamma\}x^{-1}dx,$$

where γ is Euler's constant and

$$\mathrm{Ei}(x)\equiv\int_{-\infty}^{x}e^{x}x^{-1}dx.$$

The values given here were computed by Dr. Cornish by summing the infinite series

$$J_1(x)=e^{-x}\sum_{n=0}^{\infty}x^n/n!n^2,$$

which is the most convenient method for arguments up to 13 or 15. Beyond this, it is easier to use another development

$$J_1(x)=2\sum_{n=2}^{\infty}c_nx^{-n}\Gamma_x(n+1)/\Gamma(n+1),$$

where c_n is the coefficient of x^n in the power series expansion of $\{\ln(1-x)\}^2$. Values for arguments from 13 to 50 are being computed in this way.

The Decay of Rh^{106}†

DAVID E. ALBURGER
Brookhaven National Laboratory, Upton, New York
(Received June 27, 1952)

Beta-rays with maximum energies of 3.53±0.01, 3.1±0.1, 2.44±0.07, and 2.0±0.1 Mev and relative intensities of 68, 11, 12, and 3 percent, respectively, have been found with a lens spectrometer in the decay of Rh^{106}. Internal conversion lines of 0.513 and 0.624 Mev transitions occur with intensities of 7.5×10^{-4} and 2.3×10^{-4} relative to total beta-emission. The first of these has a K/L ratio of 7.8±1, indicating an electric quadrupole radiation. Lens and scintillation spectrometer measurements show that the gamma-ray spectrum consists of lines at 0.511, 0.621, 0.87, 1.045, 1.55, and 2.41 Mev with relative intensities of 100:53:3:8:2.5:1, respectively. The results are consistent with beta-decay to states in Pd^{106} at 0, 0.513, 1.137, 1.55, and 2.42 Mev having even parities and spins of 0, 2, 0, 2, and 2, respectively. Rh^{106} is assigned spin 1 and even parity. The possibility of explaining the gamma-gamma angular correlation of Rh^{106} based on this decay scheme is mentioned.

I. INTRODUCTION

MEASUREMENT of the angular correlation of succession radiations as a means of determining certain properties of nuclear energy levels has been developed extensively during the past few years. Rh^{106}, a 30-sec beta-activity[1] which is generally used in an equilibrium condition with 1-yr Ru^{106}, was one of the early cases studied. Brady and Deutsch found[2] that the angular correlation of the gamma-rays emitted in the decay of Rh^{106} exhibited a strong anisotropy while at the same time Deutsch and Metzger showed[3] that an anisotropic effect existed in the direction-polarization correlation.

Prior to the experiments of Brady, Deutsch, and Metzger and some preliminary results reported[4] by the author, the only complex decay scheme for Rh^{106} was proposed[5] by Peacock. He found two beta-ray groups with end points at 3.55 Mev (82 percent) and 2.30 Mev (18 percent) and gamma-rays of 0.51, 0.73, and 1.25 Mev by means of a lens spectrometer. The data were interpreted as beta-decay to the ground state of Pd^{106} and to a level at 1.25 Mev, the latter being followed by either a 0.51–0.73-Mev gamma-ray cascade (17 percent) or a 1.25-Mev crossover (1 percent).

On the basis of this decay scheme Brady, Deutsch, and Metzger deduced the following from the correlation measurements: (1) the first excited state of Pd^{106} has a spin $J\geq2$; (2) the parities of the ground and second excited states are the same; and (3) if both cascade transitions are quadrupole, they are electric. They also showed that the general shape of the angular correlation most closely corresponds to a 0–2–0 cascade but that the magnitudes of the anisotropy coefficients are smaller than expected by a factor of two.

Ling and Falkoff examined[6] this case theoretically and proved that no combination of quadrupole and dipole radiations could account for the angular correlation if only a single two-step cascade were involved. The analysis was extended[7] to higher multipole orders by Spiers, but the correlation could still not be explained successfully without introducing additional cascade processes. Williams and Wiedenbeck suggested[8] that the first excited state is 2+ and that two higher levels might be present, one being 0+ and the other 1± or 3+.

The first experimental evidence for greater complexity of the Rh^{106} decay scheme was obtained[9] by Goldhaber and der Mateosian who discovered that this activity could produce photoneutrons in Be and D_2O The fraction of gamma-rays above 2.23 Mev was estimated to be approximately 1 percent of the total gamma-ray intensity and appeared to be too great to be accounted for as bremsstrahlung from the energetic beta-rays.

With this new information and the unsatisfactory situation regarding the angular and direction-polarization correlations, it was considered desirable to reinvestigate the Rh^{106} decay scheme. The results reported here show that altogether four excited states in Pd^{106} are involved in the decay of Rh^{106}. In addition to a strong 0.624–0.513-Mev gamma-ray cascade several other cascade processes are present which might conceivably contribute sufficiently large enough effects to help explain the observed correlations.

II. BETA-RAY SPECTRUM

The beta-ray spectrum of Rh^{106} was examined with a lens spectrometer set for a resolution of 2.5 percent. Sources of Ru^{106} aged for approximately two years, were mounted on 0.09 mg/cm² Nylon and the deposits were estimated to be less than 0.5 mg/cm² thick.

† Under contract with the AEC.
[1] Way, Thano, Scott, and Thew, *Nuclear Data*, National Bureau of Standards Circular No. 499 (1950).
[2] E. L. Brady and M. Deutsch, Phys. Rev. **74**, 1541 (1948); **78**, 558 (1950).
[3] M. Deutsch and F. Metzger, Phys. Rev. **74**, 1542 (1948); **78**, 551 (1950).
[4] D. E. Alburger, Phys. Rev. **85**, 734 (1952).
[5] W. C. Peacock, Phys. Rev. **72**, 1049 (1947).
[6] D. S. Ling and D. L. Falkoff, Phys. Rev. **76**, 431 (1949).
[7] J. A. Spiers, Phys. Rev. **78**, 75 (1950).
[8] A. H. Williams and M. L. Wiedenbeck, Phys. Rev. **78**, 822 (1950).
[9] M. Goldhaber and E. der Mateosian, Brookhaven National Laboratory Report BNL 51 (S-5) (1950) (unpublished).

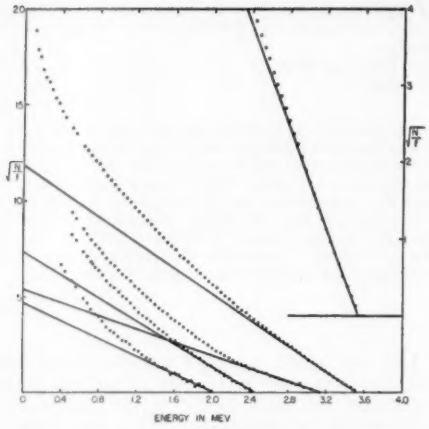

FIG. 1. Kurie plot analysis of the Rh^{106} beta-ray spectrum. An enlargement of the total curve is shown at the right.

Because of the indications of complexity found in preliminary runs, considerable care was exercised in taking and analyzing the data. The statistical accuracy was high, such that ~500,000 counts per point were recorded at the top of the curve, the points were interlaced in a random manner, and the results of a number of complete runs were averaged together in order to minimize effects of drift in the counting system. Corrections for counter dead-time and background were applied. In spite of the smooth appearance of the total curve data were taken at approximately 85 momentum settings. Calculation and analysis of the Kurie plot was carried out with the aid of a table of relativistically accurate Fermi functions kindly supplied by I. Feister of the National Bureau of Standards. An extrapolation of the table above 3.1 Mev was necessary in order to cover the full range of beta-ray energies.

Figure 1 shows a Kurie plot analysis of the Rh^{106} beta-ray spectrum. Subtraction of the various components was done in the usual manner by least squares fitting of a straight line to points near the end of each curve. In this way four beta-ray groups could be resolved consistently assuming that the allowed shape applied to each. Owing to the statistical scatter of the points below 2 Mev and the possible influence of source thickness effects, it was not considered advisable to extend the analysis further. The end-point energies of the various groups are 3.53±0.01, 3.1±0.1, 2.44±0.07, and 2.0±0.1 Mev. The relative intensities of 68, 11, 12, and 3 percent, respectively, were determined by reconstructing the momentum distributions of each component and comparing their areas as measured with a planimeter. The errors in their intensity determinations are about 15 percent for the most energetic group and 25 percent for the inner groups. The 6 percent excess intensity at low energies is not considered significant in view of the errors involved and the number of subtractions made.

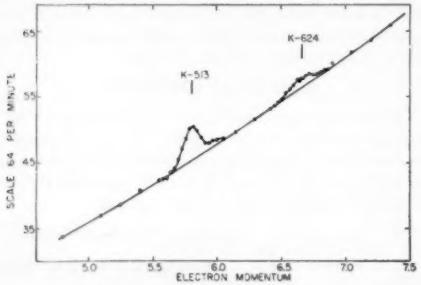

FIG. 2. Internal conversion lines of Rh^{106} superposed on the beta-spectrum.

III. INTERNAL CONVERSION LINES

Internal conversion lines were found superposed on the Rh^{106} beta-ray spectrum as shown in Fig. 2. The energies of the transitions are 513 and 624 kev in agreement with internal conversion lines also observed[10] by Hill. The intensities of the K-lines relative to total beta-radiation are 7.5×10^{-4} and 2.3×10^{-4}, respectively. No evidence for other conversion lines was found in spite of the high statistical accuracy of the points.

Measurement of the K/L ratio of the 513-kev transition was carried out at a spectrometer resolution of 1.6 percent. Good statistics were necessary since the L-line was only 2 percent above the beta-ray yield at this point. When the beta-background is subtracted, the curve in Fig. 3 is obtained from which the K/L ratio is 7.8±1. Because of higher background and lower net yield a K/L measurement was not attempted on the 624-kev transition.

IV. GAMMA-RAY MEASUREMENTS

The lens spectrometer was used to examine the photoelectron spectrum due to the gamma-rays of Rh^{106}. The results obtained with a 25-mC source and converters of lead (22 mg/cm²) and uranium (44 mg/cm²) are shown in Figs. 4 and 5. Assignments of the lines are given in each figure. It may be noted that the lead converter permits the L-0.511 and K-0.621 lines to be separated, while the corresponding conversion lines from uranium have very nearly the same energy because of binding effects. On the other hand, the uranium allows clearer observation of the K-0.87 line and in addition shows the presence of a weak 1.55-Mev gamma-ray.

Examination of Peacock's lead conversion curve[5] suggests that the L-0.511 and K-0.621 lines were not resolved and that this resulted in the misassignment of the L-0.621 peak as being the K conversion line of a 0.72 Mev gamma-ray.

[10] R. D. Hill (private communication).

The energies of the various gamma-rays were determined from the positions of the K peaks and in some cases checks were made using the extrapolated high energy edge of the line. The energies thus obtained are 0.511, 0.621, 0.87, 1.045, and 1.55 Mev with errors of not more than 1 percent.

The relative intensities were determined from the momentum plots of K conversion lines by comparing areas and correcting for photoelectric cross section according to the empirical formula of Gray.[11] The applicability of Gray's formula to the source and converter geometry used in this work was studied by examining in a similar geometry the photoelectron peaks due to sources of Na^{22} and Na^{24}. The disintegration schemes of these isotopes are known and the range of energies covered is from 0.51 to 2.76 Mev. It is found that in the energy range of the lens measurements on Rh^{106},

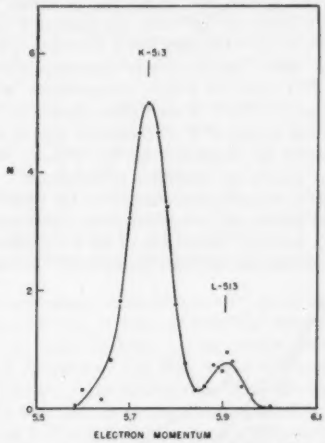

FIG. 3. K and L internal conversion lines of the 513-kev transition after subtraction of the beta-ray background.

0.51 to 1.55 Mev, Gray's formula may give results in error by as much as 50 percent at the extreme ends of this interval, while for gamma-rays between 0.5 and 1.0 Mev the errors are probably not more than 25 percent. The intensities of the Rh^{106} gamma-rays relative to the 0.511-Mev transition, as given in Fig. 7, must be regarded as having errors which increase from about 20 percent for the 0.621-Mev line to 50 percent for the 1.55-Mev gamma-ray.

As a check on the above gamma-ray measurements a 100-mC Rh^{106} source was examined recently using a uranium converter and slightly better resolution than previously. A curve closely similar to that of Fig. 5 was obtained except that the L lines of both the 0.87- and 1.55-Mev gamma-rays were visible. From this result it is more certain that all of the gamma-rays are

[11] L. H. Gray, Proc. Cambridge Phil. Soc. **27**, 103 (1931).

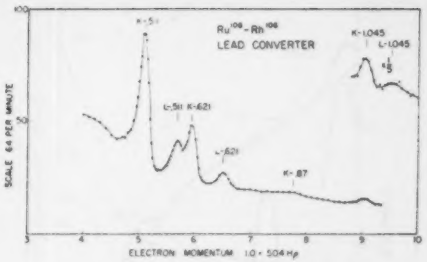

FIG. 4. Rh^{106} photoelectron spectrum using a Pb converter 22 mg/cm² thick.

due to Rh^{106} and not to impurities. With this same source the region above 1.55 Mev was examined carefully because of the photoneutron evidence previously mentioned. No photoelectron peaks were found but there appeared to be a weak Compton electron group ending at about 2.2 Mev. In spite of this result it was not felt that the presence of an additional gamma-ray had been established definitely. The evidence for a gamma-ray of 2.9 Mev previously suspected[4] was not confirmed.

In collaboration with Dr. W. F. Hornyak, a scintillation crystal spectrometer was put in operation using a 5819 photomultiplier tube together with a NaI(Tl) crystal 4 cm in diameter and 3 cm thick specially prepared by Dr. A. Schardt. The resolution of this device at 661-kev gamma-ray energy is 10.0 percent. The gamma-rays of Rh^{106} previously measured with the lens spectrometer were all observed with this instrument. To examine the region above 1.55 Mev the gamma-rays from a 200-mC Rh^{106} source were filtered through 5 cm of lead before reaching the NaI crystal. In this arrangement a high discrimination against the lower energy and more intense components was achieved. Without the lead filter the pile-up of small pulses prevented a clear examination at high energies with at the same time reasonable counting rates.

The spectrum obtained with a differential pulse-height analyser and covering energies between 1.0 and 3.2 Mev

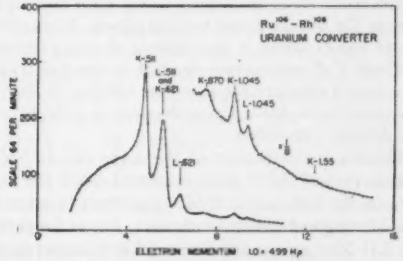

FIG. 5. Rh^{106} photoelectron spectrum using a U converter 44 mg/cm² thick.

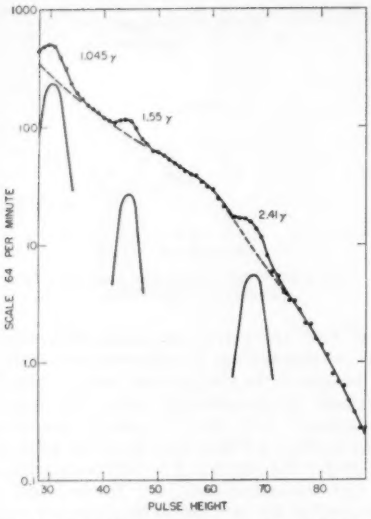

FIG. 6. Pulse-height spectrum between 1.0 and 3.2 Mev from a NaI crystal due to Rh^{106} gamma-rays.

is shown in Fig. 6. The highest energy peak is interpreted as the photoline of a 2.41±0.04 Mev gamma-ray, the energy being based on a Na^{24} calibration. In the Na^{24} spectrum peaks corresponding to pair production by the 2.76-Mev gamma-ray with the escape of one and two annihilation quanta were present in addition to the photopeak. The one-quantum escape peak was 0.16 as intense and the two-quantum escape peak 0.45 as intense as the photoline.

This information may be used to substantiate the interpretation of the Rh^{106} curve in Fig. 6. The two quantum escape peak should be measurable but it is masked by the 1.55-Mev photoline, while the one quantum escape peak should barely be visible. Since no other higher lines seem to be present it would be difficult to interpret the 2.41-Mev line as an annihilation escape peak of a higher energy gamma-ray.

The relatively slow decrease in the yield beyond 2.4 Mev in Fig. 6 is attributed to pulse pile-up. When a Na^{24} source was examined in the presence of strong fluxes of Cs^{137} and Co^{60} gamma-rays incident on the NaI crystal in order to simulate the situation existing in Rh^{106} it was possible to obtain a slow decrease in yield beyond the 2.76-Mev photoline.

The relative intensities of the 2.41- and 1.55-Mev gamma-rays of Rh^{106} were estimated using the Na^{24} data on the 1.38- and 2.76-Mev gammas to correct for lead filtering and detection efficiency. It was found that the 2.41-Mev gamma-ray is about 0.4 as intense as the 1.55-Mev component or 1 percent of the 0.513-Mev line. This corresponds to an intensity of about 0.6 percent of all gamma-rays in rough agreement with the estimates of Goldhaber and der Mateosian based on a measurement of the photoneutron yield.[9]

DISCUSSION

A decay scheme for Rh^{106} can be deduced which is consistent with the various measurements described above within their respective errors. This is shown in Fig. 7. All of the radiations were resolved except a beta-ray group, indicated by the dashed line, to a level which is thought to exist in Pd^{106} at 2.42 Mev. Such a level would explain both the 0.87- and 2.41-Mev gamma-ray transitions, the latter being equal within the probable error to the more accurate sum 0.87+1.55=2.42 Mev.

Confirmation of a considerable portion of the Pd^{106} level scheme has been obtained[12] by Hayward who has studied the gamma-ray transitions occurring in the K-capture decay of Ag^{106}. He has proposed levels at 0.511 Mev (2+), 1.131 Mev (0+), 1.54 Mev (3+), and 1.76 Mev (4+). The 0.511-Mev transition is found to have a K/L ratio of 8.2±1 in agreement with the present data on Rh^{106}. If the highest state at 1.76 Mev actually has a spin of 4, its failure to appear in Rh^{106} decay would be accounted for by beta-ray selection rules and gamma-ray transition probabilities.

The spin and parity assignments in the present work are based mainly on the measurements described in the foregoing sections. The nature of the 0.513-Mev radiation can be determined from the analysis[13] of Goldhaber

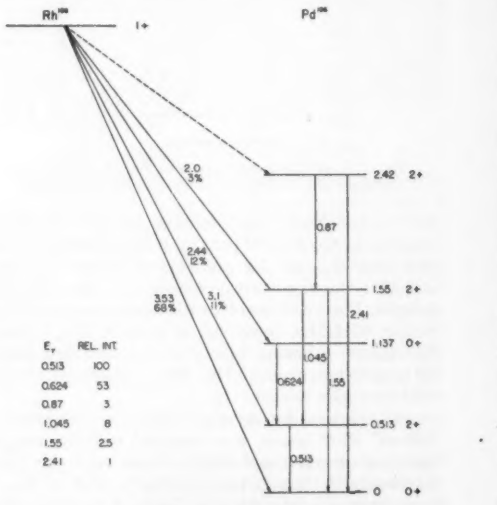

FIG. 7. Decay scheme of Rh^{106}.

[12] R. H. Hayward, Phys. Rev. **85**, 760 (1952) and private communication to M. Goldhaber.
[13] M. Goldhaber and A. W. Sunyar, Phys. Rev. **83**, 906 (1951).

and Sunyar by extrapolation of the empirical K/L ratio curves. Their data on electric transitions are given in Fig. 8 together with the point corresponding to the 0.513 Mev gamma-ray of Rh^{106}. It is evident that electric quadrupole radiation is involved, a conclusion which also fits the general rule formulated[13] by Goldhaber and Sunyar that the first excited states of most even-even nuclei have a spin of 2 and even parity.

The ratio of K conversion coefficients of the 0.513 and 0.624 Mev transitions as obtained from the internal and photoelectric conversion measurements is 1.73. This agrees well with the value 1.70 from the tables[14] of Rose *et al.* assuming both transitions are $E2$. Furthermore, if the decay scheme is accepted as being correct then the absolute K conversion coefficients of the 0.513- and 0.624-Mev transitions may be calculated. These are $(3.5\pm1)\times10^{-4}$ and $(2.1\pm1)\times10^{-3}$, respectively, which are in approximate agreement with the values 4.99×10^{-3} and 2.93×10^{-3} for electric quadrupoles taken from the tables of Rose *et al.* Although the 1.137-Mev level could then have a spin of 0 or 4 and even parity if the transitions are pure electric, the latter case is ruled out by the beta-ray measurements. The logft values of the beta-groups were calculated from the graphs[15] of Moszkowski and are as follows: 3.55-Mev group—5.2, 3.1-Mev group—5.7, 2.44-Mev group—5.3, and 2.0-Mev group—5.6. All of these would appear to be allowed according to the classification[16] of Nordheim. This would not be possible with a spin difference of 4 between the ground and second excited states.

The spins discussed thus far would explain the absence of the crossover transition from the second excited state and would account for the general trend of the angular correlation. The data would also suggest that Rh^{106} has spin 1 and even parity. With this assumption and the fact that crossover transitions occur from the levels at 1.55 and 2.42 Mev these states could have a spin of either 1 or 2 and even parity in order for the beta-transitions to be allowed. The allowed nature of a beta-transition to the 2.42-Mev state is inferred from an estimate that the branching to this state is approximately 1.5 percent, based on the gamma-ray intensities, and that the log ft value is therefore less than 5. In view of the greater intensity of the cascade gamma-rays from both of these states, even though the crossovers are more energetic, it would be more favorable to assign spins of 2 to the 1.55- and 2.42-Mev levels.

After the partial decay scheme up to and including the 1.55-Mev level had been established[4] several attempts were made to account more completely for the Rh^{106} angular correlation. Kraushaar examined[17] this case with NaI detectors in which some energy

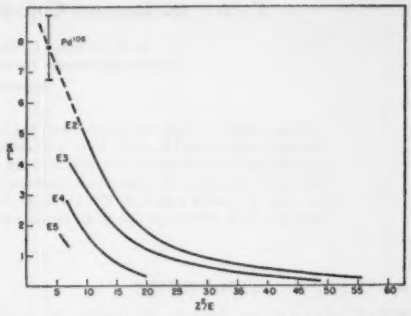

FIG. 8. Empirical K/L ratios for electric transitions from Goldhaber and Sunyar (reference 13) showing the point for the 513-kev transition in Pd^{106}.

discrimination was employed. He was able to show that the effect of the 1.04–0.51 Mev cascade is to lessen the angular correlation anisotropy caused by the 0.624–0.513-Mev main cascade but that contribution of the former is not sufficiently intense to account for the total correlation. The greatest cancellation effect would occur if the 1.55-Mev level were assigned a spin of 2 which would be consistent with the beta-decay analysis. Kraushaar suggested that a loss-of-memory might be involved in the angular correlation of the 0–2–0 cascade. This hypothesis was tested[18] by Steffen who measured the Rh^{106} angular correlation after embedding the activity in various metals and ionic crystals. No changes in the correlation could be made and it was concluded that a loss-of-memory effect was not present. Experiments similar to those of Kraushaar have been carried out[19] recently by Arfken, Klema, and McGowan. These authors were also not able to account for the total correlation effect.

Since levels at 1.55 and 2.42 Mev in Pd^{106} appear to be excited in Rh^{106} decay it is evident that in addition to the 0.624–0.513 Mev pair several weaker cascades occur, one involving three successive gamma-rays. It is possible that the angular correlation could be explained on the basis of the decay scheme presented. However, a more exact knowledge of the relative intensities of Rh^{106} gamma-rays would be desirable.

The author is indebted to Dr. M. Goldhaber for many helpful discussions of this problem. Mr. Arthur Schwarzschild gave considerable assistance in taking and analyzing the data, and Miss Elizabeth Wilson and Dr. Seymour Katcoff prepared some of the sources. Thanks are also due to Dr. W. F. Hornyak for collaborating in some of the gamma-ray measurements and to Dr. I. Feister whose Fermi function tables were used. A 200-mC Rh^{106} source used in part of this work was obtained on loan from Oak Ridge through the kind cooperation of Mr. John H. Gillette.

[14] Rose, Goertzel, Spinrad, Harr, and Strong (privately circulated).
[15] S. A. Moszkowski, Phys. Rev. **82**, 35 (1951).
[16] L. W. Nordheim, Phys. Rev. **78**, 294 (1950).
[17] J. J. Kraushaar, Phys. Rev. **85**, 727 (1952).
[18] R. M. Steffen, Phys. Rev. **86**, 632 (1952).
[19] Arfken, Klema, and McGowan, Phys. Rev. **86**, 413 (1952).

$K/(L+M)$ Internal Conversion Ratios for $M4$ Transitions*

G. A. Graves, L. M. Langer, and R. D. Moffat
Physics Department, Indiana University, Bloomington, Indiana

(Received June 27, 1952)

A high resolution magnetic spectrometer has been used to study the internal conversion lines of magnetic four-pole transitions. The $K/(L+M)$ internal conversion ratios fall lower than those predicted from the empirical curve of Goldhaber and Sunyar in the region of low values of Z^2/E. A revised curve is presented. The following values are obtained for the energy of the transition and for the $K/(L+M)$ ratio: Y^{91}, 551.2 kev, 6.00; Sr^{87}, 388.2 kev, 5.79; Y^{87}, 381.3 kev, 5.41; Ba^{137}, 661.4 kev, 4.64; In^{113}, 391.7 kev, 4.21; and In^{115}, 334.6 kev, 3.76. Values are also given for lines in Cd^{111} and In^{114}.

INTRODUCTION

THE classification of an isomerism is usually accomplished either in terms of the half-life and the energy separating the states, by measuring the internal conversion in the K-shell, or by evaluating K/L internal conversion ratios.

In employing the first of these methods, it is usually not difficult to measure the transition energy quite well. However, the half-life which one uses for comparison with the theory must be the half-life for the radiation alone and not the total half-life of the state. This means that, if there are branching transitions, a detailed knowledge of these branches is required. In addition, it often happens that the half-life for the transition is one which is difficult to measure—e.g., it may be very short. When one employs the second method, one again needs some knowledge of the decay scheme, if one determines the gamma-ray intensity indirectly by finding the intensity of the beta-rays which feed the level. However, if one obtains the internal conversion and the gamma-ray intensity directly, or if one measures the K/L internal conversion ratio, an identification of the isomerism can be made without a complete knowledge of the decay scheme.

In a recent paper,[1] Goldhaber and Sunyar have attempted to formulate a scheme for the classification of nuclear isomers by identification of the type of radiative transition between the states. These authors employed a semi-empirical approach, relying chiefly on experimental results and on well-founded theoretical calculations such as the relativistic internal conversion coefficients of Rose *et al.*[2] One result of their investigations was the publication of curves of empirical K/L internal conversion ratios for various known transition types.[3] These curves can aid in the identification of other unknown transitions for which this ratio can be measured. In addition, they can be of assistance in determining the total conversion coefficient for a given type of transition. This quantity is valuable in analyzing complex decay schemes because it is needed for a comparison of intensity between the various beta- and gamma-decay branches.

The object of this paper is to present the results of a group of experiments which have indicated that a portion of the published empirical curve for $M4$ transitions should be substantially modified. A new curve for such transitions is proposed. The modifications are based largely upon $K/(L+M)$ ratios measured in the isomeric transitions In^{113}, In^{115}, Sr^{87}, Y^{87}, Y^{91}, and Ba^{137}, and to some extent on new results in the literature.

EXPERIMENTAL PROCEDURES

All measurements were made upon chemically separated, relatively thin and uniform, electrically grounded sources in a high resolution, magnetic spectrometer of 40-cm radius of curvature.[4] The momentum spread of

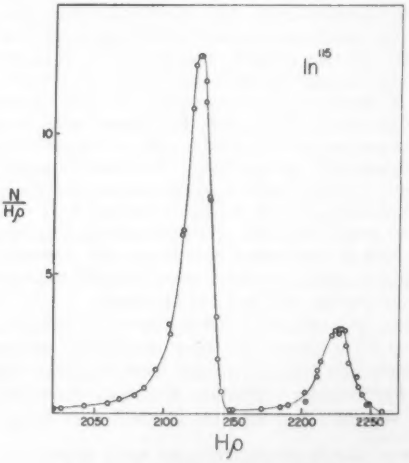

FIG. 1. Conversion electron spectrum of In^{115}.

* Assisted in part by the joint program of the ONR and AEC, and by a grant from the Frederick Gardner Cottrell Fund of the Research Corporation.

[1] M. Goldhaber and A. W. Sunyar, Phys. Rev. **83**, 906 (1951).

[2] Rose, Goertzel, and Perry, Oak Ridge National Laboratory Report No. 1023 (unpublished); also Phys. Rev. **83**, 79 (1951).

[3] Actually, these curves are a mixture of K/L and $K/(L+M)$ ratios, since conversions in the M, N, etc., shells were neglected where no separate measurements of them were available. Only for very high Z and very low energies are the L and M lines resolved, with present day techniques.

[4] L. M. Langer and C. S. Cook, Rev. Sci. Instr. **19**, 257 (1948).

the lines at half-maximum intensity ranged from 0.5 percent to 1.1 percent, depending mostly on the thickness of the source. In all cases, after the background level appropriate to any beta-spectrum present had been subtracted, the data were corrected for decay and exhibited on plots of $N/H\rho$ *vs* $H\rho$. The ratio of the areas of the internal conversion lines yields the $K/(L+M)$ ratio.[5] The ratios quoted below are believed to be correct to within 5 percent, with the possible exception of that for In^{113}, where an arbitrariness in the subtraction of a complex beta-background might introduce as much as 5 percent additional error.

The particular experimental procedure used with the various isotopes is described in the separate discussions

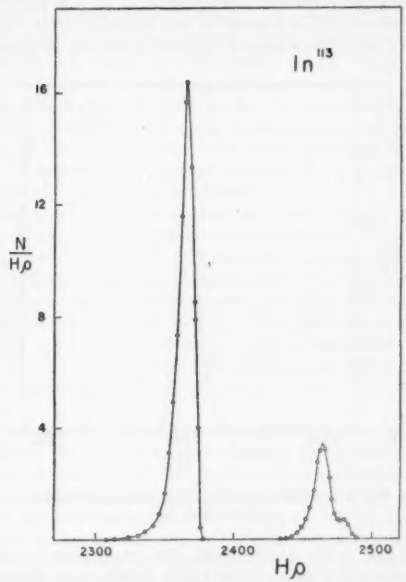

FIG. 2. Conversion electrons of 391.7-kev transition in In^{113}.

below, and these individual results are collected in a summary curve.

RESULTS

In^{115}

The study of this isotope provided one of the first indications that the $M4$ curve of Goldhaber and Sunyar might require a change.[6]

The source material was grown and extracted as

[5] The practice of evaluating conversion ratios from the ratios of the peaks in a plot of N *vs* $H\rho$ is only valid if the geometrical resolution is poor compared to the natural line width. If the sources are not thin or if the lines are not completely separated, such a procedure may lead to erroneous ratios.

[6] Langer, Moffat, and Graves, Phys. Rev. **86**, 632 (1952).

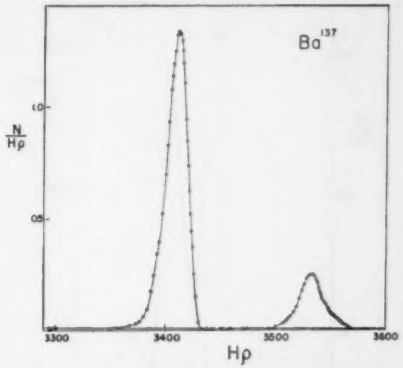

FIG. 3. Momentum distribution of conversion electrons of Ba^{137}.

$In(OH)_3$ from the 54-hour Cd^{113} parent, which had been produced by deuteron bombardment on cadmium in the cyclotron. It was deposited as a slurry on a 0.0002-in. aluminum backing. The internal conversion lines of interest are shown in Fig. 1. The energy of this 4.5-hour transition is 334.6 kev,[7] for which the corresponding value of Z^2/E is 7.12. The $K/(L+M)$ ratio is 3.76.[8] This transition presumably occurs between an excited $p_{1/2}$ state and the $g_{9/2}$ ground state, whose spin has been measured. This assignment is in agreement with the level predictions of the nuclear shell model.

In^{113}

In^{113} was prepared by a short deuteron bombardment on cadmium in the cyclotron. The source was deposited as an $In(OH)_3$ slurry upon a 0.0002-in. Al backing. The internal conversion lines from this source were superimposed on a weak beta-ray background whose decay indicated that it might arise from a mixture of 54-min In^{116} and 117-min In^{117}. From an empirical plot of this background against time, the background level existing at the time of measurement of each of the points was determined. This level was subtracted from the measured counting rate, and the residual rates were corrected for a decay of half-life 104 minutes.

The internal conversion lines are shown in Fig. 2. For this transition, the measured energy is 391.7 kev, yielding Z^2/E as 6.13, and the $K/(L+M)$ ratio is 4.21. Shell model predictions ascribe $p_{1/2}$ to the upper state and $g_{9/2}$ to the lower state of this isomeric pair.

Ba^{137}

The $M4$ transition in Ba^{137} follows a beta-decay from Cs^{137}. The source of Cs^{137} was separated from the fission products at Oak Ridge. Since the period of the isomeric

[7] Because of a typographical error, this energy was erroneously given as 333.7 kev in reference 6.

[8] This value is somewhat lower than that previously given by J. L. Lawson and J. M. Cork, Phys. Rev. **57**, 982 (1940).

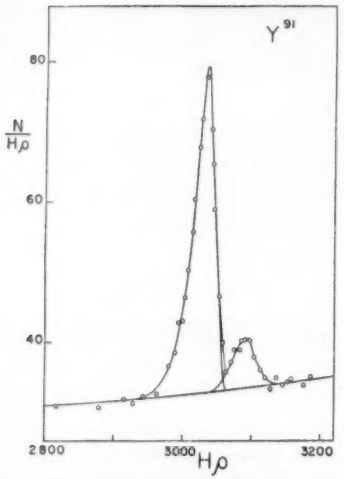

FIG. 4. Electron line spectrum in Y^{91}.

transition is very short (2.62 minutes) compared to that of the beta-decay which feeds it, its internal conversion lines are measured in equilibrium with the 37-year parent activity and no decay correction need be made. The momentum plot shown in Fig. 3 yields a $K/(L+M)$ ratio of 4.64. The gamma-ray energy is 661.4 kev, for which Z^2/E is 4.74. The decay is presumably from an excited state of $h_{11/2}$ to a $d_{3/2}$ ground state whose spin has been measured.

Y^{91}

The internal conversion lines in Y^{91} arise from a 51-minute metastable state which is fed by the 9.7-hour beta-decay of Sr^{91}. The Sr^{91} was separated from the fission products at Los Alamos, following a short neutron bombardment of fissionable material in a pile. The internal conversion electron spectrum, corrected for the 9.7-hour equilibrium decay, is shown in Fig. 4. The energy of the unconverted gamma-ray is 551.2 kev, Z^2/E is 2.76, and $K/(L+M)$ is 6.00. For this transition, the shell model predicts $g_{9/2}$ for the upper level and $p_{1/2}$ for the lower level.

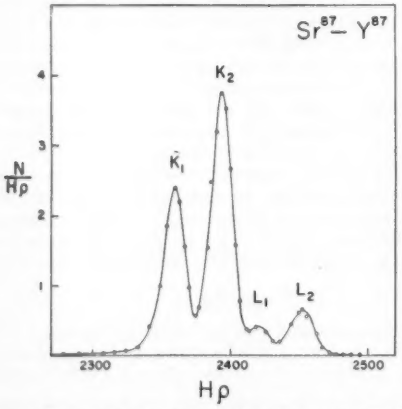

FIG. 5. Momentum plot of conversion electrons in $Sr^{87}-Y^{87}$. This curve is not decay-corrected and is introduced just to show the relative separation of these lines.

$Sr^{87}-Y^{87}$

The activity in these isotopes has a rather extensive history, to which references can be found in two recent articles.[9,10] Convincing evidence has been presented in these papers that the decay scheme, at least in part, is as follows: Y^{87} is formed in two isomeric states. The upper state undergoes a 14-hour transition of about

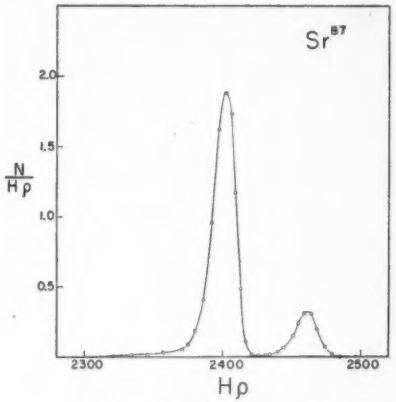

FIG. 6. Internal conversion electrons of the 388.2-kev transition in Sr^{87}.

385 kev to the ground level. This lower state in turn decays with a period of 80 hours, mainly by K-capture to an excited state in Sr^{87} at about 875 kev above its ground level. This state then undergoes a 485-kev transition to a 2.8-hr isomeric level which is about 390 kev above the ground state. No crossovers have been definitely established in this chain, although some positrons as well as some internal conversion lines in the region of 1 Mev have been reported and sometimes attributed to this decay.

Both the 14-hr and the 2.8-hr isomeric states appear to give rise to $M4$ transitions. $K/(L+M)$ ratios reported for these conversions have ranged from 6.0 to 8.3. About 0.4 percent of the 485-kev transitions occur by internal conversions, and no $K/(L+M)$ values have been previously reported for these lines.

[9] E. K. Hyde and G. D. O'Kelly, Phys. Rev. **82**, 944 (1951).
[10] L. G. Mann and P. Axel, Phys. Rev. **84**, 221 (1951).

Because of the small energy separation of the two $M4$ transitions, in the past there has been difficulty in resolving the conversion lines, which has complicated measurements on the $K/(L+M)$ ratios. The present experiment was performed with better resolution, and it was also arranged to measure the internal conversion lines of each transition with sources in which the other transition was essentially absent. This made possible a more accurate determination of the energies and of the $K/(L+M)$ ratios. Here the K and L lines are completely separated and no arbitrariness of extrapolation is necessary.

Radioactive yttrium was produced by bombarding strontium with deuterons in the cyclotron. The yttrium was separated as a hydroxide and deposited as a slurry onto a 0.0002-in. Al source backing. An examination of this source in the spectrometer about eighteen hours after the separation gave the results shown in Fig. 5. In the course of the different studies on this source, it was obvious that the lines K_1 and L_1 decayed with a 14-hr half-life, while K_2 and L_2 first grew with this half-life and later decayed with the 80-hr period. This lends support to the genetic relationships previously proposed[10] and summarized above.

One hundred and twenty-two hours after preparation of this source, its spectrum was again studied. By this time the 14-hr activity was completely gone, and the internal conversion lines of the 2.8-hour transition were easily measured in equilibrium with the 80-hr state into which the 14-hr activity had fed. These lines, which are in Sr^{87}, are corrected for the 80-hr decay and shown in Fig. 6. Our measurements ascribe 388.2 kev to the energy of the transitions, 3.72 to Z^2/E, and 5.79 to the $K/(L+M)$ ratio.

Further evidence for the correctness of the previously proposed decay scheme was obtained by separating strontium from yttrium left over in preparing the above source. This second separation was performed 90 hr after the bombardment. One portion of this Sr was used as a spectrometer source; the other was monitored by a device which automatically recorded its decay. From this, the half-life of this material was found to be 173 ± 2 minutes. Two traverses of the K-line in the spectrometer fitted to within 2 percent at their peaks when both were corrected for this decay to the same initial time. The $K/(L+M)$ ratio obtained from this separated strontium source differed from that quoted above by only 1 percent.

To investigate the conversion of the $M4$ transition in Y^{87}, strontium was bombarded with eighty microamperes of deuterons for one hour. Yttrium was separated from the strontium, a spectrometer source prepared, and the scanning of the spectrum commenced within about one hour after the bombardment. The actual counting rates are shown in Fig. 7. It is obvious from this figure that there is only a very small contribution to the counting rate from internal conversions in strontium (K_2 and L_2).

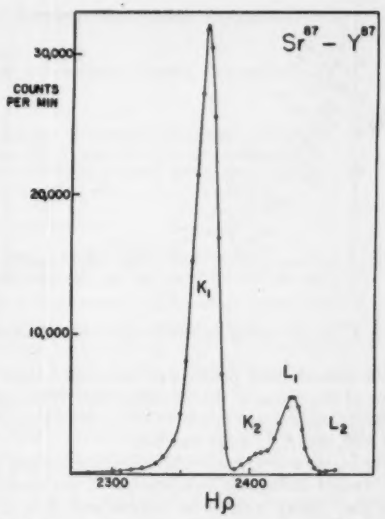

FIG. 7. Electron momentum distribution obtained shortly after separation from a source containing only yttrium at the initial time. These points have been corrected for the counter losses at high counting rates. No decay correction has been applied.

From our previous measurements on strontium it was easily determined where its spectrum had a negligible influence on these points. For these points, a 14-hr decay correction was applied, and the plot of Fig. 8 was made. The proper low energy extrapolation of the

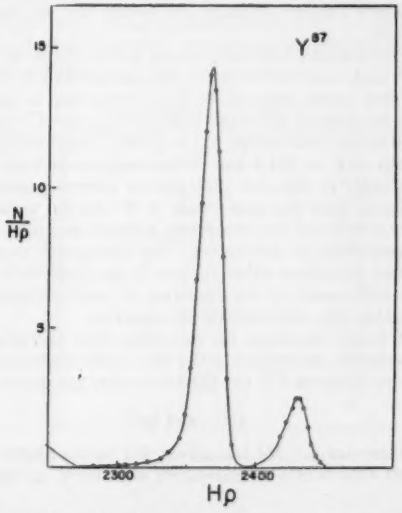

FIG. 8. Conversion elections from the 14-hr transition in Y^{87}.

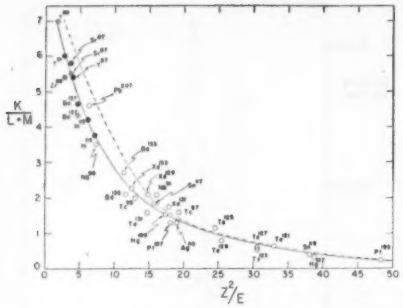

FIG. 9. $K/(L+M)$ internal conversion ratios for $M4$ transitions.

L-line beyond these points was determined from the shape of the L-line in the strontium data. The energy of this transition was measured to be 381.3 kev, Z^2/E was 3.99, and $K/(L+M)$ was 5.41.

The higher energy conversion lines in strontium were also studied during this investigation. It was confirmed that they decay with 80-hr half-life and their $K-L$ energy difference shows that they are in strontium. The transition energy is 483.4 kev, Z^2/E is 2.99, and the $K/(L+M)$ ratio was measured to be 6.64. This last quantity might be in error by as much as 25 percent, since the counting rate on these lines is low. Mann and Axel[10] measured the internal conversion coefficient for this transition, from which they concluded it was either $M1$ or $E2$, and probably $M1$. Our value of the $K/(L+M)$ ratio seems to substantiate this assignment when compared with Goldhaber and Sunyar's curves,[1] although the results are not conclusive.

The spin and level assignments previously given in Sr^{87} would seem to be correct. The ground state is $g_{9/2}$, the first excited state at 388.2 kev would then be $p_{1/2}$, and the state at 871.6 kev could be $p_{3/2}$. For Y^{87}, the shell model would assign $p_{1/2}$ to the 80-hr level and $g_{9/2}$ to the level at 381.3 kev. These assignments lead to difficulties in that one then expects allowed positron emission from the upper state of Y^{87} to the ground state of Sr^{87}, and very few, if any, positrons are observed corresponding to this branch. This discrepancy would appear to indicate either an error in the predictions of the shell model, or the operation of some additional selection rule which forbids the transition.

A search was made for conversion lines previously reported[9] in the region above 1 Mev in the spectrum of freshly prepared Y^{87}, but these lines were not found.

Cd^{111} and In^{114}

These are not $M4$ transitions, but in the course of these experiments measurements were made on some of the internal conversion electrons of these isotopes, and the results are presented here.

The source was the one from which the In^{113} data had previously been obtained. Three sets of K, L, and M lines were measured. Two of these sets represented conversions following the 68-hr beta-decay of In^{111} to Cd^{111}, and one set resulted from a 50 day $E4$ transition between isomeric states of In^{114}. The $K-L$ energy differences support the assignment of these lines to these elements.

For the two lines arising between levels in Cd^{111}, the gamma-ray energies are 170.8 kev and 245.6 kev,[11] with $K/(L+M)$ ratios of 7.03 and 4.79, respectively. The distribution among $K:L:M$ conversions for these transitions have been estimated as 875:105:20 and 827:146:24, respectively. For In^{114}, the transition energy is 189.8 kev,[11] with a $K/(L+M)$ ratio of 1.00, and with $K:L:M$ equal to 500:425:75. There is the possibility of considerable error in our estimate of the relative strength of the L and M conversions, since the lines are multiple and are not completely resolved, and this makes it difficult to determine the true contribution of each. The estimates given above seem reasonable from the data.

CONCLUSIONS

The results for the $M4$ transitions presented in this paper are shown along with results of other investigations in Fig. 9. In this figure, Z is the nuclear charge of the isomeric pair; E is the transition energy in kilovolts. The dashed curve is the original empirical curve of Goldhaber and Sunyar,[1] the solid curve is the one proposed on the basis of the new data. The solid circles represent data presented in this paper. The barred circles represent results reported by Bendel *et al.*[12] The open circles represent estimations of the best values for $K/(L+M)$, as determined by Bendel from re-evaluation of the literature.[13]

Although this new curve of $K/(L+M)$ ratios should be useful for the identification of $M4$ isomers, a curve of true K/L ratios would be of more value for a direct comparison with theory when the new theoretical results for L conversion become available.

The authors take this opportunity to express their appreciation to Dr. Milo B. Sampson and the cyclotron staff for bombardments and to Mr. Arthur Lessor for performing many of the chemical separations. We are indebted to Dr. D. P. Ames for the chemical separation of the Y^{91} sample.

[11] These energies are about two kev lower than reported by Lawson and Cork (see reference 8). The energy of the transition in In^{114} agrees well with the 190-kev energy reported by Mei, Mitchell, and Zaffarano, Phys. Rev. **76**, 1883 (1949).

[12] Bendel, Shore, Brown, and Becker, Phys. Rev. **87**, 195 (1952).

[13] We are grateful to Mr. Bendel for very kindly supplying us with his results.

The Slope of Logarithmic Plots of the Fowler-Nordheim Equation*

J. M. HOUSTON
Research Laboratory of Electronics, Massachusetts Institute of Technology, Cambridge, Massachusetts
(Received June 10, 1952)

The slope of logarithmic plots of the Fowler-Nordheim equation for electron field emission is expressed in terms of the surface work-function and a tabulated function, $s(y)$. This new function, $s(y)$, is derived from Nordheim's $v(y)$ which appears in the exponent of the Fowler-Nordheim equation. Values of $v(y)$ are also tabulated and are believed to be more exact than Nordheim's original values.

THE Fowler-Nordheim equation gives a theoretical relation between the current density of field emission electrons and the electric field at the surface of the emitter. According to the theory the only controlling quantity that depends on the emission surface used is the work-function. It is the purpose of this paper to make available a tabulated function which will aid in the evaluation of surface work-function from field emission measurements.

The Fowler-Nordheim equation can be written in the following form.[1]

$$J=1.55\times10^{-6}F^{2}\phi^{-1}\exp[-6.86\times10^{7}\phi^{\frac{1}{2}}F^{-1}v(y)],$$

where J = current density in amp/cm², F = electric field at surface in volts/cm, ϕ = surface work-function in volts, $y=3.62\times10^{-4}F^{\frac{1}{2}}/\phi$ (reference 1), and $v(y)$ = elliptic function of y (reference 2).

In experimentally testing the above equation one usually plots $\log_{10}(J/F^{2})$ *versus* $(1/F)$. Because $v(y)$ is a slowly varying function of F, the Fowler-Nordheim equation predicts for this plot a curve closely approximating a straight line over a small range of variation in F. It is useful to know the slope of this curve for two reasons: (1) It gives one an exact method of interpreting the slope of experimentally measured plots of $\log_{10}(J/F^{2})$ *versus* $(1/F)$. (2) One can predict how far the experimental plot should depart from a straight line.

To find the slope of a $\log_{10}(J/F^{2})$ *versus* $(1/F)$ plot of the Fowler-Nordheim equation, one takes the derivative with the following result:

$$\text{Slope}=\frac{d(\log_{10}J/F^{2})}{d(1/F)}=-2.98\times10^{7}\phi^{\frac{1}{2}}\left(v-\frac{y}{2}\frac{dv}{dy}\right)$$
$$=-2.98\times10^{7}\phi^{\frac{1}{2}}s(y),$$

where $s(y)=v-\frac{1}{2}ydv/dy$.

The function $s(y)$ is tabulated in Table I. Also the values of $v(y)$ are listed because my calculated values differ slightly (up to 3 percent) from the original values published by Nordheim.[2] The values of $v(y)$ given here are believed to be correct to four figures, and $s(y)$ correct to three figures.

As F is increased, the absolute value of the slope at first decreases until approximately $y=0.7$ and then increases to infinity at $y=1$. The maximum of the potential barrier at the metal surface has been pulled down to the Fermi level when $y=1$.

As an example, consider field emission from a tungsten hemisphere of radius equal to one micron. The minimum current which can be measured is about 10^{-16} ampere, which corresponds to $J=1.6\times10^{-9}$ amp/cm², $F=1.5\times10^{7}$ volt/cm, and $y=0.31$. The maximum current density which has been reported[3] is about $J=10^{7}$ amp/cm², corresponding to $I=0.6$ amp, $F=7.5\times10^{7}$ volt/cm, and $y=0.70$. Over this range the slope changes by about 3 percent.

If experimental results are plotted in the form $\log_{10}J$ *versus* $1/F$, or $\log_{e}J$ *versus* $1/F$, the function $s(y)$ can still be used to interpret the slope:

$$(\log_{10}J)\ vs\ (1/F):\ \text{slope}=-0.8686F-2.98\times10^{7}\phi^{\frac{1}{2}}s(y),$$
$$(\log_{e}J)\ vs\ (1/F):\ \text{slope}=-2F-6.86\times10^{7}\phi^{\frac{1}{2}}s(y).$$

The author wishes to thank Professor W. B. Nottingham for his advice and criticism during the solution of this problem.

TABLE I. Values of $v(y)$ and $s(y)$.

y	$v(y)$	$s(y)$
0	1.0000	1.000
0.1	0.9874	0.999
0.2	0.9565	0.995
0.3	0.9109	0.989
0.4	0.8525	0.982
0.5	0.7822	0.973
0.6	0.7002	0.964
0.65	0.6546	0.962
0.7	0.6056	0.961
0.75	0.5529	0.965
0.8	0.4956	0.976
0.85	0.4320	1.010
0.9	0.3587	1.085
0.95	0.2648	1.348
1	0	∞

* This work has been supported in part by the Signal Corps, the Air Materiel Command and the ONR.
[1] H. Sommerfeld and H. A. Bethe, *Handbuch der Physik* (J. Springer, Berlin, 1934), Vol. 24, Part 2, p. 436.
[2] L. Nordheim, Proc. Roy. Soc. (London) **121**, 626 (1928).
[3] W. P. Dyke and J. K. Trolan, Linfield College Technical Report No. 1 (September, 1951).

Radii of Mirror Nuclei

ROBERT R. WILSON
Cornell University, Ithaca, New York
(Received June 3, 1952)

A nuclear model is used in which the nucleon density is a constant out to the core radius R and then decreases as $e^{-\alpha r}/r^2$, where $\alpha^2=8MW/\hbar^2$, in which W is taken as the average binding energy per nucleon. Values of R are determined from the measured energy differences between mirror nuclei by calculating the Coulomb energy difference on the above model. If one assumes that the density of the core is constant with changing A, then $R=1.36\times10^{-13}A^{\frac{1}{3}}/(1+3/\alpha R)$ and fits the data well. This also gives values of nuclear radii in agreement with those obtained from the recent electron scattering measurements of Lyman, Hanson, and Scott even for large A. For light elements, a good approximation to the average nuclear radius, $R+1/\alpha$, is $1.4\times10^{-13}A^{\frac{1}{3}}$. Nearly half of the nucleons are in the exponential tail.

AN important method for determining nuclear radii has been through the study of mirror nuclei.[1–4] A nuclear model is assumed, and then the Coulomb energy difference between the two mirror isobars is calculated. The only parameter is the radius and this is determined by fitting the experimentally measured energy difference. Apart from the model, the only assumption is that the n–n interaction is the same as the p–p interaction. Usually a constant density spherical nucleus is assumed, in which case the radii are given by $R=1.45\times10^{-13}A^{\frac{1}{3}}$. These radii are somewhat larger than those indicated by scattering measurements,[5–7] especially for heavy elements.

In this note it is assumed that the nucleus has a constant density core but that the nucleons penetrate to the outside field free region. The nucleonic wave function outside the core will then be identical to that characteristic of the deuteron, namely, $e^{-\alpha r}/r$, where $\alpha^2=8MW/\hbar^2$ in which W is now taken as the average binding energy per nucleon. Thus in this model the density is constant out to a radius R and then falls off as $e^{-\alpha r}/r^2$.

The difference in Coulomb energy between the isobaric pair having atomic number Z and $Z+1$ for such a density distribution is given in terms of exponential integrals **Ei** by

$$\Delta E=\frac{6}{5}\frac{Ze^2}{R}\left[\frac{1+5(1+3/\alpha R)\,\mathbf{Ei}(-\alpha R)/e^{-\alpha R}-15\,\mathbf{Ei}(-2\alpha R)/\alpha R e^{-2\alpha R}}{(1+3/\alpha R)^2}\right].$$

The part outside the brackets will be recognized as the energy difference for a uniform spherical charge of radius R. The part inside the bracket which is plotted as F in Fig. 1 varies slowly with the parameter αR and is about 0.75 for typical values of αR.

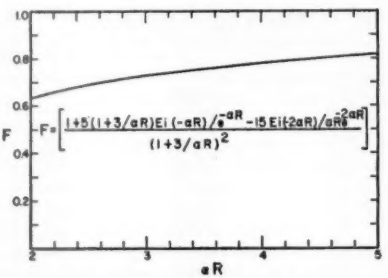

FIG. 1. The expression within the brackets of Eq. (1) of the text is plotted as a function of αR.

In Table I are listed measured energy differences,[8–12] as obtained from the positron spectra resulting from transition between mirror nuclei, and values of R resulting from calculations using the above expression. In Table II, values of b obtained from the relation $R=bA^{\frac{1}{3}}$ are given. It can be seen that b is surprisingly small, about 1.1×10^{-13} cm on the average, but not a constant. On the other hand, the quantity $R+1/\alpha$ is more nearly the average nuclear radius, and the values of $b'=(R+1/\alpha)/A^{\frac{1}{3}}$ given in the second column are nearly constant at 1.4×10^{-13} cm, the meson Compton wavelength. For comparison, values of $b''=r_0/A^{\frac{1}{3}}$ are also given where r_0 is the radius resulting from the uniform density model.

The ratio of the time a nucleon spends outside of R to the time it spends inside R is just $3/\alpha R$, and this ratio is roughly unity for light nuclei. Thus, since the

[1] E. Wigner, Phys. Rev. **51**, 947 (1937); **56**, 519 (1939).
[2] H. A. Bethe, Phys. Rev. **54**, 436 (1938).
[3] White, Creutz, Delsasso, and Wilson, Phys. Rev. **59**, 63 (1941).
[4] D. Elliot and L. King, Phys. Rev. **60**, 489 (1941).
[5] Bratenahl, Fernbach, Hildebrand, Leith, and Moyer, Phys. Rev. **77**, 597 (1950).
[6] Richardson, Ball, Leith, and Moyer, Phys. Rev. **86**, 29 (1952).
[7] Lyman, Hanson, and Scott, Phys. Rev. **84**, 626 (1951).
[8] F. Boley and D. Zaffarano, Phys. Rev. **84**, 1059 (1951).
[9] Barkas, Creutz, Delsasso, Sutton, and White, Phys. Rev. **58**, 383 (1940).
[10] White, Delsasso, Fox, and Creutz, Phys. Rev. **56**, 512 (1939).
[11] K. Siegbahn and E. Borh, Arkiv. Mat. Astron. Fysik **B30**, No. 3 (1944).
[12] K. Siegbahn and H. Slätis, Arkiv. Mat. Astron. Fysik **A32**, No. 9 (1946).
[13] V. Perez-Mendez and H. Brown, Phys. Rev. **76**, 689 (1949).

TABLE I. Values of the core radius R as obtained from $R=6Ze^2F/5\epsilon$, where $\epsilon=E_{max}+2m_ec^2+(m_n-m_p)$ and F is given as a function of αR in Fig. 1. E_{max} is the end point in Mev of the positron spectra resulting from the transitions between mirror nuclei.

A	E_{max}(Mev)	$(1/\alpha)\times10^{13}$	$R\times10^{13}$	Ref.
11	0.97±0.01	0.86	2.15	11
13	1.24±0.01	0.83	2.46	12
15	1.68±0.01	0.82	2.55	13
19	2.20±0.08	0.81	2.98	10
23	2.82±0.09	0.80	3.21	10
	2.99±0.09		3.08	8
25	2.99±0.09	0.79	3.41	10
27	3.54±0.10	0.79	3.30	9
	3.48±0.10		3.35	8
29	3.63±0.07	0.78	3.56	3
31	3.85±0.07	0.78	3.71	3
33	4.13±0.07	0.78	3.80	3
	4.06±0.12		3.86	8
35	4.38±0.07	0.78	3.90	3
	4.43±0.13		3.86	8
37	4.57±0.13	0.78	4.00	8
39	5.13±0.15	0.78	3.86	8

TABLE II. Some values of the constant b as obtained from the relation $R=bA^{\frac{1}{3}}$ are given in column 1, where R is the core radius. The second column is for the average radius, $R+1/\alpha$. The third column gives the constant of the expression $R=b''A^{\frac{1}{3}}/(1+3/\alpha R)^{\frac{1}{3}}$ which would obtain if the core density remains constant with changing A. The last column gives $b_0=r_0/A^{\frac{1}{3}}$, where r_0 is the radius calculated on the basis of the simple uniform density model.

A	$b=R\times10^{13}/A^{\frac{1}{3}}$	$b'=(R+1/\alpha)\times10^{13}/A^{\frac{1}{3}}$	$b''=R\times10^{13}(1+3/\alpha R)^{\frac{1}{3}}/A^{\frac{1}{3}}$	$b_0=r_0\times10^{13}/A^{\frac{1}{3}}$
11	0.97	1.35	1.26	1.40
13	1.05	1.40	1.32	1.45
15	1.03	1.37	1.30	1.41
19	1.11	1.42	1.36	1.45
23	1.13	1.40	1.36	1.44
	1.08	1.36	1.32	1.39
25	1.16	1.43	1.39	1.47
27	1.10	1.36	1.32	1.40
	1.12	1.38	1.33	1.41
29	1.19	1.41	1.37	1.45
31	1.18	1.42	1.39	1.45
33	1.18	1.43	1.39	1.45
	1.20	1.44	1.41	1.47
35	1.19	1.43	1.39	1.45
	1.18	1.42	1.38	1.44
37	1.20	1.43	1.39	1.47
39	1.14	1.38	1.34	1.39

nucleons spend about half of their time outside the nuclear core, we should expect considerable changes in the interpretation of some nuclear phenomena when considered on the basis of this model. The density in the core is $r_0^3/R^3(1+3/\alpha R)$ times that resulting from the uniform density model. In Fig. 2 is plotted the density distributed for carbon. It is reasonable to expect the core density to remain essentially constant as A varies. This implies that the core radius is given by the relation $R=1.36A^{\frac{1}{3}}/(1+3/\alpha R)^{\frac{1}{3}}$, where the constant 1.36 is the average of the values given in the third column of Table II. For Au, the above relation gives a value of the average radius, i.e., $R+1/\alpha$, which is consistent with the value determined by Lyman, Hanson, and Scott[7] from electron scattering measurements.

Jastrow and Roberts[14] have pointed out how a similar model can be used to explain the results of neutron and proton scattering experiments where, at low particle energies, the nucleon density tail is relatively opaque but, as the particle energy increases, the tail becomes more and more transparent. Thus the "size" of the nucleus depends in those experiments on the energy of incident particles. In the same way one must revise the interpretation of other experiments such as those related to the production and scattering of mesons in nuclei.

In conclusion, the arbitrariness of the model assumed must be emphasized. Its principal justification is the same as that for the constant density model, namely, its simplicity. A more sophisticated theory would give each nucleon its proper wave function, perhaps on the basis of the shell model.

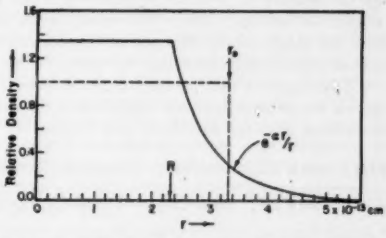

FIG. 2. The relative density of nucleons in carbon is plotted for the uniform density model (dashed curve) and for the core model with exponential tail (full curve).

I am indebted to Dr. S. T. Butler for a number of conversations on this subject.

[14] R. Jastrow and J. Roberts, Phys. Rev. **85**, 757 (1952).

Spontaneous Magnetization of a Triangular Ising Lattice

R. B. Potts
University of Adelaide, Adelaide, South Australia
(Received May 12, 1952)

The spontaneous magnetizations for the anisotropic rectangular and triangular Ising lattices are obtained by generalizing Yang's result for the isotropic square Ising lattice.

1. INTRODUCTION

ALTHOUGH exact treatments have been given for the statistics of the rectangular and triangular Ising lattices, no exact results have been obtained for these lattices in the presence of an external field. However, it has been known for some time that Onsager has obtained the long-range order (or spontaneous magnetization) for the square Ising lattice; and now that the derivation of his result has finally appeared,[1] it is appropriate to state the corresponding results for the rectangular and triangular lattices.

2. RECTANGULAR LATTICE

The surprisingly simple result for the square lattice is (in a form slightly different to that given by Yang)

$$I(S)^8=1-16x^4/(1-x^2)^4, \tag{1}$$

where $I(S)$ is the spontaneous magnetization and $x=\exp(-2H)$, using the usual notation of kTH for the energy of interaction between neighboring units. For the square (or isotropic) lattice this energy is the same whether the neighbors are in a row or in a column.

One can immediately generalize the result (1) for the case of a rectangular (anisotropic) lattice in which the energy of interaction between neighbors in a row is different from that for neighbors in a column. If this anistropy is distinguished by the variables H_x and H_y and $x=\exp(-2H_x)$, $y=\exp(-2H_y)$, then the spontaneous magnetization for the rectangular lattice is

$$I(R)^8=1-16x^2y^2/[(1-x^2)^2(1-y^2)^2]. \tag{2}$$

This result is, of course, symmetric in x and y, and it has been checked using the series solution given by Domb.[2]

Equation (2) can be written in an alternative form which permits generalization to the triangular lattice. The inversion transformation $T\rightarrow T'$ for the rectangular lattice may be written,[3] in terms of hyperbolic functions,

$$\frac{\sinh^2 2H_x'}{\sinh^2 2H_x}=\frac{\sinh^2 2H_y'}{\sinh^2 2H_y}=\frac{(\cosh^2 2H_x')(\cosh^2 2H_y')}{(\cosh^2 2H_x)(\cosh^2 2H_y)}=\frac{16x^2y^2}{(1-x^2)^2(1-y^2)^2}. \tag{3}$$

Hence the result for $I(R)$ may be written

$$I(R)^8=1-\sinh^2 2H_x'/\sinh^2 2H_x. \tag{4}$$

3. TRIANGULAR LATTICE

For the anisotropic triangular Ising lattice, with variables H_x, H_y, H_z, and $x=\exp(-2H_x)$ etc., the inversion transformation is[3,4]

$$\frac{\sinh^2 2H_x'}{\sinh^2 2H_x}=\frac{\sinh^2 2H_y'}{\sinh^2 2H_y}=\frac{\sinh^2 2H_z'}{\sinh^2 2H_z}=\frac{[(\cosh 2H_x')(\cosh 2H_y')(\cosh 2H_z')+(\sinh 2H_x')(\sinh 2H_y')(\sinh 2H_z')]^2}{[(\cosh 2H_x)(\cosh 2H_y)(\cosh 2H_z)+(\sinh 2H_x)(\sinh 2H_y)(\sinh 2H_z)]^2}$$
$$=\frac{16x^2y^2z^2}{(1+xy+yz+zx)(1+xy-yz-zx)(1-xy+yz-zx)(1-xy-yz+zx)}. \tag{5}$$

This transformation is symmetrical in x, y, and z and reduces to (3) when one of H_x, H_y, or H_z is zero.

The generalization of (4) is now obvious and leads to the result that the spontaneous magnetization of the triangular lattice is given by

$$I(T)^8=1-\sinh^2 2H_x'/\sinh^2 2H_x, \tag{6}$$

or from (5),

$$I(T)^8=1-\frac{16x^2y^2z^2}{(1+xy+yz+zx)(1+xy-yz-zx)(1-xy+yz-zx)(1-xy-yz+zx)}. \tag{7}$$

For the special case of an isotropic ($H_x=H_y=H_z$) triangular lattice,

$$I(T)^8=1-16x^6/[(1+3x^2)(1-x^2)^3], \tag{8}$$

which is not an obvious generalization of (1) or (2). The formula (8) has been checked by the low temperature series solution,

$$I(T)=1-2(x^6+6x^{10}-x^{12}+39x^{14}-12x^{16}+274x^{18}-114x^{20}+2025x^{22}+\cdots), \tag{9}$$

derived previously[5] as a consequence of an investigation of the rectangular lattice with first and second interactions.[5]

[1] C. N. Yang, Phys. Rev. **85**, 808 (1952).
[2] C. Domb, Proc. Roy. Soc. (London) **A199**, 199 (1949).
[3] R. B. Potts, unpublished D. Phil. thesis, University of Oxford (1951).
[4] R. M. F. Houtappel, Physica **16**, 425 (1950).
[5] C. Domb and R. B. Potts, Proc. Rov. Soc. (London) **A210**, 125 (1951).

The Rydberg Constant and the Atomic Mass of the Electron*

E. RICHARD COHEN
Atomic Energy Research Department, North American Aviation, Incorporated, Downey, California

(Received March 14, 1951. Revised copy received June 30, 1952)

A re-evaluation of the spectroscopic data pertinent to the Rydberg constant and the atomic mass of the electron yields the values $R_\infty = 109737.326 \pm 0.014$ cm^{-1} and $m = (54.895 \pm 0.008) \times 10^{-5}$ amu. If the "microwave" value of the electron atomic mass, $m = (54.8785 \pm 0.0019) \times 10^{-5}$, is used, the Rydberg constant is $R_\infty = 109737.311 \pm 0.012$ cm^{-1}. It is furthermore concluded that Houston's and Chu's data can be brought into agreement with that of Drinkwater, Richardson, and Williams by ascribing the discrepancy to differences in wavelength standards used by these investigators.

INTRODUCTION

IN 1941 Birge[1] published a careful study of the existing experimental data on the Hα and Dα lines and reached the conclusion that the Rydberg constant had the value $R_\infty = 109737.303 \pm 0.017$ cm^{-1} (international angstrom scale). The existence of the recently discovered fine structure splitting of the spectrum of hydrogen[2–4] and ionized helium[5–11] has indicated that small corrections must be made to the previously accepted Dirac theory. Since these corrections modify the predicted positions of the electronic energy levels, they inversely modify also the value of the Rydberg constant as inferred from the observed positions of those levels. The observed energy difference of 1062 ± 5 Mc, for example, in the $2S_{1/2} - P_{1/2}$ level of hydrogen implies a shift of 0.035 cm^{-1} in the wave number of the $3P_{3/2} - 2S_{1/2}$ transition; this in turn produces a shift of 0.010 cm^{-1} in the apparent position of the Hα_2 line, which is a blend of the $3P_{3/2} - 2S_{1/2}$ transition and the $3D_{3/2} - 2P_{1/2}$ transition with relative intensities[12] 2.08 and 5. If this line then is used to determine the hydrogen Rydberg constant, this shift will introduce an error of 0.072 cm^{-1}, which is well outside the accuracy with which the Rydberg can be determined. Furthermore, the shifts in energy levels have bearing on the spectroscopic determination of the atomic mass of the electron, which can be an important source datum in the more general question of the best values of the fundamental atomic constants.

FINE STRUCTURE OF HYDROGEN AND HELIUM

The theoretical formula for the Lamb shift has been given by several authors[12–16] and can be written as

$$\Delta E(n, 0, 1/2) = \frac{8Z^4}{n^3}\frac{\alpha^3 R}{3\pi}\left[\ln\frac{\mu}{k_0} - \ln 2 + \frac{19}{30}\right], \quad l = 0$$

$$\Delta E(n, l, j) = \frac{8Z^4}{n^3}\frac{\alpha^3 R}{3\pi}\left[\ln\frac{\alpha^2\mu}{2k_l} + \frac{3(j-l)}{2(2j+1)(2l+1)}\right], \quad l \neq 0$$

where $\mu = mc^2$, $\alpha =$ "$1/137$" $= e^2/\hbar c$, $k_l =$ average excitation energy, and $R =$ Rydberg constant associated with the atom in question.

The most complete calculation of the logarithmic terms seems to be that of Bethe, Brown, and Stehn[16], who give $\ln(2k_0/\alpha^2\mu) = 2.8121$ and $\ln(2k_1/\alpha^2\mu) = -0.0300$ for the $2S$ and $2P$ states of hydrogen. These values lead to a Lamb shift of 1051.4 megacycles. Baranger[17] has calculated the corrections to this shift, which are of order α^6, involving the effects of vacuum polarization. These much smaller quantities contribute an additional 6.89 megacycles which brings the Lamb shift to 1058.3 megacycles, in reasonably good agreement with the observed value[2] of 1062 ± 5.†

For the helium II spectrum the observed[8] Lamb shift is 14020 ± 100 megacycles for the $2S - 2P$ separation. The computed value is 14040 megacycles, including Baranger's correction term. (The shift as inferred from the calculations of Bethe, Brown, and Stehn is 13820 megacycles, and on the assumption that the proper parameter is αZ, the Baranger correction increases this by 220 megacycles).

Because of the somewhat uncertain theoretical values (there may still be further corrections of the order of a

* This investigation was carried out as a preliminary to a general re-evaluation of the values of the atomic constants by J. W. M. DuMond and the author, at the request of the National Research Council Committee on Constants and Conversion Factors, and serves in part as a report to that committee.

[1] R. T. Birge, Phys. Rev. **60**, 766 (1941).
[2] W. E. Lamb, Jr., and R. C. Retherford, Phys. Rev. **72**, 241 (1947); **75**, 1325 (1949); **79**, 549 (1950).
[3] H. Kuhn and G. W. Series, Nature **162**, 373 (1948).
[4] H. Kuhn and G. W. Series, Proc. Roy. Soc. (London) **202**, 127 (1950).
[5] W. E. Lamb, Jr., and M. Skinner, Phys. Rev. **78**, 539 (1950).
[6] J. E. Mack and N. Austern, Phys. Rev. **72**, 972 (1947); **73**, 1233 (1948); **74**, 1262 (1948).
[7] G. R. Fowles, Phys. Rev. **73**, 639 (1948); **74**, 219 (1948).
[8] H. Kopfermann and W. Paul, Nature **162**, 33 (1948).
[9] Murakawa, Suwa, and Kamei, Phys. Rev. **76**, 1721 (1949).
[10] Kopfermann, Krüger, and Öhlmann, Z. Physik **126**, 760 (1949).
[11] J. G. Hirshberger and J. E. Mack, Phys. Rev. **77**, 745 (1950).
[12] A. Sommerfeld and A. Unsöld, Z. Physik **38**, 237 (1926).
[13] H. A. Bethe, Phys. Rev. **72**, 339 (1947).
[14] J. B. French and V. F. Weisskopf, Phys. Rev. **75**, 1240 (1949).
[15] N. M. Kroll and W. E. Lamb, Jr., Phys. Rev. **75**, 388 (1949).
[16] Bethe, Brown, and Stehn, Phys. Rev. **77**, 370 (1950).
[17] M. Baranger, Phys. Rev. **84**, 866 (1951).

† *Note added in proof*[18]—W. E. Lamb, Jr., and R. C. Retherford, Phys. Rev. **86**, 1014 (1952), give a final result for the experimentally determined shift in hydrogen of 1058.27 Mc±1.0 Mc (limit of error) to be compared with a calculated shift (including further corrections for anomalous magnetic moment of the electron and reduced mass effects) 1057.27 Mc. These corrections have negligible effect on the present analysis since 3 Mc corresponds to only 0.0001 cm^{-1}.

TABLE I. Calculated fine structure of hydrogen[a] and helium.[b] The line positions are given relative to the "Balmer line," $W=R(n_0^{-2}-n_1^{-2})$.

	Transition	Intensity	Position cm^{-1}	Position of peak cm^{-1}
H	$3S_{1/2}-2P_{3/2}$	0.2	−0.06092	−0.06092
	$3D_{3/2}-2P_{3/2}$	1.0	0.03687	0.06937
	$3D_{5/2}-2P_{3/2}$	9.0	0.07298	
	$3P_{1/2}-2S_{1/2}$	1.04	0.25900	0.26303
	$3S_{1/2}-2P_{1/2}$	0.1	0.30492	
	$3P_{3/2}-2S_{1/2}$	2.08	0.36740	0.39234
	$3D_{3/2}-2P_{1/2}$	5.0	0.40271	
H	$4S_{1/2}-2P_{3/2}$	0.2	0.02114	0.02114
	$4D_{3/2}-2P_{3/2}$	1.0	0.06244	0.07615
	$4D_{5/2}-2P_{3/2}$	9.0	0.07767	
	$4P_{1/2}-2S_{1/2}$	1.04	0.34752	0.34752
	$4S_{1/2}-2P_{1/2}$	0.1	0.38698	0.41755
	$4P_{3/2}-2S_{1/2}$	2.08	0.39325	
	$4D_{5/2}-2P_{1/2}$	5.0	0.42828	
He	$4F_{7/2}-3D_{5/2}$	2.803	0.1968	0.1968
	$4D_{3/2}-3P_{3/2}$	1.073	0.6514	0.6526
	$4F_{5/2}-3D_{3/2}$	1.962	0.6532	
	$4S_{1/2}-3P_{1/2}$	0.156	1.4699	1.4699

[a] The hydrogen spectrum values can be adapted to deuterium simply by multiplying by the scale factor $R_D/R_H=1.00027$.
[b] The complete He pattern consists of 13 lines but most of these are low intensity and have never been carefully measured or even observed. Only those components are listed which have been measured.

few megacycles), we have chosen in the present calculation to use the experimentally observed separation rather than the theoretical ones. This choice is actually inconsequential with respect to the numerical results, since the spectroscopic data which we shall analyze do not have sufficient resolution more than merely to indicate the existence of this shift. The use of experimental values rather than theoretically computed ones is, however, to be preferred for logical reasons. We have, specifically, set the logarithmic term equal to zero for $l\neq 0$ and have used the observed separation to determine the value of the logarithmic term for $l=0$.

We have furthermore assumed k_0 to be independent of the principal quantum number, n; this is actually very nearly true. Such an assumption probably is not independent of the assumption that k_l is zero for all except s states and is consistent with it. This procedure cannot be completely justified, but it can be excused on the basis that it appears to be an adequate approximation within the accuracy of the experimental data.

The quantity $\Delta E(n, l, j)$ as given above is the value of the shift of the level away from the "Dirac position", and hence the complete formula for the energy levels is

$$E(n,l,j)=-\frac{1}{n^2}R-\frac{\alpha^2}{n^3}R\left[\frac{2}{2j+1}-\frac{3}{4n}\right]+\Delta E(n,l,j).$$

The pertinent experimental data are concerned with the transitions $n_1=3\rightarrow n_0=2$ and $n_1=4\rightarrow n_0=2$ for hydrogen and $n_1=4\rightarrow n_0=3$ for helium. In each case we can define the "Balmer line" by the relation $W=R(n_0^{-2}-n_1^{-2})$ and calculate the expected pattern relative to it. The Balmer line, of course, is a fictitious line and is the energy level if the fine structure were nonexistent. The theory allows us to determine the energy shift of an observed line from the Balmer line, however, and from this latter, the Rydberg constant is easily computed. In determining the shift of a line only an approximate value of the Rydberg constant is necessary, since the shifts are relatively small. In this way the shifts tabulated in Table I have been computed, and the fine structure pattern for hydrogen is shown in Fig. 1. In general, the individual lines cannot be separated—an observed line is actually a blend of two or more unresolved components and the position of the peak is determined by the superposition of the various component lines. The actual determination of this position depends on the line widths as well as their separations and intensities. A simple first-order approximation has been used that if lines are closer together than their half-widths (so that no indication of a double peaked pattern is present), the observed peak is at the center of gravity of the complex; while if two lines are well separated, one of them may cause an asymmetry in the wings of the other but there will be only a negligible shift in the peak. Fortunately, a clear separation between "close" lines and "far" lines is possible in the patterns being considered. The last column of Table I lists the position of the observed peak as the center of gravity of the components which, as indicated by the braces, fall close enough together so as to be unresolved.

OBSERVATIONAL DATA

The pertinent observations on the fine structure of hydrogen, deuterium, and helium are the data of

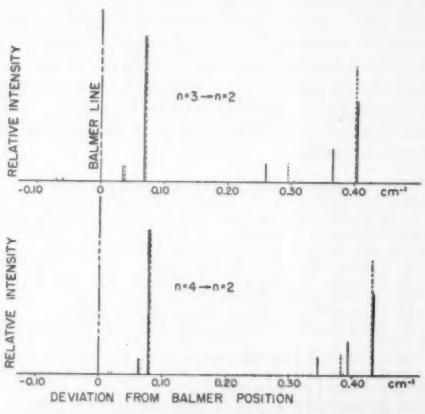

FIG. 1. Fine structure pattern for hydrogen. A comparison of the pattern with and without the Lamb-Retherford shift. The dotted lines represent positions and intensities of the Dirac-Sommerfeld pattern. The solid lines represent the positions and intensities including the line-splitting which results from the new electrodynamics.

Houston,[18] Drinkwater, Richardson, and Williams,[19] and Chu.[20] We have gone back to Houston's original paper and have decided to use all of Houston's data rather than merely the long wavelength components in calculating the Rydberg. Houston himself points out, "the asymmetry in the short wavelength component is so pronounced that it is possible to determine the position of the third component which is causing it (i.e., this third component is the $3P_{1/2}-2S_{1/2}$ transition). This is the component predicted by the theory of Sommerfeld and Unsöld and which has previously been inferred from the displacement of the maximum. . . . Because of this asymmetry, only the long wavelength component is used in the computation of the Rydberg constant." The theory of the hydrogen fine structure, however, seems to be adequately well confirmed by experiment that we feel no concern in using *all* of the experimental data, in connection with the theoretical predictions of the fine structure pattern, in the present analysis. Even the previous discrepancy in the doublet separation, in which the observed separation is less than the theoretical value, has now been fully explained. The conclusion that the discrepancy could be resolved by an arbitrary *ad hoc* shift in the energy of the n^2S levels[21,22] has been completely confirmed by the measurements of this shift (the Lamb-Retherford shift), which is the reason for the present re-examination of the entire question.

We have similarly reviewed the data of Drinkwater, Richardson, and Williams and feel confident in using both components of the doublet in our analysis. The reproducibility in the individual measurements of DRW leads, however, to probable errors which are unrealistic. This can best be seen if we compare the separation of the two main peaks with its theoretical value. DRW measure 0.3198 ± 0.0010 cm^{-1} to be the separation between what they call line 14 and line 2 in Hα and 0.3205 ± 0.0010 cm^{-1} for the corresponding separation in Dα. The theoretical value, including the effects of the blending of components 1 and 4 and the Lamb splitting of component 2 is 0.3230 cm^{-1} for Hα and 0.3231 cm^{-1} for Dα. The extent of the disagreement can also be exhibited in terms of the value of α which would be implied by the measured separations. We find $1/\alpha=137.72\pm0.15$ from hydrogen and $1/\alpha=137.44\pm0.15$ from deuterium, compared with the value given by DuMond and Cohen[23] as 137.043. (It might be pointed out that if we had tried to calculate $1/\alpha$ from the measured separations on the basis of the Dirac theory without the Lamb shift we would have obtained $1/\alpha=139.65$.) For this reason we have used the quoted errors only to determine relative weights to be assigned to the data and have made use of the external consistency to define the actual errors.

TABLE II. Observational data for the calculation of the Rydberg constant.[a]

Wavelength (air) angstroms	Wave number (vacuum) cm^{-1}	Balmer line cm^{-1}	Rydberg cm^{-1}	Source
6562.7110	15233.3972	15233.0049	109677.635	Hα_1, Houston
±0.0018	±0.0041	±0.0041	±0.030	
6562.8473	15233.0811	15233.0117	109677.684	Hα_2, Houston
±0.0009	±0.0021	±0.0021	±0.015	
	15233.3868	15232.9945	109677.560	Hα_1, DRW
	±0.0016	±0.0016	±0.012	
	15233.0670	15232.9976	109677.583	Hα_2, DRW
	±0.0014	±0.0014	±0.010	
	15233.2551	15232.9921	109677.543	Hα_3, DRW
	±0.0021	±0.0021	±0.015	
4861.2800	20564.9695	20564.5520	109677.610	Hβ_1, Houston
±0.0013	±0.0055	±0.0055	±0.029	
4861.3578	20564.6405	20564.5643	109677.676	Hβ_2, Houston
±0.0022	±0.0092	±0.0092	±0.049	
	15237.5317	15237.1393	109707.403	Dα_1, DRW
	±0.0014	±0.0014	±0.010	
	15237.2112	15237.1418	109707.421	Dα_2, DRW
	±0.0013	±0.0013	±0.009	
	15237.4127	15237.1496	109707.477	Dα_3, DRW
	±0.0021	±0.0021	±0.015	
4685.7030	21335.5431	21334.8905	109722.294	He, Houston
±0.0012	±0.0055	±0.0055	±0.028	
4685.8030	21335.0879	21334.8911	109722.297	He, Houston
±0.0026	±0.0118	±0.0118	±0.060	
4685.7017	21335.5490	21334.8964	109722.324	He, Chu
±0.0014	±0.0063	±0.0063	±0.033	
4685.8012	21335.0961	21334.8993	109722.339	He, Chu
±0.0020	±0.0090	±0.0090	±0.048	
4685.5313	21336.3247	21334.8874	109722.278	He, Chu
±0.0032	±0.0145	±0.0145	±0.074	

[a] As indicated by the errors associated with these observations, retaining 4 decimal places in the wave numbers cannot be justified in all cases. The measurements have all been carried through with four decimal places as a matter of consistency and to be certain that rounding-off errors would not build up additional uncertainties.

Chu's measurements are taken as he reported them. Birge[1] raises the question of excluding one of Chu's four plates on the basis that the doublet separation measured there is inconsistent with the separation measured on the other three plates. Birge, however, does not notice this inconsistency in the original data but finds it only when he has computed $1/\alpha$ from each of the four plates separately. It then appears that plate 126 yields $1/\alpha=139.790$, compared to the other three values 137.314, 136.971, and 136.971. (These are the actual figures quoted by Birge and calculated in his 1941 paper. They do not include corrections for the Lamb shift,[24] but the discussion would not be affected if this refinement were made since we are not interested here in the value of the fine structure constant but only in the consistency of the data.) On this basis, then, Birge questions retaining plate 126, but he does not actually exclude it. If, however, we look at the errors involved in these determinations of $1/\alpha$, we see a different picture. The values are $1/\alpha=139.8\pm1.8$, compared to $1/\alpha=137.3\pm1.2$, 137.0 ± 1.2, 137.0 ± 1.4. Plate 126 therefore differs from the other three by an amount

[18] W. V. Houston, Phys. Rev. **30**, 608 (1927).
[19] Drinkwater, Richardson, and Williams, Proc. Roy. Soc. (London) **174**, 164 (1940).
[20] D. Y. Chu, Phys. Rev. **55**, 175 (1939).
[21] E. C. Kemble and R. D. Present, Phys. Rev. **44**, 1031 (1932).
[22] S. Pasternack, Phys. Rev. **54**, 1113 (1938).
[23] J. W. DuMond and E. R. Cohen, Phys. Rev. **82**, 555 (1951).
[24] Corrected for the modification in fine structure pattern due to the Lamb shift, these values would all be raised by 0.076.

which is less than twice the error in this difference, and it would seem unwise to exclude it since the results would, in such a case, appear to have much better consistency than should reasonably be ascribed to them.

The data from all three sources are tabulated in Table II. Houston's and Chu's measurements of wavelengths in air have been corrected to vacuum using Barrell and Sears' formula[25] for refractive index:

$$(\mu-1)\times 10^6 = 272.581 + 1.5453/\lambda^2 + 0.01268/\lambda^4,$$

with λ in microns. This formula gives μ correctly to better than 1 part in 10^8. The data of DRW are given by them directly in terms of vacuum wave numbers using this expression for index of refraction, so that their results require no further correction.

Houston's measurements, as well as Chu's, are based on the value 5015.6750A for the He line. This line was measured relative to the cadmium line 6438.4696A, which is the defining standard of length, by Merrill[26] who gave the wavelength as 5015.675A and to which he appends the comments, "From the number and internal agreement of the individual determinations it seems that an error larger than 0.003A is scarcely to be expected."[27] Merrill's actual data list seven observations ranging from 0.673 to 0.677 for the fractional part of the wavelength, with a mean of 0.6752 ± 0.0008. In a survey of other measurements, however, he quotes a value of 0.678 measured by Lord Rayleigh and 0.679 by Priest. Now an increase of one milliangstrom in the accepted wavelength of this line will reduce the value of the Rydberg as inferred from the data of Houston or Chu, who use this line as their standard of length, by 0.022 cm^{-1}, and this is neither a negligible nor an improbable correction. Therefore, it is evident that in our analysis of the measurements of the Rydberg constant we cannot exclude the possibility that Houston and Chu used a wavelength standard which is different than that used by Drinkwater, Richardson, and Williams merely due to the fact that, relative to the cadmium line whose *defined* wavelength in air is 6438.4696A, the helium line actually has a wavelength which is somewhat different than 5015.6750A. We shall use as the measured wavelength of this line relative to the cadmium line

$$\lambda = 5015.6752\pm 0.0015 \quad \text{(standard deviation)},$$

where the error has been somewhat arbitrarily chosen to allow for possible systematic errors in Merrill's measurements. In our least squares analysis of all of the pertinent experimental data, it will now be necessary to include this as an observational equation and to include as part of the results of our least squares fitting the "best" value of this wavelength.

In addition to these measurements of wavelengths, measurements of the isotopic shift are useful in determining the atomic mass of the electron, although they give no direct information on the value of the Rydberg constant. The separation between the Hα lines and the Dα lines has been carefully measured by several investigators. The Hα Balmer line is given by

$$\tilde{\nu}_H = \frac{5}{36}R_H = \frac{5}{36}R_\infty\frac{H-m}{H},$$

and the Dα Balmer line is given by

$$\tilde{\nu}_D = \frac{5}{36}R_D = \frac{5}{36}R_\infty\frac{D-m}{D},$$

where m = atomic mass of the electron, H = atomic mass of the hydrogen atom, and D = atomic mass of the deuterium atom. These expressions give us

$$m = \frac{36HD}{5(D-H)}\frac{\tilde{\nu}_D-\tilde{\nu}_H}{R_\infty}.$$

Using the values of Li, Whaling, Fowler, and Lauritsen[28] for the atomic masses $H=1.008142$ and $D=2.014735$, we find (note that it is adequate here to use an approximate value of $R_\infty = 109737.3$)

$$m = (13.2393\times 10^{-5})(\tilde{\nu}_D-\tilde{\nu}_H)$$

for the atomic mass of the electron, when the isotopic shift is measured in vacuum wave numbers. The error in this coefficient due to the errors in the atomic masses is approximately 6 parts per million. A correction for the fact that the measured lines are at slightly larger wave number than the theoretical "Balmer line" would decrease the factor 36/5 by five parts per million. Both these quantities are completely negligible with respect to the accuracy of the measurements.

The pertinent data are those of Shane and Spedding,[29] Robinson,[30] and Williams.[31] In the case of Shane and Spedding it has been necessary to compute their value of the separation by working backwards from their quoted values of e/m, the Faraday, and the atomic masses. They give $e/m = 1.7579\times 10^7$ emu, which is calculated from the formula

$$\frac{e}{m} = \frac{FR_H(D-H)}{(R_D-R_H)D(H-m)},$$

[25] H. Barrell and J. E. Sears, Jr., Trans. Phil. Soc. **238**, 1 (1949).
[26] P. W. Merrill, Astrophys. J. **46**, 357 (1917).
[27] In a recent private communication Dr. Merrill informed the author that he would now say that a correction of 0.002A or 0.003A might not be at all inconceivable. It was his feeling, furthermore, that with present day techniques (the original measurements were made in 1917) improved accuracy for the wavelength of this line could easily be attained and that on the basis of this discrepancy such a measurement should probably be undertaken.
[28] Li, Whaling, Fowler, and Lauritsen, Phys. Rev. **83**, 512 (1951).
[29] C. D. Shane and F. H. Spedding, Phys. Rev. **47**, 33 (1935).
[30] C. F. Robinson, Phys. Rev. **55**, 423 (1939). See also R. T. Birge, Phys. Rev. **60**, 766 (1941).
[31] R. C. Williams, Phys. Rev. **54**, 558 (1938).

using the values: $H=1.007775$, $D=2.01363$, $R_H=109677.759$, $F=9651.1$. From this we may calculate $R_D-R_H=29.86276$ cm^{-1} and

$$\bar{\nu}_D-\bar{\nu}_H=(5/36)(29.86276)=4.147605 \text{ cm}^{-1}.$$

Since a correction for index of refraction was omitted[22] in the original paper, this value is the separation measured in air.

Robinson's measurements were made on the most intense component of Hα and Dα in air and the separation is $\Delta\bar{\nu}=4.1453\pm0.0010$ cm^{-1}. This becomes 4.14415 ± 0.0010 cm^{-1} when reduced to vacuum. (Apparently the only published data on Robinson's work is an abstract in the Bulletin of the American Physical Society. The values quoted here are reported by R. T. Birge in his 1941 paper and were communicated to him privately by Professor Houston.)

Williams measured the interference patterns of Hα and Dα with a 3-mm étalon. The measured peak-to-peak interval is given as $\Delta\bar{\nu}=4.14716\pm0.00040$ cm^{-1} in air. This value, however, must be corrected because of differential effects due to the influence of components 3 and 4 on the position of the center of component 1. The major source of this correction is due to the fact that Williams' experimental conditions were such that the Doppler broadening of the lines is less for D than for H; component 3 has an appreciable overlap with component 1 in Hα but a negligible effect in Dα. He evaluates this net correction as 0.00090 cm^{-1} so that the true isotopic shift in air is $\Delta\bar{\nu}=4.14806$ cm^{-1}. Williams' correction to vacuum appears, however, to be in error; from his published figures one would calculate an index of refraction for air $\mu=1.0002557$, whereas Barrell and Sears' value at this wavelength is $\mu=1.0002762$. Apparently this can be ascribed only to a numerical error on Williams' part. We therefore find (using Barrell and Sears' value for index of refraction) that the wave-number separation in vacuum is $\Delta\bar{\nu}=4.14691\pm0.00040$ cm^{-1}.

The data from the three sources and their probable errors are given in Table III.

TABLE III. Dα−Hα isotopic shift and calculated atomic mass of the electron.

Source	$\bar{\nu}_D-\bar{\nu}_H$ (in air) cm^{-1}	$\bar{\nu}_D-\bar{\nu}_H$ (in vacuum) cm^{-1}	$m\times10^4$ amu
C. H. Shane and F. H. Spedding	4.14761	4.14646	54.8961±0.0074
C. F. Robinson	4.1453	4.14415	54.8655±0.0132
R. C. Williams	4.14806	4.14691	54.9020±0.0053

TREATMENT OF EXPERIMENTAL DATA

In combining all these independent results it is important that the weights assigned to each individual value shall be consistent with the weights assigned to the other data, in order that the relative accuracy of the several measurements be properly represented. The errors listed in Table II are the errors reported by the respective authors, although we shall not use these values by themselves to determine the weights. It is felt that there is too much variation among the results of different observers (compared with the errors quoted by them) to believe their quoted accuracy as representing much more than an indication of the reproducibility of the measurement under a given set of experimental conditions.

If we consider the measurements on a given Balmer pattern to constitute a single determination of the Rydberg we have six independent observations: (Houston, Hα, Hβ, He; DRW, Hα, Dα; Chu, He). These independent values are obtained by taking a mean value of the Rydberg as computed from each of the lines in the pattern. The error assigned shall be the larger of the two values computed by internal and external consistency.

The procedure now is to carry out a least squares solution to determine the most consistent values for the Rydberg constants and the electron mass. In order to handle the equations conveniently we introduce approximate values for R_∞ and m and then calculate the necessary corrections to these numbers. Therefore let M_i be the atomic mass of an arbitrary nucleus and R_i the associated Rydberg constant; we can write

$$R_\infty=\left(1+\frac{m}{M_i}\right)R_i.$$

We must also take into account the fact that Houston and Chu both used the helium λ5015 line as their standard of length and hence their computed Rydberg values are to be corrected if a change is made in the wavelength standard which they used. We shall therefore write

$$R_\infty'=\left(1+\frac{m}{M_i}\right)R_i,$$

when the equation refers to the data of either Houston or Chu. We now let

$$R_\infty=R_0+x, \quad R_\infty'=R_0+y, \quad m=m_0+z\times10^{-5},$$

where $R_0=109737.3000$ cm^{-1}, $m_0=54.9000\times10^{-5}$ amu, and $M_1=1.007593$, $M_2=2.014186$, $M_4=4.002775$. Thus we obtain two linear equations

$$x-(R_i\times10^{-5}/M_i)z=(m_0R_i/M_i)+R_i-R_0$$

(for the data of Drinkwater, Richardson and Williams);

$$y-(R_i\times10^{-5}/M_i)z=(m_0R_i/M_i)+R_i-R_0$$

(for the data of Houston or Chu).

Now because we admit that the He wavelength may be in error, we shall write the correct wavelength as

$$\lambda=5015.6750+\delta,$$

where δ is the correction (measured in angstroms) to be applied to the assumed value to obtain the actual value.

[22] R. C. Williams and R. C. Gibbs, Phys. Rev. **48**, 971 (1935).

(Of course we cannot find the true value of δ but we can make a "best estimate" of this quantity.) Since Houston's standard value was 5015.6750, and the calculated value of the Rydberg constant is inversely proportional to this, we must write

$$(5015.6750)R_\infty' = (5015.6750+\delta)R_\infty,$$

which reduces to the relation

$$y = x + 21.88\delta.$$

The measurements of Drinkwater, Richardson, and Williams on the wavelength of Hα and Dα, tabulated in Table II, yield a mean value $R_1 = 109677.567 \pm 0.011$ cm^{-1} for Hα and $R_2 = 109707.424 \pm 0.018$ for Dα. The linearized equations are therefore

$$x - 1.088z = 0.026 \pm 0.011 \quad \text{wt} = 83, \qquad \text{(a)}$$

$$x - 0.544z = 0.027 \pm 0.018 \quad \text{wt} = 31. \qquad \text{(b)}$$

Houston's measurements on Hα, Hβ, and He yield mean values, respectively, of $R_1 = 109677.674 \pm 0.020$ cm^{-1}; $R_1 = 109677.626 \pm 0.037$ cm^{-1}; $R_4 = 109722.295 \pm 0.038$ cm^{-1}, and therefore yield, respectively, the equations

$$y - 1.088z = 0.133 \pm 0.020, \quad \text{wt} = 25, \qquad \text{(c)}$$

$$y - 1.088z = 0.085 \pm 0.037, \quad \text{wt} = 8, \qquad \text{(d)}$$

$$y - 0.274z = 0.044 \pm 0.038, \quad \text{wt} = 7. \qquad \text{(e)}$$

Chu's measurements on He yield $R_4 = 109722.322 \pm 0.038$, which gives us

$$y - 0.274z = 0.070 \pm 0.038, \quad \text{wt} = 7. \qquad \text{(f)}$$

Merrill's measurement of the wavelength of the He 5015 line gives, according to the previous discussion of this measurement, $\delta = 0.0002 \pm 0.0015$A, so that we have a further equation

$$x - y = -0.004 \pm 0.033, \quad \text{wt} = 9. \qquad \text{(g)}$$

Finally the spectroscopic determinations of the atomic mass of the electron by Shane and Spedding, Robinson, and Williams give three additional equations:

$$z = -0.004 \pm 0.011, \quad \text{wt} = 83, \qquad \text{(h)}$$

$$z = -0.035 \pm 0.020, \quad \text{wt} = 25, \qquad \text{(i)}$$

$$z = 0.002 \pm 0.008, \quad \text{wt} = 150. \qquad \text{(j)}$$

The errors assigned to the numerical quantities in these equations are standard deviations, and the associated weights are taken to be proportional to the reciprocal of the square of the standard deviation, an error of ± 0.100 being assigned unit weight. The least squares procedure is now to set up, in the usual way, the normal equations for the system. These equations are

$$123x - 9y - 107.168z = 2.959,$$

$$-9x + 56y - 39.740z = 4.839,$$

$$-107.168x - 39.74y + 405.539z = 8.2863,$$

and the solution of these equations is

$$x = 0.0261, \quad y = 0.0870, \quad z = -0.00502, \quad \chi^2 = 11.94.$$

The quantity χ^2 is the sum of the squares of the normalized residuals (which it is the purpose of "least squares" to make "least"). For 7 degrees of freedom—10 equations minus 3 unknowns—the expectation value of χ^2 is just equal to 7 and there is a probability of 0.10 that in a normally distributed universe χ^2 would be larger than 12.0. Therefore, considering the uncertainty with which the errors in the observational equations (a)–(j) can be assigned, the agreement is quite reasonable. Expressing this in a slightly different way we can compute the ratio of internal to external consistency as used by Birge[32]; this quantity is $r_e/r_i = 1.3$. Using the larger measure of error the final answers are

$$x = 0.0261 \pm 0.0140, \qquad y = 0.0870 \pm 0.0188,$$

$$z = -0.00502 \pm 0.0079, \quad \delta = 0.0028 \pm 0.0007.$$

The correlation coefficients for these adjusted variables are

$$r(x, y) = 0.277, \quad r(y, z) = 0.362, \quad r(z, x) = 0.530,$$

$$r(\delta, x) = -0.333, \quad r(\delta, z) = -0.044.$$

The purely spectroscopic values therefore become

$$R_\infty = 109737.326 \pm 0.014 \text{ cm}^{-1},$$

$$m = (54.895 \pm 0.008) \times 10^{-5} \text{ amu},$$

$$\lambda = 5015.6778 \pm 0.0007\text{A}.$$

The consistency of the observed data is shown graphically in Fig. 2. In order to be able to draw a two-dimensional picture of the actual three-dimensional manifold, we represent in Fig. 2 only the projection onto the x-z plane of the intersection of the surfaces of the observational equation with the surface $y = x + 0.0609$. This procedure is the geometrical equivalent of recomputing the data of Houston and of Chu on the assumption that the correct value of the wavelength of the helium green line is equal to the least squares "best" value. The ellipse at the center of the plot is the projection on the x-z plane of the ellipsoid of error. This ellipsoid is such that its projected semidiameter on any axis is the standard error of the corresponding variable.[34]

The value of m obtained here is to be compared with the value computed from the data reported by DuMond and Cohen[23, 35] on the very accurate microwave results which yield a measurement of the atomic mass of the

[32] R. T. Birge, Phys. Rev. **40**, 207 (1932).

[34] J. W. M. DuMond and E. R. Cohen, Revs. Modern Phys. **20**, 82 (1948).

[35] In the present paper m is used for the atomic mass of the electron. DuMond and Cohen use this letter for the physical mass of the electron, so that in their notation the atomic mass is Nm, where N is Avogadro's constant. Since there is no need in the present analysis to consider Avogadro's constant explicitly and since the numerical values for m are always followed by an indication of the units (amu), the present simplified notation should produce no ambiguity.

electron. Hipple, Sommer, and Thomas[36] and Bloch and Jeffries[37] have measured the ratio of the proton "cyclotron" frequency to the proton resonance frequency in the same magnetic field and a weighted average of these results is $\omega_e/\omega_p = 0.358071 \pm 0.000007$. Gardner and Purcell[38] have measured the ratio of the proton resonance frequency to the electron cyclotron frequency in the same field and find $\omega_p/\omega_e = (1.52101 \pm 0.00002) \times 10^{-3}$. Thus the ratio of electron mass to proton mass is simply $(0.358071)(1.52101) \times 10^{-3} = 54.4630 \times 10^{-5}$; and using 1.007593 for the mass of the proton we find $m = (54.8785 \pm 0.0013) \times 10^{-5}$, the error quoted being a probable error, which is smaller than the spectroscopic value by 0.016 ± 0.008.

If we use this value and neglect the spectroscopic mass determinations the Rydberg constant is $R_\infty = 109737.311 \pm 0.012$ cm^{-1}, a decrease of 0.015 which is just slightly larger than the standard deviation. This value is indicated in Fig. 2 by the small circle and the vertical line.

The over-all picture appears to be fairly consistent, although it must be remembered that there is some area of uncertainty. The assignment of a correction to the wavelength of the helium green line is certainly an assumption which should not be accepted without stronger evidence than that offered at present. Our least squares "best" value of the helium wavelength, 5015.6778±0.0007A, is larger than the value given by Merrill, 5015.675A, by 0.0028±0.0007, which is a significant correction with respect to its standard deviation and at the same time is not too great a correction with respect to the accuracy with which the spectroscopic determination was carried out. It would therefore be well worth while to redetermine the ratio of the wavelength of this line to the fundamental cadmium wavelength standard. In the absence of this, all we have actually done is to use the data of Houston and Chu as a determination of the atomic mass of the electron and determine the Rydberg constant entirely from the measurements of Drinkwater, Richardson, and Williams. The discrepancy between the spectroscopic determination and the "microwave" determination of the atomic mass of the electron may appear annoyingly large, but the difference is not statistically improbable and we shall therefore adopt as the best available present value of the Rydberg constant

$$R_\infty = 109737.311 \pm 0.012 \text{ cm}^{-1}.$$

This value is consistent with an electron mass

$$m = (54.8785 \pm 0.0013) \times 10^{-5} \text{ atomic mass units},$$

and if this is subsequently changed by methods which are independent of the Rydberg constant, a correction factor can be specified. By comparing these values with the purely spectroscopic results, we find that an increase

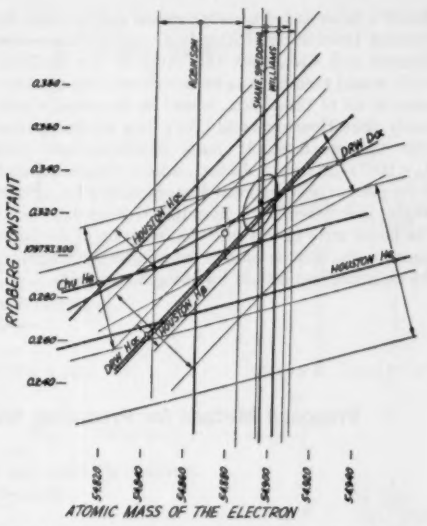

FIG. 2. A consistency diagram for the spectroscopic data determining the Rydberg constant. Each heavy line represents an experimental result. The light lines on either side of each heavy line indicate the standard deviation of the measurement. The black dot at the center of the ellipse is the least squares "best" value for the Rydberg constant and the atomic mass of the electron. The ellipse itself is the projection of the standard error ellipsoid onto the plane of the diagram and the standard error of any variable is given in turn by the projection of this ellipse on the corresponding axis. The small open circle and the vertical line to the left of, and slightly below, the ellipse is the value of the Rydberg constant if the microwave data is used to determine the electron atomic mass.

of 1 part per million in the electron mass will produce an increase of 0.0005 cm^{-1} in the Rydberg. It is important to point out, however, that there is nothing particularly fundamental in this coefficient; its value is dependent upon the values and weights of the Rydbergs for different atoms and reflects only the way in which the present data determine an observational relationship between R_∞ and m. With a different set of observational data this relationship will change.

The value given here, 109737.311 cm^{-1}, for the Rydberg constant is only slightly larger than R. T. Birge's 1941 value. This is the result of various compensating effects. If we do not use the "microwave" value for the electron mass, but restrict ourselves entirely to optical spectroscopic data the Rydberg is 109737.326 cm^{-1} or 0.023 cm^{-1} larger than Birge's value. Except for a small effect due to the difference in the treatment of the data, this change is a result of the Lamb shift corrections to the energy levels. Using the smaller "microwave" mass reduces this difference by 0.015 cm^{-1}, so that the result is only 0.008 cm^{-1} larger than Birge's value. On the other hand, if the wavelength of the green helium line is not to be changed from

[36] Hipple, Sommer, and Thomas, Phys. Rev. **76**, 1877 (1949); **80**, 487 (1950).
[37] F. Bloch and C. D. Jeffries, Phys. Rev. **80**, 305 (1950).
[38] J. H. Gardner and E. M. Purcell, Phys. Rev. **76**, 1262 (1949).

Merrill's value and if no other reason can be given for choosing Drinkwater, Richardson, and Williams over Houston and Chu, then the value of the Rydberg, which would then have to be calculated from consideration of all of these data, would be increased significantly since Houston's and Chu's data in combination with the spectroscopic mass determinations yield $R_\infty = 109737.387\ \text{cm}^{-1}$. In fact, a least squares solution of the present observational data, excluding Eq. (g) and putting in its place, $x = y$, gives $109737.346 \pm 0.019\ \text{cm}^{-1}$. The larger error in this case is a reflection of the larger spread in the data because of the inconsistency between the cadmium and helium wavelength standards.

We shall conclude by listing the Rydberg constant for the four lightest stable nuclei. In addition to the previously quoted mass we use the value 3.015899 ± 0.000011 for the mass of the He^3 nucleus (the probable errors quoted for the nuclear masses have negligible effect on the error of the results)

$$R_\infty = 109737.311 \pm 0.012\ \text{cm}^{-1},$$
$$R_H = 109677.575 \pm 0.012,$$
$$R_D = 109707.420 \pm 0.012,$$
$$R_{He^3} = 109717.346 \pm 0.012,$$
$$R_{He^4} = 109722.268 \pm 0.012.$$

PHYSICAL REVIEW VOLUME 88, NUMBER 2 OCTOBER 15, 1952

Proposed Method for Producing Short Intense Monoenergetic Ion Pulses*

R. C. MOBLEY
Department of Physics, Duke University, Durham, North Carolina
(Received June 16, 1952)

A method is outlined whereby suitable periodic deflection over the range of possible path lengths between foci of an appropriate focusing magnet is utilized to convert a continuous monoenergetic ion beam at one focus into very short duration high intensity monoenergetic ion pulses at the other focus. Time-of-flight analysis of reaction particle pulses resulting from the interaction of the ion pulses with stationary target nuclei is discussed, and the application of this method to the elastic and inelastic scattering of neutrons is considered briefly.

IN principle the interaction of a beam of high intensity short duration monoenergetic ion pulses with stationary target nuclei and time-of-flight analysis of the resultant reaction particle pulses is a form of spectroscopy applicable to all types of nuclear particles. Spacially separated, by differing times of flight from target or scatterer to an appropriately placed detector, the energy and angular distribution of any particular group of particles could then be determined without interference from other groups or in the case of scattering without interference from the source particles except for elastic scattering in the forward direction.

The problem of an appropriate method of producing a beam of high intensity, short duration, monoenergetic ion pulses appears, however, to have hindered application of this technique. One approach to this problem, which it is felt may be of sufficient general interest to warrant publication in its present design stage, is outlined in the accompanying diagram (Fig. 1).

It consists in principle of deflecting successive portions of a continuous monoenergetic ionbeam, such as that from an electrostatic generator, over progressively shorter paths between foci a and g of magnet M in a manner such that all portions of the beam so deflected arrive at g essentially simultaneously in a high intensity, short duration current pulse. These ion pulses incident in turn on an appropriate target at g produce similar short duration, high intensity, reaction particle pulses. In more detail, magnet M is a focusing magnet with an ion deflector at focus a, a target at focus g, and the property that path lengths from a to g become progressively shorter for paths entering the magnetic field at successive points from k to e. When swept at an appropriate rate from c to e by the deflector at a, all ions successively crossing line $c\,e$ in one edge of the monoenergetic ion beam can be made to emerge from the magnetic field on a cylindrical surface which collapses to a focus on its axis through g. Under these circumstances a sharply focused, relatively low intensity, long duration ion pulse entering the field of magnet M emerges greatly foreshortened along its direction of motion and arrives at g as a very short duration, high intensity pulse.

As a consequence of the quite arbitrary choice of geometry shown, the path length from c to d, due to the selection of 45° for angles $c\,b\,j$ and $d\,b\,j$, is approximately $2S$ longer than the path length from e to f. The rate at which the ion beam must be swept along line $c\,e$ on entering the field of magnet M to fulfill the above requirement is then approximately one-half the velocity of the incident beam. Swept at this rate, a segment of the deflected and chopped incident ion beam x thick and approximately $2S$ long becomes a pulse ap-

* This work was in part supported by the AEC.

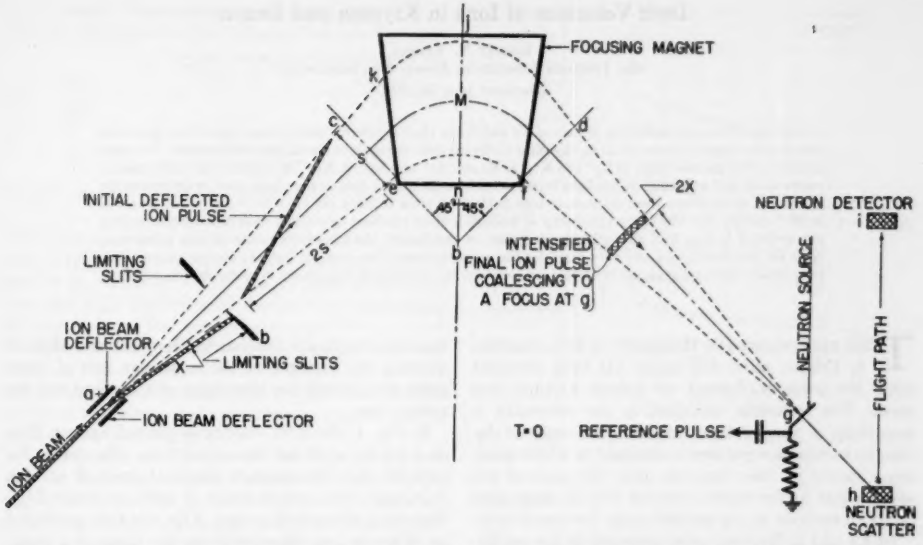

FIG. 1. A suggested experimental apparatus for the production of high intensity short duration ion pulses and its application to the measurements of energy and angular distribution of elastically and inelastically scattered neutrons.

proximately $2x$ long which coalesces to a focus on the target at g. The time duration of the ion pulses at g would then be $2x/v$, where v is the ion velocity, and the pulse current at g would be intensified by a factor of S/x over that of the beam entering the deflector at a.

The selection of a mean total deflection greater or smaller than 90° for focusing magnets of the type shown leads to pulse lengths smaller or greater, respectively, than $2x/v$. In general, the pulse length is given by approximately x/v', where v' is the sweep velocity from c to e, and the pulse current by I_0S/x, where I_0 is the steady-state ion current at a. In the case where the magnet dimension $n\,j$ is fixed it should be noted that although increasing the total deflection leads to greater pulse length and lower peak current it also results in a greater total charge per pulse.

For a single ion pulse incident on target g let the time sequence of reaction particle groups at the detector be termed an R.P.G. pattern. The maximum pulse repetition rate for nonoverlapping successive R.P.G. patterns is then determined by the length of time it takes the lowest energy particle group being observed to traverse the flight path. Since the average current at g is proportional to the pulse repetition rate and is a measure of the rapidity with which data can be gathered, it should be noted that under some circumstances higher repetition rates with attendant R.P.G. pattern overlap may be usable. With a judicious choice of repetition rate, a particle group of interest could probably still be singled out in the presence of considerable pattern overlap, although identification of such an isolated monoenergetic group might require a particle detector capable of a certain degree of energy discrimination or a knowledge of the relative positions of different particle groups as a function of detector position or repetition rate.

If the reaction particles are scattered neutrons, then for 1-Mev $Li^7(p, n)Be^7$ neutrons incident on the scatterer at h, 2.7-Mev protons with a corresponding velocity of 2.3×10^9 cm/sec would be incident on the Li target at g. For $S=20$ cm and $x=0.2$ cm the time duration of the proton pulses at g would be 1.8×10^{-10} sec, the length of time for the proton beam to sweep from c to e on entering the magnet M would be 1.8×10^{-8} sec, and the proton pulse current would be intensified by a factor of 100 over the steady proton beam current entering the deflector at a. For a flight path of 100 cm and a 100-kev lower limit on neutron energy to be observed, the flight time is 2.3×10^{-7} sec corresponding to a nonoverlapping R.P.G. pattern repetition rate of 4.4×10^6 cycles/sec. The average current at g for a steady beam of 50 μa at a would be 3.8 μa and the peak current would be 5 ma.

It should perhaps be noted that experiments of the type possible with a steady neutron flux are equally possible with the "pulsed-neutron delayed-detection" scheme outlined above, with the additional advantage of a much higher neutron flux during the appropriate brief detection period. This would in many cases result in an improved ratio of useful to background counts.

Drift Velocities of Ions in Krypton and Xenon

ROBERT N. VARNEY
Bell Telephone Laboratories, Murray Hill, New Jersey
(Received June 26, 1952)

Drift velocities and mobilities of ions of Kr and Xe in their respective parent gases have been measured over a wide range of values of E/p_0, the ratio of electric field strength to normalized gas pressure. Two ions appear in each gas identified as Kr^+ and Kr_2^+ in Kr and Xe^+ and Xe_2^+ in Xe. The relation that drift velocity varies as $(E/p_0)^{\frac{1}{2}}$ at high E/p_0 has been found to hold for the atomic ions and has been used to determine the equivalent hard sphere cross sections at high fields. The cross sections are 157×10^{-16} cm² for Kr and 192×10^{-16} cm² for Xe. The Langevin theory of mobilities gives excellent agreement with experimental results extrapolated to zero field strength provided that, in the theory, the hard sphere cross section is taken as large for the atomic ions and very small for the molecular ions. The range of the polarization forces is such as to render them insignificant in atomic ion collisions and of primary importance in molecular ion collisions.

THE work reported by Hornbeck[1] on drift velocities in helium, neon, and argon has been extended using the same equipment to include krypton and xenon. The technique described in the references is essentially a time-of-flight method. As reported by him, an oscilloscope pattern is obtained in which sharp steps appear at time intervals after the start of the sweep equal to the transit time for ions to cross from anode to cathode in the parallel-plate Townsend tube.

In Kr and in Xe, two steps appeared in the oscilloscope pattern for values of E/p_0 below 75 volts/(cm×mm Hg). (The symbol p_0 is used to indicate that pressure readings are adjusted to the value which would be produced by the same gas density at 0°C.) These two steps indicate the presence of two ions which are identified as the molecule ions Kr_2^+ and Xe_2^+ as the faster and the atomic ions Kr^+ and Xe^+, respectively, as the slower ions. The identification is supported by the further observation that the supposed molecular ions disappear at higher E/p_0 in accordance with the greater difficulty of producing these ions, the fact that they do have greater speed (see reference 1), and the mass spectrographic analysis by Hornbeck and Molnar[2] showing the presence of the molecular ions of these gases and the relative abundance of these ions and the atomic ions.

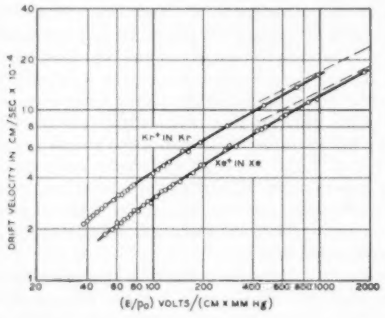

FIG. 1. The drift velocity of atomic ions in krypton and xenon as a function of E/p_0, log-log plot. The broken lines at the right of each curve have a slope of $\frac{1}{2}$.

In Fig. 1, the drift velocity is plotted against E/p_0 on a log-log scale for the atomic ions. The curves for both Kr and Xe approach slopes of one-half at high E/p_0 and tend toward slopes of unity at lower E/p_0. The slope of one-half at high E/p_0 has been predicted by Wannier and Hornbeck[3] on the basis of a hard-sphere model of the atom-ion collisions. (The use of the term "hard-sphere scattering" here simply means that cross sections are independent of velocity and that scattering is probably isotropic. It does not deny the possibility that scattering by charge exchange may in fact be occurring if that process satisfies the same criteria.) Application of their calculation to present drift velocity measurements leads to cross sections shown in Table I. The values for He, Ne, and A are added for reference.

The increase in the ion-atom cross section for krypton above the argon value may seem small, by contrast, for example, with the increase from neon to argon. It is of some interest to note that the atom-atom cross sections increase with atomic number in a similar way. Table II shows this comparison. The ratio of the two cross sections for each gas is given, and it is seen to vary over a very limited range for all the gases tested.

Figure 2 shows the values of the mobilities of the various ions observed. The mobility is defined here by the equation

$$\mu=(v/E)(p/760)(273/T).$$

The experiments were conducted at 27±1°C, and the mobilities are reduced to standard gas density by this definition. However, no correction is made for the direct influence of temperature on mobility other than through change of gas density.

The mobilities reported here for Kr^+ and Xe^+ are in excellent agreement with those of Tyndall and Mun-

[1] J. A. Hornbeck, Phys. Rev. **83**, 374; **84**, 615 (1951).

[2] J. A. Hornbeck and J. P. Molnar, Phys. Rev. **84**, 621 (1951).

[3] G. Wannier and J. Hornbeck, Phys. Rev. **82**. 458 (1951).

TABLE I. Ion-atom and atom-atom cross sections.

Gas	Ion-atom cross section from drift velocity $\times 10^{16}$ cm^2	Atom-atom cross section from viscosity $\times 10^{16}$ cm^2
He	54	15
Ne	65	21
A	134	42
Kr	157	49
Xe	192	67

son.[4] This agreement is in contrast with the observations of reference 1 in which the results for the molecular ions of He, Ne, and A obtained in these laboratories coincided with Tyndall and Munson's reported values for atomic ions. The present agreement for Kr^+ and Xe^+ also concurs qualitatively with the observations of reference 3 that molecular ions are formed in relatively lesser number to atomic ions as the molecular weight increases and hence are less likely to appear and be mistaken for atomic ions.

A comparison of the present results may be made with the Langevin theory of mobilities[5] in several ways, depending on the size of the hard sphere (range of repulsive forces) used. At one extreme, the formula gives a mobility based on polarization forces only, and in the other direction the influence of a large hard core on the scattering predominates. In the latter case, the calculation requires a cross section value which in the present paper is taken as in Table I from the high E/p_0 limit of hard-sphere scattering.

For the molecular ions, which have a small charge exchange cross section and whose mobilities are therefore likely to depend largely on polarization forces, the Langevin equation has been used in the form

$$\mu_0 = 0.5105\left(1+\frac{m_a}{m_i}\right)^{\frac{1}{2}} \Big/ [\rho(K-1)]^{\frac{1}{2}}.$$

Here m_a is the mass of the gas atoms, m_i is the mass of the ion, ρ is the gas density, and K is the dielectric constant. The experimentally observed mobility must be extrapolated to zero field for comparison with the theoretical value. The resulting comparison appears in Table III. For the atomic ions, the Langevin formula

TABLE II. Ratio of ion-atom to atom-atom cross section.

Gas	Ratio of ion-atom to atom-atom cross section
He	3.6
Ne	3.1
A	3.2
Kr	3.2
Xe	2.9

[4] A. M. Tyndall and R. J. Munson, Proc. Roy. Soc. (London) **A177**, 187 (1940).
[5] H. R. Hasse, Phil. Mag. **VII**, 1, 139 (1926).

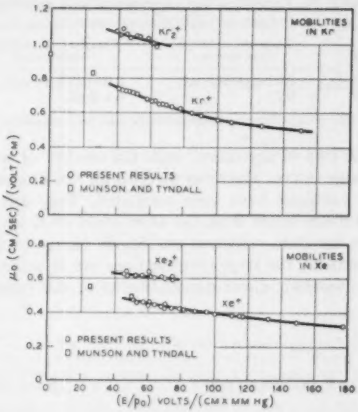

FIG. 2. The mobility at standard gas density, μ, of atomic and molecular ions in krypton and xenon as a function of E/p_0.

is taken as

$$\mu_0 = A\left(1+\frac{m_a}{m_i}\right)^{\frac{1}{2}} \Big/ [\rho(K-1)]^{\frac{1}{2}},$$

where A must be taken from Langevin's table as a function of a parameter

$$\lambda = 8\pi p\sigma^4/(K-1)e^2.$$

Here p is the gas pressure, $\pi\sigma^2$ is the experimentally determined hard-sphere cross section, e is the electronic charge, and K is again the dielectric constant. Using cross sections from Table I, the results shown in Table IV are obtained. The slightly less satisfactory agreement in Table IV compared with that in Table III is attributable to the somewhat too schematic nature of the Langevin theory.

In summary, the measurements have shown the existence of both atomic and molecular ions in krypton and in xenon, thus maintaining the same pattern previously found for helium, neon, and argon. The drift velocities for the various ions in their respective parent gases have been measured. For the atomic ions, the hard-sphere or equivalent charge exchange model of ion-atom interaction has been shown to apply at high E/p_0 values. For the molecular ions, the polarization forces between ion and atom primarily influence the drift rate. As in the case of the lighter rare gases, the molecule ions showed a higher drift velocity than the

TABLE III. Theoretical and experimental ionic mobilities.

Ion	Polarization mobility (Langevin)	Experimental mobility (extrapolated)
Kr_2^+	1.18 cm^2/volt-sec	1.1–1.2 cm^2/volt-sec
Xe_2^+	0.74	0.67–0.77

TABLE IV. Theoretical and experimental ionic mobilities.

Ion	Langevin mobility (hard sphere)	Experimental mobility (extrapolated)
Kr^+	1.01 cm²/volt-sec	0.9–0.95 cm²/volt-sec
Xe^+	0.77	0.6–0.65

atomic ions in agreement with the concept of weaker exchange forces. The cross sections for the atomic ion-atom collisions have been computed. They are some three times larger than the atom-atom cross sections. If the ion-atom collisions are largely charge exchange interactions, the large cross sections are in accordance with numerous direct measurements of this cross section (at higher energies) which show increasing size with decreasing energy.[6]

The writer is most indebted to Dr. J. A. Hornbeck for placing at his disposal the equipment designed and constructed for the earlier work on helium, neon, and argon. He is also pleased to acknowledge the assistance and the helpful suggestions of Dr. David J. Rose. Mr. F. D. Dolezal also assisted materially in the work of assembly and of taking of data. Dr. Hornbeck and Dr. G. H. Wannier very kindly reviewed and helpfully criticized the analysis and the manuscript.

[6] See, for example, Landolt-Bornstein, *Zahlenwerte und Funktionen* (Julius Springer, Berlin, 1950), Vol. 1, p. 358.

PHYSICAL REVIEW VOLUME 88, NUMBER 2 OCTOBER 15, 1952

Conductivity of Oxide Emitters*

RAY C. HUGHES AND PATRICK P. COPPOLA
Philips Laboratories, Inc., Irvington on Hudson, New York

(Received May 14, 1952)

Measurements of the conductivity of a BaSrCaO emitter over a range from room temperature to 1100°K indicate the existence, in well-activated cathodes, of a low temperature conduction mechanism having an activation energy of as little as 0.05 ev. Coincident with the temperature at which appreciable emission can be drawn, a high temperature conduction mechanism of 1 ev activation energy becomes evident. Application of a high pressure (25 atmospheres) of xenon to the cathode causes a marked decrease in conductivity in the high temperature range. These results are considered to confirm a hypothesis recently advanced by Loosjes and Vink that conduction in the high temperature region occurs predominantly through space currents in the pores of the oxide. The small activation energy of the low temperature conduction mechanism is considered to indicate the probability that this conduction occurs in a monolayer of barium on the surface of the oxide.

RECENT studies by Vink[1] and Loosjes and Vink[2] have led to the conclusion that the conduction through an oxide emitter, at operating temperature, occurs largely via space currents in an electron gas within the pore volume of the coating. In the present work, further evidence of conduction in this manner was sought.

The experimental approach has been to apply a relatively high pressure (25 atmospheres) of xenon gas to an activated emitter and to observe whether an apparent decrease in conductivity occurs. This method is based on the assumption that the electrons within the pores of the oxide will collide with the xenon molecules, and the average drift velocity under the influence of the applied field will be appreciably reduced.

The test cathode for measurement of resistance is of the design described by Loosjes and Vink, and is shown schematically in Fig. 1. A layer of oxide (BaSrCaO composition) of approximately 0.25-mm thickness is held between the flat ends of two 3-mm diameter nickel cathode sleeves of "*A*" nickel, the sleeves being spring loaded to hold the assembly under slight compression. Oxide coating on the cylindrical surfaces of the sleeve and a closely spaced anode permit measurements of emission to be made. The porosity of oxide in a processed tube was determined to be 70 percent by volume. The temperature of the sleeves is measured by thermocouples. Connections to the sleeves permit measurement of the resistance of the oxide by means of a dc bridge. The test assembly is enclosed in a metal envelope of rugged construction and is connected to the vacuum system and a gas purifying train via glass to metal seals, as shown in Fig. 2. Manipulation of gas and vacuum is provided by glass tip-off constrictions and glass percussion valves.

The xenon is treated for removal of oxidizing impurities by prolonged exposure to glowing zirconium wire and a fluffy deposit of barium obtained by evaporation from "Batalum" getters in a low pressure of the xenon. The xenon can be transferred quantitatively to the envelope of the test cathode by freezing out in a side arm on the envelope. Tipping off from the gas train

* Presented at the Twelfth Annual M.I.T. Conference on Physical Electronics, March, 1952.

[1] H. S. Vink, thesis, Leiden (1948) (unpublished).

[2] R. Loosjes and H. J. Vink, Philips Research Reports 4, 449 (1949).

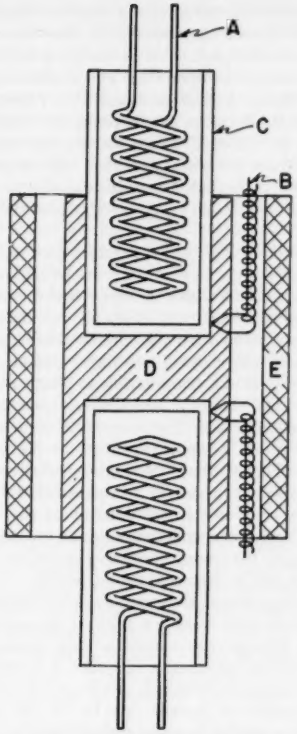

FIG. 1. Schematic representation of the experimental cathode. *A*—heater; *B*—thermocouple; *C*—nickel cathode sleeve; *D*—BaSrCaO; *E*—anode.

and expansion of the gas in the envelope volume then produces the desired pressure of 25 atmospheres. Subsequent measurements under vacuum conditions (pressure <1 mm Hg) can be made by again freezing out the gas in the side arm by immersing in a liquid nitrogen bath.

Measurements of conductivity of the emitter as a function of temperature in the range from room to 800°C were made in the following sequence:

(1) Tube on the pump and the oxide incompletely activated.

(2) Tube "tipped off" and the oxide fully activated and stabilized.

(3) Xenon admitted at $\frac{1}{2}$ atmosphere pressure.

(4) Tube "tipped off" from the gas purifying train and xenon frozen out in the side arm.

(5) Gas expanded in tube envelope to give 25 atmospheres pressure.

(6) Gas alternately frozen out and expanded to check reproducibility of the observed pressure effects.

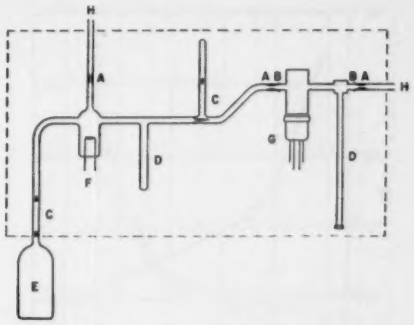

FIG. 2. The gas purifying train portion and experimental tube assembly. *A*—tip-off construction; *B*—Pyrex to Kovar seals; *C*—glass percussion valves; *D*—traps for freezing out xenon; *E*—flask of xenon; *F*—getters; *G*—experimental tube; *H*—leads to high vacuum system. The dotted lines indicate a bake-out oven.

Limited measurements of emission were made to determine the lowest temperatures at which significant emission (0.02 microampere or more) could be obtained.

EXPERIMENTAL RESULTS

Typical results of log conductivity *versus* reciprocal temperature (cathode in vacuum) are shown for three increasing degrees of activation in Fig. 3. Following activation of the cathode, and while the tube was still on the pump, plots *A* and *B* were obtained. These results, especially *A*, are very similar to those obtained

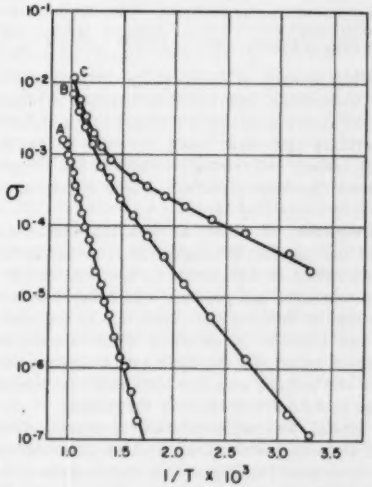

FIG. 3. Log conductivity *versus* reciprocal temperature relationships for an oxide emitter. *A*, *B*—tube on the pump, *B* more highly activated than *A*; *C*—tube tipped off.

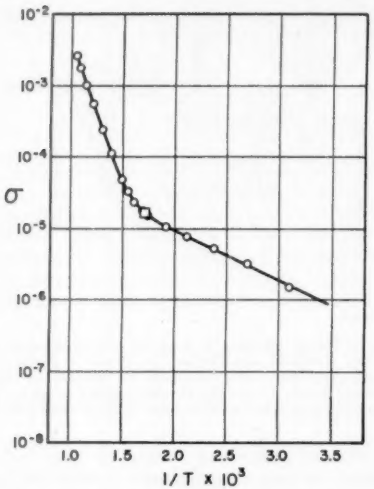

FIG. 4. Log conductivity *versus* reciprocal temperature relationships of oxide emitters. The tubes are tipped off and cathodes well activated. The point indicated by a square is the lowest temperature at which appreciable emission was obtained.

by Loosjes and Vink[2] on cathodes at the lowest state of activation. They are also similar to results presented by Hannay *et al.*[3] and by Wright[4] for measurements made with the tube on the pump. A comparison of activation energies and conductivities follows:

	Present work	Loosjes and Vink	Wright	Hannay *et al.*
Activation energy, ev	1.13	1.14	*ca* 1.1	1.1
Conductivity at 1000°K	10^{-3}	6.3×10^{-3}	3×10^{-4}	4×10^{-4}

A marked increase in conductivity, the appearance of a low temperature conduction mechanism of relatively low activation energy, and decrease in slope of the high temperature plot occur when the tube is tipped off, getters flashed, and the cathode held at 800°C until its resistance becomes stabilized. These effects are illustrated by curve *C* of Fig. 3.

Introduction of xenon at ½ atmosphere pressure caused no significant change in the conductivity-characteristics of the cathode; likewise, results obtained when the gas pressure was reduced to a very low value by freezing the xenon out in the side arm were not significantly different. Therefore, the introduction of xenon and the tipping off to confine the gas within the cathode envelope has caused no significant change in state of activation of the cathode.

A typical plot representative of results obtained under vacuum, ½ atmosphere, and low pressures conditions is presented in Fig. 4. The temperature at which appreciable emission (>0.02 microampere) could be drawn is indicated and is seen to coincide with the first detectable increase in conductivity above that of the low temperature plot. This is rather good evidence that the change in slope of the plot is associated with emission effects. Activation energies for representative measurements obtained on the pump and after tip off are given in Table I. These results are, in general, similar to those of Loosjes and Vink and confirm their conclusion that the high temperature conduction mechanism has an activation energy of approximately 1 electron volt.

Application of high xenon pressure produced a well-defined decrease in conductivity in the high temperature region. This is shown in Figs. 5 and 6. Subsequent removal of the xenon by freezing out restored the original vacuum and low pressure conductivity. Deviation between the vacuum and high pressure plots begins to occur at the temperature at which emission is detectable and becomes progressively greater as the temperature increases. The magnitude of change is by factors of 3 and 4 (approximately) for the two tubes at 700°C. Though the dependence of conductivity on xenon pressure at constant temperature could not be accurately examined, it was determined that the conductivity varied in a smooth manner as the gas pressure was changed. The changes produced in the low temperature range will be discussed subsequently.

On the logarithmic scale employed for presenting the data, it is not evident at first that the introduction of a high gas pressure has caused a large change in the conductivity of the coating. However, if we extrapolate the low temperature branch of the plot and calculate the proportion of current due to the low and high temperature mechanisms, we find at 700°C:

Tube 673	Tube 524	
2.8	1.6	percent of current carried by low temp. mechanism.
97.2	98.4	percent of current carried by high temp. mechanism, under vacuum conditions.
72	81	percent reduction in current carried by high temp. mechanism, due to high gas pressure.

TABLE I. Activation energies calculated from log conductivity *versus* reciprocal temperature.

Tube No.	Condition	Activation energy, electron volts: Low temperature mechanism	Uncorrected high temperature mechanism	High temperature mechanism, corrected for low temperature mechanism
524	on pump	...	1.13	...
	tipped off	0.13	0.68	0.94
	tipped off	0.13	0.76	0.99
	low pressure	0.13	0.76	0.99
	low pressure	0.14	0.71	0.94
673	on pump	0.31	0.86	1.24
	on pump	0.37	0.77	1.17
	tipped off	0.15	0.73	0.95
	tipped off	0.14	0.68	0.94
	tipped off	0.15	0.66	0.90
	tipped off	0.14	0.71	1.04

[3] Hannay, MacNair, and White, J. Appl. Phys. **20**, 669 (1949).
[4] D. A. Wright, Brit. J. Appl. Phys. **1**, 150 (1950).

It is to be expected that, as the gas pressure is increased, emission currents in the large pores will at first be somewhat reduced and that, as the pressure is further increased, the effect will extend to successively smaller pores and that the degree of reduction in pores previously affected will become more marked. It is thus not to be expected that the space currents within the pores will be completely eliminated. The manner of deviation between the high and low pressure curves is therefore in qualitative agreement with what might be expected.

The emission which could be drawn to the plate was strongly decreased by the introduction of $\frac{1}{2}$ atmosphere of xenon. For example, at 450°C, in vacuum, 15 microamperes was obtainable; after introduction of $\frac{1}{2}$ atmosphere pressure, 0.02 microampere could be drawn at the same temperature and plate voltage. This is a change of nearly 3 orders of magnitude. No significant change occurred in the resistance. This furnishes strong evidence that the resistance measurements are free of any spurious space current effects external to the coating volume, for the distances which must be involved in such currents are comparable to the cathode to plate separation.

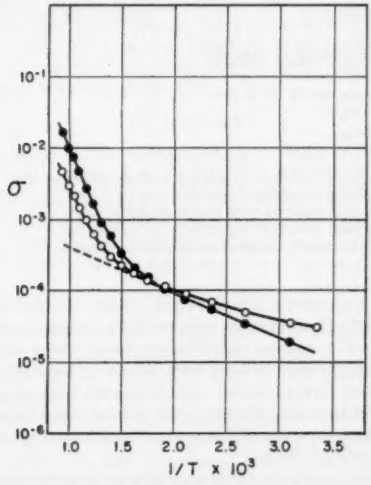

FIG. 5. Effect of high xenon pressure on conductivity of an oxide emitter. ●—vacuum and low pressure; ○—high pressure (25 atmospheres).

DISCUSSION

It remains to account for the discrepancy between the results obtained here and those of Hannay *et al.* Hannay's results were all obtained from tubes on the pumps, and without getters. Under these conditions we likewise obtain curves (see Fig. 3, curve *A*) in which the entire plot can be represented by an approximately straight line, and if two conduction mechanisms are present, these are not evident. This type of plot has been discussed in detail by Wright[4] who has observed that with any type of coating immediately after outgassing at 1300°K, a state is at once established, where σ is near $10^{-8}\Omega^{-1}$ cm^{-1} at 1100°K and where the slope of logσ *versus* $1/T$ is about 1.1 ev. Wright considers this an intermediate state, neither fully activated, nor poisoned. It is to this condition that a cathode tends to return after either poisoning in an oxidizing gas or activating in a reducing gas.

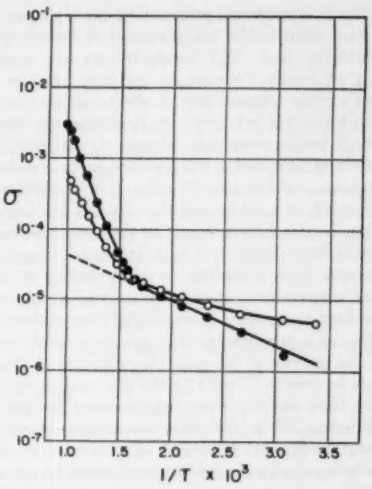

FIG. 6. Effect of high xenon pressure on conductivity of an oxide emitter. ●—vacuum and low pressure; ○—high pressure (25 atmospheres).

Comparing results obtained by different experimenters, we find that our results for the most inactive state on the pumps are closely similar to those described by Wright, an activation energy of 1.13 ev being obtained in our measurements. We concur with Wright in his belief that Hannay, McNair, and Wright have observed only this same state. We believe that Hannay *et al.* have obtained a low state of activation due to the fact that all measurements were made "on the pump," and because the activating agent employed, methane, is largely disassociated and consequently does not have the assumed effectiveness as a reducing agent. Further, operation at abnormally high temperature would have caused loss in activation both by barium evaporation and by sintering. As a result of these effects, the emission densities observed were less, by more than two orders of magnitude, than is normal for a "good" cathode. The present authors therefore conclude that the measurements of Hannay *et al.* do not represent the behavior of a well-activated cathode. The origin of the measured conductivity is not entirely evident but may well be almost entirely due to space currents in the pores of the coating.

A totally unexpected influence of the high gas pressure was noted in the low temperature branch of the conductivity plot. The conductivities are approximately equivalent for vacuum and high pressure conditions at the temperature at which emission is first detected but toward lower temperatures the vacuum and high temperature plots diverge significantly. Conductivity is increased in the low temperature region by the presence of the gas. In order to explain this fact satisfactorily it must be assumed that the low temperature conduction is determined by the surface properties of the oxide particles. It is most attractive to assume a monatomic layer of barium, as postulated by de Boer.[5] At low temperatures this surface layer of barium might be oxidized by residual gases coming from various tube surfaces at a rate greater than arrival of fresh barium from the interior of the grains by diffusion. A layer of surface barium to account for the low temperature conduction has recently been suggested by Wright[4] and by Friedenstein *et al.*[6] This assumption would also explain the general failure of all observers to detect a low temperature conduction mechanism of low slope in all cases in which measurements are made on the pumps, for under these circumstances, a monatomic barium film would be most rapidly oxidized.

The effect of a high pressure of inert gas surrounding the cathode would be to greatly impede access of oxidizing gases coming from the tube walls. The gas pressure should also reduce the rate of outgassing of the tube parts. If we assume further that protection of the surface film of barium from oxidation is never perfect, then the continuous curvature of the low temperature, high pressure plot and the rather slow increase in conductivity with increasing temperature is consistent with the view that the proportion of surface coverage is increased with increasing temperature as a consequence of the increased rate of barium diffusion. As an alternative to the assumption of an adsorbed monolayer of barium in the above speculations, one might attribute the low temperature conduction to semiconductor effects at points of contact between individual oxide crystals, the semiconductor being oxide activated by excess barium, and consider deactivation of the semiconductor by conversion of excess barium to oxide. However, the slope of the low temperature plot for the high pressure measurements decreases to 0.05 and 0.08 ev, respectively, for the two tubes. These low activation energies appear to be inconsistent with a semiconductor interpretation. In view of this low apparent slope, the supporting considerations by Wright and Friedenstein *et al.*, and the presumed efficacy of the gas in retarding the surface deactivation of the cathode, it appears most probable that the low temperature conduction is due to an adsorbed monolayer of barium.

This investigation was suggested by E. S. Rittner, to whom we are indebted for helpful discussions throughout the course of the work. Technical assistance by Richard Ahlert, George Beutel, and Martin Miller is also gratefully acknowledged.

[5] J. H. de Boer, *Electron Emission and Absorption Phenomena* (Cambridge University Press, London, 1935).
[6] Friedenstein, Martin, and Munday, Repts. Progr. Phys. **11**, 298 (1948).

PHYSICAL REVIEW VOLUME 88, NUMBER 2 OCTOBER 15, 1952

The Close Pair Effect in Cosmic-Ray Stars*

K. E. Davis, J. B. Marion,† J. F. Delord, and K. M. King‡
Reed College, Portland, Oregon
(Received May 21, 1952)

Evidence is presented to establish the existence of the close pair effect in cosmic-ray stars formed in nuclear emulsions exposed at 95,000 ft. A reasonable estimate of the magnitude of the effect may be derived from the data obtained, and this magnitude is compared with that obtained from similar studies at lower altitudes. It appears that a maximum for the excess of close pairs occurs for separations ≤ 1 mm in the emulsions exposed at balloon altitudes. It is extremely difficult to explain the effect on the basis of present knowledge.

INTRODUCTION

INDEPENDENTLY and almost simultaneously, Leprince-Ringuet and Heidmann[1] and Li and Perkins,[2] in 1948, discovered, in the analysis of a number of nuclear plates that had been exposed at about 12,000 ft in the Alps, that there were more pairs of stars with small separations between their centers (on the order of hundreds of microns) than could be explained on the basis of a random distribution. Since the numbers involved in these studies were relatively small, it was felt that further studies were indicated both at comparable and other altitudes. The present study involves a balloon exposure of 8 hours at 95,000 ft and geomagnetic latitude 55°N.

In analyzing the 19 plates that were selected for this study, it was discovered that about 50 percent fewer stars fell in the border areas of the plates than were to

* The work reported in this paper was supported by a Cottrell Grant of the Research Corporation.
† Now at Rice Institute, Houston, Texas.
‡ Now at Columbia University, New York, New York.
[1] L. Leprince-Ringuet and J. Heidmann, Nature **161**, 844 (1948).
[2] T. T. Li and D. H. Perkins, Nature **161**, 844 (1948).

be expected. This lowering of the star density near the edges of the plates is probably due to the obscuring of stars actually formed in this region by the many spurious grains rendered developable by stresses introduced in the emulsion in the cutting, handling, or binding. Accordingly, the plates were divided into a number of vertical and horizontal strips and the chi-square test applied to the numbers of stars in these areas. On the basis of this test, it was concluded that, if a region 2 mm from the long sides of the 1 in.×3 in. plates and 3 mm from the short sides was excluded, then the remaining stars would be randomly distributed over regions of about 40 mm² area.

After the border region was excluded from the counting, 1077 stars were found on 278 cm² of the 50-micron Eastman NTB emulsions that were used. A total of 241 close pairs were found, whose centers were separated by a distance[3] of 1950 microns or less.

Using the lowest possible power in both the objective lens and eyepiece of the microscope, the diameter of the field of view was slightly less than 2 mm. Distances between star centers were measured directly with a previously calibrated reticle. Error introduced by the curvature of the field was found to be negligible.

DERIVATION OF THE FORMULA FOR THE EXPECTED NUMBER OF CLOSE PAIRS

Consider a plate of area S, over which there are evenly distributed N stars; the density of stars is $n=N/S$. The number of stars within a distance r of some point is

$$q(r)=n\pi r^2, \tag{1}$$

if the point is at least r from the edge of S. Therefore, let us define a new area S', every point of which is at least r from the edge of S. Equation (1) then applies to all points within S'. For all stars within S', the sum of all pairs with separation $\leqslant r$ is

$$F(r)=nS'\cdot n\pi r^2. \tag{2}$$

If every star of the pairs counted in (2) were in S', then the total number of actual pairs would be $\frac{1}{2}F(r)$, since, in this case, each pair would have been counted twice.

Now, if M of the stars represented in (2) are outside of S' (but still within S), and if each has K neighbors in S' within a distance r, then we have the relation

$$q'(r)=\tfrac{1}{2}[F(r)+MK], \tag{3}$$

since, in counting, we consider only those pairs formed with stars falling within S'. Equation (3), then, is the formula for the expected number of close pairs with separations $\leqslant r$.

The product MK may be evaluated in the following manner: Consider a star in the area $A=S-S'$ (see Fig. 1), a distance x from the edge of S' ($x\leqslant r$, and $r\leqslant a/3$, where a is the short dimension of the plate, $S=ab$). The area of S' in which this star may form pairs is $G(x)$:

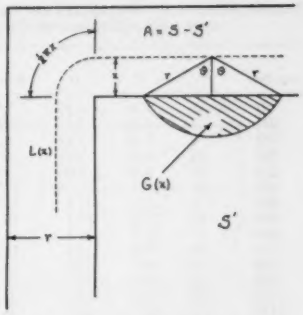

FIG. 1. Diagram to accompany the derivation of Eq. (7) for the expected number of close pairs with separations less than a given distance.

$$G(x)=\tfrac{1}{2}r^2\vartheta-xr\sin\vartheta.$$

The number of stars expected in $G(x)$ is $nG(x)$. Now, the stars in A are evenly distributed; i.e., the number of stars in any strip of width dx, which is everywhere a distance x from the edge of S', is $nL(x)$, where $L(x)$ is the length of the strip:

$$L(x)=2(a+b-4r)+2\pi x.$$

Therefore,

$$MK=\int_0^r nL(x)\cdot nG(x)\cdot dx,$$

$$MK=r^2n^2(a+b-4r)/3,$$

for $r\leqslant a/3$ and neglecting corner effects. Hence,

$$q'(r)=\tfrac{1}{2}[n^2\pi r^2S'+r^2n^2(a+b-4r)/3]. \tag{4}$$

If it is now desired to normalize (4) to 10^3 stars, it must be recalled that in the area S' there are nS' stars:

$$q''(r)=q'(r)\times 10^3/(nS'),$$

$$q''(r)=10^3\times\tfrac{1}{2}n\pi r^2[1+r(a+b-4r)/(3\pi S')], \tag{5}$$

where q'' is the normalized quantity. At the greatest distances considered ($r\approx 2$ mm), the second term in (5) amounts to only about 1.5 percent of the first term. This term becomes important only when r is about 5 mm or greater. However, we have the additional restriction that $r\leqslant a/3$. Therefore,

$$q''(r)=N\pi r^2/(2ab)\times 10^3, \quad r\leqslant a/3 \text{ and } 5 \text{ mm}. \tag{6}$$

For the total number of close pairs with separations $\leqslant r$ on the 19 plates that were analyzed, we have

$$Q(r)=10^3\times\sum_{i=1}^{19}\frac{N_i}{S_i}\frac{\pi r^2}{2ab}, \tag{7}$$

where N_i and S_i are, respectively, the total number of stars and the total usable area of the ith plate.

COMPARISON OF THE VARIOUS RESULTS

Table I summarizes the data obtained in the present investigation. P' signifies the observed number of close

[3] The distance between centers as projected on the plane of the emulsion.

TABLE I. Values of the observed (P) and expected (Q) number of close pairs with separation $\leq r$ microns.

r (microns)	P^a	P	Q	$P-Q$	$(P-Q)/Q^{\frac{1}{2}}$	(qv) (barns)
50	2	1.86	0.16	1.70	4.25	
100	5	4.64	0.63	4.01	5.05	15.4
150	6	5.58	1.42	4.16	3.5	13.5
200	10	9.30	2.54	6.76	4.2	19.8
250	10	9.30	3.96	5.34	2.7	14.5
350	21	19.5	7.76	11.7	4.2	28.9
450	27	25.1	12.8	12.3	3.4	28.4
550	40	37.2	19.1	18.1	4.1	39.9
650	47	43.7	26.8	16.9	3.3	35.7
750	54	50.2	35.4	14.8	2.5	30.2
850	75	69.7	45.8	23.9	3.5	47.7
950	86	80.0	57.2	22.8	3.0	44.2
1050	101	93.9	69.9	24.0	2.9	45.6
1150	113	105	83.8	21.2	2.3	39.4
1250	126	117	99.0	18.0	1.8	32.8
1350	141	131	115	16.0	1.5	28.5
1450	153	142	133	9.0	0.8	15.7
1550	172	160	152	8.0	0.65	13.8
1650	191	177	172	5.0	0.4	8.5
1750	205	190	194	−4.0	−0.3	
1850	229	213	217	−4.0	−0.3	
1950	241	224	241	−17.0	−1.1	

pairs with separations $\leqslant r$ microns; P signifies the normalized value. The values of $Q(r)$ were computed by Eq. (7). It is to be noted that the ratio of the observed to the expected deviations $(P-Q)/Q^{\frac{1}{2}}$ is, for $0<r\leqslant 1350$ microns, positive and greater than unity.

The excess of close pairs, $(P-Q)$, is compared graphically with the results of the previous investigations[1,2] in Fig. 2. The determinations of Leprince-Ringuet and Heidmann[1] are based on the observation of 2250 stars on 640 cm² of 100-micron Ilford emulsion, exposed for three to six weeks at 3600 m; those of Li and Perkins[2] are based on 1230 stars found in the analysis of 54 in² of boron loaded, 100-micron, Ilford C-2 emulsion, exposed for 40 days at 3650 m. All values are normalized to 1000 stars.

The results of the present investigation, which extends the range of observation to 1950 microns, indicate that the excess of close pairs reaches a maximum in the neighborhood of $r=1000$ microns and then tends downward, crossing the axis near $r=1700$ microns. Negative values of $P-Q$ then appear out as far as the measurements were carried. $P-Q$ must, of course, tend to zero as r approaches a value such that πr^2 equals the area of the plate ab.

It should be noted that at least two other investigations of the close pair effect have been carried out as side issues in the search for other data. Addario and Tamburino[4] report that in scanning plates exposed at 29,000 ft, they find a close pair effect of about the same magnitude as that found by Li and Perkins[2] at 12,000 ft. However, Salant, Hornbostel, and Dollman[5] find no observable effect in plates exposed at 100,000 ft. These two reports cannot be considered representative, however, inasmuch as only 84 stars were observed in the former and 211 in the latter case. These, certainly, do not represent statistical samples. The 1077 stars observed in the present study may not be sufficient to give an accurate representation of the magnitude of the effect at 95,000 ft; however, it is felt that they are sufficient to conclude that a close pair effect exists at this altitude and with a somewhat greater magnitude than at mountain altitudes. The increase of the magnitude of the effect with altitude is probably to be expected, since the cosmic-ray particles are much more highly energetic at great altitudes.

A second, more recent publication by Li[6] appears to indicate the following:

(a) Plates exposed at sea level under no absorber do not show an excess of P over Q, or else the effect is so small that it is outweighed by the statistical fluctuations. (This is based on only 140 stars, however.)

(b) Plates exposed at 12,000 ft under no absorber show such fluctuating values for $P-Q$ that it is impossible to estimate where any maximum might occur or whether a downward trend is indicated at large r.

(c) Plates exposed at 12,000 ft under various thicknesses of lead and ice absorbers indicate that the magnitude of the effect under these conditions is somewhat larger than in plates exposed under no absorbers at the same altitude. The $P-Q$ curve reaches a broad flat maximum, beginning at about $r=1500$ microns, and extends, with no indication of a downward trend, out to the largest distances measured (2540 microns). Since we might expect the average distance between pairs to be somewhat greater at 12,000 ft than at 95,000 ft, for, at the latter altitude, the cosmic-ray particles are much more energetic (and hence any secondary particles emitted in stars would have a greater probability of possessing sufficient energy to induce another star),

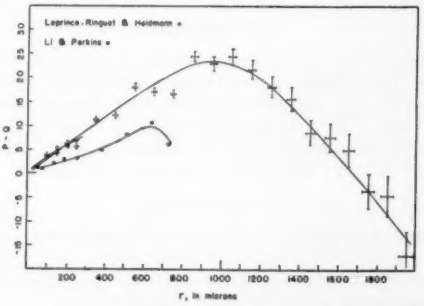

FIG. 2. Comparison of the values for the excess of close pairs, $P-Q$, for pair separations less than a given r. The values given for Leprince-Ringuet and Heidmann (reference 1) and Li and Perkins (reference 2) were obtained at 12,000 feet. The probable errors are based on a scanning efficiency of 90 percent. All values are normalized to 1000 stars.

[4] M. M. Addario and S. Tamburino, Phys. Rev. **80**, 749 (1950).
[5] Salant, Hornbostel, and Dollman, Phys. Rev. **74**, 694 (1948).
[6] T. T. Li, Phil. Mag. **41**, 1152 (1950).

this particular $P-Q$ curve would be expected to reach a maximum at a greater distance than that for the authors' curve of Fig. 2. It cannot be said with certainty whether or not this is indicated with the present results.

Li's data have since been re-analyzed by Davis.[7] He interprets his results as indicating that no effect exists. A similar analysis of our data leaves our results essentially unchanged; this is discussed in greater detail below.

THE MECHANISM OF THE CLOSE PAIR EFFECT

Three possible explanations of the close pair effect have been suggested by Leprince-Ringuet *et al.*:

(1) One of the stars emits a neutral particle[8] which gives rise to the other as a secondary star.

(2) A pair is produced by a single particle of known or unknown type.

(3) A pair is produced by a collimated shower of particles of known or unknown type.

On the basis of several assumptions, hypothesis (1) may be checked by calculating $q\sigma$, the product of q (the average number of infinitely penetrating particles capable of forming the excess of close pairs, $P-Q$, necessarily emitted by all other stars, $N-(P-Q)\approx N$, in order to account for the excess), with σ (the cross section for star production of these particles. It is further assumed that these q particles are emitted isotropically. We make the following definitions:

$$w(r)=qN\sigma Lx, \quad W(y,r)=\int_{V_0}\frac{\partial w}{\partial r}\frac{\partial r}{\partial V}dV,$$

where $w(r)$ is the number of secondary stars that would be formed within a distance r of the N primary stars in an infinite emulsion; L is the number of nuclei per cm^3 present in the emulsion (4.75×10^{22}, if the hydrogen content is neglected[9]); $W(y,r)$ is the actual number of secondary stars formed in the volume V_0 of the finite emulsion if the N primary stars are situated a distance y below the surface of the emulsion of thickness d (see Fig. 3).

$$\partial w/\partial r=qN\sigma L, \quad \partial r/\partial V=1/4\pi r^2,$$
$$dV=r^2\sin\vartheta dr d\vartheta d\varphi,$$

$$W(y,r)=\frac{q\sigma NL}{4\pi}\int_{V_0}\sin\vartheta dr d\vartheta d\varphi. \tag{8}$$

Integration yields

$$W(y,r)=\tfrac{1}{2}q\sigma NL[y\log(r/y)+(d-y)\times\log[r/(d-y)]+d]. \tag{9}$$

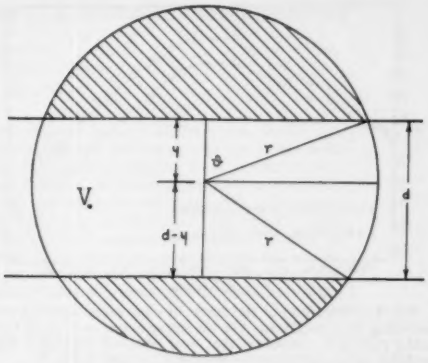

FIG. 3. Diagram to accompany the derivation of Eq. (10) for the dependence of the excess of close pairs on r, the maximum separation of their centers, based on the assumptions given in the text.

For a given r, let the term in the brackets be $f(y)$. Now, since a primary star has equal probability of occurring anywhere in the range $0\leq y\leq d$, we obtain $W(r)$ in the following manner:

$$W(r)=\tfrac{1}{2}q\sigma NLd^{-1}\int_0^d f(y)dy.$$

Hence, if we let $W(r)$ be the excess of close pairs, $P-Q=E(r)$,

$$E(r)=\tfrac{1}{2}q\sigma NLd[\tfrac{3}{4}+\log(r/d)], \quad r>d. \tag{10}$$

The various determinations of $q\sigma$ calculated by this formula are summarized in Table II.

It can be seen by the figure given by the present work in Table II, that if particles are emitted from the primary stars that have a geometrical cross section for star production (0.67 barn for the NTB emulsion, if the hydrogen content is neglected[10]), then approximately 42 such particles must be emitted from each of the N stars. Since this hypothesis yields such an unreasonably high value for q, we conclude that fast neutrons are probably not the intermediate particles. Again, if some type of neutral meson were emitted from

TABLE II. Summary of the various determinations of $q\sigma$.

Observer(s)	Reference	No. stars (N)	$q\sigma$ (barns)
Leprince-Ringuet and Heidmann	1	2250	7.5
Li and Perkins	2	1230	6.5±2.4
Li	5	2870[a]	13.8±5.4
This work		1077	28.0±5.3

[a] The 1230 stars of the second reference are included in this figure.

[7] G. Davis, Phil. Mag. **43**, 472 (1952).

[8] Since only 3 double stars (i.e., a pair connected by an ionizing particle, usually a negative pi-meson) were observed in the present study, it must be reasonably concluded that neutral particles are the responsible agency.

[9] Calculated from data listed by J. Rotblat, Prog. Nucl. Phys. **1**, 43 (1950).

[10] Calculated from data listed by the Kodak Nuclear Track Plates Manual (Eastman Research Staff, Rochester, 1950), using for the nuclear radius, $r=1.4\times10^{-13}A^{\frac{1}{3}}$ cm. The value given is the weighted mean for the NTB emulsion.

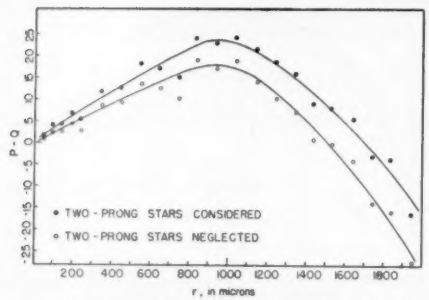
P-Q
25 20 15 10 5 0 5 10 15 20 25
• TWO-PRONG STARS CONSIDERED
○ TWO-PRONG STARS NEGLECTED
200 400 600 800 1000 1200 1400 1600 1800
r, in microns

FIG. 4. Comparison of the excess of close pairs including and excluding two-prong stars. For the upper curve, only those two-prong stars were considered that were positively identified. The probable errors (not drawn) correspond to those of Fig. 3.

these stars with an average multiplicity of, say, 3, as a maximum estimate, then a cross section for star production of at least 14 times the geometrical cross section would have to be postulated if these mesons were to account for the entire excess of close pairs. Therefore, hypothesis (1) is discounted, for the present at least, since intermediate neutrons or neutral mesons could account for only a small fraction of the observed excess of close pairs.

Hypothesis (2) leads to similar difficulties. If we again postulate that a fast neutron is the responsible agency, with a cross section for star production equal to the geometrical cross section, then its mean free path in the emulsion must be

$$p=1/(L\sigma)=31 \text{ cm}.$$

Hence, the formation of close pairs with separations $\leqslant 2$ mm is extremely unlikely.

Li[6] shows, at great length, that (*a*) edge effects (which we have taken the precaution to eliminate as far as possible), (*b*) uneven thickness of the emulsion, (*c*) inefficiency of scanning, and (*d*) the regenerative processes [hypotheses (1) and (2)] can account for only a small percentage of the observed excess of close pairs.

It is possible, however, that the pairs are produced by single, penetrating particles of unknown type. The variables in such a process could easily be chosen so as to give the observed variation of pair frequency with r.[8]

SCANNING EFFICIENCY

A close check of the scanning indicated an efficiency of at least 92 percent. Li[6] has reported 80 percent on a first search and 99 percent over-all efficiency after a second search at half the previous speed, using 98 percent as a conservative working figure. Davis[7] concludes that this latter figure should be more nearly 80 percent and that the principal stars missed were two pronged ones. He properly points out that the difficulty of identifying two-prong stars makes their inclusion unsuitable in an analysis of high accuracy. When they are eliminated from data obtained from Li's plates, no close pair effect seems indicated. However, results of performing a similar operation on our data are given in Fig. 4, and it can be seen that they are essentially unchanged by such a subtraction. A histogram of star-prong multiplicity percentages is given in Fig. 5.

CONCLUSIONS

On the basis of the results obtained in this study, it is concluded that sufficient evidence is available to establish the existence of the close pair effect at 95,000 feet. However, the number of stars taken into consideration may not be sufficient to give an accurate account of the magnitude of the effect at this altitude. The effect is essentially independent of whether positively identified two-prong stars are included or excluded. It appears that a maximum value for the excess of close pairs occurs for separations $\leqslant 1000$ microns, and negative values occur after about 1700 microns (1500 microns with two-prong stars excluded) out to the greatest distances measured. It is extremely

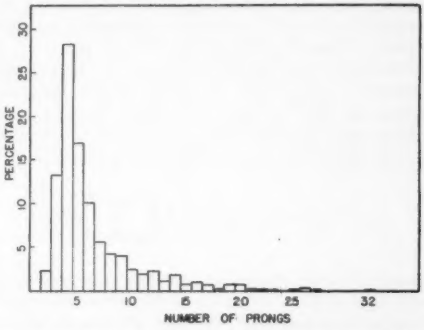

FIG. 5. Multiplicity of star prongs. Indicated value for two-prong stars is based only on those for which identification was positive.

difficult to explain the effect on the basis of present knowledge.

The rate of star production at 95,000 ft and 55° N geomagnetic latitude was found to be 2020 ± 55 stars/cm^3/day.[11] The percentage of all stars with two or more prongs that contain hammer tracks was found to be 0.39 ± 0.19.[12]

The authors wish to express their appreciation for the kind assistance of Bernard Peters of the University of Rochester, and John A. Simpson, Jr., of the University of Chicago, during the early phases of this project, and of Lawrence S. Germain of Reed College, who has taken considerable interest in the investigation. We are also indebted to the Naval Research Laboratories and the General Mills Corporation, through whose generosity the balloon exposure was made possible.

[11] E. O. Salant *et al.*, reference 4, find 2000 stars/cm^3/day at 100,000 feet.

[12] F. L. Adelman and S. B. Jones, Phys. Rev. **75**, 1468 (1949), find a percentage of 0.37.

The Free Energies and Phase Transition of a Cylindrical Superconductor*

PAUL M. MARCUS†
University of Illinois, Urbana, Illinois
(Received June 23, 1952)

The Helmholtz and Gibbs free energies for a cylindrical superconductor of arbitrary cross section in a uniform axial magnetic field are defined carefully in terms of magnetic moment or total flux for the body as a whole. These definitions, applicable for arbitrary electrodynamic description of the superconductor, are transformed to equivalent forms with different density functions, on assuming the London equations. A general expression is obtained for change of Gibbs function when the superconducting cross section contracts and normal phase appears, which gives directly the critical current density condition of London for the phase transition. Three critical fields are defined and compared, making use of several theorems on the dependence of the boundary current density on the shape and size of the cross section. The general formulas for free energies and critical fields are illustrated for several special cross sections, including an oval shape with nonuniform boundary current density. The metastability of a superconductor described by the London equations is illustrated and discussed.

1. INTRODUCTION

THE thermodynamic analysis of the behavior of a superconductor in a magnetic field is a particularly interesting application of thermodynamics to general physical systems because of the remarkably inhomogeneous nature of the field distribution and the quite explicit formulation of the magnetic contributions to the thermodynamic functions. The analysis can then lead to detailed understanding of the path of the phase transition produced by a sufficiently strong magnetic field. The thermodynamics has a special simplicity in that explicit magnetic terms are simply added to the temperature dependent terms present without the magnetic field, but a special complexity in the inhomogeneous nature of these added terms.

A simple approximation introduced by Casimir and Gorter[1] is commonly used to give the main features of the behavior, namely, that the superconducting specimen is a magnetized body such that $B=0$ within the specimen.[2] Finer details associated with the penetration of the field into the specimen, which appear in the behavior of small specimens (i.e., thin films, wires, or small spheres), are not contained in this approximation. A more detailed theory may be carried out on the basis of definite assumptions about the field penetration law, such as the London equations, but this seems to have been done only for the thin film.[3] In addition, the thin film discussion does not emphasize simplicity and generality.

The following work gives the detailed thermodynamic theory for a cylindrical specimen of arbitrary cross section in a longitudinal magnetic field using for the electrodynamic description the London equations. In this case, in which the field has only the component parallel to the axis, while the currents form closed loops in the cross section, the formulation is not much more complicated than for the simple approximation, and the free energies have particularly simple forms. At the same time the situation is general enough to give rise to phenomena not present for the film (or the circular cylinder), such as breakdown of superconductivity at one point of the cross section (actually at a line of points on the surface).

The thermodynamic functions will be defined for the body as a whole, a procedure which seems more satisfactory than the use of assumed density functions from the beginning, which are justified only for relations obtained by integration over definite volumes. In fact, the density functions are to some extent arbitrary since densities may be added which integrate to zero but are not zero everywhere, as will be illustrated later. However, there is a natural choice of density functions which appeals most to our physical understanding. The procedure will avoid using fictitious magnetization densities in the superconductor, but will use only the current densities actually present in the physical situation; however, the total magnetic moment of the specimen is a well-defined physical quantity which will be useful to introduce.

The Gibbs free energy is the appropriate quantity to use for discussion of the phase transition and will be used to deduce the critical field for first breakdown of superconductivity. This will give an alternative proof of the critical current density condition of H. London[4] based here purely on the magnetostatic description. This critical field will be compared with two other critical fields, namely, the critical field for a massive superconductor, and the critical field for which total conversion of superconductor to the normal state is thermodynamically favorable. In the course of this analysis the current density at the surface of the specimen will be studied, and some new quantitative and qualitative theorems about its behavior as a function

* Work supported by the ONR.
† Now at Carnegie Institute of Technology, Pittsburgh, Pennsylvania.
[1] C. J. Gorter and H. B. G. Casimir, Physica **1**, 305 (1934).
[2] F. London, *Superfluids* (John Wiley and Sons, Inc., New York, 1950), Vol. 1, pp. 16–19.
[3] F. London, see reference 2, pp. 126–128.
[4] H. London, Proc. Roy. Soc. (London) **A152**, 650 (1935); see also F. London, reference 2, p. 137.

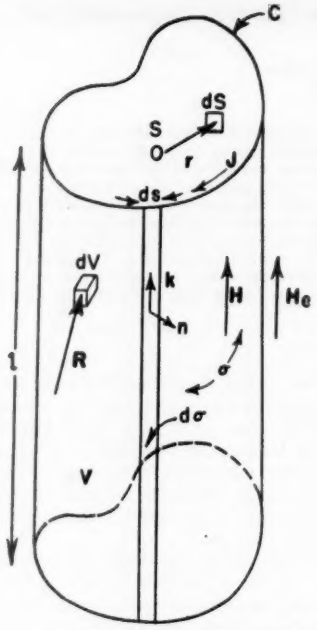

FIG. 1. Notation for the coordinates, dimensions, and vectors used in describing a cylindrical specimen in a longitudinal magnetic field.

of shape and size of the cross section will be obtained. In particular, the difference between convex and concave cross sections will appear.

Generally speaking, these results are of quantitative significance only for specimens comparable in some dimension with the penetration depth, which is of the order 5×10^{-6} cm, and hence for rather small or thin specimens.

Certain useful integral transformations (surface to line integrals) and variational theorems will be obtained which are essentially theorems about the solutions of the two-dimensional equation $\nabla^2\varphi=\beta^2\varphi$, which describes the magnetostatic behavior of the fields and currents. This equation differs in sign from the wave equation, so that the solutions are characteristically exponentials decreasing from the boundary surface toward the interior, and might be called the exponential equation.

Illustrations of the general results will be briefly noted for the film, circular cylinder and a particular oval-shaped cross section in which the exponential equation can be solved but for which the current density is not constant at the boundary.

The restriction to a situation described by the London equations is a serious one in the light of recent work on the surface energy between phases[5] and on the theories in which a variable order parameter (essentially variable Λ or λ) is introduced.[6] These treatments leave little doubt that additional terms must appear in the free energy expressions, which would have decisive effects on the phase transition. This fact is already indicated by the lack of absolute thermodynamic stability of a superconductor in a magnetic field when described by the London equations, as is brought out by London for the case of a film[7] and will be demonstrated more generally below. However, this is actually a case of metastability in that small changes of field configuration increase the Gibbs free energy, although large changes may decrease it. Thus the description by the London equations is not actually ruled out as a physical possibility by this argument unless there can be shown to exist other mechanisms or paths for altering the field configuration than those considered here, along which the free energy continually decreases.

The analysis on the basis of the London equations is useful, however, in that it constitutes a simple, self-consistent model of a superconductor which contains much of the actual physical behavior. Deviations from the behavior predicted will indicate what modifications should be made, but as yet it is not settled just what the proper modifications are. In addition, much attention has been devoted to this model in the development of the subject, and it is natural to wish to know its full consequences. Finally there may actually be situations in which the additional free energy terms are negligible, since the surface energy between phases decreases with increasing impurity content and may actually go negative.[8] In this case the present analysis would apply as it stands.

2. WORK EXPRESSIONS

Two simple expressions for the work dW done on (a length l of) the cylindrical specimen (Fig. 1) in an arbitrary infinitesimal change will be given in terms of the total flux through the specimen Φ and the magnetic moment $\mathbf{M}$, respectively. These are used later in defining the free energies.

The first expression, obtained by integrating the Poynting vector over the surface of the superconducting cylinder during the change (Appendix I), is

$$dW=(l/4\pi)H_e d\Phi, \tag{2.1}$$

where H_e is the external field, S the cross section, and

$$\Phi=\int_S H dS. \tag{2.2}$$

The second expression is derived from (2.1) by substituting the relation between $\mathbf{M}$ and Φ,

$$\mathbf{M}=(l\mathbf{k}/4\pi)\int_S (H-H_e)dS=(l\mathbf{k}/4\pi)(\Phi-H_eS), \tag{2.3}$$

[5] A. B. Pippard, Proc. Cambridge Phil. Soc. **47**, 617 (1951).

[6] L. Landau and V. Ginsburg, J. Exptl. Theoret. Phys. (U.S.S.R.) **20**, 1064 (1950); J. Bardeen (to be published).

[7] F. London, reference 2, p. 128.

[8] A. B. Pippard, reference 5, p. 624.

where $\mathbf{k}$ is a unit vector along the cylinder axis. Equation (2.3) may be derived (Appendix II) directly from the definition of magnetic moment in terms of current density $\mathbf{J}$:

$$\mathbf{M}=(1/2c)\int_V[\mathbf{R}\times\mathbf{J}]dV, \tag{2.4}$$

where the volume $V=lS$ and $\mathbf{R}$ is the radius vector of dV from an arbitrary origin.

Equation (2.3) has a simple interpretation in which a fictitious magnetization density $(H-H_e)/4\pi$ per unit volume is introduced in place of the currents, and H is considered to be the magnetic induction (i.e., the B vector) due to this magnetization. This interpretation may then be justified by showing that this magnetization actually leads to the assumed induction B.

Putting (2.3) into (2.1) gives the second form of the work expression

$$dW=H_e dM+(lS/4\pi)H_e dH_e. \tag{2.5}$$

3. THE FREE ENERGIES

The Helmholtz free energy or work function F is defined so that isothermal changes in F equal the work done on the system. It is convenient to subtract out the work done in building up the field H_e, leaving only terms referring to the specimen. Hence we write for isothermal changes

$$(dF)_T=(l/4\pi)H_e d\Phi-(lS/4\pi)H_e dH_e=H_e dM, \tag{3.1}$$

which gives on integration

$$F(H_e, T)=F(0, T)+(l/4\pi)\int_0^\Phi H_e d\Phi-lSH_e^2/8\pi. \tag{3.2}$$

Assuming now that the field configuration in the superconductor is unaltered, except in amplitude, as H_e increases (linearity of the field equations), (3.2) becomes

$$\begin{aligned}F(H_e, T)&=F(0, T)+(lH_e\Phi/8\pi)-(lSH_e^2/8\pi)\\&=F(0, T)+(H_e M/2).\end{aligned} \tag{3.3}$$

A Gibbs free energy or Gibbs function G for this system in which the intensive variables are T and H_e,[9] may be defined in terms of F by

$$\begin{aligned}G(H_e, T)&\equiv F(H_e, T)-H_e M\\&=F(H_e, T)-(lH_e/4\pi)(\Phi-H_e S);\end{aligned} \tag{3.4}$$

hence, using (3.3),

$$\begin{aligned}G(H_e, T)&=F(0, T)-H_e M/2\\&=F(0, T)-(lH_e/8\pi)(\Phi-H_e S).\end{aligned} \tag{3.5}$$

For isothermal changes

$$(dG)_T=-MdH_e=-(l/4\pi)(\Phi-H_e S)dH_e, \tag{3.6}$$

so that G remains constant in reversible isothermal changes at constant H_e and is therefore the appropriate function for discussing the phase change from the superconducting to the normal state. For irreversible processes (at constant T and H_e) G will of course decrease, and thermodynamic equilibrium corresponds to a minimum for G.

The definitions of F and G given above do not depend on assumed density functions, but are given for the body as a whole. They are quite general in that they do not depend on any special form of the electrodynamic equations of the superconductor, but (3.3) and (3.5) require linearity of these equations.[10] Thus they apply to various modifications of the London equations, such as the integral relations recently suggested by Pippard.[11] Application of an integral relation derived from the London equations, will in the present case lead below to equivalent expressions for F and G with different, and in some ways more natural, density functions.

4. INTEGRAL RELATIONS FOR SOLUTIONS OF THE LONDON EQUATIONS

The London equations will now be assumed to describe the field configuration; only their magnetostatic form will be required. Thus $\mathbf{H}$ and $\mathbf{J}$ will satisfy at all times in the superconducting phase the equations

$$\nabla\times\mathbf{H}=(4\pi/c)\mathbf{J};\quad\text{(a)}\qquad \Lambda\nabla\times\mathbf{J}=-\mathbf{H}/c;\quad\text{(b)} \tag{4.1}$$

which lead to

$$\begin{aligned}&\nabla^2 H=\beta^2 H;&&\text{(a)}\\&\nabla^2\mathbf{J}=\beta^2\mathbf{J};&&\text{(b)}\\&\beta^2=(4\pi/\Lambda c^2)=(1/\lambda^2).&&\text{(c)}\end{aligned} \tag{4.2}$$

The boundary condition $H=H_e$ on C then determines the solution of the (scalar) two-dimensional exponential equation (4.2a) for H, in the cross section of the superconductor, and hence determines $\mathbf{J}$ by (4.1a) or (II.1) (Appendix II).

Then, using (II.1) for $\mathbf{J}$, (4.2a), and various vector (surface to line) integral theorems, one can show that

$$\begin{aligned}W&=l\int_S(H^2/8\pi+\Lambda J^2/2)dS &&\text{(a)}\\&=(l/8\pi\beta^2)\oint_C H(\partial H/\partial n)ds &&\text{(b)}\\&=(lH_e/2\beta^2 c)\oint J_e ds &&\text{(c)}\\&=(lH_e/8\pi)\int_S HdS, &&\text{(d)}\end{aligned} \tag{4.3}$$

[9] The pressure is assumed constant throughout the analysis and changes of volume are ignored.

[10] For nonlinear equations, (3.2) and (3.4) would give instead of (3.5), $G(H_e, T)=F(0, T)-(l/4\pi)\int_0^{H_e}\Phi dH_e+lSH_e^2/8\pi$. (3.6) remains the same, however.

[11] A. B. Pippard, Phys. Rev. **86**, 653 (1952).

where $J_s=(c/4\pi)(\partial H/\partial n)$ is the magnitude of $\mathbf{J}$ at the boundary C, and $\mathbf{n}$ the outward normal to C. W is the total work done on the superconductor in introducing the field H_e, as one sees by integrating (2.1) and comparing with (4.3d).

Similarly one may show that the first-order change in W, when H varies around the value satisfying (4.2a) and the corresponding $\mathbf{J}$ is determined by (II.1), is

$$\Delta W=l\Delta\int_S(H^2/8\pi+\Lambda J^2/2)dS$$
$$=(l/4\pi\beta^2)\oint_C\delta H(\partial H/\partial n)ds. \tag{4.4}$$

Thus the correct solutions of the London equations in S for which $H=H_e$ on C, (hence δH, the variation of H, vanishes on C) minimize W with respect to other fields and their corresponding currents.

5. THE PHASE TRANSITION CONDITION

To obtain the condition for onset of the phase transition, a formula is first obtained for the change in G when the cross section of the superconducting phase contracts and normal phase appears. In the normal phase, under static conditions, no currents will be present, so that by (II.1) $H=H_e$ throughout.

Consider a contraction of S to S', as in Fig. 2, where H and J are solutions of (4.2) in S, and H', J' the solutions in S', both with external field H_e. Then the change in G in the contraction is given by

$$\Delta G\equiv G_s(H_e,T;S')+G_n(H_e,T;\Delta S)-G_s(H_e,T;S). \tag{5.1}$$

The notation $G_s(H_e,T;S')$ means the Gibbs function of the region S' at external field H_e and temperature T in the superconducting state[12]; similarly subscript n refers to the normal state. Then using (3.5),

$$\Delta G=G_s(0,T;S')+G_n(0,T;\Delta S)-G_s(0,T;S)$$
$$-(lH_e/8\pi)\left(\int_{S'}H'dS-\int_S HdS\right)$$
$$-(lH_e^2/8\pi)\Delta S, \tag{5.2}$$

where use has been made of

$$G_n(H_e,T)=G_n(0,T)=F_n(0,T);$$

i.e., G_n is unaffected by the field. This follows from (3.5), since by (2.3) $M=0$ when $H=H_e$.

It is shown in Appendix III that

$$(H_e/4\pi)\left(\int_{S'}H'dS-\int_S HdS\right)$$
$$=\int_{\Delta S}(\Lambda J_e^2/2-H_e^2/8\pi)dS, \tag{5.3}$$

where the contraction ΔS is arbitrary but infinitesimal. Define the intrinsic free energy densities f_{s0}, f_{n0} (densities in absence of a field) by

$$G_s(0,T;S)=f_{s0}(T)S,\quad G_n(0,T;S)=f_{n0}(T)S, \tag{5.4}$$

and put (5.3) and (5.4) in (5.2) to obtain

$$\Delta G=l\int_{\Delta S}(f_{n0}(T)-f_0(T)-\tfrac{1}{2}\Lambda J_e^2)dS. \tag{5.5}$$

Equation (5.5) gives a simple general formula for the change in Gibbs free energy when an arbitrary contraction of the cross section occurs and normal phase appears. Since $f_{n0}(T)$ and $f_{s0}(T)$ are intrinsic properties of the material, independent of cross sections and fields, (5.5) states that when the current density J_e at some point on the boundary rises to a critical value characteristic of the material (at temperature T), no increase of G will result from creation of normal phase at that point.

Thus we deduce from (5.5) the critical current density condition[13] for first breakdown of superconductivity, which occurs when at some point of the boundary, J_e attains the value J_c defined by

$$\tfrac{1}{2}\Lambda J_c^2\equiv f_{n0}(T)-f_{s0}(T). \tag{5.6}$$

This current density must also be the value of the current density along any equilibrium boundary between superconducting and normal phase at this T; otherwise displacement of the boundary could lower G.

The free energy densities determined by (3.3) and (3.5) are somewhat arbitrary since by (4.3a, d) multiples of $(H^2/8\pi+\Lambda J^2/2-H_eH/8\pi)$ may be added to the density without affecting the integral over the cross section; hence the total free energy. Thus adding this quantity once gives for G_s, the Gibbs energy of a superconducting phase,[14]

$$G_s(H_e,T)=l\int_S g_s(H,T)dS, \tag{5.7}$$

$$g_s(H,T)=f_{s0}(T)+H^2/8\pi+\Lambda J^2/2$$
$$-H_eH/4\pi+H_e^2/8\pi. \tag{5.8}$$

Similarly for a normal phase, in which $H=H_e$, $J=0$, we have

$$G_n(H_e,T)=G_n(0,T)=l\int_S g_n(H,T)dS,$$
$$g_n(H,T)=f_{n0}(T). \tag{5.9}$$

Equation (5.8) and (5.9) with (5.6) show that with this

[12] The T will occasionally be dropped from the arguments when conditions are understood to be isothermal and temperature is not of interest; similarly with S.

[13] See reference 3. The proof here is quite different from H. London's since only the magnetostatic solutions are used, but less general. The formulation in terms of the Gibbs free energy makes the breakdown condition quite apparent.

[14] This form of the free energy density agrees with that of Landau and Ginsburg, reference 6, without the terms in the gradient of the order parameter, e.g., their Eq. (15). It is a direct consequence of starting with a Hamiltonian formulation of the energy.

definition of the Gibbs density functions, the densities are spatially continuous across the phase boundary. This is a natural property for a Gibbs function, which we expect to be unaffected by a phase transition, and so (5.8) seems to be the more desirable definition.[14]

The Helmholtz free energy may similarly be defined as

$$F_s(H_e, T)=l\int_S f_s(H, T)dS, \tag{5.10}$$

$$f_s(H, T)=f_{s0}(T)+H^2/8\pi+\Delta J^2/2-H_e^2/8\pi, \tag{5.11}$$

$$f_n(H, T)=f_{n0}(T). \tag{5.12}$$

Equation (5.11) gives the Helmholtz free energy density in a "natural," i.e., readily interpretable, form as a sum of field energy, $H^2/8\pi$, the kinetic energy of the currents, $\Delta J^2/2$, plus the intrinsic energy, $f_{s0}(T)$, and minus the field energy, $H_e^2/8\pi$, which would be present if no superconductor were present.

6. CRITICAL FIELDS AND BOUNDARY CURRENT DENSITIES

Three critical fields associated with the phase transition may now be defined. First for a massive superconductor of dimensions large compared to λ, H, and J will approach the simple exponential solutions of the infinite plane boundary, for which $\Delta J^2/2=H^2/8\pi$. Hence using (5.6), the external field, H_{cm}, giving rise to the critical boundary current density in a massive specimen, is given by

$$H_{cm}^2/8\pi=\tfrac{1}{2}\Delta J_c^2=f_{n0}(T)-f_{s0}(T). \tag{6.1}$$

Thus $H_{cm}(T)$ is an intrinsic property of the material, independent of shape.

The critical field H_c, at which first breakdown of superconductivity occurs is the field for which J_s reaches the value J_c given in (5.6) or (6.1), at some point of the boundary. H_c is in general both shape and temperature dependent.

At the third critical field H_{ct}, total conversion from superconducting phase to normal phase becomes thermodynamically favorable, which means that the Gibbs free energy is unaltered by this change.[15]

Certain relations among these three fields may be found and the general result will be shown that for convex cross sections,

$$H_{cm}<H_c<H_{ct}. \tag{6.2}$$

It is shown in Appendix IV that for convex cross sections,

$$H_e^2/8\pi-\Delta J_e^2/2>0. \tag{6.3}$$

Comparing (6.3) with (6.1) gives $H_c>H_{cm}$. However, if the specimen contains a convex cavity, the proof of (6.3) may be turned around to give

$$H_e^2/8\pi-\Delta J_e^2/2<0 \text{ (convex cavity)}. \tag{6.4}$$

Hence in such a cavity, or more generally, in a deep enough concavity of the outer boundary of S, $H_c<H_{cm}$.

To discuss H_{ct}, an equation is obtained from the defining condition, using (5.8) and (4.3a, d),

$$G_n(H_{ct}, T; S)-G_s(H_{ct}, T; S)$$
$$=lS(f_{n0}-f_{s0}-H_{ct}^2/8\pi)$$
$$+l\int_S(H^2/8\pi+\Delta J^2/2)dS=0, \tag{6.5}$$

which becomes, using (6.1),

$$H_{ct}^2/8\pi=H_{cm}^2/8\pi+(1/S)\int_S(H^2/8\pi+\Delta J^2/2)dS, \tag{6.6}$$

where H and J are the solutions in S for which $H_e=H_{ct}$. Evidently $H_{ct}>H_{cm}$ under all conditions.

Finally we expect that $H_{ct}>H_c$ on the general argument that one has $\Delta G=0$ for total conversion to normal phase only if the ΔG in the first part of the contraction is highly favorable, i.e., $\Delta G\ll 0$, to make up for the unfavorable change of G in the conversion of the last superconducting core, for which $J_e\ll J_c$. But at $H_e=H_c$, the ΔG for the first contraction is $\geqslant 0$, so that H_{ct} must be still larger. This argument would be precise only if we knew that J_s decreased at every point of the boundary as S contracted, so that ΔG would continually increase for every mode of contraction. However, J_s does not always decrease in a contraction, as will be illustrated later, and a more delicate argument is required.

Suppose $H_{ct}\leqslant H_c$ for cross section S. Consider a contraction of S to $S'=S-\Delta S$, at $H_e=H_{ct}$; then by (5.5)

$$\Delta G=G_s(H_{ct}; S')+G_n(H_{ct}; \Delta S)-G_s(H_{ct}; S)\geqslant 0, \tag{6.7}$$

since $J_s\leqslant J_c$ all along C. Subtracting (6.7) from (6.5)

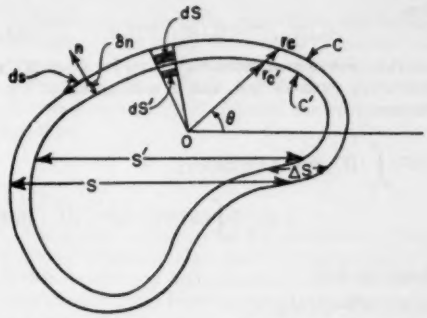

FIG. 2. Notation for a contraction of cross section and illustration of a semiconvex shape.

[14] H_{ct} is the critical threshold field used by F. London in reference 2 (pp. 131, 136), and justified there by surface energy considerations.

gives

$$G_n(H_{ct};S')-G_s(H_{ct},S')\leqslant 0. \tag{6.8}$$

But it is proved in Appendix IV that, for given H_e, a semiconvex cross section, and a uniform radial contraction,

$$(1/S')\int_{S'}(H'^2/8\pi+\Lambda J'^2/2)dS > (1/S)\int(H^2/8\pi+\Lambda J^2/2)dS. \tag{6.9}$$

Hence, by (6.5)

$$G_n(H_{ct};S')-G_s(H_{ct};S') > (S'/S)[G_n(H_{ct};S)-G_s(H_{ct};S)]=0. \tag{6.10}$$

Since (6.10) contradicts (6.8), we must have $H_{ct}>H_c$ for the semiconvex cross section.

Equation (6.9) may also be combined with (6.6) to show that H_{ct} continually increases as S contracts.

Although J_s does not decrease at every point as S contracts for given H_e, an average result follows from (6.3) and (4.3c), namely, for convex S

$$W'-W=\frac{lH_e}{2\beta^2c}\left(\oint_{C'}J_s'ds-\oint_C J_s ds\right)<0. \tag{6.11}$$

On the other hand, (6.9) gives a limit to the rate of decrease of J_s, at least for uniform contractions, since, using (4.3c),

$$\frac{W'}{S'}-\frac{W}{S}=\frac{lH_e}{2\beta^2c}\left(\frac{1}{S'}\oint_{C'}J_s'ds-\frac{1}{S}\oint_C J_s ds\right)>0. \tag{6.12}$$

Using (4.3d), (6.9) also states that for given H_e the flux of H diminishes less rapidly than the cross section, i.e., $(\Phi'/S')>(\Phi/S)$.

7. ILLUSTRATIONS OF THE GENERAL FORMULAS

Explicit formulas for the various quantities introduced above can be given in a few simple cases, and serve to illustrate and verify the general relations. Results are therefore briefly tabulated for the film, circular cylinder, circular-cylindrical cavity, and a special oval cross section defined below.

The general relations (7.1), (7.2) express Φ, M, G_s, F_s in terms of W, so that only W need be given, i.e.,

$$W=lH_e\Phi/8\pi=H_eM/2+H_e^2V/8\pi, \tag{7.1}$$

$$G_s=2Vf_{s0}-F_s=V(f_{s0}+H_e^2/8\pi)-W. \tag{7.2}$$

For a film of thickness $2a$, the fields are

$$H_z=H_e\cosh\beta x/\cosh\beta a,\qquad J_y=-(H_e c\beta/4\pi)\sinh\beta x/\cosh\beta a, \tag{7.3}$$

and for a section of width w, length along the field l, and volume $V=2awl$, (7.3) gives

$$W=(VH_e^2/8\pi)\tanh\beta a/\beta a, \tag{7.4}$$

$$H_{cm}=H_c\tanh\beta a=H_{ct}[1-(\tanh\beta a/\beta a)]^{\frac{1}{2}}. \tag{7.5}$$

Similarly for a circular cylinder of diameter $2a$,

$$H_z=H_eI_0(\beta r)/I_0(\beta a),\qquad J_\theta=-(c\beta H_e/4\pi)I_1(\beta r)/I_0(\beta a), \tag{7.6}$$

where I_0 and I_1 are the modified Bessel functions of the first kind.[16] For length l and volume $V=\pi a^2l$,

$$W=(VH_e^2/8\pi)2I_1(\beta a)/\beta aI_0(\beta a), \tag{7.7}$$

$$H_{cm}=H_cI_1(\beta a)/I_0(\beta a)=H_{ct}\{1-[2I_1(\beta a)/\beta aI_0(\beta a)]\}^{\frac{1}{2}}. \tag{7.8}$$

The circular cylindrical cavity is conveniently used to illustrate that $H_c<H_{cm}$ at a sufficiently concave boundary, as in (6.4), in contrast to the relation at a convex surface. Thus the fields in a massive superconductor surrounding a cylindrical cavity of radius a in which $H=H_e$, are

$$H_z(r)=H_eK_0(\beta r)/K_0(\beta a),\qquad J_\theta(r)=(c\beta H_e/4\pi)K_1(\beta r)/K_0(\beta a), \tag{7.9}$$

where K_0 and K_1 are the modified Bessel functions of the second kind. Then (6.4) is easily verified, since

$$(4\pi\Lambda)^{\frac{1}{2}}J_e(a)/H_e=K_1(\beta a)/K_0(\beta a)>1. \tag{7.10}$$

Equation (7.10) also shows that $J_e(a)$, the current density at the cavity surface, becomes indefinitely large as $a\to 0$, since

$$K_1(\beta a)/K_0(\beta a)\to[1/\beta a\ln(1/\beta a)]. \tag{7.11}$$

Evidently then for any value of H_e, the critical current density will be exceeded around a sufficiently small hole. Thus the superconductor is unstable with respect to penetration of flux and formation of normal phase in the interior, a well-known difficulty of this model of a superconductor. The lowest G in any external field will, in fact, correspond to uniform field $H=H_e$ and $J=0$ inside the specimen (which are solutions of the London equations), but with the material remaining in the superconducting phase. Writing (5.7), (5.8) in the form

$$G_s=l\int_S[(H-H_e)^2/8\pi+\Lambda J^2/2+f_{s0}]dS$$

clearly leads to this conclusion. To attain this state, the specimen would have to break into a fine structure of infinitesimal normal and superconducting regions, with the former of higher order than the latter, as pointed out by F. London for the film.[17]

[16] $I_p(z)=e^{-p\pi i/2}J_p(iz)$; $-\pi\leqslant$ phase $z\leqslant\pi/2$; where J_p is the Bessel function of the first kind and order p.

[17] F. London, reference 2, p. 128.

However, the superconductor in the state described by the London equations is actually in a metastable state for $H_e<H_c$ since any penetration of flux and formation of normal phase at the boundary increases G by (5.5), so that there is a potential barrier to attainment of the state of lowest G value. However, this barrier may be less for other modes of flux penetration than considered here, e.g., lateral penetration of a thin film.[18]

The final example differs from the previous cases in that the boundary current density J_e is not uniform, permitting greater generality. The contour of S is defined by

$$R\cosh\beta_x x\cosh\beta_y y=1, \quad \beta_x^2+\beta_y^2=\beta^2, \tag{7.12}$$

and depends on two parameters, R and β_y. For $\beta_y\ll\beta$, S is long and thin and becomes a film for $\beta_y=0$. The field

$$H=H_eR\cosh\beta_x x\cosh\beta_y y \tag{7.13}$$

satisfies $\nabla^2H=\beta^2H$, and the boundary condition. $\mathbf{J}$ follows from (7.13) by (II.1). Then

$$W=(lH_e/2\pi\beta_x\beta_y)\{K([1-R^2]^{\frac{1}{2}})-E([1-R^2]^{\frac{1}{2}})\}$$

$$=(lH_e/2\beta^2c)\oint_C J_e ds, \tag{7.14}$$

where K and E are complete elliptic integrals of modulus $[1-R^2]^{\frac{1}{2}}$.

A contraction of S may be obtained by increasing β_y and R such that x_0, the x intercept, remains constant, but y_0, the y intercept, decreases, where

$$\beta_x x_0=\beta_y y_0=\cosh^{-1}(1/R). \tag{7.15}$$

Then if $\beta_y\ll\beta$,

$$J_e(0, y_0)=(cH_e/4\pi)\beta_y[1-R^2]^{\frac{1}{2}} \tag{7.16}$$

will increase, since the increase in R is second order. However,

$$J_e(x_0, 0)=(cH_e/4\pi)\beta_x[1-R^2]^{\frac{1}{2}}$$

will decrease, as will $\oint_C J_e ds$ in (7.14).

The general behavior of J_e for given H_e seems to be qualitatively accounted for by the notion of shielding from penetration of the fields present at neighboring boundaries. Thus decreased shielding of a boundary point results from making the specimen thinner or more convex at this point and decreases J_e. Conversely, greater concavity, as on a concave boundary, increases J_e relative to H_e. In the example above, the decreased convexity of the sharp point when contracted more than made up for the reduction in size of S as a whole.

The author is indebted to J. Bardeen for valuable discussion and to A. B. Pippard for comments and criticism.

[18] This metastability assumes that penetration at the boundary produces normal phase and not a fine structure which has the lower free energy of superconducting phase. An additional assumption is needed here to make the model consistent; thus we could assume that superconducting or normal regions can only form greater than a minimum size, which could be arbitrarily small as long as it is finite. Metastability with respect to a fine structure of this minimum size would then exist. Once the fine structure formed at a certain field strength, it would not disappear on decreasing the field, since the lowest Gibbs energy was already attained, and no Meissner effect would be expected.

APPENDIX I

Proof of (2.1).

The general expression for the work done on length l of the superconducting cylinder by the sources of the field in an arbitrary change in time dt may be obtained from the flux of the Poynting vector through the outer surface σ (Fig. 1),

$$dW=-dt\int_\sigma(c/4\pi)[\mathbf{E}\times\mathbf{H}]\cdot\mathbf{n}d\sigma$$

$$=-(cldt/4\pi)\oint_C[\mathbf{E}\times\mathbf{H}_e]\cdot\mathbf{n}ds, \tag{I.1}$$

where $\mathbf{H}_e$ is the uniform external field parallel to the cylinder axis. Transforming the integral by taking the constant vector $\mathbf{H}_e$ outside, using the fact that $\mathbf{E}$ is in the plane of the cross section, substituting the induction law, and applying Stoke's theorem, we obtain

$$dW=(l/4\pi)H_e dt\int_S\dot{H}dS=(l/4\pi)H_e d\Phi. \tag{I.2}$$

APPENDIX II

Proof of (2.3).

The current density $\mathbf{J}$ is given by the Maxwell equation

$$\mathbf{J}=(c/4\pi)\nabla\times\mathbf{H}=(c/4\pi)\nabla H\times\mathbf{k}, \tag{II.1}$$

where H is the scalar magnitude of the field $\mathbf{H}$ and $\mathbf{k}$ is a unit vector along $\mathbf{H}$ (and the cylinder axis). Thus $\mathbf{J}$ is entirely in the cross section and tangential at the boundary, since H is constant on the boundary. Then using (II.1), a form of Stoke's theorem, and that H is constant on C, we have

$$\int_V\mathbf{J}dV=l\int_S\mathbf{J}dS=-lc/4\pi\oint_C H\mathbf{d}\mathbf{s}=0. \tag{II.2}$$

From (II.2) it follows easily that $\mathbf{M}$ is independent of origin; hence, using an origin in each S, $\mathbf{M}$ is seen to be parallel to the axis. The following transformations then lead to (2.3):

$$\mathbf{M}=(1/2c)\int_V[\mathbf{R}\times\mathbf{J}]dV$$

$$=(l/2c)(c/4\pi)\int_S\mathbf{r}\times[\nabla H\times\mathbf{k}]dS \tag{II.3}$$

($\mathbf{r}$ is a radius vector in S, see Fig. 1)

$$
\begin{aligned}
&= -(l\mathbf{k}/8\pi)\int_S \mathbf{r}\cdot\nabla H dS \\
&= -(l\mathbf{k}/8\pi)\int_S [\nabla\cdot(\mathbf{r}H) - H\nabla\cdot\mathbf{r}]dS \\
&= -(l\mathbf{k}/8\pi)\left(\oint_C H\mathbf{n}\cdot\mathbf{r}ds - 2\int_S HdS\right) \\
&= -(l\mathbf{k}/8\pi)\left(H_e\oint_C [\mathbf{r}\times d\mathbf{s}]\cdot\mathbf{k} - 2\int_S HdS\right) \\
&= -(l\mathbf{k}/8\pi)\left(2H_eS - 2\int_S HdS\right) \\
&= (l\mathbf{k}/4\pi)\int_S (H - H_e)dS.
\end{aligned}
\tag{II.4}
$$

APPENDIX III

Proof of (5.3)

From (4.3, a, d), assuming ΔS is infinitesimal (see Fig. 2),

$$
\frac{H_e}{8\pi}\left(\int_{S'} H'dS - \int_S HdS\right) = \frac{W'-W}{l}
$$

$$
= \int_{S'}\left(\frac{H'^2}{8\pi} + \frac{\Delta J'^2}{2}\right)dS - \int_S\left(\frac{H^2}{8\pi} + \frac{\Delta J^2}{2}\right)dS \tag{III.1}
$$

$$
= \int_{S'}\left(\frac{H'^2}{8\pi} + \frac{\Delta J'^2}{2} - \frac{H^2}{8\pi} - \frac{\Delta J^2}{2}\right)dS
$$

$$
- \int_{\Delta S}\left(\frac{H_e^2}{8\pi} + \frac{\Delta J_e^2}{2}\right)dS. \tag{III.2}
$$

Now consider H and J as the variation of H', J' within S' and apply the variational theorem (4.4) to give

$$
\frac{W'-W}{l} = \frac{1}{8\pi\beta^2}\oint_{C'}(H'-H)\frac{\partial H}{\partial n}ds
$$

$$
- \int_{\Delta S}\left(\frac{H_e^2}{8\pi} + \frac{\Delta J_e^2}{2}\right)dS. \tag{III.3}
$$

Putting $H'-H = (\partial H/\partial n)|\delta n|$, $|\delta n|ds = dS$ (the contraction is assumed locally flat), and $(\beta^2/8\pi)(\partial H/\partial n)^2 = \Delta J_e^2/2$ in (III.3), where $|\delta n|$ is the distance between C and C' along the normal, gives the desired result:

$$
\frac{H_e}{8\pi}\left(\int_{S'} H'dS - \int_S HdS\right) = \int_{\Delta S}\left(\frac{\Delta J_e^2}{2} - \frac{H_e^2}{8\pi}\right)dS. \tag{III.4}
$$

APPENDIX IV

Proof of (6.3).

Choose an origin O in S (Fig. 2) from which any radius cuts C and C' in only one point (cross sections for which this is possible might be called semiconvex) and define $\alpha = (r_{C'}/r_C) \leqslant 1$, where $\mathbf{r}_{C'}$ is the radius to C', $\mathbf{r}_C$ to C, both at angle θ. Let H, J be the correct field and corresponding current in S, and H' and J' for S'. Define a field $H_1'(\mathbf{r}')$ by means of the contraction α which sends $\mathbf{r}$ into $\mathbf{r}'$, translating the values of H unchanged, and let J_1' be the corresponding current. Thus

$$
H_1'(\mathbf{r}') = H_1'(\mathbf{r}\alpha) = H(\mathbf{r}), \tag{IV.1}
$$

and

$$
J_1'(\mathbf{r}') = (1/\alpha)J(\mathbf{r}), \tag{IV.2}
$$

since the same values of H are compressed in S' into a distance smaller by α (however, see below).

Then using (4.4), the theorem that H', J' minimize W' and that $\alpha^2 \leqslant 1$, we can write the inequality

$$
W'/l = \int_{S'}(H'^2/8\pi + \Delta J'^2/2)dS'
$$

$$
< \int_{S'}(H_1'^2/8\pi + \Delta J_1'^2/2)dS' \quad \text{(a)} \tag{IV.3}
$$

$$
= \int_S (H^2/8\pi + \Delta J^2/2\alpha^2)\alpha^2 dS \quad \text{(b)}
$$

$$
< \int_S (H^2/8\pi + \Delta J^2/2)dS = W/l \quad \text{(c)}
$$

(the area element in S' is written dS' to emphasize that it may be obtained by contraction of a corresponding element dS in S, where $dS' = \alpha^2 dS$). Hence, from (III.4) and (IV.3) using (4.3d),

$$
(W-W')/l = \int_{\Delta S}(H_e^2/8\pi - \Delta J_e^2/2)dS > 0. \tag{IV.4}
$$

If now (IV.4) holds for a localized infinitesimal ΔS, we have

$$
H_e^2/8\pi - \Delta J_e^2/2 > 0. \tag{IV.5}
$$

The proof of (6.9) proceeds similarly, but we now assume α is a constant, independent of θ, and define a field H_1 in S by expansion of the correct field values in S',

$$
H'(\mathbf{r}') = H_1(\mathbf{r}'/\alpha) = H_1(\mathbf{r}), \tag{IV.6}
$$

$$
J'(\mathbf{r}') = (1/\alpha)J_1(\mathbf{r}'/\alpha) = (1/\alpha)J_1(\mathbf{r}). \tag{IV.7}
$$

Then, using $\alpha < 1$ and the variational theorem (4.4),

we can write the inequality

$$(1/\alpha^2)\int_{S'}(H'^2/8\pi+\Delta J'^2/2)dS'$$

$$>\int_{S'}(H'^2/8\pi\alpha^2+\Delta J'^2/2)dS'$$

$$=\int_{S}(H_1^2/8\pi+\Delta J_1^2/2)dS$$

$$>\int_{S}(H^2/8\pi+\Delta J^2/2)dS. \quad \text{(IV.8)}$$

Since $\alpha^2=S'/S$, (IV.8) gives

$$(W'/S')>(W/S). \quad \text{(IV.9)}$$

The proofs of the inequalities (IV.3) and (IV.8) apply strictly only for constant α. This still includes a large class of contractions, since the origin is arbitrary (provided it meets the semiconvexity condition) and α is arbitrary (between 0 and 1), and is adequate for the use made in (6.9) where establishing the contradiction between (6.10) and (6.8) for any contraction, including a uniform contraction, gives the desired result.

To establish (6.3) or (IV.5), however, requires that (IV.3) and (IV.4) hold for a different type of contraction, specifically for a local contraction ΔS such that J has throughout ΔS the single value J_e of that section of the boundary. In this case α is a function of θ such that α differs from unity over an infinitesimal range $\delta\theta$ and differs by an infinitesimal amount.

Now in general when α varies with θ, (IV.2) [similarly with (IV.7)], must be replaced by

$$J_1'(r',\theta)\equiv\frac{c}{4\pi}|\nabla_{r'}H_1'(r',\theta)|$$

$$=\frac{|J|}{\alpha}\left[1+\frac{-\frac{2}{r}\frac{\partial H}{\partial\theta}\frac{\partial H}{\partial r}\frac{1}{\alpha}\frac{\partial\alpha}{\partial\theta}+\left(\frac{\partial H}{\partial r}\right)^2\frac{1}{\alpha^2}\left(\frac{\partial\alpha}{\partial\theta}\right)^2}{\left(\frac{\partial H}{\partial r}\right)^2+\frac{1}{r^2}\left(\frac{\partial H}{\partial\theta}\right)^2}\right]^{\frac{1}{2}}, \quad \text{(IV.10)}$$

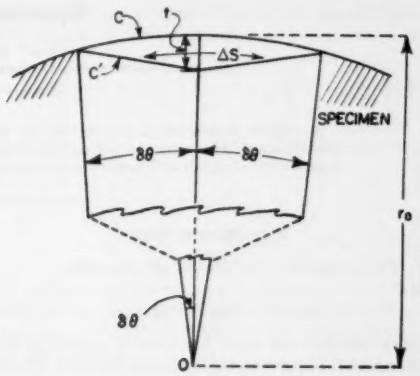

FIG. 3. Example of a flat, local, infinitesimal contraction of the cross section, required in the proof of (6.3).

where $H(r,\theta)$ is the proper field in S. The additional terms in (IV.10) vanish when $(\partial\alpha/\partial\theta)=0$, but in general will appear in (IV.3b) in a multiplier of J^2. The step (IV.3c) may still be justified, however, by showing that under certain conditions the additional terms do not unbalance the inequality. By a straightforward analysis of a flat, triangular contraction (Fig. 3) suitable for the proof of (6.3), a sufficient condition for (IV.3c) to hold may be shown to be $(1/\delta\theta)(4l/R_0/3r_0^2)^{\frac{1}{2}}<1$, where l, r_0, $\delta\theta$ are indicated in the figure and R_0 is the radius of curvature of the boundary at the point of interest. This condition requires that the curvature must be convex outward, that the contraction be sufficiently flat and small, and that the boundary be sufficiently smooth. In addition, it is plausible that a general infinitesimal contraction, which may be considered as made up of a large number of flat contractions meeting the above conditions, will also satisfy the desired inequality. Finally the derivation of the above condition suggests that even if the surface is locally concave, but not too concave, the inequality may be justified. Thus the general relation (IV.5) may also hold for semiconvex regions, although this has not been rigorously established.

Equivalent Potentials

RES JOST* AND WALTER KOHN†
Institute for Theoretical Physics, University of Copenhagen, Copenhagen, Denmark
(Received July 10, 1952)

An explicit construction is described for the entire class of potentials leading, for a particular angular momentum, to the same phase shift and energy spectrum as a given central potential. A similar procedure is applied to potentials with purely discrete spectra.

1. INTRODUCTION

LET us consider the Schrödinger equation

$$\varphi''(r)+E\varphi(r)=V_0(r)\varphi(r), \tag{1.1}$$

which describes the wave functions of a particle in a central field. In general, this equation leads to a discrete spectrum $E_i<0$ as well as a phase shift $\eta(E)$ for positive E. The question can then be asked whether this spectrum and phase shift can be reproduced by other "equivalent" potentials. In a previous paper[1] we have shown that in the case of m discrete eigenvalues the manifold of equivalent potentials is at most m-dimensional. We shall see in the present note that this manifold does in fact exist and can be easily constructed explicitly from the bound state solutions of the given potential V_0 [Eqs. (2.12), (2.10), and (2.29)]. The same is true for each higher angular momentum. However, under very general conditions, the phase shift and spectrum for any *two* angular momenta are compatible with at most one central potential.

The situation is similar in the case of a one-dimensional boundary value problem with a purely discrete spectrum. (We shall confine ourselves to the case where the wave function is required to vanish at the ends of the interval.) The equivalent potentials, i.e., potentials with the same spectrum, are then characterized by the values of a denumerably infinite set of parameters. Again explicit construction of these potentials is possible.

The case of a purely discrete spectrum has been the subject of an extensive investigation by Borg,[2] who confined himself to questions of existence and uniqueness. Very recently conditions for the existence of a boundary value problem corresponding to a given spectrum and given spectral constants [corresponding to our Γ_l, Eq. (3.5)] have been published by Gel'fand and Levitan.[3] The present work was stimulated by an interesting note[4] by Borg.

After completion of our investigation we received a manuscript by Holmberg,[5] which contains some of the results of the present paper.

2. SCATTERING PROBLEMS

We consider as an example the S-state radial Eq. (1.1) with a given potential $V_0(r)$ and corresponding spectrum $E_l=-\kappa_l^2$, $l=1, 2, \cdots, m$, and phase shift $\eta(k)$, $k=\sqrt{E}$.

Let $\psi_l(r)$ be the normalized bound state functions and $\psi(k, r)$ the continuum solutions normalized to $\sin(kr+\eta(k))$ at infinity. An infinitesimal change $\delta V(r)$ of the potential then produces the following changes of the eigenvalues and the phase shift:

$$\delta E_l=\int_0^\infty \delta V(r)[\psi_l(r)]^2dr, \tag{2.1}$$

$$\delta\eta(k)=-\frac{1}{k}\int_0^\infty \delta V(r)[\psi(k, r)]^2. \tag{2.2}$$

Thus the condition that the eigenvalues and phase shift remain unchanged is that $\delta V(r)$ be orthogonal to the squares of all the eigenfunctions.

We shall now verify that the functions $\psi_l'(r)\psi_l(r)$ have this property. Clearly,

$$\begin{aligned}
&\int_0^\infty \psi_l'\psi_l[\psi_m]^2dr \\
&=\frac{1}{2}\int_0^\infty \psi_l\psi_m[\psi_l'\psi_m+\psi_l\psi_m']dr \\
&\quad+\frac{1}{2}\int_0^\infty \psi_l\psi_m[\psi_l'\psi_m-\psi_l\psi_m']dr \\
&=\frac{1}{2}\int_0^\infty \psi_l\psi_m[\psi_l\psi_m]'dr+\tfrac{1}{2}(E_l-E_m) \\
&\quad\times\left[\int_0^\infty \psi_l(r')\psi_m(r')dr'\right]dr \\
&=\tfrac{1}{4}[\psi_l\psi_m]^2\Big|_0^\infty-\tfrac{1}{4}(E_l-E_m)\left[\int_r^\infty \psi_l\psi_m dr\right]^2=0,
\end{aligned} \tag{2.3}$$

where use has been made of the Schrödinger equation.

* Permanent address: Institute for Advanced Study, Princeton, New Jersey.
† On leave of absence from Carnegie Institute of Technology, Pittsburgh, Pennsylvania.
[1] R. Jost and W. Kohn, Phys. Rev. **87**, 979 (1952).
[2] G. Borg, Acta Math. **78**, 1 (1946).
[3] I. M. Gel'fand and B. M. Levitan, Doklady Akad. Nauk S.S.S.R. **77**, 557 (1951).
[4] G. Borg, Proceedings of the International Congress of Mathematics, Cambridge, Massachusetts, 1950, American Math. Soc. Providence, Rhode Island (unpublished).
[5] B. Holmberg, Nuovo cimento (to be published).

The same derivation holds when $\psi_m(r)$ is replaced by $\psi(k, r)$. This suggests that an m-dimensional manifold of potentials can be obtained from such infinitesimal increments by integration.

To carry out this integration it is convenient to work with the solutions $f(k, r)$, $\mathrm{Im}(k) \leqslant 0$ defined by

$$\lim_{r\to\infty} e^{ikr} f(k, r) = 1. \tag{2.4}$$

We fix our attention now on one of the bound state functions $f(-i\kappa_1, r) \equiv f_1(r)$ and look for the solution of the system of equations

$$\partial V(\lambda, r)/\partial\lambda = f_1(\lambda, r) f_1'(\lambda, r), \tag{2.5}$$

$$f_1''(\lambda, r) + E_1 f_1(\lambda, r) = V(\lambda, r) f_1(\lambda, r) \tag{2.6}$$

with the boundary conditions

$$V(0, r) = V_0(r), \quad f_1(0, r) = f_1(r) \tag{2.7}$$

and

$$\lim_{r\to\infty} e^{\kappa_1 r} f_1(\lambda, r) = 1. \tag{2.8}$$

Eliminating the potential from (2.5) and (2.6) gives

$$\frac{\partial}{\partial\lambda}\frac{f_1''(\lambda, r)}{f_1(\lambda, r)} = f_1'(\lambda, r) f_1(\lambda, r). \tag{2.9}$$

The solution of this equation satisfying (2.7) and (2.8) was obtained by a power series expansion in λ, every term being uniquely defined by the boundary conditions (2.7) and (2.8). The result is

$$f_1(\lambda, r) = f_1(r)/N(\lambda, r), \tag{2.10}$$

where

$$N(\lambda, r) = 1 + \frac{\lambda}{4}\int_r^\infty f_1^2(r')\,dr'. \tag{2.11}$$

By means of (2.6) this leads to the potential

$$V(\lambda, r) = V_0(r) + \frac{\lambda}{N} f_1(r) f_1'(r) + \frac{\lambda^2}{8N^2}[f_1(r)]^4. \tag{2.12}$$

It can be verified directly that (2.10) and (2.12) satisfy (2.5)–(2.8). Thus (2.12) constitutes a one parameter family of equivalent potentials. The conditions that the potential be regular requires that the variation of λ is restricted by

$$-4\left[\int_0^\infty f_1^2\,dr\right]^{-1} < \lambda < \infty.$$

To obtain further insight we shall construct explicitly the solutions $f(\lambda; k, r)$, for any k with $\mathrm{Im}(k) \leqslant 0$, corresponding to this family of phase equivalent potentials. An increment δV of the potential leads to

$$\delta f(k, r) = -\int_r^\infty G(k, r, r')\,\delta V(r') f(k, r')\,dr', \tag{2.13}$$

where the Greens function $G(k, r, r')$ is the solution of (1.1) defined by the initial values

$$G(k, r, r) = 0, \quad \left[\frac{\partial}{\partial r} G(k, r, r')\right]_{r=r'} = 1.^6 \tag{2.14}$$

From (2.5) and (2.13) one has therefore the equation

$$\frac{\partial f(\lambda; k, r)}{\partial\lambda} = -\int_r^\infty G(\lambda; k, r, r') f(\lambda; k, r') \times f_1(\lambda; r') f_1'(\lambda; r')\,dr'. \tag{2.15}$$

The integral can be evaluated in analogy with (2.3) by using the fact that G is a solution of the Schrödinger equation in r'.[7] The result simplifies by means of (2.14) and the equation

$$\left[\frac{\partial}{\partial r'} G(k, r, r')\right]_{r=r'} = -1 \tag{2.16}$$

to give

$$\frac{\partial f(\lambda; k, r)}{\partial\lambda} = -\frac{1}{4(k^2+\kappa_1^2)} f_1(\lambda; r) \times [f_1(\lambda; r) f'(\lambda; k, r) - f_1'(\lambda; r) f(\lambda; k, r)], \tag{2.17}$$

or equivalently,

$$\frac{\partial f(\lambda; k, r)}{\partial\lambda} = -\tfrac{1}{4} f_1(\lambda; r)\int_r^\infty f_1(\lambda; r') f(\lambda; k, r')\,dr'. \tag{2.18}$$

By putting $r = 0$ in (2.18) one obtains

$$\partial f(\lambda; k)/\partial\lambda = 0 \tag{2.19}$$

or

$$f(\lambda; k) = f(0, k) \equiv f(k). \tag{2.20}$$

Since $f(\lambda; k)$ determines the spectrum and phase shift, this equation confirms again the fact that we are dealing with a family of equivalent potentials. On the other hand, (2.17) leads to the interesting equation

$$\frac{\partial f'(\lambda; k, 0)}{\partial\lambda} = -\frac{1}{4(k^2+\kappa_1^2)}[f_1'(\lambda; 0)]^2 f(k), \tag{2.21}$$

which shows that all the $f_l'(\lambda; 0) \equiv f'(\lambda; -i\kappa_l, 0)$ stay constant except one, namely, $f_1'(\lambda; 0) \equiv f'(\lambda; -i\kappa_1, 0)$. This latter is according to (2.10) given by

$$f_1'(\lambda; 0) = f_1'(0) \Big/ \left[1 + \frac{\lambda}{4}\int_0^\infty [f_1(r)]^2\,dr\right]. \tag{2.22}$$

---

[6] $G(k, r, r')$ can be written as

$$G(k, r, r') = u(k, r) v(k, r') - u(k, r') v(k, r),$$

where u and v are those solutions of (1.1) defined by the initial values $u(k, 0) = 0$, $u'(k, 0) = 1$; $v(k, 0) = 1$, $v'(k, 0) = 0$.

[7] For this purpose one evaluates $\int_a^b \chi^2 f_1 f_1'\,dr$ where $\chi = \alpha G + \beta f$, as in (2.3) and then picks out the coefficient of $\alpha\beta$.

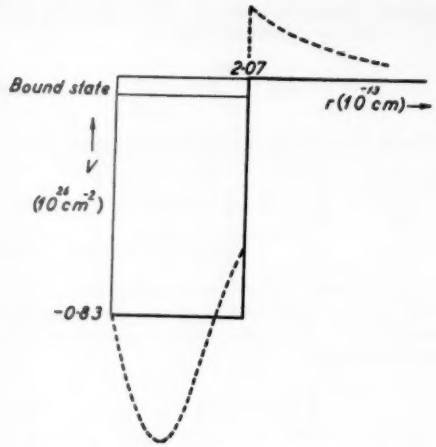

FIG. 1. The deuteron square well (——) and an equivalent potential (– – – –).

Introducing

$$\frac{1}{\Gamma_1(\lambda)} \equiv \int_0^\infty [f_1(\lambda; r)]^2 dr = \frac{1}{2i\kappa_1} \dot{f}(-i\kappa_1) f_1'(\lambda, 0), \quad (2.23)$$

where

$$\dot{f}(k) \equiv df(k)/dk \quad (2.24)$$

and the Schrödinger equation has been used, leads to

$$\lambda = 4[\Gamma_1(\lambda) - \Gamma_1(0)]. \quad (2.25)$$

As λ varies over its admissible range $-4\Gamma_1(0) < \lambda < \infty$, $\Gamma_1(\lambda)$ takes on all the values $0 < \Gamma_1(\lambda) < \infty$. Let us now generalize the definition (2.23) to the other bound state wave functions,

$$\frac{1}{\Gamma_l(\lambda)} \equiv \int_0^\infty [f_l(\lambda, r)]^2 dr = \frac{1}{2i\kappa_l} \dot{f}(-i\kappa_l) f'(\lambda, 0). \quad (2.26)$$

Then we have the following result: Each equivalent potential of the manifold (2.12) is characterized by the value of Γ_1, which varies in the range $0 < \Gamma_1 < \infty$ while all the other Γ_l are constant.

Furthermore, we may note that if one potential of this family satisfies the conditions

$$\int_0^\infty r |V(r)| dr < \infty \quad (2.27)$$

and

$$\int_0^\infty r^2 |V(r)| dr < \infty, \quad (2.28)$$

then, by (2.10), so do all the others.

In reference 1 we have proved that under the two last conditions a potential is uniquely defined by its phase, its discrete eigenvalues, and the m positive parameters Γ_l. It is therefore clear that by repeating the above construction (2.12) using the other discrete energy levels, we obtain the complete m-dimensional manifold of equivalent potentials. This construction can be explicitly performed since one can write down explicitly all the bound state functions for an arbitrary λ. In fact, integration of (2.18) leads to the following expression for the solution corresponding to arbitrary k:

$$f(\lambda; k, r) = f(0; k, r) - \frac{\lambda}{4N} f_1(r) \int_r^\infty f_1(r') f(0; k, r') dr', \quad (2.29)$$

which can be easily verified. It will be noticed that in the final equations (2.10), (2.12), and (2.29) the normalization of f_1 is irrelevant since it can be absorbed into the parameter λ.

For any higher angular momentum l, the results are completely analogous to those for S-states. Equations (2.10), (2.12), and (2.29), with the f's now denoting solutions of the radial equation for the given l, remain uncharged and lead to the totality of potentials equivalent for the l under consideration.

The following question then arises naturally: Given a potential V_0, is there another potential V_1 which leaves the spectrum and phase shifts corresponding to two angular momenta, say $l=0$ and $l=1$, unchanged?

Let us first consider the usual case where none of the S-eigenvalues $E_{i,S}$ coincide with a P-eigenvalue $E_{j,P}$. From our construction [see Eq. (2.12)] it follows that any potential V_S equivalent with V_0 as far as S-states are concerned has the property

$$\lim_{r\to\infty} V_S - V_0 / e^{-2\kappa_S r} = \text{constant}, \quad (2.30)$$

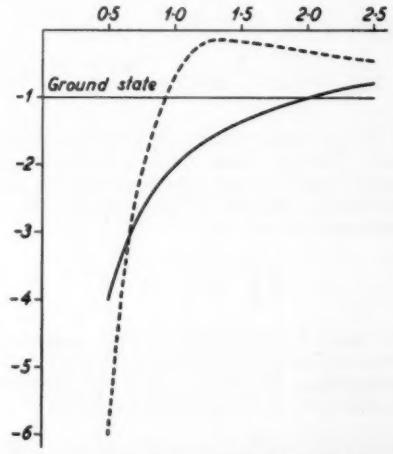

FIG. 2. The Coulomb potential (——) and an equivalent potential (– – – –).

where κ_S is the positive root of the smallest $|E_{l,S}|$ used in the construction of V_S. A corresponding result holds for any V_P reproducing the P-spectrum and phase shift. Since all $E_{l,S} \neq E_{l,P}$, $\kappa_S \neq \kappa_P$ so that $V_S \neq V_P$ unless $V_S = V_P = V_0$.

The same result can be obtained even when some of the eigenvalues coincide, provided that V_0 has an asymptotic expansion of the form

$$\sum_{s}^{\infty} a_s r^{-s}.$$

It can then be shown[9] that $f_{l,S}$ and $f_{l,P}$ have different asymptotic expansions and hence so do $V_S - V_0$ and $V_P - V_0$.

It is clear that even if V_0 falls off at infinity only like r^{-1}, Eqs. (2.10), (2.12), and (2.29) still lead to equivalent potentials.

Examples of potentials equivalent for S-states are shown in Figs. 1 and 2. They have been constructed by using the ground-state wave functions.

3. POTENTIALS WITH PURELY DISCRETE SPECTRUM

The boundary value problems which lead to purely discrete spectra fall into several subcases. We shall not make an extensive study of all of these but only exemplify the situation by discussing in some detail the case

$$\varphi''(r) + E\varphi(r) = V_0(r)\varphi(r), \tag{3.1}$$

$$\varphi(0) = \varphi(1) = 0, \tag{3.2}$$

where $V_0(r)$ is regular. We shall make a brief reference to the case of an infinite interval.

A solution of (3.1) which plays the same role as our previous function $f(k, r)$ of (2.4) can be chosen as $g(E, r)$ defined by the initial conditions

$$g(E, 0) = 0, \quad g'(E, 0) = 1. \tag{3.3}$$

The eigenvalues E_l of (3.1) and (3.2) are defined by

$$g(E_l, 1) = 0. \tag{3.4}$$

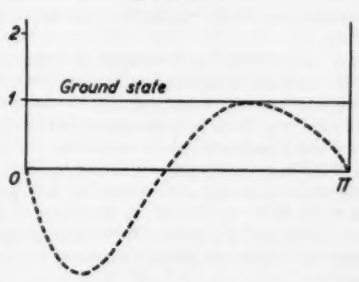

FIG. 3. The one-dimensional box (——) and an equivalent potential (– – – –).

[8] The a_s may, of course, all vanish as, for example, for cut-off or exponentially decreasing potentials.

[9] W. Sternberg, Math. Ann. **81**, 119 (1920).

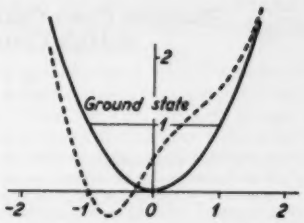

FIG. 4. The harmonic oscillator potential (——) and an equivalent potential (– – – –).

The eigenfunctions are $g(E_l, r) \equiv g_l(r)$, and we call

$$\frac{1}{\Gamma_l} \equiv \int^1 g_l^2 dr = g_l'(1)\dot{g}(E_l, 1), \tag{3.5}$$

where

$$\dot{g}(E, r) \equiv \partial g(E, r)/\partial E. \tag{3.6}$$

Again the expression g_l'/g_l is orthogonal to all the squares of the eigenfunctions and therefore—just as in Sec. 2—gives rise to a one parameter family of equivalent potentials

$$V(\lambda, r) = V_0(r) + \frac{\lambda}{4} g_1'(r) g_1(r) + \frac{\lambda^2}{8N^2}[g_1(r)]^2, \tag{3.7}$$

$$N(\lambda, r) = 1 - \frac{\lambda}{4}\int_0^r [g_1(r')]^2 dr', \tag{3.8}$$

with the solutions

$$g(\lambda; E, r) = g(0; E, r) + \frac{\lambda}{4N} g_1(r) \int_0^r g_1(r') g(0; E, r') dr'. \tag{3.9}$$

From (3.9) and (3.5) it follows that the Γ_l, $l \neq 1$ are independent of λ whereas Γ_1 varies from 0 to ∞ as λ varies from $-4\Gamma_1(0)$ to ∞. Again the manifolds of potentials and solutions, (3.7) and (3.9) are independent of the normalization of $g_l(r)$.

By an obvious modification of appendix II of reference 1 it can be shown that in the present case an equivalent potential is completely determined by the infinite set of parameters Γ_l, $l = 1, 2, \cdots$. Hence, by repeating the above construction procedure using the other eigenvalues any equivalent potential can be constructed.[10]

Also for the case of an infinite interval (e.g., the harmonic oscillator) Eqs. (3.7) to (3.9) lead to equivalent potentials, the normalization of $g_l(r)$ being arbitrary.

Potentials equivalent to a one-dimensional "box" and to a harmonic oscillator potential are shown in Figs. 3 and 4. They have been constructed by means of the ground-state wave functions.

It is a pleasure to thank Professor Niels Bohr for extending to us the hospitality of his institute.

[10] We assume here, without proof, that the process of adjusting successive Γ_l converges, under reasonable conditions, as $l \to \infty$.

Emulsion Cloud-Chamber Observations on the Interactions of High Energy Primary Cosmic Radiation*

M. F. KAPLON AND D. M. RITSON
University of Rochester, Rochester, New York

(Received June 9, 1952)

The initial investigations with the emulsion cloud chamber are surveyed. A study of some "purely electronic" showers is presented and an upper limit on the electron-photon component of the primary radiation is given as ≤ 2 percent of the proton component at energies in excess of $\sim 3\times 10^{11}$ ev. High energy nuclear interactions occurring in brass are discussed, and evidence is presented for the similarity of nucleon-nucleon and nucleon-nucleus interactions at very high energies. A study of the soft radiation produced in these interactions gives a ratio of neutral mesons to charged particles of 0.5. The primary proton spectrum is extended to energies of approximately 5×10^{12} ev, and evidence is presented for the constancy of the α-particle to proton ratio in the primary flux up to these energies.

I. INTRODUCTION

HIGH energy nuclear interactions are characterized by their resultant mixed shower cascades consisting of penetrating (nucleonic and mesonic) and soft (electronic) components. Interactions whose energies are greater than approximately 5×10^{11} ev have been previously studied by a variety of techniques: cloud chambers, counters, and photographic emulsions. Cloud chambers and counter systems have the great advantage of automatic selection (by a suitable triggering mechanism) but suffer from their lack of high resolution; usually only the resultant cascade is observed but not the initiating event. The photographic emulsion is capable of extremely high resolution and allows a detailed study of the primary interaction but suffers the lack of a method of systematic selection of events; previously high energy events have been found in photographic emulsions only in the course of surveys of many cubic centimeters of emulsion. We describe here a technique of observing high energy nuclear interactions which has the advantage of both systematic selection and high resolution.

Sensitive nuclear emulsions are exposed in an emulsion cloud chamber consisting of carefully aligned alternate layers of absorber and emulsion. A high energy particle interacts in the absorber; the emulsions directly below the absorber in which the interaction occurs show mainly the charged component produced in this interaction. Further down in the emulsion-absorber stack the electronic component begins to multiply and form well-marked electronic showers. These electronic showers form the basis for the systematic selection of high energy events.

The experimental procedure to locate high energy events then consists of a systematic survey for electronic showers in one of the emulsions deep in the stack; if the plates are carefully aligned, it is then possible to trace the shower in succeeding and preceding emulsions. As the shower is traced back towards its origin, the electronic component diminishes, and an emulsion is reached in which the shower (now primarily pure penetrating component) first appears; this is usually near the origin of the shower (which occurs in the absorber directly above this emulsion), and the tracks in this emulsion project back to the point of origin. In this fashion all those showers are located which have an energy greater than a given value (the critical energy for selection being determined by the character of the absorber), whose zenith angles are less than some critical angle (dependent upon the geometry of the stack), and which are initiated in the absorbers above the scanned detection emulsion.

As stated above, the energy range for which this technique is applicable depends upon the material of which the stack is constructed. For the experiment described in this paper (brass absorbers) we do not observe the cores of electronic showers above the background of random tracks unless their energies are greater than $\sim 10^{11}$ ev: We find that a shower consisting of 5 or more parallel tracks within a radius of $\sim 100\mu$ can be detected in the emulsions exposed in this experiment; reference to Fig. 3 shows that this corresponds to a shower whose energy is $\gtrsim 10^{11}$ ev. In an arrangement consisting solely of photographic emulsion this limit would be as high as $\sim 5\times 10^{12}$ ev, while for very high Z materials (e.g., lead) this limit would be as low as $\sim 10^{10}$ ev.

When an emulsion cloud chamber is flown at high altitudes, the high energy interactions are produced by the latitude insensitive components of the primary cosmic-ray beam. With an arrangement of this type we obtain direct experimental data on the flux and composition of the high energy primary radiation[1] (Sec. VII), information concerning the nature of the primary interactions[2] (Sec. V) as well as an estimate on the lifetime of the neutral π-meson.[3] Pure electronic showers are observed (events not directly connected to a nuclear

* This work was supported by the AEC.

[1] Kaplon, Ritson, and Woodruff, Phys. Rev. **85**, 933 (1952). See reference 16.
[2] M. F. Kaplon and D. M. Ritson, Phys. Rev. **85**, 932 (1952). See reference 16.
[3] Kaplon, Peters, and Ritson, Phys. Rev. **85**, 900 (1952). See reference 16.

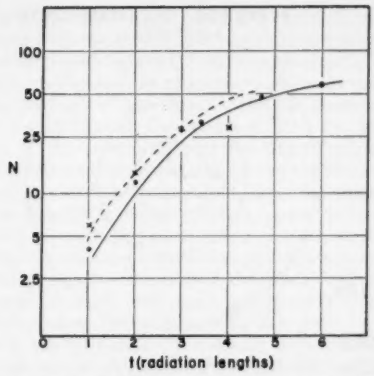

FIG. 1. Observed integral electron spectra for two different electron showers. The ordinate represents the total number of electrons exceeding the cut-off energy (defined by accepting electrons within a circle of 100 μ radius centered on the shower axis); the abscissa represents the distance in radiation lengths from the origin. The curves are the theoretical predictions normalized to the experimental data at their maxima. The dashed curve refers to a shower (×) of estimated energy $\sim 2.5\times 10^{11}$ ev and the solid curve (●) to a shower of $\sim 5\times 10^{11}$ ev.

interaction in the stack) which apparently arise from an incident electron or γ-ray. We are thus enabled to make a rather detailed study of soft shower development through several radiation lengths. These results are presented in Sec. III.

II. EXPERIMENTAL

We have extended our analysis on the emulsion cloud chamber used previously.[4] It consisted of a carefully aligned stack of 20 4-inch by 6-inch Ilford G-5 100-μ emulsions on 1.3-mm glass backing, separated by 3-mm brass absorbers (see Fig. 3 of reference 4). This arrangement was flow with the emulsion surfaces horizontal for six hours above 90,000 ft by a "Skyhook" balloon at White Sands, New Mexico (the actual flight curve is given in Fig. 2 of reference 4). The emulsions were processed by the usual methods of temperature development and after processing were cut to 3-inch by 2-inch size for microscopic observation.

The vertical spacing between successive emulsions in this experimental arrangement was 5 mm, consisting of 3 mm of brass, 1.3 mm of glass, 0.6 mm of air, and 0.1 mm of emulsion. The effective radiation length (X_0) for this combination of materials is 2.35 cm; thus, for vertical incidence 0.213 radiation lengths are traversed from plate to plate, and the entire stack in the vertical direction was 4.25 radiation lengths. The geometrical mean free path for nucleon interactions $\lambda_N[\sigma_N=\pi(1.45\times 10^{-13}A^{\frac{1}{3}})^2]$ for the above combination of materials is 16.6 cm; for vertical incidence 0.03 of a mean free path is traversed from plate to plate, and the entire stack in the vertical direction is 0.6 nuclear mean free paths. For α-particles[4] the entire stack is of the order of one mean free path.

The actual positioning of the plates during flight was determined by tracing G-rays (heavy primaries) through the stack. These particles provided straight marker lines which were used to determine the relative position of two plates. In order to predict with perfect accuracy the position of a track from one plate to the next the following details must be known:

(1) Lateral horizontal displacement of plates.
(2) Relative rotation of the plates.
(3) Spacing of the plates.
(4) Tilt of the plates.
(5) Deviations of the plates from perfect planes.

In principle, all five characteristics can be determined by setting up the equations derived from a series of G-rays passing through the plates; in practice corrections were applied only for errors due to (1). The errors due to causes (2)–(5) were minimized by the design of the stack but were in all cases of the order of the machining tolerances (several mils) involved in the construction of the brass plate assembly. In practice the precision to which the position of a track could be predicted was thus limited to a few hundred microns. This space resolution is not sufficient to completely eliminate confusion with background when tracing single minimum ionizing tracks from one plate to the next, but it is sufficient to enable one to trace unequivocally a group of several minimum ionizing tracks or a single high energy track of more than several times minimum ionization (e.g., α-particles or heavy primaries).

To use this emulsion-absorber arrangement to obtain information relevant to the high energy flux values, it was necessary to adopt criteria for shower selection to accomplish the following:

(a) Make certain that for each shower selected a primary particle could be found.
(b) Eliminate purely electronic showers.
(c) Work in a region of sufficiently high energy so that the scanning for showers is 100 percent efficient.

In order to meet the above conditions the following criteria were adopted:

(1) The zenith angle of the shower must be greater than some minimum value.
(2) The shower must either:
  (a) start 2 radiation units inside the stack;
  (b) be multicored;
  (c) or contain at least 6 collimated tracks in the first plate in which it is visible.
(3) The shower must either:
  (a) not die out within 3 radiation units;
  (b) or must be seen for at least 2 radiation units and further develop after this.

Criterion (1) is a scanning criterion and was adopted to decrease inefficiency due to increasing background and decreasing visibility of small zenith angle showers.

[4] Kaplon, Peters, Reynolds, and Ritson, Phys. Rev. 85, 295 (1952).

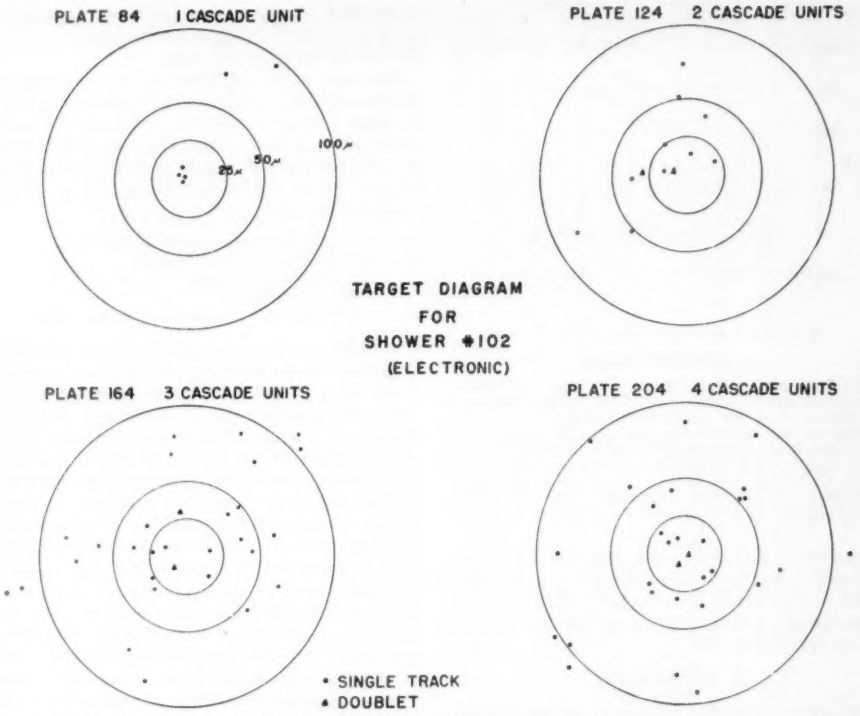

FIG. 2. Target diagrams for a typical electron shower at successive stages of its development. The points represent electron tracks projected onto a plane perpendicular to the shower axis, and the circles centered on the shower axis are of 25, 50, and 100 μ radius, respectively.

The second criterion was applied to eliminate purely electronic showers, and the third criterion was to insure that the energy cutoff is sufficiently high to make shower selection efficient. The criteria given above were adopted for selection of high energy nuclear events to obtain flux values; to obtain further events for studying the characteristics of these interactions certain of the above criteria were relaxed, particularly 2(a) and 2(b).

III. "PURELY ELECTRONIC" SHOWERS

In the introduction it was noted that electron showers were observed which were not associated directly with a nuclear event. These "purely electronic" showers apparently arise from electrons and photons incident from outside the stack. Unlike nuclear showers (see Sec. V) these events are characterized by their low initial multiplicity, in some cases originating from only a pair of minimum ionizing particles. We describe here observations on these events.

In an emulsion an electronic shower several radiation lengths from its origin appears as a highly compressed core of minimum ionizing tracks with a sharply decreasing density outside the core. This development can be described in the following qualitative fashion. The number of electrons with energies in the range E, $E+dE$ at a depth t from the point at which a photon of energy W_0 is incident on the absorber is given by the usual one-dimensional cascade function $\pi(W_0, E, t)$.[5] If in the high energy region (approximation A of reference 5) it is assumed that the lateral distribution of the electronic shower arises solely from the multiple Coulomb scattering,[6] the electrons of energy E will be spread over a circle whose radius is $\sim E_s/E$ radiation

[5] B. Rossi and K. Greisen, Revs. Modern Phys. **13**, 240 (1941).

[6] Though the assumption is commonly made that the lateral distribution of electrons in a cascade shower arises solely from multiple Coulomb scattering, this assumption does not appear completely justified. M. Stearns in Phys. Rev. **76**, 836 (1949) has shown that the angles characterizing the processes of pair formation and bremsstrahlung are $\sim(mc^2/E)\log(E/mc^2)$ radians; this is to be contrasted with the angle mc^2/E radians upon which the justification for neglecting the characteristic angular deviation as compared to multiple Coulomb scattering is usually made. For one radiation length the angle $(mc^2/E)\log(E/mc^2)$ is the same order of magnitude as the root mean square angle due to multiple scattering.

units ($E_s \sim 20$ Mev) and will make angles of $\sim E_s/E$ radians with the shower axis.[5] In this experiment, to eliminate the background of random minimum ionizing tracks, we imposed the restriction that tracks counted make an angle of less than 1° with the shower axis; this is equivalent on the average to $E>1$ Bev and to most of the observable electrons being confined to within 400 μ of the shower axis for the combination of materials used in this experiment. Thus the imposition of an angular or radial cutoff is equivalent on the average to restricting observations to electrons whose energy exceeds some cut-off value E_{c0}; this value E_{c0} is a very insensitive function of the depth t. If E_{c0} is assumed constant with depth and if the number of electrons whose energy exceeds E_{c0} at a given depth is known, the development of a shower can be calculated without any knowledge of the radial distribution in the shower. Thus,

$$N(W_0, E_{c0}, t) = \int_{E_{c0}}^{\infty} \pi(W_0, E', t) dE'$$

becomes in this approximation a function solely of the ratio W_0/E_{c0} and t; this function is that given by the one dimensional cascade theory.[5] Experimentally we determine the number of electrons N at a given depth t' and can therefore evaluate W_0/E_{c0}, thus enabling the behavior of the shower to be predicted at other depths t. In Fig. 1 is plotted the observed integral electron spectrum for two electronic showers and the integral spectrum derived theoretically.

The emulsion-absorber arrangement provided a convenient method for observing the lateral development of electron showers at varying depths t. This was accomplished by obtaining target diagrams (electron distributions projected onto the plane perpendicular to the shower axis) of several showers for different depths t. Figure 2 shows the target diagrams for a typical electron shower. This procedure gives directly the experimental core structure of the shower, that is, the number of electrons whose energy exceeds some cut-off energy E_{c0} contained within a radius R of the shower axis at a depth t. Though no completely satisfactory theory of the lateral development of soft showers has been developed (see also reference 6), the existing theories should give some agreement with the observed results. To this end we have used the theory developed by Fernbach and Eyges[7] in conjunction with the one-dimensional cascade theory[5,8] to calculate the structure function for the lateral structure of soft showers:

$$N_e(t, R, E_{\min}, W_0) = \int_{E_{\min}}^{\infty} dE \pi(W_0, E, t) \int_0^{RE/E_s} x P_R(x, s(t)) dx.$$

Here $P_R(ER/E_s, s)RdR$ is proportional to the fraction of electrons of energy E in the annular ring R, $R+dR$ at a depth t from the origin of the shower; s is defined by $\log(W_0/E)+\lambda'(s)t=0$.[5] $\pi(W_0, E, t)$ is the differential electron spectrum, and the structure function $N_e(t, R, E_{\min}, W_0)$ represents the number of electrons at a depth t and within a circle of radius R. The energy of these electrons is greater than $E_{\min}$ and they arise from an initial photon of energy W_0. The function N_e is relatively insensitive to the choice of $E_{\min}$, the major contributions arising from larger E. In Fig. 3 is plotted the structure function *versus* t parameterized for several values of R and W_0, and Figs. 4 and 5 show experimental core structures for several values of R as a

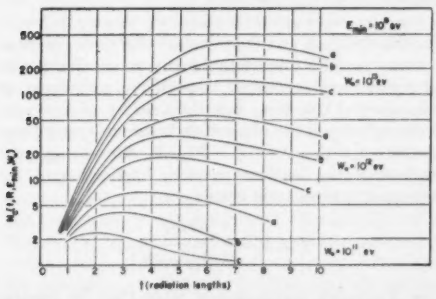

FIG. 3. The radial distribution function for photon initiated showers is plotted as ordinate *vs* radiation length as abscissa for different values of radii and incident photon energy. $N_e(t, R, E_{\min}, W_0)$ represents the number of electrons with energy in excess of $E_{\min}$ contained within a circle of radius R (centered on the shower axis) at a depth t (radian units) from the point at which a photon of energy W_0 is incident on the absorber. The curves a, b, c refer to radii of 25, 50, and 100 μ, respectively, for an absorber for which the radiation length $X_0=2.35$ cm. For other materials of radiation length X_0' cm, $R'(\mu)=(X_0'/2.35)R(\mu)$.

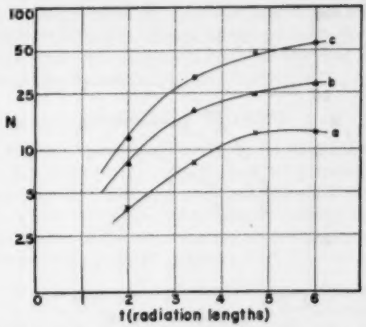

FIG. 4. Observed radial electron distributions for electron showers. The number of electrons contained within circles of radii 25, 50, and 100 μ (curves a, b, c) is plotted against the depth of the shower (radiation lengths). The shower energy is estimated $\sim 2.5\times 10^{11}$ ev.

[7] See S. Fernbach, Phys. Rev. **82**, 288 (1951).

[8] L. Janossy and H. Messel, Proc. Roy. Irish Acad. **54**, 31 (1951).

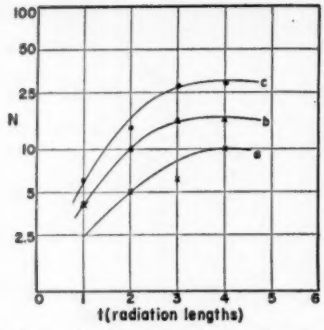

FIG. 5. Observed radial electron distributions for electron showers. The number of electrons contained within circles of radii 24, 50, and 100 μ (curves a, b, c) is plotted against the depth of the shower (radiation lengths). The shower energy is estimated $\sim 5\times 10^{11}$ ev.

function of t. It can be seen that the shape of these curves is similar to the theoretical curves of Fig. 3. This qualitative agreement does not necessarily imply the correctness of the form of P_R given by Fernbach and Eyges; the shape of N_e is relatively insensitive to the choice of P_R.

In order to make a more complete comparison with theory, both the energy and the point of origin of the shower must be known. A suitable event is furnished by the soft shower cascade observed in the "T-Star."[3] This is a double-cored soft shower arising from an energetic nuclear interaction and has been analyzed on the assumption of the two photon decay of a neutral π-meson. From opening angle and energy partition the total energy in the double cored soft shower was estimated as 1.5×10^{12} ev; using the above-mentioned calculation based on the theory of Fernbach and Eyges, we estimated 3×10^{12} ev. This discrepancy most probably arises from the fact that the calculations of radial distributions are rather inaccurate in the regions which make the major contributions to our results (small R and large E). Notwithstanding this numerical discrepancy of the order of two, the qualitative predictions are reasonably well in accord with the observations.

IV. ENERGY DETERMINATION IN NUCLEAR SHOWERS

Showers which originate from a high energy nuclear event (in contrast to "purely electronic" showers) are generally characterized by a multicored soft shower structure in the later stages of their development and by their characteristic appearance (large number of tracks projecting back to a unique origin) in the earliest observable stage.

There are three different methods that are of use in estimating the energy of high energy nuclear events in the photographic emulsion: measurement of multiple Coulomb scattering, kinematical estimate based on opening angles, and determination of the energy carried in the soft component. The applicability of each of these methods depends on the geometry and arrangement of the photographic emulsions during exposure and on the local geometry of the event with respect to the emulsion.

In order to employ fully the scattering method to determine the energies of individual tracks in high energy events extremely long path lengths must be available. With plates exposed in a horizontal geometry with respect to the source of the high energy primary particles, as in this experiment, this condition is never realized. The method of relative scattering[4] over long cell lengths is in principle applicable with our geometry, but from a practical point of view it is difficult to implement owing to the impossibility of successfully identifying the same group of minimum ionizing tracks when they are accompanied by a cascading electronic shower.

The kinematical method is most applicable, and the easiest to use for observations of high energy events in emulsions, being relatively insensitive to the particular geometry employed. Its main disadvantages lie in its inherent statistical nature and the necessity for making assumptions concerning the nature of the interaction in order to derive information relevant to the energy of the event.

The soft component method is most efficiently applicable for events of high enough energy such that the majority of the γ-rays associated with the event give rise to well-marked electronic cores. This method then requires some assumption concerning the characteristics of high energy nuclear events in order to infer their energy from the soft component energy. As the conditions of this experiment do not favor the scattering method we shall discuss only the kinematical and soft component methods.

For the kinematical analysis we assume nucleon-nucleon collisions and the existence of a center-of-mass system (c.m.) for discussing the interaction. We denote by ϑ and θ angles referred, respectively, to the c.m. or laboratory (l.) system; $\bar{\beta}$ is the velocity of the c.m., $\bar{\beta}_i$ the velocity of the ith particle in thec.m. system, and $\gamma=2\bar{\gamma}^2-1$[with $\bar{\gamma}^2=1/(1-\bar{\beta}^2)$] is the energy per nucleon of the incident particle. Application of the Lorentz transformation gives

$$\bar{\gamma}\tan\theta_i=\frac{\sin\vartheta_i}{(\bar{\beta}/\bar{\beta}_i+\cos\vartheta_i)}.$$

The reasonable assumption is made that the angular distribution of particles produced in the c.m. is symmetric about a plane transverse to the direction of motion of the incident particle; we find in the small angle approximation for laboratory angles

$$\bar{\gamma}^2\theta_p\theta_{1-p}=\frac{\sin^2\vartheta}{(\bar{\beta}^2/\bar{\beta}_0^2-\cos^2\vartheta)},$$

where the subscripts F, $1-F$ refer to the angles containing a fraction F, $1-F$ of the total number of produced particles and β_0 is the particle velocity, assumed equal for the angles ϑ and $\pi-\vartheta$. With the further assumption that $\beta/\beta_0 \approx 1$ we have in sufficient approximation $\gamma = 2/(\theta_F \theta_{1-F})$.

Kinematical energy estimates are usually made using the angle $\theta_{\frac{1}{2}}$ which involves the greatest statistical accuracy. Without prior knowledge concerning the angular distribution in the c.m. the use of the angle $\theta_{\frac{1}{2}}$ alone for an energy estimate is inherently bad. A distribution such as $\cos^2\vartheta$, for instance, in the c.m. gives in the l. system an extremely broad plateau in the neighborhood of $\theta_{\frac{1}{2}}$, so that it is possible to make an extremely gross error in energy estimate. Though the use of angles θ_F for $F \neq \frac{1}{2}$ involves greater statistical inaccuracy, one is at least enabled to obtain an internal consistency check on the energy estimate.

In order to obtain this internal check the normalized integral angular distribution in the l. system,

$$F(\theta_F) = \int_0^{\theta_F} N(\theta) d\theta / N,$$

is plotted *versus* $\log\theta_F$ (N refers to the number of charged shower particles). As $\log\gamma\theta_F = -\log\gamma\theta_{1-F}$, the plot will be symmetric with respect to reflections through the point $F=\frac{1}{2}$, $\log\theta_{\frac{1}{2}}$ as origin. The appearance of this symmetry property in our experimental angular distributions is consistent with the assumptions made concerning the c.m. distribution (but does not uniquely require this).

The method of the soft component is perhaps the most indirect of those available but has some fair degree of accuracy in the case of the highest energy events. In using this method it is assumed that the soft component resulting from high energy nuclear interactions is not directly produced but arises from the decay of some strongly coupled nuclear particle (e.g., π^0 mesons). When the energy carried by the soft component is determined, the energy of the initial event is inferred on the basis of some assumption concerning the equipartition of energy between the various produced particles (see Sec. VI).

There are two methods available to estimate the energy of the soft component. The first is applicable to the lower energy soft component, presumably arising from the decay of the slower π^0 mesons appearing at wide angles in the l. system and consists of determining the separation of relatively isolated doublets situated within a radiation length of the initial event. By assuming an average conversion behavior for the γ-rays the energy of the initiating photon can be estimated from the doublet separation.[9] The energy carried by the high energy soft component can be determined by applying the methods discussed in Sec. III.

[9] Bradt, Kaplon, and Peters, Helv. Phys. Acta 23, 24 (1950).

It has been found in some special events which are susceptible to a good measurement by both the kinematical and soft component methods that the energy estimates agree within the statistical limits.[3]

V. NUCLEAR SHOWERS

A scan for showers was made in the emulsion under the 12th brass plate; these showers were traced both deeper into the stack and back into the stack towards their point of origin. Qualitatively these showers exhibited one of the following characteristics in tracing back towards a point of origin:

(a) There was a gradual diminution of the number of minimum ionizing tracks from plate to plate until the shower consisted of only a few tracks and could not be followed further or

(b) the shower diminished in size, the multiplicity changing rather markedly from plete to plate until a plate was reached where the shower appeared as a rather compressed bundle of minimum ionizing tracks ($\sim$20 on the average); no shower of even small multiplicity was then found in the predicted region of the preceding plate.

Showers exhibiting characteristic (a) are considered to be of "purely electronic" origin (incident electron or γ-ray), while showers exhibiting characteristic (b) are considered to be of nuclear origin. A shower of nuclear origin containing on the average 5 or more neutral mesons in the central core will give rise to approximately 10 or more high energy γ-rays near the origin and will thus multiply more rapidly than a shower initiated by a single electron or γ-ray. The rapid change of multiplicity (b) is thus consistent with the assumption of the nuclear origin of these showers.

This argument is strengthened by the observation that for those showers selected as being of nuclear origin, many exhibited multicore characteristics, while no shower falling into the "purely electronic" class exhibited this characteristic. For those showers exhibiting nuclear characteristics a detailed search was made in the emulsion preceding its first appearance for a charged primary. Owing to the random background of minimum ionizing tracks, it was impossible to associate with certainty a single minimum ionizing track as being the incident primary for a given interaction; sometimes several tracks of the proper orientation were found within the predicted area (circle of $\sim 700\mu$ diameter). In those cases in which several tracks were found, any of which could possibly have been the minimum ionizing primary, their relative orientation was such that only one of them could be the desired primary; their spatial separation was also inconsistent with the possibility of any two or more of them being associated as a part of the shower. Thus it was possible to say that these showers made a transition from $\sim$20 particles to at most one particle in the preceding emulsion. This is consistent with a neutral or charged strongly interacting particle producing a high energy interaction in the intervening brass absorber. For those showers whose primaries had $Z>1$ it was always possible to uniquely

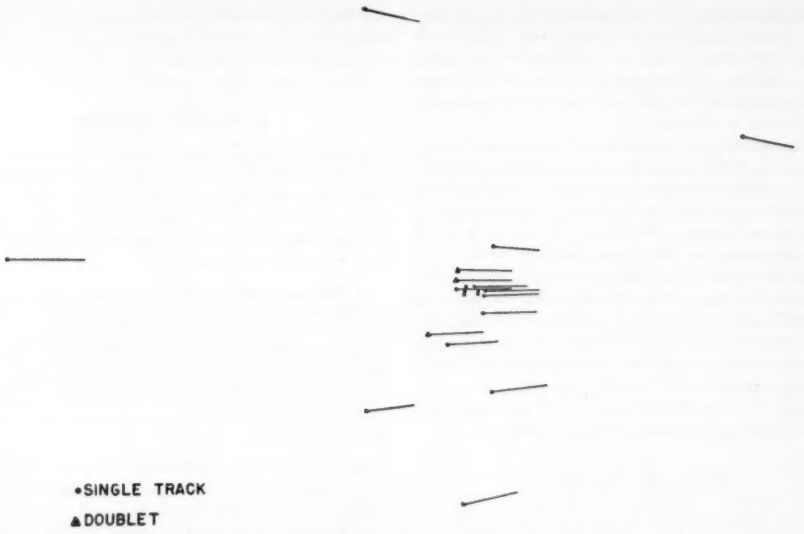

FIG. 6. Target diagram of the charged shower particles produced by an interaction in brass of an energetic cosmic-ray nucleon (shower 59 of Table I). The shower particles are projected onto a plane perpendicular to the shower axis.

locate that primary and trace it back to its point of entrance into the stack.

To extract information about the nuclear interaction, measurements were made on the shower in the emulsion directly below the absorber in which the interaction occurred. To accomplish this a target diagram of the shower was made; the entrance and exit points into and from the emulsion of those particles satisfying given geometrical criteria were accurately determined using a precision microscope stage. These tracks were then plotted as a target diagram; the plot may be direct (i.e., the shower projected onto the plane of the emulsion), but it is more convenient to project these tracks onto a plane perpendicular to the shower axis. These tracks were extended back along their trajectories and the showers of nuclear characteristics were found to project back to a common origin with the limits of accuracy of our measurements. Figures 6 and 8 are typical target diagrams for nuclear showers; Fig. 6 represents a shower made by singly charged or neutral primary, and Fig. 8 an interaction produced by a primary α-particle.

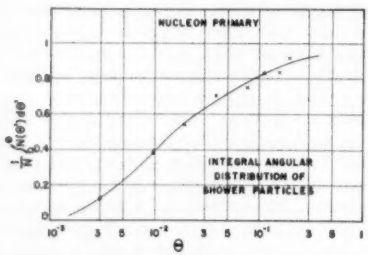

FIG. 7. Normalized integral angular distribution in the laboratory system for the shower of Fig. 6. The ordinate represents the fraction of the charged shower particles contained within the polar angle θ and is plotted *versus* logθ as abscissa.

The angular distribution of the shower particles in the laboratory system is obtained from the target diagram. By applying the kinematical methods of Sec. IV to these angular distributions an energy estimate for each shower was obtained. Figures 7 and 9 represent the normalized integral angular distributions in the l. system derived from the target diagrams of Figs. 6 and 8, respectively. The symmetry properties exhibited by these angular distributions are consistent with the assumptions underlying the kinematical method of energy estimate (see Sec. IV).

We have tacitly assumed in the above in deriving the angular distribution that the minimum ionizing tracks appearing in the first emulsion below the interaction are all shower particles emanating from the primary interaction. There are two possible sources of adulteration:

(a) conversion of γ-rays formed directly or indirectly in the primary interaction;
(b) particles produced in secondary nuclear interactions.

The contribution of electron-positron pairs from the conversion of meson "bremsstrahlung" can be neglected (see Sec. VI); those neutral mesons in the central

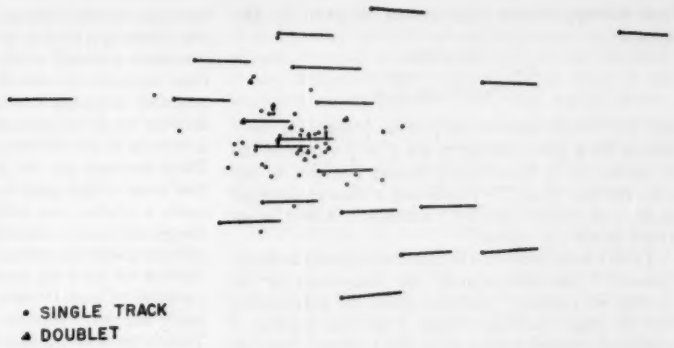

FIG. 8. Target diagram of the charged shower particles produced by an interaction in brass of an energetic cosmic-ray α-particle (shower A of Table I). The shower particles are projected onto a plane perpendicular to the shower axis.

shower core (average energy in the l. system $\sim 2-4 \times 10^{11}$ ev) have such a large Lorentz time dilation factor ($\sim 1-2.5\times 10^{2}$) that their decay into two γ-rays is sufficiently retarded (the π^0 lifetime is taken as $\sim 10^{-14}$ second[8]), so that they cannot contribute appreciably to the appearance of charged particles by pair conversion. If, however, an appreciable fraction of the soft component accompanying penetrating showers should arise from the decay of shorter lived strongly interacting particles, it is possible that the charged multiplicity we observe represents an upper limit to the actual charged multiplicity. The neutral mesons in the more diffuse part of the shower can, however, effectively decay immediately into two γ-rays; with our average conditions ($N_{ch}{}^{\text{diffuse}} \sim 10$) we have approximately 10 γ-rays traveling on the average 0.1 of a radiation length; since on the average one of these γ-rays may convert to an electron-positron pair, it is possible that two of the shower particles may in reality be electrons. The contribution of secondary interactions to the shower at its first point of observation can be neglected; secondary interactions from the diffuse shower particles are of relatively low energy and will not contribute shower particles of the proper orientation; any contributions from secondary interactions of the shower particles in the core (probability for interaction of all core particles is ~ 0.2) can be eliminated by their inability to project back to a common origin with the rest of the shower particles. We can conclude, therefore, that on the above assumptions as to the nature of the shower particles we observe an essentially unadulterated penetrating shower in the emulsion directly beneath that absorber in which the interaction occurs.

The analysis of the angular distribution in the first emulsion contains information relevant not only to the energy of the shower but also to the degree of anisotropy of the charged particle distribution in the c.m. system (we make here the same assumptions concerning the symmetry properties in the c.m. as in Sec. IV). A convenient parameter for characterizing the departure

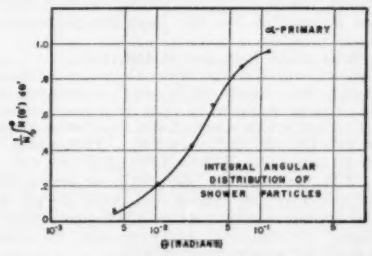

FIG. 9. Normalized integral angular distribution in the laboratory system for the shower of Fig. 8. The ordinate represents the fraction of the charged shower particles contained within the polar angle θ and is plotted *versus* logθ as abscissa.

TABLE I. Summary of high energy showers.

1 Shower, primary, target nucleus	2 Number of charged particles, N_{ch}	3 $\frac{N_{\pi^0}}{N_{ch}}$	4 $\gamma\times10^{-3}$	5 X	6 $\frac{r}{R}$	7 N_{ch} (Fermi)[b]
$A(\alpha)$, Cu	21(84)	0.6 ±0.2	3	1.17	0.18	15
178(α), Cu	23(92)	0.72±0.15	6	2	0.46	14
$R(\alpha)$,[c] Ag	14(56)	0.75±0.25	0.48	2.33	0.57	6.6
77(ρ), Cu	24	···	4	1.17	0.18	16.5
104(ρ), Cu	20	0.5 ±0.3	1.3	1.33	0.23	11.7
67(ρ,n)Cu	9	1.2 ±0.5	4.5	1.33	0.23	16
60(ρ,n)Cu	26	···	19.5	1.33	0.23	23
91(ρ,n)Cu	16	0.6 ±0.35	1.3	1.7	0.34	10.8
224(ρ,n)	24	···	1.8	1.9	0.42	11.6
63K(ρ,n)Cu	19	···	6.1	2.5	0.62	12
55K(ρ,n)Cu	18	···	1.29	3.3	0.73	6.1
17(ρ)Cu	24	1.1 ±0.3	5.1	3.7	0.76	7.9
72K(ρ,n)Cu	17	···	0.5	4	0.78	4.5
59(ρ,n)Cu	24	0.5 ±0.3	8.9	4	0.78	8.8
222(ρ,n)Cu	16	···	1	6	0.85	4.2
66(ρ,n)Cu	11	0.75±0.4	0.64	6.67	0.87	2.7
T(ρ)Cu	36	0.6 ±0.2	19.4	6.67	0.87	6.3
58K(ρ,n)Cu	15	···	30	8.7	0.9	8
179(ρ,n)Cu	24	···	0.8	20	≳1	2
67K(ρ,n)Cu	15	···	0.8	20	≳1	2
Z(ρ,n)Cu	15	0.5 ±0.25	50	24	≳1	3.4
184(ρ,n)Cu	10	···	5	33	≳1	2
45K(ρ,n)Cu	14	···	7.2	66	≳1	2
S(ρ)[d] light element	15	···	32	···	≳1	6
G-L(ρ)+Ag	18	···	23	≳9	≳1	6
		Av. 0.71±0.1				

[a] Uncorrected for secondary effects; see Sec. VI.
[b] See reference 11.
[c] See reference 9.
[d] See reference 13.
[e] See reference 14.

from isotropy in the c.m. system is given by the quantity

$$X=\frac{(\theta_{3/4}/\theta_{1/4})}{(\theta_{3/4}/\theta_{1/4})_{\text{Isotropic}}},$$

that is, X is the ratio of the $\frac{3}{4}$ to the $\frac{1}{4}$ widths in the l. system for a given shower to the $\frac{3}{4}$ to $\frac{1}{4}$ widths in the l. system for a hypothetical shower isotropic in the c.m. system. Thus $X\sim 1$ indicates a shower isotropic in the c.m. system and $X\ll 1$ indicates a shower anisotropic in the c.m. system.

Table I summarizes the results of the shower analysis. Column 1 identifies in order our designation for the shower, its primary appearing inside the parentheses, and the target nucleus; Column 2 the total number of observed charged shower particles; Column 3 the uncorrected ratio of neutral mesons to charged shower particles (see Sec. VI); Column 4 the energy per nucleon (γ) in the l. system in units of the nucleon rest mass of the initiating particle; Column 5 gives the parameter X measuring the departure of the angular distribution from isotropy in the c.m. system; Column 6 gives the impact parameter calculated from the Fermi theory[10] to give an X corresponding to that observed; and Column 7 gives the charged π-meson multiplicity calculated on the basis of Fermi's theory[11] using the energy (Column 4) and the impact parameter r/R (Column 6) as the two independent parameters.

Table I exhibits the following striking features:

(1) The similarities between high energy stars occurring in nucleon-nucleon collisions,[12,13] Ag,[13,14] and brass.

(2) The sidely varying degrees of anisotropy of those showers produced by single nucleons as compared to the isotropy of the α-particle showers.

(3) The relatively constant multiplicity of the α-particle showers.

In addition to these we have the symmetry property exhibited by the angular distribution in the l. system. These features can be rather well accounted for by adapting the statistical view presented by the Fermi theory.[10]

The similarities between the nucleon induced showers occurring in target nuclei of widely varying A indicate that subsequent collisions inside the nucleus do not contribute appreciably to the final multiplicity. The symmetry property exhibited by the angular distributions supports the view that the charged particles are produced in a single c.m. system and that their angular distribution in this system is symmetric about a plane transverse to the direction of motion of the c.m. system. These features can be explained on the assumption that most of the particles produced in an interaction inside a nucleus are sufficiently collimated in a high energy collision to interact simultaneously in the next collision inside the nucleus. On the Fermi theory[10,15] the collision of such an ensemble of particles might be expected to lead to very similar results to that of a single energetic particle interacting with a nucleon. Thus a nucleon-nucleus collision at sufficiently high energies can be effectively treated as a nucleon-nucleon collision, the only difference being in the relation of the velocity of the c.m. system to the velocity of the original primary nucleon. In the extreme case when all the particles emitted in the first interaction simultaneously collide with the next nucleon, the c.m. system for this second collision characterized by $\bar{\gamma}_2$ is related to the incident nucleon energy by $\gamma\approx 4\bar{\gamma}_2^2$; when this situation occurs n successive times the relation $\gamma\approx 2n\bar{\gamma}_n^2$ holds.[15a] These relations suggest that the primary energies listed in Column 4 of Table I, which are obtained from the relation $\gamma=2\bar{\gamma}^2$, may represent a lower limit to the actual primary energy (e.g., in brass n may reasonably be 3 or 4 and the true energies could be as high as 3 or 4 times those listed in Table I).[16] However, a definitive relation between the experimentally determined $\bar{\gamma}$ and the primary nucleon energy would depend on the fine details of each individual interaction, and thus we have adopted the relation $\gamma=2\bar{\gamma}^2$ to characterize the primary energy. (The estimate of our median acceptance energy for nuclear showers based on energy estimates for electron showers, Sec. VII, is in qualitative agreement with the median energy obtained for nuclear showers using the relation $\gamma=2\bar{\gamma}^2$.)

The features (2) and (3) lend further support to the view that at sufficiently high energies a nucleon-nucleus interaction can be effectively considered as a nucleon-nucleon interaction. On this basis the occurrence of

[10] E. Fermi, Phys. Rev. **81**, 683 (1951).

[11] The charged particle multiplicity is calculated on the basis of Fermi's theory assuming only π-mesons are produced. If one also allows for the production of nucleon-antinucleon pairs, the calculated charge multiplicity given is changed by the same factor (0.985) for each shower, independent of the impact parameter. In this case then according to the Fermi theory 40 percent of the charged particles are π^+ and π^- mesons and 60 percent of the charged particles are proton-antiproton pairs.

[12] Lord, Fainberg, and Schein, Phys. Rev. **80**, 970 (1950). The S-star is the first example observed of a star induced by a high energy proton and appears to have been formed in a glancing collision (single nucleon-nucleon) with a light nucleus of the emulsion.

[13] Two very high energy proton induced interactions occurring in emulsion have been recently observed at this laboratory; one occurs in a Ag nucleus, and the other has no black or gray prongs. Both exhibit similar characteristics to those described in the text.

[14] A. Gerosa and P. Levi-Setti, Nuovo cimento **8**, 601 (1951).

[15] U. Haber-Schaim, Phys. Rev. **84**, 1199 (1951).

[15a] Consider a collection of particles with energies and momenta E_i and P_i in the l. system and $\bar{E}_i$ and $\bar{P}_i$ in the c.m. system. Making a Lorentz transformation along the Z direction from the l. system to the c.m. with velocity $\bar{\beta}$ with respect to the l. system, we have $(\bar{\gamma}^2=1/(1-\bar{\beta}^2))$ $\Sigma_i\bar{P}_{i,z}=\bar{\gamma}(\Sigma_iP_{i,z}-\bar{\beta}\Sigma_iE_i)$. As the c.m. system is defined by $\Sigma_i\bar{P}_{i,z}=\Sigma_i\bar{P}_{i,y}=\Sigma_i\bar{P}_{i,z}=0$, we find $\bar{\beta}=P_{i,z}/\Sigma_iE_i$. For the specific case cited in the text for the nth collision with a nucleon $\Sigma_iE_i=E+nM$, where $E=\gamma M$ is the energy of the original incident nucleon and P its momentum, we find $\bar{\beta}_n=[P/(E+nM)]=(\gamma^2-1)^{\frac{1}{2}}/(\gamma+n)$ and $\bar{\gamma}_n^2=(\gamma+n)^2/(2n\gamma+n^2-1)$. For $\gamma\gg n$ we have $\gamma\approx 2n\bar{\gamma}_n^2$.

[16] These considerations apply to results previously reported, references 1, 2, and 3; in particular footnote 5 of reference 2 is in error, and the exponent in the integral primary proton flux will have larger limits of error.

widely varying degrees of anisotropy for nucleon induced showers is to be expected; if, however, the shower was produced in a series of collisions the angular distribution should tend to show a more "average" behavior. This "average" behavior is in fact observed for the α-particle induced showers in which we observe the sum behavior of 4 independently interacting nucleons. It is difficult to see any explanation of the above features on the basis of the plural theory[17] or any variant thereof.[18]

It is also of interest to consider the variation of multiplicity of shower particles as a function of the incident primary energy. We have analyzed the data of Pickup and Voyvodic[19] on lower energy emulsion showers by the kinematical methods of Sec. IV. Utilizing also the data of Perkins[20] in this lower energy region and considering the average behavior of the shower multiplicity in these different energy regions (we use $N_{ch} \approx 20$ at 4.5×10^{12}), we find that the shower multiplicity varies approximately as the $\frac{1}{4}$ power of the incident energy per nucleon (γ^1) in the l. system. For this variation of multiplicity with energy we find $N_{ch} \approx 2.5\gamma^{\frac{1}{4}}$ in agreement with the prediction of the Fermi theory of multiple meson production for 0 impact parameter; Fermi gives $N_{ch} = 2.3\gamma^{\frac{1}{4}}$. Furthermore, we do not observe any appreciable variation of multiplicity with impact parameter; the predictions of the Fermi theory in this respect probably result from the detailed assumptions made about the form of the equilibrium volume, and these assumptions do not represent a fundamental feature of the theory.

VI. RATIO OF NEUTRAL MESONS TO CHARGED PARTICLES

Observations made on the number of minimum ionizing tracks present in a shower immediately after interaction and after passage through a further small amount of absorber (some fraction of a radiation length) show that an appreciable multiplication has occurred. This multiplication arises from

(a) γ-rays converting to pairs with some subsequent cascade development;[21] these γ-rays can arise from neutral meson decay or from "bremsstrahlung" associated with the nuclear interaction. (We observe in fact that an appreciable fraction of the multiplication is in the form of pairs.)

(b) Mesons and nucleons created in a subsequent interaction by one of the penetrating shower particles.

To deduce from observations made on the increase in multiplicity the ratio of neutral mesons to charged particles we must therefore take into account the effect of the "bremsstrahlung" in (a) and the effect of the secondary multiplication in (b). The typical experimental conditions under which our observations were made were as follows: We scanned an area corresponding approximately to that defined by the median opening angle of the shower and observed the increase in multiplicity over $\sim\frac{1}{3}$ of a radiation length.

To determine the contribution of "bremsstrahlung" γ-rays to this increase, we note that only tracks lying within $\sim 2^\circ$ of the shower axis were observed. The average opening angle of an electron pair of energy E is $\sim (mc^2/E)\log(E/mc^2)$ radians,[6] and thus we observe pairs for which $E \gtrsim 50$ Mev. The fraction of energy radiated as "bremsstrahlung" in the c.m. system by a spin 0 meson of energy $\bar{E}_\mu$ (in the c.m.) is given by Schiff[22] as (α is the fine structure constant)

$$(\alpha/\pi)[\log(2\bar{E}_\mu/\mu c^2) - \tfrac{3}{2}].$$

We assume a normal "bremsstrahlung" spectrum in the l. system $dn_\gamma = K dw/w$, where w is the photon energy, the constant K is given by the expression above, and thus the number of γ-rays in the l. system with energies exceeding ~ 50 Mev arising from a single meson of energy $\bar{E}_\mu$ in the c.m. is given by

$$n_\gamma = (\alpha/\pi)[\log(2\bar{E}_\mu/\mu c^2) - \tfrac{3}{2}]\log(E_\mu/50 \text{ Mev}),$$

where E_μ is the meson energy in the l. system. For our average shower the charged multiplicity (N_{ch}) was ~ 20, $\bar{\gamma} \sim 50$, $\bar{E}_\mu \sim 3.3Mc^2$ (we assume a total multiplicity of $N \sim 30$) and $E_\mu \sim 270Mc^2$ (the assumption is made that ~ 0.8 of the total shower energy appears in the central core) for those mesons in the forward core. With these values $n_\gamma \sim 0.045$ and if two γ-rays are considered to originate from one neutral meson, the spurious neutral to charged ratio arising from meson "bremsstrahlung" is $0.045/2 \approx 0.02$.

The background due to secondary interactions is appreciably more important than that estimated above for "bremsstrahlung." To a good approximation (see Sec. IV) the fraction of shower particles falling in a given target area is proportional to $\frac{1}{3} + k\log(\theta/\theta_1)$ (we are assuming that the behavior of the angular distribution in the logarithmic plot can be approximated as

[17] W. Heitler and L. Janossy, Proc. Phys. Soc. (London) **A62**, 669 (1949).

[18] Messel, Potts, and McCusker (to be published).

[19] E. Pickup and L. Voyvodic, Phys. Rev. **82**, 265 (1951). Their data indicate a median charged multiplicity of ≈ 8 at energies of $\sim 10^{11}$ ev. (These refer to showers with $N_H = 0$.)

[20] D. H. Perkins, private communication. Perkins gives a median charged multiplicity of ≈ 13 at a median energy of $\sim 7 \times 10^{13}$ ev. (These refer to showers with $N_H \leq 5$.)

[21] To properly assess the cascade development for small radiation lengths ($t \leq 1$) we have performed a Monte Carlo calculation (in Approximation A of reference 5) in units of 1/20 of a radiation length up to one radiation length for photon induced showers. The process of electron-positron pair production by electrons (triplet process) was included in this calculation, the probability for this process being taken as 0.11 of that for pair production by a γ-ray (H. J. Bhabha, Proc. Roy. Soc. (London) **A152**, 559 (1935)). The distribution of the virtual photons responsible for this process was assumed to follow a bremsstrahlung distribution, the above cross section being calculated on this basis for all virtual photons whose energy is in excess of 10^{-4} of the incident photon energy. Energy partition in pair production by a γ-ray was taken into account using the curves on page 199 of Heitler's *Quantum Theory of Radiation* and all secondaries with energies $\geq 10^{-4}$ incident photon energy were accepted in the cascade. We find on the average 0.6 electron after $\frac{1}{3}$ a radiation length, 1.25 electrons after $\frac{2}{3}$ a radiation length, and 1.8 electrons after $\frac{3}{3}$ of a radiation length. It was found that the inclusion of the triplet process contributed negligibly.

[22] L. Schiff, Phys. Rev. **76**, 89 (1949).

a straight line in the neighborhood θ_1) where the area subtends an angle θ and the constant k is a function of the anisotropy of the shower. If $\langle\log(\theta/\theta_1)\rangle$ is determined, we can then estimate the average number of particles from secondary interactions falling in the target area. For our average conditions ($N_{ch}\sim 20$) there are approximately 10 charged secondaries near the shower axis whose average energy is of the order of $\frac{1}{15}$ of the primary energy. Thus the characteristic angle for the secondary interaction, taking into account the fact that mesons are now the primary particles, is $\theta_1^S\sim 4\theta_1^P$. Under the average geometry of our experiment, the angle subtended by the observation area at the point of secondary interaction is $\theta^S\sim 3\theta_1^P$; thus $\langle\log\theta^S/\theta_1^S\rangle\approx -0.3$ and $K\sim 0.6$ so that $\sim\frac{1}{3}$ of the secondary particles will fall in the shower area. The probability of a collision in the $\frac{1}{3}$ of a radiation unit is 0.05 per particle (geometrical cross section assumed), and the number of particles produced in the secondary interaction is $N_{ch}^S\approx 20/18^1=10$ (see Sec. V). Therefore, one charged shower particle will produce on the average in $\frac{1}{3}$ of a radiation length (0.17) charged secondaries in the observation area. As one γ-ray in $\frac{1}{3}$ of a radiation length produces on the average 0.6 secondaries,[21] the average number of spurious γ-rays is 0.28 or the spurious neutral to charged ratio from this source is 0.14.

The actual determinations of the neutral to charged ratio (Column 3 of Table I) for the showers observed were made without the above corrections but allowing for soft cascade multiplication.[21] The average figure of 0.71 ± 0.1 must now be corrected by subtracting the total correction of 0.16 due to causes (a) and (b) given above and the contribution due to background. It is difficult properly to assess the contribution of background due to the acceptance criteria being in a certain measure subjective in application; a conservative estimate of this contribution indicates that the error introduced in the neutral to charged ratio is less than 15 percent. The final value for the ratio of neutral mesons to charged particles is thus 0.49 ± 0.1 (calculated assuming a 10 percent background). In arriving at this figure we have not, however, taken into account any secondary nuclear multiplication by strongly interacting neutral particles (e.g., neutrons). It seems probable that this source does not contribute appreciably to secondary multiplication.[23,24] This source would, however, tend to lower the neutral to charged ratio. On the other hand, as the charged particle group probably contains some protons (in approximately equal numbers as neutrons) the ratio of neutral mesons to charged mesons should be equal to or greater than the neutral meson to charged ratio.

If we now consider the value 0.49 ± 0.1 representing the neutral meson to charged particle ratio[24a] and if the reasonable assumption is made that at sufficiently high energies π^0, π^+, and π^- mesons are produced with equal probability (such as predicted by the Fermi theory) we can conclude that particles other than π-mesons are inefficiently produced in this energy region; if 15 percent of the charged shower particles are protons[22] and an equal number of neutrons we predict that under our experimental conditions $N(\pi^0)/N_{ch}\approx 0.47$. If, however, the true value is 0.39 (probability of $\sim\frac{1}{3}$) then 22 percent of the charged particles can be other than π-mesons.[24]

VII. THE FLUX OF THE HIGH ENERGY RADIATION

In order to obtain data relevant to the high energy flux of the primary radiation, we have applied the selection criteria of Sec. II to an area of 70 cm^2 in the middle of the emulsion-absorber stack. This area is so located that it presents an approximately spherical geometry in the upper hemisphere to the primary radiation as well as allowing for an efficient selection of showers. Detailed examination of the showers falling in this area showed that 8 were of nuclear origin with a nucleon primary ($Z\leq 1$, see Secs. II and V) and 6 were "purely electronic" showers.

The energy of these showers has been estimated by the methods outlined previously (Sec. IV), and we find from kinematic considerations a median energy of $\sim 4.5\times 10^{12}$ ev. Using an absorption mean free path for nucleons in air of 100 g/cm^2 and geometrical interaction mean free path in the emulsion-absorber stack and with the further assumption of an isotropic flux over the upper hemisphere, the integral primary flux of nucleons at the top of the atmosphere with energies in excess of $\sim 4.5\times 10^{12}$ ev is 0.04 ± 0.015 nucleons per meter^2 per steradian per second. Assuming a power law for the integral primary spectrum and using the known values at low energies,[25] we find the integral exponent to be 1.45. Taking into account the fluctuations in the median

[23] Camerini, Davies, Fowler, Franzinetti, Muirhead, Lock, Perkins, and Yekutiel, Phil. Mag. **42**, 1241 (1951).

[24] This would indicate that at least within the context of the Fermi theory the production of nucleon-antinucleon pairs is unlikely; the Fermi theory predicts (see reference 11) that if the equilibrium state is reached 60 percent of the charged particles are proton-antiproton pairs. However, the Fermi theory predicts also in this case a rather copious production of neutron-antineutron pairs; these could contribute to the apparent charged multiplication by their secondary interactions. If we assume that that our average shower of 20 charged particles consists of $8\pi^+$ and π^- mesons and 12 charged nucleons, the Fermi theory in this form would predict a neutral to charged ratio of 0.2. If we then take into account the contribution of the 12 neutral nucleons to secondary interactions, we find that our observed neutral to charged ratio could be as low as 0.40 ± 0.1. Though we cannot therefore conclusively rule out the equilibrium production of nucleon-antinucleon pairs, it would appear that it is unlikely.

[24a] We have, in the analysis of this section, profited by a discussion with Professor B. Peters. The value of the neutral to charged ratio is relatively sensitive to both the results of cascade theory at small radiation lengths and the lifetime of the neutral π-meson. If an attempt is made to account for the finite lifetime of the π^0 meson by an analysis similar to that given in reference 9 (taking into account at the same time the results of the Monte Carlo calculation for the soft cascade), the ratio obtained above corresponds to a π^0 lifetime of less than 0.5×10^{-14} sec. A lifetime of 10^{-14} sec could give a ratio as high as 0.6 ± 0.1 on this type of analysis, and longer lifetimes would lead to still higher values.

[25] Winckler, Stix, Dwight, and Sabin, Phys. Rev. **79**, 656 (1950).

energy we find that the exponent could possibly be as low as 1.2 and as high as 1.65.[16]

In a survey including an additional 70 cm² at the same level in the stack, we find two α-particle induced showers with energies per nucleon in the same range as the nucleon induced showers. Though the statistics are low and the inclusion of the additional area makes the geometry less susceptible to a clean analysis, we believe that the existence of these two high energy α-particle showers is significant and indicates that the relative flux of α-particles to protons at this energy is approximately 10 percent. This figure is in agreement with the ratio of α-particles to protons in the latitude sensitive region and is compatible with results reported previously, which indicate a similar velocity spectrum for all components of the primary beam.[4] If this feature is maintained over the entire spectrum of particles making up the primary beam for all energies, it would indicate that the index in the power spectrum must have an extremely weak dependence on the density and path length traversed through matter in the acceleration region; e.g., in Fermi's theory of the origin of cosmic rays[26] the integral exponent γ in the power spectrum depends on the density in such a way that $\gamma_P/\gamma_\alpha = \lambda_\alpha/\lambda_P$, where λ is the absorption mean free path. As $\lambda_\alpha \sim \frac{1}{2}\lambda_P$ we find that the ratio of protons to α-particles, $N_P/N_\alpha \sim 8\times10^5$ at the energies of this experiment; the differentiation with respect to heavier nuclei would be even more extreme.

It is further possible to obtain an upper limit to the incident soft radiation for a higher energy range than heretofore reported.[27] We found that approximately $\frac{1}{2}$ of the showers observed efficiently were of a "purely electronic" nature. By using a minimum for shower density acceptance in the control area of 70 cm² to assure 100 percent detection efficiency, we estimated that all electronic showers whose energy is in excess of $\sim3\times10^{11}$ ev were detected efficiently. This estimate is in qualitative agreement with the energy estimated for the nuclear showers; we inferred a median energy of $\sim3\times10^{12}$ ev for nuclear showers which contained at least one electronic core in excess of $\sim3\times10^{11}$ ev; i.e., we estimated our average electron shower energy as being $\sim1/10$ of the average energy of the nuclear showers. Our area of 70 cm² contained 6 "purely electronic" showers with energies in excess of $\sim3\times10^{11}$ ev. As the conversion efficiency of the stack is 100 percent at this depth for electrons or photons, this corresponds to an incident flux at the flight altitude (18 g/cm² residual atmosphere) of 1.3×10^{-2} electrons and photons per meter² per second per steradian. If this is extrapolated to the top of the atmosphere, assuming an exponential absorption with a mean free path of 40 g/cm², we find that the flux of soft radiation incident at the top of the atmosphere is 2.5×10^{-2} particle per meter² per second per steradian. This figure represents in reality an upper limit, for if the soft component is in actuality incident in the form of some energy spectrum, the absorption mean free path would be longer than the interaction mean free path which is the figure used above; for an incident power spectrum of integral exponent 1.8 the absorption mean free path would be ~75 g/cm².[28] As the incident proton flux at this energy is 2.2 ± 0.9 particles per meter² per second per steradian, the incident primary flux of electrons and photons whose energy exceeds $\sim3\times10^{11}$ ev is $\lesssim2$ percent of the primary proton flux at this energy. It is not necessary, however, to assume an incident primary soft component to explain the observed electron showers; it can be accounted for in terms of the two-photon decay of π^0 mesons formed in nuclear interactions in the residual atmosphere above the flight altitude. The atmosphere above the stack in the vertical direction is equivalent in producing nuclear interactions to ≈70 percent of the matter in the stack. Thus for each interaction detected in the stack containing on the average two electronic cores, we expect 1.5 soft particles incident from the atmosphere into the stack.

We wish to thank Professor B. Peters, who was associated with this work in its early stages for his many valuable and constructive suggestions. We have enjoyed the opportunity of discussing this work with Professor E. P. George and Professor R. E. Marshak and wish to express our thanks for their comments and suggestions. We are indebted to Mrs. Edythe Woodruff for her assistance, especially in obtaining the data relevant to the high energy flux values; and for their invaluable assistance in scanning the plates we thank Mrs. Katherine Reynolds, Miss Barbara Hull, and Miss Katherine Merry.

[26] E. Fermi, Phys. Rev. **75**, 1169 (1949).
[27] Critchfield, Ney, and Oleska, Phys. Rev. **85**, 461 (1952).
[28] W. Heisenberg, *Cosmic Radiation* (Dover Publications, New York, 1946), p. 18.

The Atomic Heat of Silicon below 100°K*

N. PEARLMAN† AND P. H. KEESOM
Department of Physics, Purdue University, West Lafayette, Indiana
(Received July 7, 1952)

The atomic heat of Si containing less than 0.01 percent *P*-type impurities has been measured between 1°K and 100°K. Below 5°K, the atomic heat can be represented by the sum of a cubic term with Debye $\theta=658$°K, and a linear term equal to that of a highly degenerate "hole gas" with concentration about 10^{18} cm^{-3}. This is also the hole concentration calculated from Hall constant measurements on this material. The Debye θ calculated from elastic constants is 653°K, using a simplified procedure (described in Appendix II) based on the Hopf-Lechner method. The atomic heat is in reasonable agreement with measurements of Nernst and Schwers above 20°K, and of Anderson above 60°K. Above 5°K, θ decreases to a minimum of 456°K at $T=40$°K and then rises to 580°K at $T=100$°K.

The specific heat of glyptal lacquer, which was used to secure the heater and thermometer wires to the samples, was also measured. Below 15°K, it can be represented by

$$c=2.2\times10^{-4}T^3 \text{ joules/g deg},$$

and a table is given of values above this temperature.

I. INTRODUCTION

THE atomic heat of silicon between 1°K and 100°K has been measured as[1] part of a program of determining low temperature atomic heats in connection with irradiation studies.[1] Previous measurements, reported by Nernst and Schwers,[2] Magnus,[3] and Anderson,[4] have covered the temperature range above 20°K. Blackman and others[5] have succeeded in using the Born-von Kármán theory[6] to calculate vibration spectra in crystalline lattices. The vibration spectrum may then be used to calculate the atomic heat. Smith[7] has calculated the vibration spectrum for diamond which has the same crystal structure as Si. She has also calculated the dependence of the Debye temperature θ on absolute temperature and compared it with the observed dependence[8] in the case of diamond, down to 100°K, or about $\theta/20$. Our measurements on Si make it possible to judge if her results are applicable to the diamond lattice in general.

II. EXPERIMENT

A. Apparatus

The method used was similar to that of Nernst and Eucken.[9] The sample was suspended by threads inside a brass vacuum can. The cap of this can was soldered to a high vacuum pumping line, which had a U-section to act as a radiation trap. The electrical connections were brought out from the can through a Kovar-glass seal in its cap. Above 20°K, the sample was surrounded by a radiation shield, closed except for several small holes and having a heater wire attached. This facilitated measurements made between 20°K–50°K, and above 77°K.

Constantan heater wire (about 100 ohms per meter) was wound around the sample and attached with glyptal lacquer for heat contact. The thermometer wires were also wound on the sample and secured with glyptal. In the helium region, we used 0.05-mm phosphor-bronze wire, kindly supplied by Dr. K. W. Taconis of Leiden. In the hydrogen and nitrogen regions, we used 0.1-mm Pb wire. Above 20°K, the heater and thermometer wires were electrically insulated from the sample by cigarette paper. The increase in resistance of the sample with decreasing temperature made this unnecessary below 20°K.

B. Procedure

The rate of energy dissipation in the heater wire was determined by measuring the current passing through it and either the voltage across it or its resistance. Resistances of both heater and thermometer wires were measured by comparison with a standard 10-ohm resistor, using a Wenner potentiometer which had been certified by the National Bureau of Standards. Current and voltage were measured with instruments that had been calibrated with the standard resistor and the potentiometer. We estimate the over-all error in these measurements at about 0.3 percent.

Heating periods were begun and ended by a timing circuit which counts pulses produced photoelectrically by the pendulum of a clock. This circuit was arranged so that current could be supplied to the heater during periods which were multiples of ten seconds in length. The clock was checked against timing signals broad-

* Assisted by Signal Corps Contract.
† This article contains material from the thesis submitted by N. Pearlman to the Faculty of the Graduate School of Purdue University in partial fulfillment of the requirements for the Ph.D. degree, June, 1952.
[1] Assisted by AEC contract.
[2] W. Nernst and F. Schwers, Sitzber. preuss. Akad. Wiss., Physik-math. Kl., p. 355 (1914).
[3] A. Magnus, Ann. Physik **70**, 303 (1923).
[4] C. T. Anderson, J. Am. Chem. Soc. **52**, 2301 (1930).
[5] A bibliography is found in M. Blackman, Rept. Phys. Soc. Prog. Phys. **8**, 11 (1941). See also, e.g., E. W. Montroll, J. Chem. Phys. **10**, 218 (1942); **11**, 481 (1943); **12**, 98 (1944); **15**, 575 (1947); R. B. Leighton, Revs. Modern Phys. **20**, 165 (1948).
[6] M. Born and T. von Kármán, Physik. Z. **13**, 297 (1912); **14**, 15 (1913).
[7] H. M. J. Smith, Trans. Roy. Soc. (London) **A241**, 105 (1948).
[8] K. S. Pitzer, J. Chem. Phys. **6**, 68 (1938).
[9] A. Eucken, *Handbuch der Experimentalphysik* (Akademische Verlagsgesellschaft M.B.H., Leipzig, 1929), Vol. VIII-1.

cast by WWV, and the over-all error introduced by the timing circuit is estimated at not larger than 0.01 percent.

The thermometers were calibrated against the vapor pressures of the refrigerant liquids, using the 1939 scale for helium,[10] the NBS formula for hydrogen,[11] and the values published by Keesom and Bijl for nitrogen.[12] Above 2.2°K a correction was made to the vapor pressure above the liquid surface, to take into account the hydrostatic pressure due to the liquid above the vacuum can. When necessary, the resistance of the heater wire was also measured. The calibrations were made immediately prior to each series of heat capacity measurements. Occasionally, the calibration was checked after a run. The Pb thermometer was also compared several times with a helium gas thermometer.

It was found that the resistance-temperature curve of Pb could be approximated by a straight line above about 25°K. Below this temperature a smooth curve was drawn through the experimental calibration points. The phosphor-bronze curve was also linear below about 2°K; above this the curve could be represented by a parabola. The straight line and parabola agreed with the smooth curves drawn through the calibration points to within 0.1 percent or better. Hence, in the temperature regions where they were applicable, these expressions were used to convert resistances to temperatures and also to calculate dR/dT, which enters into the determination of ΔT, the temperature rise of the specimen resulting from heating. Between 10°K and 25°K, dR/dT was determined graphically from the Pb calibration curve.

At the conclusion of the calibration the helium gas, with which the calorimeter had been filled in order to provide heat contact between the thermometer and the bath, was pumped out and a vacuum of the order of 10^{-6} mm Hg maintained in the can. The timing circuit provided a pulse every ten seconds which was made audible by a small loudspeaker, and at every signal a galvanometer reading was taken. The galvanometer sensitivity was measured frequently, so that deflections could be converted to resistances, and hence to temperatures. The temperature drift, which was usually about 10^{-5}°K per second, was followed during a "fore-period" about 2–5 minutes long. The sample was then heated, usually for 10 or 20 seconds, producing a temperature rise of several hundredths of a degree, and thereafter the temperature drift was followed for several minutes during the "after-period." The change in temperature due to heating was determined by extrapolating the fore- and after-periods, usually to the middle of the heating period. An analysis of the heat exchange between the sample and its surroundings, including a correction for the lag of the galvanometer showed that at the lowest temperatures, the extrapolation should be carried to a point somewhat earlier than the middle of the heating period (see Appendix I). This procedure was checked by taking several points at approximately the same temperature, using different heating times and different heating currents.

C. Samples

Two samples were used, both kindly supplied by the Bell Telephone Laboratories. The first, Si I, weighed about 40 g and was stated to have an impurity concentration of about 1.5×10^{-4} percent B. Because of its small mass and the fact that its shape made it necessary to apply several tenths of a gram of glyptal to secure the heater and thermometer wires, it was impossible to measure its heat capacity accurately below 4°K. The other sample, Si II, weighed about 260 g, but its impurity concentration was not known. Its more suitable shape made it possible to use only a few mg of glyptal, and so results were obtained with this sample to below 1.5°K.

D. Measurements on Glyptal

In order to correct for the heat capacity of the glyptal, especially on the smaller sample, we measured the specific heat of glyptal from 4°K to 100°K. One set of measurements was made by adding extra glyptal to the small Si sample in several steps until a total of about 1 gram had been added. The total heat capacity was measured after each addition, and from these results the atomic heat of the Si as well as the specific heat of the glyptal could be calculated. This method gave results consistent among themselves at 4°K, and from 10 to 20°K. As an independent check, a copper disk weighing about 3 grams was coated with about 300 mg of glyptal, and the total heat capacity measured from 10 to 100°K. The heat capacity of the glyptal was about 50 percent of the total at 10°K and about 30 percent of the total at 100°K. In the overlapping temperature range, from 10 to 20°K, the two sets of results agreed to within about 15 percent.

The measured specific heat of glyptal, from which the correction was determined, could be represented below 15°K by the expression

$$c(\text{glyptal}) = 2.2\times10^{-4}\,T^2 \text{ joules/g deg.} \qquad (1)$$

Values above this temperature are given in Table I. The glyptal was air dried at room temperature after application. It is possible that different drying treatment might result in variations of polymerization which might be reflected in the specific heat. We would also like to point out that Eq. (1) is merely the simplest empirical relationship based on only a few points of not very high accuracy. Hence, while it is adequate for the required correction, any theoretical inference from its analytic form would be unwarranted.

[10] A table of T *versus* ϕ, based on this scale, has been issued by the Royal Society Mond Laboratory, Cambridge, England (1949).
[11] Woolley, Scott, and Brickwedde, J. Research Natl. Bur. Standards **41**, 379 (1948).
[12] W. H. Keesom and A. Bijl, Physica **4**, 305 (1937); Commun. Kamerlingh Onnes Lab., Leiden, No. 245d.

TABLE I. Specific heat of glyptal.

T°K	c joules/g degree
20	0.11
25	0.16
30	0.20
35	0.25
40	0.29
45	0.34
50	0.38
55	0.43
60	0.49
65	0.55
70	0.62
75	0.71
80	0.79
85	0.88
90	0.97
95	1.06
100	1.15

III. EXPERIMENTAL RESULTS

As mentioned above in Sec. II-C, measurements below 4°K were made only on Si II. Above 30°K, only Si I was measured. Between 10 and 30°K both were measured, and the values agreed to within the experimental error after the heat capacity of the smaller sample had been corrected for that of the glyptal used on it. The magnitude of this correction was almost 40 percent at 10°K, about 15 percent at 20°K, and about 2 percent at 100°K on the smaller sample. The correction for glyptal on the larger sample was negligible at all temperatures.

Below 5°K, the atomic heat of Si II can be represented by the expression

$$C_v = 6.83\times10^{-6}\,T^3 + 21.0\times10^{-6}\,T \text{ joules/mol deg.} \quad (2)$$

The spread of the experimental points from this relation is shown in Fig. 1, in which C_v/T is plotted against T^2; on this plot, Eq. (2) is a straight line. The coefficients in Eq. (1) were calculated by least squares from the values of 86 experimental points taken during runs on three different days.

The values of the experimental points for temperatures from 10 to 100°K and a smooth curve through them are plotted in Fig. 2, along with the values obtained in this temperature range by Nernst and Schwers,[2] and Anderson.[4] Our results agree fairly well with these earlier measurements. A smooth curve for the Debye θ is also drawn in Fig. 2. Values taken from both curves are listed in Table II. Although the measurements give C_p, $(C_p-C_v)/C_p$ is less than 10^{-4} below 100°K,[13] so we may compare our results directly with the theoretical calculations of C_v (see Sec. IV).

The over-all random instrumental error is probably less than 1 percent and is largely independent of the temperature range. At the lowest temperatures, the influence of the heat leak, enhanced by the smallness of the heat capacity of the sample, apparently introduces random errors of several percent, as indicated by the spread of the points. There is also the possibility of systematic error of about 1 percent in the hydrogen range due to uncertainty in the glyptal correction. The over-all error in the θ-values is probably under 1 percent, particularly below 50°K, where θ depends on the cube root of the atomic heat.

IV. DISCUSSION

A. Very Low Temperature Region, $T<5$°K

1. Lattice Contribution to the Atomic Heat

The fact that the atomic heat of Si II below 5°K can be represented by the sum of a cubic and a linear term in T indicates the possibility that we have reached the true T^3 region.[14] In this case the linear term would be due to a source other than the lattice (see paragraph 2 below). Blackman's calculations lead him to expect the true T^3 region at temperatures below $\theta/50$, or at least below $\theta/100$. θ calculated from the coefficient of the cubic term in Eq. (2) is 658°K, and therefore T is less than $\theta/100$ for T less than 5°K. Blackman also proposes a criterion for the true T^3 region, namely, that $\theta(E)$, the Debye temperature calculated from low temperature elastic constants, should equal $\theta(T)$, the Debye temperature calculated from the lattice atomic heat. Values of the elastic constants of Si and their temperature coefficients, both at room temperatures, have recently been published by McSkimin and collaborators.[15] We recalculated the temperature coefficients with a more recent value of the linear expansion

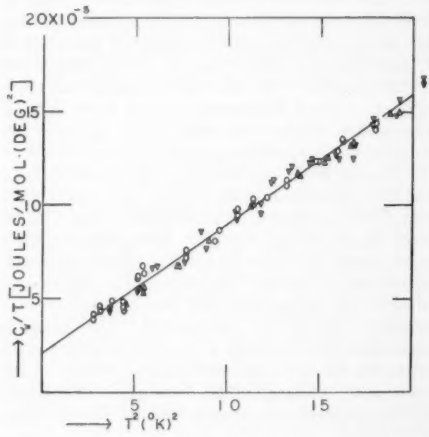

FIG. 1. C_v/T *vs* T^2 for Si. ○: 6/1/51; ▽: 5/10/51; △: 4/25/51.

[13] See, e.g., F. Seitz, *The Modern Theory of Solids* (McGraw-Hill Book Company, Inc., New York, 1940), Sec. 24.

[14] See reference 5, Sec. 3.

[15] McSkimin, Bond, Buehler, and Teal, Phys. Rev. **83**, 1080 (1951).

coefficient than that apparently used there. With these data, we obtained an estimate of the elastic constants at 0°K: $c_{11}=1.689$, $c_{12}=0.6532$, $c_{44}=0.8005$, all in units of 10^{12} dynes/cm². The method of Hopf and Lechner,[16] modified as suggested by Durand[17] (see Appendix II), was used to calculate $\theta(E)$, for which we found 653°K. This is about 1 percent lower than $\theta(T)$. The agreement is very good in view of the accuracy of the elastic constants and the approximations involved and is further evidence that the contribution of the lattice is correctly represented by the term proportional to T^3.

2. *Nonlattice Contribution to the Atomic Heat*

The nonlattice contribution to the atomic heat can thus be represented by a term linear in temperature. Such a term is observed in the low temperature atomic heat of metals, where it is identified with the heat capacity of a strongly degenerate electron gas.[18] To see if our observed linear term might have a similar origin, the number of carriers per cm³ n was determined by measuring the Hall constant R at and below room temperature on several small specimens cut from Si II. The resistivity ρ was also measured on these specimens. Table III presents the results, and for comparison, those of Pearson and Bardeen[19] on two of the samples in their series of measurements on B-doped Si.

The Hall constant and carrier concentration are related by[20]

$$R=r/ne. \tag{3}$$

Here e is the electronic charge, and r is a factor which varies between 1 and 2, depending on the ratio of resistivity due to impurities to total resistivity, for non-degenerate assemblies. For degenerate assemblies, r is unity. If R is given in units of cm³/coulomb, then

$$n=r\times 6.25\times 10^{18}/R. \tag{4}$$

Two of the specimens give for n, 10^{18} cm^{-3} from room temperature down to about 10°K for specimen B and down to about 2°K for specimen C. On these specimens contacts were soldered to Rh-plated spots. Pressure probes were used on specimen A, and reliable Hall constant measurements could not be made below room temperature with this arrangement. The agreement among the resistivity values for the three specimens is as good as can be expected, considering the inhomogeneity likely to be present in an ingot weighing over 260 grams.

The heat capacity per mole due to a highly degenerate Fermi-Dirac gas is[18]

$$C_v=1.62\times 10^{-12}Vn^{\frac{1}{3}}m^*T=\gamma T \text{ joules/mole deg}, \tag{5}$$

where V is the atomic volume of the lattice, and m^* is the ratio of effective carrier mass to electron mass. Stoner[21] has shown that this equation holds for T less than 0.1 T_D, where T_D is the degeneracy temperature, given by[22]

$$T_D=4.2\times 10^{-11}n^{\frac{1}{3}}/m^* \text{ °K}. \tag{6}$$

With n equal to 10^{18} cm^{-3}, T_D is about 40°K, when m^* equals unity. This is the value found by Pearson and Bardeen[19] for the ratio of effective mass of holes to the electron mass. Thus below about 4°K, γ according to Eq. (5) is about 20×10^{-6}j/mole deg², which is in good agreement with the coefficient of the linear term found experimentally [see Eq. (2)], 21.0×10^{-6}j/mole deg².‡

The fact that the Hall constant hardly varies with T from 300°K to 2°K while T_D is only about 40°K would seem to imply that the activation energy for the impurity levels is zero and that the Fermi level is not very near the top of the filled band. The latter supposition seems reasonable, but Pearson and Bardeen[19]

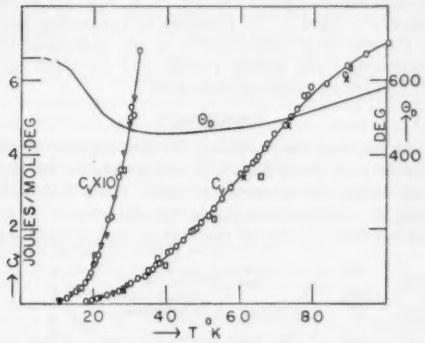

FIG. 2. C_v and θ for Si. ○: Si I; ▽: Si II; □: Nernst and Schwers; ×: Anderson.

TABLE II. Atomic heat and Debye θ of silicon.

T°K	C_v joules/mole deg	θ	T	C_v	θ
...	...	...	40	1.30	456
12	0.0130	637	45	1.78	460
13	0.0165	637	50	2.30	466
14	0.0210	623	55	2.88	472
15	0.0310	596	60	3.49	478
16	0.0400	584	65	4.08	485
17	0.0500	576	70	4.66	494
18	0.064	562	75	5.19	505
19	0.081	548	80	5.66	517
20	0.102	534	85	6.16	529
25	0.262	488	90	6.44	547
30	0.510	467	95	6.78	574
35	0.860	458	100	7.09	580

[16] L. Hopf and G. Lechner, Verhandl. deut. physik. Ges. **16**, 643 (1914).
[17] M. Durand, Phys. Rev. **50**, 449 (1944).
[18] A. Sommerfeld and H. Bethe, Handbuch der Physik (Julius Springer, Berlin, 1933), Vol. 24, part 2, pp. 347, 430.
[19] G. L. Pearson and J. Bardeen, Phys. Rev. **75**, 865 (1949).
[20] V. A. Johnson and K. Lark-Horovitz, Phys. Rev. **79**, 176 (1950); **82**, 977 (1951).
[21] E. C. Stoner, Phil. Mag. **21**, 145 (1936).
[22] V. A. Johnson and K. Lark-Horovitz, Phys. Rev. **71**, 374 (1947).

‡ *Note added in proof*:—Further electrical measurements on Si II show it to be very inhomogeneous, with both N- and P-type regions. Hence this numerical agreement may be fortuitous.

TABLE III. Electrical measurements on silicon.

Temperature region	Parameter	Our samples A	B	C	Pearson and Bardeen[a] 2	3
Room	R: cm³/coulomb	6	5	5	17	8
	ρ: ohm cm	0.14	0.14	0.10	0.14	0.06
Liquid nitrogen	R	···	5	4	200	60
	ρ	0.78	0.75	0.44	0.9	0.33
Liquid hydrogen	R (average)	···	4	4	···	···
	ρ (average)	6	3	1	···	···
Liquid helium	R (average)	···	···	5	···	···
	ρ (average)	10	130	14	···	···
Impurity atoms added to melt		?	?	?	6.7×10^{17} cm^{-3}	1.3×10^{18} cm^{-3}

[a] See reference 19.

found zero activation energy only for material having a carrier concentration at room temperature of 5×10^{15} cm^{-3} and higher. On the other hand, our resistivity values agree fairly well with those of their sample 2 both at room temperature and liquid nitrogen temperature, although only 6.7×10^{17} cm^{-3} B atoms were added to this melt. The reason for this discrepancy in the Hall constants is not clear. Further measurements are planned on a very pure single crystal of Si, in which, according to our interpretation of the present result, no linear term should be observed in the atomic heat.

B. Higher Temperature Region, $T>10°K$

It is usual to discuss the behavior in this temperature range in terms of the dependence of θ on T. Already at 12°K, the linear term in Eq. (2) is less than 2 percent of the total, so deviations from constancy of θ must be ascribed to lattice effects which are imperfectly approximated by the Debye continuum treatment.[22] Figure 3 is a plot of θ/θ_0 against T/θ_0, where θ_0 is the constant value in the true T^3 region, for Si and diamond.[24,25] For Si, θ_0 was taken as 658°K, our observed value of $\theta(T)$. For diamond, the value 1972°K was used for θ_0; this was calculated by the method of Hopf and Lechner,[16] using Smith's[7] revision of the elastic constants of diamond measured by Bhagavantam and Bhimasenachar.[26] The curve for diamond is plotted from Pitzer's measurements[8] and that for Si from the data of Table II. The circles in Fig. 3 are from θ-values calculated by Smith[7] from her determination of the elastic spectrum of diamond.

Both curves exhibit the feature found by Blackman and others in calculations on other lattices,[14] namely, that the true T^3 region ends before T equals $\theta/50$. Both curves show a dip in θ/θ_0, that for diamond being smaller and occurring at higher T/θ_0 than that for Si. This would seem to indicate that the detailed behavior of the atomic heat is not completely determined by the type of lattice.

[22] P. Debye, Ann. Physik **39**, 789 (1912).

[24] Hill and Parkinson (see reference 25) have given a similar plot, using θ_∞ as the normalizing factor rather than θ_0. θ_∞ is defined in terms of the approach of C_v to the classical value $3R$, at high temperatures.

[25] R. W. Hill and D. H. Parkinson, Phil. Mag. **43**, 309 (1952).

[26] S. Bhagavantam and J. Bhimasenachar, Proc. Roy. Soc. (London) **A187**, 381 (1946).

Katz[27] has recently shown that curves of this type may be used to derive information about the shape of the elastic spectrum. He introduces parameters q and δ_m. If the minimum in θ is θ_m and occurs at T_m, then q is given by

$$q=5T_m/\theta_0, \tag{7}$$

and δ_m is given by

$$\delta_m=(\theta_m/\theta_0)-1. \tag{8}$$

For q greater than 0.5, the spectrum is insensitive to changes in θ, so little information can be derived from q and δ_m. For q less than 0.5, a dip in θ/θ_0 corresponds to a peak in the spectrum centered about ν_p, with the weight β relative to the total area of the spectrum, where ν_p is given by

$$\nu_p=q\nu_M, \tag{9}$$

where ν_M is the maximum frequency, and β is given by

$$\beta=-11\delta_m q^3. \tag{10}$$

For the diamond curve, q is 0.5 and δ_m is -0.08, so β is 0.1. Smith[7] finds that q is 0.53 from her calculated spectrum, but the area of the peak appears to be rather larger than 10 percent of the total. These comparisons are only qualitative, since q is so large. For Si, q is 0.3, and δ_m is -0.31; β is again about 0.1. Since ν_M is proportional to θ, this would imply that ν_p for Si is about 0.2 times ν_p for diamond. These conclusions would provide a rough check on calculations of the spectrum for Si, since they apply at the low frequency end, where the accuracy of calculated spectra is poorest.

We would like to express our appreciation of the support and encouragement of Dr. K. Lark-Horovitz, who suggested the problem and provided valuable guidance in its execution. We have also benefited from stimulating discussions with Dr. H. Y. Fan. We would also like to thank Dr. D. Finlayson for performing some of the electrical measurements, L. W. Aukerman for constructing the timing circuit, and L. Babb and V. Bolyard for technical assistance.

APPENDIX I

At very low temperatures, the heat capacity of the sample is so small that it is comparable to the heat leak during one experimental point. When this is the case, the temperature during the after-period decays exponentially to that of the bath at such a rapid rate

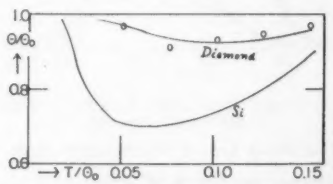

FIG. 3. θ/θ_0 vs T/θ_0 for diamond and Si. Curves are from atomic heat measurements; circles are Smith's calculated points for diamond.

[27] E. Katz, J. Chem. Phys. **19**, 488 (1951).

that extrapolation to the middle of the heating period no longer gives the true temperature rise. This problem has been treated by Keesom and Kok,[28] who assume that the temperature-recording instrument responds immediately to changes in T.[29–31] This implies that the maximum temperature will occur at the end of the heating-period, whereas we noticed that our galvanometer reached a maximum deflection at a time somewhat later than this whenever the final temperature of the sample was above that of the bath. Other evidence indicates that this lag is much longer than the thermal relaxation time of the specimen, so we assume that it is due to the momentum of the galvanometer and extend the treatment of Keesom and Kok[28] to take this effect into account. They derive the equations

$$T_h - T_f = (L/k)(1-e^{-kt/C}), \tag{11}$$

$$T_a - T_f = (L/k)(e^{kt_1/c}-1)e^{-kt/C}, \tag{12}$$

for the heating- and after-periods, respectively. The subscripts f, h, a refer to the fore-, heating-, and after-periods, respectively. T is absolute temperature, L the heat input per second during the heating period, and k the rate of heat loss to the surroundings per degree temperature difference per second. C is the heat capacity of the sample, t is time in seconds, $t=0$ corresponding to the beginning of the heating period, and $t=t_1$ to the end. We simplified this equation by assuming $T_f=0$, throughout the fore-period.

The differential equation for the deflection of a critically damped galvanometer which is recording the temperature of a resistance thermometer may be written as

$$(\tau/2\pi)^2\ddot{\alpha}+2(\tau/2\pi)\dot{\alpha}+\alpha=T, \tag{13}$$

where α is the galvanometer deflection and τ is the period of the galvanometer with no damping. This equation holds if T (measured here in arbitrary units) varies linearly with the current through the galvanometer, a condition which is very nearly satisfied in our measurements, since we operate in such small temperature intervals during each experimental point that the galvanometer sensitivity and dR/dT of the thermometer are essentially constant. The solution of Eq. (13) with T given by Eqs. (11) and (12) can be put in the form

$$\alpha = A_1 e^{-2\pi t/\tau} + A_2 t e^{-2\pi t/\tau} + A_3. \tag{14}$$

Imposing the boundary conditions

$$t=0, \quad \alpha_h = 0 = \dot{\alpha}_h, \tag{15a}$$

$$t=t_1, \quad \alpha_a = \alpha_h, \quad \dot{\alpha}_a = \dot{\alpha}_h, \tag{15b}$$

for the beginning and end of the heating period, and

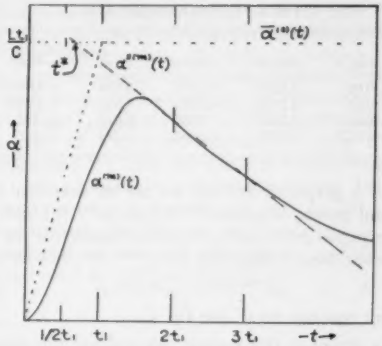

FIG. 4. Galvanometer deflection $\alpha^{(m)}(t)$ during and after heating period, illustrating extrapolation back to t^* to find true temperature rise Lt_1/C.

introducing $m=k/c$, the constants become

$$A_{1h} = (L/k)\left[\frac{4\pi^2}{(2\pi-m\tau)^2}-1\right], \tag{16a}$$

$$A_{2h} = (L/k)\left[\frac{4\pi^2}{\tau(2\pi-m\tau)}-\frac{2\pi}{\tau}\right], \tag{16b}$$

$$A_{3h} = (L/k)\left[1-\frac{4\pi^2}{(2\pi-m\tau)^2}e^{-mt}\right], \tag{16c}$$

$$A_{1a} = A_{1h}+e^{2\pi t_1/\tau}(L/k)\left[1-\frac{2\pi t_1}{\tau}-\frac{4\pi^2}{(2\pi-m\tau)^2} \times\left\{1-\frac{2\pi}{\tau}\left(1+\frac{m\tau}{2\pi}\right)t_1\right\}\right], \tag{16d}$$

$$A_{2a} = A_{2h}+e^{2\pi t_1/\tau} \times\frac{2\pi}{\tau}(L/k)\left[1-\frac{4\pi^2}{(2\pi-m\tau)^2}\left(1+\frac{m\tau}{2\pi}\right)\right], \tag{16e}$$

$$A_{3a} = \frac{4\pi^2}{(2\pi-m\tau)^2}(L/k)(e^{mt_1}-1)e^{-mt}. \tag{16f}$$

Then for the ideal case with no heat leak ($m=0$) and no lag in the galvanometer ($\tau=0$), we find the ideal temperature rise α_{id}:

$$\bar{\alpha}^{(0)}(t_1) = Lt_1/C = \alpha_{id}, \tag{17}$$

where the superscript on α indicates the value of m and the bar indicates that τ equals zero. To find α_{id} from the heating curve observed in an actual experiment, Keesom and Kok[28] extrapolate the tangent to the after-period at t_1 back to a time t^* such that

$$\alpha'^{(m)}(t^*) = Lt_1/C = \alpha_{id}, \tag{18}$$

where $\alpha'^{(m)}$ is the equation of the tangent. They find

[28] W. H. Keesom and J. A. Kok, Proc. Koninkl. Nederland. Akad. Wetenschap. **35**, 294 (1932); Commun. Kamerlingh Onnes Lab., Leiden, No. 219c.

[29] Aston and Szasz (see reference 30) and Keesom and Kurrelmeyer (see reference 31) have given generalized treatments while retaining this assumption.

[30] J. G. Aston and G. J. Szasz, J. Chem. Phys. **15**, 560 (1947).

[31] W. H. Keesom and B. Kurrelmeyer, Commun. Kamerlingh Onnes Lab., Leiden, No. 257a (1939).

TABLE IV. t^* as a function of m.

m sec^{-1}	$\alpha^{(m)}(2t_1)$	$\alpha^{(m)}(3t_1)$	t^* sec	$[\alpha^{(m)}(2t_1)-\alpha^{(m)}(3t_1)]/\alpha^{(m)}(2t_1)$
0.001	9.8693	9.7715	6.636	0.00991
0.01	8.7840	7.9494	5.342	0.09505
0.015	8.2366	7.0906	4.613	0.1391
0.033	6.5272	4.6766	1.234	0.2816

t^* by a graphical method; we use an analytical procedure instead. We find $\alpha^{(m)}(2t_1)$ and $\alpha^{(m)}(3t_1)$ from the after-period curve, and extrapolate backwards the line between them. Calling this line $\alpha''^{(m)}$, we then have

$$\alpha''^{(m)}(t^*)=Lt_1/C=\alpha_{id} \tag{19}$$

as our equation for t^* (see Fig. 4).

To illustrate this method, we indicate the manner in which it was applied to our data. Since for our galvanometer $\tau=7$ sec, we approximated $2\pi/\tau$ by unity. We have $t_1=10$ sec; and setting $L=C$, which involves no loss in generality, we have $\alpha_{id}=10$. Inserting these values in Eqs. (16), we have

$$A_{1a}=\frac{2-m}{(1-m)^2}+e^{10}\frac{(28-9m)}{(1-m)^2}, \tag{20a}$$

$$A_{2a}=\frac{1}{1-m}+e^{10}\frac{m-3}{(1-m)^2}, \tag{20b}$$

$$A_{3a}=\frac{1}{m(1-m)^2}(e^{10m}-1)e^{-mt}. \tag{20c}$$

Equation (20c), which is the third term of our result [see Eq. (14)], differs from Eq. (12) due to Keesom and Kok only by the factor $(1-m)^{-2}$. Since we now have an analytical expression for $\alpha''^{(m)}$ in the form of a transcendental equation in t^* and m, we can find t^* for any choice of m. Values of t^* found in this way are tabulated as a function of m in Table IV. The last column in the Table IV relates m to the observed points in the after-period, and so enables one to judge where to enter the table. For $m>0.033$ the extrapolation will be very uncertain due to the large slope of $\alpha''^{(m)}$. It should be pointed out that while Keesom and Kok[28] find that t^* is never greater than $t_1/2$, we find larger values of t^* for $m=0.01$ and $m=0.001$. For such small values of m, however, the difference between $\alpha''^{(m)}(t^*)$ and $\alpha''^{(m)}(t_1/2)$ will only be of the order of 0.1 percent or less, so the extrapolation can be made to $t_1/2$.

TABLE V. Calculated data.

i, j	$j\xi$	$j\xi+C$	$f(j\xi)$	$1/120\xi^i$	a_i	λ_i	$a_i(H-L)$
0	0.0	0.413	3.767	0.00833	3.767	3.000	3.771
1	0.2	0.613	2.085	0.04167	−12.702	1.000	−12.794
2	0.4	0.813	1.634	0.2083	27.983	0.743	28.354
3	0.6	1.013	0.982	1.042	−37.845	0.625	−38.473
4	0.8	1.213	0.749	5.208	27.498	0.539	28.046
5	1.0	1.413	0.595	26.04	−8.124	0.470	−8.307

APPENDIX II

The labor involved in using the Hopf-Lechner method[16] to find $\bar{v}$, defined by

$$\frac{1}{\bar{v}^3}=\frac{1}{4\pi}\cdot\frac{1}{3}\int\sum_{k=1}^{3}\frac{1}{v_k^3}d\Omega, \tag{21}$$

where the v_k are the three sound velocities in each direction, is greatly reduced by the scheme outlined below. In the notation of Born and von Kármán[22] for a cubic crystal,

$$C=c_{44}/C'', \quad C'=(c_{12}+c_{44})/C'', \quad C''=c_{11}-c_{44}, \tag{22}$$

where c_{11}, c_{12}, and c_{44} are the three independent elastic constants for a cubic crystal in Voigt's notation.[33] When $c_{11}<c_{12}+2c_{44}$ (this corresponds to $C'>1$), we define

$$5\xi=\tfrac{1}{3}(1+2C'). \tag{23}$$

This corresponds to the generalization suggested by Durand[17] of the original treatment of Hopf and Lechner. They considered only the case in which $c_{11}>c_{12}+2c_{44}$ ($C'<1$), in which case Eq. (23) must be replaced by

$$5\xi=1. \tag{24}$$

Then introducing

$$f(j\xi)=(j\xi+C)^{-1}, \quad j=0, 1, \cdots 5, \tag{25}$$

the coefficients a_i are defined by

$$a_i=\frac{1}{120\xi^i}\sum_{j=0}^{5}\alpha_{ij}f(j\xi), \tag{26}$$

where the coefficients α_{ij} are given by the matrix

$$\begin{Vmatrix} 120 & 0 & 0 & 0 & 0 & 0 \\ -274 & 600 & -600 & 400 & -150 & 24 \\ 225 & -770 & 1070 & -780 & 305 & -50 \\ -85 & 355 & -590 & 490 & -205 & 35 \\ 15 & -70 & 130 & -120 & 55 & -10 \\ -1 & 5 & -10 & 10 & -5 & 1 \end{Vmatrix}=(\alpha_{ij}). \tag{27}$$

Introducing the constants

$$\beta_1=1-C'^2, \quad \beta_0=1-3C'^2+2C'^3, \tag{28}$$

we define

$$\begin{aligned} &\lambda_0=3; \quad \lambda_1=1, \\ &\lambda_2=\left(1-\frac{2}{5}\beta_1\right), \\ &\lambda_3=\left(1-\frac{3}{5}\beta_1+\frac{1}{35}\beta_0\right), \\ &\lambda_4=\left(1-\frac{4}{5}\beta_1+\frac{4}{105}\beta_0+\frac{2}{21}\beta_1^2\right), \\ &\lambda_5=\left(1-\beta_1+\frac{1}{21}\beta_0+\frac{5}{21}\beta_1^2-\frac{1}{77}\beta_0\beta_1\right), \end{aligned} \tag{29}$$

[22] M. Born and T. von Kármán, Physik. Z. 14, 15 (1914).
[33] W. Voigt, *Lehrbuch der Kristallphysik* (B. G. Teubner, Leipzig, 1928).

and write

$$I_{HL}=\frac{1}{3}\sum_{i=0}^{5}\lambda_i a_i. \tag{30}$$

The final result is then

$$\bar{v}=(I_{HL})^{-\frac{1}{2}}(C''/\rho)^{\frac{1}{2}}\ \text{cm/sec} \tag{31}$$

and

$$\theta(E)=2.514\times10^{-8}\bar{v}/(V)^{\frac{1}{3}}, \tag{32}$$

where ρ is the density of the crystal and V the atomic volume.

It should be pointed out that Eq. (32) holds only when the Debye treatment gives an adequate approximation to the atomic heat, that is, in the true T^3 region. Thus the elastic constants should be those at 0°K. It can be seen from Eqs. (30) and (31), however, that $\theta(E)$ is not extremely sensitive to variation of the c_{ij}. To illustrate the method, we apply it to the data given by Hopf and Lechner for FeS_2: $\rho=5.03$ g/cm³, $C=0.413$, $C'=0.598$, $C''=2.555\times10^{12}$ dynes/cm². Since $C'<1$, $\xi=0.2$. From Eq. (28), $\beta_1=0.642$, $\beta_0=0.355$. Table V lists the quantities calculated from these data. The last column gives the coefficients computed by Hopf and Lechner. From this table we calculate $I_{HL}=2.25$; and $\bar{v}=5.46\times10^5$ cm/sec. The values given by Hopf and Lechner are 2.26 and 5.43×10^5 cm/sec.

PHYSICAL REVIEW VOLUME 88, NUMBER 2 OCTOBER 15, 1952

Production of the *E*-Layer in the Oxygen Dissociation Region in the Upper Atmosphere

D. C. CHOUDHURY
Institute of Radio-Physics and Electronics, Calcutta University, Calcutta, India

(Received April 25, 1952)

Starting with the generally accepted theory that the *E*-layer is formed by ionization of O_2 in the region of its dissociation, the probable value of the absorption cross section of O_2 for this ionization is calculated by utilizing the height distribution of O_2 (in the transition region) as recently obtained by Moses and Wu. It is found that, depending upon the temperature gradient and the boundary temperature chosen for the region of dissociation, the necessary absorption cross section varies from 3×10^{-19} cm² to 9×10^{-18} cm². Hence, it follows that for the two current hypotheses of *E*-layer ionization, namely, pre-ionization by solar rays in the wavelength range 900A–1000A (Nicolet) and ionization by high energy photons emitted from the solar corona (Hoyle and Bates), the ionization cross section of O_2 should also lie within this range. For the former, the rate of ion production (as obtained by application of simple Chapman formula and assuming the sun to be radiating like a blackbody) appears to be one hundred times more than the observed rate. The discrepancy is removed if it is assumed that of the molecules excited to the pre-ionization levels by absorption, only a small fraction (one in a hundred) undergoes ionization. For the high energy photons it is found that in order to have the necessary absorption cross section, the energy should be 181 ev rather than 325 ev as obtained by Hoyle and Bates. It is suggested that both the pre-ionization process and the ionization by high energy photons are operative in producing *E*-layer ionization. The former produces the normal *E*-layer and the latter (of different frequencies) intensifies the ionization at different levels producing the fine structure of the *E*-layer as reported recently.

1. INTRODUCTION

THE most generally accepted theory of the *E*-layer is that it is formed by the ionization of molecular oxygen in the region where its concentration falls rapidly with height owing to photodissociation (Mitra,[1] Bhar,[2] and Wulf and Deming[3]). There is, however, uncertainty regarding the process of ionization and the wavelength of the active radiation. According to the earlier views, the ionization of O_2 was either at its first ionization potential (Wulf and Deming[3]) or at its second ionization potential (Bhar[2]). There have, however, been objections to both these views. For the first ionization potential (12.2 ev) the absorption cross section is so small that no ionization maximum will be formed in the region of dissociation. (Ionization at the first ionization potential of O_2 is now believed to produce the *D*-region.[4]) Again, the wavelength range of the active radiation for the second ionization potential 760–661A lies within the region of strong absorption of atomic oxygen. Hence, the active radiation will all be used up before reaching the transition level. To meet these difficulties two different hypotheses have been proposed. According to one (Hoyle and Bates[5]) emissions of very high energy photons (perhaps of about 325 ev) from the solar corona is supposed to cause the ionization. According to the other (Nicolet[6]) pre-ionization of molecular oxygen by solar radiation in the energy range 12.2 to 13.55 ev (900A to 1000A) is responsible for the ionization of O_2.

In the present note the recent theoretical determinations of the distribution of molecular oxygen in the region of dissociation, as made by Moses and Wu,[7] will be utilized to first find out what should be the value of the absorption cross section of O_2, in order that the *E*-peak may be formed at the observed height.

[1] S. K. Mitra, Nature **142**, 914 (1938).
[2] J. N. Bhar, Indian J. Phys. **12**, 363 (1938).
[3] O. R. Wulf L. S. and Deming, Terr. Mag. Atmos. Elect. **43**, 283 (1938).
[4] A. P. Mitra, J. Geophys. Research **56**, 373 (1951).
[5] F. Hoyle and D. R. Bates, Terr. Mag. Atmos. Elect. **53**, 51 (1948).
[6] M. Nicolet, Mem. Roy. Met. Inst. Belge, **19**, 124 (1945).
[7] H. E. Moses and T.-Y. Wu, Phys. Rev. **83**, 109 (1951).

This value will be checked with the absorption cross section values assumed for the two ionizing processes mentioned above. The rate of ion production at the level of maximum ionization will also be determined with the help of Chapman's formula and compared with the observed rate.

2. ABSORPTION CROSS SECTION OF O_2 FOR THE IONIZING RADIATION PRODUCING THE *E*-LAYER

Theoretical Formula

According to the simple Chapman theory[8] of ionized layer formation, the absorption coefficient (A) of the ionizing radiation is given by the relation

$$A=\cos\chi/nH, \tag{1}$$

where n is the molecular concentration of the ionized gas at the level of maximum ionization, $H(=kT/mg)$ is the scale height of the region of layer formation, and χ is the zenith angle of the sun. Chapman's formula is applicable only in the case of isothermal atmosphere for which H is constant with height. H is thus really the exponential factor measuring the rate of decrease of the concentration of the active molecules. Knowing H, n may be calculated from the height of the maximum ionization (h_m) obtained from radio measurements. Hence A is known. For $\cos\chi$, a representative value is 0.9, if the mean midday value of h_m in the temperate latitude is used.

Height Distribution of O_2 in the Region of Dissociation

Of the various attempts made on this problem mention may be made of those by Rakshit,[9] by Penndorf,[10] and by Moses and Wu.[7] Rakshit has calculated the height distribution of O_2 on the assumption that the O atoms recombine by the two-body collision process. According to Rakshit's calculations, the dissociation starts at about 90-km level and is almost complete at 130 km. Between the heights 105 and 125 km the concentration of O_2 decreases approximately exponentially. Penndorf, on the other hand, assumes a three-body collision process for the recombination of the O atoms. According to Penndorf, the dissociation becomes appreciable from the height of 95 km and is almost complete at 125 km. The decrease again follows approximately an exponential law between the heights 105 km and 125 km.

The latest work on this subject is of Moses and Wu.[7] These authors have directed attention to certain incongruities in the assumptions make by Rakshit and by Penndorf in their calculations and claim that the method of calculation adopted by them does not suffer from any such defects. Further, the calculations are based on the recent knowledge of the temperature distribution of the upper atmosphere. As such, the results obtained by these authors may be taken to represent the actual distribution more closely. (Note: In calculating the equilibrium condition Moses and Wu assume, as in Rakshit's calculations, that the predominant process is two-body rather than three-body collision.)

The calculations by Moses and Wu have been made for three conditions of temperature gradient and boundary temperature starting from the hundred-km level, namely, (i) $T=300°K$, $dT/dh=10°/km$, (ii) $T=270°K$, $dT/dh=5°/km$, (iii) $T=300°K$, $dT/dh=5°/km$. In all these cases dissociation begins between the heights 90 km and 100 km and is not complete until the height of 150 km is reached. In Fig. 1 the curves (a), (b), and (c) depict, after Moses and Wu, the height distributions (in logarithmic scale) of O_2 as obtained for the three cases. It will be noticed that the distribution curves are approximately straight. Hence, we can express the height distribution of O_2 by the simple exponential formula,

$$n_h=n_0\exp(-h/H),$$

where n_0=number density of O_2 at the datum level 100 km, n=number density of O_2 at height h above the datum level, and H=effective scale height replacing the usual scale height (kT/mg) for an isothermal atmosphere of constant molecular weight.

In Table I the assumed heights of the *E*-peak are given in the first column, the number densities of O_2 at these heights (as obtained from the corresponding curves in Fig. 1) are given in the second column, the effective H values obtained from the slopes of the distribution curves are shown in the third column, and in

TABLE I. The *E*-peak will be produced at the heights shown in the first column, if the absorption coefficient of O_2 has the corresponding values as shown in the fourth column. The "effective" H values (third column) used in calculating the absorption coefficient are obtained from the slopes of these curves. The three tables are for the three cases of O_2-distribution with height as depicted in Fig. 1.

Height (km)	Number density of O_2	Effective H (km)	Absorption cross section 'A' (cm^2)
Case (i). $T=300°K$ and $dT/dh=10°/km$.			
100	$4.5\times10^{12}/cm^3$		3.0×10^{-19}
110	$8.0\times10^{11}/cm^3$	6.52	1.7×10^{-18}
120	$2.1\times10^{11}/cm^3$		6.6×10^{-18}
Case (ii). $T=270°K$ and $dT/dh=5°/km$.			
100	$3.7\times10^{12}/cm^3$		3.6×10^{-19}
110	$6.8\times10^{11}/cm^3$	6.59	2.0×10^{-18}
120	$1.8\times10^{11}/cm^3$		7.3×10^{-18}
Case (iii). $T=300°K$ and $dT/dh=5°/km$.			
100	$2.4\times10^{12}/cm^3$		5.2×10^{-19}
110	$5.0\times10^{11}/cm^3$	7.07	2.5×10^{-18}
120	$1.4\times10^{11}/cm^3$		8.8×10^{-18}

[8] S. Chapman, Proc. Phys. Soc. (London) **43**, 26, 433 (1931).
[9] H. Rakshit, Indian J. Phys. **21**, 57 (1947).
[10] R. Penndorf, J. Geophys. Research **54**, 7 (1949); Phys. Rev. **77**, 561 (1950).

the fourth column is given the corresponding absorption cross section for the ionization of O_2, as obtained from Eq. (1), as would produce the *E*-peak at the assumed level.

It is seen from the table that, depending upon the assumed height of the *E*-peak and the temperature gradient, the necessary absorption cross section varies from 3.1×10^{-19} cm² to 8.8×10^{-18} cm². Since the minimum of these values is at least one order higher than the absorption cross section for the first ionization potential, it is clear that this ionization cannot be the cause of the *E*-layer. This, of course, confirms the conclusion of the previous workers. Again, the absorption cross sections for the second, third and fourth ionization potentials, which are of the orders 10^{-16} cm², 10^{-17} cm², and 10^{-18} cm², respectively, are all much higher than the value necessary. As such, these ionizations also cannot produce the *E*-layer. Let us, therefore, consider the two other suggested ionization processes of O_2, namely, pre-ionization (Nicolet[6]) and ionization by high energy photons 325 ev (Hoyle and Bates[5]).

According to Nicolet the pre-ionization of O_2 may occur in the wavelength range 900A to 1000A where the bands of the Rydberg series terminating at the (first) ionization continuum present the character of pre-ionization. Assuming the coefficient of absorption within the band to be 10^5 times that of the ionization continuum, Nicolet estimates the absorption cross section for the process to be 10^{-15} to 10^{-16} cm². This, however, is more than one order higher than even the maximum necessary value (8.8×10^{-18} cm²). But it is quite possible that Nicolet's value is an overestimate and that the actual value is one order lower. With such value of the absorption cross section, the *E*-peak for case (ii), namely, $T=270°$K and $dT/dh=5°$/km, is produced at the 120-km height.

Let us also determine the maximum rate of ion production at the level of *E*-peak with the help of Chapman's expression,[8]

$$I_m = S_0 \cos\chi / H \exp 1,$$

where S_0 is the number of quanta incident per cm² per sec normally from above. Taking the sun as a blackbody radiator, S_0 within the wavelength range 900 to 1000A is 1.0×10^{10} per cm² per sec. Hence, corresponding to the three values of H, 6.52 km, 6.59 km, and 7.07 km for the three cases as shown in Table I, the rates of maximum ion production are 5.1×10^3/cm³, 5.0×10^3/cm³ and 4.7×10^3/cm³ per sec, respectively. (The representative value of $\cos\chi$ is taken as 0.9.) These rates are about two orders higher than the observed maximum rate which is 30 to 50 per cm³ per sec only. The discrepancy may, however, be explained if it is remembered that the rates as calculated above give actually the rates of production of O_2 molecules excited to the one or the other band level with pre-ionization characteristics. It is quite likely that of these excited

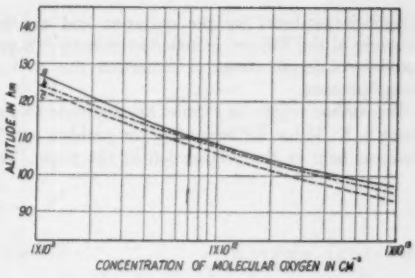

FIG. 1. Calculated number densities of molecular oxygen as functions of height (drawn after Moses and Wu). (a) $T=300°$K, $dT/dh=10°$/km; (b) $T=270°$K, $dT/dh=5°$/km; (c) $T=300°$K, $dT/dh=5°$/km.

molecules only a small fraction, say one in a hundred, undergoes pre-ionization, and the rest are removed from the excited state by spontaneous or stimulated transition.

We next examine the hypothesis of Hoyle and Bates,[5] namely, that the *E*-layer is produced by very high energy photons emitted by the solar corona. Assuming that the number density of the particles at the level of the *E*-peak is 6×10^{12}/cm³ and taking the scale height value as 10 km, Hoyle and Bates found the necessary absorption cross section for the ionizing x-rays to be 1.7×10^{-19} cm². Hence, they estimated that the ionizing radiation should be of about 325 ev energy. We note from the tables, however, that even for the lowest assumed height of the *E*-layer, namely, 100 km, the required absorption cross section is somewhat higher than 1.7×10^{-19} cm². Ionizing x-ray with such absorption should have energy of about 181 ev.[11]

3. CONCLUDING REMARKS

The above discussions show that if the height distribution of O_2 in the transition region be as that given by Moses and Wu, then both Nicolet's pre-ionization process and Bates and Hoyle's ionization by high energy photons may be operative in ionizing O_2 and producing the *E*-layer at the observed height in the region of transition as originally suggested by Mitra,[1] by Bhar[2] and by Wulf and Deming.[3] The necessary absorption cross section of O_2 for producing the ionization at the observed height is of the order 10^{-18} cm² (rather than 10^{-15} to 10^{-16} as assumed by Nicolet or 10^{-19} cm² as assumed by Hoyle and Bates). For Hoyle and Bates' process the energy of the ionizing photons should be of the order 181 ev rather than 325 ev as assumed by these authors. It is possible that both of the processes are operative in producing the *E*-layer ionization. The quasi-permanent, normally observed

[11] A. H. Compton and S. K. Allison, *X-Ray in Theory and Experiment* (MacMillan and Company, London, 1935).

E-layer is produced by pre-ionization and the fine structure of the E-layer, as reported recently,[12] is produced by intensifications of ionization due to high energy photons.

The author wishes to express his gratitude to Professor S. K. Mitra, for suggesting the problem and for constant help in the preparation of the paper. This paper forms a part of the work done in the scheme on "Ionospheric Investigations" financed by the Council of Scientific and Industrial Research, Government of India, and the author expresses his thanks to the Council for providing the necessary facilities for research work.

[12] R. Naismith, Wireless Eng. **28**, 271 (1951).

PHYSICAL REVIEW VOLUME 88, NUMBER 2 OCTOBER 15, 1952

The Backscattering of Positrons and Electrons

H. H. SELIGER
National Bureau of Standards, Washington, D. C.

(Received March 31, 1952)

Beta-rays from a point source, backscattered by materials of various atomic numbers Z have been collected over a 2π solid angle and also over narrow solid angles at various obliquities. In all cases electrons are backscattered to a greater extent than positrons. The number and energy spectrum of the backscattered beta-rays depend strongly on the direction of emergence and on Z. In spite of the use of hetero-energetic sources, the results can be interpreted qualitatively on the basis of multiple scattering, in terms of a "side-scattered" and a "diffused" component.

I. INTRODUCTION

THERE has been relatively little recent experimental work on the backscattering of fast electrons in matter and none on the backscattering of positrons. Brand[1] has studies the backscattering of cathode rays up to 32 kev in energy and Bothe[2] has extended the measurements to 680 kev using radioactive sources in a magnetic analyzer.

Recently the author reported an excess of electron backscattering over positron backscattering.[3] This excess of electron backscattering over positron backscattering is to be expected indirectly on the basis of the single scattering cross sections as calculated by Bartlett and Watson[4] for electrons and Massey[5] for positrons. A further study of the backscattering process has provided several very interesting results from which one is able to deduce a qualitative understanding of the general backscattering process.

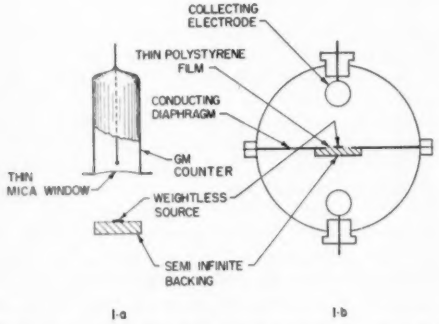

FIG. 1 (a). Schematic drawing of geometrical arrangement of the previously reported experiments; (b) schematic drawing of 4π counter arrangement.

[1] J. O. Brand, Ann. Physik **5**, 609 (1936).
[2] W. Bothe, Z. Naturforsch. **4a**, 542 (1949).
[3] H. H. Seliger, Phys. Rev. **78**, 491 (1950).

II. EXPERIMENTAL PROCEDURE

The geometry of the previous experiment (see reference 3) is indicated schematically in Fig. 1(a). If one defines an angle θ as the angle between the plane containing the front surface of the backing and the plane containing the axis of the detector and the source, then in Fig. 1(a), $\theta=90°$.

The present experiments can be divided into two parts. In the first part the backscattering coefficients for both positrons and electrons as functions of the atomic number Z of the backing material were measured for a 2π solid angle, in contrast with the solid angle of roughly 1 steradian in Fig. 1(a). These 2π backscattering coefficients were determined in 4π absolute beta-counters.[6] The geometry of the measurement is indicated schematically in Fig. 1(b). In the second part the angular distributions of the backscattered electrons and positrons, both in number and in energy, were measured as functions of Z. The arrangement of Fig. 1(a) was modified so that the solid angle subtended was only 0.01 steradian. The source approximated a point source, and the backing on which the source was

[4] J. H. Bartlett and R. E. Watson, Proc. Am. Acad. Arts Sci. **74**, 53 (1940).
[5] H. S. W. Massey, Proc. Roy. Soc. (London) **A181**, 14 (1942).
[6] H. H. Seliger and L. Cavallo, Natl. Bur. Standards J. Research **47**, 41 (1951).

mounted was constructed so that it could rotate, with its axis of rotation laying in the plane of the front surface of the backing and perpendicular to the line containing the axis of the detector. Thus by rotation of the backing relative to the counter one could sample the backscattered radiation at various angles θ. Estimates of the energy distribution of the backscattered electrons were made by means of absorption curves in aluminum. These absorption curves, extrapolated to zero total absorber, also gave the correction for the absorption due to the thickness of air and counter window.

P^{32}(E_{max} 1.71 Mev) and Na^{22}(E_{max} 0.58 Mev) were used as sources of negative and positive electrons, respectively. The backscattering was measured for Lucite, aluminum, copper, silver, platinum, and lead.

1. 2π Backscattering Coefficients

The 2π backscattering coefficients were measured in the following manner: The absolute disintegration rate of the source, N_0 was determined in the 4π counter by the method outlined in reference 6. Then the source, mounted on a thin polystyrene film, was placed on the polished face of the backing and the counting rate in the top half of the counter was measured. This is given by

$$N_t' = \tfrac{1}{2}N_0[1+\beta(1-\tau)^2], \tag{1}$$

where N_t' is the counting rate in the top half of the 4π counter, β is the backscattering coefficient, and τ is the fractional absorption in the mounting film ($\tau \ll 1$). The factor $(1-\tau)$ is taken squared because a particle must pass through the mouting film twice if it is backscattered. The procedure for determining τ is also given in reference 6. β, defined by (1) can be written as

$$\beta = \frac{1}{(1-\tau)^2}\left[\frac{N_t' - \tfrac{1}{2}N_0}{\tfrac{1}{2}N_0}\right]. \tag{2}$$

$\tau \sim 0$ for P^{32} electrons, so that β reduces to

$$\beta = (2N_t'/N_0) - 1. \tag{3}$$

In the case of Na^{22} positrons τ is not zero and a further correction is necessary because of the associated γ and annihilation radiation. It is possible that a γ or annihilation quantum accompanying a positron which is stopped in the backing will produce a count in the top half of the 4π counter, thereby making β^+ appear larger than the true value. The presence of cascade or annihilation radiation does not affect the determination of N_0 since the entire process occurs well within the resolving time of the proportional counter and amplifier for the original beta-particle ionization pulse.

A new set of 4π counter equations was derived, following the same line of reasoning as in the original paper on 4π counting, but this time taking into account the γ and annihilation radiation from the Na^{22} positrons. The final result for β gave

$$\beta = \frac{1}{(1-\tau)^2}\left[\frac{N_t' - \tfrac{1}{2}(N_0+N_b')}{\tfrac{1}{2}(N_0-N_b')}\right], \tag{4}$$

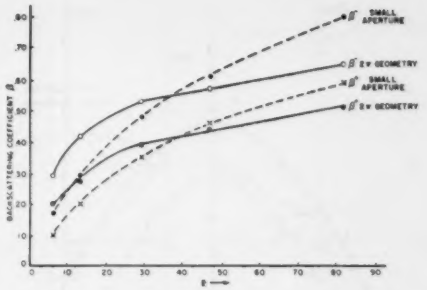

FIG. 2. Backscattering coefficients for positrons and electrons as functions of Z, measured with 2π geometry (solid curves) compared with previously measured backscattering coefficients.

where N_b', the counting rate in the bottom half of the 4π counter with the infinite backing in place, is due entirely to the effect of the photons. The total correction, including that for film absorption and for γ and annihilation radiation, amounted to roughly 5 percent.

Another possible correction involved in the case of the Na^{22} positrons is introduced by the finite probability that a positron will be annihilated in motion. However, even in the case of lead, this probability is of the order of 1 or 2 percent.[7] For lower Z it would be still smaller. No corrections were made for this effect.

2. Angular Distribution Measurements

An arrangement was used here whereby the point source was evaporated on a thin film and supported below the detector. The backing could be brought up directly in contact with the thin film and then backing and film could be rotated so as to sample the radiation at various angles θ. A complete absorption curve in aluminum was measured for the source mounted on the thin film with no backing behind it. The angular distribution of this unscattered or direct radiation was effectively isotropic from $\theta = +10°$ to $\theta = -10°$, the limiting angular range of the experimental arrangement. A slight asymmetry due to difficulty in exact centering of the source was present, but the average of the values for plus and minus θ removed this effect. Next, similar absorption curves were measured for $\theta = \pm 10°$, $\pm 20°$, $\pm 30°$, $\pm 60°$, and 90° with the various backings in position. At each angle θ, the difference between the latter set of readings and the former or unscattered readings gave the net backscattered radiation reaching the detector through that particular absorber. These differences plotted as functions of the thickness of aluminum absorber represent the absorption of the net backscattered radiation. Corrections were made in the case of Na^{22} for the γ-ray background.

[7] W. Heitler, *Quantum Theory of Radiation* (Oxford University Press, London, 1947), second edition, p. 231.

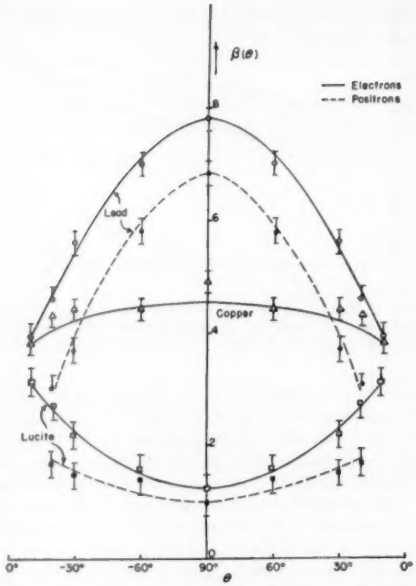

FIG. 3. Angular distribution of the backscattering coefficients for positrons and electrons for high, medium, and low Z backing materials.

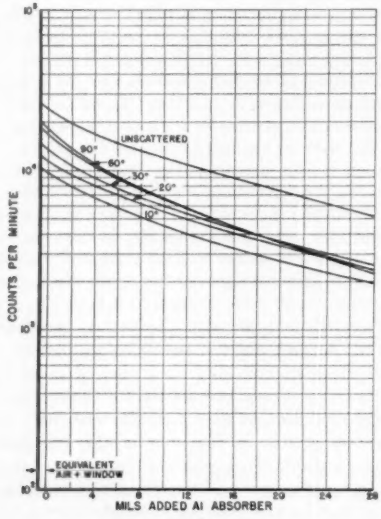

FIG. 4. Absorption in aluminum of the net backscattered P^{32} electrons from a lead backing. The unscattered absorption curve is shown for comparison.

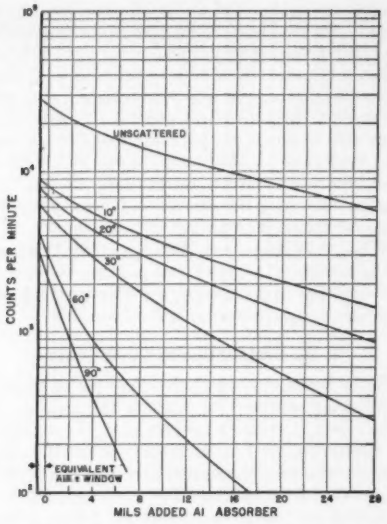

FIG. 5. Absorption in aluminum of the net backscattering P^{32} electrons from a Lucite backing. The energy loss can be estimated by comparison with the unscattered absorption curve.

III. RESULTS

Except for quantitative values, the positrons exhibited the same characteristics as electrons so that the discussion will be limited to electrons.

The final results for the 2π backscattering coefficients as measured in the 4π counter are shown by the solid lines in Fig. 2. The dashed line curves are the results of the previous measurement with the geometry of Fig. 1(a). The differences in backscattering between the two

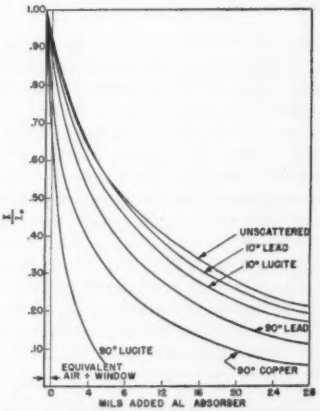

FIG. 6. Relative transmission of P^{32} backscattered electrons from low, medium, and high Z for $\theta = 10°$ and $\theta = 90°$.

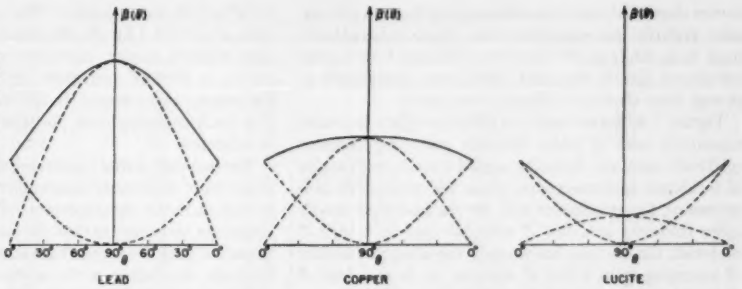

FIG. 7. Relative contributions to $\beta(\theta)$ of the diffusion effect (concave downward dashed curves) and the side scattering effect (concave upwards dashed curves), assuming a cosine distribution for the diffusion effect. The solid lines are taken from Fig. 3 for electrons.

types of geometries and especially the lower values of β at high Z and higher values of β at low Z measured over the 2π solid angle point up the anisotropy of the angular distribution of the backscattered radiation. The magnitude of this anisotropy is shown more clearly in Fig. 3, where the backscattering coefficient β is plotted as a function of the angle θ. Here $\beta(\theta)$ is defined by

$$\beta(\theta)=N(\theta)/N_\infty, \tag{5}$$

where $N(\theta)$ is the net extrapolated backscattered radiation at the angle θ, and N_∞ is the extrapolated value of the unscattered radiation, both at zero total absorber. From the $\beta(\theta)$ curves of Fig. 3 one can infer the results of Fig. 2, since

$$\langle\beta(\theta)\rangle_{Av}=\int_0^{\pi/2}\beta(\theta)\cos\theta d\theta.$$

Therefore, $\langle\beta(\theta)\rangle_{Av}<\beta(90°)$ for high Z and $\langle\beta(\theta)\rangle_{Av}>\beta(90°)$ for low Z. In addition to the values of $N(\theta)$, the absorption curves in aluminum of the net backscattered radiation give very important results concerning the relative energy degradation of the backscattered particles as functions of θ and of Z. Figures 4 and 5 show curves representing the absorption of P^{32} electrons backscattered from lead and from Lucite, respectively.

It is seen that electrons emerging at $\theta=90°$ from low Z materials are tremendously degraded in energy while those emerging at $\theta=10°$ are only slightly degraded. In the case of high Z materials the electrons emerging at $\theta=90°$ are only slightly different in energy from those emerging at 10°. The relative energy degradation as a function of θ and Z is brought out more clearly by Fig. 6 where the fractional transmission from lead, copper, and Lucite backings is plotted for $\theta=10°$ and $\theta=90°$. Here one can see that the particles emerging at small angles θ have a similar energy spectrum to the original unscattered electrons, while the spectrum of those emerging at large angles θ is quite different and has a large Z dependence.

IV. DISCUSSION

An important feature and a fortunate simplification in the interpretation of the present experimental results is the fact that the backscattering is approximately energy independent in the energy range considered. This was shown in abundant detail by Brand[1] and Bothe[2] for monoenergetic electrons and by Burtt,[8] Zumwalt,[9] and the author[3] for hetero-energetic radioactive sources with widely differing end points. Blanchard and Fano have shown[10] that the shape of the distribution function which describes the angular distribution of an electron inside a scatterer with respect to its original direction at any point along its path depends on the energy loss E_0-E and the original energy E_0 principally as the ratio $(E_0-E)/E_0$. Although a 100-kev electron beam will penetrate deeper into a scatterer than a 50-kev electron beam, both beams will lose their original "sense" of direction, or become isotropic at the same fractional loss of energy. Therefore the same fraction of each should be reflected in any given Z element. However, the ratio of elastic to inelastic scattering is proportional to Z, so that an electron in a high Z material will become isotropic with much less energy loss than it would in a low Z material, thereby increasing its probability of escape from the high Z material. The angular distribution of diffusing electrons emerging from any plane surface follows a cosine φ law where the angle φ is defined by $\varphi=(90°-\theta)$.

A qualitative estimate of the diffusion effect can be obtained by normalization of the experimental curves of Fig. 3 to a cosine distribution at $\theta=90°$. In Fig. 7 this is represented by the dashed concave downward curves. The difference between the experimental or solid line curves in Fig. 7 and the cosine distribution curves is given by the dashed concave upward curves. This distribution is due to the incompletely diffused or sidescattered electrons. Electrons initially incident and subsequently emerging at small angles with the surface lose only a small fraction of their original energy in being deflected and it is to those electrons that the adjective "side scattered" is applied. Since the ratio of scattering to absorption cross sections is still proportional to Z, the sidescattered electrons will lose less energy in the high Z material than in the low Z material. However, since little energy is lost even in low Z materials, the degradation for the sidescattering effect will be very much less than the degradation for the complete diffusion effect. In Fig. 6 the 10° transmission

[8] B. P. Burtt, Nucleonics 5, No. 2, 28 (1949).
[9] L. R. Zumwalt, unpublished report Mon C 397 (1950).
[10] C. H. Blanchard and U. Fano, Phys. Rev. 82, 767 (1951).

curves show that electrons sidescattered from Lucite are only slightly less energetic than those sidescattered from lead, while at 90° electrons diffusing from Lucite are almost totally degraded, being very much lower in energy than electrons diffusing from lead.

Figure 7 indicates that the diffusion effect increases materially with Z while the side scattering remains relatively constant. It can be argued that at small angles of incidence and emergence, while the mean deflection necessary for emergence will be reached after many more collisions in a low Z material than in a high Z material, the electron has roughly the same probability of emerging from a low Z material as from a high Z material, although it will be slightly less energetic upon emerging from the low Z material.

Miller[11] has made calculations of the ratio β^-/β^+, using Bartlett and Watson's and Massey's cross section calculations in a classical multiple scattering theory originally given by Bothe[12] for electrons. He estimates $\beta^-/\beta^+=1.16$ for mercury. The experimental results show $\beta^-/\beta^+=1.3$ for $Z=80$, which is in fair agreement with Miller's results, especially since the initial conditions in Bothe's derivation are not exactly those of the present experiments. In any case an excess of electron backscattering over positron backscattering is to be expected.

The isotropic initial conditions of the experiments are those most commonly encountered in actual practice in radioactivity measurements. It is therefore quite important to recognize that the backscattering is anisotropic, so that the proper backscattering correction can be made, depending on the geometry used. The curves of Fig. 2 should be especially helpful to those working with C^{14}, S^{35} and other low energy beta-emitters, where a 2π windowless counter is often used.

The author wishes to thank Miss L. Cavallo and Miss S. V. Culpepper for their valuable assistance in making these measurements, and Dr. U. Fano and Dr. C. H. Blanchard for many stimulating and enlightening discussions.

[11] W. Miller, Phys. Rev. **82**, 452 (1951).
[12] W. Bothe, Ann. Physik **6**, 44 (1949).

PHYSICAL REVIEW VOLUME 88, NUMBER 2 OCTOBER 15, 1952

Thermal Neutron Capture Cross Sections

H. POMERANCE
Oak Ridge National Laboratory, Oak Ridge, Tennessee
(Received June 11, 1952)

The thermal neutron capture cross sections of more than one hundred isotopes, including all the isotopes of 24 elements, plus several others, have been measured with the Oak Ridge National Laboratory pile oscillator.

THE thermal neutron capture cross sections of the elements have been measured by many techniques, but the cross sections for the individual isotopes[1] of those elements have been determined for the most part only by activation methods. Activation methods may be used only with roughly half of all stable isotopes, namely, those that become radioactive upon thermal neutron capture, and other techniques must be used for the remainder. A few measurements have been made by determining with a mass spectrometer the depletion produced by prolonged neutron bombardment, and some measurements have recently been made by counting directly the neutron capture gamma-rays; in both these methods natural samples can be employed. This paper reports on work with the Oak Ridge National Laboratory pile oscillator, which can measure directly the thermal neutron capture of any stable isotope sample. The more than one hundred enriched isotopic samples used in these measurements were produced by electromagnetic separation in the Stable Isotope Research Division of Oak Ridge National Laboratory.

The pile oscillator has been previously described and has been used to measure the cross sections of 69 elements.[2] It operates by pulsing the current of a boron-coated ionization chamber by moving the sample back and forth through the chamber, and by integrating these pulses which are proportional to the capture area of the sample. By operating in the reflector of the graphite reactor, the pile oscillator uses principally thermal neutrons; the cadmium ratio on indium is about 30, indicating that even for as unfavorable a case as indium the nonthermal capture contributions are at most 3.2 percent. The thermal capture cross sections for the isotopes as for the elements have been measured relative to gold for which the cross section has been taken to have a value of 95 barns for neutrons of 2200 m/sec velocity.[2]

The values of the isotopic cross sections are listed in Table I. The isotopic cross sections are for the pure isotopes; the atomic cross sections listed in the last column are the contributions of the isotopes to the natural elements and are found by multiplying the isotopic cross sections by the natural relative abundances. The errors are estimated from the average per-

[1] Cross section values with bibliographical references may be found in *Nuclear Data*, Nat. Bur. Standards Circular No. 499 (1950).

[2] H. Pomerance, Phys. Rev. **83**, 641 (1951).

TABLE I. Thermal neutron capture cross sections (in barns).

Isotope	Isotopic value	Estimated error (percent)	Atomic value[a]
Magnesium 24	0.033	30	0.026
25	0.27	30	0.027
26	0.06	100	0.006
Silicon 28	0.081	30	0.075
29	0.27	30	0.012
30	0.41	100	0.013
Potassium 39	1.87	8	1.74
40	66.	30	0.01
41	1.19	8	0.08
Calcium 40	0.22	20	0.21
42	39.7	8	0.25
Titanium 46	0.57	30	0.05
47	1.62	20	0.13
48	8.0	8	5.86
49	1.8	25	0.10
50	0 (+0.4)	—	0
Chromium 50	16.3	8	0.73
52	0.73	8	0.61
53	17.5	8	1.65
54	0 (+0.3)	—	0
Iron 54	2.17	8	0.13
56	2.55	8	2.34
57	2.4	12	0.05
58	2.5	80	0.02
Nickel 58	4.2	8	2.87
60	2.54	8	0.67
61	1.9	50	0.02
62	14.6	15	0.54
Copper 63	4.3	8	2.96
65	2.11	8	0.65
Gallium 69	1.99	8	1.20
71	4.9	8	1.95
Germanium 70	3.25	8	0.69
72	0.94	10	0.26
73	13.7	8	1.08
74	0.60	10	0.22
76	0.35	20	0.02
Selenium 74	48	15	0.42
76	82	8	7.42
77	40	10	3.05
78	0.4	100	0.09
80	0.59	10	0.29
82	2.0	70	0.19
Zirconium 90	0.1	70	0.06
91	1.52	8	0.17
92	0.25	30	0.04
94	0.08	50	0.01
96	0.1	100	0
Molybdenum 92	0 (+0.3)	—	0
95	13.4	8	2.11
96	1.2	50	0.20
97	2.1	30	0.20
98	0.4	100	0.09
100	0.5	100	0.05
Silver 107	29.9	8	15.4
109	84	8	40.6
Antimony 121	5.7	8	3.25
123	3.94	8	1.69
Tellurium 120	68	100	0.07
122	2.7	35	0.07
123	390	8	3.49
124	6.5	20	0.30
125	1.49	10	0.10
126	0.77	25	0.14
128	0.3	100	0.09
130	0.5	50	0.18
Barium 134	2	100	0.06
135	5.6	15	0.37
136	0.4	100	0.03
137	4.9	8	0.55
138	0.68	15	0.49
Cerium 136	25	100	0.05
138	8.7	70	0.02
140	0.63	10	0.56
142	1.76	15	0.20
Neodymium 142	18.5	12	5.01
143	292	8	35.67
144	4.8	12	1.15
145	52	8	4.28
146	9.8	8	1.68
148	3.3	30	0.19
150	2.9	50	0.16
Hafnium 174	500	100	0.9
176	15	100	0.8
177	375	8	69.3
178	72	15	19.5
179	50	50	6.9
180	13	40	4.5
Tungsten 180	30	−100, +400	0.03
182	19.2	10	4.95
183	10.9	10	1.55
184	1.97	15	0.60
186	34.1	8	9.95
Rhenium 185	100	8	37.3
187	63	8	39.6
Thallium 203	11.0	8	3.20
205	0.77	10	0.55
Lead 204	0.9	70	0.01
206	0.1	100	0.03
207	0.70	10	0.15
208	0 (+0.03)	—	0
Thorium 232	7.0	5	7.0

[a] The atomic value is the product of the isotopic value with the relative abundance of that isotope in the natural element.

formance of the pile oscillator and from the adequacy of the available sample of enriched material.

The limit of detection of the pile oscillator is a capture area of somewhat less than 0.1 mm², and the limit of precision is the same, but for this report exactly 0.1 mm² was used. This means that a sample of 0.5 mm² capture area was assumed to be measured with a precision of 20 percent, and 1.0 mm² with a precision of 10 percent. Although the values for the elements were thought to be accurate to 5 percent, a limit of 8 percent is listed for the isotopic measurements, principally because only one sample of each material was available. The extra 3 percent refers to the problem of getting an adequate chemical analysis of a small sample without destroying a large part of it. If the sums of the isotopic contributions to the natural element values are compared with the previously published values for the elements, it will be seen that 8 percent is a fair estimate of the error.

The cross section values of Table I are not original data for the samples but are derived numbers, because the enrichment was not usually sufficient to insure that all the capture came from the enriched isotope. For each element a set of simultaneous equations was solved, using the isotopic assays of the samples and the pile oscillator measurements as the primary data. The isotopic assays, performed by the Assay Department of the Y-12 plant, were more precise than the pile oscillator work and contributed no error to the final values of the cross sections. The computational data are not given in Table I, but the estimated errors allow for the contributions of the various isotopes to the total for the sample that was employed.

The author is indebted to Miss Thelma Arnette for her aid in this work.

Letters to the Editor

PUBLICATION of brief reports of important discoveries in physics may be secured by addressing them to this department. The closing date for this department is five weeks prior to the date of issue. No proof will be sent to the authors. The Board of Editors does not hold itself responsible for the opinions expressed by the correspondents. Communications should not exceed 600 words in length and should be submitted in duplicate.

The Influence of Binary Collisions on Molecular Gas Flow

J. W. HIBY AND M. PAHL
Forschungsstelle für Spektroskopie in der Max-Planck Gesellschaft, Hechingen Hohenzollern, Germany
(Received August 22, 1952)

BINARY collisions occurring in a molecular gas flow (mean free path $\lambda \gg d$, d being the diameter or other characteristic dimension of cross section) cause a deviation from the limiting value of ideal free-molecule flow ($\lambda \to \infty$). The conductance or specific flow F (gas flow per unit difference of pressure) is therefore a function of the mean pressure $\bar{p}$, depending on the geometrical form of the flow resistance. Pollard and Present[1] have deduced an approximate function $F(\bar{p})$ for the case of a very long capillary tube. They employ a rigorous mathematical method but make use of the assumption that by mutual collisions the molecules are scattered isotropically, thus neglecting the "persistence of molecular velocities" (Jeans). A simple correction for persistence as in the case of the elementary treatment of gaseous self-diffusion is not possible here, because the distribution of molecule path directions in the flow resistance and its change by the collisions must be considered.

If the pressure drop $p_1 - p_2$ along the flow resistance is small relative to $\bar{p}$, one can reduce the kinetics of relatively rare binary collisions to the problem of single scattering of molecules in a gas with Maxwell velocity distribution. Recently we have deduced[2] an approximate distribution function of the directions of scattering, assuming the molecules to be rigid elastic spheres. Consistent insertion of this scattering distribution into the integral of Pollard and Present would lead to great mathematical difficulties; but by using graphical methods we have found approximate solutions of first order in d/λ, representing the pressure variation of molecular conductance for the most important flow resistances. The relations agree with experimental results.

For a long circular tube of radius a we find for the ratio between its conductance F and the limiting value F_0 (corresponding to $\bar{p} \to 0$, $\lambda \to \infty$):

$$F/F_0 = 1 - 0.75(a/\lambda)\ln(\lambda/3.56a). \quad (1)$$

By this equation F_0 can be calculated from experimental results at small pressures. From the best observations of Knudsen and Gaede on the conductance of capillary tubes, F_0 is found slightly larger than calculated by Knudsen's formula for free-molecule flow; we conclude that Maxwell's coefficient f (fraction of molecules reflected diffusely at the walls) for several gases at a glass wall has a mean value $f = 0.98 \pm 0.01$, and that the minimum which the F vs $\bar{p}$ curve reaches in the transition region to laminar flow (beyond the range of validity of our equation) lies nine percent below F_0, not five percent as Knudsen assumed.

For a narrow slit between two plane parallel plates we find a more complicated formula; two constants are adjusted by comparison with experiments of Gaede.[3] In such a slit, the binary collisions cause a much stronger decrease of specific flow with increasing pressure than in a circular tube.

With short tubes F becomes a linear function of $\bar{p}$. If $2a$ is the tube diameter, l the tube length (or mean length of straight sections of a tube with sharp corners), and if $l \ll \lambda$, then

$$F/F = 1 + \kappa \cdot 2a/\lambda. \quad (2)$$

For $l/2a \approx 4$, we find $\kappa = 0$. With longer tubes κ becomes negative, with shorter tubes positive. For a circular orifice we find $\kappa = 0.12$, in agreement with experimental observations of Knudsen.[4]

Equation (2) will also apply to a porous medium, as it resembles a network of short capillaries. Assuming a plausible mean ratio $l/2a \approx 3$, we find that in the molecular region κ has the same order of magnitude as the slope factor 0.0738 of the Poiseuille equation for laminar flow. This agrees with experiments of Carman[5] on the permeability of fine powders; the flattening of the curve in the molecular region observed by Barrer and Grove[6] may be caused by a different pore structure.

Detailed publication will appear in the *Zeitschrift für Naturforschung*.

[1] W. G. Pollard and R. D. Present, Phys. Rev. **73**, 762 (1948).
[2] J. W. Hiby and M. Pahl, Z. Physik **129**, 517 (1951); **130**, 348 (1951).
[3] W. Gaede, Ann. Physik **41**, 289 (1913).
[4] M. Knudsen, Ann. Physik **28**, 999 (1909).
[5] P. C. Carman, Proc. Roy. Soc. (London) **A203**, 55 (1950).
[6] R. M. Barrer and D. M. Grove, Trans. Faraday Soc. **47**, 826 (1951).

Spin-Spin Interaction in HD Nuclear Resonance

B. SMALLER, E. L. YASAITIS, E. C. AVERY, AND D. A. HUTCHISON
Chemistry Division, Argonne National Laboratory, Chicago, Illinois
(Received September 2, 1952)

THE existence of a nuclear spin-spin interaction has been postulated by Hahn and Maxwell[1] and McNeil, Slichter, and Gutowsky[2] to account for the slow-beat phenomenon in the spin-echo nuclear resonance technique. Ramsey and Purcell[3] have proposed a second-order perturbation arising from higher electronic triplet states of the molecule to account for the interaction. For the case of the HD molecule they have calculated the magnetic level shifts to be approximately 70 $I_H \cdot I_D$, which implies that the proton resonance in HD would consist of a triplet structure with a 70 cps separation between components.

We have completed a series of measurements on the resonance line structure of the proton in H_2 and in HD which are in agreement with the predictions of Ramsey and Purcell. The equipment used has been described elsewhere.[4] The proton resonance in HD was obtained in a sample of H_2-D_2 that had been allowed to equilibrate under 1200 lb/in.[2] pressure for 18 months. A typical mass spectrometer analysis gave 2.4 percent H_2; 26.3 percent HD; 69.5 percent D_2 in good agreement with the assumption of a K_{eq} of 3.25. Resolution of the component lines was not feasible because of magnetic field homogeneity limitations, and thus resonance line widths were the criteria of structure. Since relaxation times can contribute to line broadening, line width measurements were made on pure H_2 at 1200 lb/in[2] and on a freshly prepared H_2-D_2 mixture where the H concentration was equal to that in the HD equilibrated sample. No significant difference in line width was detected. To insure that saturation broadening did not occur, the rf power was kept well below the saturation value. To insure the constancy of the field inhomogeneity over the gas sample volumes, interchange of the gas samples was made without moving the position of the gas chamber coil assembly in the magnet. The dc sweeping field rate was calibrated in terms of cycles per second by using a modulated radiofrequency source and by noting the separation of the resonances due to the sideband frequencies.

Operating at a radiofrequency of 30 Mc/sec, the results of 30 measurements on the H_2 proton resonance gave a line width (full width at $\frac{1}{2}$ maximum) at 109 ± 7 cps, while from 32 measurements of the H_2:HD proton resonances the average line width was found to be 138 ± 4 cps, the indicated error being the standard deviation of the mean. Obviously the triplet structure, revealed only in a broadening of the resonance line, cannot be deduced from the experimental evidence. However, with an *a priori* postulation of the structure one can deduce quite easily, by graphical analysis, the required separation of components to give agreement with

experiment. Taking into account both the H_2 and HD contribution to the line width, the required separation of components is found to be 52±6 cps. The result can be considered in good agreement with the theoretical predictions, since relatively crude wave functions[8] were used in predicting the separation.

We are indebted to Dr. Ramsey and Dr. Purcell[6] for their invaluable suggestions and information and to Dr. O. C. Simpson of this laboratory who encouraged us to made these measurements.

[1] E. L. Hahn and D. E. Maxwell, Phys. Rev. **84**, 1246 (1951).
[2] McNeil, Slichter, and Gutowsky, Phys. Rev. **84**, 1245 (1951).
[3] N. F. Ramsey and E. M. Purcell, Phys. Rev. **85**, 143 (1952).
[4] B. Smaller, Phys. Rev. **83**, 812 (1951).
[5] N. F. Ramsey, private communication.
[6] We have been informed recently that H. Y. Carr, using pulse echo techniques in HD, has obtained results in substantial agreement with our own.

The Probability of Internal Conversion of *K* Series Radiation of Au Arising from the Interaction of the *L* Subshells*

J. W. MIHELICH
Brookhaven National Laboratory, Upton, New York
(Received August 25, 1952)

IF a vacancy is created in the *K* shell of an atom, for example, by a *K* capture event, an *L* electron can fall into this vacancy, losing energy either by emission of an x-ray photon or by transfer of energy to an outer electron (Auger effect). Calculations have been made by Massey and Burhop[1] for the probability of internal conversion of the *K* series radiation for gold arising from the interaction of the L_IL_I, L_IL_{II}, and L_IL_{III} shells. They used the Møller correspondence principle, employing Dirac wave functions, and treat the process as a transition between states of equal energy of the system comprised of the two electrons. Two approximations were made: (1) the treatment of the problem as a two-electron problem, neglecting the perturbation of the wave function of the atomic electrons due to the ionization of the atom; (2) the use of screened hydrogen-like wave functions for the atomic electrons. They obtained the probability of the Auger transitions $L_IL_I \rightarrow K,\infty$, $L_IL_{II}\rightarrow K,\infty$, and $L_IL_{III}\rightarrow K,\infty$ for gold. These results for the relativistic theory were compared with those obtained in the nonrelativistic approximation of Burhop[2] (see Table I).

We have obtained an experimental value for the relative probability of the Auger transitions for which they made calculations, and in addition, we have obtained values for the transitions $L_{II}L_{II}\rightarrow K,\infty$, $L_{II}L_{III}\rightarrow K,\infty$, and $L_{III}L_{III}\rightarrow K,\infty$. The source, Hg^{197m}, which decays to Au^{197m} by *K* capture, was prepared by Dr. A. DeShalit by irradiating Au with protons in the Princeton cyclotron.[3] The Auger electrons were analyzed in a 180° permanent magnet photographic spectrograph. The measured energies of the lines, along with the energies expected using a recent compilation of x-ray level energies,[4] are listed in Table I. The measured intensities are compared with the two sets of theoretical calculations. It may be noted here that energy and intensity considerations eliminate the possibility of these Auger lines arising in Hg^{197m}.

TABLE I. Experimental and theoretical energies and intensities for Auger transitions in Au involving two *L* electrons.

Transition	Energy (kev) Meas.	Energy (kev) Calc.[a]	Intensity Theoretical Nonrel.[b]	Intensity Theoretical Rel.[c]	Intensity Measured This work	Intensity Measured $Z=83$[d]
$L_IL_I\rightarrow K\infty$	51.87	52.00	1.0	1.0	1	1.0
$L_IL_{II}\rightarrow K\infty$	52.51	52.62	1.14	5.5	1.7	1.83
$L_IL_{III}\rightarrow K\infty$	54.26	54.43	2.28	5.3	1.2	1.33
$L_{II}L_{II}\rightarrow K\infty$	53.10	53.24			~0.3	<0.2
$L_{II}L_{III}\rightarrow K\infty$	54.89	55.05			1.4	2.33
$L_{III}L_{III}\rightarrow K\infty$	56.64	56.86			0.8	1.25

[a] Using x-ray critical absorption edge energies (see reference 4).
[b] See reference 2.
[c] See reference 1.
[d] See reference 5.

In addition, Ellis[5] has obtained similar data for Auger transitions in $Z=83$ [using Th(B+C)], which are listed in the table.

It is clear that the experimental data on intensities, which have an experimental uncertainty of about 25 percent, are incompatible with the relativistic results of Massey and Burhop, who suggested the experiment as a test for the extension of the Dirac equation to two bound electrons, believing it was not likely that the inaccuracies in the approximations discussed above would be great enough to mask the relativistic effect. However, it may be that a recalculation of this effect, using the Hartree self-consistent field method as suggested by Massey and Burhop, would modify the theoretical values. One would hesitate to question the validity of the Dirac equation on the basis of existing calculations for this Auger effect.

Two additional points are of interest. First, we observe the L_{II}, $L_{II}\rightarrow K,\infty$ transition which Ellis did not detect and for which he set an upper limit of 0.2 of the intensity of the other transition. Second, Ellis notes that the Auger electron energies were less (by ~0.2 kev) than the calculated values ($E_K-2E_{L_I}$), etc., where E_K and E_{L_I} are the x-ray absorption edge energies for the *K* and L_I shells. This is a measure of the additional energy required to remove an *L* electron from an atom ionized in the *L* shell. Robinson and Cassie[6] have noted a similar energy defect (~0.07 kev) for Cu, by directly comparing the energies of photoelectrons with the energies of Auger electrons. We also observe such an energy defect (~0.15 kev) which is just outside experimental error.

Thanks are due Dr. A. DeShalit, for preparation of the source, and Professor J. H. Bartlett, Dr. M. Goldhaber, and Dr. John Miskel for discussion.

* Work performed under contract with AEC.
[1] H. S. W. Massey and E. H. S. Burhop, Proc. Roy. Soc. (London) **A153**, 661 (1936). See also *The Auger Effect and Other Radiationless Transitions*, E. H. S. Burhop (Cambridge University Press, London, 1952).
[2] E. H. S. Burhop, Proc. Roy. Soc. (London) **A148**, 272 (1935). Similar nonrelativistic results have been calculated by E. G. Ramberg and R. K. Richtmyer, Phys. Rev. **51**, 913 (1937). See also L. Pincherle, Nuovo cimento **12**, 81 (1935).
[3] The source was prepared in connection with an investigation of the decay of Hg^{197m} and Au^{197m} [A. DeShalit and J. W. Mihelich (to be published)].
[4] Hill, Church, and Mihelich, Rev. Sci. Instr. (to be published).
[5] C. D. Ellis, Proc. Roy. Soc. (London) **139**, 336 (1933).
[6] H. R. Robinson and A. M. Cassie, Proc. Roy. Soc. (London) **113**, 282 (1926).

Interaction between Nuclear Spins in HD Gas*

H. Y. CARR† AND E. M. PURCELL
Harvard University, Cambridge, Massachusetts
(Received September 3, 1952)

A NUMBER of nuclear resonance experiments have disclosed effects that could be explained only by an internuclear interaction of the form $\mathbf{I}_1\cdot\mathbf{I}_2$, I_1 and I_2 being the spins of the two nuclei involved.[1-5] Ramsey and Purcell[4] have pointed out that such an interaction can arise from the indirect coupling of one nuclear spin to another via the exchange-coupled electrons of the molecule and that an especially clear test of this theory would be afforded by the molecule HD. In this molecule the interaction should split both the H and the D resonances into multiplets. The separation of the multiplets is calculable and should be field independent.

Fine structure in both the H and D resonances of HD gas has now been observed. Furthermore, the fine structure has been observed in the H resonance at both 30 Mc/sec and 5 Mc/sec and found to be field independent. According to the theoretical prediction, the H resonance should consist of three equally intense lines, equally spaced in frequency, the separation between the central line and the satellites being denoted δ cps. The D resonance should consist of two equally intense lines, δ cps apart. This is the structure observed. An approximate calculation based on Heitler-London wave functions gave 70 cps as the order of magnitude of δ. The observed δ is 43.5±1 cps, which agrees with the theoretical prediction as well as one could expect.

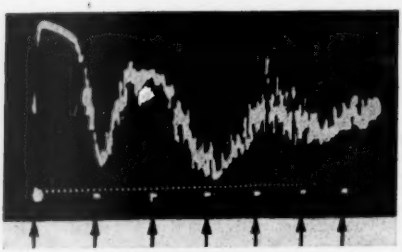

FIG. 1. Deuteron signal from HD.

The method of observation consisted of the application of an intense 15-μsec rf pulse at the resonant frequency to a tuned coil containing the sample in the static magnetic field. The intensity and duration of the pulse were such as to cause the net nuclear magnetic moment vector to nutate 90°. This enabled the observation of maximum signal amplitude due to the free ringing or precession of the moment vector when the 15-μsec pulse was removed.[5] The homogeneity of the static field was good enough to allow the observation of the nuclear free-ringing signal or "tail" with its modulation pattern[6] for 100,000 μsec. The ultimate limitation on the observation of the fine structure modulation in the nuclear signal was the relaxation time.

The modulation pattern on the "tail" in the D resonance in HD at 4.4 Mc/sec is shown in Fig. 1. It is a simple beat pattern of two signals of equal amplitude. The two spin groups correspond to the two possible orientations of the neighboring H magnetic moment. Figure 2 shows the pattern observed in the H resonance at the same frequency. This is the slightly more complicated but typical beat pattern of three signals of equal frequency separation and amplitude. The three groups in this case correspond to the three possible orientations of the neighboring D magnetic moment. In addition to the fine structure modulation, both tails decay due to the normal relaxation processes.

The most accurate value for the separation δ, 43.5±1 cps, was obtained from the fifth minimum on a picture of the H resonance at 4.4 Mc/sec. The ±1 cps is the estimated maximum limit of error. The limits in the D resonance at 4.4 Mc/sec and the H resonance at 30.0 Mc/sec were somewhat greater. To within the latter limits, all separations observed in the D resonances and the H resonances agreed with the value quoted above.

The samples used consisted of substantially pure HD gas sealed in a glass bulb of 0.1 cc volume, in amount such that the pressure at room temperature would be about 300 atmospheres. The samples were prepared by admitting a known volume of the gas at known pressure and temperature through 25 cm of capillary to the bulb where the gas was frozen by immersing in liquid helium. While the bulb was still immersed and the gas still frozen, the upper end of the capillary was sealed off. The observations were then made at liquid nitrogen temperature.

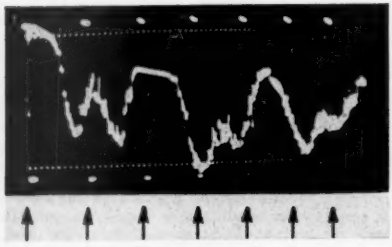

FIG. 2. Proton signal from HD.

We are greatly indebted to Mr. David G. White of the Department of Chemistry for the preparation of the gas which was subsequently sealed off. The method of preparation involved the reaction of D_2O with lithium aluminum hydride in a manner similar to that described by Fookson, Pomerantz, and Rich.[7] In the present work the final fractionation process was omitted. Two of their samples prepared by the same method as the present samples were analyzed mass spectrographically before fractionation and were found to contain 98.1 percent and 97.0 percent hydrogen deuteride, respectively.

* This work was partially supported by the joint program of the ONR and AEC.
† Now at Rutgers University, New Brunswick, New Jersey.
[1] Gutowsky, McCall, and Slichter, Phys. Rev. **84**, 589 (1951).
[2] McNeil, Slichter, and Gutowsky, Phys. Rev. **84**, 1245 (1951).
[3] E. L. Hahn and D. E. Maxwell, Phys. Rev. **84**, 1246 (1951).
[4] N. F. Ramsey and E. M. Purcell, Phys. Rev. **85**, 143 (1952).
[5] E. L. Hahn, Phys. Rev. **77**, 297 (1950).
[6] E. L. Hahn, Phys. Rev. **80**, 580 (1950), Part G.
[7] Fookson, Pomerantz, and Rich, J. Research Natl. Bur. Standards **47**, 31 (1951).

The Theory of Secondary Emission*

J. F. MARSHALL
Bartol Research Foundation, Franklin Institute, Swarthmore, Pennsylvania
(Received August 7, 1952)

SEVERAL authors[1,2] have treated the problem of the interaction between energetic primary electrons and the weakly-bound lattice electrons of a solid. However, owing to considerations involving the orthogonality of Bloch wave functions, certain conclusions based upon these theories are incorrect.

The differential cross section for the process in which a primary electron undergoes a transition from a state $\mathbf{K}$ to a state $\mathbf{K}'$, within a solid angle $d\Omega'$, is given by

$$d\sigma(\mathbf{K}\to\mathbf{K}')=\Sigma_{\mathbf{q}}d\sigma_{\mathbf{q}}, \tag{1}$$

where

$$d\sigma_{\mathbf{q}}=[4m^2e^4K'/h^4S^4K]\times|\Sigma_{\mathbf{m}}a_{\mathbf{m}+\mathbf{q}}(\mathbf{k})a_{\mathbf{m}}{}^*(\mathbf{k}')|^2d\Omega'. \tag{2}$$

Here, $\mathbf{S}=\mathbf{K}-\mathbf{K}'$, $\mathbf{m}$ and $\mathbf{q}$ are vectors with integer components, and $\mathbf{k}$ and $\mathbf{k}'$ are wave vectors corresponding to initial and final states of the lattice electron. The $a_{\mathbf{m}}$ are the coefficients in the Fourier expansion of the eigenfunctions for a cubic lattice of lattice constant a.
These have the form

$$\Psi_{\mathbf{k}}(\mathbf{r})=V^{-\frac{1}{2}}\exp[i\mathbf{k}\cdot\mathbf{r}]\Sigma_{\mathbf{m}}a_{\mathbf{m}}(\mathbf{k})\exp[i(2\pi/a)\mathbf{m}\cdot\mathbf{r}]. \tag{3}$$

It is found that for each $\mathbf{q}$ the following conservation relation holds:

$$\mathbf{S}+\mathbf{k}-\mathbf{k}'+2\pi\mathbf{q}/a=0. \tag{4}$$

For given $\mathbf{K}$, $\mathbf{K}'$, $\mathbf{k}$, and $\mathbf{q}$, $\mathbf{k}'$ is uniquely specified by Eq. (4), and the summation indicated in Eq. (1) is equivalent to an integration over final states $\mathbf{k}'$.

Because of the presence of S^4 in the denominator of Eq. (2) $d\sigma_{\mathbf{q}}$ is appreciable only when $\mathbf{K}'$ has values for which S is near its minimum $S_{\min}$. For primary energies above several hundred ev, $\mathbf{S}_{\min}$ is considerably smaller than any of the other terms in Eq. (4), and, in the region of interest, $\mathbf{k}'$ is given approximately by

$$\mathbf{k}'\approx\mathbf{k}+2\pi\mathbf{q}/a. \tag{5}$$

It is consequently assumed for purposes of integration over Ω' that $a_{\mathbf{m}}(\mathbf{k}')$ can be replaced by $a_{\mathbf{m}}(\mathbf{k}+2\pi\mathbf{q}/a)$. This approximation leads to the total cross section of the Wooldridge theory:

$$\sigma_{\mathbf{q}}=\frac{16\pi m^2e^4}{h^4}\,\frac{|\Sigma_{\mathbf{m}}a_{\mathbf{m}+\mathbf{q}}(\mathbf{k})a_{\mathbf{m}}{}^*(\mathbf{k}+2\pi\mathbf{q}/a)|^2}{[(2\pi\mathbf{q}/a)\cdot(2\pi\mathbf{q}/a+2\mathbf{k})]^2}. \tag{6}$$

However, expressions for secondary yields and energy losses based upon this cross section actually vanish since, in this approximation, σ_q is zero, a fact not recognized in previous theories. This is an immediate consequence of the orthogonality relation between the lattice eigenfunctions belonging to $\mathbf{k}$ and $\mathbf{k}+2\pi\mathbf{q}/a$,

$$\int \psi_{\mathbf{k}}\psi_{\mathbf{k}+2\pi\mathbf{q}/a}^{*}d\tau=0. \quad (7)$$

Substitution of Eq. (3) into Eq. (7) yields

$$\frac{1}{V}\Sigma_{\mathbf{m},\mathbf{n}}a_{\mathbf{n}}(\mathbf{k})a_{\mathbf{m}}^{*}(\mathbf{k}+2\pi\mathbf{q}/a)\int\exp[(2\pi i/a)(\mathbf{n}-\mathbf{q}-\mathbf{m})\cdot\mathbf{r}]d\tau$$
$$=\Sigma_{\mathbf{m}}a_{\mathbf{m}+\mathbf{q}}(\mathbf{k})a_{\mathbf{m}}^{*}(\mathbf{k}+2\pi\mathbf{q}/a)=0. \quad (8)$$

Substitution of Eq. (8) into Eq. (6) yields a zero cross section. In order to obtain a finite result, it is necessary to take into account the variation of $a_{\mathbf{m}}(\mathbf{k}')$ with $\mathbf{K}'$. This can be accomplished by a Taylor series expansion of $a_{\mathbf{m}}(\mathbf{k}')$ about the point $\mathbf{k}'=\mathbf{k}+2\pi\mathbf{q}/a$. This results in a cross section which for sufficiently high energies has the same form as that obtained by Bethe[3] for the ionization of atoms, namely,

$$\sigma_q=(A/E)\ln(E/E'), \quad (9)$$

where E is the energy of the primary electron and A and E' are parameters characteristic of the medium. A similar expression is obtained for the rate of energy loss by electrons passing through solids. These results are entirely different from those obtained on the basis of Eq. (4), which have previously been interpreted[1,2] to mean that both the rate of production of secondaries and the rate of energy loss should be practically independent of the energy of the primary. Actually, these quantities are zero in the approximation leading to Eq. (4), and as indicated by Eq. (9) and the equivalent expression for the energy loss, they decrease rapidly with energy.

It should be pointed out that the above considerations do not apply to the case of free electrons ($\mathbf{q}=0$), which has been treated by Baroody[4] and by Dekker and van der Ziel[2], since values of $\mathbf{S}$ in the neighborhood of $\mathbf{S}_{\min}$ are forbidden because they correspond to transitions to occupied states.

The questions outlined here will be treated in more detail in a forthcoming paper.

* Supported by the ONR.

[1] D. E. Wooldridge, Phys. Rev. **56**, 562 (1939).
[2] A. J. Dekker and A. van der Ziel, Phys. Rev. **86**, 755 (1952).
[3] H. Bethe, Ann. phys. **5**, 325 (1930).
[4] E. M. Baroody, Phys. Rev. **78**, 780 (1950).

Alpha-Particle Ionization in Mixtures of the Noble Gases

WILLIAM P. JESSE AND JOHN SADAUSKIS
Argonne National Laboratory, Chicago, Ill.
(Received September 2, 1952)

DURING the course of experiments to determine for polonium alpha-particles the absolute value of W, the average energy required to produce an ion pair in various gases, erratic results soon showed that the effect of minute gaseous impurities in such measurements is much greater than is commonly recognized. Accordingly, experiments have been carried out where a contaminant in measured quantities could be added to the gas under investigation and the effect of the impurity on the total ionization observed. Preliminary experiments on helium and neon have shown rather striking results.

In the measurements a short collimating system directed the polonium alpha-particles along the axis of a long cylindrical ionization chamber. The effective path length was about 20 cm. The ions produced by each alpha-particle were collected and measured by a method already described.[1] From a knowledge of the capacity of the system and the change of potential of the system produced by the ionization from each alpha-particle, the absolute number of ion pairs produced may be determined. The average energy W to produce an ion pair is, of course, the energy of the polonium alpha-particle (5.298 Mev) divided by this number.

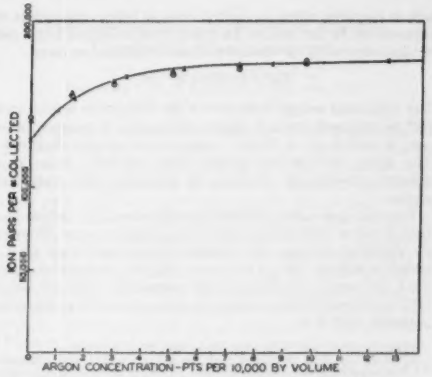

FIG. 1. Ion pairs collected per alpha-particle as a function of argon concentration in helium. Runs △ and ○ represent commercial "spectroscopically pure" He. Run × represents this He after further purification.

The ionization chamber was pumped and baked for twelve hours at a temperature above 200°C at the beginning of the measurements, and extreme care was taken to minimize gaseous impurities from the system.

The graph in Fig. 1 shows the effect on the ionization produced per alpha-particle of adding extremely small quantities of argon to pure helium. The ionization per alpha-particle at first increases rapidly with increasing argon concentration and then more slowly, apparently approaching finally a saturation value. The points on the curve may be indefinitely repeated by adding argon in measured quantities and then removing it by repeated passage over coconut charcoal at liquid air temperature.

The addition of argon to pure neon gives a curve of the same type as that shown in Fig. 1, but with higher ionization values throughout. Data for helium and neon with argon as an impurity are shown in Table I.

TABLE I. Polonium alpha-ionization measurements in helium and neon.

Gas	Ion pairs per Po alpha-particle	W = average energy per ion pair, ev/ion pr
Purest helium used	128,300	41.3
Helium +0.13% argon	178,400	29.7
Purest neon	146,000	36.3
Neon +0.12% argon	203,000	26.1

It is of interest to note that, for the purest gases used here, the number of ion pairs produced per alpha-particle is much smaller, and the W correspondingly larger, than the results heretofore given in the literature. In fact, the value of W for helium commonly given in the literature, about 30 ev/ion pair, is in much closer agreement with the above value for helium saturated with argon as an impurity. This suggests the presence of impurities in previous determinations.

Experiments with a small radium source placed in a standard position with regard to the chamber show a similar increase in gamma-ray ionization as the argon concentration in helium is increased. Here the total relative current through the chamber was measured, rather than the effect of single gamma-rays.

A plausible explanation[2] for the increase in ionization observed, both for alpha-particles and gamma-rays, is that this increase results from a transfer of energy from the metastable states in

helium (or neon) when an excited atom of helium encounters an argon atom. In the process the argon atom is ionized and a pair of ions collected in the chamber. Thus for helium, we have

$$He^* + A \rightarrow He + A^+ + e^-.$$

Any additional energy imparted by the metastable helium atom He^* to the argon atom A, above that energy to produce an ion pair, is carried off as kinetic energy in the ejected electron e^-. The above reaction has already been studied[2,4] under quite different experimental conditions in connection with metastable atoms.

Krypton and carbon dioxide as contaminants in helium have been found to yield results, in general, similar to argon. However, no significant increase in ionization is observed when neon is added to helium. This is in accord with the explanation above, since the energy available in the metastable state for helium (19.8 ev) is insufficient to ionize the neon atom with an ionization potential of 21.5 ev.

[1] Jesse, Forstat, and Sadauskis, Phys. Rev. **77**, 782 (1950).
[2] The authors wish to express their thanks to Dr. Roland E. Meyerott for first suggesting this explanation and for many stimulating discussions of the whole subject.
[3] A. A. Kruithof and M. J. Druyvesteyn, Physica **4**, 450 (1937).
[4] M. A. Biondi, Phys. Rev. **83**, 653 (1951).

The Reaction $Li^6(\gamma,d)He^4$ at 2.76 Mev

HOWARD B. GLENN
Argonne National Laboratory, Chicago, Illinois
(Received August 4, 1952)

A SEARCH has been made for the $Li^6(\gamma,d)He^4$ reaction using 2.76-Mev γ-rays from Na^{24}. Ilford C2 nuclear emulsions loaded with enriched Li^6 were used. Using fused NaF irradiated in the Argonne heavy water pile, the Li^6 plates were exposed to approximately 10 r using $\frac{1}{8}$ in. of Al to filter out the beta-rays from Na^{24}. Using the accepted mass values[1] for Li^6, He^4, and H^2, the reaction threshold is found to be 1.48 Mev and there is 1.28 Mev available for the reaction products. From the kinetics of the problem, neglecting γ-ray momentum, the alpha-particle receives $\frac{1}{3}$ and the deuteron receives $\frac{2}{3}$ of this energy. These correspond to ranges of 2 and 8 microns, respectively, in the emulsions used.

During preliminary investigations, one example of the reaction was found. Searching was continued on a plate which had the maximum exposure, but with a tolerable gamma-background. In 7500 fields of view, corresponding to $\frac{3}{4}$ cm^2, only two possible events were found. Figure 1 shows the first example to be found. The ranges for the alpha and the deuteron tracks are 2 and 8 microns, respectively, as predicted, and the track density shows the two-body nature of the event. The photograph does not show the two tracks and the point of disintegration as clearly as they appear under the microscope.

On the basis of this evidence, an upper limit for the cross section for the reaction can be placed at

$$\sigma[Li^6(\gamma,d)He^4]_{2.76\ Mev} = (4\pm4)\times10^{-30}\ cm^2.$$

The only other work reported[3] on this reaction was done using a mixture of 14.8-Mev and 17.6-Mev γ-rays from the $Li^7(p,\gamma)$ reaction.

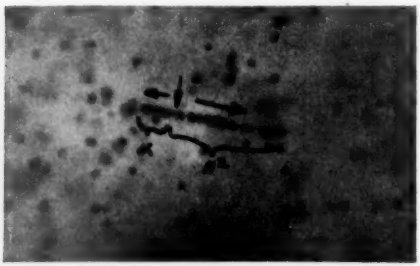

FIG. 1. Example of the reaction $Li^6(\gamma,d)He^4$.

[1] Li, Whaling, Fowler, and Lauritsen, Phys. Rev. **83**, 512 (1951).
[2] E. W. Titterton, Proc. Phys. Soc. (London) **A63**, 915 (1950).

Mean Free Paths of Electrons in Evaporated Metal Films

F. W. REYNOLDS AND G. R. STILWELL
Bell Telephone Laboratories, Murray Hill, New Jersey
(Received August 28, 1952)

RECENT work on the evaporation of metals, particularly Cu and Ag, has made available thin films of these metals, in the thickness range from about 100–2000 angstroms, which have resistivities and resistance-temperature coefficients predictable from existing theories. These results suggest approximate values for the mean free paths l of the conduction electrons in these metals at room temperatures.

It is well known that the resistivity ρ' of a thin metallic film is greater than ρ for the bulk metal, and that the ratio ρ'/ρ increases with decrease in film thickness t. Thomson[1] was the first to suggest a theory of this effect involving the mean free path and the film thickness. Subsequently, this theory has been modified and extended by others, including Fuchs[2] and Dingle.[3] A comprehensive review of this subject has been given recently by Sondheimer.[4] Andrew,[5] working with Sn and Hg using relatively thick layers $>3\mu$ and wires $>6\mu$ in diameter, has obtained experimental confirmation of this theory at low temperatures. Similar results appear lacking in the literature for thinner layers and for higher temperatures. In general, thin metallic films exhibit wide variations in properties with method of preparation and have much larger resistivities than would be predicted from theory. Our recent work has been successful in minimizing these variations by selection and control of the rate of evaporation and residual gas pressure. Optimum conductivity is obtained by using fast rates of evaporation, for example, 500–1000 angstroms per second, and low residual gas pressure, for example, 10^{-5} mm. At these rates and pressures satisfactory films can be obtained in the thickness range previously mentioned. Films deposited at much slower rates and/or higher pressures show considerable departure from calculated values.

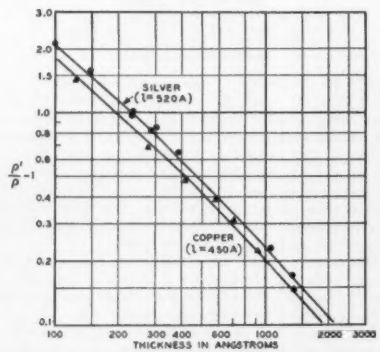

FIG. 1. Experimental points involving resistivity measurements of Cu and Ag films at room temperature, shown with curves calculated from theory to obtain approximate values of mean free paths.

Methods of film preparation other than evaporation have been tried, such as chemical deposition and electrolysis. The films thus obtained had much higher resistivities, in some cases by factors as large as fivefold, and in this respect were comparable to films evaporated under adverse conditions.

Evaporated Cu films have been examined in greatest detail. These films, formed under optimum conditions, show large aging effects immediately after evaporation. Their resistance drops rapidly during the first few minutes, reaching an approximate equilibrium in about 1–2 hours in vacuum. These films, stored in dry air, remain essentially constant in resistance over a period of many months. Fast evaporated Cu films are highly crystallized.

Figure 1 is a plot of $(\rho'/\rho)-1$ *versus* film thickness in angstroms. The solid lines are computed from Dingle's tabulations for the case of inelastic scattering at the film boundaries using values of mean free paths l of 520 and 450 angstroms for Ag and Cu, respectively, to approximate the experimental data. This value of l for Ag is in good agreement with that calculated from Sommerfield's theory assuming N_e/N_a, the number of free electrons per atom, is unity. The experimental value of l for Cu is about 15 percent higher than calculated. It may be of practical interest to note that since these plots are nearly straight lines, Planck's[6] empirical equation, $\rho'/\rho=1+c\delta/l$, agrees within about five percent with the more exact theory down to thicknesses of $t=l/10$ where c is assigned an arbitrary value of 0.4.

Resistance-temperature coefficients α' have been determined for these fast evaporated films. Results for Cu and Ag are given in Fig. 2. The solid lines are calculated, and the circles represent

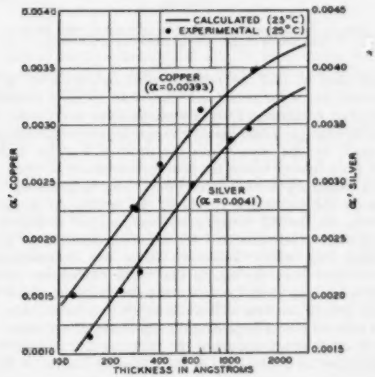

FIG. 2. Comparison of measured and calculated resistance-temperature coefficients.

experimental points. These calculations are based on the assumption that $\rho'\alpha'=\rho\alpha$, where ρ, α are the bulk values, and ρ', α' are the corresponding film quantities. Films not deposited under optimum conditions have smaller values of α' than indicated by these curves. Such films have larger values of ρ' than normal, but the product $\rho'\alpha'$ remains essentially constant for a given metal, indicating that Matthiessen's rule is followed.

The following bulk metal values at 25°C have been used in the calculations:

	ρ(Microhm-cm)	α(deg C^{-1})
Ag	1.623	0.0041
Cu	1.705	0.00393

[1] J. J. Thomson, Proc. Cambridge Phil. Soc. **11**, 120 (1901).
[2] K. Fuchs, Proc. Cambridge Phil. Soc. **34**, 100 (1938).
[3] R. B. Dingle, Proc. Roy. Soc. (London) **201**, 545 (1950).
[4] E. H. Sondheimer, Advances in Phys. **1**, 1 (1952).
[5] E. R. Andrew, Proc. Phys. Soc. (London) **62**, 77 (1949).
[6] W. Planck, Physik. Z. **15**, 563 (1914).

The Geometrical Correction in Angular Correlation Measurements*

E. L. CHURCH AND J. J. KRAUSHAAR
Brookhaven National Laboratory, Upton, New York
(Received August 28, 1952)

THE presence of the effects of mixtures of multipole radiations and disturbing extra-nuclear fields in angular correlation studies necessitates an accurate evaluation of the correlation function. The largest correction that must be applied to the experimental data before an appropriate analysis can be made is that due to finite instrumental angular resolution. The problem of accounting for such effects has been discussed by Walter *et al.*,[1] Frankel,[2] and Frauenfelder.[3] The object of the present note is to present a simple procedure for correcting the data directly in terms of the experimental resolution curve and to indicate that the corrections so introduced are greater than has heretofore been assumed. The method outlined, an extension of the procedure of Frankel, is applied to a particular case and verified at two different geometries. The corrections are found to be large and sensitively dependent on the shape of the resolution curve.

The directional correlation function for a $\gamma-\gamma$ cascade may be written in the form

$$W(\theta)=N(\theta)/N(\tfrac{1}{2}\pi)=\Sigma_M A_{2M}P_{2M}(\cos\theta), \tag{1}$$

where the coefficients A are functions of the cascade parameters. The resolution curve $f(\delta)$, corresponding to a particular geometry, is determined using annihilation radiation and is conveniently expanded as

$$f(\delta)=N(\pi-\theta)=\Sigma_m B_m P_m(\cos\delta). \tag{2}$$

Assuming the counters to be individually symmetric, the observed correlation function $W'(\theta)$ may be compounded out of (1) and (2) as

$$W'(\theta)=\int W(\theta')f(\delta')d\Omega', \tag{3}$$

where θ,θ', and δ' are the three sides of a triangle on the surface of the unit sphere. The integral (3) can be evaluated by an application of the addition theorem for spherical harmonics as shown by Frankel.[2] One finds

$$W'(\theta)=\sum_M\left[\left(\frac{4\pi}{2M+1}\right)B_{2M}\right]A_{2M}P_{2M}(\cos\theta)=\sum_M A_{2M}'P_{2M}(\cos\theta). \tag{4}$$

The effect of finite counter geometry is therefore one of altering the original coefficients by a simple factor.

The coefficients B_{2M} are obtained by direct numerical integration over the experimental resolution curve as shown below. To within an arbitrary factor which cancels in the subsequent normalization of $W(\theta)$,

$$\left(\frac{4\pi}{1}B_0\right)=\int f(\mu)P_0(\mu)d\mu,\ \left(\frac{4\pi}{5}B_2\right)=\int f(\mu)P_2(\mu)d\mu,\ \left(\frac{4\pi}{9}B_4\right)=\int f(\mu)P_4(\mu)d\mu, \tag{5}$$

where $\mu=\cos\delta$.

If the resolution curve can be approximated by a triangular or Gaussian distribution, these coefficients can be estimated by means of the expansions[4]

$$\begin{aligned}\left(\frac{4\pi}{1}B_0\right)&=1-\frac{6.092}{7.325}(-5)\delta_0^2+\ldots,\\ \left(\frac{4\pi}{5}B_2\right)&=1-\frac{6.092}{7.325}(-4)\delta_0^2+\frac{1.609}{2.930}(-7)\delta_0^4-\ldots,\\ \left(\frac{4\pi}{9}B_4\right)&=1-\frac{1.889}{2.271}(-3)\delta_0^2+\frac{1.460}{2.659}(-6)\delta_0^4\\ &\qquad-\frac{0.631}{2.133}(-9)\delta_0^6+\ldots,\end{aligned} \tag{6}$$

where δ_0 is the half-width at half-maximum of the resolution curve expressed in degrees. The upper coefficients refer to a triangular, and the lower to a Gaussian distribution.

In practice, directional correlation results are usually represented in the form

$$W'(\theta)=1+a_2'\cos^2\theta+a_4'\cos^4\theta, \tag{7}$$

where the coefficients a' have been determined by a weighted least squares fitting procedure to the experimental data. The corresponding coefficients A' in (4) may then be determined by relationships such as those given by Lloyd.[6] After calculation of the unprimed coefficients A by the appropriate divisions of A' by (5), the data may then be returned to the original form (7) in a reverse fashion.[6]

To verify the usefulness of the above procedure, the directional correlation of Rh^{106}, with no appreciable bias on the counters, was measured with $\delta_0=6.6°$ and 12.0° with effectively a point source. The values of a_2 and a_4 obtained for the two cases before and after applying the calculated geometrical corrections are shown in Table I. It is seen that the correction is considerable and

TABLE I. Directional correlation coefficients for Rh^{106}.

	$\delta_0=12.0°$		$\delta_0=6.6°$		Theor. (0–2–0)	
	a_2	a_4	a_2	a_4	a_2	a_4
Uncorrected	−1.718 ±0.074	+2.294 ±0.085	−2.086 ±0.049	+2.782 ±0.056		
Corrected	−2.248	+2.921	−2.244	+2.968	−3.000	+4.000

that the adjusted values for the two geometries are in agreement within the indicated rms statistical errors.

The possible discrepancy between the measured correlation function of Rh^{106} and that expected for a 0–2–0 cascade will be discussed in a subsequent publication,[6] both in the light of the above data and the recent work of Arfken *et al.*[7]

We wish to acknowledge helpful discussions of this problem with M. Fuchs.

* Research carried out under contract with the AEC.
[1] Walter, Huber, and Zünti, Helv. Phys. Acta **23**, 697 (1950).
[2] S. Frankel, Phys. Rev. **83**, 673 (1951).
[3] H. Frauenfelder, *Annual Review of Nuclear Science*, Vol. 2 (to be published).
[4] The numbers in parentheses represent powers of ten by which the coefficients should be multiplied.
[5] S. P. Lloyd, Phys. Rev. **83**, 716 (1951).
[6] J. J. Kraushaar and M. Goldhaber (to be published).
[7] Arfken, Klema, and McGowan, Phys. Rev. **86**, 413 (1952).

High Frequency Breakdown in Neon

A. D. MACDONALD
Department of Physics, Dalhousie University, Halifax, Nova Scotia
(Received August 15, 1952)

THE breakdown electric field in neon gas at frequencies in the 3000-Mc/sec region has been measured for a pressure range of from 0.5 mm of Hg to 300 mm of Hg. The method used is similar to that employed in the investigation of He and H_2, and the experimental equipment and procedure are described in detail elsewhere.[1–3] Spectroscopically pure neon was used. The vacuum system was such that the pressure remained at less than 10^{-6} mm of Hg for a period longer than that required for a run. The breakdown fields are shown in Figs. 1 and 2 for cylindrical cavities of heights 0.317 cm and 0.634 cm, respectively. The accuracy of the pressure measurements is one percent and of the electric field measurements five percent. On the same plots are shown theoretically derived curves. The theory is similar to that reported for helium and hydrogen[2,3] in that the electron velocity distribution function is derived as a solution of the Boltzmann Transport equation, considering diffusion to the walls to be the predominant electron loss mechanism. The changes in electron energy produced by the field and by elastic and inelastic collisions are included in the equation. The theory differs from that previously used in that the collision cross sections have different functional forms for neon, and these lead to more complicated differential equations. These equations have not yielded exact solutions over the whole pressure range. Separate approximations are made for the cases where the pressure is either higher or lower than that at which the collision frequency is equal to the radian frequency of the electric field. This is indicated by the break in the theoretical curves in the figures. As in previous theories, the derived distribution functions are combined with kinetic theory formulas and the diffusion equation to give an equation from which breakdown fields may be computed. It may be seen from the figures that these breakdown equations which use no gas discharge data other than collision cross sections predict breakdown field within the accuracy determined by these cross sections over a large range of experimental variables.

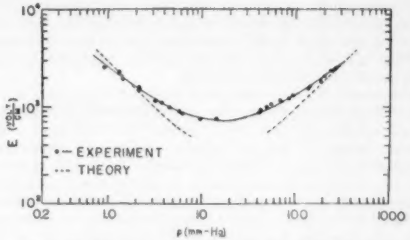

FIG. 1. Breakdown electric field in neon gas at 3000 Mc/sec. The height of the cylindrical cavity is 0.317 cm.

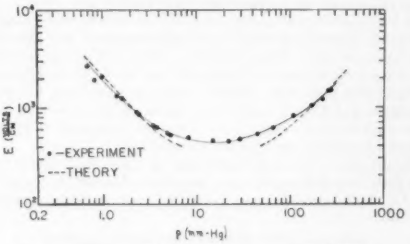

FIG. 2. Breakdown electric field in neon gas at 3000 Mc/sec. The height of the cylindrical cavity is 0.634 cm.

A detailed report, including the mathematical derivation, will be published at a later date in the Canadian Journal of Physics.

[1] M. A. Herlin and S. C. Brown, Phys. Rev. **74**, 291 (1948).
[2] A. D. MacDonald and S. C. Brown, Phys. Rev. **75**, 411 (1949).
[3] A. D. MacDonald and S. C. Brown, Phys. Rev. **76**, 1634 (1949).

Photomesons from the Deuteron

JOSEPH A. THIE*
Newman Laboratory of Nuclear Studies, Cornell University, Ithaca, New York
(Received August 27, 1952)

THE theory of Chew and Lewis[1] is applied here in the calculation of the coincidence cross section between a meson or its decay product and a recoiling nucleon of the disintegrated deuteron. It is desirable to do this in order that theory might be compared with the interesting results of Keck and Littauer[2] on π^- production and also in anticipation of possible future study of π^0's from neutrons by this method.

That P, θ_p, μ, and θ_μ, if restricted to a plane, are four independent variables follows from four-momenta conservation and velocity addition, $P\cos(\theta_p-\theta_D)=\mathbf{k}_f\cdot\mathbf{D}/D+D/2$, where $\mathbf{P}=\mathbf{k}_f$

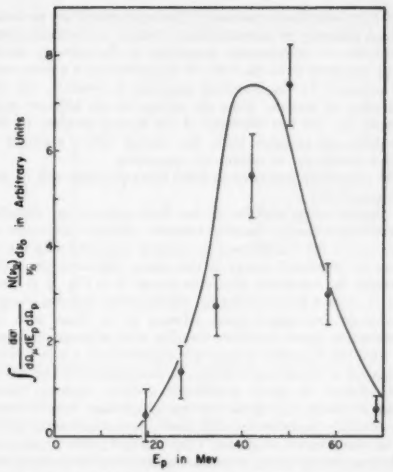

FIG. 1. Energy distribution of protons at 30° in coincidence with 56±9-Mev mesons at 90° produced by 310-Mev bremsstrahlung. The experimental points are those of Keck and Littauer. Normalization is to equal maximum ordinates.

$+\mathbf{D}/2$ is the nucleon's laboratory momentum composed of internal and center-of-mass momentum. $\mathbf{P}$ and $\mathbf{D}$ make angles θ_p and θ_D, respectively, with $\mathbf{v}$. Using these relations the easily derived $d\sigma/d\mu d\mathbf{k}_f$ is transformed to

$$\frac{d\sigma}{d\Omega_\mu dE_p d\Omega_p} = \frac{MP\mu\mu_0[\mu(\mu_0+2M)-\mu_0 v_0\cos\theta_\mu]}{32\pi^2|\mu(\mu_0+M)+\mu_0 P\cos(\theta_p+\theta_\mu)-\mu_0 v_0\cos\theta_\mu|}\mathfrak{F}, \quad (1)$$

where $E_p=P^2/2M$, and $\mathfrak{F}$ is $(K^3+L^3)[|O_f|^2+\frac{1}{3}(|E_f|^2-|O_f|^2)\times\cos^2\gamma]$ for $\pi^\pm$, and $(K_n{}^3+L_n{}^3+K_p{}^3+L_p{}^3)[\frac{1}{3}(|O_f|^2+|E_f|^2)+(|E_f|^2-|O_f|^2)\cos\delta]$ for π^0, with $\cos^2\gamma=K^2/(K^2+L^2)$ and $\cos\delta=\mathrm{Re}(\frac{1}{3}\mathbf{K}_n{}^*\cdot\mathbf{K}_p+L_n{}^*L_p)/(K_n{}^3+L_n{}^3+K_p{}^3+L_p{}^3)$.

One possible application is the nucleon's energy spectrum for sharply defined θ_p and θ_μ. For free nucleons these two variables determine a $\bar{\mu}_0$ and $\bar{E}_p$. In coincidence with the deuteron's mesons in a range $\Delta\mu_0$ at $\bar{\mu}_0$ one expects nucleons with energies distributed about a peak at $\bar{E}_p$. Multiplication of the above by $d\nu_0 N(\nu_0)/\nu_0$ and integration over $\nu_0(\mu_0)$ gives the yield at a particular E_p. The dependence of K^3+L^3 on ν_0 can be had from free nucleon excitation functions. The dominant behavior of the above is given by $|E_f|^2$ and $|O_f|^2$, which are, when one uses plane waves to describe the final two-nucleon system,

$$\frac{\alpha(\beta^2-\alpha^2)^2}{2\pi^2(1-\alpha\rho_1)}\left\{\frac{1}{(P^2+\alpha^2)(P^2+\beta^2)} \pm \frac{1}{(P^2+\alpha^2-2\mathbf{k}_f\cdot\mathbf{D})(P^2+\beta^2-2\mathbf{k}_f\cdot\mathbf{D})}\right\}^2, \quad (2)$$

the upper and lower signs for $|E_f|^2$ and $|O_f|^2$, respectively. These peak at $\bar{E}_p$, $\bar{\mu}_0$. For the particular case of Fig. 1 the plane wave approximation is quite good, but results are insensitive to γ. Correction for the finite experimental $\Delta\theta_p$ and $\Delta\theta_\mu$ widens the theoretical curve by several Mev at half-maximum, but does not affect the location of the maximum. Thus both the half-width and the location of the maximum are at variance with experiment. This is not understood, although a number of suggestions have been investigated. The theory already includes a 3-Mev shift of the peak to higher energies due to the deuteron's binding energy.

The effect on photomeson production of a model suggested by various authors, particularly Wilson,[3] has also been investigated. If mesons are produced while the nucleons are within a meson Compton wavelength of each other, which is about $\frac{1}{4}$ of the time, then reabsorption and photodisintegration are assumed to result. In this model one then expects photomeson production cross sections roughly 20 percent below the Chew and Lewis value. The above energy widths are likewise different in this model. At present statistics on the deuterium to hydrogen ratios are not good enough to either establish or refute this model.

The author is indebted to Professor H. A. Bethe for his encouragement and to Mr. M. E. Miles for doing the numerical calculations.

* AEC Postdoctoral Fellow.

[1] G. F. Chew and H. W. Lewis, Phys. Rev. **84**, 779 (1951). The notation of these authors is used throughout ($c=\hbar=$meson mass$=1$).
[2] J. Keck and R. Littauer, Phys. Rev. **88**, 139 (1952).
[3] R. R. Wilson, Phys. Rev. **86**, 125 (1952).

Domain Properties in $BaTiO_3$

WALTER J. MERZ
Bell Telephone Laboratories, Murray Hill, New Jersey
(Received August 21, 1952)

WE have investigated the arrangements and movements of the ferroelectric domains with an electric field in very good single crystals of $BaTiO_3$. The behavior has been studied both in so-called *a* plates, where the polar axis lies in the plane of the plate, and in *c* plates, where it is perpendicular.

Published descriptions of domains in $BaTiO_3$ have heretofore reported only so-called 90° walls, i.e., those between domains having their polar axes perpendicular to each other. It has usually been assumed that domains polarized antiparallel must also be present, so that each region heretofore called a domain is made up of many smaller antiparallel regions which are the true domains. These 180° walls have now been observed and studied in our work.

Domain boundaries in $BaTiO_3$ crystals are observable, owing to strain birefringence and changes in the refractive index. The strains are larger around a 90° wall than around a 180° wall which makes the 90° wall much sharper and more pronounced. However, the 180° walls can also be seen more easily if one applies an electric dc field perpendicular to the antiparallel domains. The field turns the polar axis of the antiparallel domains a little in opposite directions which increases the internal strain and also shifts the extinction position by a small angle in opposite directions. The antiparallel domains are shown in Fig. 1 by the light and dark lines, for example, at *A*.

Another evidence of the 180° walls is shown in crystals where the antiparallel domains cross 90° walls, which are in this case

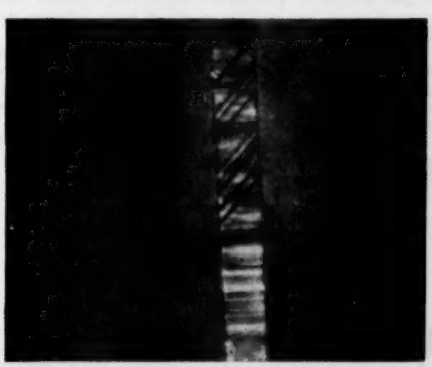

FIG. 1. Edge of a *c* crystal. Total width of crystal $=4\times10^{-4}$ cm.

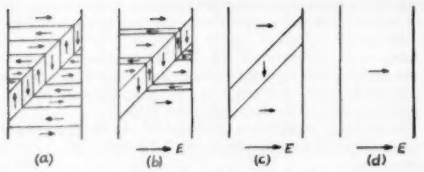

FIG. 2. Schematic arrangements of domains as in Fig. 1 when a field is applied. Observe the head-to-tail arrangement.

at about 45° to the a and c directions. We then can see sharp zigzag lines as in B of Fig. 1. This is shown schematically in Fig. 2(a). If a field is applied in the $+c$ direction, one can move the whole zig-zag line until everything is polarized parallel to the $+c$ direction except the 45° band itself as in Fig. 2(c). At higher field strengths this band also disappears [Fig. 2(d)].

The average width of the antiparallel domains as measured by microscope is from 10^{-5} cm. to about 10^{-3} cm. Whether the width depends on the length of the domain cannot be decided yet.

The observation of antiparallel domains by looking at the edge of a c crystal when an electric field is applied in the c direction was made simultaneously with the observation of the hysteresis loop. Going through the cycle very slowly (using a dc amplifier), we could compare every step of the hysteresis loop with the corresponding domain movements. The loop obtained for the best crystals is shown in Fig. 3.

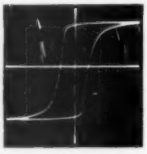

FIG. 3. Hysteresis loop of $BaTiO_3$.

In contrast to the behavior of domain walls in ferromagnetics, it seems to be energetically easier to create new domains than to make an existing properly polarized domain grow larger. We observe hundreds of small new domains which appear very suddenly when a field is applied, thus causing the "low field corner" of the hysteresis loop to be sharp. When more than about half of the domains point in the direction of the applied field, a further increase in the field causes the remaining oppositely orientated domains to change orientation. This wall motion process goes more slowly and requires higher field strengths. This difference can be seen optically as well as in the fact that the "high field corner" of the loop is round.

More detailed studies of the number of domains, their velocities and relaxation times are being carried out by applying very short square electrical pulses. We are especially interested in the dependence of the domain motions on length and amplitude of the applied pulses and the changes with temperature.

I would like to thank Dr. P. W. Anderson and Dr. J. K. Galt for many helpful discussions and Mr. J. Remeika for the preparation of the very good crystals.

Scintillators and Energy Transfer Processes

C. REID
Department of Chemistry, University of British Columbia, Vancouver, Canada

(Received September 3, 1952)

KALLMANN and Furst[1-3] have investigated the relative efficiencies as scintillation counters for γ-rays and α-particles of various organic molecules in solution. The phenomena occurring in such systems are briefly summarized in Fig. 1. For an efficient scintillation process (e) the requirements are obviously: (a) high efficiency of solvent-solvent transfer of electronic energy (i) relative to radiationless quenching in the solvent, so that energy transport from the body of the solvent to a solvent molecule adjacent to the dissolved molecule is possible; (b) high probability of transfer from the solvent to an adjacent solute molecule (t), but low efficiency of the reverse process; (c) high probability of emission from the excited solute molecule (e) relative to self- (c), or solvent (s), quenching.

The conditions necessary to fulfill these processes will be dealt with separately.

1. Solvent-solvent transfer. It has been pointed out elsewhere[4] that efficient energy transfer between identical molecules will occur only if the transfer process is rapid compared with the rate of loss of vibrational energy in the excited electronic state, since otherwise the remaining electronic energy (b in Fig. 2) is insufficient to excite a second molecule, which process requires energy a. Accordingly, we expect good solvents to be those with high polarizability (good electronic coupling with adjacent molecules) but with few branches or long side chains which would facilitate dissipation of vibrational energy. An examination of the solvents most efficient in liquid scintillator systems (xylene, toluene, aniline, benzene, etc.) show that they are, in fact, usually polarizible aromatic molecules of this kind. Any substituents present are of the electron donating kind which further increase the π-electron density of the aromatic ring and thus the polarizibility.

2. Solvent-solute transfer. High efficiency at the solvent-solute transfer step is dependent on good electronic coupling between the two kinds of molecules, but retransfer back to the solvent must be prevented by rapid loss of excited state vibrational energy by the solute. This can be best attained if the molecule is of a "flapping" kind with low vibrational frequencies. Thus we find the most efficient solution scintillators often among this kind of molecule (terphenyl, diphenyl hexatriene, phenyl-α-naphthylamine, etc.). For such molecules both retransfer to the solvent and "self-transfer" (st) to other dissolved molecules is minimized.

3. Emission of radiation. The last-mentioned process, self-transfer between solute molecules, results in a decreased emission probability per unit time and consequently increases the chance of energy loss by competing radiationless processes. Condition (3), like (2), is therefore best met by solutes for which the loss of upper state vibrational energy is rapid.

It has already been shown experimentally[4] that some aromatic substances show self-transfer in solid solutions in inert solvents at low temperature, whereas others do not. Clearly, molecules

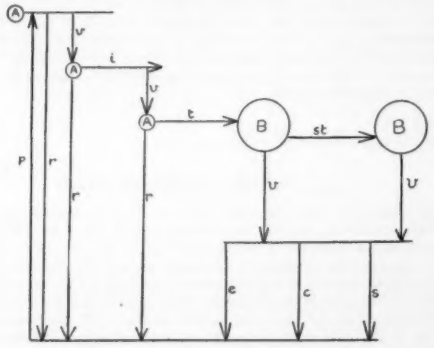

FIG. 1. Steps involved in liquid scintillation. A = solvent molecule energy levels; B = solute molecule energy levels; p = primary excitation of solvent by γ-ray; r = nonradiative solvent quenching; v = loss of vibrational energy (this step may include radiationless crossover to lower electronic levels of the same molecule); t = solvent-solute transfer process; st = self-transfer in solute; e = light emission; c = self-quenching; s = solvent quenching.

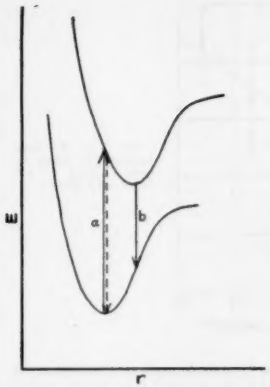

FIG. 2. Typical potential curve relationship. a = energy required to excite molecule; b = energy available after loss of upper state vibrational energy; dotted line = energy available for transfer before vibrational energy is lost.

for which such self-transfer occurs should be in the class of inefficient scintillators, whereas those showing no self-transfer should be efficient scintillators. This is in general the case. Efficient self-transferring substances such as anthracene are relatively inefficient as solution scintillators when compared with, say, terphenyl or diphenyl hexatriene, which show no sign of self-transfer phenomena in low temperature glasses. Whereas this relationship holds for most of the substances examined, there are a few cases for which its validity is doubtful. For example, fluoranthene and pyrene do not show self-transfer but are only moderately good scintillators. Such apparent exceptions are probably explained by the comparatively low quantum yields of fluorescence shown by these substances in the pure state as a result of radiationless internal conversion to the ground state within the molecule. This process was not considered in the above arguments.

[1] H. Kallmann and M. Furst, Phys. Rev. **79**, 857 (1950).
[2] H. Kallmann and M. Furst, Phys. Rev. **81**, 853 (1951).
[3] H. Kallmann and M. Furst, Phys. Rev. **85**, 816 (1952).
[4] M. M. Moodie and C. Reid, J. Chem. Phys. **20**, 1510 (1952).

The Reaction $Li^7(\alpha,\gamma)B^{11}$ and States of B^{11}

G. A. JONES AND D. H. WILKINSON
Cavendish Laboratory, Cambridge, England
(Received September 2, 1952)

WE have used NaI(Tl) crystals to study gamma-ray transitions from states in B^{11} at 8.93, 9.19, and 9.28 Mev formed by bombarding Li^7 with alpha-particles.[1] Figure 1 shows the gamma-rays which we have detected, together with the previously known[2] locations of the energy levels.

Table I lists the labeled gamma-rays, the probability of the mode of de-excitation of which they form a part (normalized to unity for each initial state), their energy as expected from the known[2] levels, and their energy as measured in the present investigation.

TABLE I. Gamma-rays from B^{11}.

Gamma-ray	Probability	Expected energy (Mev)	Measured energy (Mev)
γ_1	0.89	8.926 ±0.012	8.91 ±0.03
γ_2	0.07	3.892 ±0.018	3.90 ±0.12
γ_3	0.07	5.034 ±0.014	5.05 ±0.08
γ_4	0.04	6.788 ±0.018	6.80 ±0.10
γ_5	0.97	4.731 ±0.018	4.728 ±0.023
γ_6	0.97	4.459 ±0.014	4.470 ±0.023
γ_7	0.03	6.808 ±0.013	6.80 ±0.03
γ_8	0.10	9.276 ±0.012	9.27 ±0.03
γ_9	0.83	4.817 ±0.018	4.806 ±0.013
γ_{10}	0.83	4.459 ±0.014	4.464 ±0.013
γ_{11}	0.07	2.468 ±0.018	2.53 ±0.06
γ_{12}	0.07	6.808 ±0.013	6.83 ±0.03

The status of γ_4 is a little uncertain; it is possible that the doublet around 6.8 Mev is involved rather than the 2.14-Mev level. The lifetime of the 4.46-Mev level is less than a few times 10^{-14} sec—it displays a Doppler shift.[3] The radiative widths of the 8.93-, 9.19-, and 9.28-Mev levels are, very roughly, 0.1, 1, and 10 ev, respectively.

We have also carried out the following angular distribution and correlation measurements:[4] $\alpha-\gamma_1$, $\alpha-\gamma_5$, $\alpha-\gamma_6$, $\gamma_5-\gamma_6$ (in two planes), $\alpha-\gamma_7$, $\alpha-\gamma_8$, $\alpha-\gamma_9$, $\alpha-\gamma_{10}$, $\gamma_9-\gamma_{10}$ (in two planes), $\alpha-\gamma_{12}$; coincidences between γ_{11} and γ_{12} have been detected. If we take the ground states of both Li^7 and B^{11} to be $3/2-$ we are able to assign, with fair certainty, spins and parities to the levels in B^{11} at 4.46, 6.81, 8.93, 9.19, and 9.28 Mev; under reasonable assumptions these assignments lead to spin assignments for the levels at 2.14 and 5.03 Mev. These results are shown in Fig. 1 and in Table II.

TABLE II. Experimental characteristics of levels of B^{11} and shell model assignments.

Level	0	2.14	4.46	5.03	6.76	6.81	7.30	8.57	8.93	9.19	9.28
Expt.	$3/2-$	$\frac{1}{2}\pm$	$5/2+$	$\frac{1}{2}\pm$		$3/2+$			$3/2+$	$7/2+$	$5/2-$
Shell	$1p_{3/2}$	$1p_{\frac{1}{2}}$	$1d_{5/2}$	$2s_{\frac{1}{2}}$	$M(3/2-)$	$1d_{3/2}$	$1f_{7/2}$	$2p_{3/2}$	M	M	$1f_{5/2}$

We have been tempted to apply the shell model to B^{11} even at high excitation; the resulting identifications appear in Fig. 1 and in Table II where M stands for a state of multiple excitation; the first, at 6.76 Mev, is probably $3/2-$, i.e., $(1p_{\frac{1}{2}})^2(1p_{\frac{3}{2}})^{-1}$.

In defense of this rather speculative shell scheme, it must be said that it agrees with all our experimental findings and contradicts none; that it may not be completely sophistical is further suggested by three remarks:

(a) All transitions from the 9.28-Mev level, assigned by the scheme to a single-particle state, agree with the predictions of

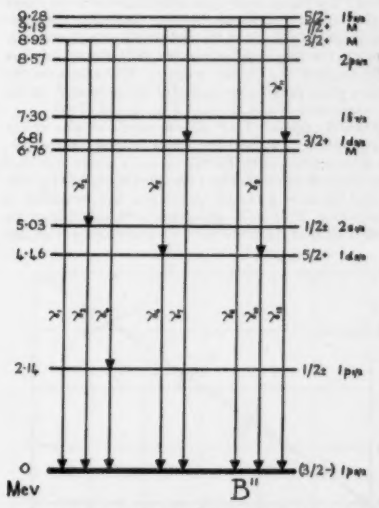

FIG. 1. Decay scheme of 8.93-, 9.19-, and 9.28-Mev levels of B^{11}. Arrows indicate the observed modes of de-excitation; the labeled gamma-rays are those whose energy has been measured. To the right of the levels are their experimental assignments with their description by the shell model. (M stands for a state of multiple excitation.)

the single-particle model;[5] those from the 8.93- and 9.19-Mev levels, supposed by the scheme to be of multiple excitation, show preferred $E2$ transitions[6] to be expected from such states of more general excitation.

(b) The splittings of the supposed p, d, and f doublets are 2.1, 2.4, and 2.0 Mev, respectively, all of the correct order.

(c) The separation of the supposed $1d_{5/2}-2s_{\frac{1}{2}}$ levels is 0.57 Mev, in good accord with the nearest known examples of this separation in O^{17} and F^{17} of 0.55 and 0.87 Mev, respectively.[7]

We would like to point out the considerable interest that attaches to the parity assignments which would be available from a study of $B^{10}(d,p)B^{11}$ stripping.

A full account of this work is in preparation.

[1] Bennett, Roys, and Toppell, Phys. Rev. **82**, 20 (1951).
[2] From the $B^{10}(d,p)B^{11}$ reaction by Van Patter, Buechner, and Sperduto, Phys. Rev. **82**, 248 (1951).
[3] G. A. Jones and D. H. Wilkinson, Phil. Mag. (to be published).
[4] $\alpha-\gamma_a$ means the angular distribution of γ_a relative to the alpha-particle beam; $\gamma_a-\gamma_m$ means the angular correlation between γ_a and γ_m.
[5] V. F. Weisskopf, Phys. Rev. **83**, 1073 (1951).
[6] M. Goldhaber and A. W. Sunyar, Phys. Rev. **83**, 906 (1951).
[7] R. A. Laubenstein and M. J. W. Laubenstein, Phys. Rev. **84**, 18 (1951).

The Quenching of *Ortho*-Positronium Decay by a Magnetic Field*

JOHN WHEATLEY† AND DAVID HALLIDAY
University of Pittsburgh, Pittsburgh, Pennsylvania
(Received September 2, 1952)

WE have measured the quenching of three-quantum annihilation from positronium by a magnetic field.[1] This effect has been detected by Deutsch and Dulit[2] and by Pond and Dicke[3] using different methods. Positronium was formed in SF_6 gas in a chamber placed between the poles of a magnet. The positron source was ~0.01 mC Na^{22} on a Zapon film. The decay of the $^3S_1$ positronium was detected by three NaI scintillation counters placed with their axes 120° apart in the plane perpendicular to the magnetic field.[4] The background triple coincidence rate was found by letting nitric oxide into the gas chamber. Generally, the background was about ten percent of the total triple coincidence rate. The magnet was specially designed and the 5819 photomultipliers magnetically shielded to eliminate magnetic field effects on the counters. At a given pressure we measured the ratio $n(H)$ of the true triple coincidence rate at the field H to that at $H=0$.

If one plots $n(H)$, against $(1-n)/H^2$, one should obtain—at low enough gas densities—a straight line whose intercept is the fraction of the rate contributed by the $^3S_1$, $m_J=\pm1$ states. A typical experimental curve is shown in Fig. 1 for a density of 0.052 g/cm³. It is clear that the $m_J=\pm1$ states supply less than two-thirds of the zero field rate. This is in agreement with calculations by Drisko[5] who finds that the probability for annihilation from any particular m_J substate of the $^3S_1$ state depends on the angle of the plane of the annihilation with the external field. In the special case corresponding to our geometry, Drisko finds that the $m_J=0$ state contributes one-half of the zero field rate. All our data are in agreement with this result.

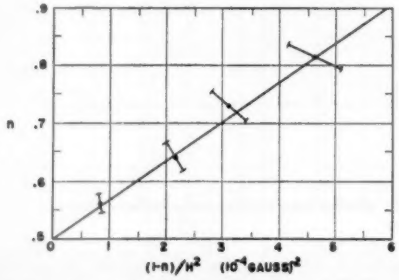

FIG. 1. A quenching plot for an SF_6 density of 0.052 g/cm³.

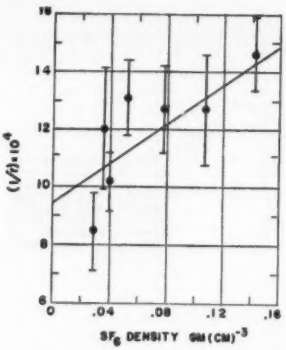

FIG. 2. A least squares line whose intercept gives r_0 and whose slope gives σ.

If collisions are ignored, the theoretical expression for $n(H)$ for our geometry is

$$n(H)=(2+a^2r_0)/(2+2a^2r_0),$$

where $r_0=\tau_3/\tau_1=1120$ as given theoretically by Ore and Powell,[6] and $a=2\mu_0H/\Delta E$ with ΔE the ground state splitting as determined recently by Deutsch and Brown.[7] If one includes the possibility that collisions with gas atoms can cause transitions from $J=1$ to $J=0$ (probability per unit time $\lambda=Nv\sigma$) and transitions in which m_J changes with $\Delta J=0$ (probability per unit time $\lambda'=Nv\sigma'$), the situation is more complicated.[8] Transitions of the latter type cause $n(H)$ to approach a high field limit of less than $\frac{1}{3}$.

At high fields the quenching is relatively more sensitive to λ' than to λ. We found by measuring $n(H)$ as a function of gas density at $H=7100$ gauss that $\sigma'<\frac{1}{4}\sigma$. This conclusion depends on making use of a value of σ reported by Siegel and De Benedetti[9] for SF_6 ($\sigma\cong10^{-21}$ cm²). Using this approximate limit for σ', we find that for $H<3000$ gauss and for gas densities less than 0.15 g/cm³ the effect of the λ' transitions on the quenching is negligible and that, in fact, the quenching is given by Eq. (1) with r_0 replaced by $r=r_0/(1+r_3\lambda)$.

In order to obtain an experimental value for r_0 and to check σ, we make the definite assumption that λ' transitions are negligible. For each density we then determine the best value for r, using only data with $H<3000$ gauss. Consequently, the plot shown in Fig. 2 should be linear. The probable errors are large because $1/r$ is relatively sensitive to n; a one percent change in n produces at least a six percent change in $1/r$. The intercept and slope of the least squares line fitted to the data give the values of r_0 and σ. Our procedure requires only that Siegel and De Benedetti's value of σ be correct as to order to magnitude, justifying neglect of the λ' transitions; in this sense only is our value of σ independent. In computing σ from λ, we have assumed the dominance of single collisions. We find $r_0=1050\pm140$ compared with Ore and Powell's theoretical result of $r_0=1120$, and we find $\sigma=8\times10^{-22}$ cm² compared with $\sigma=10^{-21}$ cm² obtained by Siegel and De Benedetti.[9]
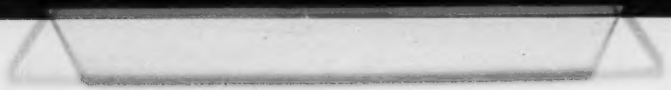
* Work done in Sarah Mellon Scaife Radiation Laboratory. Support of the ONR is acknowledged.
† Now at the University of Illinois, Urbana, Illinois.
[1] J. Wheatley and D. Halliday, Phys. Rev. **87**, 235 (1952).
[2] M. Deutsch and E. Dulit, Phys. Rev. **84**, 601 (1951).
[3] T. A. Pond and R. H. Dicke, Phys. Rev. **85**, 489 (1952).
[4] S. De Benedetti and R. Siegel, Phys. Rev. **85**, 371 (1952).
[5] R. Drisko, private communication.
[6] A. Ore and J. L. Powell, Phys. Rev. **75**, 1696 (1949).
[7] M. Deutsch and S. C. Brown, Phys. Rev. **85**, 1047 (1952).
[8] O. Halpern, Phys. Rev. **88**, 232 (1952).
[9] R. Siegel and S. De Benedetti, Phys. Rev. **87**, 235 (1952).